**NATIONAL TECHNICAL UNIVERSITY OF ATHENS**
**SCHOOL OF CIVIL ENGINEERING**
**GEOTECHNICAL DEPARTMENT**

**ΕΘΝΙΚΟ ΜΕΤΣΟΒΙΟ ΠΟΛΥΤΕΧΝΕΙΟ**
**ΣΧΟΛΗ ΠΟΛΙΤΙΚΩΝ ΜΗΧΑΝΙΚΩΝ**
**ΤΟΜΕΑΣ ΓΕΩΤΕΧΝΙΚΗΣ**

# CONSTITUTIVE MODELLING OF THE MECHANICAL BEHAVIOUR OF UNSATURATED SOILS

# ΚΑΤΑΣΤΑΤΙΚΗ ΠΡΟΣΟΜΟΙΩΣΗ ΤΗΣ ΜΗΧΑΝΙΚΗΣ ΣΥΜΠΕΡΙΦΟΡΑΣ ΜΗ ΚΟΡΕΣΜΕΝΩΝ ΕΔΑΦΩΝ

**DOCTORAL THESIS**
of
**PANAGIOTIS Chr. SITARENIOS**
*Diploma of Civil Engineering, University of Patras*
*M.Sc. National Technical University of Athens*

**ΔΙΔΑΚΤΟΡΙΚΗ ΔΙΑΤΡΙΒΗ**
του
**ΠΑΝΑΓΙΩΤΗ Χρ. ΣΙΤΑΡΕΝΙΟΥ**
*Διπλ. Πολιτικός Μηχανικός Πανεπιστημίου Πατρών*
*Μ.Δ.Ε. Εθνικό Μετσόβιο Πολυτεχνείο*

Supervisor:
**Michael J. Kavvadas**
*Associate Professor, NTUA*

Επιβλέπων:
**Μιχαήλ Ι. Καββαδάς**
*Αναπληρωτής Καθηγητής Ε.Μ.Π*

**Athens, July 2016**

**Αθήνα, Ιούλιος 2016**

**ΕΘΝΙΚΟ ΜΕΤΣΟΒΙΟ ΠΟΛΥΤΕΧΝΕΙΟ**
**ΣΧΟΛΗ ΠΟΛΙΤΙΚΩΝ ΜΗΧΑΝΙΚΩΝ**
**ΤΟΜΕΑΣ ΓΕΩΤΕΧΝΙΚΗΣ**

# ΚΑΤΑΣΤΑΤΙΚΗ ΠΡΟΣΟΜΟΙΩΣΗ ΤΗΣ ΜΗΧΑΝΙΚΗΣ ΣΥΜΠΕΡΙΦΟΡΑΣ ΜΗ ΚΟΡΕΣΜΕΝΩΝ ΕΔΑΦΩΝ

**ΔΙΔΑΚΤΟΡΙΚΗ ΔΙΑΤΡΙΒΗ**

**ΠΑΝΑΓΙΩΤΗ Χρ. ΣΙΤΑΡΕΝΙΟΥ**

*Διπλ. Πολιτικός Μηχανικός, Πανεπιστημίου Πατρών*
*Μ.Δ.Ε. Εθνικό Μετσόβιο Πολυτεχνείο*

Η διατριβή υποβάλλεται στη Σχολή Πολιτικών Μηχανικών του Εθνικού Μετσόβιου Πολυτεχνείου προς εκπλήρωση των προϋποθέσεων του τίτλου του Διδάκτορος Μηχανικού

**ΤΡΙΜΕΛΗΣ ΣΥΜΒΟΥΛΕΥΤΙΚΗ ΕΠΙΤΡΟΠΗ:**

1. Μ. ΚΑΒΒΑΔΑΣ, Αν. Καθηγητής ΕΜΠ (Επιβλέπων)
2. Γ. ΜΠΟΥΚΟΒΑΛΑΣ, Καθηγητής ΕΜΠ
3. Β. ΓΕΩΡΓΙΑΝΝΟΥ, Αν. Καθηγήτρια ΕΜΠ

**ΕΠΤΑΜΕΛΗΣ ΕΞΕΤΑΣΤΙΚΗ ΕΠΙΤΡΟΠΗ:**

1. Μ. ΚΑΒΒΑΔΑΣ, Αν. Καθηγητής ΕΜΠ (Επιβλέπων)
2. Γ. ΜΠΟΥΚΟΒΑΛΑΣ, Καθηγητής ΕΜΠ
3. Β. ΓΕΩΡΓΙΑΝΝΟΥ, Αν. Καθηγήτρια ΕΜΠ
4. Γ. ΓΚΑΖΕΤΑΣ, Καθηγητής ΕΜΠ
5. A. GENS, Καθηγητής UPC (Barchelona Tech)
6. Ν. ΓΕΡΟΛΥΜΟΣ, Επικ. Καθηγητής ΕΜΠ
7. Α. ΠΑΠΑΔΗΜΗΤΡΙΟΥ, Επικ. Καθηγητής ΕΜΠ

Αθήνα, Ιούλιος 2016

**NATIONAL TECHNICAL UNIVERSITY OF ATHENS**
**SCHOOL OF CIVIL ENGINEERING**
**GEOTECHNICAL DEPARTMENT**

# CONSTITUTIVE MODELLING OF THE MECHANICAL BEHAVIOUR OF UNSATURATED SOILS

**DOCTORAL THESIS**

**PANAGIOTIS Chr. SITARENIOS**

*Dipl. Civil Engineer, University of Patras*
*M.Sc. National Technical University of Athens*

The thesis is submitted to the School of Civil Engineering of the National Technical University of Athens in fulfilment of the requirements for the Degree of Doctor of Philosophy

**ADVISORY COMMITTEE:**

1. M. KAVVADAS, Assoc. Professor NTUA (Supervisor)

2. G. BOUCKOVALAS, Professor NTUA

3. V. GEORGIANNOU, Assoc. Professor NTUA

**EXAMINATION COMMITTEE:**

1. M. KAVVADAS, Assoc. Professor NTUA (Supervisor)

2. G. BOUCKOVALAS, Professor NTUA

3. V. GEORGIANNOU, Assoc. Professor NTUA

4. G. GAZETAS, Professor NTUA

5. A. GENS, Professor UPC (Barchelona Tech)

6. N. GEROLYMOS, Asst. Professor NTUA

7. A. PAPADIMITRIOU, Asst. Professor NTUA

Athens, July 2016

This document was created using LaTeX.

# Thesis Structure \ Δομή Τεύχους Διατριβής

# Αντί Προλόγου

Έφτασε η ώρα για να γραφτεί με διαφορά το πιο δύσκολο κομμάτι αυτού του τεύχους: Οι ευχαριστίες... Μα πως είναι δυνατό να χωρέσουν σε δύο-τρεις σελίδες τόσοι άνθρωποι, τόσες εμπειρίες, τόσα γεγονότα; Πως γίνεται να μην ξεχάσεις κάποιον; Ίσως αν τα πάρει κάνεις χρονολογικά να είναι μία καλή λύση. Θα σας πω λοιπόν μία σύντομη ιστορία!

Το τεύχος που κρατάτε στα χέρια σας συμβολίζει ένα ορόσημο στην πορεία μου ως Πολιτικού Μηχανικού και ειδικότερα ως Γεωτεχνικού Μηχανικού, ή έτσι τουλάχιστον το αισθάνομαι. Είναι το αποκορύφωμα μίας ερευνητικής προσπάθειας που ξεκίνησε, θεωρητικά, το Σεπτέμβριο του 2007 αλλά πρακτικά ξεδιπλώθηκε, σε πλήρη έκταση και ένταση, από τον Σεπτέμβριο του 2011. Στην πραγματικότητα όμως θα έλεγα ότι οι πρώτες βάσεις μπήκαν πολύ παλιότερα κάπου το 2001, όταν για πρώτη φόρα ήρθα σε επαφή με το αντικείμενο της Εδαφομηχανικής σε ένα αμφιθέατρο του Πανεπιστημίου Πατρών. Ήταν οι εκεί δάσκαλοί μου, Καθηγητές κκ. Δημήτρης Ατματζίδης, Γιώργος Αθανασόπουλος και ο αείμνηστος Λέκτορας Δημήτρης Χρυσικός, οι πρώτοι άνθρωποι που μου μετέδωσαν και μου εμφύσησαν την αγάπη στο αντικείμενο της Γεωτεχνικής Μηχανικής. Από αυτούς μπήκαν οι βάσεις και τους οφείλω το πρώτο χρονικά ευχαριστώ!

Με την ολοκλήρωση των προπτυχιακών μου σπουδών, ήρθε το μεταπτυχιακό των υπογείων έργων στο Εθνικό Μετσόβιο Πολυτεχνείο. Εκεί έγινε και η πρώτη γνωριμία με τον επιβλέποντά μου, Αν. Καθηγητή κ. Μιχάλη Καββαδά. Η εμπιστοσύνη με την οποία με περιέβαλλε, από την πρώτη στιγμή, είναι σχεδόν συγκλονιστική. Συνεργαζόμαστε (δική του η επιλογή της λέξης...) πλέον επί 12 συναπτά χρόνια στον Τομέα Γεωτεχνικής του Ε.Μ.Π στην έρευνα, διδασκαλία, επίβλεψη διπλωματικών και μεταπτυχιακών εργασιών. Οι γνώσεις και η εμπειρία που έχω αποκομίσει από την συνεργασία αυτή είναι απλά ανεκτίμητες. Η παράθεσή τους σε ένα φύλλο χαρτί το μόνο που θα επιτύγχανε είναι να τις αδικήσει και για αυτό θα αρκεστώ στο... Κύριε Καββαδά... ΕΥΧΑΡΙΣΤΩ ΠΟΛΥ!

Λένε ότι το διδακτορικό είναι μία κατά βάση μοναχική ακαδημαϊκή και ερευνητική διαδρομή. Παρόλα αυτά εγώ είχα την τύχη να έχω πολλούς αρωγούς με τους οποίους να μοιράζομαι τους προβληματισμούς μου, να περιγράφω τις ερευνητικές μου ανασφάλειες, να με βοηθούν να βρίσκω λύσεις. Ξεχωριστή θέση μεταξύ τους έχουν δύο άνθρωποι. Οι διδάκτορες Μιχάλης Μπαρδάνης και Γιώργος Μπελόκας. Μου προσέφεραν απλόχερα την βοήθειά τους και για αυτό τους ευχαριστώ πολύ! Ένα μεγάλο ευχαριστώ οφείλω αναμφισβήτητα και στους διδάκτορες κκ. Πέτρο Φορτσάκη και Γιώργο Προυντζόπουλο, καθώς ήταν αυτοί οι οποίοι με μύησαν στα μυστικά του Abaqus αλλά και του Τομέα (βλ. παρακάτω). Ένα πολύ μεγάλο ευχαριστώ οφείλω να εκφράσω και στον πιο κοντινό μου άνθρωπο στο πλαίσιο της ερευνητικής μας ομάδας, τον Κωσταντίνο Τζιβάκο, πολύτιμο φίλο, συνάδελφο και συνεργάτη σε κάθε ακαδημαϊκή (και μη) δραστηριότητα εντός και εκτός ομάδας. Σημαντικός επιστημονικός συνοδοιπόρος μου αυτά τα χρόνια ήταν και ο Δρ. Αλέξανδρος Καλός. Μαζί περάσαμε ατελείωτες ώρες στην μελέτη και εμβάθυνση στο αντικείμενο της πλαστικότητας, ήταν η ασφάλειά μου σε κάθε μαθηματικό υπολογισμό και για αυτό τον ευχαριστώ ιδιαίτερα. Από ένα ξεχωριστό ευχαριστώ οφείλω και στους νεότερους υποψηφίους διδάκτορές μας, Δημήτρη Λίτσα και Φίλιππο Χόρτη σημαντικούς συνεργάτες τα τελευταία χρόνια στο πλαίσιο της έρευνας της ομάδας μας στο αντικείμενο των σηράγγων.

Η χρηματοδότηση της ερευνάς μου δεν ήταν εξασφαλισμένη από την αρχή. Αυτό με έσπρωξε στο να αναζητήσω παράλληλα την τύχη μου στην αγορά εργασίας. Είχα την τύχη, την χαρά και την τιμή να βρεθώ σε ένα από τα μεγαλύτερα γραφεία τεχνικών μελετών στην Ελλάδα, τον Όμιλο Τεχνικών Μελετών Α.Τ.Ε. Εκεί μου δόθηκε η ευκαιρία να εργασθώ και να εμβαθύνω πάνω στο αντικείμενο της Γεωτεχνικής Μηχανικής και της Σηραγγοποιείας σε σημαντικά έργα ανά την Ελλάδα. Εκτός από πολύ μεγάλο σχολείο, ο «Όμιλος» υπήρξε για μένα και ένα ευχάριστο και ασφαλές περιβάλλον εργασίας. Η συνεισφορά και η βοήθεια όλων των συναδέλφων ήταν καθοριστική. Πάνω από όλους όμως, ξεχωριστή θέση κατέχουν ο κ. Παναγιώτης Βέττας και η κα. Σταυρούλα Σχινά. Τους οφείλω ένα πολύ μεγάλο ευχαριστώ!

Διέκοψα την συνεργασία μου με τον «Όμιλο» το 2011, όταν συνειδητοποίησα ότι η ολοκλήρωση ενός διδακτορικού και η επαγγελματική ενασχόληση με το αντικείμενο δεν είναι εύκολο να συμβαδίζουν για μεγάλο χρονικό διάστημα. Αυτό είναι κάτι το οποίο θα ήθελα να μοιραστώ και ως συμβουλή – στον βαθμό που μου επιτρέπεται - σε νέους συναδέλφους που σκέφτονται να κάνουν ένα τέτοιο διπλό βήμα στη ζωή τους.

Θα την συνόψιζα απλά στο: «γίνεται... αλλά δεν συνίσταται».

Η αφοσίωση πλέον στην εκπόνηση της Διατριβής, μου έδωσε την ευκαιρία για την πραγματοποίηση ενός πολύ σημαντικού βήματος (σχεδόν ονείρου για όποιον ασχολείται με την μηχανική των μη κορεσμένων εδαφών). Την μετάβαση μου, το 2012, στο Universitat Polytechnica de Catalunya (UPC) στην Βαρκελώνη. Η μετενσάρκωση αυτού του ονείρου σε πραγματικότητα θα τολμούσα να πω ότι οφείλεται αποκλειστικά στον άνθρωπο σύμβολο του Τομέα Γεωτεχνικής του ΕΜΠ, στον αγαπητό μας δάσκαλο και φίλο, Ομότιμο Καθηγητή κ. Ανδρέα Αναγνωστόπουλο. Από την συνεχή και ακόρεστη (!) προσπάθειά του να βοηθήσει τον καθέναν στον Τομέα, με όποιο τρόπο και αν μπορεί, δεν «γλίτωσα» (ευτυχώς!) ούτε εγώ. Ήταν αυτός που μου έλεγε όπου με έβλεπε και όπου με απαντούσε... «τι θα γίνει επιστήμονα;... θα πας στην Βαρκελώνη;... να γράψω στον Gens;»... και φυσικά το κατάφερε. Δάσκαλε σε ευχαριστώ!

Η περίοδος της Βαρκελώνης υπήρξε καταλυτική. Είχα την τύχη να βρεθώ στην πηγή της γνώσης και της έρευνας, στο «Βατικανό» της Μηχανικής των μη κορεσμένων εδαφών (δεν είναι δικός μου προσδιορισμός), αποκομίζοντας συμπυκνωμένη γνώση και εμπειρία. Για την περίοδο της Βαρκελώνης οφείλω ένα ξεχωριστό ευχαριστώ σε δύο ανθρώπους. Στον υπεύθυνο Καθηγητή μου, Καθηγητή κ. Antonio Gens και στην φίλη μου και πολύτιμη αρωγό μου, μεταδιδακτορική ερευνήτρια τότε, Επίκουρη Καθηγήτρια πλέον στο πανεπιστήμιο Tor Vergata της Ρώμης, Δόκτορα Francesca Casini. Τον Καθηγητή κ. Antonio Gens οφείλω να τον ευχαριστήσω επιπρόσθετα και για την τιμή που μου έκανε να ταξιδέψει ως την Αθήνα για να αποτελέσει μέλος της επταμελούς εξεταστικής μου επιτροπής, συμβάλλοντας με τον τρόπο αυτό και στην τελική διαμόρφωση της διατριβής. *Profesor Antonio Gens e Dr. Francesca Casini muchas gracias para su ayuda e hospitalidad en Barcelona.*

Η επιστροφή μου από την Βαρκελώνη (το φθινόπωρο του 2012) με έβαλε πλέον στην τελική και ουσιαστικότερη πορεία προς την ολοκλήρωση του διδακτορικού. Ατελείωτες ώρες στο δεύτερο (ίσως και πρώτο αν μετρήσουμε πραγματικές ώρες...) σπίτι μου, τον Τομέα Γεωτεχνικής του Εθνικού Μετσόβιου Πολυτεχνείου. Αν με ρωτήσει κανείς να απαντήσω με το χέρι στην καρδιά... τί ήταν αυτό που συνέβαλλε περισσότερο στην επιτυχή κατάληξη αυτής της ερευνητικής πορείας θα έλεγα αβίαστα... «ο Τομέας μας». Αν τώρα με ρωτήσει και το γιατί... τα πράγματα δυσκολεύουν. Θα έλεγα, όσο υπεροπτικό και αν ακούγεται, ότι δεν είναι εύκολο να το καταλάβει κανείς αν δεν το ζήσει. Παρόλα αυτά θα κάνω μία προσπάθεια να το

αποτυπώσω σε λίγες γραμμές.

Ξεκινώντας, θα έλεγα ότι είναι τα μέλη ΔΕΠ του τομέα μας τα οποία με την συστηματική ερευνητική και διδακτική εργασίας τους, πολλά χρόνια τώρα, έχουν προάγει τον τομέα σε ένα εργαστήριο παραγωγής έρευνας και γνώσης διεθνώς αναγνωρισμένο και καταξιωμένο. Ένα περιβάλλον εργασίας το οποίο σε κάνει περήφανο και σε τιμά το να αποτελείς μέλος του. Προσωπικά, από τα μέλη ΔΕΠ του τομέα μας, ένα μεγαλύτερο ευχαριστώ οφείλω στα μέλη της τριμελούς μου συμβουλευτικής επιτροπής Καθηγητή κ. Γεώργιο Μπουκοβάλα και Αναπληρώτρια Καθηγήτρια κ. Βασιλική Γεωργιάννου, για την συμβολή τους στην ομαλή πορεία αυτής της διατριβής, αλλά και στα μέλη τις επταμελούς εξεταστικής μου επιτροπής Καθηγητή κ. Γιώργο Γκαζέτα, και Επίκουρους Καθηγητές κκ. Νίκο Γερόλυμο και Αχιλλέα Παπαδημητρίου για την συμβολή τους στην τελική διαμόρφωση της διατριβής.

Σε οποιοδήποτε περιβάλλον εργασίας όμως, είναι αδύνατο να σε κερδίσει μόνο η δουλειά. Αυτό που σε κερδίζει είναι το κλίμα. Είναι όλο αυτό που έχουμε καταφέρει στον τομέα και απλά αποτυπώνεται με την φράση…«μία παρέα»… όλοι οι συν-υποψήφιοι πρώην και νυν διδάκτορες. Μια παρέα που μπορεί να κάνει την πιο σύνθετη επιστημονική συζήτηση αλλά και τον πιο μεγάλο χαβαλέ με την ίδια ευκολία. Είναι τα γέλια, τα ξενύχτια, τα τραγούδια, τα «ψητούρια», οι απρογραμμάτιστες και προγραμματισμένες έξοδοι, οι εκδρομές, τα ταξίδια (συνεδριακά, ερευνητικά και μη)… οι διακοπές!; Διακοπές; και όμως ναι διακοπές!… γιατί επιτυχία ή μάλλον ευτυχία είναι να θες να μοιραστείς στιγμές με συναδέλφους και όταν είσαι εκτός του αυστηρού πλαισίου της δουλείας. Γιατί πλέον αυτοί οι άνθρωποι αποτελούν την διασκέδασή σου, την παρηγοριά σου, το αγχολυτικό σου. Είναι πλέον η παρέα σου, οι φίλοι σου. Όλοι τους κατέχουν ξεχωριστή θέση στην καρδία μου και τους ευχαριστώ για όλη αυτή την απίστευτη καθημερινότητα που μου εξασφάλιζαν. Όσο όμως και αν προσπαθήσω να αποφύγω ονομαστικές αναφορές απλά δεν γίνεται (συγνώμη…) να μην αναφέρω τρεις ανθρώπους. Βρίσκονται ένα σκαλοπάτι πιο πάνω μέσα στην καρδιά μου και δεν μπορώ παρά να τους ξεχωρίσω. Κωνσταντίνε Τ., Δημήτρη Κ. και Γιάννη Χ. σας ευχαριστώ ιδιαιτέρως!

Και μιας και που πιάσαμε τα σκαλοπάτια, θα μου επιτρέψετε να ανέβουμε άλλο ένα για να συναντήσουμε τις παρέες μου εκτός ΕΜΠ. Τις παλιότερες και πλέον διαχρονικές. Οι φίλοι και οι φίλες μου, παρέες που δοκιμασμένα πλέον έχουν

χαρίσει χαρές και γέλια έχουν περάσει λύπες και παρεξηγήσεις και έχουν αντέξει. Είναι όλοι αυτοί οι άνθρωποι που απαρτίζουν τις παρέες της Πάτρας και της Σαντορίνης. Και εδώ δεν θα μπω πραγματικά σε προσωπικές αναφορές γιατί θα είναι αδικία. Ξέρουν... τους αγαπώ και τους ευχαριστώ όλους!

Τέλος είναι ώρα να ξεφύγουμε από κάθε χρονική παράθεση και κάθε κλίμακα γενικότερα και ειδικότερα. Γιατί απλά πρόκειται για τους ανθρώπους οι οποίοι πάντα βρίσκονται ψηλά μέσα στην καρδιά μας. Είναι οι άνθρωποι που μας μεγαλώνουν, οι άνθρωποι στους οποίους οφείλουμε τα πάντα. Είναι η οικογένεια και ειδικά οι γονείς μας. Είχα την τύχη να μεγαλώσω σε ένα υγιές και εύρωστο οικογενειακό περιβάλλον, συναισθηματικό, ψυχικό και οικονομικό αρωγό σε κάθε μου βήμα. Και τί περίεργο... είναι οι άνθρωποι στους οποίους συνήθως εκφράζουμε πιο σπάνια από όλους τα συναισθήματά μας, θες γιατί τους θεωρούμε δεδομένους, θες γιατί είναι δύσκολο να τα εκφράσεις. Η διατριβή λοιπόν αυτή τους αφιερώνεται δικαιωματικά ως ένα μικρό δείγμα της ευγνωμοσύνης και της αγάπης μου!

Παναγιώτης Χρ. Σιταρένιος
Αθήνα, Ιούνιος 2016

Η παρούσα έρευνα έχει χρηματοδοτηθεί από:

- Τον Ειδικό Λογαριασμό Κονδυλίων Έρευνας (Ε.Λ.Κ.Ε) του Εθνικού Μετσόβιου Πολυτεχνείου, μέσω του προγράμματος υποτροφιών προς υποψήφιους διδάκτορες, για το ακαδημαϊκό έτος 2009 - 2010.
- Το Ίδρυμα Κρατικών Υποτροφιών (Ι.Κ.Υ), μέσω υποτροφίας του προγράμματος Erasmus, για την περίοδο εκτέλεσης της διατριβής στην Βαρκελώνη (Ιανουάριος 2012 - Ιούλιος 2012).
- Το ερευνητικό πρόγραμμα "NeTTUN: New Technologies for Tunnelling and UNderground works" χρηματοδοτούμενο από την Ευρωπαϊκή Επιτροπή (7th Framework Programme - FP7), για την περίοδο Σεπτέμβριος 2012 - Ιούνιος 2016.

Ο συγγραφέας αισθάνεται την υποχρέωση να ευχαριστήσει όλους τους εμπλεκόμενους φορείς για την υποστήριξή τους.

# Abstract

The main objective of the present doctoral thesis is the development of a constitutive model for unsaturated soils, its validation and further numerical implementation in the finite element method computer code Simulia Abaqus. From a practical point of view, partial saturation usually concerns either natural or compacted soils. Both natural and compacted soils tend to exhibit strong evidence of anisotropy. For this reason, the proposed constitute model includes anisotropic features to account for the effect of stress induced anisotropy on the mechanical behaviour of soils. Hence, the final deliverable comprises of a new constitutive model for anisotropic and unsaturated soils implemented as a user defined material, in the finite element method computer code Simulia Abaqus.

The main features of the developed constitutive model can be summarized as follows:

- It incorporates the anisotropic, distorted elliptical yield surface of Kavvadas (1982) to account for the non-isotropic yield locus of anisotropically consolidated soils.

- Plastic strains accumulation follows a non-associated flow rule, defined through a plastic potential surface with a similar shape but different orientation, with respect to the yield surface. The proposed flow rule can be calibrated to account for the desired plastic dilation in radial stress paths (with emphasis on 1D compression) and further enhances the control over the position of the critical state line on the void ratio – mean effective stress plane.

- It incorporates a new mixed hardening rule consisting of three different parts:

    a) a new isotropic part based on the Intrinsic Compressibility Framework of Belokas & Kavvadas (2011), which in combination with the kinematic

part of the rule describes the dependence of the virgin compression lines on the level of the stress induced anisotropy;

b) the kinematic hardening rule of Kavvadas (1982) to describe the evolution of the orientation of the yield surface with plastic deviatoric straining, and;

c) a new kinematic hardening rule, which describes a progressive elimination of the soil's memory of anisotropy with the onset of plastic deviatoric strains. It aims to reproduce in a simple, natural and unified way the strain softening behaviour that anisotropically consolidated soils tend to exhibit when subjected to undrained triaxial loading (anisotropy degradation) together with a unique critical state, independent of the initial anisotropy and of the stress path undertaken;

- Extension in the unsaturated regime is realized through Bishop's average skeleton stress, using the macro-structural degree of saturation as a scaling parameter. Such a selection allows for a natural representation of the nonlinear increase in shear strength and of the evolution of elastic compressibility with partial saturation. Bishop's average skeleton stress, also, ensures a smooth transition between saturated and unsaturated conditions, as it recalls Terzaghi's effective stress upon saturation.

- It includes a Loading – Collapse (LC) surface, derived from a new compressibility framework proposed within the present thesis. The latter describes a constantly evolving compressibility even under constant suction as a result of its double dependence of the unsaturated compression lines on both suction and degree of saturation.

The developed constitutive model is implemented in an incremental driver which solves the constitutive equations, using an explicit integration scheme. The developed incremental driver is utilized to simulate common laboratory stress paths at a single material point, but also for the implementation in the computer code Simulia Abaqus, in the latter as a user defined material. To allow for the simulation of unsaturated problems, the developed single material point algorithm incorporates a simple hydromechanical coupling based on the Gallipoli et al. (2003) water retention model.

To validate and evaluate the constitutive model the following steps where undertaken:

- A parametric study was performed for: a) validating the model predictions against the underlying mechanical framework; b) a qualitative comparison of the model's predictions against common experimental observations; c) investigating the effect of various model parameters, and; d) comparing the simulation results derived with the single material point algorithm with the results of finite element analyses, both concerning simple common laboratory stress paths in order to validate the proposed numerical tools.

- The proposed model is calibrated and evaluated against available experimental data. Laboratory measurements from three individual experimental studies are used, namely: a) the Gens (1982) experimental investigation on the anisotropic behaviour of the Lower Cromer Till; b) the Casini (2008) experimental investigation on the unsaturated behaviour of anisotropically consolidated Jossigny Silt samples, and; c) the Barrera (2002) experimental investigation on the hydromechanical behaviour of the Barcelona Clayey Silt.

- The proposed model is applied in the finite element analyses of two common engineering problems. The first application is related to the anisotropic features of the model and deals with face stability of an EPB excavated tunnel. The results derived with the proposed model are compared with their MCC counterparts, to reveal how the anisotropy degradation mechanism included in the proposed model results to increased tunnel deformation. To test the unsaturated capabilities of the proposed model, an additional numerical investigation of the behaviour of a typical shallow footing, laying on an unsaturated soil profile is performed, revealing the effect of partial saturation on bearing capacity and deformation.

The proposed constitutive model was found to provide sound results, in line with the general behavioural trends of anisotropic and unsaturated soils, while it is relatively easily calibrated with the experimental results of common laboratory tests. Moreover, the developed numerical tools can efficiently handle complicated numerical analyses facilitating the investigation of the effects of anisotropy and partial saturation on common engineering problems as part of future research. Highlights of the main simulation capabilities of the proposed model include:

- Efficient description of the evolution of the intrinsic compression curves with evolving stress induced anisotropy.

- The incorporated flow rule can successfully represent the accumulation of plastic strains during both radial compression and drained triaxial compression tests.
- The proposed new hardening rule, describing the degradation of anisotropy with plastic deviatoric straining, can efficiently reproduce both the desired strain softening behaviour and a unique critical state independent of the initial anisotropy and of the imposed stress path.
- The incorporation of Bishop's average skeleton stress can successfully account for the nonlinear evolution of shear strength with suction.
- The proposed compressibility framework can efficiently represent the evolution of compressibility with suction and degree of saturation and is capable of reproducing; a) unique compression lines for saturated material states, irrespectively of the level of applied suction; b) a constantly evolving compressibility under constant suction compression and a maximum of collapse.

Future versions of the proposed constitutive model should focus on addressing its main drawbacks, namely:

a) the hardening rule of Kavvadas (1982) needs to be enhanced towards an increased versatility of the orientation of the yield surface during radial stress paths, in order to reduce the model's tendency to over-predict the peak strength of anisotropically consolidated soil samples. In the present version, an accurate representation of the peak strength can be achieved through proper calibration;

b) due to its extended elastic domain, the simulations regarding highly overconsolidated soils, lack in precision compared to their normally consolidated counterparts. To address this issue, the proposed model needs to evolve to a bounding surface plasticity model (bubble model), by incorporating a small plastic yield envelope which will account for small strain stiffness, similar to the Belokas (2008) and Kalos (2014) proposals;

c) the flow rule needs to better accommodate the increase in dilatancy with increasing suction, typically observed in experimental studies. A direct dependance of the plastic potential function on the level of the applied suction can hold as a possible solution.

# Περίληψη

Ο κύριος σκοπός της παρούσας διδακτορικής διατριβής είναι η ανάπτυξη ενός καταστατικού προσομοιώματος για μη κορεσμένα εδάφη, η τεκμηρίωσή του και η εισαγωγή του στο πρόγραμμα πεπερασμένων στοιχείων Simulia Abaqus. Ο μερικός κορεσμός σε πρακτικό επίπεδο αφορά κυρίως φυσικά ή συμπυκνωμένα εδάφη με κοινό τους χαρακτηριστικό την ανισοτροπία της μηχανικής τους συμπεριφοράς. Για τον λόγο αυτό επιλέχθηκε στο προτεινόμενο καταστατικό προσομοίωμα να συμπεριληφθεί η δυνατότητα πρόβλεψης της ανισοτροπίας, με αποτέλεσμα το τελικό παραδοτέο να αποτελεί ένα νέο καταστατικό προσομοίωμα για ανισότροπα στερεοποιημένα, μη κορεσμένα εδαφικά υλικά, με δυνατότητα εξωτερικής ενσωμάτωσης στον κώδικα πεπερασμένων στοιχείων Simulia Abaqus.

Τα κυριότερα χαρακτηριστικά του προτεινόμενου καταστατικού προσομοιώματος συνοψίζονται ως εξής:

- Χρησιμοποιεί το στρεβλό ελλειψοειδές του Kavvadas (1982) ως την επιφάνεια πλαστικής διαρροής ανισότροπα στερεοποιημένων εδαφικών υλικών.

- Ενσωματώνει έναν μη συσχετισμένο νόμο ροής, η διατύπωση του οποίου βασίζεται στην ενσωμάτωση μίας επιφάνειας πλαστικού δυναμικού, όμοιου σχήματος και διαφορετικού προσανατολισμού σε σχέση με την επιφάνεια διαρροής. Ο προτεινόμενος νόμος ροής μπορεί να βαθμονομηθεί ώστε να προβλέπει την επιθυμητή πλαστική διαστολικότητα σε ακτινικές τασικές οδεύσεις (με έμφαση σε συνθήκες μονοδιάστατης παραμόρφωσης) ενώ ταυτόχρονα επιτρέπει τον ανεξάρτητο έλεγχο της θέσης της γραμμής κρίσιμης κατάστασης στο επίπεδο λόγου κενών $v$ – μέσης ενεργού τάσης $p$.

- Ενσωματώνει έναν νέο μικτό νόμο κράτυνσης ο οποίος περιλαμβάνει τρία επιμέρους μέρη:

  α') έναν νέο νόμο ισότροπης κράτυνσης, ο οποίος ενσωματώνει το πλαίσιο

εγγενούς συμπίεσης των Belokas & Kavvadas (2011) και δύναται, σε συνδυασμό με τον νόμο κινηματικής κράτυνσης, να περιγράψει με ακρίβεια τη συσχέτιση των καμπυλών εγγενούς συμπίεσης με το επίπεδο της επιβαλλόμενης τασικής ανισοτροπίας,

β') τον κινηματικό νόμο κράτυνσης του Kavvadas (1982), ο οποίος περιγράφει την εξέλιξη του προσανατολισμού της επιφάνειας διαρροής με την εξέλιξη της ανισοτροπίας και

γ') έναν νέο νόμο κινηματικής κράτυνσης, ο οποίος μέσω των διεκτροπικών πλαστικών παραμορφώσεων περιγράφει τη σταδιακή «απώλεια μνήμης» της ανισοτροπίας σε τασικές οδεύσεις που προκαλούν αστοχία. Ο προτεινόμενος νόμος κινηματικής κράτυνσης αποσκοπεί στην ενοποιημένη και στη φυσική περιγραφή, αφενός της τασικής χαλάρωσης που επιδεικνύουν ανισότροπα στερεοποιημένα εδαφικά υλικά σε δοκιμές αστράγγιστης τριαξονικής συμπίεσης, αφετέρου μίας ενιαίας και μοναδικής κρίσιμης κατάστασης, ανεξάρτητης τόσο της αρχικής ανισοτροπίας όσο και της επιβαλλόμενης τασικής διαδρομής που οδηγεί στην αστοχία.

- Η επέκταση του καταστατικού προσομοιώματος για εδαφικές καταστάσεις μερικού κορεσμού γίνεται με χρήση της τάσης εδαφικού σκελετού του Bishop ως η πρώτη καταστατική παράμετρος, καθώς και της μύζησης και του βαθμού κορεσμού ως επιπλέον καταστατικές παραμέτρους. Η χρήση της τάσης του Bishop επιτρέπει τη φυσική περιγραφή της εξέλιξης της αντοχής με τη μύζηση και επιπρόσθετα επιτρέπει την προσομοίωση μίας ομαλής μετάβασης από καταστάσεις πλήρους κορεσμού σε καταστάσεις μερικού κορεσμού και το αντίθετο.

- Τέλος, ενσωματώνει μία καταστατική επιφάνεια τύπου Φόρτισης – Κατάρρευσης (Loading - Collapse) για την περιγραφή πλαστικών καταστάσεων που συνδέονται με φόρτιση επί καταστάσεων παρθενικής συμπίεσης υπό διαφορετικά επίπεδα μύζησης και με τις ογκομετρικές μεταβολές που προκαλούνται λόγω μεταβολής της μύζησης. Βασίζεται σε ένα νέο πλαίσιο συμπιεστότητας για καταστάσεις μερικού κορεσμού, το οποίο προβλέπει γραμμές παρθενικής συμπίεσης με κλίση εξαρτώμενη τόσο από τη μύζηση όσο και από τον βαθμό κορεσμού.

Το προτεινόμενο καταστατικό προσομοίωμα ενσωματώνεται σε αλγόριθμο επίλυσης των καταστατικών εξισώσεων σε υλικό σημείο, ο οποίος χρησιμοποιείται τόσο για την εκτέλεση απλών προσομοιώσεων τυπικών τασικών οδεύσεων φόρτισης και μεταβολής της μύζησης σε υλικό σημείο, όσο και για την ενσωμάτωση του προσομοιώματος στον κώδικα πεπερασμένων στοιχείων Simulia Abaqus. Για την πραγματοποίηση προσομοιώσεων της συμπεριφοράς μη κορεσμένων εδαφών, ενσωματώνονται στον αλγόριθμο ενσωματώνονται δυνατότητες συζευγμένης ανάλυσης της μηχανικής και υδραυλικής συμπεριφοράς μέσω του μαθηματικού προσομοιώματος περιγραφής της καμπύλης συγκράτησης ύδατος των Gallipoli et al. (2003). Για την επαλήθευση και αξιολόγηση του καταστατικού προσομοιώματος εκτελέστηκαν οι ακόλουθες επιμέρους εργασίες:

- Εκτελέστηκε ικανό πλήθος παραμετρικών αναλύσεων με σκοπό: α) την επαλήθευση της συμμόρφωσης του προσομοιώματος με τις προβλέψεις του πλαισίου μηχανικής συμπεριφοράς, β) την ποιοτική σύγκριση των προβλέψεων του προσομοιώματος με τα συνήθη ευρήματα εργαστηριακών διερευνήσεων, γ) την αποσαφήνιση της επιρροής διαφόρων παραμέτρων με σκοπό τη διευκόλυνση της βαθμονόμησής του και δ) τη σύγκριση των αποτελεσμάτων αναλύσεων υλικού σημείο με τα αποτελέσματα αναλύσεων πεπερασμένων στοιχείων σε επίπεδο απλών τασικών οδεύσεων συνήθων εργαστηριακών δοκιμών για την επαλήθευση των αριθμητικών εργαλείων.

- Το προσομοίωμα βαθμονομήθηκε με βάση διαθέσιμα εργαστηριακά δεδομένα από την βιβλιογραφία. Χρησιμοποιήθηκαν δεδομένα από τρεις διαφορετικές πηγές (διδακτορικές διατριβές) επιλεγμένες με γνώμονα τόσο την πληρότητα σε επίπεδο δοκιμών και διαφορετικών τασικών οδεύσεων, όσο και την ύπαρξη επαρκούς τεκμηρίωσης. Συγκεκριμένα, χρησιμοποιούνται αποτελέσματα από την εργαστηριακή διερεύνηση: α) της Lower Cromer Till από τον Gens (1982), β) της Jossigny Silt από την Casini (2008) και γ) της Barcelona Clayey Silt από τον Barrera (2002).

- Εκτελέστηκαν σύνθετες αναλύσεις συνοριακών συνθηκών με τον κώδικα πεπερασμένων στοιχείων Simulia Abaqus. Εξετάστηκαν δύο διαφορετικά γεωτεχνικά προβλήματα μηχανικού. Το πρώτο αφορά στη μηχανοποιημένη διάνοιξη σήραγγας και εστιάζει στην επιρροή της ανισοτροπίας και κυρίως της προκαλούμενης τασικής χαλάρωσης στην υπολογιζόμενη έκθλιψη του μετώπου

και κατ' επέκταση στην ευστάθειά του. Το δεύτερο πρόβλημα αφορά στη μηχανική συμπεριφορά ενός επιφανειακού θεμελίου και στην επιρροή του πάχους της μη κορεσμένης ζώνης σε αυτήν.

Προέκυψε ότι το προτεινόμενο καταστατικό προσομοίωμα δύναται να περιγράψει με επιτυχία τα κυριότερα μηχανικά χαρακτηριστικά ανισότροπα στερεοποιημένων εδαφών τόσο σε καταστάσεις πλήρους όσο και μερικού κορεσμού, ενώ η διατύπωσή του είναι σχετικά απλή και οι παράμετροί του εύκολα διακριβώσιμες στη βάση συνήθων εργαστηριακών δοκιμών. Επιπρόσθετα, τα αναπτυχθέντα υπολογιστικά εργαλεία αριθμητικής επίλυσης των εξισώσεων του προσομοιώματος αποδεικνύεται ότι μπορούν να διαχειριστούν με επιτυχία σύνθετες αναλύσεις πεπερασμένων στοιχείων επιτρέποντας τη μελλοντική χρήση του προσομοιώματος τόσο σε πρακτικές εφαρμογές όσο και στην ερευνητική διερεύνηση της επίδρασης της ανισοτροπίας και του μερικού κορεσμού σε προβλήματα μηχανικού. Οι κυριότερες δυνατότητες του προτεινόμενου προσομοιώματος μπορούν να συνοψιστούν στα εξής:

- Δύναται να περιγράψει με ακρίβεια την εξάρτηση των καμπυλών εγγενούς συμπίεσης από τον βαθμό της επιβαλλόμενης τασικής ανισοτροπίας.

- Ο προτεινόμενος νόμος ροής περιγράφει επιτυχώς τις πλαστικές παραμορφώσεις τόσο σε δοκιμές ακτινικής συμπίεσης όσο και σε στραγγισμένες δοκιμές τριαξονικής φόρτισης.

- Ο προτεινόμενος νόμος κράτυνσης για την «απώλεια μνήμης» της ανισοτροπίας με τη συσσώρευση διεκτροπικών πλαστικών παραμορφώσεων περιγράφει επιτυχώς τόσο την τασική χαλάρωση που επιδεικνύουν ανισότροπα στερεοποιημένα εδαφικά υλικά όσο και μία ενιαία κρίσιμη κατάσταση.

- Η εφαρμογή της τάσης εδαφικού σκελετού του Bishop περιγράφει με επιτυχία την εξέλιξη της διατμητικής αντοχής με τη μύζηση σε καταστάσεις μερικού κορεσμού.

- Το προτεινόμενο πλαίσιο συμπιεστότητας για καταστάσεις μερικού κορεσμού, προσομοιώνει επιτυχώς την εξέλιξη της συμπιεστότητας με τη μύζηση και τον βαθμό κορεσμού και δύναται να προβλέπει: α) καμπύλες συμπίεσης ανεξάρτητες της μύζησης για καταστάσεις πλήρους κορεσμού, β) συνεχή μεταβολή της συμπιεστότητας για καταστάσεις φόρτισης υπό σταθερή μύζηση

καθώς και γ) ένα μέγιστο στις ογκομετρικές παραμορφώσεις λόγω διαβροχής (κατάρρευση).

Μελλοντικές εκδόσεις του προσομοιώματος θα πρέπει να εστιάσουν στην άρση των κυριότερων αδυναμιών του προσομοιώματος, ως εξής:

- Το προσομοίωμα τείνει να υπερεκτιμά τη μέγιστη αντοχή ανισότροπα στερεοποιημένων εδαφών. Απαιτείται τροποποίηση του νόμου κινηματικής κράτυνσης του Kavvadas (1982) με σκοπό τη δυνατότητα μεγαλύτερης ευελιξίας ως προς τον προσανατολισμό της επιφάνειάς διαρροής σε ακτινικές τασικές οδεύσεις. Στην παρούσα έκδοση το πρόβλημα αυτό μπορεί να ξεπεραστεί μέσω κατάλληλης βαθμονόμησης των παραμέτρων του προσομοιώματος.

- Λόγω της μεγάλης ελαστικής περιοχής, οι προβλέψεις του προσομοιώματος υστερούν σε καταστάσεις που αναφέρονται σε έντονα υπερστερεοποιημένα εδαφικά υλικά. Για την βελτίωση των προβλέψεων απαιτείται η εισαγωγή εσωτερικής επιφάνειας πλαστικής διαρροής για την μετατροπή του προσομοιώματος σε προσομοίωμα οριακής πλαστικότητας, όμοια με τα προσομοιώματα των Belokas (2008) και Kalos (2014).

- Ο νόμος ροής απαιτεί βελτίωση με σκοπό την καλύτερη πρόβλεψη της αύξησης της τάσης για διαστολική συμπεριφορά που τα μη κορεσμένα εδαφικά υλικά επιδεικνύουν με την αύξηση της μύζησης. Η ενσωμάτωση κάποιου τύπου άμεσης εξάρτησης της επιφάνειας πλαστικού δυναμικού από το επίπεδο της μύζησης θα μπορούσε να αποτελεί έναν πιθανό τρόπο βελτίωσης των προσομοιώσεων.

# Εκτενής Περίληψη

## 1 Εισαγωγή

### 1.1 Σκοπός της Διατριβής

Σε πολλά μέρη του Κόσμου, ακόμα και σε περιοχές με εύκρατο κλίμα όπως η Ελλάδα, επικρατούν ξηρές ή ημίξηρες κλιματολογικές συνθήκες, με αποτέλεσμα τα ανώτερα τμήματα του εδάφους να είναι μη κορεσμένα. Ως μη κορεσμένο ορίζεται ένα έδαφος, το οποίο έχει βαθμό κορεσμού μικρότερο του $100\%$ ($S_r < 100\%$). Εδάφη με βαθμό κορεσμού ίσο με $100\%$ καλούνται πλήρως κορεσμένα ενώ με βαθμό κορεσμού ίσο με το μηδέν ξηρά.

Σημαντικός αριθμός έργων Πολιτικού Μηχανικού θεμελιώνονται ή κατασκευάζονται σε μη κορεσμένους εδαφικούς σχηματισμούς, ενώ ο μερικός κορεσμός επηρεάζει σημαντικά τη μηχανική συμπεριφορά των εδαφών, τόσο σε επίπεδο αντοχής όσο και παραμορφωσιμότητας. Παρόλα αυτά, κατά την μελέτη τέτοιων έργων σπάνια λαμβάνεται υπόψη η παρουσία της μη κορεσμένης ζώνης, είτε σε αναλυτικές είτε σε αριθμητικές προσεγγίσεις της μηχανικής τους συμπεριφοράς. Οι συνήθεις παραδοχές συνίστανται στην θεώρηση ενός είτε πλήρως κορεσμένου είτε πλήρως ξηρού υλικού για το εδαφικό προφίλ πάνω από τη στάθμη του υδροφόρου ορίζοντα.

Οι κύριοι λόγοι που επιβάλουν τη θεώρηση ενός τέτοιου εξιδανικευμένου εδαφικού προφίλ είναι η πολυπλοκότητα των μηχανισμών που σχετίζονται με τη μηχανική συμπεριφορά των μη κορεσμένων εδαφών και η περιορισμένη διαθεσιμότητα και διάδοση κατάλληλων υπολογιστικών εργαλείων και εργαστηριακών συσκευών. Επιπρόσθετα η περιορισμένη εξοικείωση του μέσου μηχανικού με την μηχανική συμπεριφορά των μη κορεσμένων εδαφών συντελεί σημαντικά προς αυτή την κατεύθυνση. Η βασική τεκμηρίωση μιας απλουστευμένης προσέγγισης είναι ότι αυτή είναι προς την μεριά της ασφάλειας καθώς εν γένει ο

μερικός κορεσμός αυξάνει την αντοχή και μειώνει την παραμορφωσιμότητα των εδαφών.

Παρότι η χρησιμοποιούμενη τεκμηρίωση είναι εν γένει ορθή, υπάρχουν περιπτώσεις που η θεώρησή της είναι προβληματική καθώς αδυνατεί να περιγράψει φαινόμενα που σχετίζονται με μεταβολές του βαθμού κορεσμού στην ακόρεστη ζώνη. Χαρακτηριστικά παραδείγματα τέτοιων γεωτεχνικών προβλημάτων είναι οι ανυψώσεις (αρνητικές καθιζήσεις) σε θεμελιώσεις επί διογκώσιμων εδαφών, οι καθιζήσεις λόγω διαβροχής σε κοινούς μη διογκώσιμους αργιλικούς σχηματισμούς καθώς και η προοδευτική αστοχία τεχνητών η φυσικών πρανών λόγω μεταβολής του βαθμού κορεσμού (π.χ μετά από περιόδους παρατεταμένης βροχόπτωσης).

Τα τελευταία χρόνια η εξέλιξη στις εργαστηριακές μεθόδους μέτρησης και επιβολής της μύζησης, η ανάπτυξη ειδικών συσκευών για τη μελέτη της μηχανικής συμπεριφοράς των μη κορεσμένων εδαφών καθώς και οι συντονισμένες ερευνητικές προσπάθειας για την διατύπωση αναλυτικών εργαλείων πρόβλεψης της μηχανικής τους συμπεριφοράς έχουν συμβάλει σε μεγάλο βαθμό στην κατανόηση της συμπεριφοράς των μη κορεσμένων εδαφών με αποτέλεσμα η εφαρμογή τους σε πραγματικά και πρακτικά προβλήματα μηχανικού να γίνεται ολοένα και πιο προσιτή.

Στο πλαίσιο αυτό εντάσσεται και η παρούσα Διδακτορική Διατριβή, ο κύριος σκοπός της οποίας είναι η διατύπωση ενός καταστατικού προσομοιώματος για μη κορεσμένα εδάφη και η εισαγωγή του στο πρόγραμμα πεπερασμένων στοιχείων Simulia Abaqus. Ο μερικός κορεσμός, σε πρακτικό επίπεδο, αφορά κυρίως φυσικά ή συμπυκνωμένα εδάφη με κοινό τους χαρακτηριστικό την ανισοτροπία της μηχανικής τους συμπεριφοράς. Για τον λόγο αυτό επιλέχθηκε στο προτεινόμενο καταστατικό προσομοίωμα να συμπεριληφθεί η δυνατότητα προσομοίωσης της ανισοτροπίας, με αποτέλεσμα το τελικό παραδοτέο να αποτελεί ένα **νέο καταστατικό προσομοίωμα για ανισότροπα, μη κορεσμένα εδαφικά υλικά, με δυνατότητα εξωτερικής ενσωμάτωσης σε έναν εμπορικό κώδικα πεπερασμένων στοιχείων**.

## 1.2 Ερευνητικά βήματα

Προς επίτευξη του στόχου της διατριβής, η παρούσα έρευνα περιέλαβε τρεις βασικές ενότητες επιμέρους εργασιών. Η **πρώτη ενότητα** αφορά την εκτενή βιβλιογραφική ανασκόπηση και κατανόηση της θεωρίας της πλαστικότητας, της μηχανικής

συμπεριφοράς και καταστατικής προσομοίωσης ανισότροπων εδαφών και της μηχανικής συμπεριφοράς και καταστατικής προσομοίωσης των μη κορεσμένων εδαφών.

Η **δεύτερη ενότητα** περιλαμβάνει τη διατύπωση του προτεινόμενου πλαισίου μηχανικής συμπεριφοράς των ανισότροπων και μη κορεσμένων εδαφών, με έμφαση στη συμπιεστότητα των εδαφών και πώς αυτή επηρεάζεται από την τασική ανισοτροπία, από τη μύζηση (αρνητική πίεση του νερού των πόρων) και τον βαθμό κορεσμού. Ακολουθεί η εξέλιξη του προτεινόμενου πλαισίου συμπεριφοράς σε ένα πλήρως διατυπωμένο καταστατικό προσομοίωμα για τη συμπεριφορά των ανισότροπων και μη κορεσμένων εδαφικών σχηματισμών. Η ενότητα αυτή ολοκληρώνεται με την ανάπτυξη κατάλληλων αριθμητικών αλγορίθμων επίλυσης των καταστατικών εξισώσεων σε επίπεδο υλικού σημείου, τόσο για την επαλήθευση και αξιολόγηση του προσομοιώματος σε απλές τασικές διαδρομές σε υλικό σημείο όσο και για την εφαρμογή του στην επίλυση προβλημάτων συνοριακών συνθηκών στον κώδικα πεπερασμένων στοιχείων Simulia Abaqus.

Η **τρίτη ενότητα** αφορά την επαλήθευση και αξιολόγηση των προβλέψεων του καταστατικού προσομοιώματος και των αναπτυχθέντων εργαλείων αριθμητικής επίλυσης. Περιλαμβάνει τρεις επιμέρους εργασίες. Αρχικά, μέσω πλήθους παραμετρικών αριθμητικών αναλύσεων, επαληθεύονται και ελέγχονται οι προβλέψεις του καταστατικού προσομοιώματος, έναντι αφενός του θεωρητικού πλαισίου συμπεριφοράς και αφετέρου ποιοτικών στοιχείων επί πειραματικών παρατηρήσεων. Ακολουθεί η βαθμονόμηση των παραμέτρων του προσομοιώματος στη βάση συγκεκριμένων εργαστηριακών αποτελεσμάτων και η σύγκριση της προβλεπόμενης συμπεριφοράς με τα εργαστηριακά αποτελέσματα. Παρατίθενται τρεις διαφορετικές «ασκήσεις» βαθμονόμησης και προσομοίωσης εργαστηριακών αποτελεσμάτων επί διαφορετικών εδαφών και σε πλήθος διαφορετικών τασικών οδεύσεων, ενώ οι διεξαχθείσες προσομοιώσεις επιλέχθηκαν με σκοπό να καλυφθεί ολόκληρο το φάσμα των μηχανικών χαρακτηριστικών του προσομοιώματος (ανισοτροπία, μερικός κορεσμός, ανεξάρτητα και σε συνδυασμό). Η τρίτη ενότητα ολοκληρώνεται με την εφαρμογή του προτεινόμενου καταστατικού προσομοιώματος στην επίλυση σύνθετων προβλημάτων συνοριακών συνθηκών. Συγκεκριμένα, αναλύεται ένα πρόβλημα ευστάθειας μετώπου σήραγγας και ένα πρόβλημα φέρουσας ικανότητας και καθιζήσεων επιφανειακού θεμελίου, με έμφαση στην επιρροή της ανισοτροπίας και του μερικού κορεσμού αντίστοιχα. Η συγκεκριμένη επιμέρους εργασία δε συνιστά

ολοκληρωμένη διερεύνηση των σχετικών μηχανισμών, παρά μόνο περιλαμβάνει ενδεικτικές αναλύσεις με κύριο σκοπό την περαιτέρω τεκμηρίωση της ορθής εφαρμογής του προσομοιώματος στον κώδικα πεπερασμένων στοιχείων Simulia Abaqus .

# 2 Καταστατική προσομοίωση εδαφικών υλικών

Η παρούσα ενότητα παρουσιάζει τους σημαντικότερους άξονες της θεωρίας πλαστικότητας και της θεωρίας κρίσιμης κατάστασης εδαφικών υλικών καθώς και το βασικό καταστατικό προσομοίωμα Modified Cam Clay (MCC).

## 2.1 Βασικές αρχές της θεωρίας της πλαστικότητας

Το καταστατικό προσομοίωμα αποτελεί αναπόσπαστο τμήμα οποιασδήποτε ανάλυσης συνοριακών συνθηκών (είτε με τη μέθοδο των πεπερασμένων στοιχείων είτε με τη μέθοδο των πεπερασμένων διαφορών). Περιγράφει τη μηχανική συμπεριφορά του υλικού (π.χ. έδαφος) και βασίζεται στην έννοια της **κατάστασης** του υλικού (material state).

Η κατάσταση ενός υλικού περιγράφεται από δύο ομάδες μεταβλητών. Τις **εξωτερικές μεταβλητές κατάστασης** (external variables), οι οποίες περιγράφουν την φόρτιση (loading) του υλικού και τις **εσωτερικές μεταβλητές κατάστασης**, οι οποίες περιγράφουν τη μνήμη του υλικού. Η κατάσταση ενός υλικού αλλάζει μόνο εφόσον αλλάξει κάποια από τις μεταβλητές κατάστασης. Οι πιθανές καταστάσεις ενός υλικού διακρίνονται σε **ελαστικές καταστάσεις** κατά τις οποίες οποιαδήποτε απειροστή φόρτιση (infinitesimal loading) προκαλεί μόνο αναστρέψιμες μεταβολές των εξωτερικών μεταβλητών κατάστασης και σε **πλαστικές καταστάσεις** όταν κάθε απειροστή φόρτιση προκαλεί μη αναστρέψιμες μεταβολές των εξωτερικών μεταβλητών κατάστασης.

Ανάλογα με την κατάσταση ενός υλικού ορίζεται ως **ελαστική φόρτιση** οποιαδήποτε απειροστή φόρτιση, είτε από μία ελαστική κατάσταση είτε από μία πλαστική κατάσταση, η οποία συνδέεται με μεταβολή αποκλειστικά των εξωτερικών μεταβλητών κατάστασης. Σε κάθε άλλη περίπτωση συμβαίνει **πλαστική φόρτιση** με τις εσωτερικές μεταβλητές κατάστασης να αλλάζουν μόνο κατά τη διάρκεια πλαστικών φορτίσεων.

Η διάκριση μεταξύ ελαστικών και πλαστικών καταστάσεων επιτυγχάνεται μέσω

της **επιφάνειας διαρροής**, η οποία περιγράφεται μαθηματικά από τη **συνάρτηση διαρροής** ($f(\boldsymbol{\sigma})$)[1].

Καταστάσεις επί της επιφάνειας διαρροής ($f(\boldsymbol{\sigma}) = 0$) θεωρούνται πλαστικές, ενώ καταστάσεις εντός της επιφάνειας διαρροής ($f(\boldsymbol{\sigma}) < 0$) θεωρούνται ελαστικές. Καταστάσεις εκτός της επιφάνειας διαρροής θεωρούνται μη εφικτές και για τον λόγο αυτό κατά τη διάρκεια πλαστικής φόρτισης η επιφάνεια διαρροής μεταβάλλεται ως προς το σχήμα, το μέγεθος ή/και τη θέση της ώστε κάθε νέα πλαστική κατάσταση να βρίσκεται επί της επιφάνειας διαρροής. Η μεταβολή του σχήματος, μεγέθους ή/και θέσης της επιφάνειας διαρροής ονομάζεται **κράτυνση** και συνδέεται με τη μεταβολή των μεταβλητών κράτυνσης. Οι **μεταβλητές κράτυνσης** αποτελούν μεταβλητές της συνάρτησης διαρροής, οι οποίες μεταβάλλονται μόνο κατά τη διάρκεια πλαστικής φόρτισης και ως εκ τούτου συνιστούν εσωτερικές μεταβλητές κατάστασης.

Η μηχανική συμπεριφορά του υλικού κατά τη διάρκεια ελαστικών φορτίσεων περιγράφεται από τον ελαστικό νόμο συμπεριφοράς ή **ελαστικότητα**, με τη γραμμική ισότροπη ελαστικότητα να αποτελεί την απλούστερη μορφή τέτοιου νόμου. Κατά τη διάρκεια πλαστικών φορτίσεων ο **νόμος ροής** περιγράφει τη συσσώρευση πλαστικών (μη αναστρέψιμων) παραμορφώσεων. Ανάλογα με τις παραδοχές του εκάστοτε καταστατικού προσομοιώματος, ένας νόμος ροής μπορεί να είναι συσχετισμένος ή μη συσχετισμένος. Σε έναν συσχετισμένο νόμο ροής η κατεύθυνση των πλαστικών παραμορφώσεων θεωρείται κάθετη στην επιφάνεια διαρροής στον εξαεδρικό χώρο των τάσεων, ενώ σε κάθε άλλη περίπτωση θεωρείται ότι οι πλαστικές παραμορφώσεις περιγράφονται από έναν μη συσχετισμένο νόμο ροής. Τέλος, η μεταβολή των παραμέτρων κράτυνσης κατά τη διάρκεια πλαστικών φορτίσεων περιγράφεται από τον **νόμο κράτυνσης**.

Τα πρώτα καταστατικά προσομοίωματα που αναπτύχθηκαν για εδαφικά υλικά βασίστηκαν σε υφιστάμενα προσομοίωματα για μέταλλα, συσχετίζοντας την επιφάνεια διαρροής με μία περιβάλλουσα αστοχίας. Χαρακτηριστικά τέτοια προσομοίωματα αποτελούν το προσομοίωμα Mohr-Coulomb και το προσομοίωμα Drucker-Prager. Πρόκειται για ελαστικά - απολύτως πλαστικά (απουσία κράτυνσης) καταστατικά προσομοίωματα, τα οποία είναι απλά στη χρήση και τη βαθμονόμησή τους, με τα κυριότερα μειονεκτήματά τους να συνοψίζονται στην υπερεκτίμηση της ελαστικής συμπεριφοράς των γεωυλικών, καθότι αφενός σε τασικές οδεύσεις που οδηγούν στην αστοχία η διαρροή συμπίπτει με την αστοχία και

[1] Απλουστευτικά θεωρείται ότι η συνάρτηση διαρροής εξαρτάται μόνο από τον τανυστή της τάσης.

αφετέρου τασικές οδεύσεις που δεν οδηγούν στην αστοχία θεωρούνται οιονεί ελαστικές.

## 2.2 Εδαφομηχανική της κρίσιμης κατάστασης - Το καταστατικό προσομοίωμα Modified Cam Clay (MCC)

Το πρώτο σύνθετο καταστατικό προσομοίωμα για εδαφικά υλικά είναι το καταστατικό προσομοίωμα Modified Cam Clay (MCC) (Roscoe & Burland (1968)). Στο καταστατικό προσομοίωμα MCC η επιφάνεια διαρροής περιγράφεται από μία ισότροπη ελλειψοειδή επιφάνεια στον χώρο των τάσεων ενώ η αστοχία σχετίζεται με την **κρίσιμη κατάσταση** των εδαφικών υλικών, κατά την οποία ένα εδαφικό στοιχείο παραμορφώνεται υπό συνθήκες ισόογκης παραμόρφωσης χωρίς περαιτέρω αύξηση της έντασης. Κατά τη διάρκεια πλαστικών τασικών οδεύσεων και πριν την αστοχία η επιφάνεια διαρροής κρατύνεται είτε αυξάνοντας είτε μικραίνοντας σε μέγεθός (τασική κράτυνση έναντι τασικής χαλάρωσης αντίστοιχα).

Η μεγάλη επιτυχία του καταστατικού προσομοιώματος MCC οφείλεται στο πλαίσιο μηχανικής συμπεριφοράς των εδαφικών υλικών στο οποίο βασίζεται, αυτό της Εδαφομηχανικής της κρίσιμης κατάστασης. Εντός της Εδαφομηχανικής της κρίσιμης κατάστασης [Schofield & Wroth (1968)] έχει αναπτυχθεί πληθώρα καταστατικών προσομοιωμάτων με σκοπό την προσομοίωση διάφορων και διαφορετικών μηχανικών συμπεριφορών σχετιζόμενων μεταξύ άλλων με την ανισοτροπία [π.χ. Kavvadas (1982), Dafalias (1986)], την δέση [π.χ. Belokas & Kavvadas (2010)], τον μερικό κορεσμό [π.χ. Alonso et al. (1990)] και τον ερπυσμό [π.χ. Kalos (2014)]. Βασικό κοινό τους χαρακτηριστικό είναι η χρήση του MCC ως προσομοιώματος βάσης για την περιγραφή της μηχανικής συμπεριφορά ισότροπα στερεοποιημένων και κορεσμένων εδαφικών υλικών.

Οι βασικές αρχές της Εδαφομηχανικής της κρίσιμης κατάστασης που έχουν διατυπωθεί στη βάση εργαστηριακών παρατηρήσεων της μηχανικής συμπεριφοράς αναζυμωμένων και ισότροπα επανασυμπιεσμένων αργιλικών εδαφικών υλικών μπορούν να συνοψιστούν στα εξής:

- Η παρθενική συμπίεση αναζυμωμένων και ισότροπα στερεοποιημένων εδαφικών υλικών προσομοιώνεται μέσω ευθείας γραμμής στο επίπεδο ειδικού όγκου ($v = 1 + e$, όπου $e$ ο λόγος κενών) – λογαρίθμου της μέσης ενεργού τάσης ($\ln(\sigma \equiv p)$), η οποία ονομάζεται καμπύλη ισότροπης παρθενικής συμπίεσης (isotropic virgin

compression line). Περιγράφεται μαθηματικά ως: $v = N_{iso} - \lambda \ln p$ όπου $N_{iso}$ ο ειδικός όγκος που αντιστοιχεί σε μέση ενεργό τάση ίση με $p = 1kPa$ και $\lambda$ η κλίση της ευθείας (βλ. Σχήμα 1α). Καταστάσεις επί της καμπύλης παρθενικής συμπίεσης περιγράφονται μόνο από την τρέχουσα τασική κατάσταση $\boldsymbol{\sigma}$ και τον λόγο κενών $e$ και χαρακτηρίζονται ως μη δομημένες (structureless) σύμφωνα με τους Leroueil & Vaughan (1990) ή και ως εγγενής (intrinsic) σύμφωνα με τον Burland (1990).

- Σε καταστάσεις φόρτισης - επαναφόρτισης, η συμπεριφορά στο επίπεδο $v - \ln p$ μπορεί να περιγραφεί μέσω μίας ομάδας ευθειών αποφόρτισης – επαναφόρτισης (swelling lines) με κλίση $\kappa$ (βλ. Σχήμα 1α). Η αποφόρτιση οδηγεί σε δομημένες (structured) καταστάσεις καθώς η τάση προστερεοποίησης (μέγιστη τάση ιστορίας φόρτισης) αποτελεί παράμετρο μνήμης του υλικού, απαραίτητη για την περιγραφή της εδαφικής κατάστασης.

- Η τελική κατάσταση (ultimate state) των εδαφικών υλικών σε τασικές οδεύσεις που οδηγούν σε αστοχία είναι κοινή και ανεξάρτητη των αρχικών συνθηκών και της τασικής όδευσης, βρίσκεται δε επί μίας ενιαίας γραμμής στον χώρο μέσης ενεργού τάσης $p$ - διεκτροπικής τάσης $q$ - ειδικού όγκου $v$, της γραμμής κρίσιμης κατάστασης (critical state line). Η προβολή της στο επίπεδο $v - \ln p$ είναι μία ευθεία παράλληλη στη γραμμή παρθενικής συμπίεσης και περιγράφεται από την εξίσωση $v = \Gamma - \lambda \ln p$, ενώ στο επίπεδο $p - q$ περιγράφεται από μία ευθεία με εξίσωση $q = M \cdot p$ διερχόμενη από την αρχή των αξόνων.

- Κανονικοποιημένες τασικές οδεύσεις (Hvorslev κανονικοποίηση) στραγγισμένων και αστράγγιστων τριαξονικών φορτίσεων επί κανονικά στερεοποιημένων εδαφικών υλικών περιγράφουν στον χώρο $v - p - q$ μία καταστατική επιφάνεια με όρια την καμπύλη ισότροπης παρθενικής συμπίεσης και τη γραμμή κρίσιμης κατάστασης, ονομάζεται δε επιφάνεια Roscoe (βλ. Σχήμα 1β). Η επιφάνεια Roscoe, για μη δομημένα εδαφικά υλικά, αποτελεί το όριο μεταξύ εφικτών και μη εφικτών καταστάσεων.

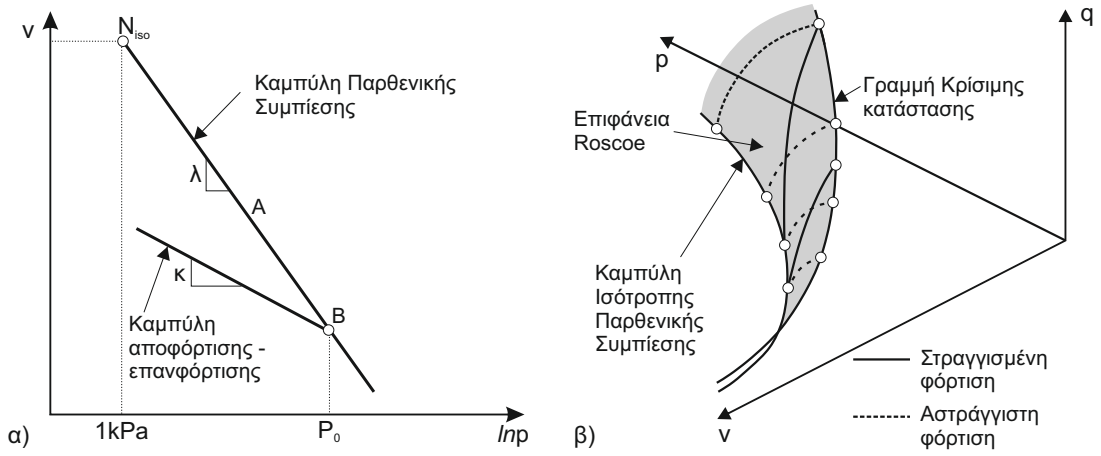


**Σχήμα 1:** α) Οι γραμμές ισότροπης παρθενικής συμπίεσης και αποφόρτισης - επαναφόρτισης στο επίπεδο $v - \ln p$ και β) η επιφάνεια Roscoe στον χώρο $v - p - q$.

# 3 Μηχανική συμπεριφορά και καταστατική προσομοίωση της εδαφικής ανισοτροπίας

Τα εδαφικά υλικά στη φύση αποτελούν συνήθως προϊόν ιζηματογένεσης, κατά την οποία διαδοχικές στρώσεις εδάφους εναποτίθενται και συμπιέζονται υπό συνθήκες μονοδιάστατης παραμόρφωσης (παρεμπόδιση πλευρικών παραμορφώσεων). Η μονοδιάστατη συμπίεση οδηγεί σε μη ισότροπο τασικό πεδίο καθώς συνήθως η αναπτυσσόμενη οριζόντια ενεργός τάση $\sigma_h$ αποτελεί μέρος της αντίστοιχης κατακόρυφης $\sigma_v$, περιγράφεται δε μέσω του συντελεστή πλευρικών τάσεων $K$ ως: $\sigma_h = K \cdot \sigma_v$. Η συμπίεση ενός εδαφικού υλικού υπό μη ισότροπο εντατικό πεδίο προσδίδει στο έδαφος **τασική ανισοτροπία** (stress induced anisotropy), η οποία οδηγεί σε ανισοτροπία στη μηχανική συμπεριφορά.

## 3.1 Μηχανική συμπεριφορά ανισότροπα στερεοποιημένων εδαφών

Στη διεθνή βιβλιογραφία υφίσταται ικανός αριθμός δημοσιεύσεων σχετικών με τη μηχανική συμπεριφορά ανισότροπα στερεοποιημένων εδαφικών υλικών [π.χ. Ladd & Varallyay (1965), Donaghe & Townsend (1978), Gens (1982), Rampello et al. (1997)], με την εργαστηριακή διερεύνηση του Gens (1982) επί της συμπεριφοράς της Lower Cromer Till να αποτελεί ακόμα και σήμερα ίσως την πλέον ολοκληρωμένη σχετική μελέτη.

Για τη μελέτη της μηχανικής συμπεριφοράς ανισότροπα στερεοποιημένων εδαφών στο εργαστήριο δύο είναι οι βασικότερες εργαστηριακές δοκιμές που χρησιμοποιούνται, ικανές να επιβάλλουν συγκεκριμένα επίπεδα τασικής ανισοτροπίας. Η δοκιμή συμπιεσομέτρου (ή οιδημέτρου) και η δοκιμή τριαξονικής ακτινικής τασικής όδευσης. Επιπρόσθετα, ανισότροπα στερεοποιημένα δοκίμια επιβάλλονται σε δοκιμές τριαξονικής φόρτισης για τη μελέτη της επίδρασης της τασικής ανισοτροπίας στην αντοχή τους. Η πλειονότητα των δημοσιευμένων αποτελεσμάτων συγκλίνουν σε κοινές παρατηρήσεις επί της μηχανικής συμπεριφοράς ανισότροπα στερεοποιημένων εδαφικών υλικών, οι οποίες συνοψίζονται παρακάτω:

- Η παρθενική συμπίεση αναζυμωμένων και ανισότροπα στερεοποιημένων εδαφικών υλικών υπό διαφορετικούς λόγους οριζόντιας προς κατακόρυφη ενεργό τάση $K$, μετά από σημαντική συσσώρευση πλαστικών παραμορφώσεων, οδηγεί σε σταθεροποίηση της τασικής ανισοτροπίας, κατά την οποία το δοκίμιο για περαιτέρω συμπίεση παραμορφώνεται υπό σταθερή διαστολικότητα $d_q = \dot{\varepsilon}_q/\dot{\varepsilon}_{vol}$, ενώ στο επίπεδο $v - \ln p$ οι καμπύλες παρθενικής συμπίεσης περιγράφονται από διαφορετικές αλλά παράλληλες ευθείες κλίσης $\lambda$ (όμοια με την καμπύλη ισότροπης συμπίεσης και τη γραμμή κρίσιμης κατάστασης). Η θέση τους στο επίπεδο $v - \ln p$ εξαρτάται από το επίπεδο της επιβαλλόμενης ανισοτροπίας, όπως αυτό περιγράφεται από τον λόγο $K$ ή τον λόγο της διεκτροπικής τάσης $q$ προς τη μέση ενεργό τάση $p$ ($n = q/p$). Αύξηση του λόγου $n$ οδηγεί σε μικρότερους λόγους κενών υπό δεδομένο επίπεδο μέσης τάσης, αντικατοπτρίζοντας την ευεργετική επίδραση της παρουσίας διάτμησης στη μείωση των κενών ενός εδαφικού υλικού (βλ. Σχήμα 2).

- Η μετρούμενη διαστολικότητα υπό συνθήκες ακτινικής τασικής όδευσης αυξάνει συνεχώς με την αύξηση του λόγου $n$ από μηδέν για συνθήκες ισότροπης συμπίεσης ($n = 0$) έως και θεωρητικού απειρισμού για ακτινική τασική όδευση ίση με την κλίση της γραμμής κρίσιμης κατάστασης $M$ ($n = M$). Στο σημείο αυτό θα πρέπει να σημειώσουμε ότι εδαφικά υλικά που, συμπιεζόμενα υπό ισότροπες συνθήκες από πολτό παρουσιάζουν διεκτροπικές παραμορφώσεις, εμφανίζουν στοιχεία εγγενούς ανισοτροπίας (μη τασική ανισοτροπία).

- Υπό συνθήκες μονοδιάστατης παραμόρφωσης επιβάλλεται στο δοκίμιο σταθερή

διαστολικότητα $d_q = 2/3$, η οποία υπό συνθήκες σταθερής ανισοτροπίας οδηγεί σε συγκεκριμένο λόγο οριζόντιας προς κατακόρυφη τάση $K$. Ο λόγος αυτός αναφέρεται σε συνθήκες παρεμπόδισης των πλευρικών παραμορφώσεων και αντιπροσωπεύει την εντατική κατάσταση ηρεμίας στο πεδίο (γεωστατική κατάσταση). Καλείται συντελεστής οριζοντίων ωθήσεων ηρεμίας ή συντελεστής γεωστατικών τάσεων $K_0$, με συνήθεις τιμές από $0.4$ έως $0.6$.

- Κατά την αποφόρτιση από συνθήκες παρθενικής συμπίεσης, όμοια με τα ισότροπα στερεοποιημένα εδαφικά υλικά, στο επίπεδο $v - \ln p$ η συμπεριφορά μπορεί να εξιδανικευτεί μέσω ενός πλήθους καμπυλών αποφόρτισης - επαναφόρτισης με κλίση $\kappa$. Σε αποφόρτιση υπό συνθήκες μονοδιάστατης παραμόρφωσης ο λόγος οριζόντιας ώθησης αυξάνει, εξαρτώμενος συνήθως από το επίπεδο προφόρτισης όπως αυτό περιγράφεται από τον λόγο προστερεοποίησης $OCR = \sigma_p/\sigma_v$ της μέγιστης κατακόρυφης τάσης της ιστορίας φόρτισης του γεωυλικού (τάση προφόρτισης, $\sigma_p$) προς την τρέχουσα κατακόρυφη ενεργό τάση ($\sigma_v$).

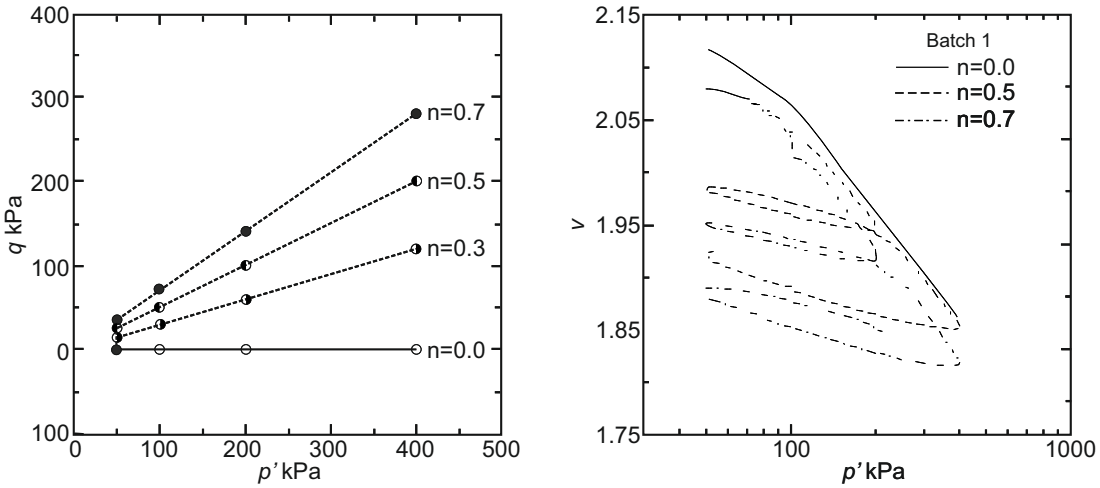


**Σχήμα 2:** Αποτελέσματα δοκιμών ακτινικής συμπίεσης επί αναζυμωμένων δοκιμίων Vallerica Clay· α) οι επιβαλλόμενες τασικές οδεύσεις στον χώρο $p - q$ και β) οι καμπύλες συμπίεσης στο επίπεδο $v - \ln p$. (Rampello et al. (1997))

Σε ότι αφορά τη συμπεριφορά ανισότροπα στερεοποιημένων εδαφικών υλικών υποβαλλόμενων σε τασικές οδεύσεις που οδηγούν στην αστοχία μπορούμε να σημειώσουμε τα ακόλουθα:

- Δοκιμές αστράγγιστης τριαξονικής συμπίεσης καταδεικνύουν ότι τα ανισότροπα στερεοποιημένα εδαφικά υλικά επιδεικνύουν μία μέγιστη τιμή της αντοχής

(διεκτροπικής τάσης) (peak strength), η οποία ακολουθείται από τασική χαλάρωση προς την επίτευξη μίας μικρότερης οριακής αντοχής (ultimate strength). Τόσο η μέγιστη τιμή της αντοχής όσο και η παρατηρούμενη τασική χαλάρωση (διαφορά μεταξύ κορυφαίας και οριακής τιμής της αντοχής) μειώνονται με τη μείωση της αρχικής ανισοτροπίας (αυξανόμενο λόγο $K$) και με την αύξηση της προστερεοποίησης (π.χ. τα ισότροπα στερεοποιημένα ή τα έντονα υπερστεροποιημένα δοκίμια δεν επιδεικνύουν τασική χαλάρωση) (βλ. Σχήμα 3).

- Σε στραγγισμένες δοκιμές τριαξονικής συμπίεσης δεν εμφανίζεται τασική χαλάρωση, με τη μέγιστη και την οριακή τιμή της αντοχής να συμπίπτουν. Αύξηση του αρχικού επιπέδου ανισοτροπίας οδηγεί σε μείωση της μετρούμενης κορυφαίας αντοχής ενώ επιδεικνύεται συστηματικά συστολική συμπεριφορά, με τη μετρούμενη ογκομετρική παραμόρφωση να μειώνεται με την αύξηση του αρχικού επιπέδου ανισοτροπίας και την αύξηση της προστερεοποίησης.

- Οι τασικές οδεύσεις, τόσο υπό συνθήκες στραγγισμένης όσο και αστράγγιστης φόρτισης, κανονικοποιούνται ως προς την τάση προφόρτισης ενώ η οριακή κατάσταση (κρίσιμη κατάσταση) εμφανίζεται κοινή και ανεξάρτητη της αρχικής ανισοτροπίας και της ακολουθούμενης τασικής όδευσης, επιτρέποντας έτσι την από κοινού μελέτη της μηχανικής συμπεριφοράς των ανισότροπα και ισότροπα στερεοποιημένων εδαφών, εντός του πλαισίου της Εδαφομηχανικής της Κρίσιμης Κατάστασης.

- Ο γεωμετρικός τόπος των σημείων διαρροής ανισότροπα στερεοποιημένων εδαφικών υλικών συνήθως εμφανίζεται μη συμμετρικός ως προς τον ισότροπο άξονα, αντικατοπτρίζοντας την ανάπτυξη προτιμητέων διευθύνσεων στον χώρο των τάσεων ως αποτέλεσμα της επιβαλλόμενης τασικής ανισοτροπίας.

## 3.2 Καταστατική προσομοίωση της εδαφικής ανισοτροπίας

Στη διεθνή βιβλιογραφία υπάρχει ικανό πλήθος καταστατικών προσομοιωμάτων τα οποία στοχεύουν στην περιγραφή της μηχανικής συμπεριφοράς ανισότροπα στερεοποιημένων εδαφών [π.χ. Kavvadas (1982), Dafalias (1986), Wheeler & Karube (1996), Dafalias et al. (2002)]. Τα βασικότερα κοινά τους χαρακτηριστικά συνοψίζονται στα παρακάτω σημεία:

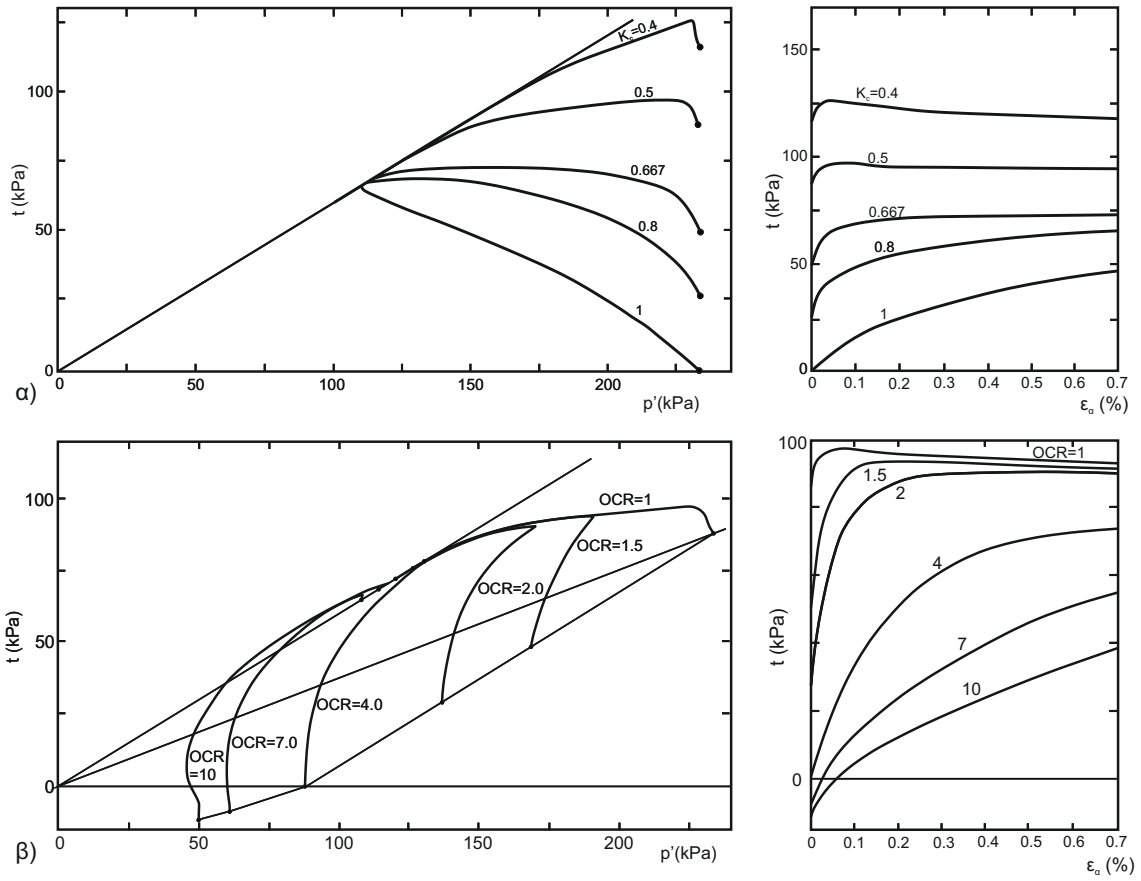


**Σχήμα 3:** Αποτελέσματα δοκιμών αστράγγιστης τριαξονικής φόρτισης επί ανισότροπα στερεοποιημένων δοκιμίων Lower Cromer Till· α) η επίδραση της αρχικής ανισοτροπίας και β) η επιρροή της προφόρτισης (Gens (1982)).

- Ενσωματώνουν μη ισότροπες καταστατικές επιφάνειες, με τα περισσότερα να υιοθετούν ένα είδος στρεβλού ελλειψοειδούς, ο κύριος άξονά του οποίου προσανατολίζεται προς την διεύθυνση της επιβαλλόμενης τασικής όδευσης (βλ. Σχήμα 4).

- Υιοθετούν μη συσχετισμένους νόμους ροής με σκοπό να περιγράψουν την εξάρτηση της διαστολικότητας από το επίπεδο της τασικής ανισοτροπίας.

- Ενσωματώνουν μικτούς νόμους κράτυνσης (ισότροπη και κινηματική κράτυνση), με τον νόμο ισότροπης κράτυνσης να ελέγχει το μέγεθος της επιφάνειας διαρροής (συνήθως υιοθετείται ο νόμος ισότροπης κράτυνσης του MCC) και τον νόμο κινηματικής κράτυνσης να περιγράφει τη στροφή – στρέβλωση ή κίνηση της επιφάνειας διαρροής ως απόρροια μεταβολής της ανισοτροπίας.

- Τα περισσότερα υιοθετούν ογκομετρικούς νόμους κινηματικής κράτυνσης για να περιγράψουν την εξέλιξη της ανισοτροπίας, με το προσομοίωμα των Wheeler & Karube (1996) να αποτελεί το πρώτο προσομοίωμα το οποίο περιλαμβάνει εξάρτηση της εξέλιξης της τασικής ανισοτροπίας και από τις πλαστικές διεκτροπικές παραμορφώσεις, επισημαίνοντας τη σημασίας μίας τέτοιας επιλογής στη σωστή πρόβλεψη μίας ενιαίας κρίσιμης κατάστασης.

Οι κυριότερες αδυναμίες των υφιστάμενων καταστατικών προσομοιωμάτων έγκεινται στην δυσκολία ακριβούς προσομοίωσης της εξάρτησης της θέσης των καμπυλών εγγενούς συμπίεσης από το επίπεδο της τασικής ανισοτροπίας και στη δυσκολία πρόβλεψης μίας ενιαίας κρίσιμης κατάστασης, ανεξάρτητης της αρχικής ανισοτροπίας και της ακολουθούμενης τασικής όδευσης προς την αστοχία.

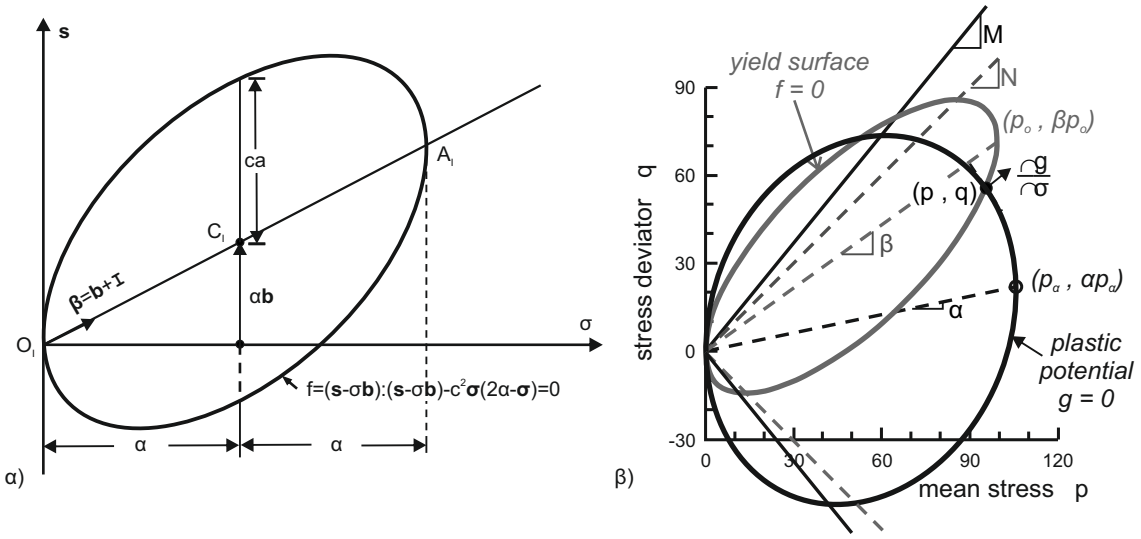


**Σχήμα 4:** Χαρακτηριστικές καταστατικές επιφάνειες των προσομοιωμάτων των α) Kavvadas (1982) και β) Dafalias et al. (2002)

# 4 Μηχανική συμπεριφορά και καταστατική προσομοίωση των μη κορεσμένων εδαφών

Οποιοδήποτε κορεσμένο εδαφικό στοιχείο δύναται κάτω από κατάλληλες υδραυλικές ή ατμοσφαιρικές συνοριακές συνθήκες να απολέσει μέρος του νερού των πόρων του με αποτέλεσμα ο βαθμός κορεσμού του να γίνει μικρότερος της μονάδας ($S_r < 100\%$). Στους πόρους ενός μη κορεσμένου εδαφικού στοιχείου (unsaturated

soil) συνυπάρχουν η υγρή και η αέρια φάση, αλληλεπιδρώντας τόσο μεταξύ τους όσο και με τη στερεή φάση (κόκκοι, αργιλικά πλακίδια ή και συσσωματώματα). Η αλληλεπίδραση αυτή οδηγεί σε σημαντικές μεταβολές της μηχανικής συμπεριφοράς του εδάφους σε σχέση με την κορεσμένη κατάσταση.

## 4.1 Η Μύζηση και η Καμπύλη Συγκράτησης Ύδατος

Η **μύζηση** (suction) αποτελεί την πιο καθοριστική παράμετρο τάσης σε ένα μη κορεσμένο έδαφος. Ορίζεται ως η περίσσεια της πίεσης της αέριας φάσης ($u_a$) ως προς την πίεση της υγρής φάσης ($u_w$):

$$s = u_a - u_w \tag{1}$$

Σε πρακτικό επίπεδο η μύζηση θεωρείται παράμετρος τάσης, απλουστευτικά δε όταν η πίεση της αέριας φάσης λαμβάνεται ίση με το μηδέν (επίπεδο αναφοράς) θεωρούμε ότι η μύζηση συμπίπτει με την αρνητική πίεση του νερού των πόρων. Παρόλα αυτά, στην πραγματικότητα οι μηχανισμοί που συνδέονται με την παρουσία μύζησης σε ένα έδαφος είναι αρκετά πιο σύνθετοι από ότι υποδηλώνει μία αρνητική πίεση πόρων. Η μύζηση σε ένα έδαφος οφείλεται σε διαφορετικά φαινόμενα τα οποία συνυπάρχουν και αλληλοεπηρεάζονται, όπως τα τριχοειδή φαινόμενα, τα φαινόμενα προσρόφησης και τα ωσμωτικά φαινόμενα.

Από θερμοδυναμικής σκοπιάς η μύζηση αντιστοιχεί σε ενεργειακό δυναμικό (potential), το οποίο καθορίζει την ροή της υγρής φάσης στο έδαφος. Επιπρόσθετα, η μύζηση μέσω της εξίσωσης του Kelvin[2] συνδέεται με τη σχετική υγρασία (relative humidity, RH) της αέριας φάσης (και κατ' επέκταση με τις επικρατούσες κλιματολογικές συνθήκες). Μείωση της σχετικής υγρασίας της αέριας φάσης οδηγεί σε αύξηση της μύζησης σε ένα δεδομένο έδαφος υπό σταθερή πίεση και θερμοκρασία.

Η χαρακτηριστική καμπύλη εδάφους - νερού (soil water characteristic curve) ή **Καμπύλη Συγκράτησης Ύδατος** (Water Retention Curve) αποτελεί την πιο σημαντική καταστατική σχέση στη μελέτη της συμπεριφοράς των μη κορεσμένων εδαφών. Συνδέει την περιεκτικότητα ενός εδάφους σε νερό (π.χ. βαθμός κορεσμού, υγρασία) με τη μύζηση και προσδιορίζεται εργαστηριακά χρησιμοποιώντας συνήθως

[2] Η εξίσωση του Kelvin συνδέει τη μύζηση $s$ με τη σχετική υγρασία $RH$ ως: $s = -\frac{RT}{M_w} \ln RH$. Διατυπώθηκε αρχικά σε όρους θερμοδυναμικού δυναμικού από τον William Thomson το 1871, γνωστό και ως Λόρδο Kelvin.

συνδυασμό διαφορετικών εργαστηριακών μεθοδολογιών επιβολής της μύζησης (π.χ. μέθοδος μετατόπισης άξονα, μέθοδος υδατικών διαλυμάτων, κλπ.). Στο Σχήμα 5 απεικονίζεται μία τυπική μορφή καμπύλης συγκράτησης ύδατος σε όρους βαθμού κορεσμού ($S_r$) – φυσικού λογαρίθμου της μύζησης ($\ln s$). Στο ίδιο σχήμα παρουσιάζεται σκαριφηματικά και η εξέλιξη της συνύπαρξης της υγρής και της αέριας φάσης του εδάφους καθώς και το πώς αυτή συνδέεται ενδεικτικά με χαρακτηριστικές περιοχές της καμπύλης, οριοθετούμενες από χαρακτηριστικές τιμές της μύζησης.

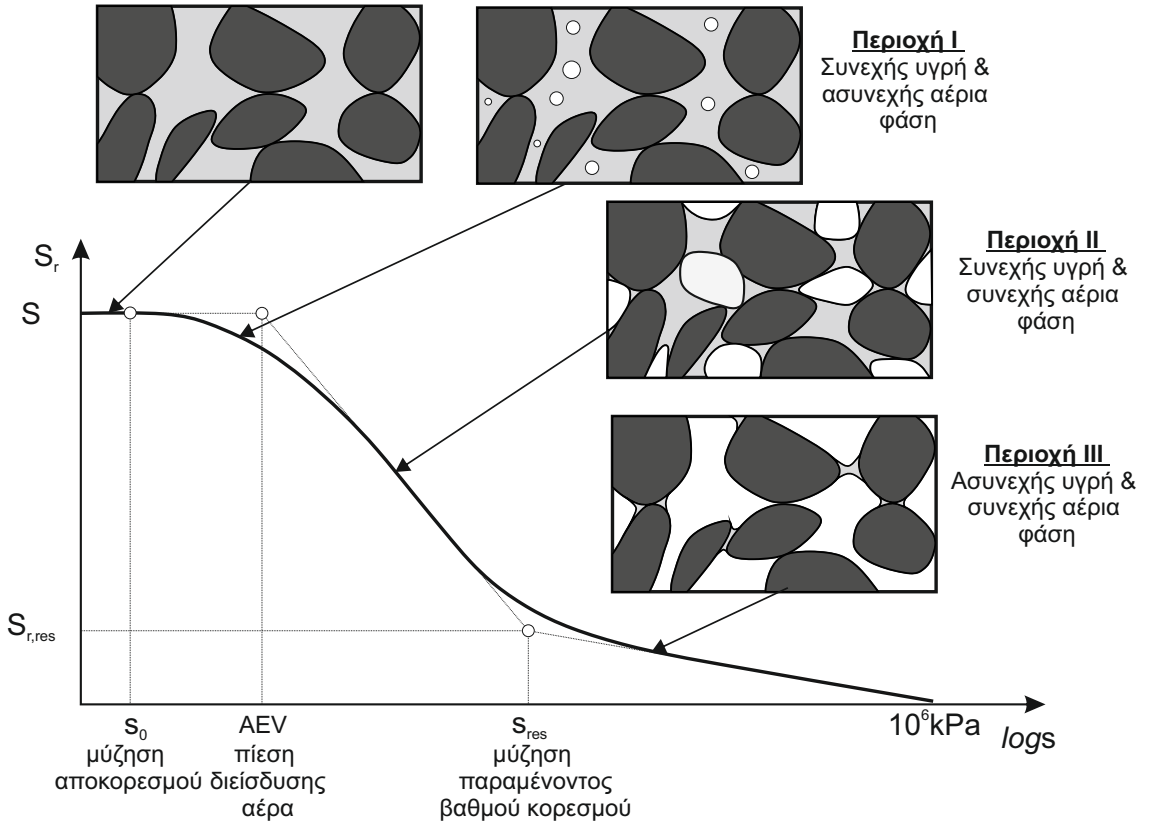


**Σχήμα 5:** Τυπική μορφή Καμπύλης Συγκράτησης Ύδατος σε όρους βαθμού κορεσμού ($S_r$) - φυσικού λογαρίθμου της μύζησης ($\ln s$).

Η καμπύλη συγκράτησης ύδατος εξαρτάται από τον τύπο του εδάφους (π.χ. όσο πιο λεπτόκοκκο ένα έδαφος τόσο μεγαλύτερο βαθμό κορεσμού μπορεί να διατηρήσει υπό δεδομένη τιμή της μύζησης), από τον λόγο κενών (μείωση του λόγου κενών αυξάνει την ικανότητα συγκράτησης ύδατος ενός δεδομένου εδάφους) καθώς και από το εάν εξετάζεται η ξήρανση ή η ύγρανση ενός εδάφους. Ο εργαστηριακός προσδιορισμός της καμπύλης συγκράτησης ύδατος καταλήγει σε ένα πλήθος εργαστηριακών δεδομένων σε διάφορα εύρη μύζησης, ανάλογα με τη

χρησιμοποιούμενη εργαστηριακή μέθοδο. Όμως σε επίπεδο αριθμητικής ανάλυσης της μηχανικής συμπεριφοράς των μη κορεσμένων εδαφών, είναι απαραίτητη η περιγραφή της καμπύλης συγκράτησης ύδατος μέσω μιας συνεχούς και συνεχώς παραγωγίσιμης μαθηματικής εξίσωσης.

Για τον σκοπό αυτό έχουν αναπτυχθεί διάφορα αριθμητικά προσομοιώματα περιγραφής της καμπύλης συγκράτησης ύδατος (water retention models) [π.χ. Van Genuchten (1980), Fredlund & Xing (1994), Gallipoli et al. (2003), Tarantino et al. (2009)]. Χρησιμοποιούνται κυρίως για την περιγραφή των εργαστηριακών δεδομένων μέσω αναλύσεων εύρεσης της βέλτιστης καμπύλης προσαρμογής αλλά και για την εκτίμηση της καμπύλης συγκράτησης ύδατος όταν δεν υπάρχουν διαθέσιμα εργαστηριακά. Τέτοιες εκτιμήσεις παρέχονται είτε μέσω εμπειρικών μεθόδων συσχέτισης των μεταβλητών των προσομοιωμάτων με φυσικά χαρακτηριστικά του εδάφους [π.χ. Zapata et al. (2000), Ganjian et al. (2007), Sitarenios et al. (2012)], είτε μέσω στατιστικών μεθόδων συσχέτισης της κοκκομετρικής διαβάθμισης των εδαφών με την δυνατότητα συγκράτησης ύδατος [π.χ. Arya & Paris (1981), Fredlund et al. (1997b), Fredlund et al. (2002)].

## 4.2 Η μηχανική συμπεριφορά των μη κορεσμένων εδαφών

Οι πρώτες απόπειρες συστηματικής μελέτης της μηχανικής συμπεριφοράς των μη κορεσμένων εδαφών επικεντρώθηκαν στην αναζήτηση μίας ενεργού παραμέτρου τάσης η οποία να δύναται να περιγράψει ενοποιημένα την αντοχή και την παραμορφωσιμότητα των μη κορεσμένων εδαφών κατά αντιστοιχία με την ενεργό τάση κατά Terzaghi για τα πλήρως κορεσμένα εδάφη (π.χ. Hilf (1956), Jennings (1957), Bishop (1959)).

Σήμερα είναι πλέον κοινά αποδεκτό ότι τέτοια παράμετρος τάσης δεν υφίσταται για τα μη κορεσμένα εδάφη και ως αποτέλεσμα η ανάλυση της μηχανικής τους συμπεριφοράς απαιτεί την υιοθέτηση **δύο ξεχωριστών παραμέτρων τάσης** για την περιγραφή της κατάστασης (Matyas & Radhakrishna (1968), Fredlund & Morgenstern (1977)) . Δύο είναι οι βασικοί συνδυασμοί παραμέτρων που έχουν επικρατήσει:

1. Η **ανοιγμένη ολική τάση** (net stress), η οποία αντιστοιχεί στην περίσσεια της

ολικής τάσης[3] ως προς την πίεση της αέριας φάσης:

$$\overline{\boldsymbol{\sigma}} = \overline{\boldsymbol{\sigma}} - u_a \tag{2}$$

σε συνδυασμό με τη **μύζηση** $s$.

2. Η **σταθμισμένη τάση του εδαφικού σκελετού του Bishop** (Bishop's average skeleton stress) υπολογιζόμενη ως:

$$\sigma = (\overline{\boldsymbol{\sigma}} - u_a) + \chi \cdot s \tag{3}$$

όπου $\chi$ παράμετρος στάθμισης της συνεισφοράς της μύζησης στην τάση του εδαφικού σκελετού. Η παράμετρος $\chi$ λαμβάνει τιμές από $0$ για ξηρό έδαφος έως και $1$ για πλήρως κορεσμένες εδαφικές καταστάσεις, με την απλούστερη επιλογή να αποτελεί η απευθείας αντιστοίχισή της με τον βαθμό κορεσμού ($\chi = S_r$). Και η τάση του Bishop χρησιμοποιείται σε συνδυασμό με τη **μύζηση** $s$, καθώς από μόνη της δεν είναι αρκετή για την πλήρη περιγραφή της μηχανικής συμπεριφοράς του εδάφους, **δεν αποτελεί δηλαδή ενεργό τάση**.

Ο πρώτος συνδυασμός (ολική τάση, μύζηση) προσφέρει έναν απλό και εύχρηστο τρόπο απεικόνισης συνήθων διαδρομών τάσης και για αυτό χρησιμοποιείται ευρέως στην επεξεργασία εργαστηριακών αποτελεσμάτων και στη διατύπωση αναλυτικών πλαισίων περιγραφής της μηχανικής συμπεριφοράς μη κορεσμένων εδαφών. Το βασικό μειονέκτημα της χρήση της ολικής τάσης έγκειται στην αδυναμία της να περιγράψει με έναν ενοποιημένο τρόπο τη μηχανική συμπεριφορά των εδαφών τόσο σε καταστάσεις μερικού όσο και πλήρους κορεσμού.

Από την άλλη μεριά, η τάση του Bishop σε καταστάσεις πλήρους κορεσμού μεταπίπτει στην ενεργό τάση κατά Terzaghi και δύναται να περιγράψει με έναν φυσικό τρόπο τη μετάβαση από καταστάσεις πλήρους σε καταστάσεις μερικού κορεσμού και το αντίστροφο, διευκολύνοντας σημαντικά την ταυτόχρονη και ενοποιημένη αριθμητική περιγραφή συνήθων πρακτικών προβλημάτων. Επιπρόσθετα, έχει αποδειχτεί ότι η τάση του Bishop δύναται να περιγράψει φυσικά την εξέλιξη της διατμητικής αντοχής με τη μύζηση ελαχιστοποιώντας την ανάγκη πρόσθετων παραδοχών σε καταστατικά προσομοίωματα της μηχανικής συμπεριφοράς μη κορεσμένων εδαφών.

[3]Στην παρούσα διατριβή τόσο για την ολική όσο και για την ανοιγμένη ολική τάση χρησιμοποιείται ο ίδιος συμβολισμός αφού πρακτικά συμπίπτουν.

Πλήθος εργαστηριακών διερευνήσεων της μηχανικής συμπεριφοράς μη κορεσμένων εδαφών υπάρχουν στην διεθνή βιβλιογραφία [π.χ. Escario & Saez (1973), Lawton et al. (1989), Wheeler & Sivakumar (1995), Cui & Delage (1996), Rampino et al. (2000), Barrera (2002), Casini (2008), Bardanis (2016)]. Τα

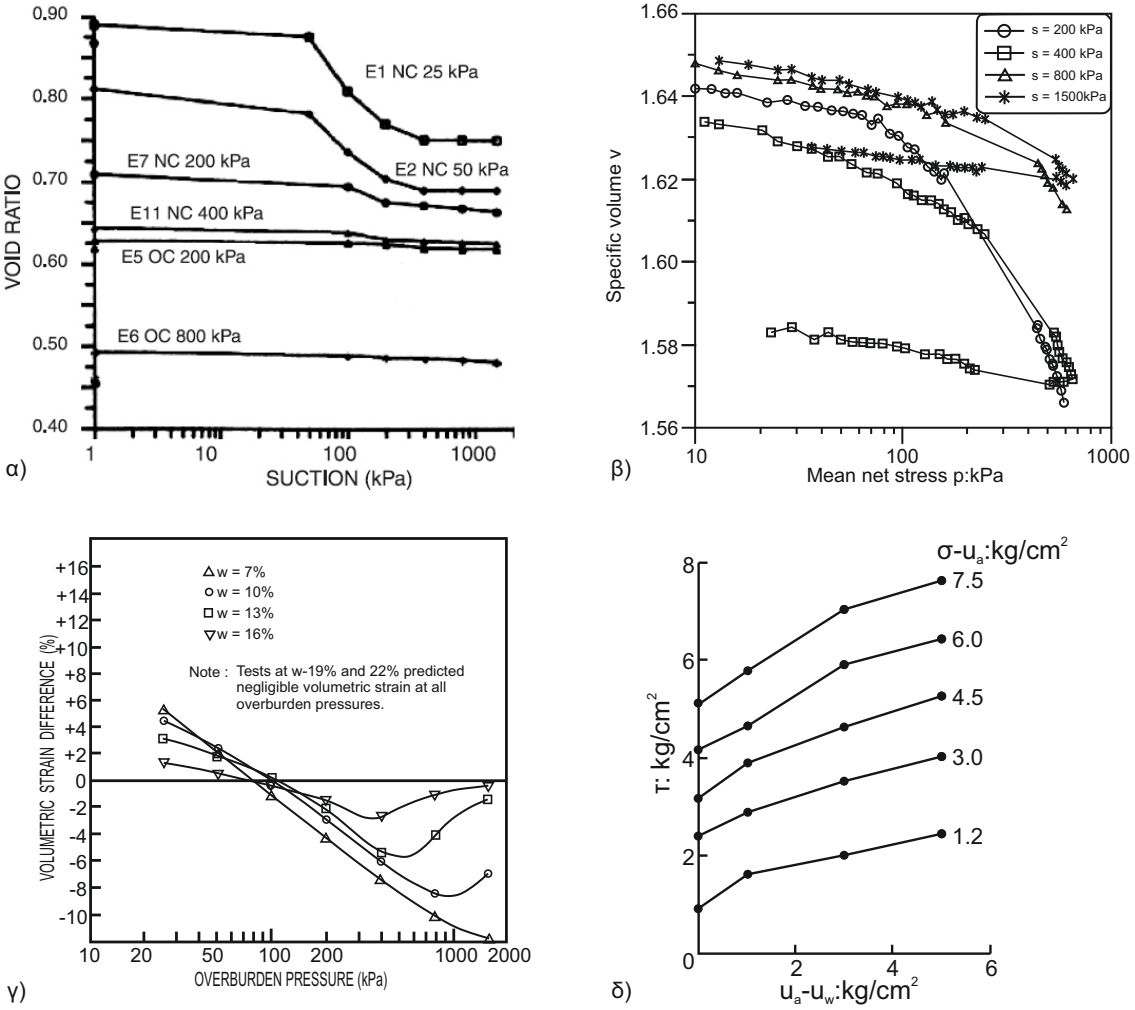


**Σχήμα 6:** α) Καμπύλες ξήρανσης αναζυμωμένης Josigny Silt (VICOL (1990)), από τους Cui & Delage (1996), β) καμπύλες ισότροπης συμπίεσης της Josigny Silt σε διαφορετικά επίπεδα μύζησης (Cui & Delage (1996)), γ) ογκομετρικές παραμορφώσεις κατά τη διαβροχή για μία συμπυκνωμένη αμμώδη αργιλο (Lawton et al. (1989)) και δ) εξέλιξη της διατμητικής αντοχής με τη μύζηση για ένα αργιλικό έδαφος (Escario & Saez (1986)).

κυριότερα μηχανικά χαρακτηριστικά των μη κορεσμένων εδαφών συνοψίζονται στα παρακάτω σημεία:

- Η ξήρανση (αύξηση της μύζησης) ενός αρχικώς πλήρως κορεσμένου εδαφικού στοιχείου οδηγεί σε αποκορεσμό, ο οποίος συνοδεύεται από μείωση του λόγου

κενών (όγκου). Η μείωση του λόγου κενών καταλήγει σε μία οριακή τιμή (residual void ratio), για την οποία περαιτέρω αύξηση της μύζησης αδυνατεί να μειώσει πρακτικά τον λόγο κενών (βλ. Σχήμα 6α).

- Ο μερικός κορεσμός αυξάνει την τάση διαρροής των εδαφών, τα οποία εμφανίζουν μία φαινόμενη τάση προφόρτισης (apparent preconsolidation pressure) ακόμα και εάν είναι κανονικά στερεοποιημένα στην πλήρως κορεσμένη κατάσταση. Η φαινόμενη τάση προφόρτισης αυξάνει με την αύξηση της μύζησης ακολουθώντας μειούμενο ρυθμό (βλ. Σχήμα 6β).

- Αύξηση της μύζησης οδηγεί σε μείωση της συμπιεστότητας, με τη συμπεριφορά να εξαρτάται και από το επίπεδο της επιβαλλόμενης τάσης (βλ. Σχήμα 6β).

- Σε κοινούς, μη διογκώσιμους εδαφικούς σχηματισμούς (non-expansive soils), η διαβροχή (μείωση της μύζησης) ενός εδάφους από μία αρχική κατάσταση μερικού κορεσμού δύναται να προκαλέσει είτε διόγκωση (swelling) είτε ογκομετρική κατάρρευση (volumetric collapse). Η συμπεριφορά εξαρτάται τόσο από το αρχικό επίπεδο της μύζησης όσο και από το επίπεδο τάσης υπό το οποίο λαμβάνει χώρα η διαβροχή. Αύξηση της αρχικής μύζησης καθώς και αύξηση της τάσης εγκιβωτισμού υπό δεδομένο αρχικό επίπεδο μύζησης ευνοεί την επίδειξη κατάρρευσης έναντι διόγκωσης. Οι παρατηρούμενες ογκομετρικές παραμορφώσεις λόγω διαβροχής είναι μη γραμμική συνάρτηση της επιβαλλόμενης τάσης, με την κατάρρευση λόγω διαβροχής από ένα δεδομένο αρχικό επίπεδο μύζησης να εμφανίζει μέγιστο (maximum of collapse) για κάποιο επίπεδο τάσης (εξάρτηση του τύπου του εδάφους και της αρχικής μύζησης) και σταθεροποίηση ή και μείωση για περαιτέρω αύξηση της τάσης (βλ. Σχήμα 6γ).

- Ο μερικός κορεσμός οδηγεί σε αύξηση της διατμητικής αντοχής των εδαφών. Η αύξηση αυτή είναι έντονα μη γραμμική, συνήθως λαμβάνει μία μέγιστη τιμή με τη μύζηση και ανάλογα με τον τύπο του εδάφους μπορεί να παρατηρηθεί και μείωση της αντοχής (σε σχέση με τη μέγιστη) για περαιτέρω αύξηση της μύζησης. Για παράδειγμα, αργιλικά εδάφη παρουσιάζουν συνήθως συνεχή αύξηση της αντοχής με τη μύζηση (με μειούμενο ρυθμό αύξησης) (βλ. Σχήμα 6δ), ενώ πιο χονδρόκοκκα εδάφη (ιλύες και άμμοι) παρουσιάζουν αρχικά αύξηση της αντοχής μέχρι σταθεροποίησής της περί μία μέγιστη τιμή που μπορεί να συνοδευτεί και από πτώση της αντοχής για περαιτέρω ξήρανση.

## 4.3 Καταστατική προσομοίωση των μη κορεσμένων εδαφών

Το πρώτο ολοκληρωμένο καταστατικό προσομοίωμα για μη κορεσμένα εδάφη είναι το Barcelona Basic Model (BBM). Το BBM διατυπώθηκε στον χώρο ολικής τάσης $\boldsymbol{\sigma}$ – μύζησης $s$ από τους Alonso et al. (1990) και οι βασικές ιδέες και αρχές που το διέπουν επηρέασαν καθοριστικά τη μετέπειτα διατύπωση καταστατικών προσομοιωμάτων καθώς - λίγο έως πολύ - κάθε καταστατικό προσομοίωμα της «μετά BBM εποχής» αποτελεί τροποποίηση ή βελτίωσή του. Τα βασικά χαρακτηριστικά του BBM συνοψίζονται ως εξής:

- Βασίζεται στις αρχές της Εδαφομηχανικής της Κρίσιμης Κατάστασης χρησιμοποιώντας ως προσομοίωμα βάσης το MCC για την περιγραφή της επιφάνειας διαρροής στον διεκτροπικό χώρο των τάσεων.

- Η επέκταση σε καταστάσεις μερικού κορεσμού υλοποιείται μέσω της καμπύλης φόρτισης – κατάρρευσης (loading-collapse), μιας καταστατικής επιφάνειας στον χώρο τάσης – μύζησης, η οποία περιγράφει με ενοποιημένο τρόπο την πλαστική διαρροή σε διαδρομές αύξησης της τάσης υπό σταθερή μύζηση και σε διαδρομές μείωσης της μύζησης υπό σταθερή τάση.

- Προβλέπει αύξηση της φαινόμενης τάσης προφόρτισης και της αντοχής με τη μύζηση καθώς και μείωση της συμπιεστότητας.

- Ενσωματώνει μια επιπρόσθετη επιφάνεια πλαστικής διαρροής σχετιζόμενη με τασικές διαδρομές αύξησης της μύζησης, η οποία μαζί με την επιφάνεια Φόρτισης - Κατάρρευσης οριοθετούν την ελαστική περιοχή στο επίπεδο $\overline{p}$ - $s$.

Στο σχήμα 7 παρουσιάζονται οι βασικές καταστατικές επιφάνειες του BBM.

Ακολουθώντας τις βασικές αρχές του BBM έχουν διατυπωθεί αρκετά καταστατικά προσομοίωματα στον χώρο ολικής τάσης - μύζησης [π.χ. Josa et al. (1992), Wheeler & Sivakumar (1995), Vaunat et al. (2000), Tang & Graham (2002), Georgiadis (2003)]. Τα περισσότερα περιλαμβάνουν τροποποιήσεις που σχετίζονται είτε με την πρόβλεψη της συμπιεστότητας είτε με την πρόβλεψη της αντοχής. Στοχεύουν στην εξάλειψη των σημαντικότερων αδυναμιών του BBM οι οποίες είναι: α) η πρόβλεψη μίας συνεχούς και γραμμικής αύξησης της αντοχής με τη μύζηση, β) η συνεχής μείωση του λόγου κενών με την αύξηση της μύζησης και γ) η αδυναμία πρόβλεψης ενός μέγιστου κατάρρευσης κατά τη διαβροχή. Επιπρόσθετα, το πλαίσιο μηχανικής συμπεριφοράς του BBM έχει χρησιμοποιηθεί και για την περιγραφή της μηχανικής

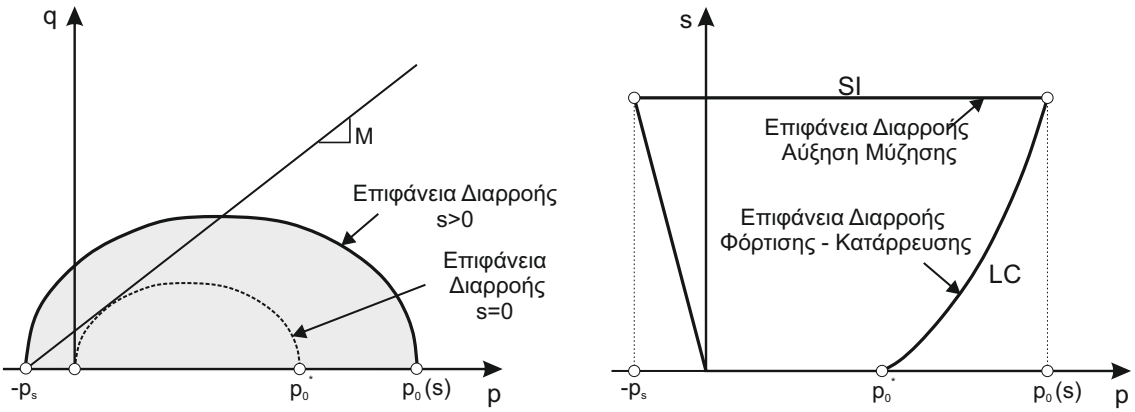


**Σχήμα 7:** Οι βασικές καταστατικές επιφάνειες του Barcelona Basic Model στον χώρο $p-q$ και στον χώρο $p-s$.

συμπεριφοράς μη κορεσμένων και ανισότροπα στερεοποιημένων εδαφικών υλικών [π.χ. Cui & Delage (1996), Stropeit et al. (2008)] ή και για τη συμπεριφορά των άμμων σε καταστάσεις μερικού κορεσμού [π.χ. Rampino et al. (2000)].

Τα τελευταία χρόνια ακολουθώντας κάποιες πρώτες προσπάθειες από τους Kohgo et al. (1993) και Bolzon et al. (1996), τα σύγχρονα καταστατικά προσομοίωματα για μη κορεσμένα εδάφη βασίζονται στη χρήση της τάσης του Bishop ως την **πρώτη καταστατική μεταβλητή** (First Constitutive Variable). Ορόσημο θεωρείται η δουλειά της Jommi (2000), η οποία ξεκινώντας από το καταστατικό προσομοίωμα MCC αντικατέστησε την ενεργό τάση με την τάση του Bishop για να μελετήσει την προκύπτουσα συμπεριφορά σε επίπεδο ολικής τάσης - μύζησης συγκρίνοντάς τη με τις προβλέψεις του BBM.

Συμπέρανε ότι η εφαρμογή της τάσης του Bishop σε καταστατικά προσομοίωματα για κορεσμένα εδάφη αρκεί για να περιγραφεί η εξέλιξη της αντοχής και της κρίσιμης κατάστασης με τη μύζηση, καθώς και η συμπεριφορά σε ελαστικές φορτίσεις που οφείλονται τόσο σε μεταβολές της τάσης όσο και σε μεταβολές της μύζησης. Επισήμανε δε και τόνισε το γεγονός ότι είναι απαραίτητη η εισαγωγή μιας επιπλέον, **δεύτερης καταστατικής μεταβλητής** (Second Constitutive Variable) - πέραν της τάσης του Bishop - η οποία θα περιγράφει την εξέλιξη της συμπιεστότητας με τον μερικό κορεσμό σε πλαστικές φορτίσεις, θα περιγράφει δηλαδή την καμπύλη φόρτισης – κατάρρευσης.

Στη διεθνή βιβλιογραφία υφίστανται διάφορες επιλογές σχετικά με τη δεύτερη καταστατική παράμετρο σε καταστατικά προσομοίωματα που υιοθετούν την τάση του Bishop ως την πρώτη τους καταστατική παράμετρο. Βασικότερες επιλογές δεύτερης καταστατικής παραμέτρου αποτελούν: α) η μύζηση [π.χ. Jommi

(2000), Loret & Khalili (2000), Gonzalez & Gens (2011)], β) η τροποποιημένη μύζηση [π.χ. Gallipoli et al. (2003)] και γ) ο βαθμός κορεσμού [π.χ. Zhang & Ikariya (2011), Zhou et al. (2012a), Casini (2012)].

# 5 Το προτεινόμενο πλαίσιο συμπιεστότητας

Το παρόν εδάφιο παρουσιάζει ένα νέο πλαίσιο συμπιεστότητας για ανισότροπα στερεοποιημένα, μη κορεσμένα εδάφη. Βασίζεται στο **πλαίσιο εγγενούς συμπιεστότητας** των Belokas & Kavvadas (2011) για καταστάσεις πλήρους κορεσμού ενώ η επέκτασή του για καταστάσεις μερικού κορεσμού υλοποιείται μέσω της υιοθέτησης καμπυλών παρθενικής συμπίεσης με συμπιεστότητα εξαρτώμενη τόσο από τη μύζηση όσο και από τον βαθμό κορεσμού.

Το πλαίσιο των Belokas & Kavvadas (2011) ακολουθεί την πρόταση των Lewin & Burland (1970) και προβλέπει ότι εγγενείς καταστάσεις ανισότροπα στερεοποιημένων εδαφικών υλικών υπό διαφορετικές τιμές του λόγου $K$ ή $n$, περιγράφονται στο επίπεδο $v - \ln p$ από μία απειρία παράλληλων καμπυλών οι οποίες ονομάζονται **καμπύλες εγγενούς συμπίεσης** (βλ. Σχήμα 8). Οι καμπύλες εγγενούς συμπίεσης περιγράφουν τη σχέση ειδικού όγκου (ή λόγου κενών) - μέσης ενεργού τάσης υπό διαφορετικά επίπεδα σταθεροποιημένης τασικής ανισοτροπίας και όπως φαίνεται στο σχήμα 8 αποτελούν καταστάσεις αναφοράς για ακτινικές τασικές οδεύσεις. Περιγράφονται από την εξίσωση:

$$v = N_n - \lambda \ln p \tag{4}$$

όπου $\lambda$ η κλίση και $N_n = f(n)$ παράμετρος, η οποία ελέγχει τη θέση των καμπυλών εγγενούς συμπίεσης στο επίπεδο $v - \ln p$.

Στο Σχήμα 8 παρατηρούμε ότι η γραμμή ισότροπης συμπίεσης και η γραμμή κρίσιμης κατάστασης περιγράφουν οριακές καταστάσεις φράζοντας την περιοχή πιθανής θέσης των καμπυλών εγγενούς συμπίεσης. Η ισότροπη συμπίεση προκαλεί την χαλαρότερη δυνατή δομή (ανώτερη τιμή του λόγου κενών), στην οποία μπορεί να βρεθεί ένα μη δομημένο (αναζυμωμένο σε πολτό) έδαφος ενώ η όλο και μεγαλύτερη παρουσία διάτμησης (μείωση $K$ ή αύξηση $n$) οδηγεί σε μειωμένες τιμές του δείκτη πόρων υπό δεδομένη μέση ενεργό τάση, με το κατώτερο όριο να περιγράφεται από τη γραμμή κρίσιμης κατάστασης (Gens (1982)). Κατά συνέπεια, η παράμετρος $N_n$ λαμβάνει τιμές από $N_{iso}$ για ισότροπη συμπίεση $K = 1.0 \rightarrow n = 0.0$ έως και $\Gamma$ για καταστάσεις επί της γραμμής κρίσιμης κατάστασης $n = M$.

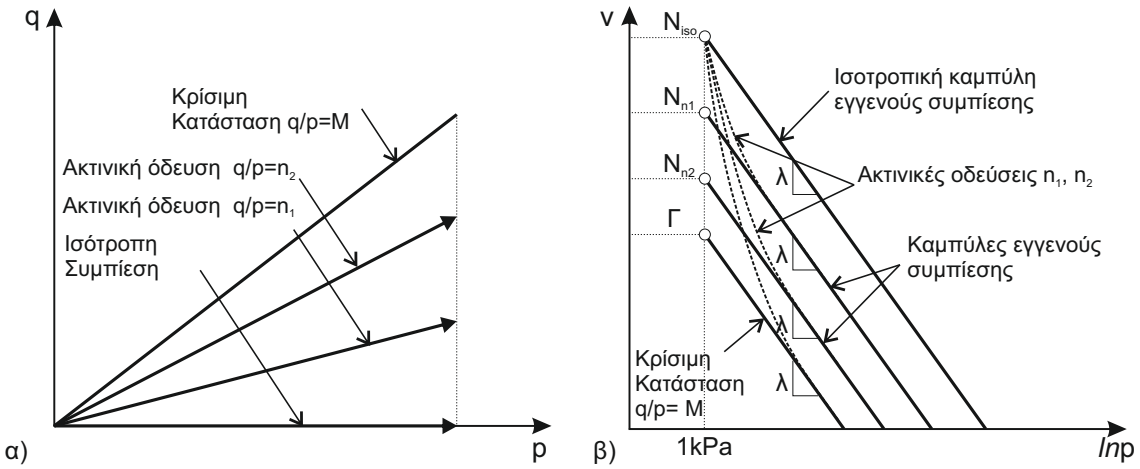


**Σχήμα 8:** α) Ακτινικές τασικές οδεύσεις στον χώρο $p$ - $q$ και β) οι καμπύλες εγγενούς συμπίεσης στο επίπεδο $v$ - $\ln p$.

Για την περιγραφή της συσχέτισης μεταξύ της επιβαλλόμενης τασικής ανισοτροπίας και της θέσης της αντίστοιχης καμπύλης εγγενούς συμπίεσης προτείνεται η σχέση:

$$N_n = \Gamma + (N_{iso} - \Gamma)\left(1 - \frac{(q/p)^2}{M^2}\right)^{r_s} \tag{5}$$

για τριαξονικές εντατικές καταστάσεις, η οποία μπορεί να γενικευτεί στον τριδιάστατο χώρο των τάσεων ώς:

$$N_n = \Gamma + (N_{iso} - \Gamma)\left(1 - \frac{\frac{1}{c^2}(\boldsymbol{s} : \boldsymbol{s})}{\sigma^2}\right)^{r_s} \tag{6}$$

Στις παραπάνω εξισώσεις η παράμετρος $r_s$ αποτελεί σταθερά του υλικού και πρέπει να υπολογίζεται για κάθε έδαφος ξεχωριστά από διαθέσιμα εργαστηριακά αποτελέσματα. Οι εξισώσεις 5 και 6 βασίζονται στις αντίστοιχες προτάσεις των Belokas & Kavvadas (2011), είναι δε ελαφρά τροποποιημένες με σκοπό την απλούστευση των μαθηματικών εκφράσεων που προκύπτουν για τον νόμο κρατύνσης του καταστατικού προσομοιώματος.

Για την επέκταση του πλαισίου συμπιεστότητας σε καταστάσεις μερικού κορεσμού χρησιμοποιείται η τάση του Bishop (εξίσωση 3). Για την παράμετρο $\chi$ χρησιμοποιείται ο **βαθμός κορεσμού του μακροπορώδους** (macro-structural degree of saturation), ο οποίος θα αναφέρεται ως **ενεργός βαθμός κορεσμού** και θα συμβολίζεται στο εξής $S_r^e$. Για τον υπολογισμό του ενεργού βαθμού κορεσμού υιοθετείται ο απλός εκθετικός

νόμος που προτάθηκε από τους Alonso et al. (2010):

$$S_r^e = (S_r)^\alpha \tag{7}$$

όπου $\alpha \geq 1.0$ παράμετρος του υλικού.

Η χρήση του ενεργού βαθμού κορεσμού στον υπολογισμό της τάση του Bishop βασίζεται σε εργαστηριακές παρατηρήσεις, οι οποίες συνηγορούν σε μία φυσική περιγραφή της εξέλιξης της διατμητικής αντοχής αλλά και της ελαστικής συμπεριφοράς των μη κορεσμένων εδαφικών υλικών με τη μύζηση όταν αυτός χρησιμοποιείται αντί του συνήθους συνολικού (μικρο- και μακρο-πορώδους) βαθμού κορεσμού. Το φυσικό νόημα του ενεργού βαθμού κορεσμού μπορεί να γίνει καλύτερα αντιληπτό σε αργιλικά εδάφη. Για παράδειγμα, ένα συμπυκνωμένο εδαφικό υλικό με ικανό αργιλικό κλάσμα συνήθως αναπτύσσει δύο επίπεδα πορώδους: α) ένα μικροπορώδες που αντιστοιχεί στους πόρους μεταξύ των αργιλικών πλακιδίων σε επίπεδο συσσωματωμάτων (intra-aggregate) και β) ένα μακροπορώδες μεταξύ των συσσωματωμάτων (inter-aggregate). Σε κοινούς, μη διογκώσιμους εδαφικούς σχηματισμούς η μηχανική συμπεριφορά ελέγχεται κυρίως από τη συνύπαρξη της υγρής και της αέριας φάσης μέσα στους μεγαλύτερους πόρους, με το μικροπορώδες να παραμένει πρακτικά πλήρως κορεσμένο για συνήθεις τιμές της μύζησης που απαντώνται σε προβλήματα μηχανικού.

Το γεγονός αυτό επιβάλει την απομείωση του βαθμού κορεσμού που χρησιμοποιείται στην περιγραφή της μηχανικής συμπεριφοράς, καθώς σε αντίθετη περίπτωση η τάση του Bishop λαμβάνει ιδιαίτερα υψηλές, μη ρεαλιστικές τιμές. Είναι προφανές ότι η απομείωση γίνεται τόσο πιο έντονη όσο πιο αργιλικό είναι ένα έδαφος, κάτι το οποίο αντικατοπτρίζεται και στις τιμές που μετρήθηκαν και προτάθηκαν από τους Alonso et al. (2010) για την παράμετρο $\alpha$ και κυμαίνονται από πολύ κοντά στη μονάδα για αμμώδη εδάφη, γύρω στο $2.0$ με $3.0$ για ιλυώδη εδάφη και έως και μεγαλύτερες από $6.0$ για αργίλους.

Όπως συζητήθηκε και στο προηγούμενο εδάφιο, η χρήση της τάσης του Bishop από μόνης της δεν είναι αρκετή για να περιγράψει την εδαφική συμπεριφορά καθώς δεν αποτελεί ενεργό παράμετρο. Η ανάγκη για επιπρόσθετες ανεξάρτητες καταστατικές παραμέτρους προκύπτει από την ανάγκη περιγραφής της εξέλιξης της συμπιεστότητας και της φαινόμενης τάσης προφόρτισης με τον μερικό κορεσμό. Το προτεινόμενο πλαίσιο μηχανικής συμπεριφοράς χρησιμοποιεί τόσο τη μύζηση $s$ όσο και τον ενεργό βαθμό κορεσμού $S_r^e$ ως επιπλέον καταστατικές παραμέτρους. Παρόλα

αυτά, πρακτικά μόνο η μύζηση αποτελεί πραγματικά ανεξάρτητη παράμετρο τάσης καθώς ο βαθμός κορεσμού είναι απόρροια της δυνατότητας συγκράτησης ύδατος του εδάφους και υπολογίζεται μέσω της καμπύλης συγκράτησης ύδατος.

Το Σχήμα 9 παρουσιάζει την επέκταση του πλαισίου εγγενούς συμπιεστότητας σε καταστάσεις μερικού κορεσμού. Παρατηρούμε ότι καταστάσεις μερικού κορεσμού θεωρούνται δομημένες καταστάσεις, βρίσκονται δε στα δεξιά των καμπυλών εγγενούς συμπίεσης στο επίπεδο $v - \ln p$ στη μετασταθερή (meta-stable) περιοχή συμπεριφοράς σύμφωνα με τον Kavvadas (2000). Στο προτεινόμενο πλαίσιο συμπιεστότητας η παρθενική συμπίεση μη κορεσμένων εδαφικών υλικών περιγράφεται από καμπύλες συμπίεσης με κλίση εξαρτώμενη τόσο από τη μύζηση όσο και από τον ενεργό βαθμό κορεσμού, ενώ η θέση τους ορίζεται επί της αντίστοιχης καμπύλης εγγενούς συμπίεσης (κορεσμένη κατάσταση) σε μία πίεση αναφοράς $p^c$. Για την περιγραφή της εξέλιξης της συμπιεστότητας προτείνεται η σχέση:

$$\lambda(s, S_r^e) = \lambda - (\lambda - \lambda(s))\,(1 - S_r^e)^\gamma \tag{8}$$

Στη σχέση 8 ο όρος $\lambda(s)$ περιγράφει την εξέλιξη της συμπιεστότητας αποκλειστικά με τη μύζηση. Μπορεί να ενσωματωθεί οποιαδήποτε κατάλληλη έκφραση που να προβλέπει μείωση της συμπιεστότητας με αύξηση της μύζησης ($\lambda(s) < \lambda$). Ο όρος $(1 - S_r^e)^\gamma$ προβλέπει αύξηση της συμπιεστότητας με την αύξηση του βαθμού κορεσμού και ενσωματώνεται για τους παρακάτω λόγους:

- Εξασφαλίζει ότι σε καταστάσεις πλήρους κορεσμού, ανεξαρτήτως του επίπεδου της επιβαλλόμενης μύζησης [4], η συμπιεστότητα του εδάφους περιγράφεται από τις εγγενείς καμπύλες. Αυτό είναι πολύ σημαντικό για πλαίσια μηχανικής συμπεριφοράς που κάνουν χρήση της τάσης του Bishop καθώς αυτή, στον πλήρη κορεσμό, συμπίπτει με την ενεργό τάση κατά Terzaghi και η μηχανική συμπεριφορά ακολουθεί αυτή των κορεσμένων εδαφών.

- Σε καταστάσεις συμπίεσης υπό σταθερή μύζηση η μείωση του λόγου κενών προκαλεί αύξηση της δυνατότητας συγκράτησης ύδατος ενός δεδομένου εδάφους, με αποτέλεσμα ο βαθμός κορεσμού να αυξάνεται. Καμπύλες συμπίεσης εξαρτώμενες αποκλειστικά από το επίπεδο της μύζησης προβλέπουν συμπίεση υπό σταθερή συμπιεστότητα, ενώ στην πραγματικότητα η μεταβολή

[4] Ένα έδαφος μπορεί να παραμείνει κορεσμένο ακόμα και υπό σημαντικά επίπεδα αρνητικής πίεσης πόρων (π.χ. ύψος τριχοειδούς ανύψωσης)

του βαθμού κορεσμού ακόμα και υπό σταθερή μύζηση επηρεάζει τη μηχανική συμπεριφορά των εδαφών.

Αυτό γίνεται καλύτερα κατανοητό αν αναλογιστούμε ότι εν γένει η μειωμένη συμπιεστότητα ενός μη κορεσμένου εδάφους οφείλεται στην ανάπτυξη εφελκυστικών δυνάμεων στον εδαφικό σκελετό μεταξύ των κόκκων ή και των συσσωματωμάτων (π.χ. λόγω υδατικών μηνίσκων), οι οποίες δρουν παρόμοια με άλλους παράγοντες επιβολής δομής, όπως για παράδειγμα η σιμέντωση. Το πλήθος των δυνάμεων αυτών ελέγχεται κυρίως από το βαθμό κορεσμού ενώ η έντασή τους από τη μύζηση (Gallipoli et al. (2003)). Καθώς λοιπόν ο βαθμός κορεσμού αυξάνεται κατά τη συμπίεση, ένα διαρκώς μειούμενο πλήθος ελκτικών δυνάμεων μεταξύ των κόκκων δρα στον εδαφικό σκελετό, με αποτέλεσμα προοδευτικά να αυξάνεται η συμπιεστότητα του εδαφικού σκελετού (βλ. διακεκομμένη γραμμή στο Σχήμα 8).

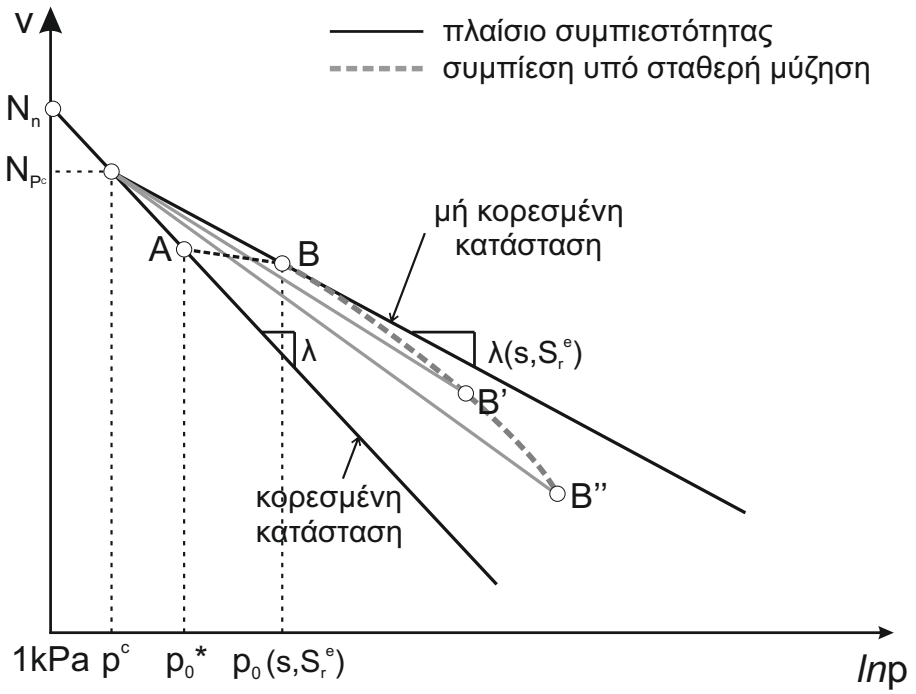


**Σχήμα 9:** Επέκταση του πλαισίου συμπιεστότητας για καταστάσεις μερικού κορεσμού. Η συμπεριφορά στο επίπεδο $v - \ln p$.

Επανερχόμενοι στον όρο $\lambda(s)$, στο προτεινόμενο πλαίσιο μηχανικής συμπεριφοράς υιοθετείται η εξίσωση του BBM:

$$\lambda(s) = \lambda \left[ (1 - r)\, e^{-\beta s} + r \right] \tag{9}$$

Η εξίσωση 9 απομειώνει τη συμπιεστότητα με την αύξηση της μύζησης, με μειούμενο ρυθμό ελεγχόμενο μέσω της παραμέτρου $\beta$, ενώ προσεγγίζει εκθετικά ένα ελάχιστο επίπεδο ελεγχόμενο από την παράμετρο $r$. Και οι δύο προαναφερθείσες παράμετροι θεωρούνται εδαφικές σταθερές. Αντικαθιστώντας την εξίσωση 9 στην εξίσωση 8 προκύπτει τελικώς η εξίσωση:

$$\lambda(s, S_r^e) = \lambda \left[1 - (1 - r)\left(1 - S_r^e\right)^{\gamma} \left(1 - e^{-\beta s}\right)\right] \tag{10}$$

Με βάση το προτεινόμενο πλαίσιο μηχανικής συμπεριφοράς, η φαινόμενη τάση προφόρτισης που αναπτύσσει ένα εδαφικό υλικό κατά την ξήρανση ($p_0(s, S_r^e)$) μπορεί να συνδεθεί με την αντίστοιχη τάση προφόρτισης υπό συνθήκες πλήρους κορεσμού $p_0^*$. Η αντιστοίχιση, όμοια με το BBM, γίνεται μέσω κατάλληλης καμπύλης αποφόρτισης - επαναφόρτισης με κλίση $\kappa$ (βλ. ευθεία A-B στο Σχήμα 9), ενώ συνδέοντας μαθηματικά τον δείκτη πόρων σε καθεμία από τις καταστάσεις προκύπτει:

$$p_0(s, S_r^e) = p^c \left(\frac{p_0}{p^c}\right)^{\frac{\lambda - \kappa}{\lambda(s, S_r^e) - \kappa}} \tag{11}$$

Η εξίσωση 11 περιγράφει την εξέλιξη της φαινόμενης τάσης προφόρτισης με τη μύζηση και τον βαθμό κορεσμού και χρησιμοποιείται στο εδάφιο που ακολουθεί για την περιγραφή της καμπύλης Φόρτισης - Κατάρρευσης του προτεινόμενου καταστατικού προσομοιώματος.

# 6 Το προτεινόμενο καταστατικό προσομοίωμα

Το παρόν εδάφιο παρουσιάζει τη μαθηματική διατύπωση του προτεινόμενου νέου καταστατικού προσομοιώματος για ανισότροπα, μη κορεσμένα εδάφη. Το προσομοίωμα διατυπώνεται στον γενικευμένο χώρο των τάσεων ($\sigma, \boldsymbol{s}$) και αποσκοπεί στην περιγραφή της μηχανικής συμπεριφοράς κοινών, μη διογκώσιμων αργιλικών εδαφών. Βασίζεται στην Εδαφομηχανική της Κρίσιμης Κατάστασης και στις αρχές της γενικευμένης θεωρίας της πλαστικότητας, κατάλληλα διατυπωμένης για καταστάσεις μερικού κορεσμού. Για την περιγραφή της κατάστασης απαιτούνται οι ακόλουθες εξωτερικές και εσωτερικές μεταβλητές κατάστασης:

- **Εξωτερικές μεταβλητές κατάστασης**:
  - ◇ ο τανυστής της τάσης του Bishop, $\boldsymbol{\sigma} = (\overline{\boldsymbol{\sigma}} - u_a \cdot \boldsymbol{I}) + S_r^e \cdot s \cdot \boldsymbol{I}$

- η μύζηση, $s$
- ο ενεργός βαθμός κορεσμού, $S_r^e$
- ο τανυστής των παραμορφώσεων, $\boldsymbol{\varepsilon}$
- ο ειδικός όγκος $v = 1 + e$, όπου $e$ ο λόγος κενών

- **Εσωτερικές μεταβλητές κατάστασης**:
  - η προβολή του κέντρου της επιφάνειας διαρροής ($a$) στον ισότροπο άξονα υπό κορεσμένες συνθήκες
  - ο τανυστής ανισοτροπίας ($\boldsymbol{b}$), ο οποίος περιγράφει τη μνήμη της τασικής ανισοτροπίας

Το προτεινόμενο καταστατικό προσομοίωμα κάνει χρήση της βασικής κινηματικής παραδοχής της θεωρίας της πλαστικότητας περί του διαχωρισμού της συνολικής επαύξησης της παραμόρφωσης σε μία ελαστική $\dot{\boldsymbol{\varepsilon}}^e$ (αναστρέψιμη) και μία πλαστική $\dot{\boldsymbol{\varepsilon}}^p$ (μη αναστρέψιμη) συνιστώσα:

$$\dot{\boldsymbol{\varepsilon}} = \dot{\boldsymbol{\varepsilon}}^e + \dot{\boldsymbol{\varepsilon}}^p \tag{12}$$

## 6.1 Ελαστικότητα

Για την περιγραφή της ελαστικής συμπεριφοράς το προτεινόμενο προσομοίωμα υιοθετεί τον ποροελαστικό νόμο συμπεριφοράς του MCC, κάνοντας χρήση της τάσης του Bishop αντί της ενεργού τάσης του Terzaghi, τροποποίηση η οποία θεωρείται επαρκής για την πλήρη περιγραφής της ελαστικής συνιστώσας της παραμόρφωσης τόσο σε καταστάσεις πλήρους όσο και μερικού κορεσμού. Το μέτρο ισότροπης συμπίεσης $K$ υπολογίζεται ως:

$$K = \frac{v\sigma}{\kappa} \tag{13}$$

ενώ το μέτρο διάτμησης υπολογίζεται ως:

$$G = \frac{1}{2}\left(\frac{2G}{K}\right)K \tag{14}$$

όπου $\kappa$ η κλίση των καμπυλών αποφόρτισης επαναφόρτισης στο επίπεδο $v - \ln\sigma$. Η ποσότητα $\dfrac{2G}{K}$ θεωρείται παράμετρος του υλικού και υπολογίζεται μέσω του λόγου του Poisson με χρήση της σχέσης:

$$\frac{2G}{K} = \frac{3\,(1-2\nu)}{1+\nu} \tag{15}$$

Έχοντας υπολογίσει τοσό το μέτρο ισότροπης συμπίεσης όσο και το μέτρο διάτμησης, με βάση τη γραμμική ισότροπη ελαστικότητα μία επαύξηση του τανυστή της Bishop τάσης υπολογίζεται ως:

$$\dot{\boldsymbol{\sigma}} = \boldsymbol{C^{\varepsilon}} : \dot{\boldsymbol{\varepsilon}}^e \Rightarrow \begin{Bmatrix} \dot{\sigma} \\ \dot{\boldsymbol{s}} \end{Bmatrix} = \begin{pmatrix} K & \mathbf{0} \\ \mathbf{0} & 2G \end{pmatrix} : \begin{Bmatrix} \dot{\varepsilon}^e \\ \dot{\boldsymbol{e}}^e \end{Bmatrix} \tag{16}$$

όπου $\boldsymbol{C^{\varepsilon}}$ το ελαστικό μητρώο στιβαρότητας ή ελαστική Ιακωβιανή (Elastic Jacobian).

## 6.2 Επιφάνεια Διαρροής

Το προτεινόμενο καταστατικό προσομοίωμα περιλαμβάνει μοναδική καταστατική επιφάνεια, η οποία αποτελεί την επιφάνεια διαρροής και διαχωρίζει μεταξύ ελαστικών και πλαστικών καταστάσεων. Πρόκειται για ένα στρεβλό ελλειψοειδές, το οποίο βασίζεται στην πρόταση εξίσωσης διαρροής του Kavvadas (1982). Η επέκτασή της για καταστάσεις μερικού κορεσμού γίνεται μέσω της εξίσωσης 11 για την περιγραφή της εξέλιξης του μεγέθους του ελλειψοειδούς ως συνάρτηση της μύζησης και του ενεργού βαθμού κορεσμού, καταλήγοντας στην ακόλουθη **εξίσωση διαρροής**:

$$f\left(\sigma, \boldsymbol{s}, \alpha\left(s, S_r^e\right), \boldsymbol{b}\right) = \frac{1}{k^2}(\boldsymbol{s}-\sigma\boldsymbol{b}) : (\boldsymbol{s}-\sigma\boldsymbol{b}) - \sigma(2\alpha\left(s, S_r^e\right) - \sigma) \tag{17}$$

όπου:

- $\sigma$: η μέση τάση του Bishop, $\sigma = \frac{1}{3}\boldsymbol{\sigma} : \boldsymbol{I}$
- $\boldsymbol{s}$: η διεκτροπική συνιστώσα του τανυστή τάσης, $\boldsymbol{s} = \boldsymbol{\sigma} - \sigma\boldsymbol{I}$
- $k$: παράμετρος του υλικού που καθορίζει την αναλογία των αξόνων του ελλειψοειδούς σε κάθε διεκτροπικό επίπεδο

- $\boldsymbol{b}$: ο τανυστής ανισοτροπίας· περιγράφει την κλίση του κύριου άξονα του ελλειψοειδούς σε κάθε διεκτροπικό επίπεδο και αποτελεί παράμετρο κράτυνσης

- $\alpha\left(s, S_r^e\right)$: η προβολή του κέντρου του ελλειψοειδούς στον ισότροπο άξονα που καθορίζει το μέγεθος του ελλειψοειδούς και περιγράφεται από την εξίσωση:

$$\alpha(s, S_r^e) = \frac{p^c}{2}\left(\frac{2\cdot\alpha}{p^c}\right)^{\frac{\lambda-\kappa}{\lambda(s,S_r^e)-\kappa}} \tag{18}$$

όπου:

  - $\alpha$: παράμετρος ισότροπης κράτυνσης του προσομοιώματος, πάντα αναφερόμενη σε καταστάσεις πλήρους κορεσμού και
  - $\lambda(s, S_r^e)$: η κλίση των καμπυλών συμπίεσης με βάση την εξίσωση 10 του προτεινόμενου πλαισίου συμπιεστότητας.

Το Σχήμα 10 παρουσιάζει την επιφάνεια διαρροής του προτεινόμενου καταστατικού προσομοιώματος. Η κλίση του ελλειψοειδούς ως προς τον ισότροπο άξονα, όπως περιγράφεται από τον τανυστή $\boldsymbol{b}$, αναπαριστά την ανάπτυξη προτιμητέων διευθύνσεων του εδαφικού υλικού στον χώρο των τάσεων ως απόρροια της επιβαλλόμενης τασικής ανισοτροπίας. Καταστάσεις εντός της επιφάνειας διαρροής θεωρούνται ελαστικές ενώ η διακεκομμένη ομοιόθετη επιφάνεια μικρότερου μεγέθους σηματοδοτεί τη θέση της επιφάνεια διαρροής για κορεσμένες καταστάσεις.

Παρατηρούμε ότι ο μερικός κορεσμός αυξάνει το μέγεθος της ελαστικής περιοχής, αυξάνοντας το μέγεθος του ελλειψοειδούς κατά τη διεύθυνση της αρχικής ανισοτροπίας που αναφέρεται στην κορεσμένη κατάσταση. Η αύξηση ακολουθεί τη φαινόμενη τάση προφόρτισης μέσω της επιφάνειας Φόρτισης - Κατάρρευσης. Η επιφάνεια Φόρτισης - Κατάρρευσης αποτελεί και αυτή επιφάνεια διαρροής του προσομοιώματος και μαζί με το στρεβλό ελλειψοειδές οριοθετούν την ελαστική περιοχή στον χώρο $\sigma - \boldsymbol{s} - s$. Επιπρόσθετα η επιφάνεια διαρροής σε καταστάσεις πλήρους κορεσμού και μηδενικής τασικής ανισοτροπίας ($\boldsymbol{b} = \boldsymbol{0}$) μεταπίπτει στην επιφάνεια διαρροής του MCC.

Έχοντας ορίσει την επιφάνεια διαρροής μπορούμε να ορίσουμε ότι οποιαδήποτε ελαστική φόρτιση σχετίζεται με μία από τις ακόλουθες δύο καταστάσεις:

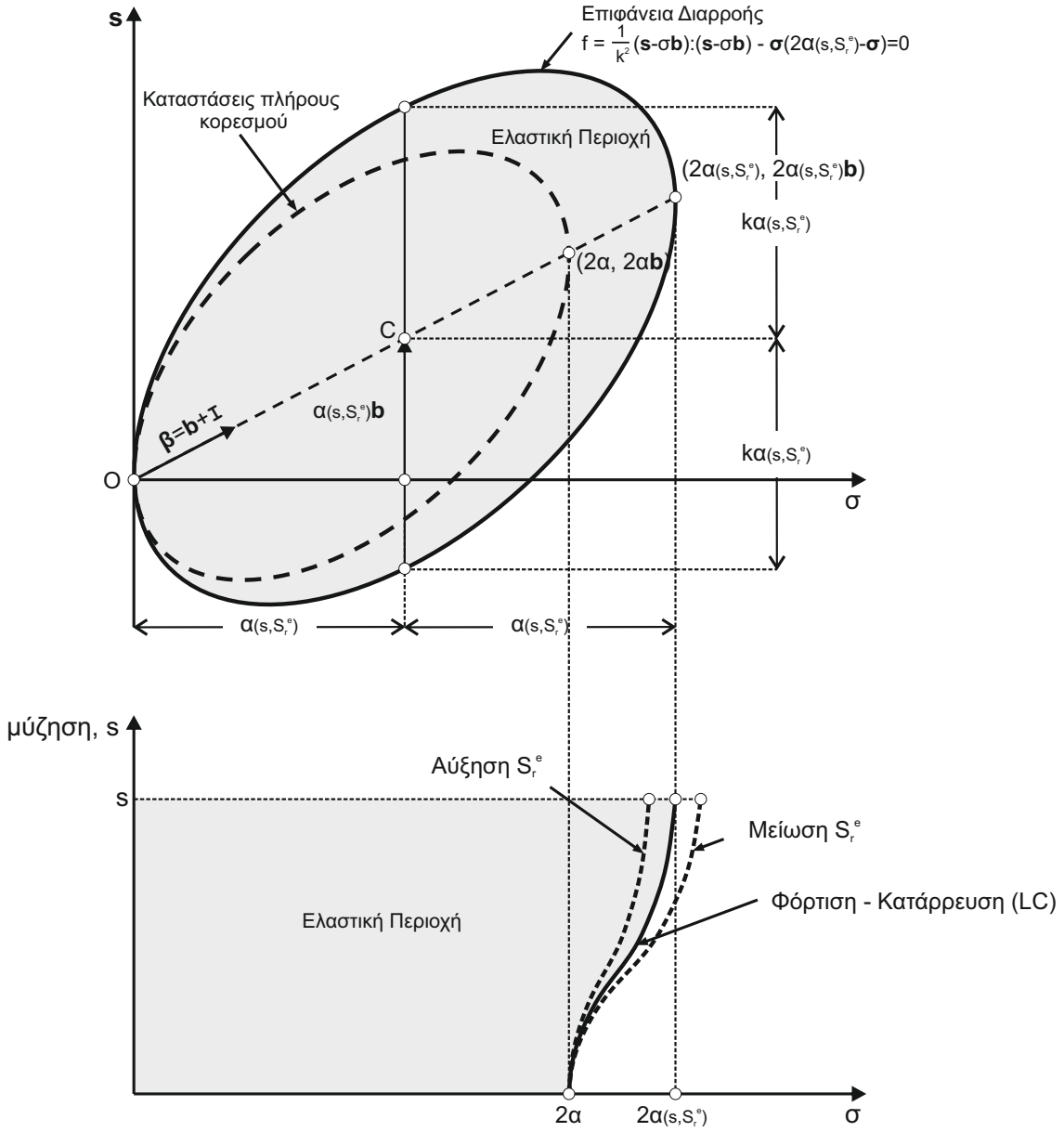


**Σχήμα 10:** Οι βασικές καταστατικές επιφάνειες του προτεινόμενου καταστατικού προσομοιώματος στον χώρο $\sigma - \boldsymbol{s} - s$.

1. Μία ελαστική αρχική κατάσταση ($f(\boldsymbol{\sigma}, s, S_r^e) < 0$) και
   μία ελαστική τελική κατάσταση ($f(\boldsymbol{\sigma} + \dot{\boldsymbol{\sigma}}, s + \dot{s}, S_r^e + \dot{S}_r^e) < 0$)

2. Μία πλαστική αρχική κατάσταση ($f(\boldsymbol{\sigma}, s, S_r^e) = 0$) και
   μια ελαστική τελική κατάσταση ($f(\boldsymbol{\sigma} + \dot{\boldsymbol{\sigma}}, s + \dot{s}, S_r^e + \dot{S}_r^e) < 0$)

Επιπρόσθετα, με δεδομένο ότι η επιλεγμένη επιφάνεια πλαστικής διαρροής είναι: α) μονοτονική συνάρτηση τόσο της μύζησης όσο και του βαθμού κορεσμού και β) ότι

οι προβολές της σε κάθε διεκτροπικό επίπεδο είναι κοίλες επιφάνειες, μπορούμε να υπολογίσουμε πως με αναφορά μία πλαστική αρχική κατάσταση ($f(\boldsymbol{\sigma}, s, S_r^e) = 0$) μία τελική ελαστική κατάσταση ($f(\boldsymbol{\sigma} + \dot{\boldsymbol{\sigma}}, s + \dot{s}, S_r^e + \dot{S}_r^e) < 0$) απαιτεί:

$$\boldsymbol{Q} : \dot{\boldsymbol{\sigma}} + \frac{\partial f}{\partial s}\dot{s} + \frac{\partial f}{\partial S_r^e}\dot{S}_r^e < 0 \tag{19}$$

όπου $\boldsymbol{Q} = \frac{\partial f}{\partial \boldsymbol{s}}$. Τέτοιες ελαστικές φορτίσεις, οδηγούν σε καθαρά ελαστική παραμόρφωση ($\dot{\boldsymbol{\varepsilon}} = \dot{\boldsymbol{\varepsilon}}^e$) και με βάση τον ελαστικό νόμο του προσομοιώματος μπορούμε να υπολογίσουμε:

$$\dot{\boldsymbol{\sigma}} = \boldsymbol{C}^e : \dot{\boldsymbol{\varepsilon}}^e = \boldsymbol{C}^e : \dot{\boldsymbol{\varepsilon}} \tag{20}$$

Αντικαθιστώντας την επαύξηση της τάσης στην εξίσωση 19 με την εξίσωση 20 αποδεικνύεται ότι **ελαστική φόρτιση συμβαίνει όταν**:

$$\boldsymbol{Q} : \boldsymbol{C}^e : \dot{\boldsymbol{\varepsilon}} + \frac{\partial f}{\partial s}\dot{s} + \frac{\partial f}{\partial S_r^e}\dot{S}_r^e < 0 \tag{21}$$

Ορίζουμε ότι **για να συμβεί πλαστική φόρτιση πρέπει**:

$$\boldsymbol{Q} : \boldsymbol{C}^e : \dot{\boldsymbol{\varepsilon}} + \frac{\partial f}{\partial s}\dot{s} + \frac{\partial f}{\partial S_r^e}\dot{S}_r^e \geq 0 \tag{22}$$

Είναι σημαντικό να σημειωθεί ότι η πλαστική φόρτιση μπορεί να συμβεί ανεξάρτητα της τιμής της ποσότητας $\boldsymbol{Q} : \dot{\boldsymbol{\sigma}} + \frac{\partial f}{\partial s}\dot{s} + \frac{\partial f}{\partial S_r^e}\dot{S}_r^e > 0$. Πιο συγκεκριμένα, μπορούμε να ορίσουμε τις ακόλουθες τρεις **υποπεριπτώσεις πλαστικής φόρτισης**:

- $\boldsymbol{Q} : \dot{\boldsymbol{\sigma}} + \frac{\partial f}{\partial s}\dot{s} + \frac{\partial f}{\partial S_r^e}\dot{S}_r^e > 0$: **πλαστική κράτυνση**,
- $\boldsymbol{Q} : \dot{\boldsymbol{\sigma}} + \frac{\partial f}{\partial s}\dot{s} + \frac{\partial f}{\partial S_r^e}\dot{S}_r^e = 0$: **ουδέτερη φόρτιση** και
- $\boldsymbol{Q} : \dot{\boldsymbol{\sigma}} + \frac{\partial f}{\partial s}\dot{s} + \frac{\partial f}{\partial S_r^e}\dot{S}_r^e < 0$: **πλαστική χαλάρωση**.

## 6.3 Νόμος Ροής

Για τον υπολογισμό του πλαστικού μέρους της παραμόρφωσης που αναπτύσσεται κατά τη διάρκεια πλαστικών φορτίσεων το προτεινόμενο καταστατικό προσομοίωμα χρησιμοποιεί έναν μη συσχετισμένο νόμο ροής. Η επαύξηση των πλαστικών παραμορφώσεων υπολογίζεται μέσω μίας επαυξητικά γραμμικής σχέσης της

μορφής:

$$\dot{\boldsymbol{\varepsilon}}^p = \dot{\Lambda}\boldsymbol{P} \tag{23}$$

όπου $\dot{\Lambda}$ βαθμωτό μέγεθος που εκφράζει το μέτρο της επαύξησης των παραμορφώσεων, $H$ το πλαστικό μέτρο κράτυνσης και $\boldsymbol{P}$ ο τανυστής του πλαστικού δυναμικού, ο οποίος ελέγχει την κατεύθυνση των πλαστικών παραμορφώσεων.

Το βαθμωτό μέγεθος $\dot{\Lambda}$ υπολογίζεται μέσω της έκφρασης:

$$\dot{\Lambda} = \frac{1}{H}\left(\boldsymbol{Q} : \dot{\boldsymbol{\sigma}} + \frac{\partial f}{\partial s}\dot{s} + \frac{\partial f}{\partial S_r^e}\dot{S}_r^e\right) \tag{24}$$

Σε ότι αφορά τον τανυστή πλαστικού δυναμικού, αυτός υπολογίζεται μέσω του νόμου της καθετότητας ($\boldsymbol{P} = \dfrac{\partial g}{\partial \boldsymbol{\sigma}}$) επί της επιφάνειας πλαστικού δυναμικού (συνάρτηση $g$) του σχήματος 11. Παρατηρούμε ότι η υιοθετούμενη επιφάνεια πλαστικού δυναμικού είναι ένα στρεβλό ελλειψοειδές, παρόμοιας μορφής με την επιφάνεια διαρροής. Για την περιγραφή της χρησιμοποιείται η ακόλουθη **συνάρτηση πλαστικού δυναμικού**:

$$g(\sigma, \boldsymbol{s}, \theta, \boldsymbol{d}) = \frac{1}{c^2}(\boldsymbol{s} - \sigma\boldsymbol{d}) : (\boldsymbol{s} - \sigma\boldsymbol{d}) - \sigma(2\theta - \sigma) \tag{25}$$

όπου $\sigma$ η μέση τάση του Bishop, $\boldsymbol{s}$ η διεκτροπική συνιστώσα του τανυστή τάσης, $\theta$ παράμετρος που ελέγχει το μέγεθος της επιφάνειας πλαστικού δυναμικού, $\boldsymbol{d}$ τανυστής αντίστοιχος του τανυστή ανισοτροπίας, ο οποίος καθορίζει την κλίση του κύριου άξονα της επιφάνειας πλαστικού δυναμικού σε κάθε διεκτροπικό επίπεδο. Η παράμετρος $c$ είναι σταθερά του υλικού και περιγράφει την αναλογία των αξόνων του ελλειψοειδούς σε κάθε διεκτροπικό επίπεδο. Μπορεί να συσχετιστεί με την κλίση της γραμμής κρίσιμης κατάστασης $M$ του MCC μέσω της σχέσης:

$$c = \sqrt{2/3}M \tag{26}$$

Η κλίση της επιφάνειας πλαστικού δυναμικού επιλέχθηκε να ακολουθεί την αντίστοιχη της επιφάνειας διαρροής μέσω ενός συντελεστή αναλογίας $\chi$, ο οποίος συνδέει τον τανυστή $\boldsymbol{d}$ με τον τανυστή ανισοτροπίας $\boldsymbol{b}$:

$$\boldsymbol{d} = \chi\boldsymbol{b} \tag{27}$$

Η παράμετρος $\chi$ ελέγχει την πλαστική διαστολικότητα του προσομοιώματος και μπορεί να βαθμονομηθεί κατάλληλα στη βάση διαθέσιμων εργαστηριακών αποτελεσμάτων.

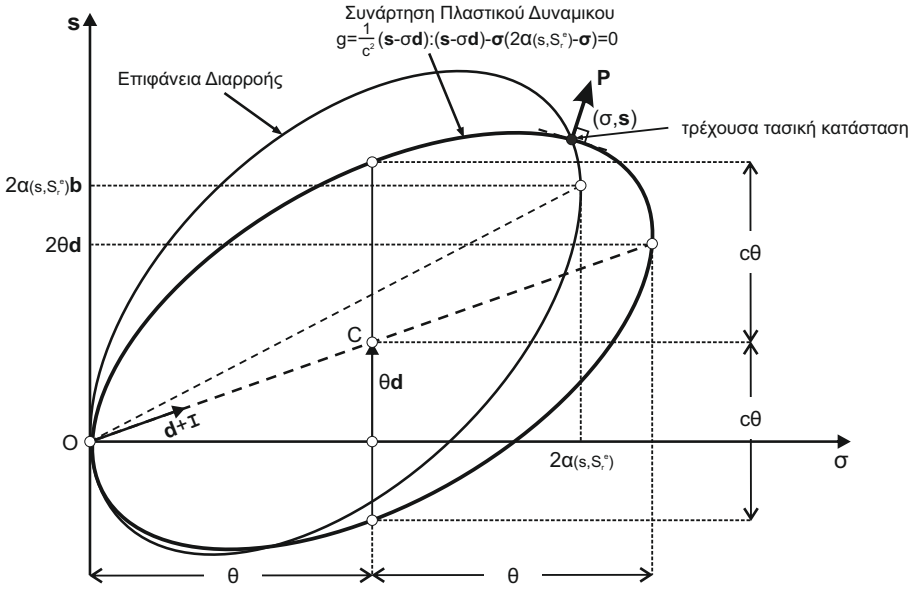


**Σχήμα 11:** Η επιφάνεια πλαστικού δυναμικού του προτεινόμενου μη σχετισμένου νόμου ροής.

Τέλος, το μέγεθος της επιφάνειας πλαστικού δυναμικού $\theta$ υπολογίζεται μέσω της απαίτησης η επιφάνεια πλαστικού δυναμικού να περνάει από την τρέχουσα τασική κατάσταση, καταλήγοντας στη σχέση:

$$\theta = \frac{1}{2}\left(\sigma + \frac{\frac{1}{c^2}\left(\boldsymbol{s} - \sigma\boldsymbol{d}\right) : \left(\boldsymbol{s} - \sigma\boldsymbol{d}\right)}{\sigma}\right) \tag{28}$$

Έχοντας διατυπώσει τον νόμο ροής του καταστατικού προσομοιώματος, οποιαδήποτε επαύξηση της τάσης μπορεί να υπολογιστεί ως:

$$\dot{\boldsymbol{\sigma}} = \boldsymbol{C}^e : \dot{\boldsymbol{\varepsilon}}^e = \boldsymbol{C}^e : \left(\dot{\boldsymbol{\varepsilon}} - \dot{\boldsymbol{\varepsilon}}^p\right) = \boldsymbol{C}^e : \left(\dot{\boldsymbol{\varepsilon}} - \dot{\Lambda}\boldsymbol{P}\right) \tag{29}$$

Επιπρόσθετα, αποδεικνύεται ότι το βαθμωτό μέγεθος $\dot{\Lambda}$ μπορεί να εκφραστεί ως συνάρτηση της επαύξησης των παραμορφώσεων με βάση τη σχέση:

$$\dot{\Lambda} = \frac{\boldsymbol{Q} : \boldsymbol{C}^e : \dot{\boldsymbol{\varepsilon}} + \frac{\partial f}{\partial s}\dot{s} + \frac{\partial f}{\partial S_r^e}\dot{S}_r^e}{H + \boldsymbol{Q} : \boldsymbol{C}^e : \boldsymbol{P}} \tag{30}$$

## 6.4 Νόμος Κράτυνσης

Το προτεινόμενο καταστατικό προσομοίωμα ενσωματώνει έναν μικτό νόμο κινηματικής κράτυνσης. Περιλαμβάνει μία ισότροπη συνιστώσα, η οποία περιγράφει την εξέλιξη του μεγέθους της επιφάνειας πλαστικής διαρροής ($\alpha$) κατά τη διάρκεια πλαστικών φορτίσεων και μία κινηματική συνιστώσα που περιγράφει την εξέλιξη του τανυστή ανισοτροπίας $\boldsymbol{b}$.

Τα περισσότερα διαθέσιμα καταστατικά προσομοιώματα για ανισότροπα στερεοποιημένα εδαφικά υλικά υιοθετούν τον νόμο ισότροπης κράτυνσης του MCC. Το μειονέκτημα μίας τέτοιας παραδοχής είναι ότι δεν είναι δυνατός ο έλεγχος της προκύπτουσας συμπεριφοράς στο επίπεδο $v - \ln\sigma$ κατά την προσομοίωση ανισοτροπικών συμπιέσεων. Αντίθετα, στο προτεινόμενο καταστατικό προσομοίωμα ο νόμος ισότροπης κράτυνσης εξάγεται βάσει της επιθυμητής συμπεριφοράς στο επίπεδο $v - \ln\sigma$ και αποσκοπεί στην ακριβή πρόβλεψη των καμπυλών εγγενούς συμπιεστότητας του πλαισίου συμπιεστότητας, στην ακριβή πρόβλεψη δηλαδή της εξάρτησης της ογκομετρικής παραμόρφωσης από την αναπτυσσόμενη τασική ανισοτροπία. Περιγράφεται από την ακόλουθη εξίσωση:

$$\dot{a} = A\dot{a^*} + \dot{A}a^* \tag{31}$$

όπου:

$$A = exp\left[\frac{\Gamma - N_{iso}}{\lambda - \kappa}\left(1 - \left(1 - \frac{1}{c^2}\boldsymbol{b} : \boldsymbol{b}\right)^{r_s}\right)\right] \tag{32}$$

και

$$a^* = \frac{1}{2}exp\left(\frac{N_{iso} - v - \kappa\ln\sigma}{\lambda - \kappa}\right) \tag{33}$$

ενώ η προσαύξηση κάθε ποσότητας υπολογίζεται ως:

$$\dot{A} = \frac{2Ar_s}{(\kappa - \lambda)}\,\frac{(N_n - \Gamma)}{\left(1 - \frac{1}{c^2}\boldsymbol{b} : \boldsymbol{b}\right)}\,\frac{1}{c^2}\boldsymbol{b} : \dot{\boldsymbol{b}} \tag{34}$$

και

$$\dot{a^*} = \frac{v}{\lambda - \kappa}a^*\dot{\varepsilon^p} = \frac{v}{\lambda - \kappa}a^*\dot{\Lambda}P \tag{35}$$

Παρατηρούμε ότι στην εξίσωση 31, μέσω του όρου $A$ (βλ. εξίσωση 32), υπεισέρχονται στον νόμο κράτυνσης οι παράμετροι του πλαισίου συμπιεστότητας ($r_s$, $N_{iso}$, $\Gamma$), καθώς και η εξέλιξη της ανισοτροπίας (κλίση της επιφάνειας διαρροής) μέσω του τανυστή ανισοτροπίας $\boldsymbol{b}$. Το Σχήμα 12 αποδίδει το σκεπτικό της διατύπωσης του

νόμου ισότροπης κράτυνσης του προσομοιώματος. Παρουσιάζει την επιθυμητή συμπεριφορά σε μία τυχαία ακτινική συμπίεση από ισότροπες αρχικές συνθήκες, όπου παρατηρούμε ότι μετά από σημαντική πλαστική φόρτιση η κλίση της επιφάνεια διαρροής σταθεροποιείται, με τον κύριο άξονα του ελλειψοειδούς ευθυγραμμισμένο με την επιβαλλόμενη τασική όδευση ενώ ταυτόχρονα η προκύπτουσα συμπεριφορά στο επίπεδο $v - \ln p$ βρίσκεται επί συγκεκριμένης καμπύλης εγγενούς συμπίεσης σύμφωνα με τις προβλέψεις του πλαισίου εγγενούς συμπιεστότητας.

Η μεταβολή της κλίσης του κύριου άξονα του ελλειψοειδούς κατά τη διάρκεια πλαστικών φορτίσεων περιγράφεται μέσω του νόμου κινηματικής κράτυνσης. Ο προτεινόμενος νόμος κινηματικής κράτυνσης περιλαμβάνει δύο επιμέρους συνιστώσες, τις $\dot{\boldsymbol{b}}_{\boldsymbol{o}}$ και $\dot{\boldsymbol{b}}_{\boldsymbol{d}}$, οι οποίες αθροιζόμενες περιγράφουν την επαύξηση του τανυστή ανισοτροπίας:

$$\dot{\boldsymbol{b}} = \dot{\boldsymbol{b}}_o + \dot{\boldsymbol{b}}_d \tag{36}$$

όπου:

$$\dot{\boldsymbol{b}}_o = \frac{1}{\alpha(s, S_r^e)} \psi (\boldsymbol{s} - \sigma \boldsymbol{b}) \dot{\varepsilon^p} \tag{37}$$

και

$$\dot{\boldsymbol{b}}_d = -\frac{1}{a(s, S_r^e)^2} \boldsymbol{b} \left(\boldsymbol{s} - \sigma \boldsymbol{b}\right) : \left(\boldsymbol{s} - \sigma \boldsymbol{b}\right) \zeta_q^p \dot{\varepsilon_q^p} \tag{38}$$

Ο όρος $\dot{\boldsymbol{b}}_o$ είναι ίδιος με τον νόμο κινηματικής κράτυνσης που προτάθηκε από τον Kavvadas (1982). Μέσω του όρου $(\boldsymbol{s} - \sigma \boldsymbol{b})$ έλκει τον προσανατολισμό της επιφάνειας διαρροής προς την επιβαλλόμενη τασική όδευση, μία βασική παραδοχή τόσο του προσομοιώματος του Kavvadas (1982) όσο και άλλων καταστατικών προσομοιωμάτων. Πρόκειται για μία ογκομετρική συνιστώσα κράτυνσης, καθώς η αλλαγή στη διεύθυνση της ανισοτροπίας θεωρείται ανάλογη της επαύξησης των ογκομετρικών παραμορφώσεων με την παράμετρο $\psi$ να καθορίζει τον ρυθμό μεταβολής της ανισοτροπίας.

Ο όρος $\dot{\boldsymbol{b}}_d$ ενσωματώνεται στο προτεινόμενο καταστατικό προσομοίωμα με σκοπό να επαναπροσανατολίζει την επιφάνεια διαρροής προς τον ισότροπο άξονα κατά τη διάρκεια τασικών οδεύσεων που οδηγούν στην αστοχία. Η δυνατότητα αυτή ενσωματώνεται με σκοπό να περιγράψει με έναν ενιαίο τρόπο α) την παρατηρούμενη τασική χαλάρωση σε δοκιμές αστράγγιστης τριαξονικής φόρτισης ανισότροπα στερεοποιημένων εδαφικών δοκιμίων και β) μία ενιαία κρίσιμη κατάσταση ανεξάρτητη της αρχικής ανισοτροπίας και της τασικής όδευσης που οδηγεί στην αστοχία. Βασική παραδοχή του προσομοιώματος είναι ότι η κοινή κρίσιμη

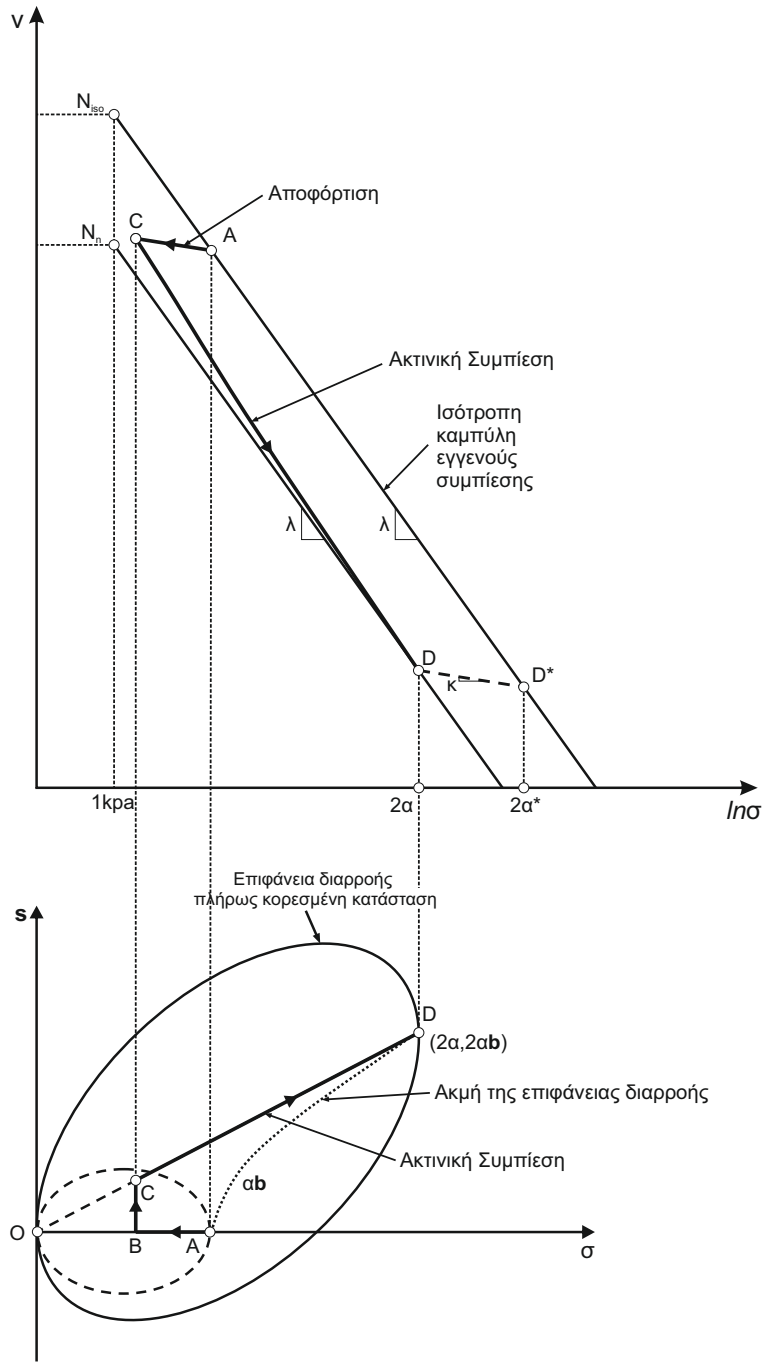


**Σχήμα 12:** Η σύνδεση του πλαισίου εγγενούς συμπίεσης με την κλίση της επιφάνειας διαρροής και τον κινηματικό νόμο κράτυνσης.

κατάσταση αντιπροσωπεύεται από μία ισότροπη επιφάνεια διαρροής, δηλαδή ότι το έδαφος κατά την αστοχία έχει απολέσει πλήρως την όποια μνήμη προτιμητέων διευθύνσεων ανισοτροπίας. Ο προτεινόμενος νόμος συσχετίζει την απώλεια μνήμης της τασικής ανισοτροπίας με την επαύξηση των πλαστικών διεκτροπικών

παραμορφώσεων ($\dot{\varepsilon}_q^p = \sqrt{\frac{2}{3}(\dot{\boldsymbol{e}}_p : \dot{\boldsymbol{e}}_p)}$), με την παράμετρο $\zeta_q^p$ να ελέγχει τον ρυθμό επαναπροσανατολισμού της επιφάνειας διαρροής και σε επέκταση το επίπεδο της διεκτροπικής παραμόρφωσης που αντιστοιχεί στην κρίσιμη κατάσταση.

## 6.5 Συνθήκη Συμβατότητας - Πλαστικό μέτρο κράτυνσης - Ελαστοπλαστικός Τανυστής Στιβαρότητας

Κατά τη διάρκεια πλαστικών φορτίσεων τόσο η αρχική όσο και η τελική κατάσταση του υλικού είναι πλαστική, βρίσκεται δηλαδή επί της επιφάνειας διαρροής. Μαθηματικά αυτό εξασφαλίζεται μέσω της συνθήκης συμβατότητας η οποία απαιτεί:

$$\dot{f} = 0 \Rightarrow \dot{f} = \boldsymbol{Q} : \dot{\boldsymbol{\sigma}} + \frac{\partial f}{\partial s}\dot{s} + \frac{\partial f}{\partial S_r^e}\dot{S}_r^e + \frac{\partial f}{\partial \alpha}\dot{\alpha} + \frac{\partial f}{\partial \boldsymbol{b}} : \dot{\boldsymbol{b}} = 0 \tag{39}$$

Συνδυάζοντας την εξίσωση 39 με την εξίσωση 24 υπολογίζεται το πλαστικό μέτρο κράτυνσης $H$:

$$H = -\left(\frac{\partial f}{\partial \alpha}\overline{\alpha} + \frac{\partial f}{\partial \boldsymbol{b}} : \overline{\boldsymbol{b}}\right) \tag{40}$$

όπου:

$$\dot{a} = \dot{\Lambda}\overline{a} \tag{41}$$

και

$$\dot{\boldsymbol{b}} = \dot{\Lambda}\overline{b} \tag{42}$$

Τέλος, οποιαδήποτε επαύξηση της τάσης συσχετίζεται με μία δεδομένη επαύξηση των παραμορφώσεων, της μύζησης και του ενεργού βαθμού κορεσμού μέσω της εξίσωσης:

$$\dot{\boldsymbol{\sigma}} = \boldsymbol{C}^{ep} : \dot{\boldsymbol{\varepsilon}} + \boldsymbol{W}_s\dot{s} + \boldsymbol{W}_{S_r^e}\dot{S}_r^e \tag{43}$$

όπου ο κλασσικός ελαστοπλαστικός τανυστής στιβαρότητας τάσεων παραμορφώσεων υπολογίζεται ως:

$$\boldsymbol{C}^{ep} = \boldsymbol{C}^e - \frac{1}{\Omega}(\boldsymbol{C}^e : \boldsymbol{P}) \otimes (\boldsymbol{Q} : \boldsymbol{C}^e) \tag{44}$$

όπου:

$$\Omega = H + \boldsymbol{Q} : \boldsymbol{C}^e : \boldsymbol{P} \tag{45}$$

Στον υπολογισμό υπεισέρχονται δύο επιπλέον τανυστές στιβαρότητας (ιακωβιανές), οι οποίοι συσχετίζουν την επαύξηση της τάσης με την επαύξηση της μύζησης και του

ενεργού βαθμού κορεσμού. Υπολογίζονται ως:

$$\boldsymbol{W}_s = -\frac{1}{\Omega}\frac{\partial f}{\partial s}(\boldsymbol{C}^e : \boldsymbol{P}) \tag{46}$$

και

$$\boldsymbol{W}_{S_r^e} = -\frac{1}{\Omega}\frac{\partial f}{\partial S_r^e}(\boldsymbol{C}^e : \boldsymbol{P}) \tag{47}$$

# 7 Αριθμητική επίλυση των καταστατικών εξισώσεων

Για την αξιολόγηση του προτεινόμενου καταστατικού προσομοιώματος σε αναλύσεις υλικού σημείου αλλά και για την ενσωμάτωσή του στον κώδικα πεπερασμένων στοιχείων Simulia Abaqus αναπτύσσεται κατάλληλος αλγόριθμος επίλυσης των καταστατικών εξισώσεων στη γλώσσα προγραμματισμού Fortran. Ο αναπτυχθείς αλγόριθμος χρησιμοποιεί την έμπροσθεν ολοκλήρωση (explicit integration), όπου με δεδομένη μία αρχική κατάσταση (γνωστές εσωτερικές και εξωτερικές μεταβλητές) και την επιβαλλόμενη επαύξηση των παραμορφώσεων ($\dot{\boldsymbol{\varepsilon}}$), της μύζησης ($\dot{s}$) και του ενεργού βαθμού κορεσμού ($\dot{S}_r^e$), υπολογίζει την τελική κατάσταση του υλικού. Η επίλυση γίνεται μέσω της επιβολής απειροστών μεταβολών των παραπάνω ποσοτήτων, γραμμικά εντός του απειροστού βήματος.

Για την πραγματοποίηση αναλύσεων σε απλό υλικό σημείο αναπτύχθηκε κατάλληλος κώδικας, επίσης στη γλώσσα προγραμματισμού Fortran, ο οποίος επιβάλλει στον αλγόριθμο επίλυσης των καταστατικών εξισώσεων πεπερασμένες μεταβολές των παραμορφώσεων ($\dot{\boldsymbol{\varepsilon}}$), της μύζησης ($\dot{s}$) και του ενεργού βαθμού κορεσμού ($\dot{S}_r^e$), όπως αυτές αντιστοιχούν στις βασικότερες εργαστηριακές δοκιμές Εδαφομηχανικής (π.χ. δοκιμές συμπιεσομέτρου, ακτινικές συμπιέσεις, τριαξονική φόρτιση, απλή διάτμηση κλπ.). Ο αναπτυχθείς κώδικας αποτελεί εξέλιξη υφιστάμενων υπολογιστικών εργαλείων (Belokas (2008)), τα οποία τροποποιούνται και αναβαθμίζονται σημαντικά εντός του πλαισίου της παρούσας διατριβής. Οι υλοποιηθείσες τροποποιήσεις κινούνται κυρίως στην κατεύθυνση της ενσωμάτωσης δυνατότητας προσομοίωσης εργαστηριακών δοκιμών που άπτονται της μηχανικής συμπεριφοράς των μη κορεσμένων εδαφών. Προς εκπλήρωση του σκοπού αυτού υλοποιούνται τα παρακάτω βήματα:

- Εισάγεται η δυνατότητα πραγματοποίησης δοκιμών μεταβαλλόμενης μύζησης (π.χ. ξήρανση, ύγρανση) καθώς και η δυνατότητα προσομοίωσης συνήθων

δοκιμών Εδαφομηχανικής (π.χ. ακτινική συμπίεση, μονοδιάστατη παραμόρφωση, τριαξονική φόρτιση, κλπ.) υπό μη κορεσμένες συνθήκες (π.χ. σταθερή μύζηση). Απαιτήθηκε η τροποποίηση των εξισώσεων υπολογισμού των συνοριακών συνθηκών των δοκιμών ώστε να συμμορφώνονται με την εξίσωση 44.

- Ενσωματώνεται στον αλγόριθμο το μαθηματικό προσομοίωμα των Gallipoli et al. (2003) για την προσομοίωση της καμπύλης συγκράτησης ύδατος. Χρησιμοποιείται στον υπολογισμό του βαθμού κορεσμού που αντιστοιχεί σε ένα δεδομένο επίπεδο μύζησης και λόγου κενών καθώς και στον υπολογισμού της μεταβολής του βαθμού κορεσμού που αντιστοιχεί σε μία δεδομένη επαύξηση της μύζησης ή του λόγου κενών. Το μαθηματικό προσομοίωμα των Gallipoli et al. (2003) περιγράφεται από την παρακάτω εξίσωση:

$$S_r = \frac{1}{[1 + ((\phi(v-1)^{\psi})\, s)^n]^m} \tag{48}$$

όπου $\phi$, $\psi$, $n$, $m$ παράμετροι του υλικού και $v$ ο ειδικός όγκος.

- Τροποποιείται ο τρόπος προσομοίωσης αστράγγιστων φορτίσεων από δοκιμές μηδενικής μεταβολής του όγκου ($\dot{e} = 0$) σε δοκιμές σταθερής υγρασίας ($\dot{w} = 0$), με σκοπό να δύναται να χρησιμοποιηθεί και για μη κορεσμένες εδαφικές καταστάσεις.

Για την ενσωμάτωση του καταστατικού προσομοιώματος στον κώδικα πεπερασμένων στοιχείων Simulia Abaqus χρησιμοποιείται το περιβάλλον User Defined MATerial (UMAT). Η υπορουτίνα UMAT είναι προσανατολισμένη στην ενσωμάτωση καταστατικών προσομοιωμάτων που βασίζονται στην κλασσική θεωρία της πλαστικότητας για κορεσμένα εδαφικά υλικά. Απαιτήθηκε η επιπρόσθετη χρήση του περιβάλλοντος User Defined Field προκειμένου να καταστεί δυνατή η ανταλλαγή μεταξύ του κυρίως προγράμματος και του αλγορίθμου επίλυσης των καταστατικών εξισώσεων της μύζησης, του βαθμού κορεσμού αλλά και των προς επιβολή επαυξήσεών τους.

Η κύρια αδυναμία της πραγματοποιηθείσας εξωτερικής ενσωμάτωσης του καταστατικού προσομοιώματος στον κώδικα πεπερασμένων στοιχείων Simulia Abaqus πηγάζει από την αδυναμία του κώδικα να προσομοιώσει την εξάρτηση της καμπύλης συγκράτησης ύδατος από τον λόγο κενών, γεγονός το οποίο επηρεάζει σε

σημαντικό βαθμό κάποιες από τις δυνατότητες προσομοίωσης του προτεινόμενου καταστατικού προσομοιώματος. Δυστυχώς, δεν παρέχεται η δυνατότητα εξωτερικής ενσωμάτωσης αλγορίθμου προσομοίωσης της καμπύλης συγκράτησης ύδατος.

Τα υπολογιστικά εργαλεία που αναπτύχθηκαν χρησιμοποιούνται εκτενώς στα επόμενα εδάφια σε αναλύσεις αξιολόγησης και τεκμηρίωσης του προτεινόμενου καταστατικού προσομοιώματος.

# 8 Αξιολόγηση των προβλέψεων του καταστατικού προσομοιώματος

Στο παρόν εδάφιο το προτεινόμενο καταστατικό προσομοίωμα αξιολογείται μέσω απλών αριθμητικών αναλύσεων που προσομοιώνουν συνήθεις εργαστηριακές δοκιμές. Εξετάζονται αποτελέσματα είτε από αναλύσεις σε μεμονωμένο υλικό σημείο είτε από απλά προσομοιώματα πεπερασμένων στοιχείων με το βασικό σκοπό της εν λόγω διερεύνησης να συνοψίζεται στα ακόλουθα σημεία:

- Σύγκριση των προβλέψεων του προσομοιώματος με την συμπεριφορά του πλαισίου μηχανικής συμπεριφοράς στο οποίο βασίζεται.
- Ποιοτική σύγκριση των προβλέψεων με τα συνήθη ευρήματα εργαστηριακών δοκιμών.
- Αποσαφήνιση της επιρροής διαφόρων παραμέτρων του καταστατικού προσομοιώματος.
- Σύγκριση των αποτελεσμάτων μεταξύ αναλύσεων μεμονωμένου υλικού σημείου και απλών αναλύσεων πεπερασμένων στοιχείων για την τεκμηρίωση των αναπτυχθέντων υπολογιστικών εργαλείων.

Τα αποτελέσματα που εξετάζονται βασίζονται κυρίως σε σταθερές τιμές για τις περισσότερες από τις παραμέτρους του καταστατικού προσομοιώματος. Εξετάζεται η συμπεριφορά του προσομοιώματος σε διαφορετικούς τύπους εργαστηριακών δοκιμών (π.χ. ισοτροπική και ανισοτροπική συμπίεση, τριαξονική φόρτιση, κλπ.) και στην επιρροή διαφορετικών επιπέδων τασικής ανισοτροπίας και μερικού κορεσμού στις προβλέψεις του προσομοιώματος. Ο πίνακας 1 παρουσιάζει τις τιμές που επιλέχθηκαν για τις διάφορες παραμέτρους του εδάφους. Εξετάζονται παραμετρικά

μόνο οι παράμετροι $\psi$, $\zeta_q^p$ του προτεινόμενου νόμου κράτυνσης προκειμένου να αποσαφηνιστεί η επιρροή τους, καθώς δε μπορούν να εκτιμηθούν απευθείας κατά την βαθμονόμηση του προσομοιώματος επί εργαστηριακών αποτελεσμάτων αλλά απαιτούν την εκτέλεση αναλύσεων δοκιμής και σφάλματος. Οι επιλεγμένες τιμές παραμέτρων του πίνακα 1 είναι υποθετικές, παρόλα αυτά επιλεγμένες με γνώμονα να αποτελούν μία συναφή ομάδα παραμέτρων που ανταποκρίνεται στη συνήθη συμπεριφορά ενός ιλυώδους εδάφους.

**Πίνακας 1:** Οι τιμές των παραμέτρων του καταστατικού προσομοιώματος που χρησιμοποιούνται στις αναλύσεις του εδαφίου 8.

| Βασικές παράμετροι | | Ανισοτροπία | | Μερικός κορεσμός | |
|---|---|---|---|---|---|
| Παράμετρος | Τιμή | Παράμετρος | Τιμή | Παράμετρος | Τιμή |
| $\kappa$ | $0.01^{*1}$ | $r_s$ | 0.75 | $r$ | 0.8 |
| $\lambda$ | $0.07^{*2}$ | $\Gamma$ | $2.0584^{*4}$ | $\beta$ | 100.0 $kPa^{-1}$ |
| $\nu$ | 1/3 | $\chi$ | $0.469^{*5}$ | $\gamma$ | 0.8 |
| $k$ | $0.93897^{*3}$ | $\psi$ | 1 - 50 | $p^c$ | 1 $kPa$ |
| $c$ | $0.93897^{*3}$ | $\zeta_q^p$ | 1 - 100 | | |
| $N_{iso}$ | 2.1 | | | | |

$^{*1}$ αντιστοιχεί σε $C_r \approx 0.023$.
$^{*2}$ αντιστοιχεί σε $C_c \approx 0.16$.
$^{*3}$ είναι ισοδύναμο με $M = 1.15$ και αντιστοιχεί σε ένα υλικό με $\phi \approx 28^o$ σε συμπίεση.
$^{*4}$ αντιστοιχεί σε $\Gamma = N_{iso} - (\lambda - \kappa)\ln 2$ ως απόρροια της επιλογής $k = c$.
$^{*5}$ βαθμονομημένο για $K_0 = 0.55$.

Για την βήμα προς βήμα αξιολόγηση των δυνατοτήτων του προσομοιώματος εκτελούνται σταδιακά αναλύσεις αυξανόμενης πολυπλοκότητας. Αρχικά οι αναλύσεις επικεντρώνονται στην πρόβλεψη της επιρροής της τασικής ανισοτροπίας, στη συνέχεια αξιολογούνται τα χαρακτηριστικά του προσομοιώματος που άπτονται του μερικού κορεσμού αγνοώντας την επιρροή της ανισοτροπίας και τελευταία εκτελούνται αναλύσεις για τη συναξιολόγηση της επιρροής της τασικής ανισοτροπίας και του μερικού κορεσμού.

## 8.1 Επίδραση της Τασικής Ανισοτροπίας

Για την αξιολόγηση των μηχανικών χαρακτηριστικών του προσομοιώματος που άπτονται της τασικής ανισοτροπίας εκτελείται ικανός αριθμός προσομοιώσεων δοκιμών ακτινικής συμπίεσης, ισότροπης συμπίεσης και δοκιμών οιδημέτρου. Επιπρόσθετα προσομοιώνονται δοκιμές τριαξονικής φόρτισης τόσο σε κανονικά όσο και σε υπερστεροποιημένα εδαφικά υλικά υπό αστράγγιστες και υπό στραγγισμένες συνθήκες με σκοπό την εξέταση της επιρροής διαφορετικών επιπέδων αρχικής τασικής ανισοτροπίας επί των αποτελεσμάτων.

Στο Σχήμα 13a παρουσιάζονται χαρακτηριστικά αποτελέσματα[5] από δοκιμές συμπίεσης, στις οποίες μεταβάλλεται η ανισοτροπία (ακτινική συμπίεση και μονοδιάστατη παραμόρφωση σε αρχικά ισότροπο υλικό, ισότροπη συμπίεση σε αρχικά ανισότροπο υλικό), στο Σχήμα 13b από τριαξονικές δοκιμές φόρτισης υπό αστράγγιστες και στραγγισμένες συνθήκες σε αρχικά ανισότροπο υλικό και στο Σχήμα 13c αποτελέσματα δοκιμών σε διαφορετικές διευθύνσεις φόρτισης (εκτός και εντός επιπέδου αρχικής ανισοτροπίας).

Παρακάτω συνοψίζονται τα βασικότερα ευρήματα της διερεύνησης:

- Το προτεινόμενο καταστατικό προσομοίωμα δύναται να περιγράψει την εξέλιξη της ανισοτροπίας κατά τη διάρκεια δοκιμών που οδηγούν σε αλλαγή των προτιμητέων διευθύνσεων της ανισοτροπίας και προβλέπει μοναδικές καμπύλες εγγενούς συμπίεσης, οι οποίες εξαρτώνται από το επίπεδο της τασικής ανισοτροπίας σε συμφωνία με το προτεινόμενο πλαίσιο συμπιεστότητας στο οποίο βασίζεται. (βλ. Σχήμα 13a). Η παράμετρος $\psi$ περιγράφει επιτυχώς διαφορετικούς ρυθμούς εξέλιξης της τασικής ανισοτροπίας με το πλέον ρεαλιστικό εύρος τιμών της παραμέτρου να κυμαίνεται από $\psi = 20$ έως $\psi = 40$.

- Ο νέος νόμος κινηματικής κράτυνσης που ενσωματώνεται προβλέπει επιτυχώς τόσο την τασική χαλάρωση που παρατηρείται σε δοκιμές αστράγγιστης τριαξονικής φόρτισης επί ανισότροπα στερεοποιημένων δοκιμίων όσο και μία μοναδική και ενιαία κρίσιμη κατάσταση ανεξάρτητη του επιπέδου της αρχικής ανισοτροπίας (βλέπε Σχήμα 13b & c). Η παράμετρος $\zeta_q^p$ ελέγχει αποτελεσματικά την απώλεια μνήμης της τασικής ανισοτροπίας κατά τη διάρκεια τασικών οδεύσεων που οδηγούν στην αστοχία και το προτεινόμενο εύρος τιμών κυμαίνεται από $\zeta_q^p = 20$ σε $\zeta_q^p = 50$.

[5] Η εκτενής και λεπτομερής παράθεση των αποτελεσμάτων όλων των προσομοιώσεων που εκτελέστηκαν είναι μη εφικτή στα πλαίσια της παρούσας εκτενούς περίληψης.

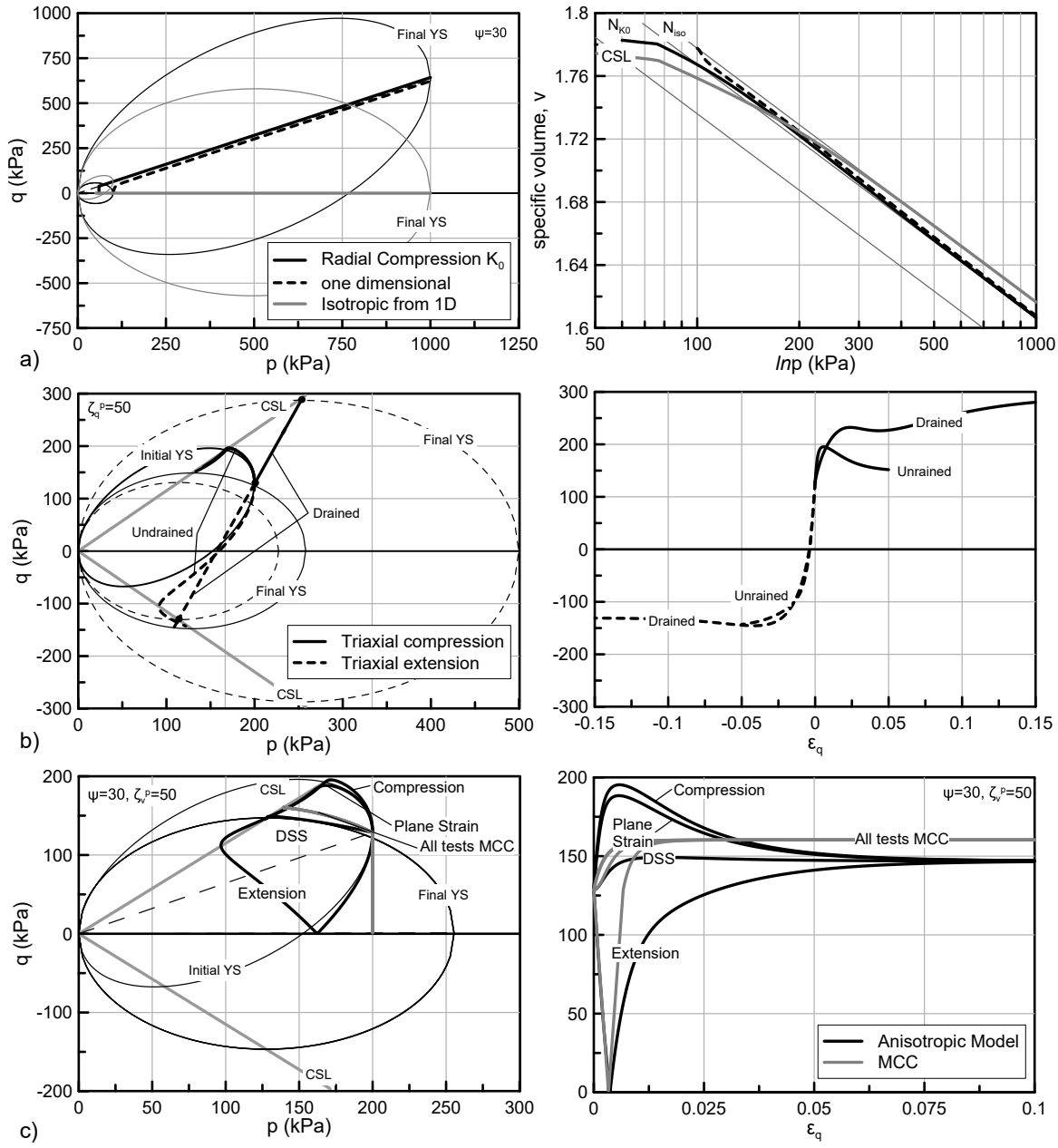


**Σχήμα 13:** Χαρακτηριστικές προσομοιώσεις με το προτεινόμενο καταστατικό προσομοίωμα: α) δοκιμές ακτινικής συμπίεσης και μονοδιάστατης παραμόρφωσης, β) τριαξονικής φόρτισης ανισότροπα στερεοποιημένων δοκιμίων και γ) τριαξονικής φόρτισης, απλής διάτμησης και επίπεδης παραμόρφωσης ανισότροπα στερεοποιημένων δοκιμίων.

- Με την κατάλληλη επιλογή συνδυασμού παραμέτρων $\psi$ και $\zeta_q^p$ είναι εφικτή η ταυτόχρονη προσομοίωση μίας συνεχώς κρατυνόμενης συμπεριφοράς κατά τη

διάρκεια στραγγισμένων τριαξονικών φορτίσεων καθώς και τασικής χαλάρωσης κατά τη διάρκεια αστράγγιστων τριαξονικών φορτίσεων.

- Το προτεινόμενο καταστατικό προσομοίωμα προβλέπει ικανοποιητικά την εξέλιξη τόσο της κορυφαίας όσο και της παραμένουσας αντοχής ως συνάρτηση της αρχικής ανισοτροπίας (βλ. Σχήμα 14).

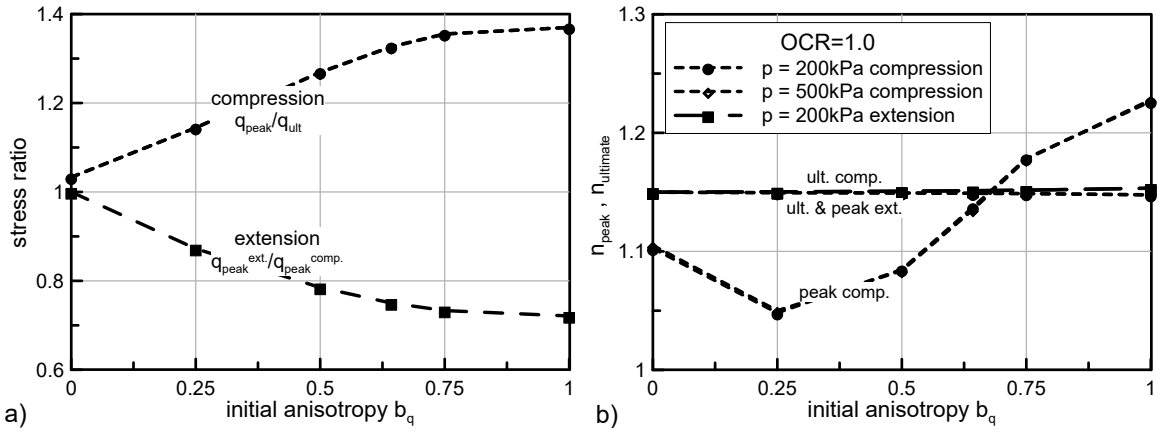


**Σχήμα 14:** Κανονικοποιημένα διαγράμματα της εξέλιξης της μέγιστης και παραμένουσας αντοχής με την αρχική ανισοτροπία. Αναφέρονται σε δοκιμές τριαξονικής συμπίεσης και εφελκυσμού.

- Ο νόμος ροής του προσομοιώματος περιγράφει με ακρίβεια την πλαστική διαστολικότητα για την οποία έχει βαθμονομηθεί ή αντίστοιχα προβλέπει με ακρίβεια την επιθυμητή τιμή του λόγου $K_0$ σε δοκιμές συμπιεσομέτρου. Εν γένει προβλέπει αύξηση της διαστολικότητας με την αύξηση του επιπέδου της τασικής ανισοτροπίας.

- Οι προβλέψεις του προσομοιώματος που αφορούν στη συμπεριφορά υπερστεροποιημένων εδαφικών καταστάσεων επηρεάζονται σαφώς από τη μεγάλη ελαστική περιοχή που ενσωματώνει το προσομοίωμα (προσομοίωμα μοναδικής επιφάνειας). Για παράδειγμα προβλέπει τασική χαλάρωση σε δοκιμές αστράγγιστης τριαξονικής φόρτισης σε αντίθεση με συνήθη εργαστηριακά αποτελέσματα, τα οποία συνιστούν μία συνεχώς κρατυνόμενη συμπεριφορά.

- Το προτεινόμενο προσομοίωμα, σε αντίθεση με ισότροπα καταστατικά

προσομοιώματα (π.χ. MCC) προβλέπει διαφορετική συμπεριφορά σε φορτίσεις υπό διαφορετικές διευθύνσεις στον χώρο των τάσεων (π.χ. τριαξονική συμπίεση, τριαξονικός εφελκυσμός, απλή διάτμηση, επίπεδη παραμόρφωση) ως απόρροια της μνήμης προτιμητέων διευθύνσεων της ανισοτροπίας (βλ. Σχήμα 13b & c).

## 8.2 Επίδραση του Μερικού Κορεσμού

Η αξιολόγηση του προσομοιώματος σε καταστάσεις μερικού κορεσμού επικεντρώνεται σε δοκιμές ισότροπης συμπίεσης υπό διαφορετικά επίπεδα μύζησης, δοκιμές τριαξονικής φόρτισης υπό διαφορετικά επίπεδα μύζησης καθώς και σε δοκιμές διαβροχής (μείωση της μύζησης) υπό διαφορετικά επίπεδα ολικής τάσης και αρχικής μύζησης. Οι αριθμητικές αναλύσεις που εκτελέστηκαν δε λαμβάνουν υπόψη την επιρροή της ανισοτροπίας καθώς επιλέγεται μία αρχικώς ισότροπη επιφάνεια διαρροής $\boldsymbol{b} = \mathbf{0}$ και τα «ανισοτροπικά χαρακτηριστικά» του προσομοιώματος ακυρώνονται επιλέγοντας $\psi = 0$ και $\zeta_q^p = 0$, απενεργοποιώντας στην ουσία τον νόμο κινηματικής κράτυνσης.

Για τη μελέτη της συμπεριφοράς των μη κορεσμένων εδαφών είναι απαραίτητη η γνώση της καμπύλης συγκράτησης ύδατος. Ο πίνακας 2 παρουσιάζει τις τιμές των παραμέτρων που χρησιμοποιούνται στην περιγραφή της σχέσης μύζησης - ενεργού βαθμού κορεσμού.

**Πίνακας 2:** Οι παράμετροι του προσομοιώματος της Καμπύλης Συγκράτησης Ύδατος του Gallipoli et al. (2003) (βλέπε εξίσωση 48) που χρησιμοποιούνται στις αναλύσεις καθώς και η επιλεγμένη τιμή της παραμέτρου $\alpha$ για τον υπολογισμού του ενεργού βαθμού κορεσμού σύμφωνα με τον εκθετικό νόμο του Alonso et al. (2010).

| Καμπύλη Συγκράτησης Ύδατος | | Alonso et. al. (2005) power law | |
|---|---|---|---|
| Παράμετρος | Τιμή | Παράμετρος | Τιμή |
| $\phi$ | 0.011 | $\alpha$ | 2.5 |
| $n$ | 1.005 | | |
| $m$ | 0.567 | | |
| $\psi$ | 4.0 | | |

Στο Σχήμα 15 παρουσιάζονται τα αποτελέσματα δοκιμών ισότροπης συμπίεσης υπό διαφορετικά επίπεδα μύζησης, επί των οποίων μπορούμε να συμπεράνουμε:

- Το προτεινόμενο καταστατικό προσομοίωμα προβλέπει μη γραμμική αύξηση της φαινόμενης τάσης προφόρτισης με την αύξηση της μύζησης.
- Υπό σταθερά επίπεδα μύζησης το καταστατικό προσομοίωμα προβλέπει συνεχώς αυξανόμενη συμπιεστότητα με την αύξηση του επιπέδου της τάσης ως απόρροια της εξάρτησης του πλαισίου συμπιεστότητας από τον ενεργό βαθμό κορεσμού.

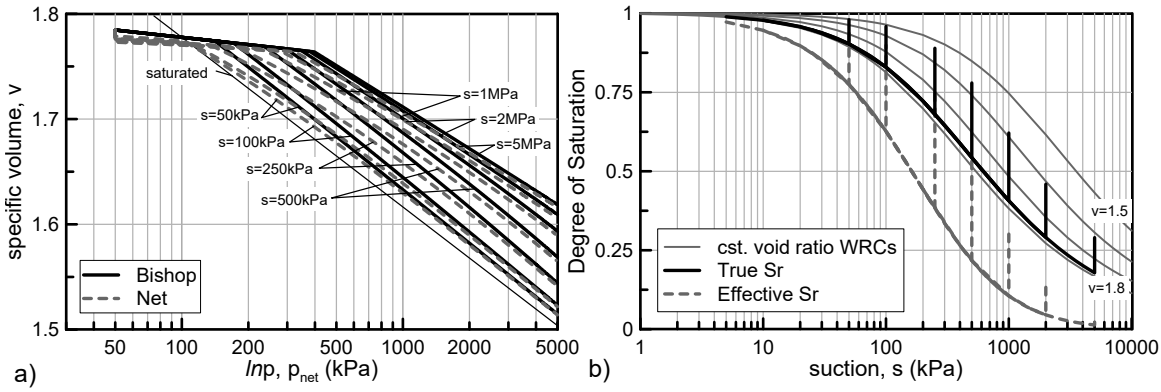


**Σχήμα 15:** Οι προβλέψεις του προτεινόμενου καταστατικού προσομοιώματος σε δοκιμές ισότροπης συμπίεσης υπό διαφορετικά, σταθερά επίπεδα μύζησης.

Στο Σχήμα 16 παρουσιάζεται η εξέλιξη της κορυφαίας αντοχής που προβλέπει το προσομοίωμα με βάση αποτελέσματα τριαξονικών δοκιμών υπό διαφορετικά και σταθερά επίπεδα μύζησης. Παρατηρούμε ότι το προσομοίωμα δύναται να προβλέπει μη γραμμική αύξηση της διατμητικής αντοχής με τη μύζηση, απόρροια της επιλογής της τάσης του Bishop ως βασικής καταστατικής μεταβλητής. Η εξέλιξη της αντοχής με τη μύζηση ακολουθεί ποιοτικά τη μεταβολή του μεγέθους $s \cdot S_r^e$. Επιπρόσθετα, παρατηρούμε ότι η επιρροή του μερικού κορεσμού στην αύξηση της αντοχής φθίνει με την αύξηση του επιπέδου της τάσης εγκιβωτισμού.

Το Σχήμα 17 παρουσιάζει χαρακτηριστικές προβλέψεις του προσομοιώματος σε δοκιμές διαβροχής από διαφορετικά επίπεδα αρχικής μύζησης και τάσης εγκιβωτισμού. Παρατηρούμε ότι το προτεινόμενο καταστατικό προσομοίωμα δύναται να προσομοιώσει ένα μέγιστο στις παραμορφώσεις κατάρρευσης λόγω διαβροχής, με τις παραμορφώσεις να εξαρτώνται τόσο από το αρχικό επίπεδο της μύζησης όσο και

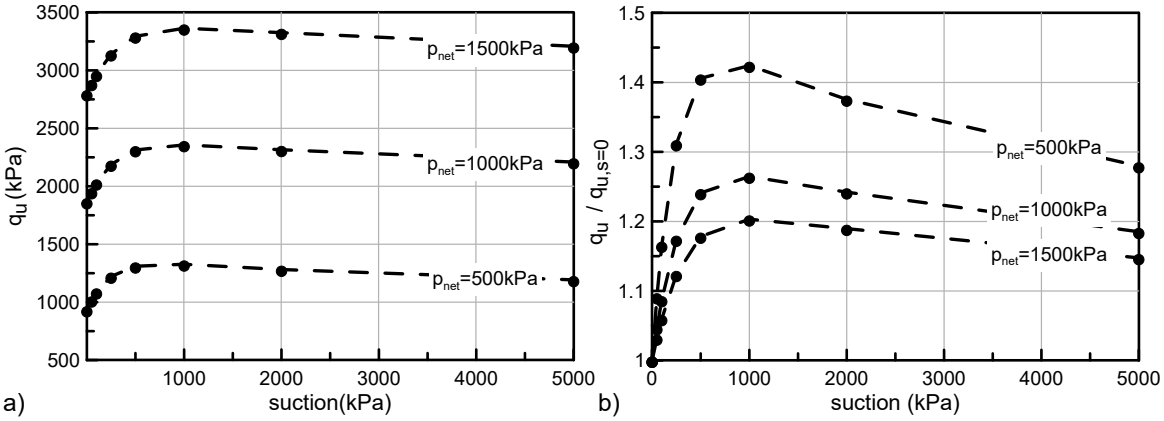


**Σχήμα 16:** Η εξέλιξη της αντοχής με τη μύζηση, υπό διαφορετικά επίπεδα μέσης ολικής τάσης, όπως προκύπτει από δοκιμές τριαξονικής φόρτισης υπό σταθερή μύζηση με το προτεινόμενο καταστατικό προσομοίωμα.

από το επίπεδο της τάσης σε συμφωνία με την συνήθη παρατηρούμενη εργαστηριακή συμπεριφορά.

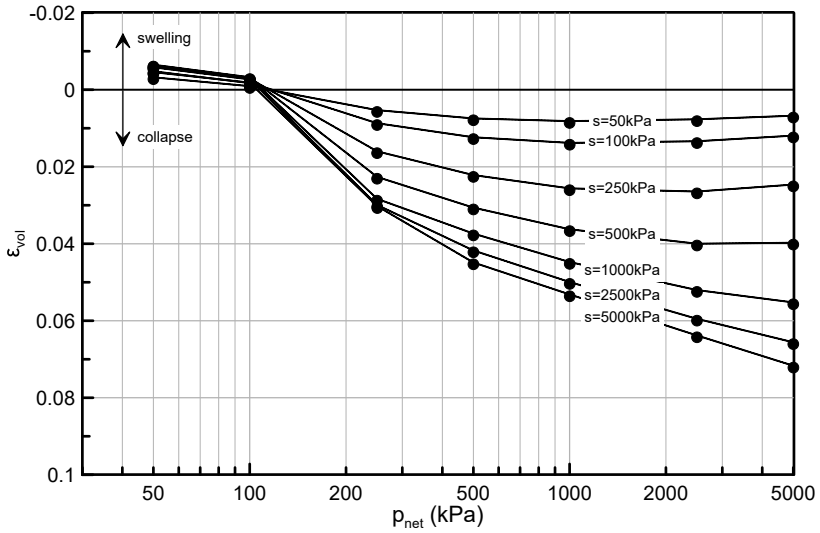


**Σχήμα 17:** Πρόβλεψη της ογκομετρικής παραμόρφωσης με τη διαβροχή για διαφορετικά επίπεδα αρχικής μύζησης και διαφορετικά επίπεδα τάσης εγκιβωτισμού.

## 8.3 Συνδυαστική επίδραση της Τασικής Ανισοτροπίας και του Μερικού Κορεσμού

Οι προβλέψεις του προσομοιώματος σε τασικές οδεύσεις που μεταβάλουν την ανισοτροπία μη κορεσμένων εδαφικών υλικών αποτελούν στην ουσία έναν συνδυασμό των προβλέψεων του προσομοιώματος όπως συνοπτικά παρουσιάστηκαν στις δύο προηγούμενες παραγράφους. Για παράδειγμα στο Σχήμα 18 συγκρίνονται αποτελέσματα από δοκιμές μονοδιάστατης παραμόρφωσης με αποτελέσματα δοκιμών ισότροπης συμπίεσης υπό διαφορετικά επίπεδα μύζησης. Παρατηρούμε ότι και στην περίπτωση της μονοδιάστατης παραμόρφωσης το προσομοίωμα προβλέπει μία μη γραμμική αύξηση στη φαινόμενη τάση προφόρτισης με τη μύζηση καθώς και συνεχώς αυξανόμενη συμπιεστότητα. Ταυτόχρονα, η εξέλιξη της ανισοτροπίας αντικατοπτρίζεται στη μετατόπιση των καμπυλών συμπίεσης που αντιστοιχούν στις δοκιμές συμπιεσομέτρου στα αριστερά των αντίστοιχων ισότροπων, σύμφωνα με το προτεινόμενο πλαίσιο συμπιεστότητας.

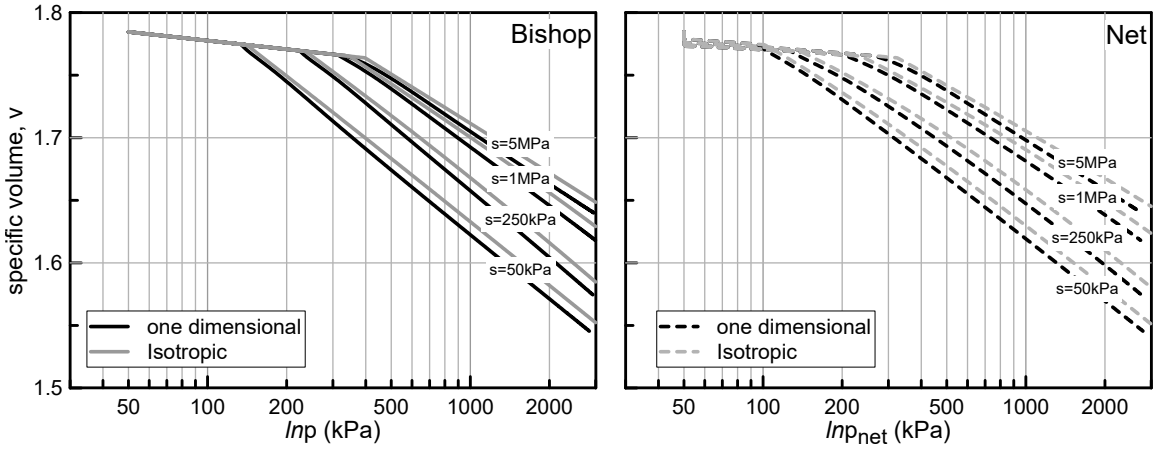


**Σχήμα 18:** Αποτελέσματα δοκιμών ισότροπης και μονοδιάστατης συμπίεσης υπό διαφορετικά επίπεδα μύζησης.

Επιπρόσθετα, αξίζει να σημειώσουμε ότι από την διεξαχθείσα διερεύνηση προκύπτουν οι παρακάτω παρατηρήσεις:

- Ο μερικός κορεσμός οδηγεί σε μείωση του ρυθμού εξέλιξης της ανισοτροπίας.
- Οποιαδήποτε ακτινική τασική όδευση επιβάλλεται σε επίπεδο ολικής τάσης αντιστοιχεί σε μία όδευση μικρότερης κλίσης στον χώρο της τάσης του Bishop.

- Ο μερικός κορεσμός οδηγεί σε μείωση του συντελεστή ωθήσεων ηρεμίας που προβλέπει το προσομοίωμα.

Μέρος των αναλύσεων στις οποίες βασίζεται η αξιολόγηση των προβλέψεων του προσομοιώματος πραγματοποιήθηκαν τόσο σε υλικό σημείο όσο και μέσω απλών προσομοιωμάτων πεπερασμένων στοιχείων στον κώδικα Simulia Abaqus, επιτρέποντας τον εκτεταμένο έλεγχο των υπολογιστικών εργαλείων που αναπτύχθηκαν. Πρέπει να σημειώσουμε πως διαπιστώθηκε ότι η αδυναμία του κώδικα πεπερασμένων στοιχείων Simulia Abaqus να περιγράφει καμπύλες συγκράτησης ύδατος εξαρτώμενες του λόγου κενών επηρεάζει σημαντικά τις προβλέψεις του προσομοιώματος, ακυρώνοντας ουσιαστικά τη δυνατότητα πρόβλεψης μίας μεταβαλλόμενης συμπιεστότητας σε δοκιμές φόρτισης υπό σταθερή μύζηση και επηρεάζοντας επιπρόσθετα τη δυνατότητα πρόβλεψης μεγίστου στην ογκομετρική παραμόρφωση κατά την διαβροχή. Η δυνατότητα ορθής περιγραφής της εξέλιξης της διατμητικής αντοχής με τη μύζηση δεν επηρεάζεται σημαντικά.

# 9 Βαθμονόμηση και σύγκριση των προβλέψεων του καταστατικού προσομοιώματος με εργαστηριακά αποτελέσματα

Το παρόν εδάφιο πραγματεύεται τη βαθμονόμηση και σύγκριση των προβλέψεων του προτεινόμενου καταστατικού προσομοιώματος βάσει διαθέσιμων πειραματικών δεδομένων από τη διεθνή βιβλιογραφία. Τρεις εργαστηριακές έρευνες χρησιμοποιούνται για τον σκοπό αυτό και πιο συγκεκριμένα: α) η έρευνα του Gens (1982) στην επιρροή της τασικής ανισοτροπίας σε ένα ιλυώδες έδαφος, β) η εργαστηριακή διερεύνηση της Casini (2008) σχετικά με την επιρροή του μερικού κορεσμού στη συμπεριφορά της Jossigny Silt και γ) η εργαστηριακή διερεύνηση της συμπεριφοράς της Barcelona Clayey Silt σε καταστάσεις μερικού κορεσμού του Barrera (2002).

## 9.1 Σύγκριση με τα εργαστηριακά αποτελέσματα του Gens (1982)

Η εργαστηριακή διερεύνηση του Gens (1982) επικεντρώνεται στην επιρροή της τασικής ανισοτροπίας στη συμπιεστότητα και στην αντοχή ενός ιλυώδους εδάφους χαμηλής πλαστικότητας, της Lower Cromer Till. Το εξεταζόμενο έδαφος χαρακτηρίζεται ως Αργιλώδης Άμμος (SC) σύμφωνα με το ενιαίο σύστημα κατάταξης εδαφών (U.S.C.S.). Οι εργαστηριακές δοκιμές εκτελέστηκαν επί αναζυμωμένων σε πολτό και επανασυμπιεσμένων εδαφικών δοκιμίων. Περιλαμβάνουν μεταξύ άλλων δοκιμές ισοτροπικής και ανισοτροπικής συμπίεσης υπό διαφόρους λόγους τάσης καθώς και τριαξονικές φορτίσεις υπό στραγγισμένες και αστράγγιστες συνθήκες σε ανισότροπα στερεοποιημένα δοκίμια. Από τη βαθμονόμηση του καταστατικού προσομοιώματος επί των διαθέσιμων εργαστηριακών αποτελεσμάτων προέκυψαν οι τιμές του πίνακα 3.

**Πίνακας 3:** Οι τιμές των παραμέτρων του καταστατικού προσομοιώματος όπως προέκυψαν από τη βαθμονόμηση στα διαθέσιμα εργαστηριακά δεδομένα του Gens (1982).

| Παράμετρος | Τιμή | Παράμετρος | Τιμή | Παράμετρος | Τιμή |
|---|---|---|---|---|---|
| $\kappa$ | 0.008 | $c$ | 0.91287 | $\chi$ | 0.49444 |
| $\lambda$ | 0.067 | $N_{iso}$ | 1.7950 | $\psi$ | 30 |
| $\nu$ | 1/3 | $\Gamma$ | 1.7450 | $\zeta_q^p$ | 40 |
| $k$ | 0.79046 | $r_s$ | 0.47 | | |

Στο Σχήμα 19 συγκρίνονται οι καμπύλες συμπίεσης που προβλέπει το προτεινόμενο καταστατικό προσομοίωμα με τα αποτελέσματα εργαστηριακών δοκιμών ανισοτροπικής συμπίεσης. Αξίζει να σημειωθεί ότι κατά τη βαθμονόμηση του καταστατικού προσομοιώματος έχουν ληφθεί υπόψη αποκλειστικά τα εργαστηριακά αποτελέσματα που αναφέρονται σε ισότροπη συμπίεση και σε δοκιμές συμπιεσομέτρου και όχι αυτά που αναφέρονται σε ακτινικές συμπιέσεις, με αποτέλεσμα οι τελευταίες να αποτελούν «τυφλές προβλέψεις» (blind predictions). Προκύπτει ότι το προτεινόμενο καταστατικό προσομοίωμα δύναται να προβλέψει ικανοποιητικά την εξάρτηση των καμπυλών συμπίεσης από το επίπεδο της αναπτυσσόμενης ανισοτροπίας, ακόμα και όταν η βαθμονόμηση γίνεται μόνο βάσει

αποτελεσμάτων μονοδιάστατης παραμόρφωσης, που είναι συνήθως διαθέσιμα σε πρακτικές εφαρμογές.

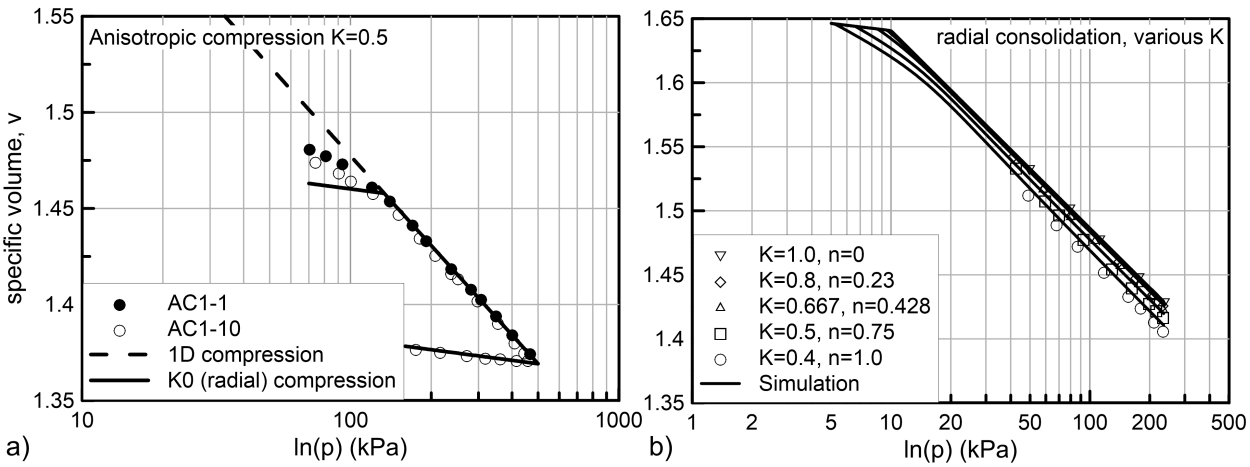


**Σχήμα 19:** Προσομοίωση δοκιμών ανισότροπης συμπίεσης του Gens (1982).

Στο Σχήμα 20 συγκρίνονται τα αποτελέσματα προσομοιώσεων δοκιμών τριαξονικής φόρτισης υπό αστράγγιστες και στραγγισμένες συνθήκες σε αρχικά ανισότροπα στερεοποιημένα δοκίμια με τα διαθέσιμα εργαστηριακά αποτελέσματα. Προκύπτει ότι ο προτεινόμενος νόμος κινηματικής κράτυνσης προβλέπει ικανοποιητικά την παρατηρούμενη τασική χαλάρωση σε δοκιμές αστράγγιστης τριαξονικής φόρτισης καθώς και την τελική, κρίσιμη κατάσταση, ανεξάρτητα της αρχικής ανισοτροπίας. Ικανοποιητικά κρίνονται και τα αποτελέσματα της προσομοίωσης των εργαστηριακών δοκιμών υπό στραγγισμένες συνθήκες (δε λήφθηκαν υπόψη στη βαθμονόμηση) τόσο στο επίπεδο της σχέσης τάσεων - παραμορφώσεων όσο και αναφορικά με την προβλεπόμενη διαστολικότητα.

Θα πρέπει να σημειωθεί ότι τα αποτελέσματα του σχήματος 20 προέκυψαν υιοθετώντας αρχικές τιμές του τανυστή ανισοτροπίας μικρότερες κατά 60% αυτών που αντιστοιχούν στην κλίση της τασικής διαδρομής κατά τη συμπίεση. Η επιλογή αυτή έγινε καθώς διαπιστώθηκε ότι τουλάχιστον για συγκεκριμένα εργαστηριακά αποτελέσματα η βασική παραδοχή του προσομοιώματος σχετικά με τον προσανατολισμό της επιφάνεια διαρροής κατά τη διάρκεια ανισοτροπικών συμπιέσεων οδηγεί σε μετέπειτα σημαντική υπερεκτίμηση της κορυφαίας αντοχής που προβλέπεται σε τριαξονικές δοκιμές.

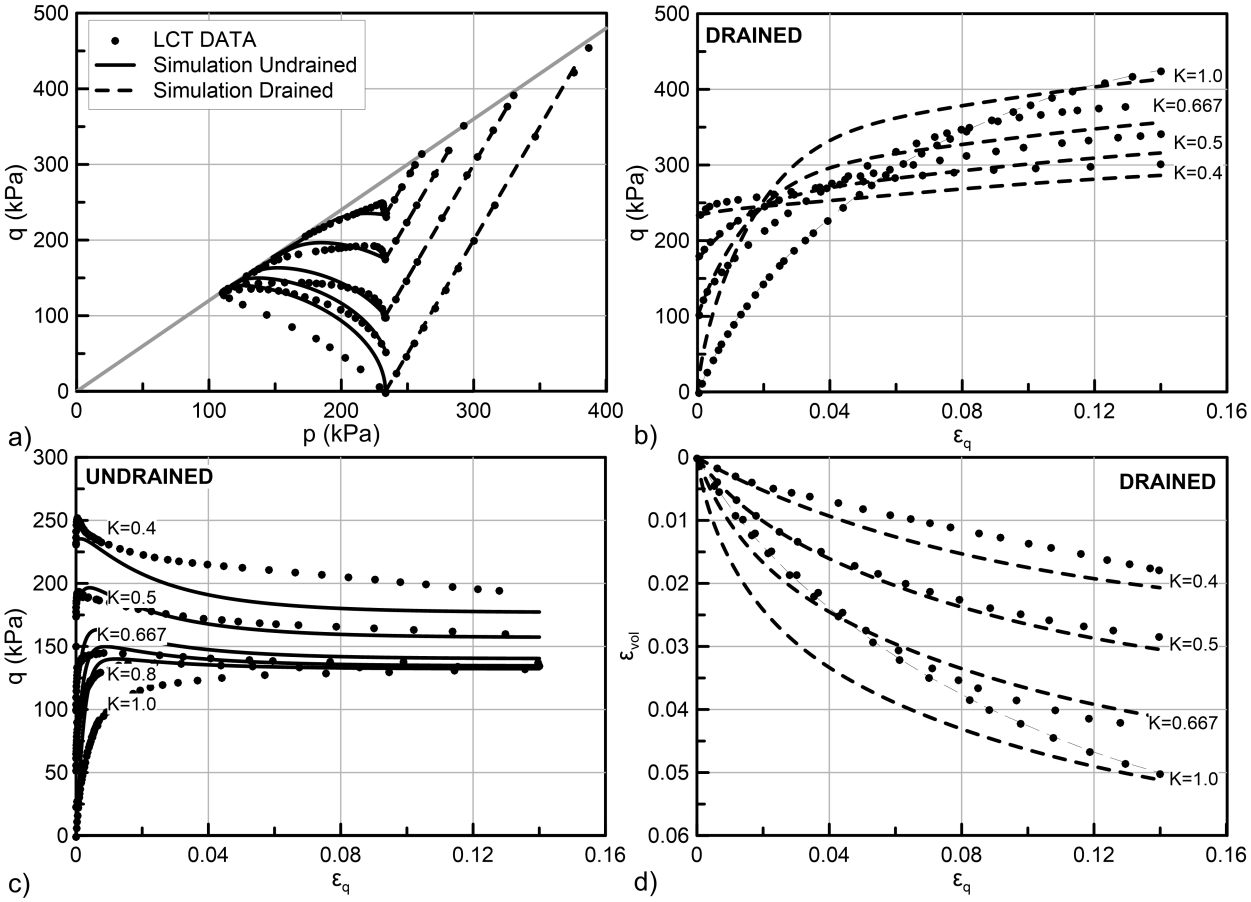


**Σχήμα 20:** Προσομοίωση δοκιμών τριαξονικής φόρτισης (στραγγισμένης και αστράγγιστες συνθήκες) του Gens (1982), υπό διαφορετικά επίπεδα αρχικής ανισοτροπίας.

## 9.2 Τα εργαστηριακά αποτελέσματα της Casini (2008)

Η εργαστηριακή διερεύνηση της Casini (2008) επικεντρώνεται στη συμπεριφορά μη κορεσμένων και ανισότροπα στερεοποιημένων δοκιμίων της Jossigny Silt. Το εν λόγω έδαφος σύμφωνα με το ενιαίο σύστημα κατάταξης εδαφών χαρακτηρίζεται ως Ιλυώδης Άργιλος χαμηλής πλαστικότητας (CL). Χρησιμοποιήθηκαν δοκίμια που προέκυψαν από στατική συμπύκνωση αναζυμωμένου εδάφους σε ποσοστά κοντά στη φυσική του υγρασία. Οι δοκιμές πραγματοποιήθηκαν με χρήση τριαξονικής κυψέλης και συμπιεσομέτρου, αμφότερα με έλεγχο της μύζησης μέσω της μεθόδου μετατόπισης του άξονα (axis translation technique).

Τα εργαστηριακά αποτελέσματα που εξετάστηκαν στο πλαίσιο της παρούσας διατριβής αφορούν δοκιμές οιδημέτρου υπό διαφορετικά επίπεδα μύζησης καθώς και δοκιμές ακτινικής συμπίεσης και τριαξονικής φόρτισης υπό σταθερή μύζηση ίση με $s = 200kPa$. Ο πίνακας 4 παρουσιάζει τις τιμές παραμέτρων που προέκυψαν από

τη βαθμονόμηση του προσομοιώματος στα διαθέσιμα εργαστηριακά αποτελέσματα. Τα Σχήματα 21 και 22 παρουσιάζουν χαρακτηριστικές συγκρίσεις αριθμητικών προσομοιώσεων με εργαστηριακά αποτελέσματα σε δοκιμές μονοδιάστατης παραμόρφωσης υπό διαφορετικά επίπεδα μύζησης και σε δοκιμές τριαξονικής φόρτισης αντίστοιχα.

**Πίνακας 4:** Οι τιμές των παραμέτρων του καταστατικού προσομοιώματος όπως προέκυψαν από τη βαθμονόμηση στα διαθέσιμα εργαστηριακά δεδομένα της Casini (2008).

| Βασικές παράμετροι | | Ανισοτροπία | | Μερικός κορεσμός | |
|---|---|---|---|---|---|
| Παράμετρος | Τιμή | Παράμετρος | Τιμή | Παράμετρος | Τιμή |
| $\kappa$ | 0.006 | $r_s$ | 2.0 | $r$ | 0.4 |
| $\lambda(0)$ | 0.11 | $\psi$ | 20.0 | $\beta$ | 30.0 $MPa^{-1}$ |
| $\nu$ | 0.333 | $\zeta_q^p$ | 20.0 | $\gamma$ | 1.0 |
| $c$ | 1.0206 | $\chi$ | 0.4945 | $p^c$ | 6 $kPa$ |
| $k$ | 1.0206 | Alonso et. al. (2005) power law | | | |
| $N_{iso}$ | 2.25 | $\alpha$ | 1.5 | | |
| $\Gamma$ | 2.178 | | | | |
| Καμπύλη Συγκράτησης Ύδατος | | | | | |
| $\phi$ | 1.318 | $n$ | 1.34 | | |
| $\psi$ | 6.04 | $m$ | 0.15 | | |
| Αρχικές τιμές παραμέτρων κράτυνσης | | | | | |
| $p_0^*$ | $40kPa$ | $b_q$ | 0.15 | | |

Με βάση τα αποτελέσματα της εν λόγω άσκησης βαθμονόμησης και προσομοίωσης των εργαστηριακών αποτελεσμάτων της Casini (2008) μπορούμε να επισημάνουμε τα κατωτέρω:

- Η διπλή εξάρτηση της κλίσης των καμπυλών συμπίεσης από τη μύζηση και τον βαθμό κορεσμού που υιοθετείται στο προτεινόμενο καταστατικό προσομοίωμα αποδεικνύεται καθοριστικής σημασίας στην κατά το δυνατόν ακριβέστερη περιγραφή της μεταβαλλόμενης συμπιεστότητας σε δοκιμές υπό σταθερή μύζηση που επιδεικνύουν τα εξεταζόμενα εργαστηριακά αποτελέσματα.

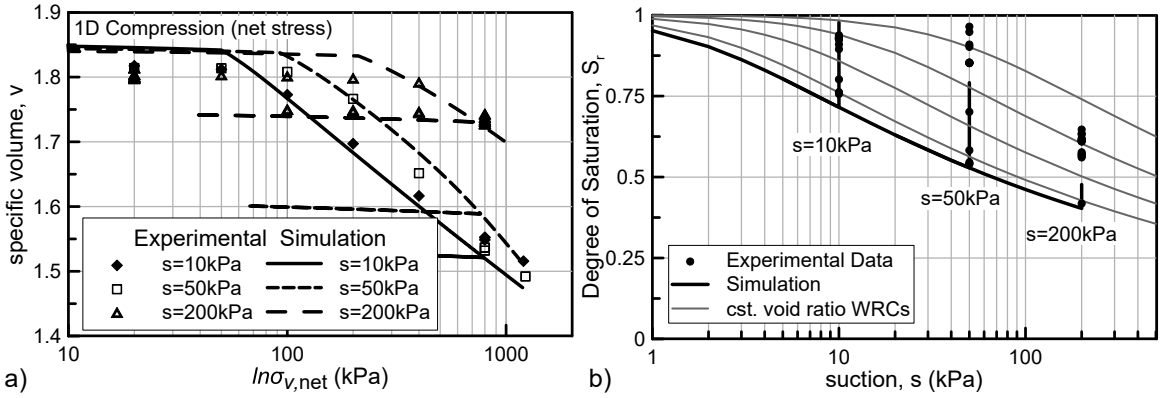


**Σχήμα 21:** Προσομοίωση δοκιμών συμπιεσομέτρου της Casini (2008), υπό διαφορετικά επίπεδα μύζησης.

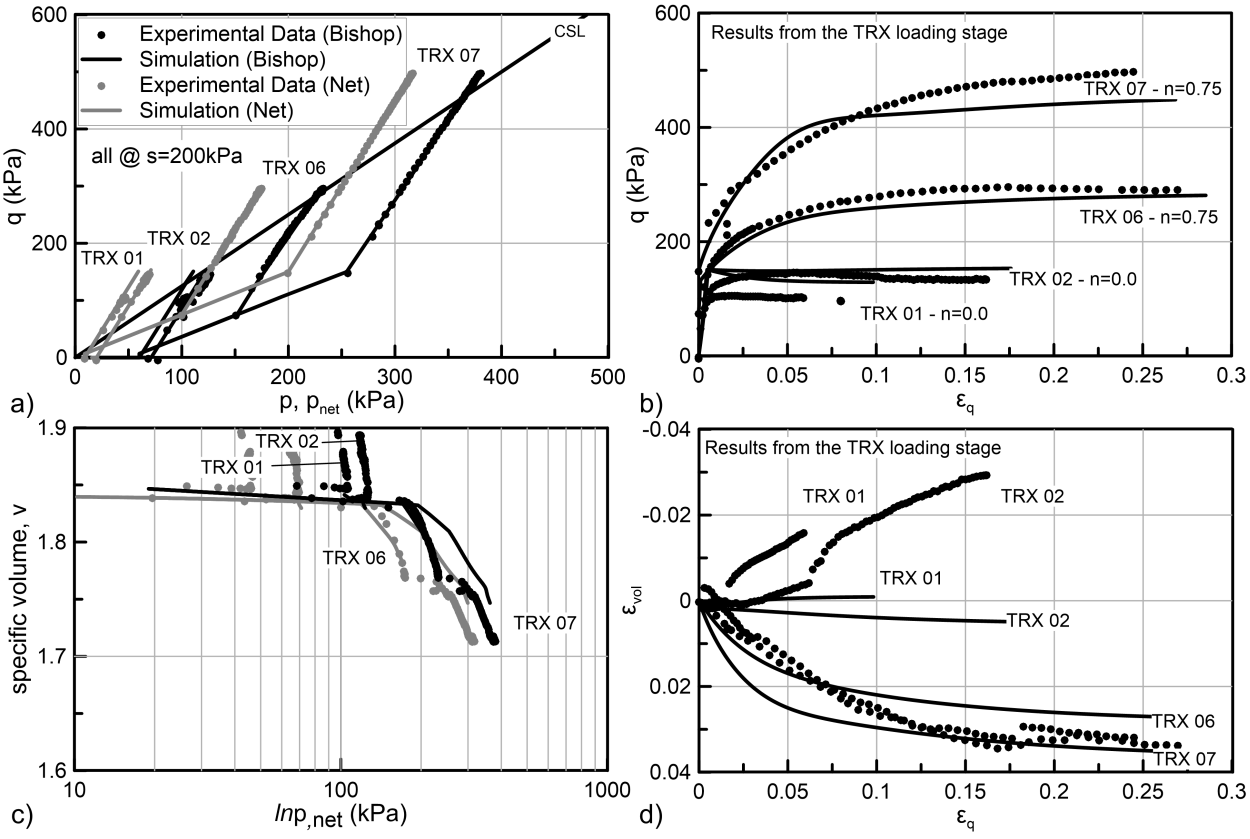


**Σχήμα 22:** Προσομοίωση δοκιμών τριαξονικής φόρτισης της Casini (2008), υπό μη κορεσμένες συνθήκες και υπό διαφορετικά επίπεδα αρχικής ανισοτροπίας.

- Το προσομοίωμα περιγράφει ικανοποιητικά τη σχέση τάσεων παραμορφώσεων και την αντοχή που μετρήθηκε σε δοκιμές τριαξονικής φόρτισης, τόσο σε

αρχικώς ισότροπα όσο και σε ανισότροπα στερεοποιημένα και μη κορεσμένα δοκίμια.

- Σημαντική συνεισφορά στις καλές προβλέψεις του προσομοιώματος κατέχει και το υιοθετούμενο προσομοίωμα της καμπύλης συγκράτησης ύδατος του Gallipoli et al. (2003), το οποίο παρέχει καλή περιγραφή της σχέσης βαθμού κορεσμού - μύζησης όσο και της εξέλιξης του βαθμού κορεσμού με τον λόγο κενών σε προσομοιώσεις υπό σταθερή μύζηση.

- Αναφορικά με την περιγραφή της ογκομετρικής παραμόρφωσης κατά τη διάρκεια δοκιμών τριαξονικής φόρτισης υπό σταθερή μύζηση προκύπτει ικανοποιητική σύγκριση των αποτελεσμάτων σε δοκιμές επί αρχικά ανισότροπων δοκιμίων και λιγότερο ακριβής σε δοκιμές σε αρχικά ισότροπα στερεοποιημένα δοκίμια, όπου το προσομοίωμα αποτυγχάνει στην πρόβλεψη της έντονα διαστολικής συμπεριφοράς που καταδεικνύουν τα εργαστηριακά αποτελέσματα.

## 9.3 Τα εργαστηριακά αποτελέσματα τού Barrera (2002)

Η τρίτη και τελευταία προσπάθεια αξιολόγησης των προβλέψεων του καταστατικού προσομοιώματος βάσει διαθέσιμων εργαστηριακών αποτελεσμάτων, βασίζεται στη μελέτη του Barrera (2002) σχετικά με τη μη κορεσμένη μηχανική συμπεριφοράς της Barcelona Clayey Silt, ενός αργιλώδους εδάφους χαμηλής πλαστικότητας (CL). Η ενασχόληση με τα συγκεκριμένα εργαστηριακά αποτελέσματα επικεντρώνεται σε περιορισμένο πλήθος δοκιμών, δίνοντας έμφαση στη δυνατότητα του προσομοιώματος να περιγράψει την κατάρρευση λόγω διαβροχής.

Ο πίνακας 9.11 παρουσιάζει τις παραμέτρους που επιλέχθηκαν για την προσομοίωση ενώ το Σχήμα 23 παρουσιάζει ενδεικτική σύγκριση της πρόβλεψης του προσομοιώματος με την ογκομετρική μεταβολή σε έναν κύκλο ύγρανσης και επαναξήρανσης, όπως αυτή προσδιορίστηκε εργαστηριακά.

Προκύπτει ότι το προτεινόμενο καταστατικό προσομοίωμα δύναται να περιγράψει επιτυχώς τις ογκομετρικές μεταβολές εντός κύκλων διαβροχής και επαναξύρανσης. Παρόλα αυτά, υπερεκτιμά τη φαινόμενη τάση προφόρτισης που αναπτύσσεται στο τέλος ενός τέτοιου κύκλου.

**Πίνακας 5:** Οι τιμές των παραμέτρων του καταστατικού προσομοιώματος όπως προέκυψαν από τη βαθμονόμηση στα διαθέσιμα εργαστηριακά αποτελέσματα του Barrera (2002).

| Βασικές παράμετροι | | Καμπύλη συγκράτησης ύδατος | | Μερικός κορεσμός | |
|---|---|---|---|---|---|
| Παράμετρος | Τιμή | Παράμετρος | Τιμή | Παράμετρος | Τιμή |
| $\kappa$ | 0.015 | $\phi$ | 0.038 | $r$ | 0.892 |
| $\lambda$ | 0.095 | $\psi$ | 2.00 | $\beta$ ( $MPa^{-1}$) | 100.0 |
| $\nu$ | 0.333 | $n$ | 1.30 | $\gamma$ | 0.1 |
| $c$ | 0.9390[*1] | $m$ | 0.23 | $p^c$ $(kPa)$ | $1.5 \cdot 10^{-6}$ |
| $k$ | 0.9390 | Alonso et. al. (2010) power law | | | |
| $N_{iso}$ | 2.055 | $\alpha$ | 1.25 | | |
| $\Gamma$ | 1.999[*2] | | | | |

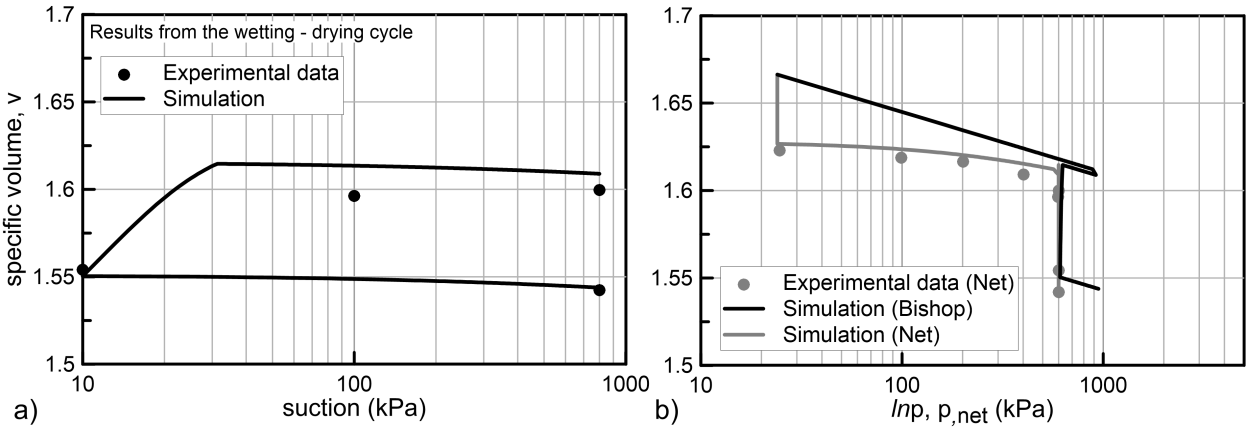


**Σχήμα 23:** Προσομοίωση δοκιμής διαβροχής από τα εργαστηριακά δεδομένα του Barrera (2002).

# 10 Εφαρμογή του καταστατικού προσομοιώματος στην αριθμητική επίλυση γεωτεχνικών προβλημάτων

Η τελευταία ενότητα της διδακτορικής διατριβής πραγματεύεται την εφαρμογή του προτεινόμενου καταστατικού προσομοιώματος σε σύνθετες γεωτεχνικές αναλύσεις συνοριακών συνθηκών με τον κώδικα πεπερασμένων στοιχείων Simulia Abaqus.

Αναλύεται η επιρροή της ανισοτροπίας στην ευστάθεια του μετώπου σήραγγας, εκσκαπτόμενης με μηχανοποιημένη όρυξη, καθώς και η επιρροή του μερικού κορεσμού στην οριακή φέρουσα ικανότητα και τις καθιζήσεις επιφανειακού θεμελίου.

Οι αναλύσεις που διεξάγονται είναι κατά βάση ενδεικτικές και αποσκοπούν στην τεκμηρίωση της ορθής εφαρμογής του καταστατικού προσομοιώματος στο Simulia Abaqus. Σε καμιά περίπτωση δεν αποτελούν ολοκληρωμένη διερεύνηση των εξεταζόμενων μηχανικών προβλημάτων.

## 10.1 **Αναλύσεις ευστάθειας μετώπου σήραγγας**

Για τις αναλύσεις ευστάθειας μετώπου σήραγγας χρησιμοποιήθηκε ένα τρισδιάστατο προσομοίωμα πεπερασμένων στοιχείων, στο οποίο αναλύεται η εκσκαφή κυκλικής σήραγγας διαμέτρου $D = 8m$ με ύψος υπερκειμένων $H_c = 16m$. Το Σχήμα 24 παρουσιάζει το προσομοίωμα πεπερασμένων στοιχείων. Πραγματοποιούνται συζευγμένες αναλύσεις της υδραυλικής και μηχανικής συμπεριφοράς του προβλήματος ενώ τόσο η ασκούμενη πίεση υποστήριξης στο μέτωπο όσο και η αντοχή και η παραμορφωσιμότητα του εδάφους αποτέλεσαν αντικείμενο παραμετρικής διερεύνησης. Αναλύθηκαν $30$ διαφορετικοί συνδυασμοί τριών διαφορετικών πιέσεων υποστήριξης και δέκα διαφορετικών συνδυασμών αντοχής και παραμορφωσιμότητας του γεωυλικού εντός του οποίου πραγματοποιείται η εκσκαφή. Συνολικά προέκυψαν $60$ αναλύσεις καθώς για κάθε έναν από τους προηγούμενους συνδυασμούς εκτελέστηκαν δύο αναλύσεις, μία με θεώρηση μηδενικής τασικής ανισοτροπίας και μία με αρχική ανισοτροπία που συμπίπτει με την ανισοτροπία του γεωστατικού τασικού πεδίου.

Η αποτίμηση της ευστάθειας μετώπου γίνεται στη βάση διαγραμμάτων εξέλιξης της έκθλιψης (οριζόντια μετακίνηση του μετώπου της σήραγγας) με τη μείωση της αντοχής του γεωυλικού εντός του οποίου λαμβάνει χώρα η διάνοιξη (βλ. Σχήμα 25), ακολουθώντας την πρόταση του Prountzopoulos (2008). Το βασικό συμπέρασμα που προέκυψε σε ότι αφορά την επιρροή της ανισοτροπίας είναι ότι αυτή οδηγεί σε αύξηση της υπολογιζόμενης έκθλιψης ενώ η επιρροή της γίνεται τόσο πιο εμφανής όσο μικρότερη είναι η ασκούμενη πίεση στο μέτωπο και όσο πιο ασθενές είναι το εξεταζόμενο γεωυλικό.

Η συμπεριφορά αυτή εξηγείται από το γεγονός ότι η αύξηση της έκθλιψης είναι απόρροια της προοδευτικής μείωσης της αντοχής (τασικής χαλάρωσης) που

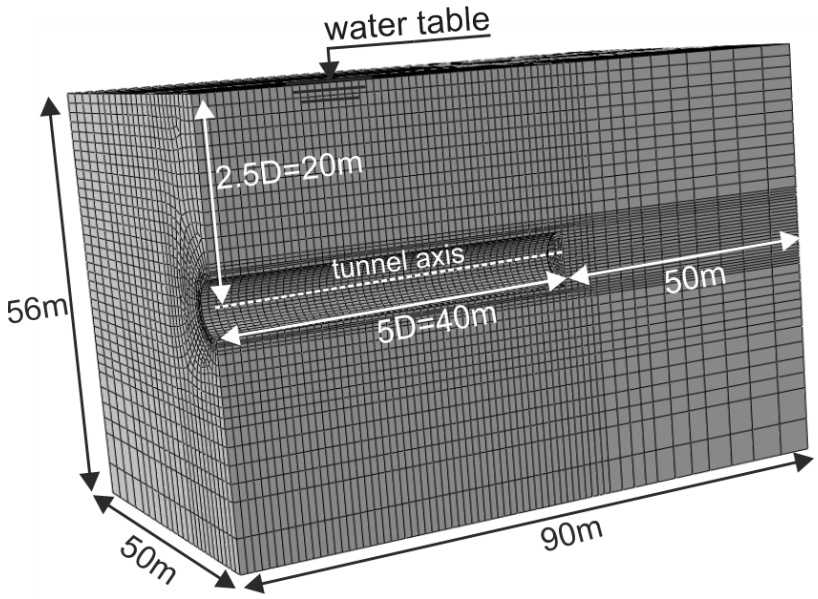


**Σχήμα 24:** Το προσομοίωμα πεπερασμένων στοιχείων που χρησιμοποιήθηκε στις αναλύσεις ευστάθειας μετώπου.

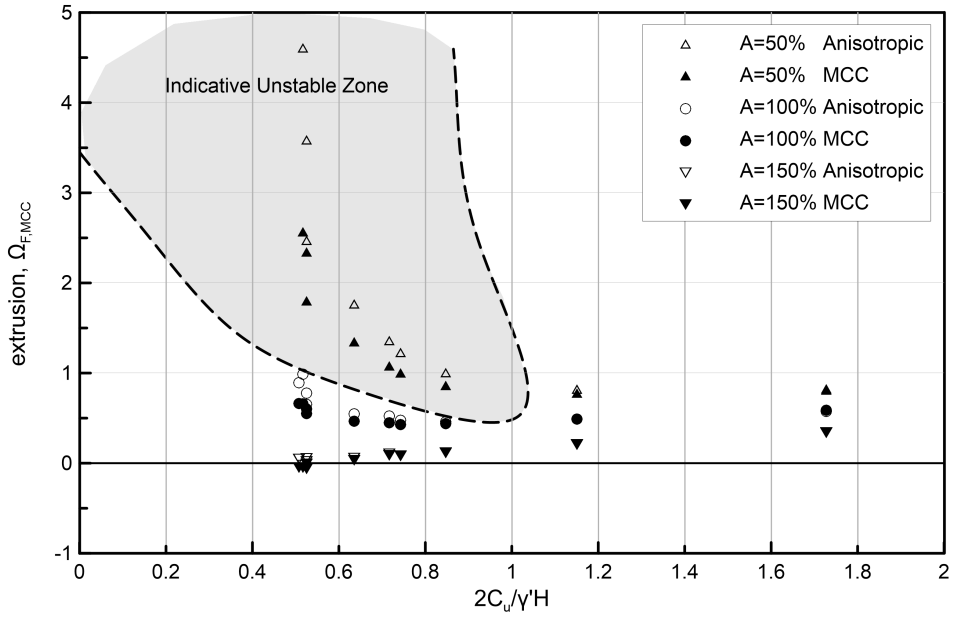


**Σχήμα 25:** Εξέλιξη της έκθλιψης του μετώπου της σήραγγας με την αντοχή του γεωυλικού για τρεις διαφορετικές πιέσεις υποστήριξης. Η επιρροή της ανισοτροπίας.

παρουσιάζουν ανισότροπα στερεοποιημένα εδάφη σε συνθήκες αστράγγιστης φόρτισης, με την τασική χαλάρωση να εντείνεται όσο αυξάνεται η πλαστική παραμόρφωση. Η ανάπτυξη πλαστικών παραμορφώσεων είναι τόσο πιο έντονη αφενός όσο πιο πτωχά είναι τα μηχανικά χαρακτηριστικά του εξεταζόμενου

γεωυλικού και αφετέρου όσο μικρότερη είναι η ασκούμενη πίεση υποστήριξης στο μέτωπο. Θα πρέπει να σημειωθεί ότι παρότι η τασική ανισοτροπία συντελεί στην αύξηση της έκθλιψης του μετώπου, σε επίπεδο αποτίμησης της ευστάθειας του μετώπου δε μεταβάλλει τα συμπεράσματα που προκύπτουν από απλούστερες αναλύσεις με αγνόηση της επιρροής της ανισοτροπίας.

## 10.2 Η επιρροή του μερικού κορεσμού στη φέρουσα ικανότητα και τις καθιζήσεις ενός επιφανειακού θεμελίου

Στην παράγραφο αυτή εξετάζεται η μηχανική συμπεριφορά ενός απειρομήκους, επιφανειακού, ακάμπτου θεμελίου και η επιρροή του μερικού κορεσμού σε αυτήν. Πρόκειται για ένα πρόβλημα επίπεδης παραμόρφωσης και για αυτό χρησιμοποιείται διδιάστατο προσομοίωμα. Πιο συγκεκριμένα, προσομοιώνεται θεμελιολωρίδα πλάτους $B = 2.0m$, εδραζόμενη στην επιφάνεια μαλακού, λεπτόκοκκου σχηματισμού με παραμέτρους που αντιστοιχούν στη συμπεριφορά της Jossigny Silt, όπως αυτές παρουσιάστηκαν στο προηγούμενο εδάφιο (βλ. πίνακα 4).

Οι αναλύσεις επικεντρώνονται στην εξέταση της επιρροής που έχουν διαφορετικά πάχη μη κορεσμένης ζώνης στην αριθμητικά υπολογιζόμενη καμπύλη φορτίου ($P$) - καθίζησης ($\delta$). Εξετάζονται έξι διαφορετικές στάθμες του υπόγειου υδροφόρου ορίζοντα οι οποίες αντιστοιχούν σε πέντε διαφορετικά βάθη από την επιφάνεια του εδάφους $d_w = 1.0, 2.0, 3.0, 4.0$ και $5.0m$ καθώς στην περίπτωση πλήρως κορεσμένου εδαφικού προφίλ ($d_w = 0.0$). Η φόρτιση γίνεται μέσω ταχείας επιβολής κατακόρυφης μετατόπισης του θεμελίου $\delta = 1.0m$ σε χρονικό διάστημα μόλις μίας ώρας ώστε να προσομοιωθούν αστράγγιστες συνθήκες φόρτισης. Εκτελέστηκαν δύο ομάδες αναλύσεων με θεώρηση και αγνόηση της αρχικής ανισοτροπίας αντίστοιχα για λόγους σύγκρισης.

Στο Σχήμα 26 παρουσιάζονται οι καμπύλες $P$-$\delta$ που προέκυψαν. Συγκριτικά παρατηρούμε ότι ο μερικός κορεσμός, όπως αυτός αντιπροσωπεύεται από την αύξηση του πάχους της μη κορεσμένης ζώνης, οδηγεί σε αύξηση της δυνατότητας ανάληψης φορτίου του εξεταζόμενου θεμελίου. Η αύξηση αυτή οφείλεται στην αυξημένη αντοχή και στη μειωμένη παραμορφωσιμότητα του μη κορεσμένου εδαφικού προφίλ, συνοδεύεται δε από σταδιακή μεταβολή του μηχανισμού αστοχίας από μηχανισμό αστοχίας σε αστράγγιστη φόρτιση προς αστοχία σε διάτρηση (βλ. Σχήμα 27). Η επιρροή της ανισοτροπίας προκύπτει μικρή σε σχέση με την αντίστοιχη επιρροή του μερικού κορεσμού, ενώ μεταβάλλεται και με την αλλαγή του

μηχανισμού αστοχίας.

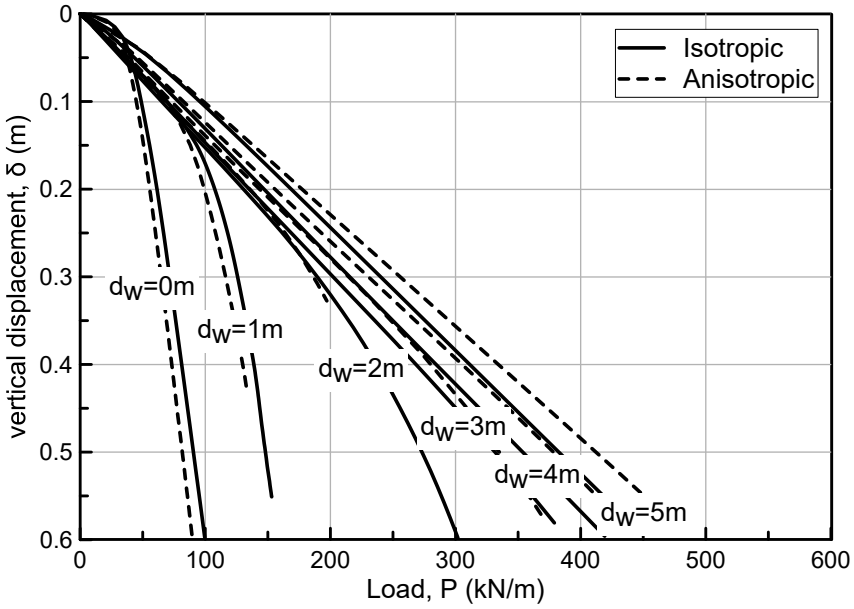


**Σχήμα 26:** Καμπύλες φορτίου $P$ - καθίζησης $\delta$ θεμελιολωρίδας πλάτους $2.0m$ για έξι διαφορετικές θέσεις του υπόγειου υδροφόρου ορίζοντα.

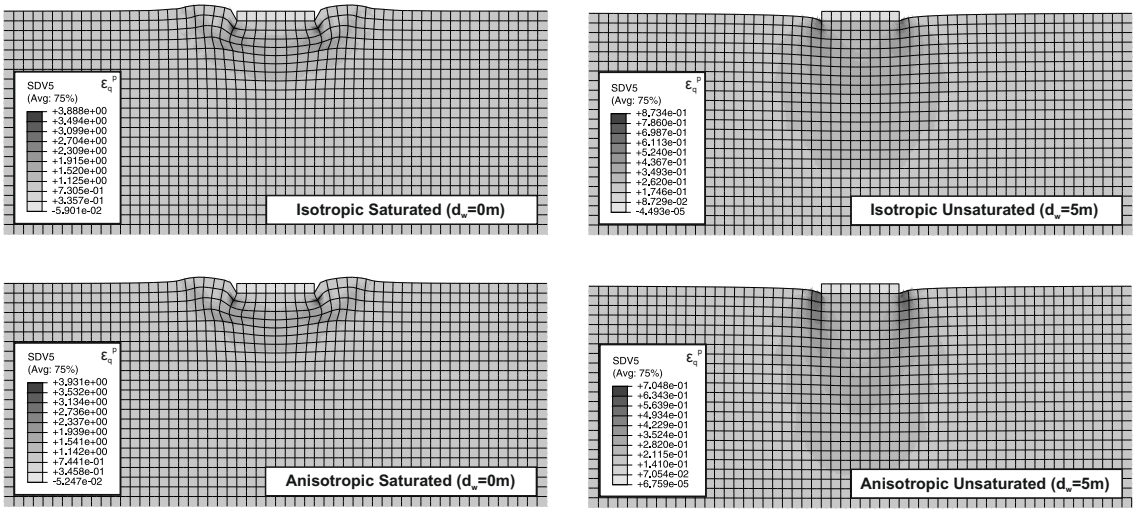


**Σχήμα 27:** Ο παραμορφωμένος κάναβος για δύο διαφορετικές θέσεις του υδροφόρου ορίζοντα.

Τέλος, εξετάζεται η επιρροή της ανόδου της στάθμης του υδροφόρου ορίζοντα σε επιφανειακό θεμέλιο εδραζόμενο επί αρχικά μη κορεσμένου εδαφικού προφίλ ($d_w = 5.0m$), στο οποίο ασκείται κατακόρυφο φορτίο σημαντικά μικρότερο του οριακού του

φορτίου. Στο Σχήμα 28, παρατηρούμε ότι η άνοδος της στάθμης του υδροφόρου ορίζοντα οδηγεί σε καθίζηση του θεμελίου ως αποτέλεσμα ογκομετρικής κατάρρευσης του εδάφους κάτω από το θεμέλιο. Αντίθετα, η ελεύθερη επιφάνεια του εδάφους σε απόσταση από το θεμέλιο ανυψώνεται καθώς η διαβροχή συμβαίνει υπό μειωμένο πεδίο τάσεων και οδηγεί σε διόγκωση.

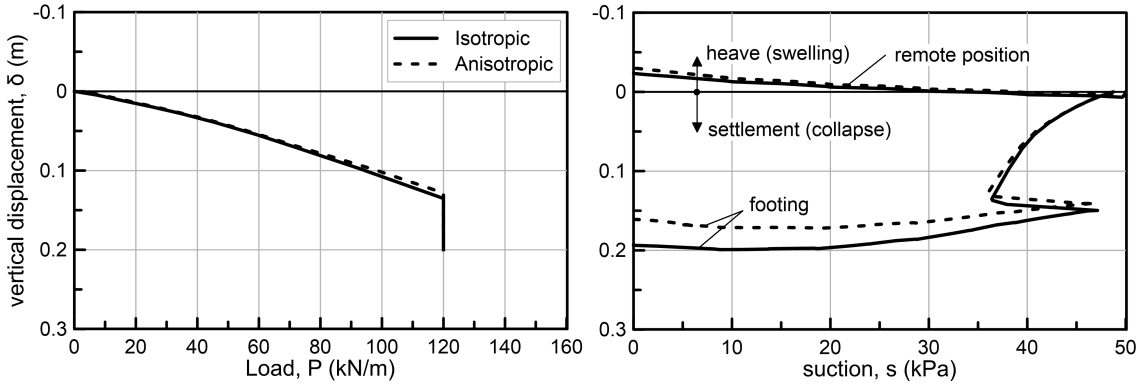


**Σχήμα 28:** Εξέλιξη των κατακόρυφων μετακινήσεων του θεμελίου και της ελεύθερης επιφάνειας του εδάφους κατά την άνοδο του υδροφόρου ορίζοντα.

# 11 Συμπεράσματα - Προτάσεις μελλοντικής έρευνας

Η παρούσα διδακτορική διατριβή είχε ως κύριο σκοπό την ανάπτυξη, αριθμητική εφαρμογή και τεκμηρίωση ενός νέου καταστατικού προσομοιώματος για μη κορεσμένα εδάφη με δυνατότητα περιγραφής της επιρροής της τασικής ανισοτροπίας. Προτάθηκε ένα προσομοίωμα μοναδικής επιφάνειας βασισμένο στις αρχές της Εδαφομηχανικής της κρίσιμης κατάστασης ενώ η μαθηματική του διατύπωση ακολουθεί τις βασικές αρχές της θεωρίας της πλαστικότητας. Περιλαμβάνει ένα στρεβλό ελλειψοειδές στον χώρο των τάσεων για την περιγραφή προτιμητέων διευθύνσεων της ανισοτροπίας, έναν μη συσχετισμένο νόμο ροής και έναν μικτό νόμο κινηματικής κράτυνσης. Ενσωματώνει μία επιφάνεια Φόρτισης - Κατάρρευσης για την ενοποιημένη περιγραφή της συμπεριφοράς τόσο σε καταστάσεις φόρτισης υπό μερικό κορεσμό όσο και σε τασικές οδεύσεις μεταβολής της μύζησης.

Οι προβλέψεις του προσομοιώματος αξιολογήθηκαν και τεκμηριώθηκαν στη βάση ποιοτικών παρατηρήσεων μέσω σημαντικού πλήθους παραμετρικών αναλύσεων αλλά και ποσοτικά μέσω ασκήσεων βαθμονόμησης και σύγκρισης της προσομοιούμενης

συμπεριφοράς με εργαστηριακά δεδομένα από τη διεθνή βιβλιογραφία. Τέλος, επιδείχθηκε η δυνατότητα εφαρμογής του προσομοιώματος σε σύνθετες αναλύσεις συνοριακών συνθηκών στον κώδικα πεπερασμένων στοιχείων Simulia Abaqus.

Προέκυψε ότι το προτεινόμενο καταστατικό προσομοίωμα δύναται να περιγράψει με επιτυχία τα κυριότερα μηχανικά χαρακτηριστικά ανισότροπα στερεοποιημένων εδαφών τόσο σε καταστάσεις πλήρους όσο και μερικού κορεσμού, ενώ η διατύπωσή του είναι σχετικά απλή και οι παράμετροί του εύκολα διακριβώσιμες στη βάση συνήθων εργαστηριακών δοκιμών. Επιπρόσθετα, αποδεικνύεται ότι τα υπολογιστικά εργαλεία που αναπτύχθηκαν για την αριθμητική επίλυση των εξισώσεων του προσομοιώματος μπορούν να διαχειριστούν με επιτυχία σύνθετες αναλύσεις πεπερασμένων στοιχείων, επιτρέποντας τη μελλοντική χρήση του προσομοιώματος τόσο σε πρακτικές εφαρμογές όσο και στην ερευνητική διερεύνηση της επίδρασης της ανισοτροπίας και του μερικού κορεσμού σε προβλήματα μηχανικού.

Οι κυριότερες δυνατότητες του προτεινόμενου προσομοιώματος μπορούν να συνοψιστούν στα εξής:

- Δύναται να περιγράψει με ακρίβεια την εξάρτηση των καμπυλών εγγενούς συμπίεσης από τον βαθμό της επιβαλλόμενης τασικής ανισοτροπίας.

- Ο προτεινόμενος νόμος ροής περιγράφει επιτυχώς τις πλαστικές παραμορφώσεις, τόσο σε δοκιμές ακτινικής συμπίεσης όσο και σε στραγγισμένες δοκιμές τριαξονικής φόρτισης.

- Ο προτεινόμενος νόμος κράτυνσης για την «απώλεια μνήμης» της ανισοτροπίας με τη συσσώρευση διεκτροπικών πλαστικών παραμορφώσεων περιγράφει επιτυχώς τόσο την τασική χαλάρωση που επιδεικνύουν ανισότροπα στερεοποιημένα εδαφικά υλικά όσο και μία ενιαία κρίσιμη κατάσταση.

- Η εφαρμογή της τάσης εδαφικού σκελετού του Bishop περιγράφει με επιτυχία την εξέλιξη της διατμητικής αντοχής με τη μύζηση σε καταστάσεις μερικού κορεσμού.

- Το προτεινόμενο πλαίσιο συμπιεστότητας για καταστάσεις μερικού κορεσμού προσομοιώνει επιτυχώς την εξέλιξη της συμπιεστότητας με τη μύζηση και τον βαθμό κορεσμού και δύναται να προβλέπει: α) καμπύλες συμπίεσης ανεξάρτητες της μύζησης για καταστάσεις πλήρους κορεσμού, β) συνεχή μεταβολή της συμπιεστότητας για καταστάσεις φόρτισης υπό σταθερή μύζηση,

καθώς και γ) ένα μέγιστο στις ογκομετρικές παραμορφώσεις λόγω διαβροχής (κατάρρευση).

Στο άμεσο μέλλον η σχετιζόμενη με την εξέλιξη του προτεινόμενου προσομοιώματος έρευνα θα πρέπει να εστιάσει στην άρση των κυριότερων αδυναμιών του προσομοιώματος:

- Το προσομοίωμα τείνει να υπερεκτιμά τη μέγιστη αντοχή ανισότροπα στερεοποιημένων εδαφών. Απαιτείται τροποποίηση του νόμου κινηματικής κράτυνσης του Kavvadas (1982) με σκοπό τη δυνατότητα μεγαλύτερης ευελιξίας ως προς τον προσανατολισμό της επιφάνειας διαρροής σε ακτινικές τασικές οδεύσεις. Στην παρούσα έκδοση το πρόβλημα αυτό μπορεί να ξεπεραστεί μέσω κατάλληλης βαθμονόμησης των παραμέτρων του προσομοιώματος.

- Λόγω της μεγάλης ελαστικής περιοχής, οι προβλέψεις του προσομοιώματος υστερούν σε καταστάσεις που αναφέρονται σε έντονα υπερστερεοποιημένα εδαφικά υλικά. Για τη βελτίωση των προβλέψεων απαιτείται η εισαγωγή εσωτερικής επιφάνειας πλαστικής διαρροής για τη μετατροπή του προσομοιώματος σε προσομοίωμα οριακής πλαστικότητας, όμοιο με τα προσομοιώματα των Belokas (2008) και Kalos (2014).

- Ο νόμος ροής απαιτεί βελτίωση με σκοπό την καλύτερη πρόβλεψη της αύξησης της τάσης για διαστολική συμπεριφορά που τα μη κορεσμένα εδαφικά υλικά επιδεικνύουν με την αύξηση της μύζησης. Η ενσωμάτωση κάποιου τύπου άμεσης εξάρτησης της επιφάνειας πλαστικού δυναμικού από το επίπεδο της μύζησης θα μπορούσε να αποτελεί έναν πιθανό τρόπο βελτίωσης των προσομοιώσεων.

# Thesis Main Body

# Contents

# List of Figures

# List of Tables

# List of Symbols

| Symbol | Units | Description |
|---|---|---|
| $\boldsymbol{\sigma}$ | Pascal | Bishop's stress tensor; coincides with Terzaghi's effective stress at Saturation |
| $\sigma \equiv p$ | Pascal | Bishop's mean stress; coincides with Terzaghi's mean effective stress at Saturation |
| $\boldsymbol{s}$ | Pascal | deviatoric stress tensor |
| $q$ | Pascal | equivalent stress or Von Mises stress; it is a measure of the stress deviator equal to $\sqrt{\frac{3}{2}\boldsymbol{s} : \boldsymbol{s}}$, called deviatoric stress for brevity. In the present dissertation, when triaxial extension is examined, it is assumed that $q = \sigma_v - \sigma_h$ allowing $q$ to obtain negative values |
| $\overline{\boldsymbol{\sigma}}$ | Pascal | net or total stress tensor; If air pressure $u_a$ is assumed equal to zero net and total stress coincide |
| $\overline{\sigma} \equiv \overline{p}$ | Pascal | mean net or total stress |
| $\boldsymbol{\varepsilon}$ | – | strain tensor |
| $\varepsilon \equiv \varepsilon_{vol}$ | – | volumetric strain |
| $\boldsymbol{e}$ | – | deviatoric strain tensor |
| $\varepsilon_q$ | – | deviatoric strain; it is a measure of the stain deviator equal to $\sqrt{\frac{2}{3}\boldsymbol{e} : \boldsymbol{e}}$. In the present dissertation, when triaxial extension is examined, it is assumed that $\varepsilon_q = \frac{2}{3}(\varepsilon_v - \varepsilon_h)$ allowing $\varepsilon_q$ to obtain negative values |
| $d_q$ | – | dilatancy |
| $\boldsymbol{\varepsilon}^{e,p}$ | – | elastic (e) or plastic (p) strain tensor |
| $\varepsilon^{e,p}$ | – | elastic (e) or plastic (p) volumetric strain |
| $\boldsymbol{e}^{e,p}$ | – | elastic (e) or plastic (p) deviatoric strain tensor |
| $\varepsilon_q^{e,p}$ | – | elastic (e) or plastic (p) deviatoric strain |

| Symbol | Units | Description |
|---|---|---|
| $\boldsymbol{q}$ | | vector (regardless whether there is a tensor involved within the definition of $\boldsymbol{q}$), representing the hardening variables |
| $\boldsymbol{I}$ | – | Second order unit tensor |
| $K$ | Pascal | bulk Modulus |
| $G$ | Pascal | shear Modulus |
| $\nu$ | – | Poisson's ratio |
| $f$ | Pascal$^2$ | yield function |
| $\boldsymbol{Q}$ | Pascal | gradient of the yield function |
| $\boldsymbol{C^e}$ | Pascal | elastic stiffness tensor |
| $g$ | Pascal$^2$ | plastic potential function |
| $\boldsymbol{P}$ | Pascal | plastic potential tensor |
| $\dot{\Lambda}$ | Pascal$^{-1}$ | plastic multiplier |
| $H$ | Pascal$^3$ | plastic modulus |
| $\boldsymbol{C^{ep}}$ | Pascal | elastoplastic stiffness tensor |
| $v$ | – | specific volume equal to $1+e$, where $e$ the void ratio |
| $\lambda$ | – | MCC compressibility parameter, defining the slope of the virgin compression lines in the $v-lnp$ plane |
| $\kappa$ | – | MCC compressibility parameter, defining the slope of the swelling lines in the $v-lnp$ plane |
| $N_{iso}$ | – | specific volume corresponding to the isotropic virgin compression line at a mean effective stress equal to $1kPa$ |
| M | – | slope of the critical state line in the $p-q$ space (triaxial stress space) |
| $\Gamma$ | – | specific volume corresponding to the critical state line at a mean effective stress equal to $1kPa$ |
| $\alpha$ | Pascal | halfsize of the yield surface - comprises an isotropic hardening variable |
| $p_0$ | Pascal | isotropic preconsolidation pressure |
| $R_p$ | – | isotropic overconsolidation ratio $p_0/p$ |
| $n$ | – | stress ratio $q/p$ |
| $K$ | – | horizontal stress ratio $\sigma_h/\sigma_v$ |
| $K_0$ | – | geostatic stress ratio, corresponding to 1D conditions (zero horizontal strains) |

| Symbol | Units | Description |
|---|---|---|
| $K_{0,NC}$ | – | geostatic stress ratio of normally consolidated materials |
| $\sigma_p$ | Pascal | vertical preconsolidation pressure $\sigma_p/\sigma$ |
| $OCR$ | – | (One dimensional) over consolidation ratio |
| $K_{0,OC}$ | – | geostatic stress ratio of over-consolidated materials |
| $S_r$ | – | degree of saturation |
| $s$ | Pascal | suction |
| $s_m$ | Pascal | matric suction |
| $s_c$ | Pascal | capillary component of suction |
| $s_a$ | Pascal | absorptive component of suction |
| $s_o$ | Pascal | osmotic component of suction |
| $s_0$ | Pascal | desaturation suction |
| $u_a$ | Pascal | gas (air) phase pressure |
| $u_w$ | Pascal | liquid (water) phase pressure |
| $T_s$ | Pascal | surface tension |
| $P_v$ | Pascal | vapour pressure |
| $T$ | $^o$K or $^o$C | temperature |
| $RH$ | – | relative humidity |
| $w$ | – | gravimetric water content |
| $\theta$ | – | volumetric water content |
| $e_w$ | – | water ratio |
| $WC$ | – | normalized water content expression (may refer to either $S_r$, $w$ or $\theta$) |
| $S_{r,M}$ or $S_r^e$ | – | macro-structural or effective degree of saturation |
| $wPI$ | – | weighted plasticity index |
| $\phi_b$ | $^o$ | friction angle related to suction |
| $N_n$ | – | specific volume corresponding to an anisotropic compression line at a mean effective stress equal to $1kPa$ |
| $\lambda(s, S_r^e)$ | – | unsaturated compressibility |
| $p_0(s, S_r^e)$ | Pascal | the apparent preconsolidation pressure |
| $\boldsymbol{b}$ | – | anisotropy tensor |
| $\boldsymbol{d}$ | – | plastic potential surface orientation tensor |
| $k$ | – | aspect ratio of the yield surface |

| Symbol | Units | Description |
|---|---|---|
| $c$ | – | aspect ratio of the plastic potential surface |
| $r_s$ | – | compressibility parameter |
| $\psi$ | – | hardening rule parameter |
| $\zeta_q^p$ | – | hardening rule parameter |
| $\chi$ | – | flow rule parameter |
| $r$ | – | unsaturated compressibility parameter |
| $\beta$ | Pascal$^{-1}$ | unsaturated compressibility parameter |
| $\gamma$ | – | unsaturated compressibility parameter |
| $p^c$ | Pascal | reference pressure |
| $D$ | meter | tunnel diameter |
| $H$ | meter | tunnel axis depth |
| $H_c$ | meter | tunnel crown depth |

# List of Abbreviations

| Abbreviation | Description |
|---|---|
| FEM | Finite Element Method |
| YS | Yield Surface |
| PPS | Plastic Potential Surface |
| CSSM | Critical State Soil Mechanichs |
| SBS | State Boundary Surface |
| NCL | Normal Compression Line |
| ICL | Intrinsic Compression Line |
| CSL | Critical State Line |
| MCC | Modified Cam Clay |
| PTL | Phase Transformation Line |
| PYE | Plastic Yield Envelope |
| CL | Compression Line |
| INCL | Isotropic Normal Compression Line |
| 1D-NCL | One Dimensional Normal Compression Line |
| LCT | Lower Cromer Till |
| ICF | Intrinsic Compressibility Framework |
| ISE | Intrinsic Strength Envelope |
| SSE | Structure Strength Envelope |
| BSE | Bond Strength Envelope |
| WRC | Water Retention Curve |
| AEV | Air Entry Value |
| MIP | Mercury Intrusion Porosimetry |
| ESM | Electron Scanning Microscopes |
| WRM | Water Retention Model |
| ILS | Ioannina Lake Silt |

| Abbreviation | Description |
|---|---|
| CM | Corinth Marl |
| TEM | Tempi Silt |
| CSC | Chania Silty Clay |
| KM | Kifissia Marl |
| KC | Kifissia Clay |
| CHM | Chalkoutsi Marl |
| BBM | Barcelona Basic Model |
| CVs | Constitutive Variables |
| FCV | First Constitutive Variable |
| SCV | Second Constitutive Variable |
| LC | Loading - Collapse |
| SI | Suction Increase |
| SD | Suction Decrease |
| ICE | Intrinsic Compressibility Envelope |
| TSS | Transformed Stress Space |
| SMP | Single Material Point |
| TRX | Triaxial |
| PS | Plain Strain |
| DSS | Direct Simple Shear |
| JS | Jossigny Silt |
| BCS | Barcelona Clayey Silt |
| EPB | Earth Pressure Balance |
| TBM | Tunnel Boring Machine |

# Chapter 1

# Introduction

## 1.1 General

A significant portion of the earth's surface, even in areas with a temperate climate, is subjected to arid or semi-arid climatic conditions. In such cases, the underground water table is usually located at an appreciable depth from the ground's surface, leaving the soil profile above the phreatic surface unsaturated ($0 < S_r < 100\%$). This zone is usually called the unsaturated or the vadose zone. The water content within the vadose zone depends on a variety of different factors, with the most important being the type of the soil and the prevailing atmospheric conditions. For instance, the type of the soil defines how capable a soil is to retain water under a given negative water pressure (i.e., height of capillary rise), while the atmospheric conditions affect the hydrologic cycle (i.e., evapotranspiration, precipitation) and thus, define the variation of the water content with time.

Although a significant number of civil engineering projects interact with the vadose zone (i.e, foundations of buildings/infrastructures, man-made slopes etc.), when it comes to the analysis of their mechanical response, the common approach in both practice and research is to neglect the presence of the unsaturated zone, either by setting the phreatic to the soil surface (saturated profile) or by assuming a completely dry soil profile above the phreatic surface.

The main reason for such simplifications is the complexity involved with the behaviour of unsaturated soils, arising primarily from the following factors:

- The difficulty in measuring the properties of a material which involves three distinct phases instead of two, namely the solid phase, the water phase and the

air phase. Common laboratory equipment is orientated towards saturated soils.

- The complexity of the interplay between the underlying mechanisms involved with the behaviour of a three-phase porous material. The fact that unsaturated soils do not obey the principle of effective stress, is simply indicative of this complexity.

- The lack of engineering insight in the behaviour of unsaturated soils, obviously related to the aforementioned complexity of the associated mechanisms and also stemming from the fact that unsaturated soil mechanics is scarcely taught in either undergraduate or post-graduate engineering courses.

The justification accompanying the assumption to neglect the unsaturated zone is that such an approach proves conservative. To some extend the aforementioned statement holds true. For instance, partial saturation favours an increased shear strength and a decreased compressibility. However, in many engineering problems, neglecting the unsaturated zone is not or should not be an option. For instance, heave or collapse of foundations due to fluctuations of the water table cannot be efficiently studied without accounting for the unsaturated nature of the foundation soil. Another illustrative example, is the progressive failure of man-made or natural slopes, especially after periods of significant precipitation, originating from a decrease in the shear strength caused by the increase in water content.

In recent years, advances in experimental techniques allowed for a more systematic study of the behaviour of unsaturated soils, leading to the evolution of a new "branch" of geotechnical discipline, the Unsaturated Soil Mechanics. The three fundamental ideas of modern Unsaturated Soil Mechanics are summarized here below:

- An unsaturated soil is a specific state of a soil and not a special soil. Thus, the unsaturated soil behaviour should be considered as an extension of the classical soil mechanics for saturated soils and not as a special case of soil behaviour.

- The Water Retention Curve (WRC), describing the relationship between suction (negative water pressure) and water content, is the most fundamental relation of unsaturated soil mechanics.

- Two independent constitutive variables are essential to describe the behaviour, contrary to saturated soils, where the effective stress is only required.

Nowadays, an ensemble of theoretical frameworks, constitutive models and analytical tools exist in the international literature, which allow for a comprehensive study of the unsaturated soil behaviour. Such tools may be utilized in the analysis of various engineering problems where partial saturation plays a key role in the soil response. Characteristic engineering problems include:

- wetting induced settlements in foundations laying on collapsible soils;
- heave due to wetting of foundations laying on expansive soils;
- failure of artificial or natural slopes following a water content increase;
- reverse analysis of slope failures;
- the behaviour of compacted soils (i.e, railway or highway embankments, earth dams etc.)
- the long-term storage of high-level radioactive nuclear waste in deep geological repositories (unsaturated backfill isolates the canisters from the surrounding ground).

## 1.2 Scope of Work

The main scope of the present Doctoral Thesis is to formulate a constitutive model for unsaturated soils and further implement it in the Finite Element Method computer code Simulia Abaqus. Geotechnical boundary value problems are usually numerically solved utilizing either the Finite Element or the Finite Difference methods. In both cases, the constitutive model provides the crucial link between external loading agents (i.e., stress increment, suction increment) and the corresponding strains accumulating in the ground.

The developed constitutive model is part of a coordinated research effort, taking place during a period of several years in the Geotechnical Department at the National Technical University of Athens to develop advanced soil constitutive behavioural frameworks. Characteristic contributions include the Kavvadas & Amorosi (2000) and Belokas & Kavvadas (2010) for anisotropic and structured clayey soils, the Kalos (2014) viscoelastoplastic model including structure degradation and small-strain stiffness characteristics, as well as the Papadimitriou et al. (2001) and the Tasiopoulou & Gerolymos (2016) constitutive frameworks for sands.

Unsaturated soils are either natural or compacted soils, both involving consolidation or compaction under anisotropic, usually one dimensional, conditions. In both cases, the resulting anisotropic fabric is reflected on their mechanical behavioural characteristics. In that respect, the present research uses an anisotropic critical state constitutive model as the saturated reference model, namely the Kavvadas (1982) MIT-E1 model. Significant enhancements are realized before it is extended in the unsaturated regime. Hence, the proposed model should be considered as an improved constitutive model for anisotropic soils which can additionally account for the behaviour of unsaturated soils, thus comprising a new anisotropic - unsaturated constitutive behavioural framework.

With the proposed model being developed for a commercial numerical code implementation, research effort was concentrated in keeping a balance between accuracy of the predictions, and simplicity of the formulation (i.e. minimizing model parameters), with the latter favouring robustness, efficiency and practical usability. The main features of the developed constitutive model are summarized bellow:

- It incorporates an anisotropic, distorted elliptical yield surface to account for the yield locus of anisotropically consolidated soils.
- It utilizes a novel mixed hardening rule consisting of:
  a) an isotropic part, which in cooperation with the kinematic part, is capable of describing distinct and parallel compression curves depending on the level of stress induced anisotropy. It is based on an Intrinsic Compressibility Framework proposed in Belokas & Kavvadas (2011) and further enhanced within the present research;
  b) a kinematic hardening part, based on a novel idea for reorienting the yield surface towards the isotropic axis at critical state. The kinematic hardening rule can reproduce in a simple, natural and unified way the strain softening behaviour that anisotropically consolidated soils exhibit during triaxial loading under undrained conditions (anisotropy strength degradation) and also reproduce unique critical state conditions irrespective of the initial anisotropy and of the stress path towards the critical state;
- Plastic strains accumulation follow a non-associated flow rule; Contrary to the Kavvadas (1982) and Belokas & Kavvadas (2010) proposal, directly postulating the plastic potential tensor, the proposed flow rule is based on a plastic

potential function, represented through a distorted ellipse. Such a selection increases the simplicity of the formulation and reduces the number of the required parameters, without practically sacrificing the model's predictions.

- Extension in the unsaturated regime is realized through Bishop's average skeleton stress, using the macrostructural degree of saturation as a scaling parameter. Such a selection allows for a natural representation of the nonlinear increase in shear strength and elastic compressibility with partial saturation. Bishop's average skeleton stress also ensures a natural transition between saturated and unsaturated conditions, as it recalls Terzaghi's effective stress upon saturation;

- It additionally includes a Loading- Collapse surface, derived from a new compressibility framework proposed within the present thesis. The latter describes a double dependance of the unsaturated compressibility on suction and degree of saturation; the developed framework can reproduce:

  a) unique compression lines for saturated material states, irrespectively of the level of the applied suction;

  b) a constantly evolving stiffness for compression under constant suction;

  c) a maximum of collapse.

The model includes a total of fifteen (15) material parameters which can be reduced to thirteen (13) through commonly utilized assumptions. Five of them correspond to the Modified Cam Clay parameters; four (4) are required to activate its anisotropic characteristics and another four (4) for its unsaturated module. The model under isotropic conditions upon saturation reduces to the Modified Cam Clay model. Its unsaturated and anisotropic behavioural characteristics are in fact decoupled, allowing for a simplified calibration of the model parameters, all of which hold a strong physical meaning. Each of the anisotropic or unsaturated features can be deployed separately or in parallel.

The model additionally requires a hydromechanical coupling with a void ratio dependant Water Retention Model (WRM), to provide the degree of saturation vs suction relationship. The Gallipoli et al. (2003) WRM is implemented in the developed numerical algorithm. When it comes to the Simulia Abaqus implementation, the code incorporates a simple water retention model with no void ratio dependance, while it does not allow for a user defined water retention law. Unfortunately, this fact

poses severe limitations on the model's unsaturated capabilities, mostly affecting its ability to reproduce a maximum of collapse.

Additionally, the proposed model focuses on the behaviour of common, clayey soils which usually collapse when water soaked. It cannot account for the behaviour of highly expansive active clays, as their simulation requires specialized mechanical frameworks and constitutive models. Finally, it is a single yield surface model and thus cannot account for small strain stiffness. The latter affects the model's simulation capabilities in highly overconsolidated soils.

## 1.3 Research Methodology - Outline of the Thesis

The research methodology to establish the proposed anisotropic - unsaturated constitutive behavioural framework is summarized by the following five (5) main Research Steps (RS):

RS.1: an extensive literature review of the theory of classical soil plasticity, the mechanical behaviour and constitutive modelling of anisotropic soils followed by a comprehensive study of the mechanical behaviour and constitutive modelling of unsaturated soils. Chapters 2 through 4 address the aforementioned task;

RS.2: the development of the underlying mechanical framework and the formulation of the proposed constitutive model, presented in detail in chapters 5 and 6 respectively;

RS.3: the numerical implementation of the proposed constitutive model, addressed in chapter 7;

RS.4: the evaluation - calibration of the proposed model, addressed in chapters 8 and 9;

RS.5: the indicative application of the proposed model to common engineering problems in chapter 10.

In more detail, chapter 2 reviews the main concepts of the theory of plasticity, definitions of the external and internal variables, the material state and loading conditions. It presents the main features of any constitutive model, namely the yield surface, the elasticity, the flow and the hardening rules. The review is limited to invisid elastoplastic formulations for saturated material states, while all the necessary

modifications to address the behaviour of unsaturated soil elements are presented in chapter 6. Emphasis is given on how the selection of a non-associated flow rule can still ensure stability of the solution, by imposing specific limitations to the selection of both the flow and the hardening rules. Chapter 2 further includes a review of the most important basic constitutive models for soil analysis, with emphases on Critical State models and specifically on the Modified Cam Clay model. The behaviour of re-constituted, isotropically consolidated soils is presented and the theory of plasticity is used to demonstrate how a conceptual framework can be formulated to a constitutive model for soils, with respect to the Modified Cam Clay model.

Chapter 3 extends the previous discussion on the mechanical behaviour of anisotropically consolidated soils. The study concentrates on the compressibility behaviour of radially and/or one-dimensionally consolidated soil specimens, as both tests induce anisotropic behavioural aspects. The behaviour of anisotropically consolidated soil samples under shear tests is analyzed, as an extension of the theory of Critical State Soil Mechanics. The discussion is based on well documented experimental results from the international literature, including drained or undrained stress paths, both compression and extension tests on soil samples subjected to different levels of initial stress induced anisotropy. The review identifies the most critical aspects of the mechanical behaviour of anisotropically consolidated soils, to be included within the proposed model. The second part of chapter 3 reviews existing constitutive models for anisotropic soils, identifying their advantages and limitations.

Chapter 4 comprises of a comprehensive study on the behaviour of unsaturated soils. It is quite extended and for a reader who is familiar with the behaviour of unsaturated soils, its first part may seem redundant. Nevertheless, considering that the majority of practitioners and researchers may lack fundamental knowledge of the nature and mechanical behaviour of unsaturated soils, the first section addresses the two fundamental concepts of unsaturated soil mechanics, namely the soil suction and the water retention curve. The section dealing with the water retention curve, additionally includes some original work partially conducted within the context of the present Doctoral Thesis to numerically simulate the water retention behaviour of typical soils from Greece. The utilized experimental data comprise of part of the Bardanis (2016) research work. The effect of partial saturation on the mechanical behaviour of soils is presented next, including the inevitable discussion on the stress - constitutive variables required for an adequate representation of the soil behaviour. The effect of

partial saturation on the yield, volumetric and shear strength is addressed. Chapter 4 concludes with the presentation of the state of the art of unsaturated soils constitutive modelling, categorized based on the selection of constitutive variables. Emphasis is given on the pioneering work of Alonso et al. (1990), concerning the Barcelona Basic Model and also on the latest modelling trends which favour the utilization of Bishop's average skeleton stress, in combination with suction and/or degree of saturation as extra constitutive variables.

Although chapters 2 to 4 comprise the necessary literature review accompanying this thesis, it was attempted to avoid a strict quotation of available sources. Instead, available literature resources are utilized as needed within a hierarchical approach, attempting to present in a didactic way the theory of plasticity, and the behaviour of anisotropic and unsaturated soils respectively. The following six (6) chapters (chapter 5 to 10), concern solely the original contribution of the present Doctoral Thesis.

Chapter 5 introduces the compressibility mechanical framework which underlines the formulation of the proposed model. It is founded on the Intrinsic Compressibility framework of Belokas & Kavvadas (2011), slightly enhanced with an eye towards reduced mathematical complexity and thus, increased implementation robustness. The framework is extended in the unsaturated regime by incorporating a double dependance of the compression curves on both suction and macro-structural degree of saturation. In fact, the proposed framework handles partial saturation as a structure generating mechanism which translates material states towards the meta-stable domain. The inter-particle forces arising from partial saturation phenomena (i.e., water menisci, increased short-range absorptive phenomena) are considered the bonding agent, while their intensity and distribution depends on both suction and water content.

Following the introduction of the mechanical framework, chapter 6 presents the mathematical formulation of the proposed constitutive model. Bishop's average skeleton stress is used as the first constitutive variable, while suction and the macro-structural degree of saturation are handled as additional external constitutive variables. The addition of suction and degree of saturation within the formulation calls for modifications on the theory of plasticity, mainly related to the definition of different types of loading. The model is formulated in a transformed generalized stress space which favours the simplicity of the numerical algorithm. The mathematical expressions related to the yield surface, elasticity, flow rule and hardening rules are

presented in detail. The consistency condition is employed to derive the plastic modulus, while the strain, suction and degree of saturation related elastoplastic Jacobians are introduced.

Chapter 7 integrates the proposed model in an explicit incremental driver which solves the constitutive equations. The FORTRAN programming language is used. The derived incremental driver was used in two seperate applications. The first one involves a simple material point algorithm which simulates typical laboratory stress paths, using the developed incremental driver for solving the constitutive equations. The single material point algorithm is based on an existing program from Belokas (2008), enhanced and further modified in order to allow for the simulation of unsaturated stress paths (i.e., constant suction compression and shear tests, constant water content tests, suction increase and decrease stress paths, etc.). For this purpose, the algorithm also includes a simple hydromechanical coupling, based on a void ratio dependant water retention model. The proposed model's incremental driver is also integrated in the Simulia Abaqus Finite Element method computer code, using the UMAT environment suitable for Lagrangian Analyses (Abaqus Standard). Significant modifications were also required in the UMAT preamble, to handle unsaturated material states. The chapter focuses on the required modifications for unsaturated soils analysis which consist the original contribution of the present thesis in terms of numerical implementation. The developed numerical tools are initially evaluated through simple Modified Cam Clay simulations, which allow for comparisons with the build-in Abaqus model.

Chapter 8 uses the developed numerical tools to evaluate the predictions of the proposed constitutive model, mainly from a qualitative point of view. A parametric study is conducted for those model parameters that are usually calibrated through a trial and error procedure, while for the remaining constitutive parameters, a coherent set of values is assumed corresponding to a silty clay. The necessary simulations are mainly performed with the developed material point algorithm, while additionally some of the simulations are also performed with simple Abaqus numerical models and compared against their material point algorithm counterparts to identify potential discrepancies in the numerical integration. Chapter 8 includes three main sections; the first one deals with the anisotropic features of the model, the second one with the unsaturated features assuming an isotropic stress background and the third one with the combined effect of anisotropy and partial saturation. The behaviour

is examined in common laboratory stress paths like drained or undrained loading, isotropic and anisotropic compression, suction increase and suction decrease tests, evaluating the model's prediction under different states of stress induced anisotropy and partial saturation. The performed simulations evaluate the model's ability to perform according to the conceptual mechanical framework and to reproduce qualitatively the usually experimentally determined behaviour. Moreover, it familiarizes the potential user with its simulation capabilities and clarifies the influence of various model parameters.

Chapter 9 addresses the necessity to calibrate the proposed model and further evaluate its predictions towards experimental measurements. Results from three individual experimental studies are raised and used. The results of the Gens (1982) experimental investigation on the anisotropic behaviour of the Lower Cromer Till are utilized to evaluate the anisotropic features of the models. The results from the Casini (2008) experimental investigation on the unsaturated behaviour of anisotropically consolidated Jossigny Silt samples provide the opportunity to evaluate the model's capabilities in simulating the unsaturated and anisotropic behaviour of a natural soil. The final simulation exercise regards the model's predictions during wetting tests and its ability to predict wetting induced collapse. The results of Barrera (2002) on the hydromechanical behaviour of compacted Barcelona Clayey Silt specimens are used to this end.

Chapter 10 applies the proposed model in Finite Element analyses of two common engineering problems. Its main goal is to demonstrate that the proposed model and the accompanying UMAT subroutine can handle complicated two-dimensional and three-dimensional numerical problems in the large scale. The first application is related to the anisotropic features of the model and deals with face stability of an EPB excavated tunnel beneath the groundwater table. Analyses results with the proposed model are compared with their MCC counterparts to reveal how the anisotropic strength degradation mechanism included in the proposed model results to increased tunnel deformation. The presented investigation comprises an investigation conducted from the author within the framework of the NeTTUN research program where amongst other research activities, the proposed model is utilized in various analyses to assess the effects of anisotropy on tunnel behaviour. Regarding unsaturated soils analyses, chapter 10 additionally includes a numerical investigation of the behaviour of a typical shallow footing laying on an unsaturated soil profile.

Characteristic analyses are performed, revealing the effect of partial saturation on bearing capacity and deformation, while a typical analysis in which the water table is gradually raised and associated with the increase in settlements under constant load is included to demonstrate the model's ability to reproduce collapse.

Finally, chapter 11 summarizes the main points of the conducted research, highlights its main achievements and also identifies the required improvements, towards increased simulation capabilities and more accurate predictions.

# Chapter 2

# Constitutive Modelling of Soils

## 2.1 General

The solution of any boundary value problem requires the use of adequate constitutive models to provide the response of a particular material to any external stimuli. In civil engineering nowadays, boundary value problems are usually solved utilizing either the finite element or the finite difference methods, to associate the stress and displacement field of a given structure subjected to external loading. A mechanical constitutive model is needed to provide the crucial link between the stress $\boldsymbol{\sigma}$ and strain $\boldsymbol{\varepsilon}$ fields developed in the medium of concern (i.e., concrete, steel, ground etc.). Combining the constitutive equations with the laws that govern the physical problem (i.e., the equations of equilibrium of motion, strain - displacement compatibility equations) the solution of the boundary problem can be obtained.

The simplest mechanical constitutive model is Hook's linear elastic law. Unfortunately materials usually involved in engineering problems, exhibit a nonlinear elastoplastic mechanical behaviour, where the application of an external load is associated with the onset of inelastic strains. Thus, a comprehensive description of the mechanical behaviour of engineering materials required for the development of a sound and general framework to allow for the prediction of the plastic, non-recoverable upon load removal, strains. Historically, such a framework was initially developed for metals (theory of metal plasticity) and was later extended for geomaterials, leading to the formulation of the classical theory of soil plasticity. The combination of the general principles of theory of soil plasticity with different conceptual mechanical frameworks, has led to the development of a huge variety of different soil constitutive models.

The initial section of the current chapter reviews the concepts of the theory of plasticity for soils, with a scope to familiarize the reader with the basic assumptions, definitions and formulations involved in the constitutive modelling of soils. It is followed by a second section which presents a brief historical review on the development of soil constitutive models is presented, emphasizing to major contributions in the international literature.

## 2.2 Theory of Plasticity

### 2.2.1 Definitions - Basic Kinematic Assumption

Constitutive models for soils describe the mechanical behaviour, namely the stress - strain relationship, of a soil element. As a soil element, a characteristic soil volume is implied, sufficiently small (infinitesimal) to justify differential calculations but at the same time sufficiently large to allow for the use of continuum mechanics. The latter addresses the multiphasial nature of soils. Soils consist of solid particles (soil grains) and voids, the pore space formed between the solid particles. Voids can be occupied by more than one fluids (i.e., gas, liquid). In natural soils, the gas phase (usually atmospheric air) and the liquid phase (usually water) coexist and interact, governing the mechanical response of the soil.

In that sense, a soil element needs to be large enough to include a sufficient portion of all coexisting phases, for the soil to be assumed as a continuum medium. Moreover, the coexistence of more than one phases in the soil skeleton calls for a proper constitutive stress capable of representing the influence of different phases.

In saturated soils, where all voids are filled with water, it is widely acknowledged that any alteration in terms of strength or strain is associated with a corresponding alteration in the effective stress $\boldsymbol{\sigma'}$ (Terzaghi 1925). In classical saturated inviscid soil plasticity, Terzaghi's effective stress principle dominated the development of various constitutive models, within the general framework of plasticity, due to the fact that a single stress tensor was sufficient to fully describe the mechanical behaviour. However, such principle does not stand for the case of unsaturated soils, where additional constitutive variables are needed.

Nevertheless, in the following lines the classical theory of plasticity, applied to saturated soils, will be presented as a starting basis for the subsequent extension in the unsaturated domain. Any modifications required for an adequate description of

the mechanical behaviour of unsaturated soils are introduced later on, in chapter 6, which presents the mathematical formulation of the proposed constitutive model for unsaturated soils.

The **material state** is uniquely defined by a set of state variables. We may define the following two sets of state variables:

1. **external variables**: they define the loading conditions. The stress and strain tensors, temperature, chemical concentrations, soil suction, degree of saturation, void ratio comprise the most commonly utilized external variables;

2. **internal variables**: they represent the soil's "memory". Internal variables may be scalar and/or tensorial quantities and reflect the effect that any change of the external variables may have in the material response.

As a material state is fully described by the state variables (external and internal), **a material state changes if and only if any of the state variables change**. The external variables may change without a change of the internal variables; on the contrary, a change of the internal variables requires a change of the external variables. A change in the state of a soil is usually associated with a corresponding change of the strain (straining), expressed by a strain increment ($\dot{\boldsymbol{\varepsilon}}$). However, it is possible for a material state to change without straining (i.e., if the temperature of a restrained block is altered). On the contrary, straining is always associated with changes in the external variables.

Any agent altering the material state is called **loading**. Note that the term loading is not used with the classical sense of an increase of the applied loads (as contrasted to unloading) since in the case of multidimensional loading some components may increase and some decrease. A very small loading is called infinitesimal loading.

Material states are separated to:

- **elastic states**: material states in which any infinitesimal loading causes only reversible changes in the external state variables. (i.e., when the loading is reversed, external variables are reversed too.);

- **inelastic states**: all non-elastic material states. For instance, all material states in which infinitesimal loading causes a change in the external variables which is not fully reversible (i.e., it includes both reversible and irreversible components). In invisid (rate independent) theory of plasticity, inelastic states coincide with **plastic states**.

Following elastic and inelastic states definition, we may further define as:

- **elastic loading**: any infinitesimal loading either from an elastic state or from a plastic state causing only change of the external variables. Thus, any elastic loading is not associated with change of the internal variables.

- **inelastic loading**: any non-elastic loading. Internal state variables change only during inelastic loading. In invisid (rate independent) theory of plasticity, inelastic loading coincides with **plastic loading**.

A constitutive law or constitutive behaviour describes the material behaviour, providing a quantitative description of the material state and of material state alterations. Elastic material behaviour or elastic law or "elasticity" is the quantitative description of changes in the material state during "elastic loading" and is expressed only via changes of the external variables. Inelastic material behaviour is associated with "inelastic loading", while when viscous phenomena are neglected it coincides with the plastic material behaviour or "plasticity".

In the present thesis, theory of plasticity is described in its incremental form and dots over symbols are used to indicate an infinitesimal increment of the corresponding quantity. Moreover, as viscous phenomena are not considered, the term plastic instead of the more general inelastic is systematically used. Within the range of small deformations and rotations, the basic kinematic assumption of the additive decomposition of the total strain increment ($\dot{\boldsymbol{\varepsilon}}$) in an elastic $\dot{\boldsymbol{\varepsilon}}^{\mathbf{e}}$ and a plastic $\dot{\boldsymbol{\varepsilon}}^{\mathbf{p}}$ component is assumed:

$$\dot{\boldsymbol{\varepsilon}} = \dot{\boldsymbol{\varepsilon}}^{\mathbf{e}} + \dot{\boldsymbol{\varepsilon}}^{\mathbf{p}} \tag{2.1}$$

**Elastic strains** are associated with elastic loading and thus are reversible. **Plastic strains** correspond to the remaining portion of the total strain that is assumed irreversible.

Summarizing we may say that a given material state is described by the state variables. Assuming that the soil element is subjected to an infinitesimal loading, the constitutive law provides the corresponding change of the state variables and thus the updated material state. By applying the above rule recursively the final state of a soil material can be defined for any finite loading.

The formulation of any constitutive law necessitates at least one (or all) of the following entities:

- an **elastic law** to calculate the elastic strain;

- a **yield surface** to distinguish between elastic and plastic states;
- a **flow rule** to determine the plastic strain during plastic loading;
- a **hardening rule** to provide the evolution of suitably selected internal variables associated with the evolution of the yield surface.

Before proceeding to the description of the above entities, we shall define some certain auxiliary quantities associated with the stress and the strain tensor. The effective stress tensor $\boldsymbol{\sigma'}$ can be decomposed to an isotropic and a deviatoric component. It is noted that henceforth, the prime ($'$) indicating effective stress will be omitted for brevity, without the risk of ambiguity, since the total stresses do not appear anywhere in the formulations. The isotropic component of the stress is defined as:

$$\sigma = \frac{1}{3}\boldsymbol{\sigma} : \boldsymbol{I} \tag{2.2a}$$

where $\boldsymbol{\sigma}$ is the effective stress tensor, $\boldsymbol{I}$ is the second order unit tensor and (:) indicates tensorial product. It is obvious that the isotropic component of the stress tensor is the octahedral stress and is also equal to the mean effective stress $p$. By subtracting the isotropic stress component from the stress tensor the deviatoric component $\boldsymbol{s}$ of the stress tensor is defined:

$$\boldsymbol{s} = \boldsymbol{\sigma} - \sigma\boldsymbol{I} \tag{2.2b}$$

In a similar way we may define the isotropic (volumetric) component ($\varepsilon$) and deviatoric component ($\boldsymbol{e}$) of the strain tensor ($\boldsymbol{\varepsilon}$):

$$\varepsilon = \boldsymbol{\varepsilon} : \boldsymbol{I} \tag{2.3a}$$

$$\boldsymbol{e} = \boldsymbol{\varepsilon} - \frac{1}{3}\varepsilon\boldsymbol{I} \tag{2.3b}$$

Equations 2.2 and 2.3 can be written in the same form for infinitesimal changes of the stress and the strain tensors, respectively, using the "super-dot" introduced previously. Moreover, equations 2.3, hold true also for the elastic and the plastic component of the strain tensor.

### 2.2.2 Elastic law

Elasticity is employed to describe the elastic component ($\dot{\boldsymbol{\varepsilon}}^e$) of the incremental strain tensor. To understand the necessity and importance of the elastic law, let's examine

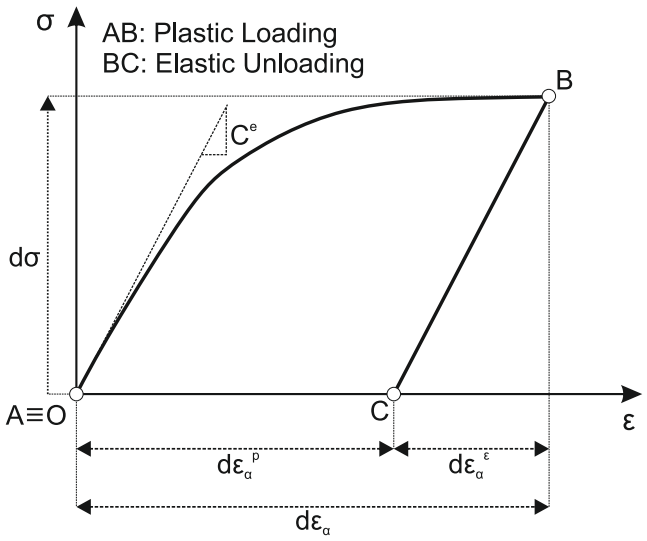


**Figure 2.1:** The elastic $\dot{\varepsilon}_a^e$ and plastic $\dot{\varepsilon}_a^p$ axial strains associated with an infinitesimal elasto-plastic loading (path AB) corresponding to an increase of the axial stress ($\dot{\sigma}_a$).

the simple case of a uniaxial compression test (fig. 2.1). An infinitesimal elastoplastic loading (AB), attributed to an increment of the axial stress $\dot{\sigma}_a$ will lead to an elasto-plastic axial strain increment $\dot{\varepsilon}_a$. The elastic strain portion $\dot{\varepsilon}_a^e$ corresponds to this part of deformation that would be recovered if the agent that caused it, in this case the stress increment $\dot{\sigma}_a$, was removed (path BC). Assuming a linear elastic law we may write that:

$$\dot{\sigma}_a = C^e \cdot \dot{\varepsilon}_a^e \tag{2.4}$$

where in this case of a uniaxial compression $C^e$ corresponds to the well known Elastic Modulus $E$. Following this simple example, we may generalize for the case of multi-axial loading, and relate an increment of the elastic strain tensor to the corresponding increment of the stress tensor via an incrementally linear expression:

$$\dot{\boldsymbol{\sigma}} = \boldsymbol{C^e} : \dot{\boldsymbol{\varepsilon}}^e \tag{2.5}$$

where $\boldsymbol{C^e}$ is the forth order elastic stiffness tensor. By employing the incremental isotropic and deviatoric components of stress and strain the elasticity formulation

(eq 2.5) may be reformed as follows:

$$\dot{\sigma} = K \cdot \dot{\varepsilon}^e + \boldsymbol{X} \cdot \dot{\boldsymbol{e}}^e \tag{2.6a}$$

$$\dot{\boldsymbol{s}} = \Psi \cdot \dot{\varepsilon}^e + 2G \cdot \dot{\boldsymbol{e}}^e \tag{2.6b}$$

and also rewritten as:

$$\begin{Bmatrix} \dot{\sigma} \\ \dot{\boldsymbol{s}} \end{Bmatrix} = \begin{pmatrix} K & \boldsymbol{X} \\ \boldsymbol{\Psi} & 2G \end{pmatrix} : \begin{Bmatrix} \dot{\varepsilon}^e \\ \dot{\boldsymbol{e}}^e \end{Bmatrix} \tag{2.7}$$

In the above expressions $K$ stands for the elastic bulk modulus, $G$ is the elastic shear modulus and $\boldsymbol{X}$, $\boldsymbol{\Psi}$ are the conjugated stiffness moduli. Finally, in the case of isotropic elasticity, where there is no coupling between the isotropic strain and the strain deviator, the elastic constitutive relations can be further simplified:

$$\dot{\sigma} = K \cdot \dot{\varepsilon}^e \tag{2.8a}$$

$$\dot{\boldsymbol{s}} = 2G \cdot \dot{\boldsymbol{e}}^e \tag{2.8b}$$

or:

$$\begin{Bmatrix} \dot{\sigma} \\ \dot{\boldsymbol{s}} \end{Bmatrix} = \begin{pmatrix} K & \boldsymbol{0} \\ \boldsymbol{0} & 2G \end{pmatrix} : \begin{Bmatrix} \dot{\varepsilon}^e \\ \dot{\boldsymbol{e}}^e \end{Bmatrix} \tag{2.9}$$

### 2.2.3 Yield Surface

The **Yield Surface** (YS) defines the set of plastic states in the state variables space. Mathematically it is described by the **yield function**:

$$f(\boldsymbol{\sigma}, \boldsymbol{q}) = 0 \tag{2.10}$$

It is assumed that negative values ($f(\boldsymbol{\sigma}, \boldsymbol{q}) < 0$) represent elastic states inside the yield surface, while plastic states lie always on the yield surface ($f(\boldsymbol{\sigma}, \boldsymbol{q}) = 0$). It is evident that positive values ($f(\boldsymbol{\sigma}, \boldsymbol{q}) > 0$) correspond to inaccessible states outside of the yield surface. During plastic loading both the initial and the final state of the soil element are on the yield surface. Hence, plastic loading is associated with changes of the size, shape or position of the yield surface, a process controlled by suitably selected internal variables called the **hardening variables**, represented by

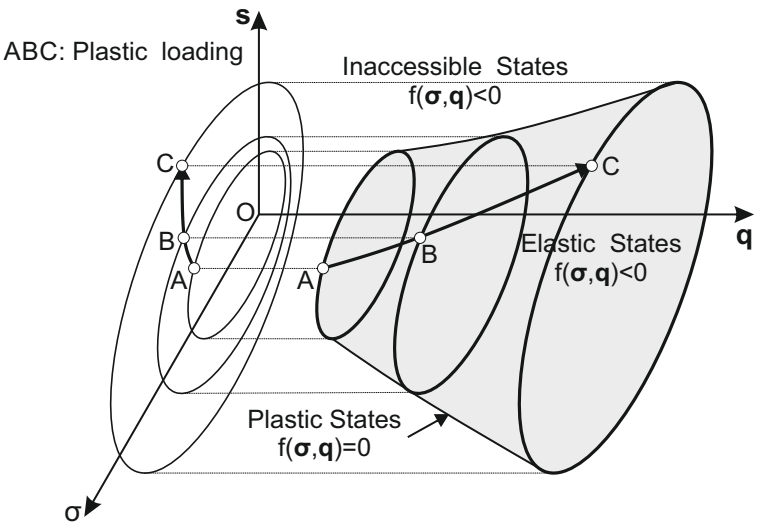


**Figure 2.2:** A yield surface in the state variables space and the corresponding elastic, plastic and inaccessible states.

$\boldsymbol{q}$ [1]. Hardening variables do not change during elastic loading, thus:

$$\dot{\boldsymbol{\varepsilon}}^p = 0 \Rightarrow \dot{\boldsymbol{q}} = 0 \tag{2.11}$$

To further simplify the analysis, it is assumed that projections of the yield surface on the stress subspace correspond to convex curves. Figure 2.2 portrays such a yield surface in the state-variable space. We can define the gradient of the yield surface in the stress space:

$$\boldsymbol{Q} = \frac{\partial f}{\partial \boldsymbol{\sigma}} \tag{2.12}$$

The gradient $\boldsymbol{Q}$ is a second order tensor and can be represented by a "vector" perpendicular to the yield surface. The isotropic and the deviatoric component of the gradient tensor can be computed as:

$$Q = \boldsymbol{Q} : \boldsymbol{I} \tag{2.13a}$$

$$\boldsymbol{Q}' = \boldsymbol{Q} - \frac{1}{3} Q \boldsymbol{I} \tag{2.13b}$$

[1] Hardening variables may be scalar or tensorial quantities; a tensor is used in favour of generality.

After some algebra it can be shown that:

$$Q = \frac{\partial f}{\partial \sigma} \tag{2.14a}$$

$$\boldsymbol{Q}' = \frac{\partial f}{\partial \boldsymbol{s}} - \frac{1}{3}\left(\frac{\partial f}{\partial \boldsymbol{s}} : \boldsymbol{I}\right)\boldsymbol{I} \tag{2.14b}$$

#### 2.2.3.1 Elastic vs Plastic loading

With the yield surface separating elastic from plastic states, we can further elaborate on the definitions of elastic and plastic loading. Starting from an elastic state, any infinitesimal change of the loading is assumed elastic, leading to a new elastic state inside the yield surface[2]. On the other hand, starting from a plastic state, either elastic loading or plastic loading may occur. Nevertheless, during elastic loading, the stress state will retract from the yield surface, leading to an elastic state. Thus, **elastic loading** is associated with;

- an elastic initial state ($f(\boldsymbol{\sigma}) < 0$) and an elastic updated state ($f(\boldsymbol{\sigma} + \dot{\boldsymbol{\sigma}}) < 0$);
- a plastic initial state ($f(\boldsymbol{\sigma}) = 0$) and an elastic updated state ($f(\boldsymbol{\sigma} + \dot{\boldsymbol{\sigma}}) < 0$).

In a convex yield surface, starting from a plastic state ($f(\boldsymbol{\sigma}) = 0$), an updated elastic state ($f(\boldsymbol{\sigma} + \dot{\boldsymbol{\sigma}}) < 0$), necessitates that the inner product of the gradient of the yield surface with the stress increment is:

$$\boldsymbol{Q} : \dot{\boldsymbol{\sigma}} < 0 \tag{2.15}$$

Given that the corresponding strain increment is purely elastic ($\dot{\boldsymbol{\varepsilon}} = \dot{\boldsymbol{\varepsilon}}^e$), application of the elastic law (eq. 2.5) yields that during **elastic loading** from a plastic state the following condition holds true:

$$\boldsymbol{Q} : \boldsymbol{C}^{\mathbf{e}} : \dot{\boldsymbol{\varepsilon}} < 0 \tag{2.16}$$

We state that **plastic loading** is associated with:

$$\boldsymbol{Q} : \boldsymbol{C}^{\mathbf{e}} : \dot{\boldsymbol{\varepsilon}} \geq 0 \tag{2.17}$$

[2] A finite loading may move the stress point on or even outside of the yield surface. In such cases, the corresponding loading must be divided to an elastic portion moving the state on the yield surface and to the remaining plastic one.

It is important to note that plastic loading does not require $\boldsymbol{Q} : \dot{\boldsymbol{\sigma}} > 0$. The following three subcases of plastic loading are defined:

- $\boldsymbol{Q} : \dot{\boldsymbol{\sigma}} > 0$: The stress increment moves outwards the yield surface, plastic strains accumulate ($\dot{\boldsymbol{\varepsilon}}^p \neq 0$) and the hardening variables evolve ($\dot{\boldsymbol{q}} \neq 0$), so that the updated state to lie on the yield surface. This is the case of **plastic hardening**;
- $\boldsymbol{Q} : \dot{\boldsymbol{\sigma}} = 0$: The stress increment moves tangential to the yield surface. This is a special case called **neutral loading**. According to the **continuity condition** (Prager 1949; Desai & Siriwardane 1984), neutral loading is considered purely elastic ($\dot{\boldsymbol{\varepsilon}}^p = 0$) and thus no hardening takes place ($\dot{\boldsymbol{q}} = 0$);
- $\boldsymbol{Q} : \dot{\boldsymbol{\sigma}} < 0$: The stress increment moves inwards the yield surface but contrary to elastic loading the stress point does not retract from it. The hardening variables evolve ($\dot{\boldsymbol{q}} \neq 0$) for the yield surface to follow the stress increment and plastic strains accumulate ($\dot{\boldsymbol{\varepsilon}}^p \neq 0$). This is the case of **plastic softening**.

Figure 2.3 summarizes schematically the aforementioned different loading conditions.

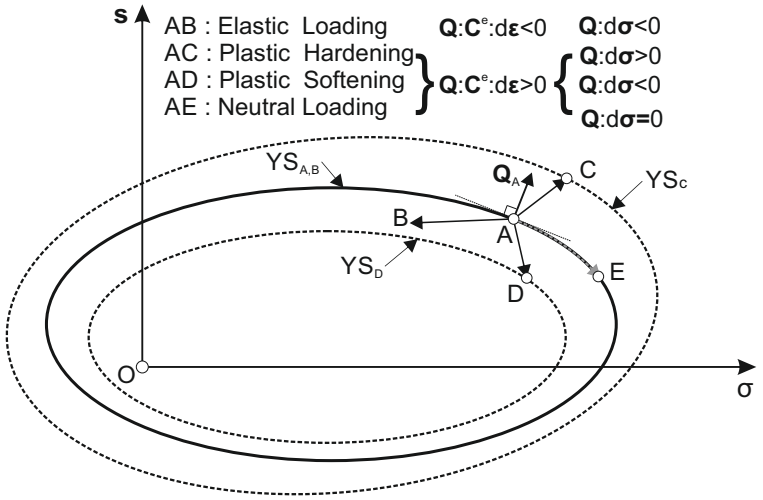


**Figure 2.3:** Different loading conditions associated with an initially plastic state.

### 2.2.4 Flow Rule

Flow rule is used to determine the magnitude and direction of the plastic strain increment whenever plastic loading occurs. The simplest mathematical form to describe

an incrementally linear strain increment is:

$$\dot{\boldsymbol{\varepsilon}}^p = \dot{\Lambda}\boldsymbol{P} \tag{2.18}$$

where $\dot{\Lambda}$ is a scalar quantity giving the magnitude of the plastic strain increment, and $\boldsymbol{P}$ the plastic potential tensor defining the direction of the plastic strain increment[3]. The scalar quantity $\dot{\Lambda}$ is assumed to be a function of the gradient $\boldsymbol{Q}$ and the stress tensor increment $\dot{\boldsymbol{\sigma}}$:

$$\dot{\Lambda} = \frac{1}{H}\left(\boldsymbol{Q} : \dot{\boldsymbol{\sigma}}\right) \tag{2.19}$$

where $H$ the so called **plastic modulus** that will be defined later by employing the consistency condition. Combining equations 2.18 and 2.19 the plastic strain increment can be expressed as:

$$\dot{\boldsymbol{\varepsilon}}^p = \frac{1}{H}\left(\boldsymbol{Q} \otimes \boldsymbol{P}\right)\dot{\boldsymbol{\sigma}} \tag{2.20}$$

indicating that the calculated plastic strain increment is incrementally linear with respect to the stress increment.

The expression for the scalar quantity $\dot{\Lambda}$ (see eq. 2.19) ensures that during neutral loading, where $\boldsymbol{Q} : \dot{\boldsymbol{\sigma}} = 0$, the incremental plastic tensor will be null, satisfying the continuity condition. Moreover, it is observed that when the plastic modulus is zero ($H = 0$), the magnitude of the plastic strain increment tensor tends to infinity ($\dot{\boldsymbol{\varepsilon}}^p \to \infty$). This situation is defined as **failure**.

Starting from the elastic law (eq. 2.5) and using the basic kinematic assumption (eq. 2.1) we may write:

$$\dot{\boldsymbol{\sigma}} = \boldsymbol{C}^e : \dot{\boldsymbol{\varepsilon}}^e = \boldsymbol{C}^e : \left(\dot{\boldsymbol{\varepsilon}} - \dot{\boldsymbol{\varepsilon}}^p\right) \tag{2.21}$$

Using the flow rule to calculate the plastic strain increment we obtain:

$$\dot{\boldsymbol{\sigma}} = \boldsymbol{C}^e : \left(\dot{\boldsymbol{\varepsilon}} - \dot{\Lambda}\dot{\boldsymbol{P}}\right) \tag{2.22}$$

Multiplying both parts with the gradient $\boldsymbol{Q}$ and utilizing equation 2.19 we obtain:

$$\dot{\Lambda}H = \boldsymbol{Q} : \dot{\boldsymbol{\sigma}} = \boldsymbol{Q} : \boldsymbol{C}^e : \left(\dot{\boldsymbol{\varepsilon}} - \dot{\Lambda}\boldsymbol{P}\right) \tag{2.23}$$

[3] $\boldsymbol{P}$ is not a unit tensor and thus, to some extend, also controls the magnitude of the plastic strain increment.

and finally solving for the scalar quantity $\dot{\Lambda}$ we derive:

$$\dot{\Lambda} = \frac{\boldsymbol{Q} : \boldsymbol{C}^e : \dot{\boldsymbol{\varepsilon}}}{H + \boldsymbol{Q} : \boldsymbol{C}^e : \boldsymbol{P}} \tag{2.24}$$

allowing for the calculation of $\dot{\Lambda}$ as a function of the incremental strain tensor.

As far as the second order plastic potential tensor $\boldsymbol{P}$ is concerned, similar to the gradient tensor $\boldsymbol{Q}$, its isotropic and deviatoric components can be calculated:

$$P = \boldsymbol{P} : \boldsymbol{I} \tag{2.25a}$$

$$\boldsymbol{P}' = \boldsymbol{P} - \frac{1}{3} P \boldsymbol{I} \tag{2.25b}$$

Equation 2.3 combined with eq. 2.25 give:

$$\dot{\varepsilon}^p = \dot{\Lambda} P \tag{2.26a}$$

$$\dot{\boldsymbol{e}}^p = \dot{\Lambda} \boldsymbol{P}' \tag{2.26b}$$

The isotropic component of the plastic potential tensor is of great importance in soil behaviour. It can be seen that $P = 0$ defines the **phase transformation state** where $\dot{\varepsilon}^p = 0$, corresponding to the transition between contractant ($\dot{\varepsilon}^p > 0$) and dilatant ($\dot{\varepsilon}^p < 0$) plastic response[4]. For $\dot{\varepsilon}^p \neq 0$ the plastic potential tensor controls the reproduced plastic dilation:

$$d_q^p = \frac{\dot{\varepsilon}_q^p}{\dot{\varepsilon}^p} = \frac{\sqrt{\frac{2}{3}\dot{\boldsymbol{e}}^p : \dot{\boldsymbol{e}}^p}}{\dot{\varepsilon}^p} = \frac{\sqrt{\frac{2}{3}\boldsymbol{P}' : \boldsymbol{P}'}}{P} \tag{2.27}$$

where $\dot{\varepsilon}_q^p = \sqrt{\frac{2}{3}\dot{\boldsymbol{e}}^p : \dot{\boldsymbol{e}}^p}$ is a measure of the deviatoric strain increment.

The plastic potential tensor can be arbitrarily selected to reproduce the desired plastic dilatancy. Nevertheless, it is more elegant to describe $\boldsymbol{P}$ as the gradient of a certain surface, in the state variables space, called the **Plastic Potential Surface** (PPS) and represented from the **plastic potential function**:

$$g(\boldsymbol{\sigma}, \boldsymbol{q}) = 0 \tag{2.28}$$

[4]The soil mechanics convention is used throughout the thesis, where compressive stresses and strains are considered positive.

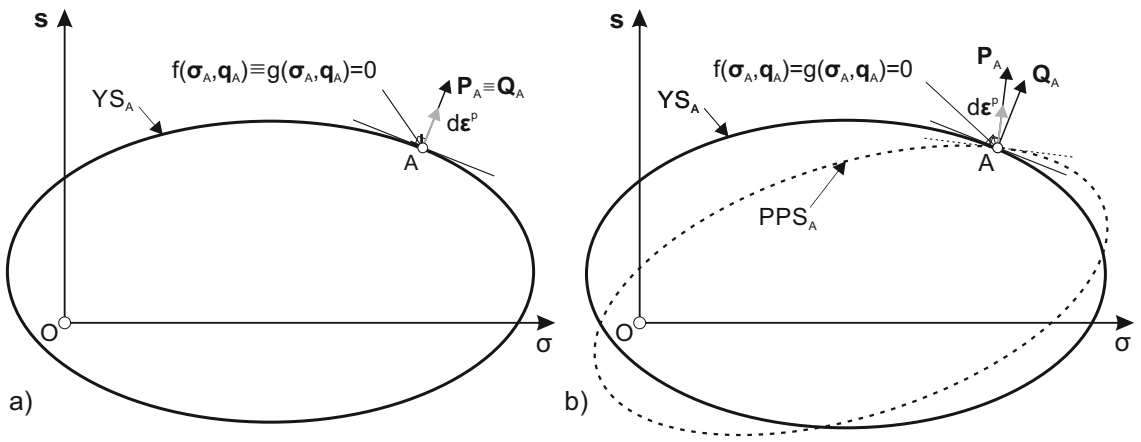


**Figure 2.4:** Selection of; a) an associated flow rule and; b) and a non-associated flow rule.

In such cases, tensor $\boldsymbol{P}$ is given by:

$$\boldsymbol{P} = \frac{\partial g}{\partial \boldsymbol{\sigma}} \tag{2.29}$$

In soil's plasticity, it is quite common to assume that the plastic potential function coincides with the yield function:

$$g(\boldsymbol{\sigma}, \boldsymbol{q}) \equiv f(\boldsymbol{\sigma}, \boldsymbol{q}) \tag{2.30}$$

It is evident that such a selection leads to $\boldsymbol{P} \equiv \boldsymbol{Q}$, corresponding to the so-called **associated flow rule**, while in any other case ($\boldsymbol{P} \neq \boldsymbol{Q}$) a **non-associated flow rule** is assumed. Figure 2.4 presents an indicative plastic strain increment derived from an associated and a non-associated flow rule.

Associated flow rules are also called normality rules due to the fact that the direction of the plastic strain increment is normal to the yield surface. Moreover, they are in favour of uniqueness[5] and thus lead to more stable solutions. At the same time, their main shortcoming is that they usually do not allow for a realistic simulation of the accumulated plastic strains, in line with experimental results.

Still, a non-associated flow rule can ensure uniqueness and thus stability of the solution, provided that the plastic potential tensor and the hardening rule have been properly selected to satisfy specific conditions. We start by stating that the plastic

[5]Uniqueness requires the existence of a unique association between the incremental state and the incremental strain response variables.

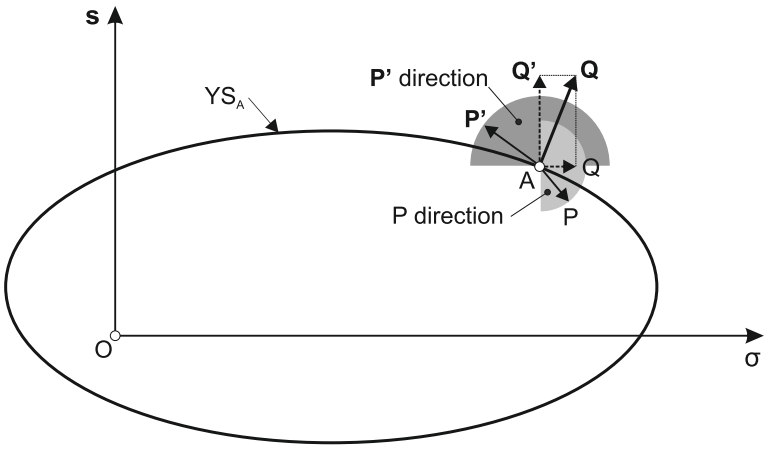


**Figure 2.5:** The limitations imposed in the isotropic and deviatoric components of the plastic potential tensor.

potential tensor must be selected to conform with the following two conditions:

$$P \cdot Q > 0 \tag{2.31a}$$

$$\boldsymbol{P}^{'} : \boldsymbol{Q}^{'} > 0 \tag{2.31b}$$

The limitation imposed in the direction of the plastic strain increment is portrayed in figure 2.5. In addition, the incorporation of an isotropic elastic law (eq. 2.9) yields:

$$\boldsymbol{Q} : \boldsymbol{C}^{e} : \boldsymbol{P} = KPQ + 2G\left(\boldsymbol{Q}^{'} : \boldsymbol{P}^{'}\right) > 0 \tag{2.32}$$

where the Bulk modulus $K$ and the Shear Modulus $G$ are assumed positive definite.

### 2.2.5 Hardening Rule

As already discussed, the hardening variables $\boldsymbol{q}$, are suitably selected internal variables controlling the evolution of the shape, size or position of the yield surface during plastic loading. In that end, the hardening rule of a constitutive relationship determines the aforementioned evolution of the hardening variables $\dot{\boldsymbol{q}}$ during a plastic loading increment. A simple form of such a rule is:

$$\dot{\boldsymbol{q}} = \dot{\Lambda}\boldsymbol{h} \tag{2.33}$$

where the quantity $\boldsymbol{h}$ (not necessarily tensorial) gives the direction of the change of the hardening variables (and to some extend the magnitude).

The hardening rule may include an **isotropic**[6] or/and a **kinematic** part. The isotropic part controls the size of the yield surface. Hence, incorporation of only an isotropic hardening rule, implies that the yield surface can only alter its size homothetically transforming with respect to a fixed point. Changes in the position and/or the shape of the yield surface are described through the kinematic part of the hardening rule, while combined isotropic and kinematic hardening leads to a **mixed** hardening rule. Figure 2.6 gives a qualitative description of the effect of different types of hardening in the evolution of a given elliptical yield surface during a given plastic loading.

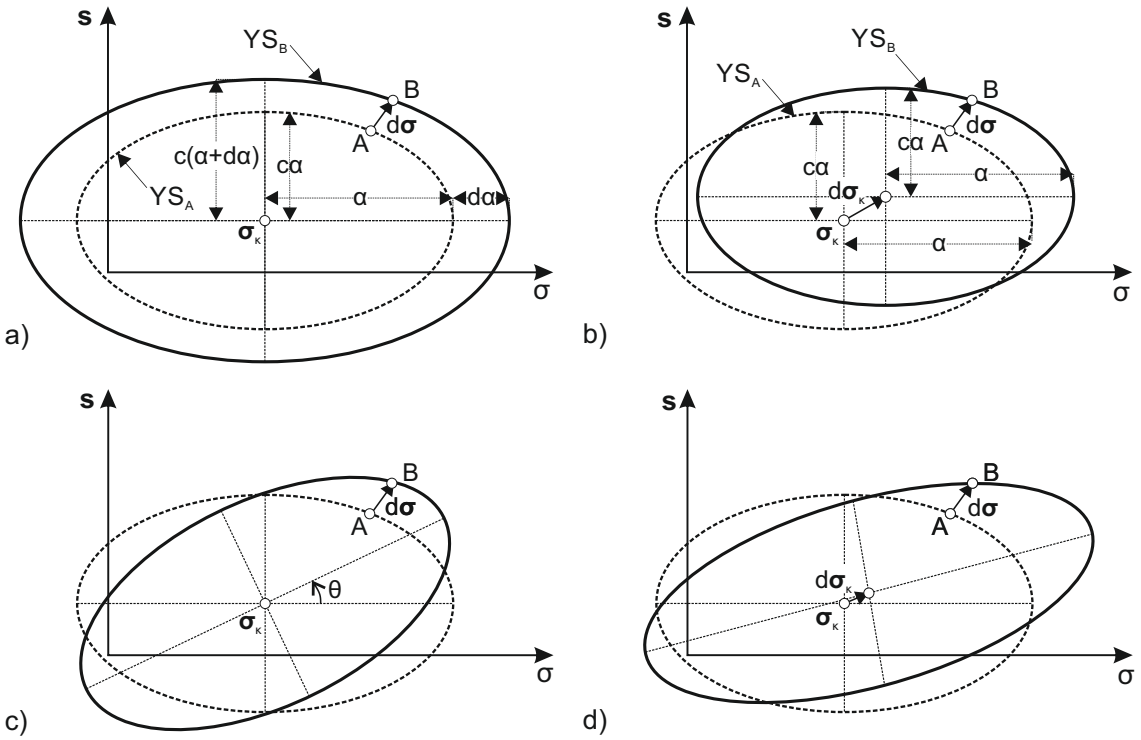


**Figure 2.6:** Schematic representation of the effect that different types of hardening have on a given yield surface; a) isotropic hardening; b)kinematic - translational hardening; c) kinematic rotational hardening and; d) mixed hardening.

### 2.2.6 Consistency Condition - Plastic Modulus

The yield surface, the elastic law, the flow rule and the hardening rule comprise all the necessary constitutive relationships required for a complete constitutive law

[6]The term isotropic should not be confused with the isotropic component of the hardening variables tensor.

developed within the framework of classical theory of plasticity for geomaterials. In this framework, the only quantity that remains to be explicitly defined is the plastic modulus $H$. It is derived by utilizing the consistency condition and as described in the following lines, it is an outcome of the already made assumptions.

**Consistency condition** (Prager 1949) ensures that during plastic loading, the material state remains plastic. In the incremental formulation of plasticity, the consistency condition requires that both the initial and the final state of a plastic increment lie on the yield surface:

$$f(\boldsymbol{\sigma}, \boldsymbol{q}) = f(\boldsymbol{\sigma} + \dot{\boldsymbol{\sigma}}, \boldsymbol{q} + \dot{\boldsymbol{q}}) = 0 \Rightarrow \dot{f} = 0 \tag{2.34}$$

Differentiating the yield function (eq. 2.10) we derive:

$$\dot{f} = 0 \Rightarrow \dot{f} = \frac{\partial f}{\partial \boldsymbol{\sigma}} : \dot{\boldsymbol{\sigma}} + \frac{\partial f}{\partial \boldsymbol{q}} : \dot{\boldsymbol{q}} = 0 \Rightarrow \tag{2.35a}$$

$$\dot{f} = \boldsymbol{Q} : \dot{\boldsymbol{\sigma}} + \frac{\partial f}{\partial \boldsymbol{q}} : \dot{\boldsymbol{q}} = 0 \tag{2.35b}$$

Employing eq. 2.19 and the hardening rule (eq. 2.33), equation 2.35b can be further elaborated and rewritten:

$$\dot{\Lambda} H + \frac{\partial f}{\partial \boldsymbol{q}} : \left(\dot{\Lambda} \boldsymbol{h}\right) = 0 \tag{2.36}$$

For non-zero values of the scalar quantity $\dot{\Lambda}$ ($\dot{\Lambda} \neq 0$) we can solve for the plastic modulus $H$:

$$H = -\frac{\partial f}{\partial \boldsymbol{q}} : \boldsymbol{h} \tag{2.37}$$

Equation 2.37 indicates that $H$ derives from the selected yield function and hardening rule.

So far, no restrictions have been imposed on the constitutive relations comprising the hardening rule. However, some limitations are needed to ensure the "stability" of the mechanical response. The issue of stability was first addressed by Drucker (1951), who stated that a stable material should always exhibit a strain hardening response and also follow the normality rule (associated flow rule), implying that even during an infinitesimal elastoplastic strain increment the second order plastic work should be positive:

$$\dot{W}_p = \dot{\boldsymbol{\sigma}} : \dot{\boldsymbol{\varepsilon}} > 0 \tag{2.38}$$

It is obvious that Drucker's stability postulate is too restrictive, especially when it

comes to the simulation of geomaterials, where strain softening behaviour is quite common. Many authors (Bland 1957; Mroz 1963; Mandel 1966) have raised concerns on Drucker's postulate, demonstrating that: a) it does not follow from purely thermodynamic considerations and; b) although it ensures uniqueness and stability, it is not a necessary condition.

Prevost & Höeg (1975) concluded that when it comes to the incremental theory of plasticity, where only infinitesimal strain increments are of concern, if uniqueness is satisfied in the response during an infinitesimal increment of the state of the material, then the material can be regarded locally stable, even during strain softening. Hill (1958) postulated that during an infinitesimal elastoplastic loading the second order net work must be positive:

$$\dot{W} = \dot{\boldsymbol{\sigma}} : \dot{\boldsymbol{\varepsilon}} > 0 \tag{2.39}$$

Hill's postulate allows for the simulation of strain softening (Mroz 1963; Darve et al. 1995) and also for the simulation of strain hardening with a non-associated flow rule, while at the same time ensures uniqueness and thus a locally stable behaviour. It is evident that eq. 2.39 allows for the second order plastic work to become negative, during an elastoplastic strain increment, as far as the corresponding elastic second order work (positive definite), produced during the same increment, is bigger:

$$\dot{W}^p = \dot{\boldsymbol{\sigma}} : \dot{\boldsymbol{\varepsilon}}^p > -\dot{\boldsymbol{\sigma}} : \dot{\boldsymbol{\varepsilon}}^e \tag{2.40}$$

It is proved that satisfaction of the above inequality condition further requires:

$$\frac{\boldsymbol{Q} : \boldsymbol{C}^e : \boldsymbol{P}}{H + \boldsymbol{Q} : \boldsymbol{C}^e : \boldsymbol{P}} > 0 \tag{2.41}$$

As long as the previous assumptions ensure that $\boldsymbol{Q} : \boldsymbol{C}^e : \boldsymbol{P}$ is always positive (see eq. 2.32), then the following condition is sufficient for eq. 2.41 to hold true::

$$H + \boldsymbol{Q} : \boldsymbol{C}^e : \boldsymbol{P} > 0 \tag{2.42}$$

Inequality 2.42 restricts the value of the plastic modulus $H$ and thus the underlaying

hardening rule (through eq. 2.37):

$$H < \boldsymbol{Q} : \boldsymbol{C}^e : \boldsymbol{P} \Rightarrow \tag{2.43a}$$

$$-\frac{\partial f}{\partial \boldsymbol{q}} : \dot{\boldsymbol{h}} < \boldsymbol{Q} : \boldsymbol{C}^e : \boldsymbol{P} \tag{2.43b}$$

It is worth noticing that the aforementioned condition (eq. 2.42) combined with the definition of plastic loading ($\boldsymbol{Q} : \boldsymbol{C}^e : \dot{\boldsymbol{\varepsilon}} > 0$), dictates that during plastic loading, the scalar quantity $\dot{\Lambda}$ (eq. 2.24) is:

$$\dot{\Lambda} = \frac{\boldsymbol{Q} : \boldsymbol{C}^e : \dot{\boldsymbol{\varepsilon}}}{H + \boldsymbol{Q} : \boldsymbol{C}^e : \boldsymbol{P}} > 0$$

Therefore, if plastic loading is always associated with a positive definite $\dot{\Lambda}$, then according to equation 2.19, for $\dot{\Lambda} = \frac{1}{H}\left(\boldsymbol{Q} : \dot{\boldsymbol{\sigma}}\right) > 0$, the following two conditions may hold true:

- $H > 0$ and $\boldsymbol{Q} : \dot{\boldsymbol{\sigma}} > 0$ corresponding to plastic hardening;
- $H < 0$ and $\boldsymbol{Q} : \dot{\boldsymbol{\sigma}} < 0$ corresponding to plastic softening;

Uniqueness of solution is still lost for $H = 0$ as $\dot{\Lambda}$ (eq. 2.19) becomes indeterminate, but as long as $H = 0$ has already been associated with failure, lost of uniqueness is reasonable. In soils, failure usually is associated with critical state. At critical state the material is neither hardening nor softening ($\dot{\boldsymbol{q}} = 0$) and thus failure is associated with perfectly plastic response ($\boldsymbol{Q} : \dot{\boldsymbol{\sigma}} = 0$). In this case, the scalar quantity $\dot{\Lambda}$ can still be determined through equation 2.24.

Many researches, usually begin their constitutive formulations by a priory restricting the values of $\dot{\Lambda}$ associated with plastic loading to the $\dot{\Lambda} > 0$ domain. It is evident that such an assumption implies that the constitutive equations incorporated, need a priori to satisfy both inequality 2.32 and 2.42. If not, then although uniqueness of solution is ensured, it is rather enforced in a mathematical way than being an outcome of the assumed constitutive equations.

For this reason, in the present dissertation, a straight forward procedure was selected and described, where all the necessary limitations are gradually imposed at different parts of the formulations (elasticity, flow rule, hardening rule), leading to the desirable uniqueness and stability. We should mention that although the conditions imposed on the plastic potential tensor (eq. 2.31) and on the elastic law employed

(isotropic elasticity) ensure that condition 2.32 will be satisfied, they should not be treated as necessary ones. Different assumptions on the selection of the flow rule and the elastic law can also ensure that condition 2.32 is fulfilled. For instance, when an associated flow rule has been selected, there is no need to impose any further restrictions on the selected elastic law.

### 2.2.7 Elastoplastic Jacobian

The elastoplastic stiffness matrix $\boldsymbol{C}^{ep}$ or elastoplastic Jacobian, relates the stress increment $\dot{\boldsymbol{\sigma}}$ with the total strain increment $\dot{\boldsymbol{\varepsilon}}$. It is of great importance in the solution process of boundary value problems using finite element codes, as it is employed in the prediction of any forthcoming state associated with loading from an initially plastic state.

To calculate it we start from the elastic law (eq. 2.5), in combination with the basic kinematic decomposition of strain (eq. 2.1) as will as with the flow rule (eq. 2.18); we derive:

$$\dot{\boldsymbol{\sigma}} = \boldsymbol{C}^{ep} : \dot{\boldsymbol{\varepsilon}} = \boldsymbol{C}^{e} : \dot{\boldsymbol{\varepsilon}}^{e} = \boldsymbol{C}^{e} : (\dot{\boldsymbol{\varepsilon}} - \dot{\boldsymbol{\varepsilon}}^{p}) = \boldsymbol{C}^{e} : \left(\dot{\boldsymbol{\varepsilon}} - \dot{\Lambda} \cdot \boldsymbol{P}\right) \tag{2.44}$$

By further employing expression 2.24 the elastoplastic stiffness tensor is formulated as follows:

$$\begin{aligned}
&\boldsymbol{C}^{ep} : \dot{\boldsymbol{\varepsilon}} = \boldsymbol{C}^{e} : (\dot{\boldsymbol{\varepsilon}} - \dot{\boldsymbol{\varepsilon}}^{p}) = \boldsymbol{C}^{e} : \left(\dot{\boldsymbol{\varepsilon}} - \frac{\boldsymbol{Q} : \boldsymbol{C}^{e} : \dot{\boldsymbol{\varepsilon}}}{H + \boldsymbol{Q} : \boldsymbol{C}^{e} : \boldsymbol{P}} \cdot \boldsymbol{P}\right) \Rightarrow \\
&\boldsymbol{C}^{ep} : \dot{\boldsymbol{\varepsilon}} = \boldsymbol{C}^{e} : \dot{\boldsymbol{\varepsilon}} - \frac{(\boldsymbol{Q} : \boldsymbol{C}^{e} : \dot{\boldsymbol{\varepsilon}}) \cdot (\boldsymbol{C}^{e} : \boldsymbol{P})}{H + \boldsymbol{Q} : \boldsymbol{C}^{e} : \boldsymbol{P}} \Rightarrow \\
&\boldsymbol{C}^{ep} : \dot{\boldsymbol{\varepsilon}} = \boldsymbol{C}^{e} : \dot{\boldsymbol{\varepsilon}} - \frac{(\boldsymbol{Q} : \boldsymbol{C}^{e}) \otimes (\boldsymbol{C}^{e} : \boldsymbol{P})}{H + \boldsymbol{Q} : \boldsymbol{C}^{e} : \boldsymbol{P}} : \dot{\varepsilon} \Rightarrow \\
&\boldsymbol{C}^{ep} : \dot{\boldsymbol{\varepsilon}} = \{\boldsymbol{C}^{e} : -\frac{(\boldsymbol{Q} : \boldsymbol{C}^{e}) \otimes (\boldsymbol{C}^{e} : \boldsymbol{P})}{H + \boldsymbol{Q} : \boldsymbol{C}^{e} : \boldsymbol{P}}\} : \dot{\varepsilon} \Rightarrow \\
&\boldsymbol{C}^{ep} = \boldsymbol{C}^{e} - \frac{1}{\Omega} (\boldsymbol{Q} : \boldsymbol{C}^{e}) \otimes (\boldsymbol{C}^{e} : \boldsymbol{P})
\end{aligned} \tag{2.45}$$

where $\Omega$ is calculated as:

$$\Omega = H + \boldsymbol{Q} : \boldsymbol{C}^{e} : \boldsymbol{P} \tag{2.46}$$

It is evident that when the initial state is elastic (stress state not on the yield surface), the elastoplastic Jacobian coincides with the elastic one:

$$\boldsymbol{C}^{ep} = \boldsymbol{C}^{e} \tag{2.47}$$

In the solution process commonly used in finite element codes, the incremental strain tensor needs to be forecasted for any given increment of the stress tensor, and thus the inverted Jacobian is required:

$$\dot{\boldsymbol{\varepsilon}} = \boldsymbol{D} : \dot{\boldsymbol{\sigma}} \tag{2.48}$$

where:

$$\boldsymbol{D} = \boldsymbol{C}^{ep^{-1}} \tag{2.49}$$

corresponding to the so called compliance matrix. For the elastoplastic Jacobian to be inverted, a non-zero determinant is required ($|\boldsymbol{C}^{ep}| \neq 0$). Uniqueness of solution as has already been expressed through inequalities 2.32 and 2.42, also ensures that the elastoplastic stiffness matrix (eq. 2.45) can be inverted.

## 2.3 Constitutive Modelling Strategies

### 2.3.1 Elastic Perfectly Plastic and Cup Hardening Models

The main characteristic of an elastic - perfectly plastic model is the absence of hardening. Hence, the yield surface cannot evolve with plastic straining and there is no need for hardening variables, leading to a yield function that depends solely on the stress variables ($f(\boldsymbol{\sigma}) = 0$). Perfectly plastic response is associated with $H = 0$, and thus plastic states correspond to failure and the yield surface coincides with the failure envelope. For this reason, usually a failure criterion is employed to describe the yield surface.

The most popular failure criterion used in geotechnical practice is the well known Mohr-Coulomb criterion described, in the generalized stress space, by the following expression:

$$h = \frac{1}{6\sqrt{2}}[3(1+\sin\phi)\sin\theta + \sqrt{3}(3-\sin\phi)\cos\theta]\sqrt{\boldsymbol{s} : \boldsymbol{s}} - \sigma\sin\phi - c\cos\phi = 0 \tag{2.50}$$

where, $c$ and $\phi$ are the well known strength parameters cohesion and angle of internal friction, respectively, while $\theta$ corresponds to the Lode angle. A graphical representation of the Mohr Coulomb failure envelope is given in fig. 2.7. It is a an expanding hexagonal pyramid where the shear strength depends on the mean effective stress and on the stress path followed. When equation 2.50 is used as a yield function, it is obvi-

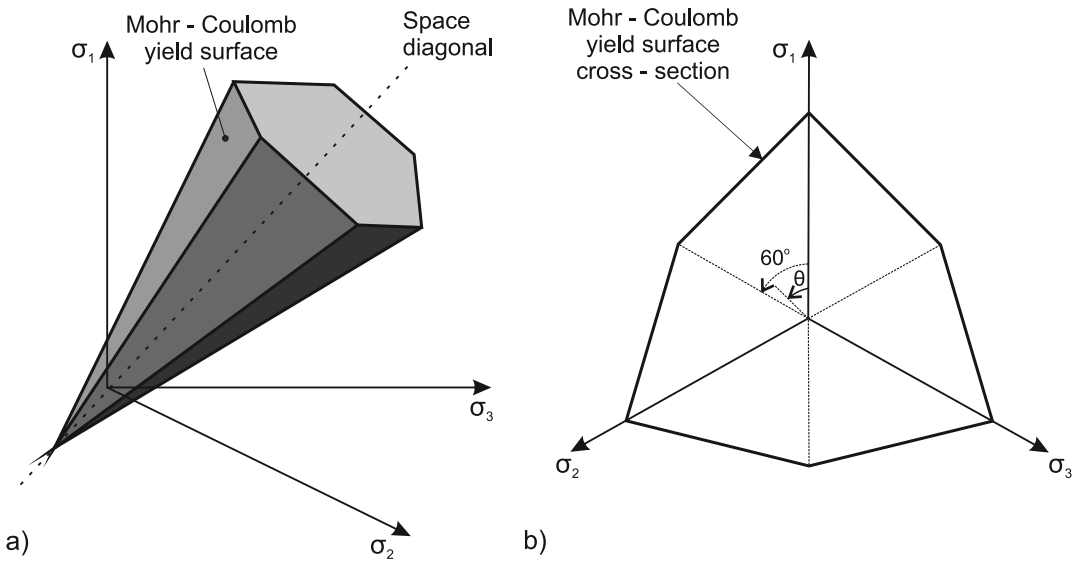


**Figure 2.7:** The Mohr - Coulomb failure envelope in the: a) principal stress space and; b) $\pi$-plane

ous that gradient $\boldsymbol{Q}$ (eq. 2.29) becomes indeterminant whenever the examined state lies on one of the edges of the hexagonal pyramid. To overcome the aforementioned shortcoming several modifications of the Mohr Coulomb failure envelope have been proposed; the three most popular are listed below:

- Drucker & Prager (1952) proposed that the Von - Misses yield criterion, originally proposed for metals, can be modified to the so called extended Von - Misses to describe a conical failure envelope that can be suitably calibrated to match the Mohr-Coulomb envelope. As shown in figure 2.8a the size of the Von-Misses failure envelope failure envelope depends highly on the Lode angle selected for calibration, meaning that the calibration performed needs to be stress path dependant, otherwise the predicted shear strength can be either over- or under-estimated.

- Lade & Duncan (1975) proposed a failure envelope, which provided it has been calibrated to match the Mohr-Coulomb criterion at its major vertices, it only slightly overestimates the predicted shear strength at any other loading direction (see fig. 2.8b).

- Matsuoka & Nakai (1974) proposed a failure criterion which given an appropriate selection of parameters, describes a failure envelope that matches the Mohr-Coulomb strength envelope at both major and minor vertices (see fig. 2.8b).

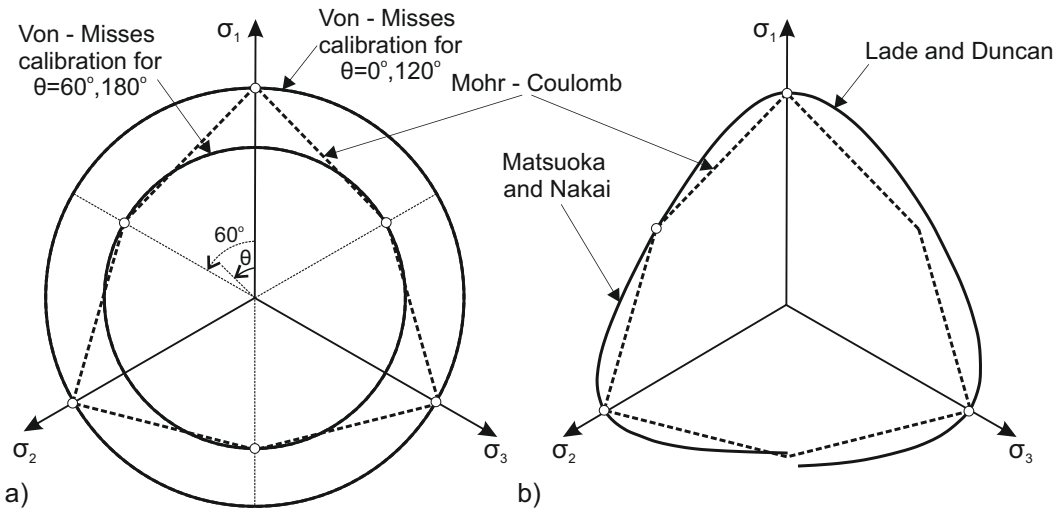


**Figure 2.8:** Projection on the $\pi$-plane of: a) the Von-Mises failure criterion, calibrated to match the Mohr-Coulomb criterion at two different Lode Angle values ($\theta = 0^o, 60^o$) (after Belokas (2008)) and; b) the Lade & Duncan and Matsuoka & Nakai failure criterions (after Davis & Selvadurai (2002)).

The elastic - perfectly plastic Mohr - Coulomb model still nowadays dominates everyday geotechnical practice, mainly due to the fact that $c$ and $\phi$ comprise the most commonly utilized soil strength parameters. The price that one has to pay its for simplicity is reflected in the following Mohr - Coulomb model's shortcomings:

- The yield envelope is a priory defined to coincide with the strength envelope and thus, plastic (irreversible) strains start to accumulate only upon failure. Such an assumption is far from realistic as soils tend to accumulate inelastic strains even when loading occurs before failure envelope is reached.

- The yield envelope is open in the space diagonal and thus radial stress paths that do not lead to failure (i.e., isotropic compression, $K_0$ consolidation) are assumed purely elastic.

- If an associated flow rule is selected, then the reproduced dilatancy coincides with the angle of internal friction $\phi$ and thus only dilant behaviour can be simulated, while even when a non-associated flow rule is selected, the reproduced dilatancy is constant and needs to be properly assigned by the user, to much the desired one under the stress path and stress level examined. The flow rule of the Mohr-Coulomb model is given in figure 2.9.

A significant improvement over the elastic perfectly plastic models are the strain

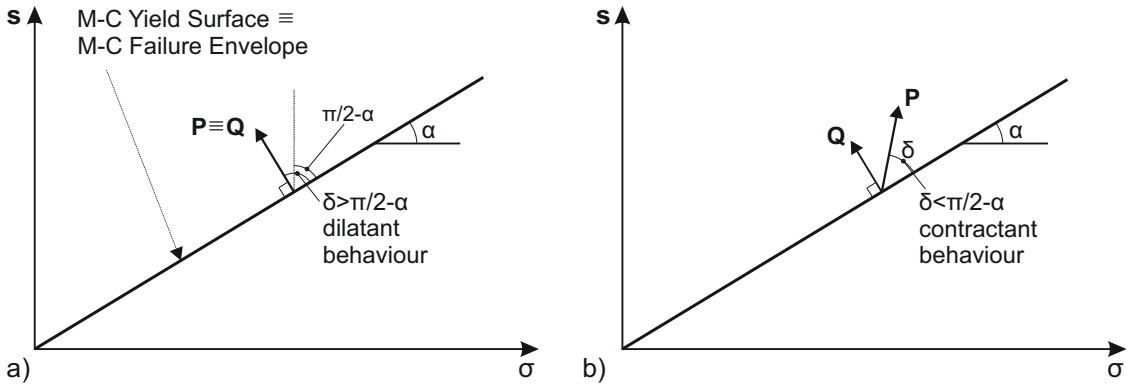


**Figure 2.9:** The Mohr- Coulomb failure criterion and selection of: a) an associated flow rule and; b) a non-associated flow rule.

hardening cup models first proposed by Drucker et al. (1957). They introduced a spherical end-cap (see fig. 2.10) to the Drucker-Prager failure envelope. As the soil hardens, the cup and the yield surface evolve, describing an increase in the size of the elastic domain (isotropic hardening). Cup hardening models can reproduce plastic strains under radial stress paths and also an initially contractant behaviour for normally consolidated soils that are sheared to failure. They also introduced the concept of using a measure of the soil density (i.e., void ratio) to control hardening. The strain hardening cup models was a major advancement towards a more realistic representation of soil behaviour and influenced a lot the development of more sophisticated constitutive models like the Modified Cam-Clay described in the following section.

### 2.3.2 Critical State Soil Mechanics - Cambridge Models

The Cambridge models, Cam Clay (Roscoe et al. 1958; Schofield & Wroth 1968) and Modified Cam Clay (Roscoe & Burland 1968), represent some of the early attempts to develop comprehensive constitutive laws for soils. They are the outcome of an extensive research conducted in the University of Cambridge, including experimental investigation of the mechanical behaviour of the clay from Cam river, after which the models are named. Within the aforementioned research, the work of Hvorslev and that of Rendulic should be considered of great importance. It was their work that led to the development of the Critical State Soil Mechanics (CSSM) (Schofield & Wroth 1968), a generalized framework capable of describing in a unified way the mechanical behaviour of soils under different stress paths and initial conditions.

To follow the discussion regarding critical state models it is essential to distinguish

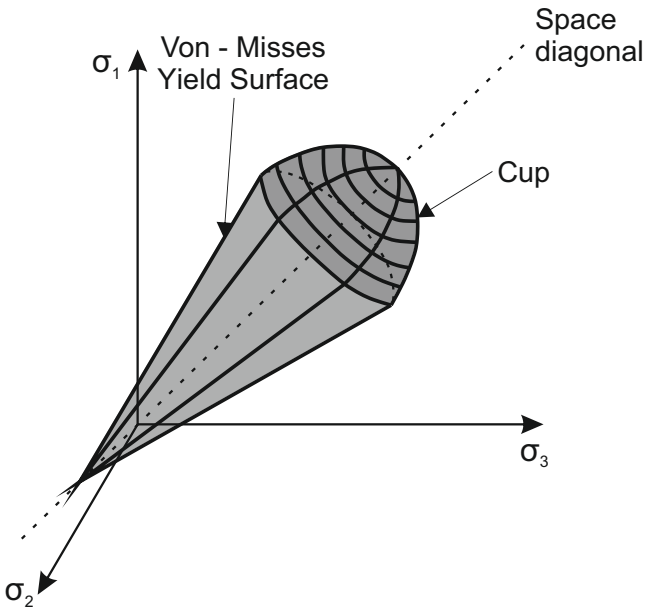


**Figure 2.10:** The yield surface of the Cup Hardening model in the principal stress space.

between structureless and structured material states:

- **Structureless or Intrinsic states**: Following Leroueil & Vaughan (1990), we define as a structureless soil state any state where all properties depend only on the current void ratio $e$ and the current effective stress tensor $\boldsymbol{\sigma}$. Such material states are also characterized as intrinsic according to Burland (1990);

- **Structured states**: Any soil state that is not intrinsic can be characterized as structured. In structured states, behaviour depends on additional parameters (apart from current $e$ and $\boldsymbol{\sigma}$), such as the preconsolidation pressure or parameters associated with structure agents (i.e., cementation, thixotropy, etc.).

Critical State Soil Mechanics is based on the observation, that for structureless material states, a bounding surface exists in the $v-p-q$ space, the State Boundary Surface (SBS), defining the boundary between accessible and not accessible material states. To better understand the CSSM principles we should examine the behaviour of a reconstituted soil under: a) isotropic compression tests and; b) shear tests.

#### 2.3.2.1 Isotropic Compression - Intrinsic States

Let's examine the behaviour of a reconstituted soil subjected to an isotropic consolidation test. It is convenient to plot the results of compression tests in the $v-p$ plane,

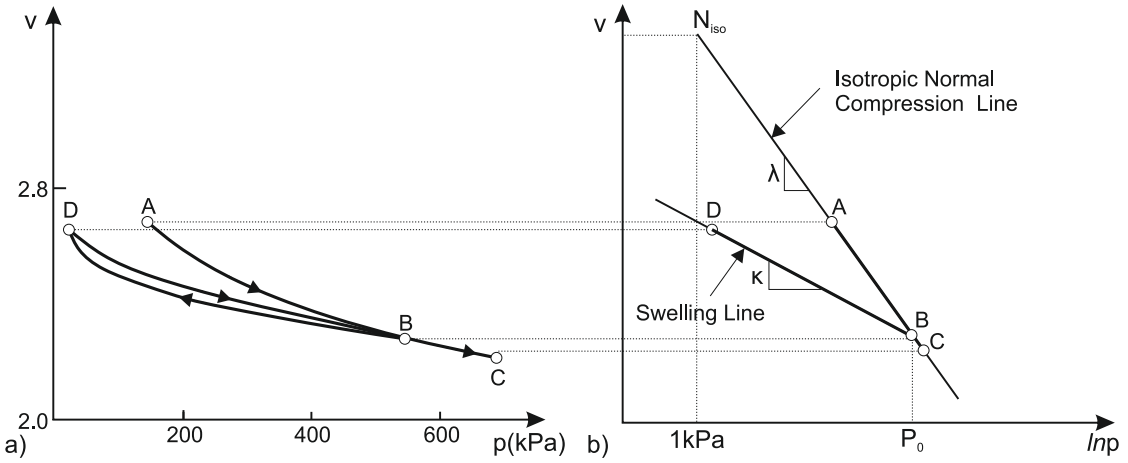


**Figure 2.11:** a) an isotropic compression test on a Kaolin clay (Amerasinghe 1973) (after Atkinson & Bransby (1977)) and; b) the idealized compressibility framework.

where $v = 1 + e$ the specific volume and $p$ the mean effective stress. In figure 2.11a we may see the results of an isotropic compression test on a sample of reconstituted Kaolin Clay, involving loading by increasing p from A to B, unloading to D and then reloading along D-B-C. The observed behaviour, neglecting the small loop in the unloading and reloading cycle B-D-B, can be idealized by two straight lines in the $v - \ln p$ plane (see fig. 2.11b). It has been found that compression tests on most reconstituted clayey soils can all be similarly idealized and represented by:

- a straight line in the $v-\ln p$ plane, called the Isotropic Normal Compression Line (NCL), mathematically represented through $v = N_{iso} - \lambda \ln p$, where $\lambda$ defines the slope, and $N_{iso}$ the position of the NCL in the $v - \ln p$ plane. A soil state lying on the NCL represents a normally loaded (normally consolidated) soil, where its current stress state is also the maximum stress state ever imposed on the given soil during its loading history. Soil states to the right of the isotropic NCL line cannot be attained[7]; thus, the NCL comprises a state boundary line;

- a set of parallel unloading - reloading lines (also called swelling lines), representing pre-loaded (overconsolidated) material states. The slope of the swelling lines is represented by $\kappa$ and their position can be defined through the maximum mean effective stress $P_0$ imposed in the soil. In the examined case, the $P_0$, also called the preconsolidation pressure, corresponds to the soil state at B.

[7]Structured soil states may exist on the right of the NCL, but at this point the presented analysis is restricted only to structureless states

Parameters $\kappa$, $\lambda$ and $N_{iso}$ are regarded as soil constants. Their values depend on the particular soil and are experimentally determined. Burland (1990) proposed the term intrinsic to describe soil properties of reconstituted clays. Intrinsic states hold as a reference frame, with which the mechanical behaviour of natural soils is compared in order to quantify the effect of potential structure inducing agents (i.e., ageing, thixotropy, bonding) on soil behaviour. Following Burland's definition, a material state lying on the aforementioned NCL, can be characterized as intrinsic, while the corresponding compression line as an Intrinsic Compression Line (ICL).

#### 2.3.2.2 Shear Tests - The Roscoe and Hvorslev surfaces

In the previous section, we examined the behaviour of isotropically compressed reconstituted materials and defined a state boundary line in the $v-p$ plane, the isotropic NCL. In this section, we examine the behaviour of isotropically consolidated soils during triaxial loading that leads to failure. In doing so, it is convenient to start from the behaviour of normally consolidated soil samples. Considering triaxial loading tests, initiating from various initial conditions ($p$, $v$), under either drained or undrained conditions, the following comments can been made:

- Specimens initially compressed in higher $p$ values sustain higher values of deviatoric stress $q$ at failure, but the shape of the deviatoric stress ($q$) - deviatoric strain ($\varepsilon_q$) curves are similar.

- The failure data points define a single straight line passing through the axes origin in the $p-q$ plane and also a single curved line in the $v-p$ plane. It turns out that the latter, in the $v-\ln p$ plane is a straight line, parallel to the normal compression line. This single and unique line in the $v-p-q$ space is defined as the Critical State Line (CSL). We may say that the CSL defines the failure of all normally consolidated samples, irrespective of the initial conditions and of the stress path followed. It represents the state of the soil at which large shear strains accumulate under constant stress state ($p$, $q$) and constant specific volume $v$.

- Both drained and undrained stress paths follow a unique surface in the $v-p-q$ space, connecting the isotropic normal compression line with the critical state line, called the Roscoe surface. Roscoe surface is a limiting surface where all

stress paths of normally or even lightly overconsolidated soil elements undergoing triaxial loading should finally lie on, while states outside of the Roscoe surface cannot be achieved. Therefore, Roscoe Surface, is also a State Boundary Surface (SBS).

In figure 2.12 the stress paths of typical drained (A to B) and undrained (C to D) triaxial shear tests are presented together with the corresponding response in the $q - \varepsilon_q$, $v - p$ and $\varepsilon_q$-$\varepsilon_{vol}$ or $\Delta U$ planes. The failure points (B, D) lie on the critical state line, while simultaneously deviatoric strains accumulate under constant $p, q$ and $v$. Figure 2.13 presents the Roscoe surface in the $v - p - q$ space and also various

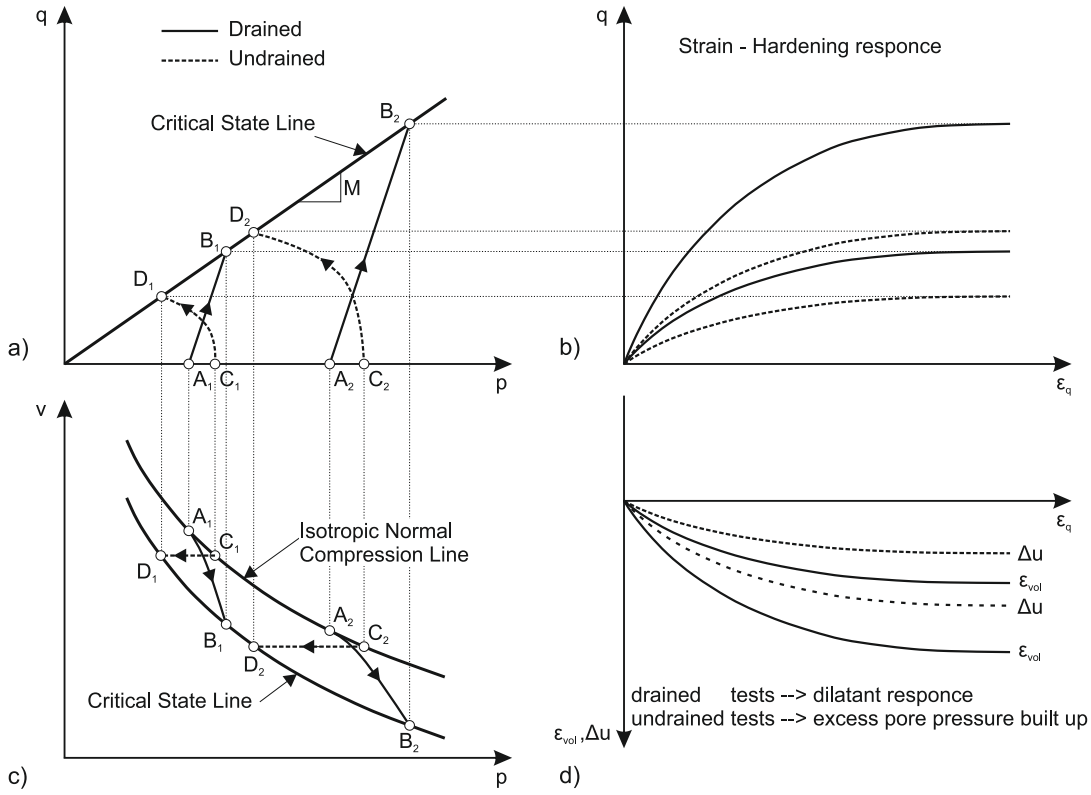


**Figure 2.12:** Typical drained (A-B) and undrained (C-D) triaxial compression tests on normally consolidated soil samples. In a) the stress paths in the $p - q$ plane; b) the corresponding stress - strain curve; c) the behaviour in the $v - \ln p$ plane and; d) the volumetric response (drained) or the excess pore pressure (undrained).

projections of the Roscoe Surface, corresponding to different specific volume values.

The critical state line in the $p-q$ plane is described through the following equation:

$$q = M \cdot p \tag{2.51}$$

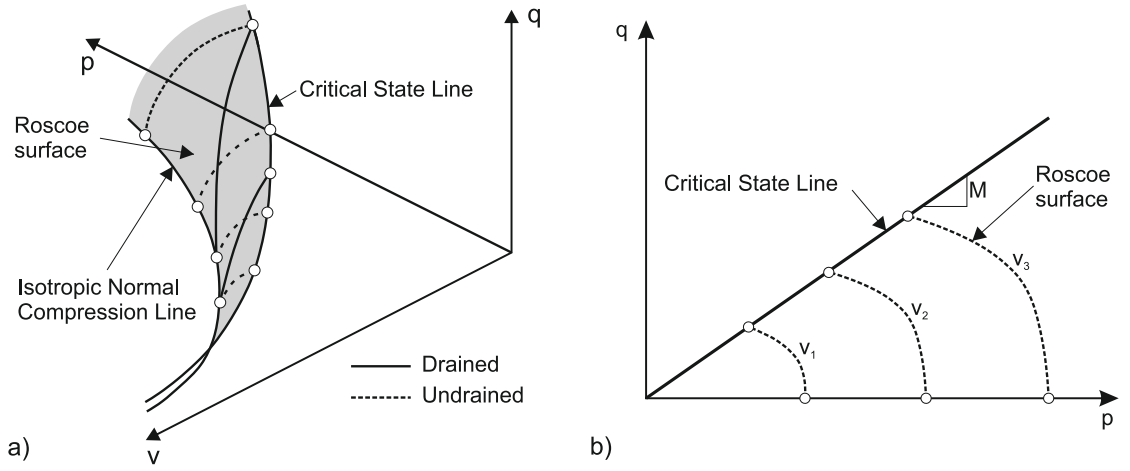


**Figure 2.13:** In a) the Roscoe surface in the $v-p-q$ space and in; b) various projections for different specific volume values in the $p-q$ plane.

where M represents the CSL slope, while in the $v-\ln p$ it is idealized as a straight line, parallel to the normal compression line, described by:

$$v_{cs} = \Gamma - \lambda \ln p \tag{2.52}$$

where $\lambda$ the slope of the NCL and $\Gamma$ corresponds to $v_{cs}$ at $p = 1kPa$.

The behaviour of overconsolidated soils can be similarly described, in a unified way, through the Hvorslev state boundary surface depicted in figure 2.14a. Test paths of overconsolidated soil specimens move above the critical state line in the $p-q$ space exhibiting a peak strength followed by a post peak strain softening behaviour before reaching their residual strength, also lying on the critical state line. The peak strength is represented by the Hvorslev surface. The Hvorslev surface intersects with the Roscoe surface at the critical state line, while towards the axes origin it is limited by the tension failure plane representing the maximum value that the $q/p$ ratio may obtain if the soil is assumed incapable of withstanding any true tensile stress.

The complete State Boundary Surface is portrayed in figure 2.14a. Using a normalization procedure based on Hvorslev equivalent pressure $p_e$:

$$p_e = \frac{\exp\left(N_{iso} - v\right)}{\lambda} \tag{2.53}$$

constant $v$ sections of the complete SBS can be plotted in the $p/p_e - q/q_e$ plane. Figure 2.14b presents such a plot.

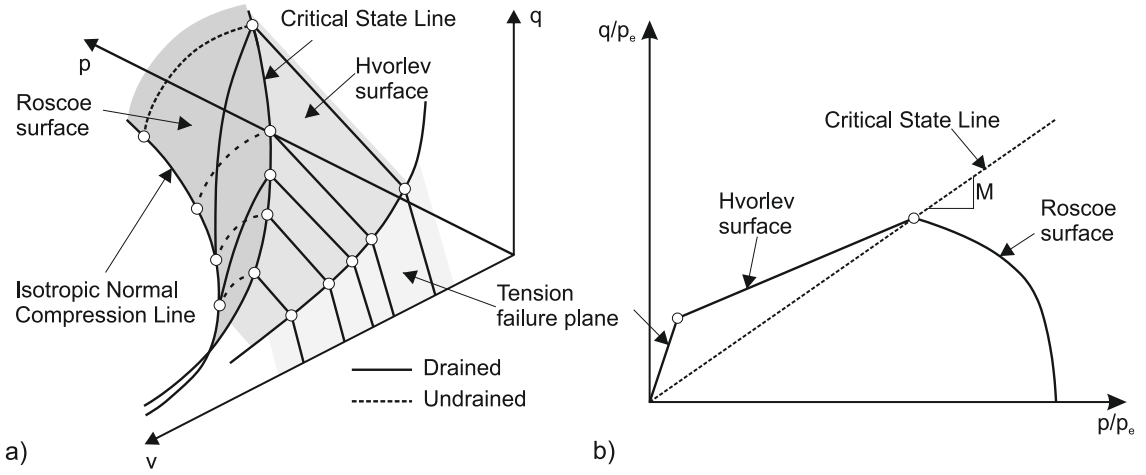


**Figure 2.14:** The complete state boundary surface (Roscoe - Hvorslev); a) in the $v-p-q$ space and ; b) in the normalized $p/p_e - q/q_e$ plane.

#### 2.3.2.3 The Modified Cam Clay

Based on the mechanical framework of Critical State Soil Mechanics, Roscoe et al. (1958) introduced the Cam - Clay constitutive model. It was later enhanced by Roscoe & Burland (1968), with an eye towards increased mathematical stability, in the well known Modified Cam - Clay (MCC) constitutive model.

MCC adopts an ellipsoidal yield surface in the $p-q$ plane, symmetric about the hydrostatic axis, that is assumed to harden only isotropically (without changing its shape) by expanding homothetically with respect to the $p$, $q$ axis intersection. The adopted yield surface (see fig. 2.15), in the generalized stress space, is described through the following yield function:

$$f\left(\sigma, \boldsymbol{s}, \alpha\right) = \frac{1}{c^2}\boldsymbol{s} : \boldsymbol{s} - \sigma(2\alpha - \sigma) = 0 \tag{2.54}$$

where $\alpha$ the hardening variable corresponding to the mean effective stress $\sigma$ at the center of the ellipse and $c$ a material constant describing the ratio of the axes of the ellipsoid. In MCC, the ratio $c$ in fact represents the slope of the critical state line and can be computed through the following expression:

$$c = \sqrt{\frac{2}{3}}M \tag{2.55}$$

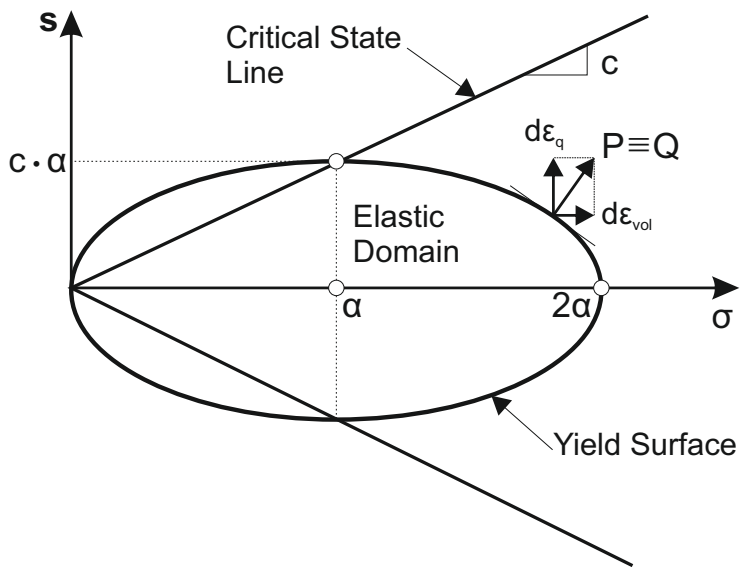


**Figure 2.15:** The yield surface of the Modified Cam Clay constitutive model.

Gradient $\boldsymbol{Q}$ equals to:

$$\boldsymbol{Q} = \{Q, \boldsymbol{Q}^{'}\} = \{2\,(\sigma - \alpha)\,, \frac{2}{c^2}\boldsymbol{s}\} \tag{2.56}$$

while the derivative of the yield function with respect to the hardening variable $\alpha$ gives:

$$\frac{\partial f}{\partial \alpha} = -2\sigma \tag{2.57}$$

Comparing figures 2.14b and 2.15, we observe that the MCC yield surface approximates a constant volume section of the Hvorslev-Roscoe SBS, while by employing a volumetric hardening rule the complete SBS in the $v - p - q$ space can be simulated.

MCC assumes an associated flow rule ($\boldsymbol{P} \equiv \boldsymbol{Q}$) and thus the yield surface also represents the plastic potential surface. Elastic behaviour inside the yield surface is simulated using the so called "poroelasticity". Poroelasticity is formulated based on the observed behaviour during unloading and reloading stress paths under isotropic and uniaxial conditions. As already discussed, the volumetric behaviour of unloaded and reloaded soil specimens is approximated by a family of swelling lines in the $v - \ln\sigma$ plane (see fig. 2.11b). Let's assume an initially elastic state ($\sigma$, $v$) lying on a swelling line with slope $\kappa$ while its position is defined through ($\sigma_0$, $v_0$) (fig. 2.16a).

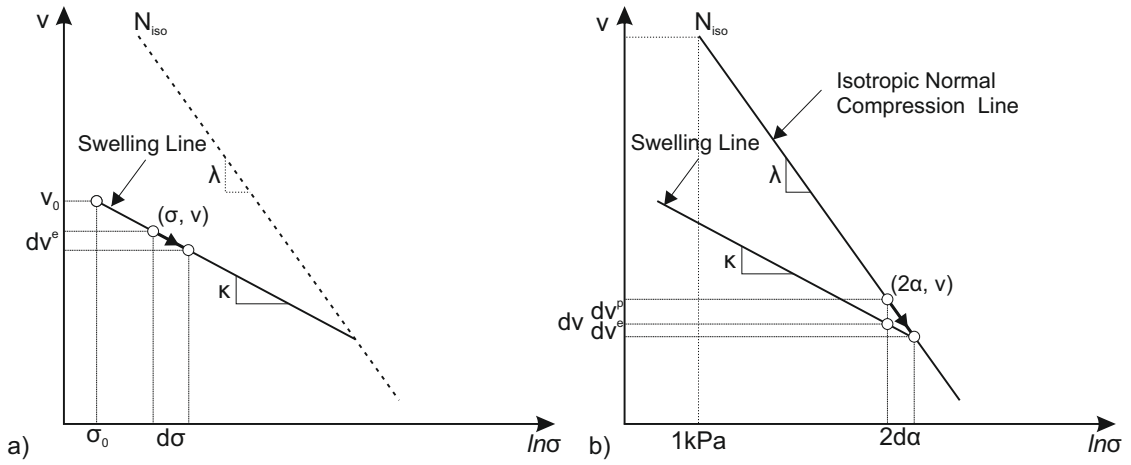


**Figure 2.16:** a) an elastic strain increment and; b) an elastoplastic strain increment, used to defining the porous elastic behaviour and the hardening rule of MCC respectively.

The aforementioned swelling line can be mathematically described as:

$$v = v_0 - \kappa \ln \frac{\sigma}{\sigma_0} \tag{2.58}$$

An infinitesimal elastic stress increment $\dot{\sigma}$ corresponds to an infinitesimal elastic volumetric strain increment $\dot{\varepsilon}^e$ that can be computed by differentiating eq. 2.58:

$$\dot{v} = -\kappa \frac{\partial \ln \frac{\sigma}{\sigma_0}}{\partial \sigma} \dot{\sigma} = -\kappa \frac{\dot{\sigma}}{\sigma} \Rightarrow \dot{\varepsilon}^e \dot{v} = \kappa \frac{\dot{\sigma}}{\sigma} \Rightarrow \dot{\varepsilon}^e = \frac{\kappa}{v\sigma} \dot{\sigma}$$

while by considering expression 2.9 we define the tangent bulk modulus $K$:

$$K = \frac{v\sigma}{\kappa} \tag{2.59}$$

It is evident that the calculated bulk modulus is a pressure dependant modulus which depends on the current mean effective stress $\sigma$ and specific volume $v$. Hence, as during loading both quantities undergo changes, the bulk modulus evolves and poroelasticity predicts non-zero values of the second order work along a full loading-unloading cycle. Such a behaviour is regarded as conservative (Belokas 2008). As far as the shear modulus is concerned it can be defined as:

$$G = \frac{1}{2} \left( \frac{2G}{K} \right) K \tag{2.60}$$

where the quantity $\frac{2G}{K}$ is assumed a material constant directly related to Poisson's ratio through expression:

$$\frac{2G}{K} = \frac{3\,(1-2\nu)}{1+\nu} \tag{2.61}$$

The isotropic hardening rule of the MCC is defined in a similar manner based on the isotropic NCL. The state of an isotropically normally consolidated soil should lie on the isotropic normal compression line in the $v - \ln\sigma$ plane, and also on the tip of the yield surface (along the isotropic axis) corresponding to $2\alpha$. Any infinitesimal loading under isotropic conditions should cause the yield surface to expand (increasing its size by $2\dot{\alpha}$) and also the material state on the $v - ln\sigma$ to move along the isotropic NCL towards a higher stress value equal to $2\alpha + 2\dot{\alpha}$ (see fig. 2.16). Starting from the governing equation of the NCL where current stress $\sigma$ is assumed equal to $2\alpha$, we may write:

$$v = N_{iso} - \lambda \ln 2a \tag{2.62}$$

Differentiating we define:

$$\dot{v} = -\lambda\frac{\partial \ln 2\alpha}{\partial 2\alpha}2\dot{\alpha} = -\lambda\frac{2\dot{\alpha}}{2\alpha} \Rightarrow \dot{\varepsilon}v = -\lambda\frac{\dot{\alpha}}{\alpha} \Rightarrow \dot{\varepsilon} = \frac{\lambda}{v\alpha}\dot{\alpha}$$

Within the aforementioned total volumetric strain increment $\dot{\varepsilon}$ the elastic strain increment $\dot{\varepsilon}^e$ is defined through poroelasticity as:

$$\dot{\varepsilon}^e = \frac{\kappa}{v\alpha}\dot{\alpha}$$

According to the basic kinematic assumption (eq. 2.1) the plastic volumetric strain increment equals:

$$\dot{\varepsilon}^p = \dot{\varepsilon} - \dot{\varepsilon}^e \Rightarrow \dot{\varepsilon}^p = \frac{\lambda}{v\alpha}\dot{\alpha} - \frac{\kappa}{v\alpha}\dot{\alpha}$$

Solving for $\dot{\alpha}$ and using the flow rule definition (eq. 2.18) we have:

$$\dot{\alpha} = \frac{v\alpha}{\lambda-\kappa}\dot{\varepsilon}^p \Rightarrow \dot{\alpha} = \dot{\Lambda}\frac{v\alpha}{\lambda-\kappa}P$$

Furthermore taking into account the associated flow rule assumed, where $P$ equals $Q$, given by expression 2.56, we end up with:

$$\dot{\alpha} = \dot{\Lambda}\frac{v\alpha}{\lambda-\kappa}2\,(\sigma-\alpha) \tag{2.63}$$

Comparing eq. 2.63 with eq. 2.33, we derive that in MCC, $h$ is a scalar quantity defined as:

$$h = 2\frac{v\alpha}{\lambda - \kappa}(\sigma - \alpha) \tag{2.64}$$

Finally, having defined the hardening rule, equation 2.37 is utilized to calculate the plastic modulus $H$:

$$H = -\frac{\partial f}{\partial \boldsymbol{q}} : \boldsymbol{h} \Rightarrow H = -\frac{\partial f}{\partial \alpha} \cdot h \Rightarrow H = 4\frac{v}{\lambda - \kappa}\sigma\alpha(\sigma - \alpha) \tag{2.65}$$

According to the MCC constitutive relationships the predicted mechanical behaviour can be separated in the following two zones:

- **Wet side**: The wet side corresponds to states at the right hand side of the CSL in the $\sigma - \boldsymbol{s}$ plane, where $\sigma - \alpha > 0$. At the wet side eq. 2.65 dictates that: $\sigma - \alpha > 0 \Rightarrow H > 0$ and thus strain hardening response is expected. Hence, a soil specimen that is triaxially loaded at the wet side will yield upon reaching the yield surface, elastoplastic strains will start accumulating and the yield surface will expand. Deviatoric stress will continuously increase until the state reaches the CSL where $\sigma - \alpha = 0 \Rightarrow H = 0$, corresponding to failure. At the same time, the associated flow rule assumed represents a contractant behaviour ($\dot{\varepsilon} > 0$).

- **Dry side**: On the dry side, at the left hand side of the CSL, $\sigma - \alpha < 0 \Rightarrow H < 0$ and thus strain softening behaviour is reproduced. In that end a soil specimen that is triaxially loaded from an initially elastic state, upon reaching the yield surface on the dry side it will have reached its peak strength value and further plastic loading will result in the contraction of the yield surface (strain softening) reproducing a decrease of the deviatoric stress towards the residual strength, finally reached when the material state reaches the critical state line. A dilatant behaviour is reproduced ($\dot{\varepsilon} < 0$).

The aforementioned behaviour is schematically summarized in figure 2.17, where the stress path of two drained triaxial compression tests, one on the wet side and the other on the dry side are demonstrated. It should also be mentioned that in MCC the CSL apart from defining the failure states also plays the role of a Phase Transformation Line (PTL), where the transition between dilatant and contractant behaviour takes place.

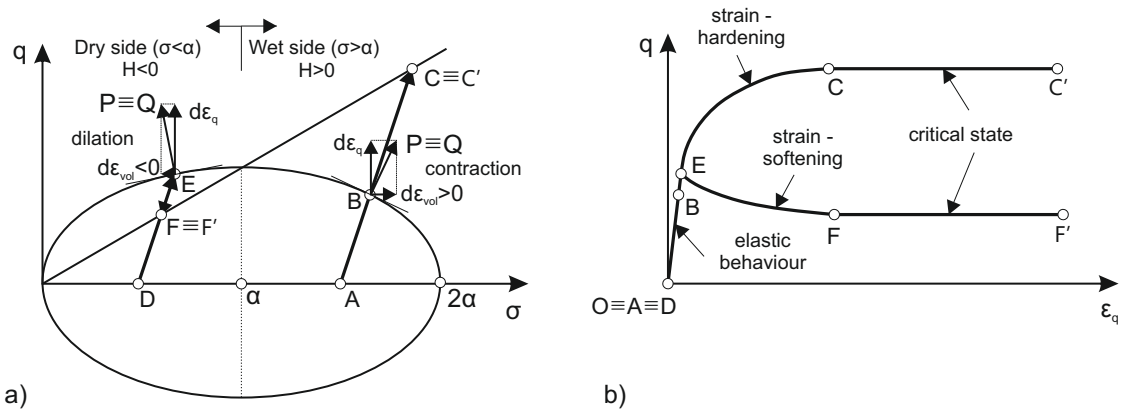


**Figure 2.17:** Two typical drained triaxial compression tests and the corresponding MCC model's predictions at the wet and the dry side. a) the stress paths in the $q - \sigma$ plane and b) the corresponding stress strain curves.

The MCC is a simple but at the same time very efficient constitutive model. It has been based on the sound and solid mechanical framework of the Critical State Soil Mechanics theory, and thus can represent essential features of the mechanical behaviour of isotropically consolidated structureless soils, with parameters easily accessible through conventional laboratory tests (i.e., isotropic compression test, triaxial drained and undrained loading).

At the same time, considering that MCC is one of the first attempts for a comprehensive description of soil behaviour, it is reasonable to expect that it will not be able to represent complex mechanical characteristics that natural soils usually exhibit due to anisotropy, structure, partial saturation or viscous effects. Following MCC principles, many researches have presented advanced constitutive models to address some of the aforementioned types of behaviour. For instance, Kavvadas (1982) and Dafalias (1986) proposed critical state models to represent the behaviour of anisotropically consolidated soils, Kavvadas & Amorosi (2000) presented a constitutive model for structured soils, while Alonso et al. (1990) extended the MCC principles in the unsaturated regime.

### 2.3.3 Bounding Surface Plasticity - Bubble Models

In Modified Cam-Clay, the selected State Boundary Surface (SBS) also represents the yield surface and thus describes the Plastic Yield Envelope (PYE) of the model, separating elastic from plastic states. Such an assumption results in an extended elastic domain where accumulated strains are recoverable upon removal of the loading

increment. Experimental results indicate that even small strains, in the order of $10^{-3}\%$, can be considered irreversible (Georgiannou 1988; Smith et al. 1992), and in that respect, an assumption of an extended elastic domain seems quite unrealistic.

The issue of small strain stiffness response gave raise to a new family of constitutive models called "bubble models", formulated within the principles of Bounding Surface Plasticity (Dafalias & Popov 1975; Dafalias & Herrmann 1982). Bubble models separate yield from the State Boundary Surface. In doing so, a relatively small PYE is incorporated, usually assumed to be related to the SBS through a proportionality ratio. PYE encloses the purely elastic domain, and can move inside the SBS following any imposed stress path. In such models the SBS plays the role of a characteristic surface bounding all the accessible material states. Both PYE and SBS can harden, following isotropic, kinematic or even mixed hardening rules. One of the major characteristics of bubble models is the need for an appropriate mapping rule to describe the variation in the plastic modulus H during loading from plastic states (on the PYE) that move towards the SBS.

Bubble models are quite more complicated, compared to single yield surface models, but give more realistic results when the behaviour during subsequent loading - unloading - reloading cycles are of importance (i.e., seismic excitations). In addition to that, in models for structured soils, a realistic representation of the plastic strains within the SBS is of great importance, as such models usually employ structure degradation rules to describe the gradual loss of structure with the onset of plastic strains.

Various bubble models have been proposed in the literature to address the mechanical behaviour of anisotropic soils (Belokas et al. 2007), structured soils (Kavvadas & Amorosi 2000; Belokas & Kavvadas 2010) and also for time-dependent behaviour (Kalos 2014). Moreover, Bounding Surface Plasticity has been extensively used in describing the cyclic response of sands (Manzari & Dafalias 1997; Papadimitriou et al. 2001). Figure 2.18 presents the characteristics surfaces employed in some of the aforementioned models.

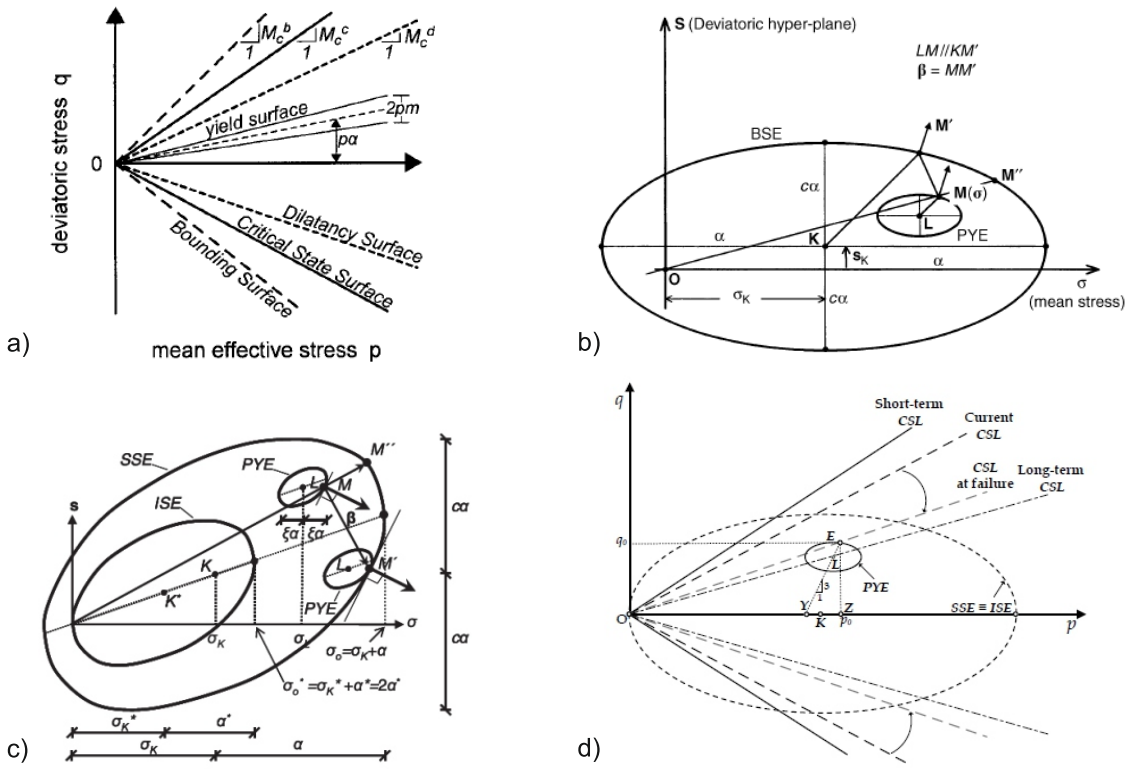


**Figure 2.18:** Characteristic surfaces of four bounding surface plasticity models; a) the Manzari & Dafalias (1997) model; b) the Kavvadas & Amorosi (2000) model; c)the Belokas & Kavvadas (2010) model and; d) the Kalos (2014).

## 2.4 Concluding Remarks

The present chapter presented the basic principles of the classical, inviscid theory of plasticity for saturated geomaterials, while all the necessary modifications to account for the behaviour of partially saturated soils will be presented in chapter 6, together with the formulation of the proposed model. It was followed by a brief historical review regarding the development of different types of soil constitutive models, emphasizing on Critical State Plasticity and on the Modified Cam Clay model. Such a review was deemed necessary as the developed constitutive model is also a critical state model, in fact extending the MCC basic ideas to account for anisotropy and partial saturation. The main points of the present chapter are summarized in the next few lines.

The formulation of any constitutive model within the framework of the classical theory of plasticity requires the definitions of the following:

- the necessary external (i.e., stress variables) and internal variables (i.e., hardening variables), which can adequately represent the state of the material;
- a yield surface, through a proper yield function $f(\boldsymbol{\sigma}, \boldsymbol{q}) = 0$ to separate elastic from plastic states;
- elastic and plastic loading;
- an elastic law for the material behaviour during elastic loading;
- a flow rule to calculate the plastic strains during plastic loading. Although it is widely accepted that an associated flow rule favours stability of the numerical solution, it was proved that even a non-associated flow rule can ensure the same level of solution's stability, provided that the selected plastic potential tensor $\boldsymbol{P}$ conforms with the $\boldsymbol{Q} : \boldsymbol{C}^e : \boldsymbol{P} > 0$ inequality;
- a hardening rule to describe the evolution of the hardening variables during plastic loading;

Following the aforementioned definitions, the consistency condition, ensuring that during plastic loading the material state remains on the yield surface, is employed to calculate the Plastic Modulus $H$, while finally the elastoplastic Jacobian $\boldsymbol{C}^{ep}$ is formulated to provide the desired link between an increment of the strain tensor and the associated stress tensor increment ($\dot{\boldsymbol{\sigma}} = \boldsymbol{C}^{ep} : \dot{\boldsymbol{\varepsilon}}$).

The first constitutive models developed for geomaterials were in fact simple elastic-perfectly plastic models (no hardening), incorporating a failure criterion as their yield surface, for instance the Mohr-Coulomb model. However, in soils, yield (initiation of plastic loading) and failure do not coincide. Following early attempts to differentiate between yield and failure (i.e., the cap-hardening model), the first sophisticated constitutive model for soils was proposed, the well-known Modified Cam Clay (MMC) (Roscoe & Burland 1968). The MCC model incorporates an isotropic elliptical yield surface, while failure is associated with the Critical State, corresponding to a material state where only deviatoric plastic stains accumulate under constant volume ($\varepsilon \dot{=} 0$) and constant mean effective stress ($\sigma \dot{=} 0$). Prior to failure, during plastic loading, the MCC's yield surface can either increase or decreases in size, reproducing either a strain hardening or a strain softening response respectively.

The MCC model dominated the subsequent development of soil constitutive models, as practically any advanced constitutive model for soils can be regarded as an

extension of the MCC. Its broad success lays on its underlying conceptual framework, the Critical State Soil Mechanics (CSSM) framework. It was founded on experimental observations of the drained and undrained shear behaviour of isotropically consolidated, reconstituted clayey soils. The main aspects of the Critical State Soil Mechanics are summarized as:

- The virgin compression of a reconstituted isotropically consolidated soil element is idealized by a straight line in the $v-\ln p$ plane with a slope $\lambda$ and position defined through parameter $N_{iso}$ corresponding to the specific volume under $1kPa$ of mean effective stress, both being material constants. It is called the Isotropic Virgin Compression Line and it defines a virtual boundary of all structureless material states.

- The loading - reloading behaviour is idealized by a group of parallel swelling lines with slope $\kappa$.

- The ultimate conditions (failure) observed in common shear tests, lie on a unique curve in the $v-p-q$ space, called the Critical State Line (CSL). Its projection on the $v-\ln p$ plane is a line parallel to the virgin compression line, while in the deviatoric stress space $p-q$ it is a straight line passing through the origin with a slope $M$.

- The normalized stress paths of either drained or undrained triaxial compression tests on normally consolidated soils (originated from the virgin compression line) follow a unique surface in the $v-p-q$ space called the Roscoe surface, limiting the domain of attainable structureless material states and thus comprising a bounding surface.

- A similar state boundary surface can be derived for overconsolidated soil states, called the Hvorslev surface.

Next chapter focuses on the mechanical behaviour of anisotropically consolidated soils and presents the most significant contributions in constitutive modelling of soil anisotropy.

# Chapter 3

# Anisotropic Soils: Mechanical behaviour and Constitutive Modelling

## 3.1 General - Definition(s) of Anisotropy

In the previous chapter, the Critical State Soil mechanics theory along with the Modified Cam-Clay constitutive model were introduced. Both were developed based on experimental results of isotropically consolidated reconstituted soils. The isotropic background of the MCC model is quite profound as it includes an isotropic yield surface (main axis orientated along the isotropic axis) and an isotropic hardening rule.

However, soils in nature are rarely found under an isotropic stress field. Natural soils are usually deposited under one - dimensional ($1D$) conditions. $1D$ conditions refer to one-dimensional compression imposed to soils during their formation through the sedimentation process and is associated with the onset of vertical strains under zero horizontal deformation ($\varepsilon_h = 0$). Anisotropic consolidation induces an anisotropic fabric in the soil, a phenomenon that is more profound in clayey soils where the platy, elongated, particles and particle groups (aggregates) tend to align with their long axes in the major principal plane (Mitchell & Soga 2005).

Fabric anisotropy on a macroscale usually leads to mechanical behaviour anisotropy. This issue has been raised by many authors in the international literature (i.e., Gens (1982)). Anisotropic soil behaviour is mainly studied through 1D consolidation (oe-

dometer) tests or radial consolidation tests on reconstituted soils. Triaxial shear tests (both drained and undrained) are also utilized to investigate the strength and deformation of initially anisotropically consolidated soils. Comparison of the obtained results with their counterparts regarding isotropically consolidated soils reveals that anisotropy severely affects the mechanical behaviour. This fact gave rise to an ensemble of constitutive models for anisotropic soils existing in the international literature (i.e., Kavvadas (1982), Dafalias (1986)).

This chapter introduces the main mechanical features of anisotropically consolidated soils, based on experimental results available in the international literature. We will first examine the typical soil behaviour under 1D compression and radial consolidation tests, before focusing on the behaviour under shear tests which produce failure. A review of the most important contributions in constitutive modelling of soil anisotropy concludes the chapter. Before proceeding with the rest of this chapter we need to discuss basic definitions of soil anisotropy.

Casagrande & Carillo (1944) distinguished between two forms of anisotropy in soils, namely the inherent and induced. Inherent anisotropy was defined as a physical characteristic inherent in the material and entirely independent of the applied stresses, whereas induced anisotropy was defined as the one due to the strains associated with the applied stresses. In this thesis we prescribe to the aforementioned definition distinguishing bewtween the stress induced and the inherent anisotropy, while moreover, defining also the bond-strength anisotropy that can either be seen as a subcase of stress induced or inherent anisotropy. In more detail we define:

- **Stress induced anisotropy**: Stress induced anisotropy corresponds exclusively to stress induced preferred directions. In that end, stress induced anisotropy, is the anisotropy that reconstituted soils acquire when they are anisotropically consolidated in the laboratory or the anisotropy possessed by natural soils which have been sedimented under 1D conditions. Stress induced anisotropy is associated with either intrinsic (structureless) or structured states;

- **Inherent anisotropy**: Any kind of anisotropy that is not attributed to an anisotropic stress field is characterized as inherent. For instance, inherent anisotropy is the anisotropy of a reconstituted and isotropically consolidated soil element which exhibits anisotropic behaviour despite its isotropic stress background;

- **Bond-Strength anisotropy**: Bond strength anisotropy corresponds solely to structured material states and represents the effect that a potentially anisotropic distribution of inter-particle bonding forces (i.e., due to cementation or partial saturation) may have on the mechanical behaviour of a given soil. An anisotropic distribution of inter-particle forces in a structured soil is usually an outcome of a pre-existing anisotropy before the action of the structure inducing agent. Thus, bond-strength anisotropy can be the outcome of either stress induced or inherent anisotropy.

For the rest of this chapter we will focus on the effects of stress induced anisotropy on the mechanical behaviour of soils. The term anisotropy without defining the type will be used sometimes for brevity, implying primary the effects of stress induced anisotropy. Moreover, the term **anisotropic fabric** is used to mention the anisotropic arrangement and interaction of soil grains/particles, irrespective of its origin.

## 3.2 Mechanical behaviour of Anisotropic soils

In section 2.3.2.3 we examined the behaviour of reconstituted soils subjected to isotropic compression tests and also to shear tests. We demonstrated that according to the CSSM theory, there exists a bounding curve in the $v - p$ plane (line in the $v - \ln p$ plane) that defines the locus of all structureless material states of isotropically consolidated soil samples, called the isotropic normal compression curve (or line). Moreover, it was discussed how normalized (Hvorslev normalization) stress paths follow a unique surface in the $v - p - q$ space (Roscoe surface).

In this section we focus on the behaviour of soil samples that have been consolidated under non-isotropic conditions. The most common non-isotropic consolidation tests are the one dimensional compression test (oedometer test) and the radial consolidation[1].

### 3.2.1 Anisotropic Consolidation

Both oedometer and radial consolidation tests impose axis-symmetric, non-isotropical conditions and thus induce an anisotropic fabric in the tested soil specimen. 1D compression imposes a constant dilatancy $d_q = \dot{\varepsilon}_q / \dot{\varepsilon}_{vol} = ct$, while radial consolidation

[1]The term radial corresponds to the direction of the imposed stress path and not to the direction of water drainage during the consolidation process.

tests impose a constant stress ratio $n = \dot{q}/\dot{p} = ct$. Under triaxial conditions, $q = \sigma_v - \sigma_h$ and $p = \frac{1}{3}(\sigma_v + 2\sigma_h)$ and thus the stress ratio $n = q/p$ can be correlated with the horizontal stress ratio $K = \sigma_h/\sigma_v$, where $\sigma_h$ and $\sigma_v$ correspond to the horizontal (radial) and vertical effective stress respectively. The following expression can be derived:

$$n = \frac{q}{p} = \frac{3(1-K)}{1+2K} \tag{3.1}$$

#### 3.2.1.1 One Dimensional (1D) Compression

The one dimensional compression test is a very common test both in research and in engineering practice. It is a convenient and relatively simple test, performed in the oedometer. In 1D compression the vertical load is increased (usually in steps), while the horizontal displacement is restrained as the soil sample is constrained within a relatively stiff steel ring. Thus, in $1D$ compression ($\varepsilon_h = 0$), $\varepsilon_q = \frac{2}{3}\varepsilon_v$ and $\varepsilon_{vol} = \varepsilon_v$ resulting in an imposed constant dilatancy equal to $d_q = 2/3$.

During 1D compression the horizontal effective stress follows the increase or decrease (during unloading) of the imposed vertical effective stress and adjusts to maintain zero horizontal strains ($\varepsilon_h = 0$). The corresponding horizontal stress ratio is usually called coefficient of earth pressure at rest or geostatic stress ratio and it is denoted as $K_0$. This is due to the fact that 1D compression resembles the sedimentation process in natural soils, where successive layers of soil are compressed under their own weight, while due to symmetry (in a relatively flat ground) no horizontal strains can develop.

Figure 3.1 presents the compression curve of a kaolin clay in the oedometer. It turns out that in a similar fashion to isotropic soils (see section 2.3.2.1), the obtained compression curve can be idealized by two straight lines in the $v - \ln p$ plane, namely the 1D Normal Compression Line (1D-NCL) and the swelling (unloading-reloading) line.

Figure 3.2a presents the variation of the horizontal effective stress with respect to the applied vertical effective stress. During the initial compression stage (A to B) the horizontal effective stress increases linearly following the increase of the applied vertical effective stress, while during unloading (from B to D) the decrease of the horizontal effective stress is much slower compared to the vertical stress reduction. The above trend is associated with the deformational behaviour during a loading - unloading stress path, where the recoverable (elastic) part of deformation is very

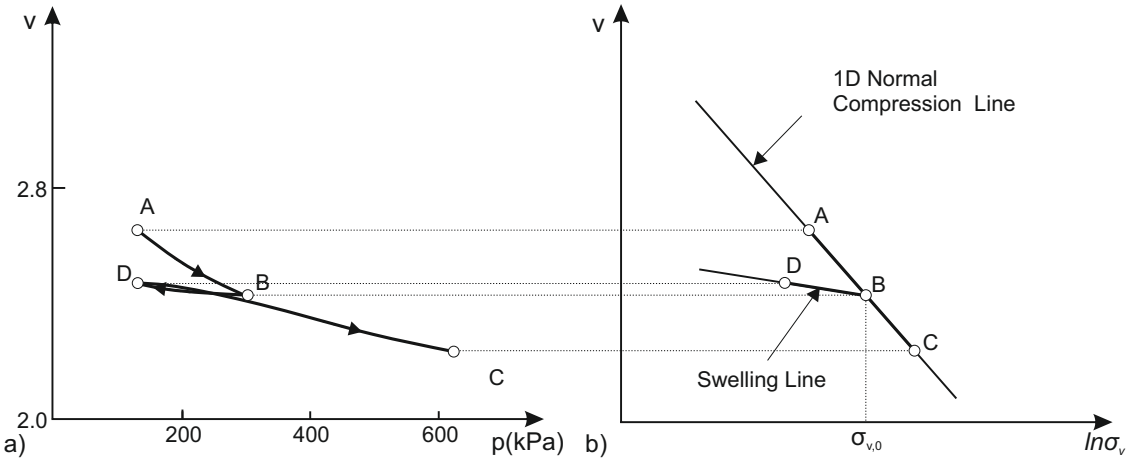


**Figure 3.1:** a) An one dimensional compression test on a Kaolin clay (Nadarajah 1973) (after Atkinson & Bransby (1977)) and; b) the idealized compressibility framework.

limited. Thus, the soil particles remain in a relatively dense arrangement, associated with the maximum vertical stress imposed in their loading history, limiting the horizontal effective stress reduction. Figures 3.2b & c show the corresponding variation in the value of the horizontal stress ratio $K_0$. It is observed that during loading (from A to B) where the soil is regarded normally consolidated, the $K_0$ remains constant and usually obtains values in the range of 0.4 to 0.7, while during unloading it increases significantly and may even obtain values higher than unity.

**Table 3.1:** $K_0$ correlations for normally consolidated soils.

| $K_{0,NC}$ | Reference |
|---|---|
| $1 - \sin\phi$ [*1] | Jaky (1944) |
| $0.95 - \sin\phi$ [*1] | Brooker & Ireland (1965) |
| $\frac{1-\sin\phi-11.5^o}{1+\sin\phi-11.5^o}$ [*1] | Bolton (1991) |

[*1] $\phi$ the friction angle of the normally consolidated material.

Various relationships exist in the literature which correlate the $K_0$ with characteristic soil properties. In tables 3.1 and 3.2 characteristic expressions are given for the coefficient of earth pressure at rest for normally consolidated ($K_{0,NC}$) and over-consolidated ($K_{0,OC}$) soils, respectively. The $K_{0,NC}$ is usually estimated from the friction angle ($\phi$) of the material, while for overconsolidated materials the $K_{0,OC}$

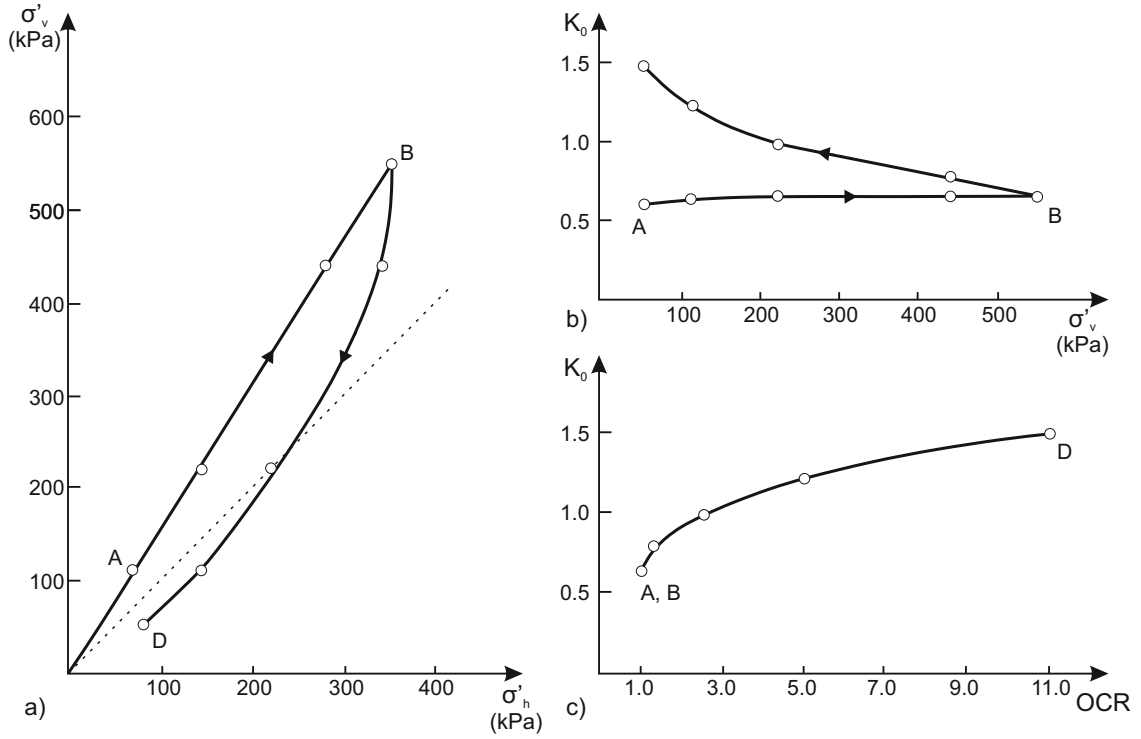


**Figure 3.2:** a) variation of the horizontal effective stress $\sigma_h$ with the vertical effective stress $\sigma_v$ in an one dimensional compression test on a Kaolin clay (Nadarajah 1973); b) the corresponding variation in the $K_0$ with $\sigma_v$ c) the $OCR$ variation. (Atkinson & Bransby 1977)

**Table 3.2:** $K_0$ correlations for overconsolidated soils.

| $K_{0,OC}$ | Reference |
|---|---|
| $K_{0,NC}(OCR) - \frac{\nu}{1-\nu}(OCR-1)$ *1 | Wroth (1978) |
| $K_{0,NC}(OCR)^{\sin 1.2\phi}$ *2 | Schmidt (1966) |
| $K_{0,NC}\sqrt{OCR}$ | Mayerhof (1976) |
| $K_{0,NC}(OCR)^{\sin\phi}$ *2 | Mayne & Kulhawy (1982) |

*1 $\nu$ the Poisson ratio.
*2 $\phi$ the friction angle of the normally consolidated material.

is usually expressed as a function of the $K_{0,NC}$ and of the overconsolidation ratio $OCR = \frac{\sigma_{v,p}}{\sigma_v}$ which represent the soil's memory of its loading history; $\sigma_{v,p}$ is the maximum vertical effective stress ever imposed in the soil of interest, called also the vertical preconsolidation pressure, while $\sigma_v$ represents the current vertical effective stress.

Figure 3.3 plots the idealized 1D compression line in the $v - \ln p$ plane and compares it with its isotropic counterpart (see also figure 2.11b). We observe that the 1D-NCL plots to the left of the I-NCL and that the two lines are almost parallel. In that respect, it is fair to assume that the slope of both lines is represented by the MCC compressibility parameter $\lambda$. The same trend holds true for the swelling lines as well and thus, both may be represented by the slope $\kappa$. In that end, the 1D-NCL is mathematically described as:

$$v = N_{1D} - \lambda \ln p \tag{3.2}$$

where $N_{1D}$ locates the line (corresponds to the specific volume at $p = 1kPa$). The 1D-NCL plots to the left of the I-NCL due to the fact that soils compressed under anisotropic conditions ($q \neq 0$), tend to acquire a denser soil fabric compared to soils compressed under isotropic conditions ($q = 0$), as a reflection of the beneficial effect of shear forces in solid particles rearrangement. It is for that reason why Roscoe et al. (1958) describe the I-NCL as the line corresponding to the maximum void ratios or to the loosest packing obtainable by a material consolidated from a slurry.

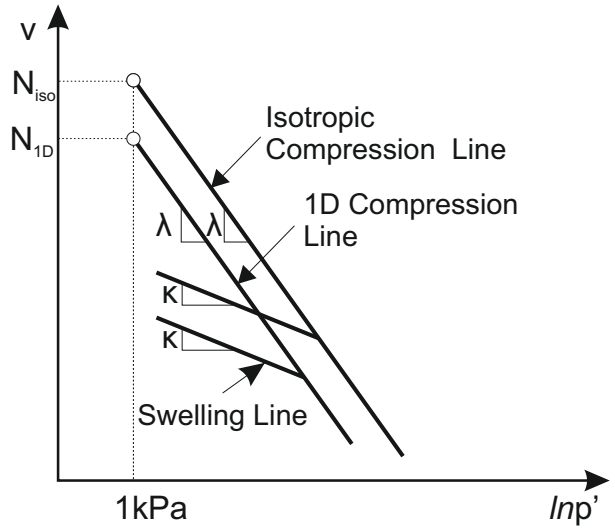


**Figure 3.3:** The idealized isotropic and one dimensional compression lines. (Atkinson & Bransby 1977)

The 1D Intrinsic - Normal Compression line is also of a great importance in accessing the effect that structure has on natural soils. Burland (1990) proposed a normalization procedure to plot together 1D Intrinsic Compression Lines for various fine-grained materials. The author introduced a normalization parameter called the

void index $I_v$:

$$I_v = \frac{e - e^{**}_{100}}{e^{**}_{100} - e^{**}_{1000}} \tag{3.3}$$

where $e^{**}_{100}$ and $e^{**}_{1000}$ correspond to the void ratio at $100kPa$ and $1000kPa$ respectively. It turned out that a reasonably unique line was achieved. Then the ICL was used as a reference frame to compare with the in-situ state of natural clays, represented by the Sedimentation Compression Curve, corresponding to the measured void ratio from undisturbed samples of natural soils. It was found that the sedimentation curve of most natural materials plots well above the corresponding ICL, while its position depends on both depositional conditions (i.e., speed of sedimentation) and post depositional processes (i.e., leaching). Figure 3.4a shows the normalized ICL of various materials in comparison with data corresponding to sedimentation curves for the same materials.

Kavvadas & Anagnostopoulos (1998) state that the in situ state of a natural soil may lie anywhere in the $e-p$ plane depending on the structure inducing process (see fig. 3.4b). Ageing (path $O \rightarrow A$) and overconsolidation (path $O \rightarrow B$) move the material state to the left of the ICL, in the para-stable domain (Kavvadas et al. 1993), while diagenesis during sedimentation, leaching and partial saturation, move the material state to the right of the ICL (path $F \rightarrow I$) in the meta-stable domain (Vaughan et al. 1988). The relative position of the in-situ state with respect to the ICL also affects the soil response during shearing. In general, soils in para-stable states dilate and strain harden while soils in the meta-stable states contract, strain soften and are prone to collapse.

#### 3.2.1.2 Radial Consolidation

As already discussed, in an 1-D consolidation test the soil specimen is compressed under a constant dilatancy $d_q = 2/3$, arising from the boundary conditions of the oedometer apparatus. The stress path adjusts to the imposed dilatancy, and after some straining, acquires a constant ratio $n_{q,1D}$ equal to:

$$n_{1D} = \frac{q}{p} = \frac{3\,(1 - K_0)}{1 + 2K_0} \tag{3.4}$$

Apart from 1-D compression, an anisotropic fabric can be induced to a soil specimen in the triaxial apparatus by applying radial stress paths of a constant $n_q = ct \neq 0$[2].

[2] $n_q = 0$ corresponds to isotropic compression tests that do not induce anisotropy.

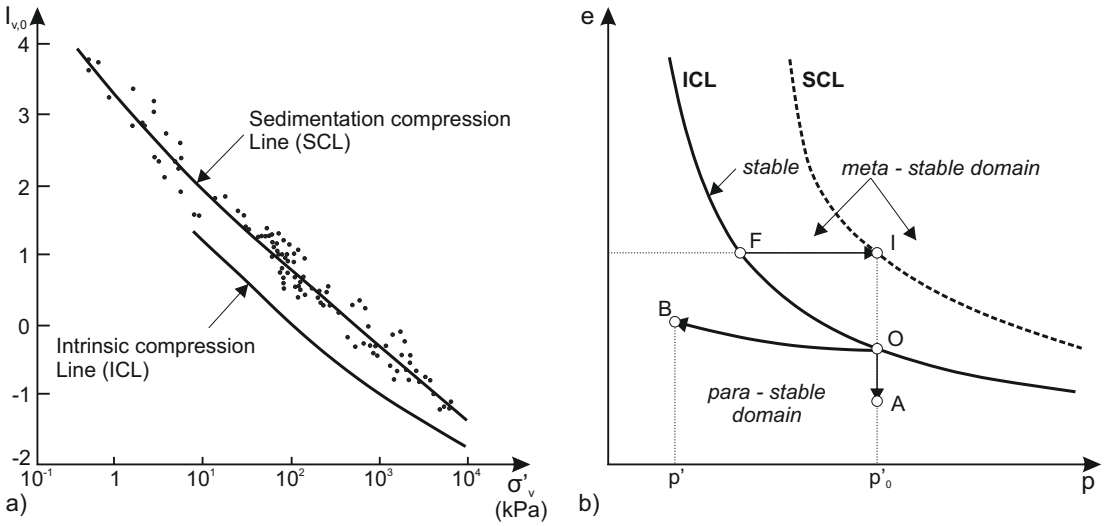


**Figure 3.4:** a) the intrinsic compression line and an averaged sedimentation curve from various normally consolidated soils after Burland (1990) and b) various mechanisms causing structure after Kavvadas & Anagnostopoulos (1998).

After substantial plastic straining an initially reconstituted soil will achieve a certain degree of anisotropy and will deform under a stabilized constant dilatancy $d_q$. Various researchers have studied the behaviour of reconstituted soils under radial stress paths.

Gens (1982) performed radial consolidation tests at different $K$ values on reconstituted samples of the Lower Cromer Till (LCT). In figure 3.5 we observe that parallel

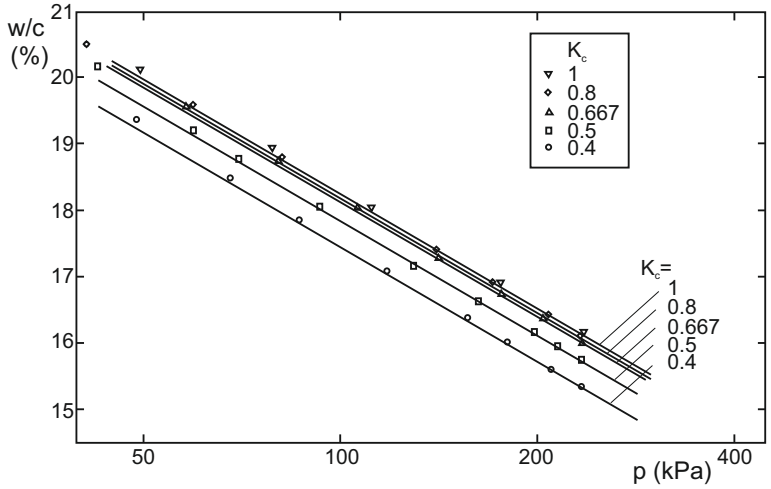


**Figure 3.5:** Water content variation with the mean effective stress during constant K consolidation tests. (Gens 1982)

consolidation lines with a constant slope can be assumed representative of the soil

behaviour in the $w/c - \ln p$ plane[3]. The results are also in good agreement with the framework proposed by Lewin & Burland (1970) based on consolidation tests of slate dust (see figure 3.6). Similar results have also been reported by Donaghe & Townsend

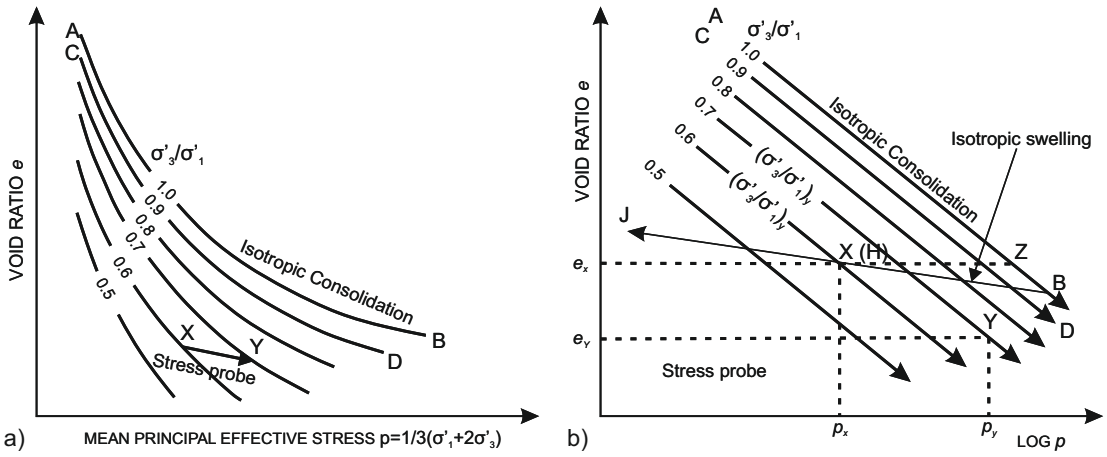


**Figure 3.6:** Anisotropic consolidation lines on the: a) $e-p$ and; b) $e-\log p$ planes. (Lewin & Burland 1970)

(1978), Georgiannou (1988) and even more recently by Rampello et al. (1997) and Belokas et al. (2007) for Vallerica Clay (see figures 3.7 and 3.8 respectively). The vast majority of the results agree on the fact that soil elements consolidated under radial stress paths of different $K$, plot in the $v-\ln p$ plane on different but practically parallel normal consolidation lines. Thus, once again it is a fair approximation to assume that the intrinsic, virgin compression lines raising from radial consolidation tests are described by the Modified Cam Clay compressibility parameter $\lambda$, while their position depends on the applied stress ratio $n$. Similarly to 1-D consolidated soils, the compression lines of radially consolidated soil samples plot on the left of the isotropic compression line. Once again the observed behaviour is attributed to the denser soil fabric induced by stress anisotropy, due to the beneficial effect of shear forces in solid particles rearrangement. Belokas & Kavvadas (2011) proposed an Intrinsic Compressibility Framework (ICF) (see figure 3.9) to reproduce and quantify the observed behaviour. Belokas ICF will be further analyzed in chapter 5 as it plays a key role in the hardening rule of the developed constitutive model. At this point it is worth mentioning that the observed behaviour under radial stress paths is consistent with Rendulic's statement that "changes in the specific volume are independent of the

[3]For saturated soil samples undergoing drained compression, the behaviour in the $w/c-\ln p$ and $v-\ln p$ planes is similar.

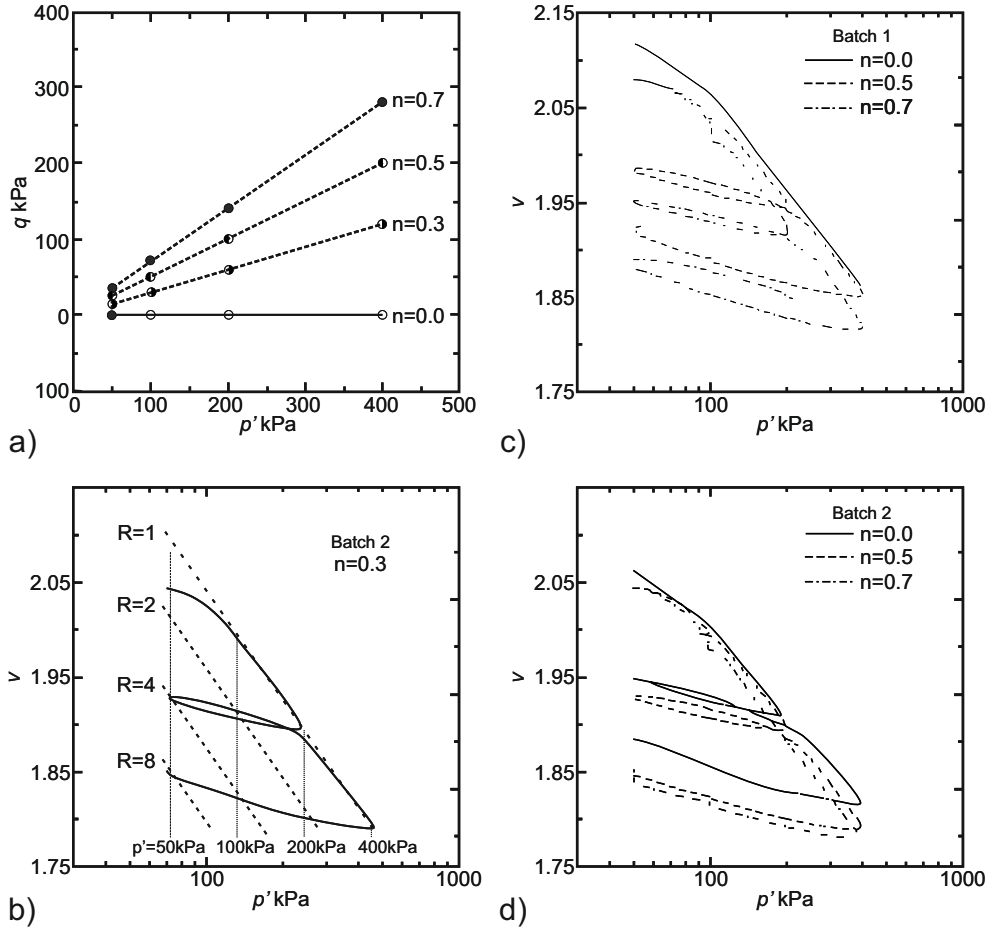


**Figure 3.7:** Anisotropic compression of Vallericca Clay; a) the applied stress paths on the $p-q$; b) a typical sequence of the applied compression states and; c,d) the corresponding behaviour in the $v-\ln p$ plane. (Rampello et al. 1997)

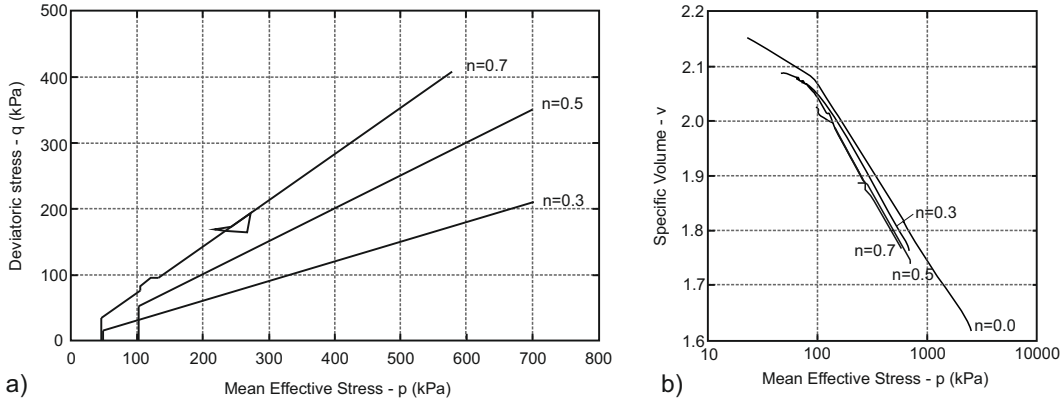


**Figure 3.8:** Anisotropic compression of Vallericca Clay. a) The applied stress paths on the $p-q$ and; b) the corresponding behaviour in the $v-\ln p$ plane. (Belokas 2008)

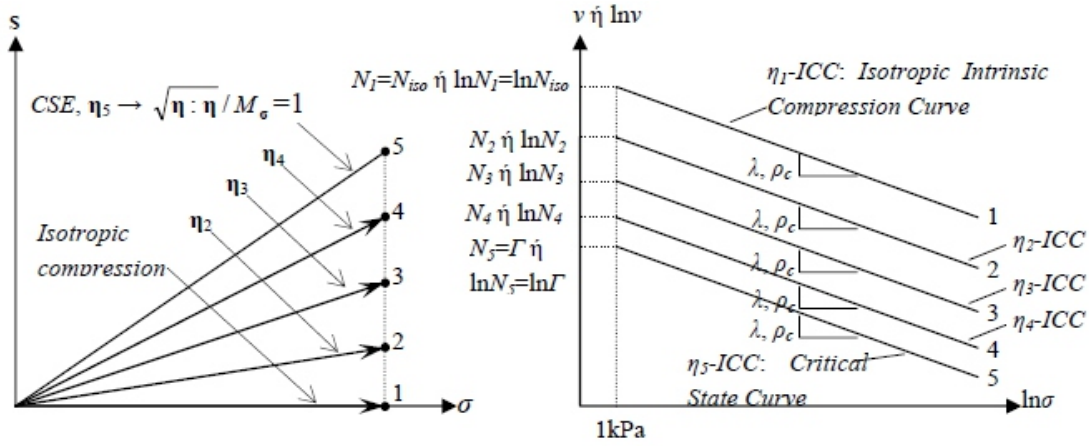


**Figure 3.9:** The Belokas & Kavvadas (2011) Intrinsic Compressibility Framework (ICF).

direction of the applied stress path", but does not confirm Rutledge's hypothesis that "the specific volume is independent of the direction of the applied stress path". It is true that some experimental results (Lee & Morrison 1970; Broms & Ratman 1963) have been found to agree also with Rutledge's hypothesis, raising a unique line in the vertical effective stress - water content plane; nevertheless, according to Gens (1982) this can be attributed to the fact that they were testing compacted soils remoulded in a relatively low water content and not reconstituted soils.

Anisotropic consolidation is also associated with the onset of deviatoric strains. Plots of the strains usually measured under such drained consolidation tests indicate that a constant dilatancy is reproduced, apart from the early stages of the consolidation test which includes the adjustment of the deviatoric stress $q$ to the desired $K$ (Gens 1982) (see figure 3.10a). In figure 3.10b, we may observe that, during isotropic consolidation of reconstituted soil samples, zero deviatoric strains are reproduced ($\frac{\dot{\varepsilon_a}}{\dot{v}} = \frac{1}{3}$), while an increased consolidation stress ratio $K$ is associated with increased deviatoric strains. Finally, for further increase in the slope of the consolidation stress path the deviatoric strains tend to infinity as the consolidation ratio approaches the slope of the critical state line, which is reasonable as long as critical state is associated with failure. Gens (1982) plotted together the strain ratios measured during consolidation tests from several authors alongside with his results on LCT (see figure 3.11). To account for differences in the soil behaviour, the observed strain ratios have been plotted against a normalized stress ratio $n/M$. The results suggest a nonlinear increase in the observed dilatancy. Table 3.3 summarises the data utilized by Gens (1982) in plotting graph 3.11. Figures 3.12 and 3.13 present

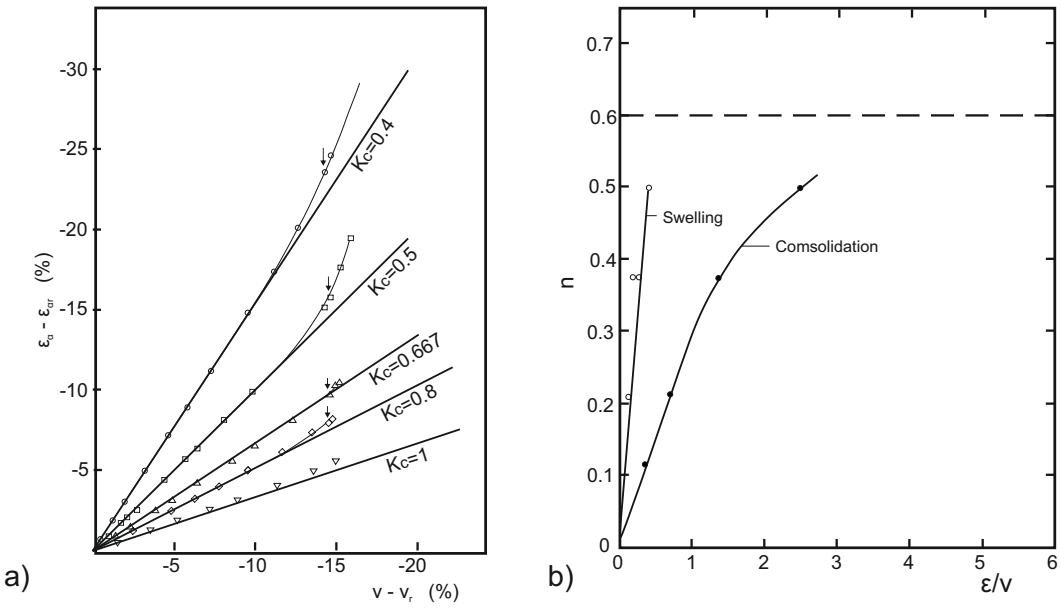


**Figure 3.10:** a) Volumetric strain vs axial strain curves and; b) variation of the strain increment ratio with stress ratio $n = \frac{1}{2}\frac{q}{p}$ during constant $K$ consolidation and swelling tests of Lower Cromer Till (LCT). (Gens 1982)

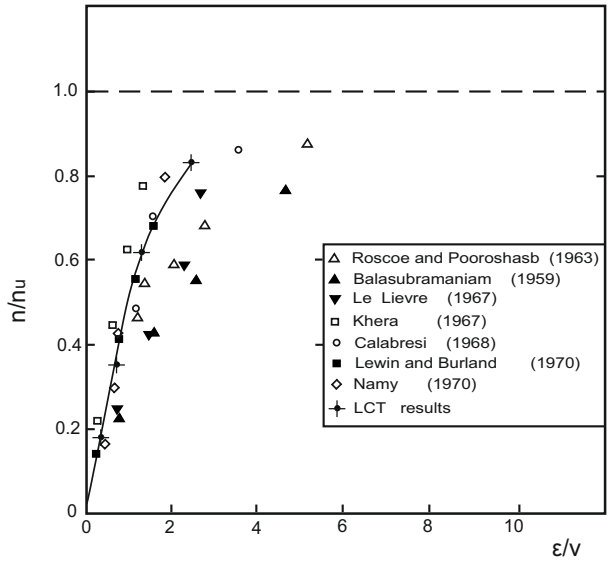


**Figure 3.11:** Variation of strain increment ratios vs normalized stress ratio for various soils (see table 3.3). (Gens 1982)

the strains measured during consolidation tests on Vallerica clay samples (Rampello et al. 1997; Belokas & Kavvadas 2010). The results confirm the trend of figure 3.11.

Regarding the behaviour during unloading, Gens (1982) plotted together the water content changes observed during unloading of soils samples that have been initially anisotropically consolidated to various $K$ ratios; the state of the soil at the end of the

**Table 3.3:** The experimental data utilized in figure 3.11.

| Soil name | Reference [*1] |
|---|---|
| Kaolin | Roscoe & Poorooshasb (1963) |
| Speston Kaolin | Balasubramannian (1969) |
| Edga Kaolin | Le Lievre (1967) |
| Grundite Clay | Khera (1967) |
| Silty Clay | Calabresi (1968) |
| Slate dust | Lewin & Burland (1970) |
| Newfield clay | Namy (1970) |

[*1] as quoted in Gens (1982).

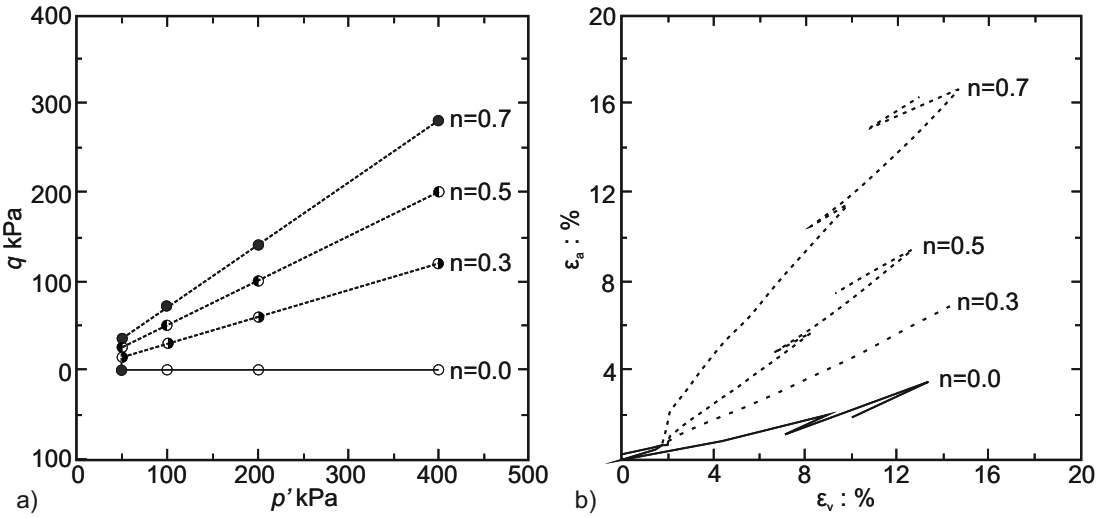


**Figure 3.12:** Vallerica clay radial consolidation tests; a) the applied stress paths and; b) the measured strains. (Rampello et al. 1997)

consolidation is considered as a reference state. Figure 3.14 reveals that a common swelling curve seems to exist, which can be approximated with a straight line in the $v - \ln p$ plane. As far as the deviatoric strains measured during unloading are concerned, it is reported that due to the limited straining occurring during unloading, it is rather difficult to ascertain whether a constant dilatancy applies during swelling or not. In figure 3.15 the axial vs volumetric strains measured are presented. It is evident that although the strain ratios increase with increasing stress ratio, they are much smaller compared to their counterparts during normal compression, indicating

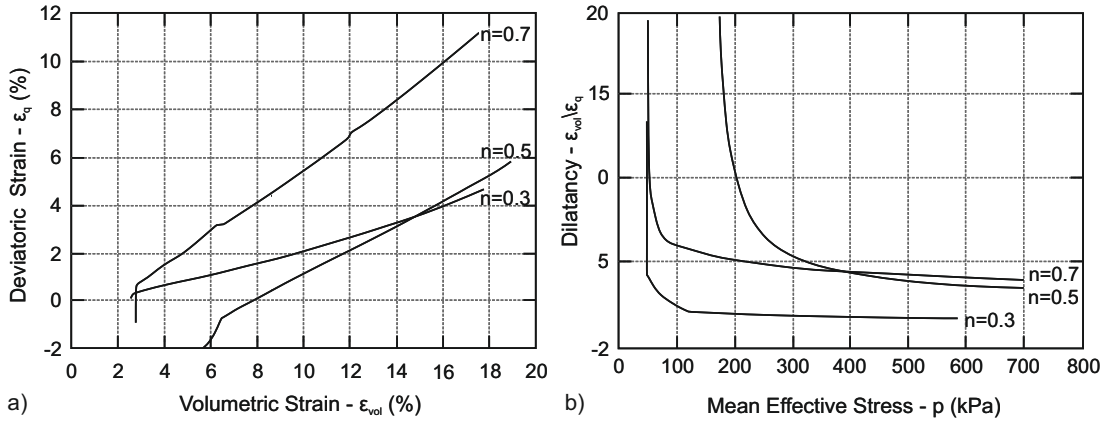


**Figure 3.13:** Vallerica clay radial consolidation tests; a) the measured strains and b) the evolution of total dilatancy with increasing mean effective stress. (Belokas & Kavvadas 2010)

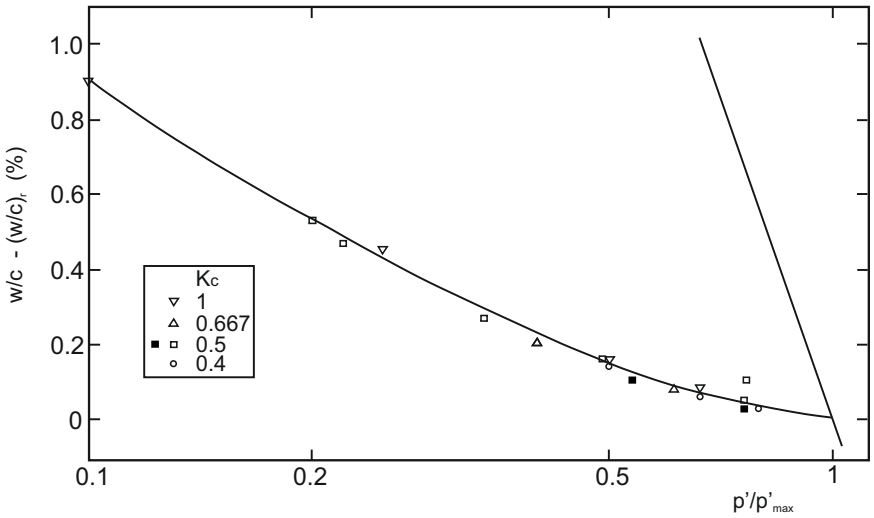


**Figure 3.14:** Water content changes observed during LCT constant $K$ swelling tests. (Gens 1982)

that the measured shear strains are proportionally much smaller. This is reasonable and in good agrement with the observed behaviour during 1-D consolidation tests. In more detail, in 1-D compression the total dilatancy during both loading and unloading is constant and there is a change in the stress ratio due to the horizontal effective stress reducing with a pace that is much smaller compared to the reduction of the vertical effective stress. In that respect, it is reasonable to expect that during unloading under a constant stress ratio the aforementioned different loading and unloading behaviour will be reflected on the anticipated strains.

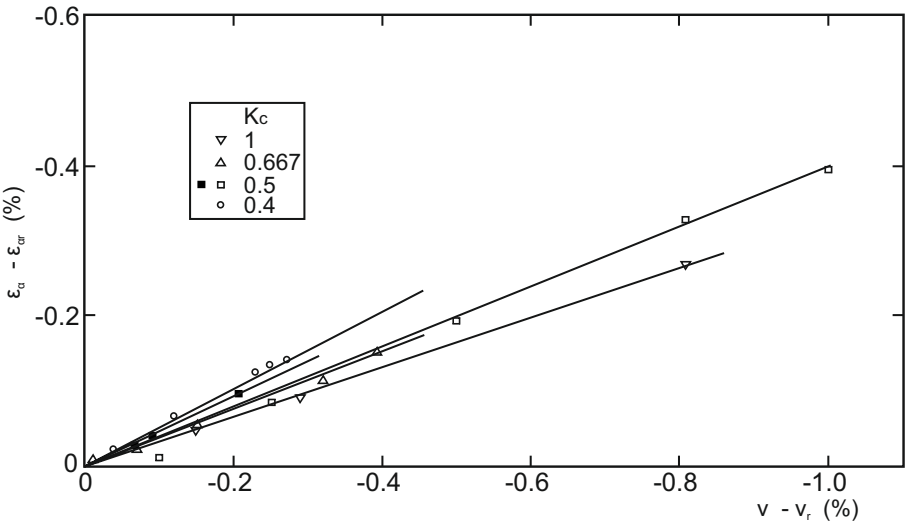


**Figure 3.15:** Axial vs volumetric strains observed during LCT constant $K$ swelling tests. (Gens 1982)

### 3.2.2 Shear Strength and Yielding of Anisotropically Consolidated Clayey Soils

In section 2.3.2 we studied the behaviour of isotropically consolidated reconstituted soils that are sheared under drained and undrained triaxial conditions. It was discussed how the behaviour of such soils, being initially either normally or even over - consolidated is described through a unified theoretical framework. As reported in Jardine et al. (2004), Bjerrum (1973) emphasized that for laboratory shear strength measurements to be representative of the in situ behaviour, soil samples should be reconsolidated to their anisotropic in situ stress conditions before sheared to failure. Ladd & Varallyay (1965) report the results of a systematic study on the behaviour of reconstituted Boston Blue Clay. They performed undrained triaxial compression and extension tests on soil specimens initially consolidated either; a) isotropically ($K = 1.0$), or anisotropically with; b) $K = 0.54$ ($\sigma_v > \sigma_h$) and c) $K = 1.85$ ($\sigma_h > \sigma_v$). Figure 3.16 presents the obtained effective stress paths. It is apparent that there are significant differences between the behaviour of isotropically and anisotropically consolidated soils.

Even nowadays, probably the most systematic study on the effects of anisotropic consolidation on shear behaviour has been offered by Gens (1982). For the rest of this section we will mainly focus on the results reported in the aforementioned contribution. Simultaneously results from other recent works will be raised as needed

to offer an as complete as possible discussion on the shear behaviour of anisotropically consolidated soils. The author worked with reconstituted samples of a sandy

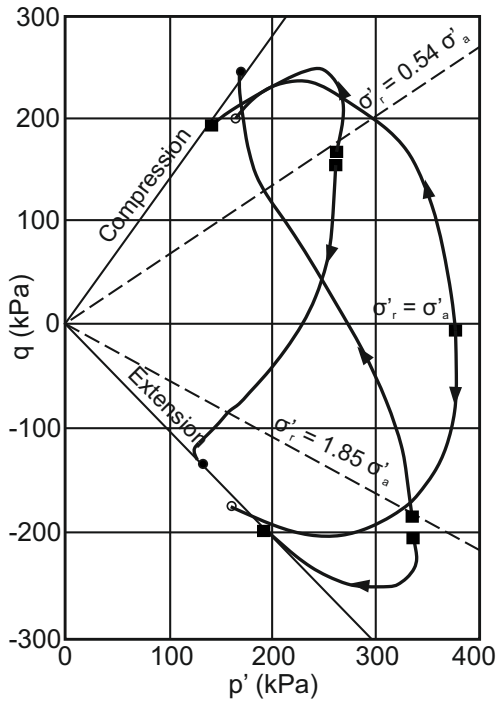


**Figure 3.16:** Boston Blue Clay undrained compression and extension tests (Ladd & Varallyay 1965), normally consolidated under three different stress ratios. (after Jardine et al. (2004))

clay of low plasticity, the Lower Cromer Till. The study includes an extensive set of laboratory tests investigating the drained and undrained behaviour of LCT under both compression and extension and for both isotropically and anisotropically consolidated soils. The reported results concern both normally consolidated soils and also soil samples that have been swelled back to various overconsolidation ratios. One of the objectives of the study was to investigate whether the behaviour exhibited from anisotropically consolidated soils depicts within the critical state framework, concentrating on whether the concept of a unique State Boundary Surface (SBS) applies for anisotropic soils as well. In doing so, the author investigated whether the behaviour of anisotropically consolidated soils undergoing triaxial loading to failure is normalizable in terms of the maximum preconsolidation pressure.

#### 3.2.2.1 Undrained behaviour

Figure 3.17a presents the normalized results of undrained triaxial compression tests on anisotropically normally consolidated samples consolidated to different vertical stresses (200, 350 and $700kPa$), all under the same stress ratio $K = 0.5$. It is observed that the achieved normalization is very satisfactory. Similar plots of results on overconsolidated soils (see fig. 3.17b) indicate that also the stress paths obtained from overconsolidated soils are normalizable with respect to the maximum consolidation pressure. The achieved normalization indicates that the behaviour of anisotropically consolidated soils can be studied in a similar fashion to their isotropically consolidated counterparts, by testing for a single maximum consolidation pressure and assuming a proportional behaviour for other stress levels.

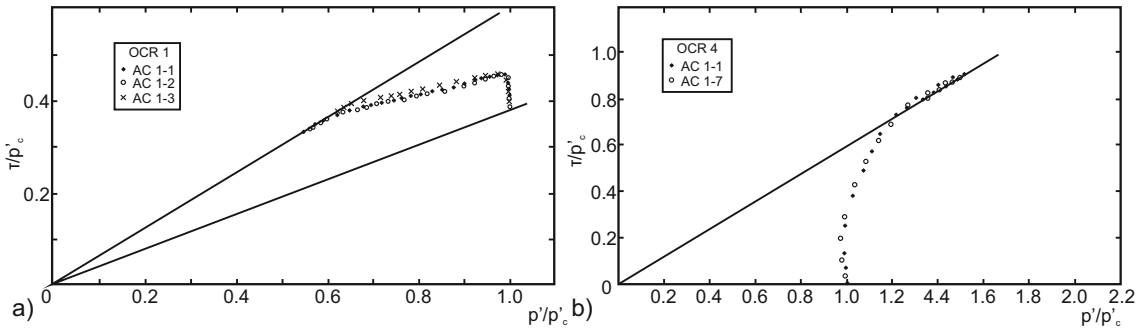


**Figure 3.17:** Undrained triaxial compression normalized stress paths, corresponding to anisotropically ($K = 0.5$); a) normally consolidated and; b) overconsolidated LCT samples. (Gens 1982)

Figure 3.18 presents the results of six undrained compression tests on soil samples initially consolidated to a maximum vertical consolidation pressure of $\sigma_v = 350kPa$ under a constant stress ratio of $K_0 = 0.5$, corresponding to a preconsolidation pressure $p \approx 233kPa$. We shall mention that $K = 0.5$, corresponds to the coefficient of lateral earth pressure at rest for the LCT and was selected for the imposed radial consolidation to resemble 1D consolidation conditions. The author reports that during this radial consolidation, the actually measured radial strains where almost zero, confirming that $K = 0.5$ corresponds to $K_0$. One of the samples was sheared directly after consolidation while the rest where unloaded to different over-consolidation ratios ($R_p$), namely; $1.5, 2.0, 4.0, 7.0$ and $10.0$. In Figure 3.18a, the initial stress states of the overconsolidated samples correspond to stress ratios different than $K = 0.5$, indicating that the soil samples where swelled back under 1D conditions by adjusting the cell pressure to maintain zero radial displacements.

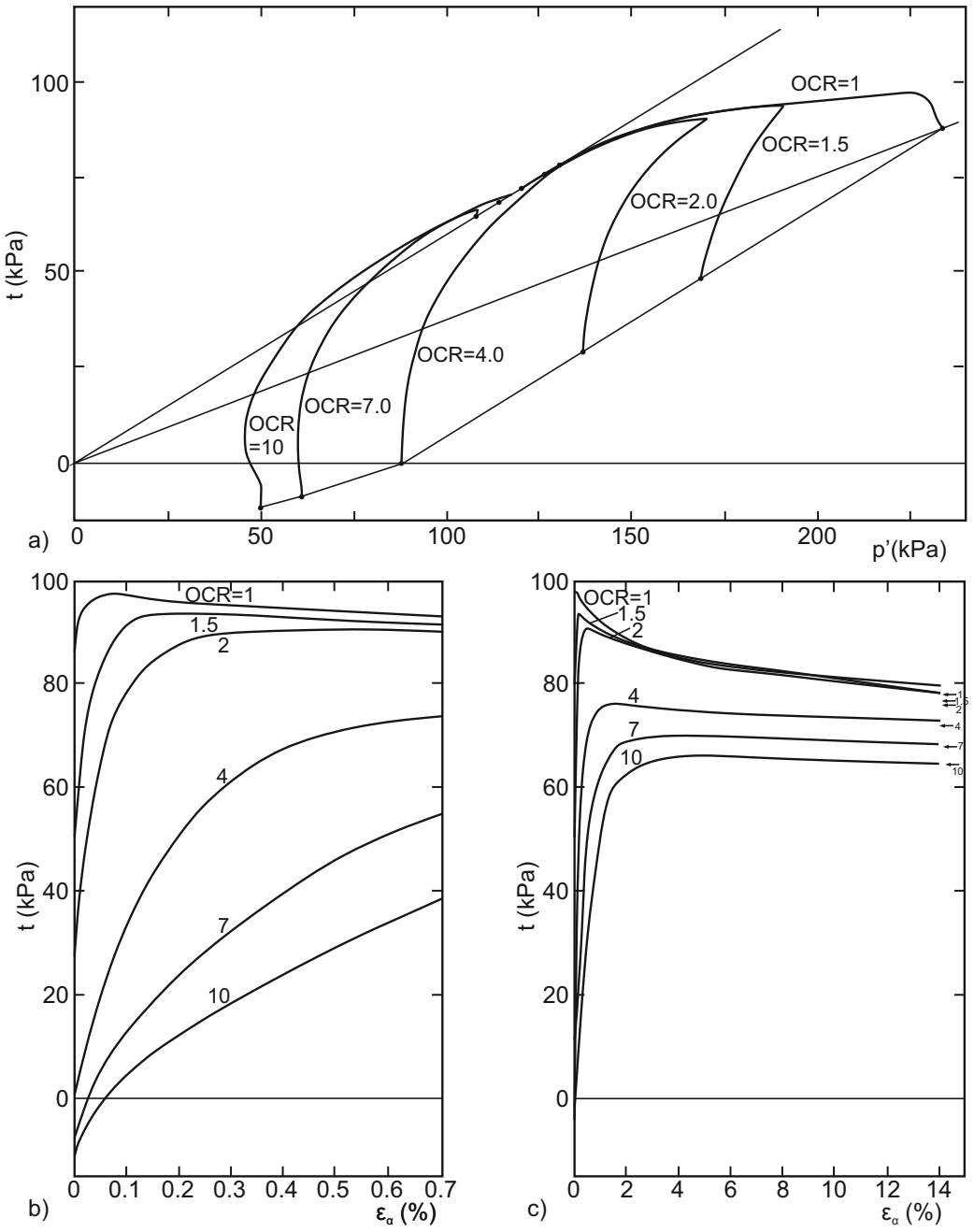


**Figure 3.18:** Undrained triaxial compression of anisotropically ($K = 0.5$) consolidated LCT samples in various overconsolidation ratios $OCR$; a) effective stress paths ($t$ vs $p$) and; b,c) the corresponding deviatoric stress - axial strain curves (in (c)) the small strain regime). (Gens 1982)

Normally or even slightly overconsolidated samples with $OCR = 1.5$ and $OCR = 2.0$ exhibit a brittle behaviour associated with a clearly defined peak followed by a decrease in the deviatoric stress towards an ultimate (residual) shear strength. On the other hand, samples swelled to $R_p$ values greater than four (4) seem to strain

harden all the way up to their ultimate shear strength; in this case peak and residual strengths coincide. Overall, we may say that initially anisotropically consolidated soils exhibit a brittle behaviour when compressed under undrained conditions, with a well defined peak, while both their brittleness and their peak strength decrease with increasing overconsolidation.

Probably the most interesting part of the aforementioned results is the one concerning the ultimate strength. It seems that the ultimate points of the performed tests are all very close to the line $\tau = 0.6p$ which corresponds to a critical state line with slope $M = 1.2$, similar to the one obtained from their isotropically consolidated counterparts. The same applies for the ultimate points in the $w/c - \log p$ plane (see fig 3.19) where the ultimate points indicate a common CSL for both anisotropically and isotropically consolidated soils. Ultimate strength results offer an area of com-

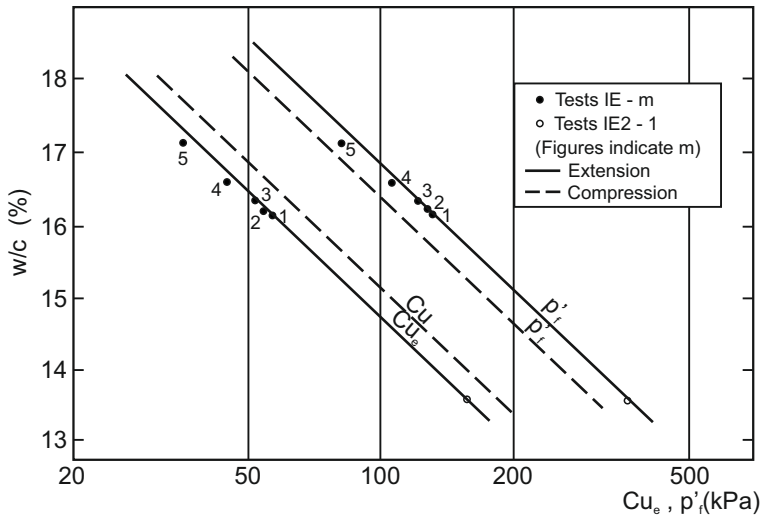


**Figure 3.19:** Undrained triaxial compression of anisotropically ($K = 0.5$) consolidated LCT samples. The corresponding peak and ultimate points on the $w/c - logp_f, C_u$ planes. (Gens 1982)

mon behaviour for both isotropically and anisotropically consolidated soils, while also indicate that the conditions prevailing at critical state are unique and independent of the initial anisotropy and of the soil's memory of its stress history. Gens (1982) also investigated the effect of the strain rate applied during shearing (see figure 3.20). The ultimate strength of anisotropically normally consolidated samples seem also independent of the applied strain rate contrary to the behaviour during the first part of the test and the associated peak strength.

Regarding other similar results, Gens (1982) reports a series of existing at the

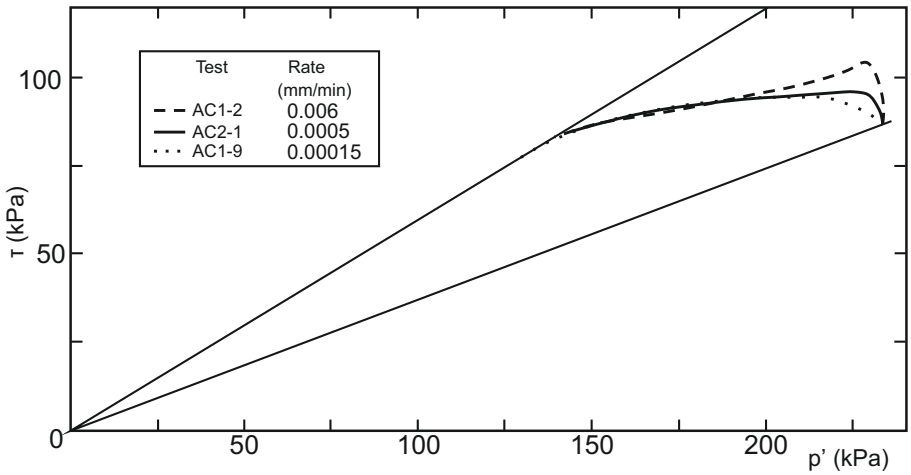


**Figure 3.20:** Undrained triaxial compression on normally consolidated LCT samples; the effect of different strain rates. (Gens 1982)

time experimental works from the international literature dealing with shear strength of anisotropically consolidated clayey soils (Donaghe & Townsend 1978; Ladd & Varallyay 1965; Koutsoftas 1981; Ladd & Lambe 1963; Vaid & Campanella 1974; Noorany & Seed 1965; Henkel & Sowa 1963; Mitachi & Kitago 1979; Parry & Nadarajah 1974). The author claims that according to his literature review in most of the cases authors report a brittle behaviour for anisotropically consolidated tests although there are some exceptions to the rule reported from Mitachi & Kitago (1979) and Parry & Nadarajah (1974). It is concluded that it seems that there exists a relation between the ratio $\tau_p/\tau_u$ with the plasticity of the tested soils with brittleness reducing as PI increases. Regarding the ultimate state it seems that the observation of a common ultimate strength between isotropically and anisotropically consolidated soils is a very general rule with only a few exceptions as those reported by Mitachi & Kitago (1979) and Parry & Nadarajah (1974) that can probably be attributed to the level of the axial strains imposed being insufficient to lead to ultimate conditions.

To examine the effect that different degrees of stress induced anisotropy have on the observed behaviour, the author performed undrained triaxial loading tests on reconstituted samples that were normally consolidated along various constant K stress paths, namely; $K = 0.4$, 0.5, 0.667, 0.8 and 1.0, with the latter corresponding to an isotropically consolidated soil sample for comparison. The obtained results (see figure 3.21) indicate that there is a strong influence of K on the stress path. The results are in favour of an increasing degree of brittleness associated with a decreasing initial anisotropy. This brittleness is more profound in the recorded stress - strain

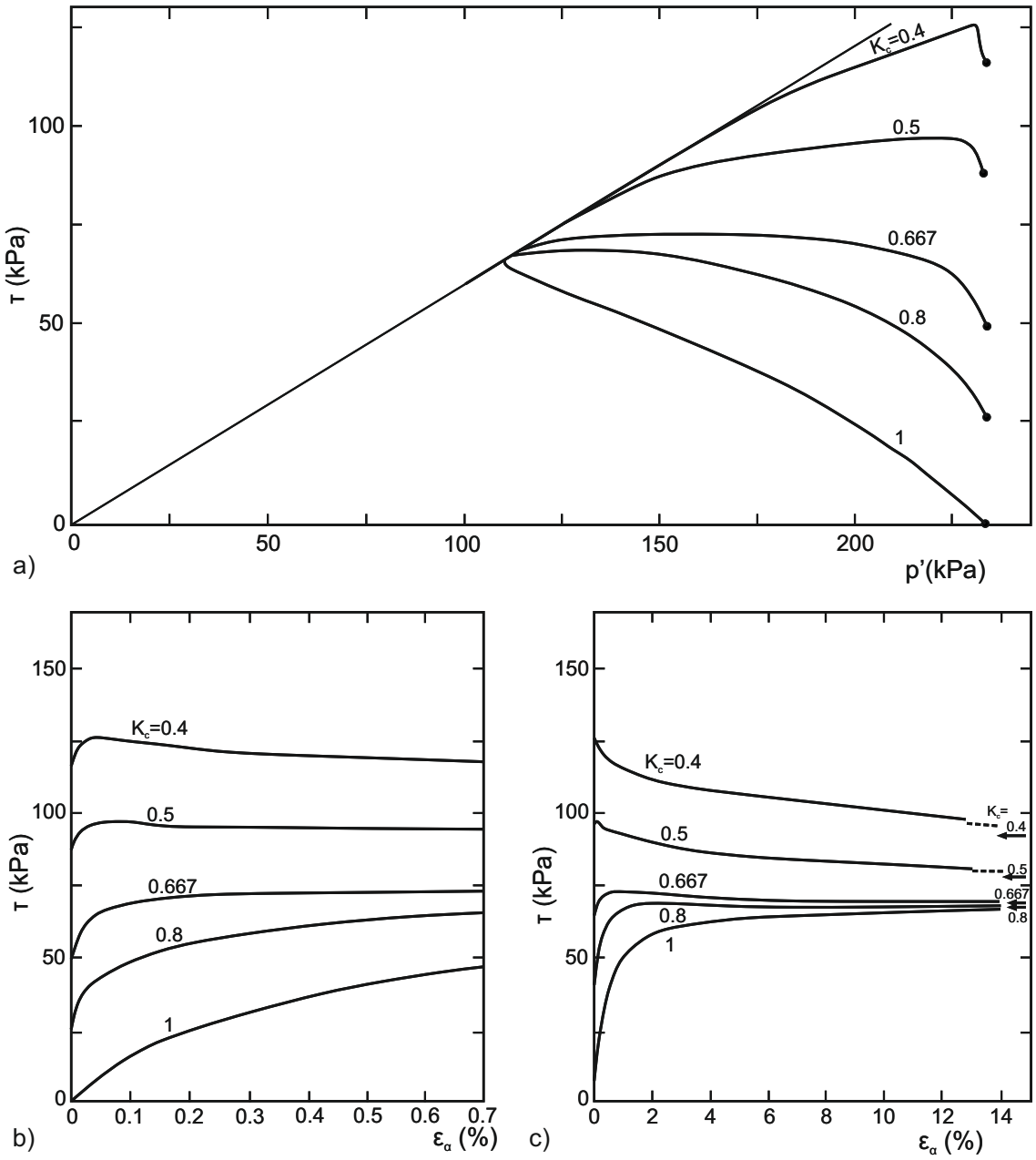


**Figure 3.21:** Undrained triaxial compression on LCT samples initially normally consolidated under various $K$ ratios; a) the $t$ vs $p$ stress paths and; b,c) the corresponding deviatoric stress - axial strain curves (in (v) the small strain regime). (Gens 1982)

curves (figures 3.21b and c). A tendency towards a unique ultimate shear strength, almost independent of the initial degree of anisotropy is observed both in the stress paths but also in the stress-strain curves. It should be noted that as mentioned by the author the tests on $K = 0.4$ and $K = 0.5$ could not reach an ultimate state because

the maximum axial strain imposed was bounded from apparatus limitations.

Figure 3.22 compares; a) the stress ratio $n = q/p$ corresponding to peak and ultimate conditions and; b) the ratio between the shear stress in peak and ultimate conditions ($\tau_p/\tau_u = q_p/q_u$) both plotted with the invert of the imposed consolidation stress ratio $1/K$. The stress ratio $n_u$ representing the ultimate conditions appears independent of the initial anisotropy and also consistent with the stress ratio at critical state defined from the isotropically consolidated samples.

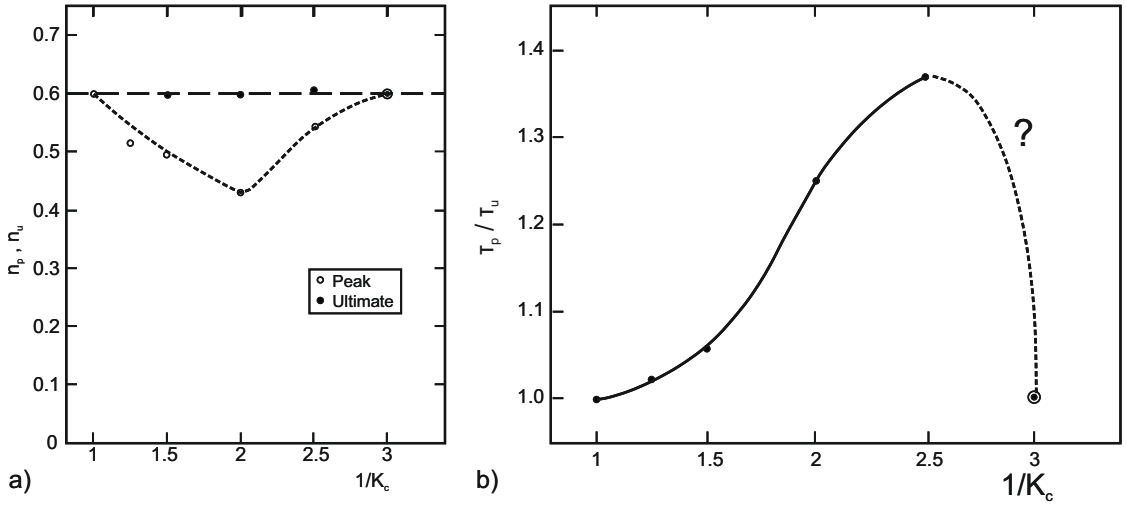


**Figure 3.22:** LCT undrained triaxial compression; variation of: a) the peak and ultimate consolidation ratio and; b) of brittleness with the consolidation stress ratio $K$. (Gens 1982)

On the other hand, the peak stress ratio $n_p$ is systematically less than the corresponding ultimate with a minimum value observed for the $K = 0.5$ sample, the one representing 1D consolidation conditions. The variation on the $\tau_p/\tau_u$ presented in figure 3.22b, reflects the already discussed increased brittleness with a decreased consolidation stress ratio. The author reports that experimental studies of the undrained behaviour of soils consolidated in various $K$ is quite limited. From what was available in the time of his thesis preparation, Donaghe & Townsend (1978) and Lee & Morrison (1970) found similar trends for the variations of peak and ultimate strength with $K$ while to the contrary only in Khera (1967) no significant brittleness was observed.

#### 3.2.2.2 Drained Behaviour

Gens 1982 also reports results from drained triaxial compression tests. In figure 3.23 the results from anisotropically consolidated soil samples with $K = 0.5$ triaxially

compressed under drained conditions initiating from various overconsolidation ratios namely; $R_p = 1.0$, 1.5, 2, 4 and 7 are given. We may observe that there are no indications of appreciable strain softening response as all tests systematically strain harden towards a common peak (coincides with ultimate) strength envelope, once again similar to the ultimate strength envelop defined from undrained compression tests on both isotropically and anisotropically consolidated samples. A very interesting observation is how reminiscent the normalized stress paths of figure 3.23b, are of the undrained stress paths of figure 3.17a.

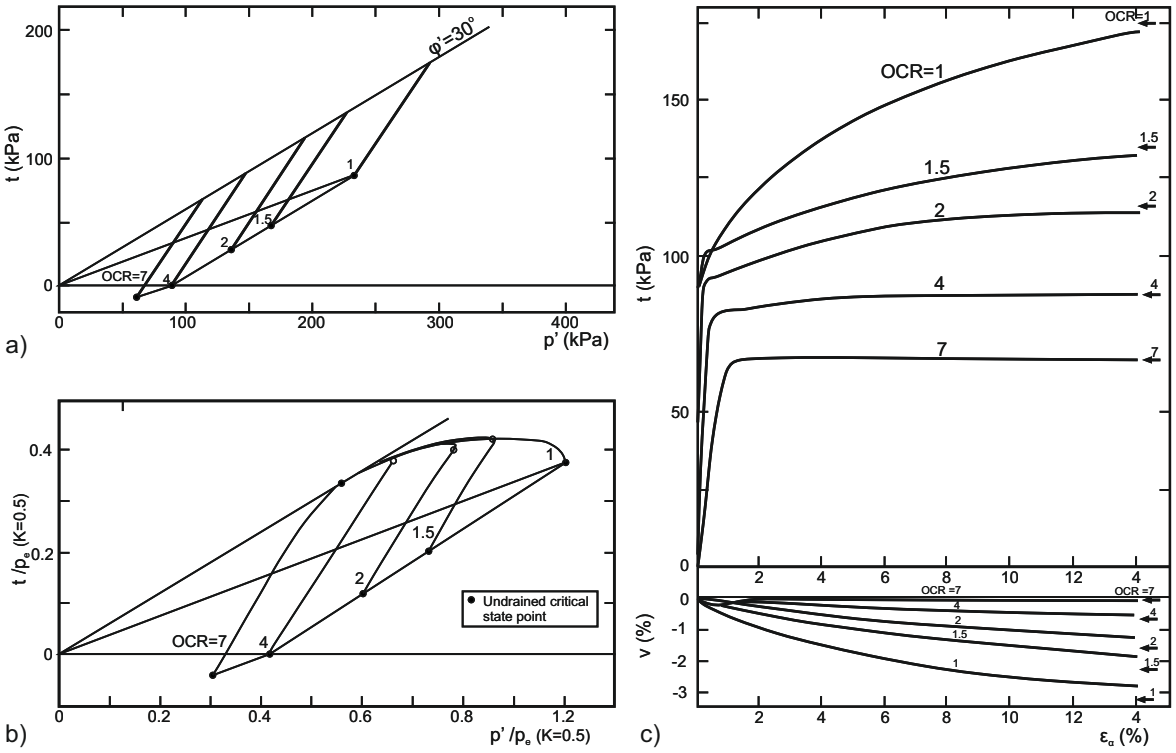


**Figure 3.23:** Drained triaxial compression of anisotropically ($K = 0.5$) consolidated LCT samples under various overconsolidation ratios $OCR$; a) effective stress paths in $t$ vs $p$; b) normalized stress paths and; c) the corresponding deviatoric stress - axial strain and volumetric strain - axial strain curves. (Gens 1982)

To further investigate the effect of anisotropic consolidation in the observed drained behaviour Gens (1982) reports two additional tests of normally consolidated samples with $K = 0.4$ and 0.667, presented in figure 3.24. Once again there is no evidence of strain softening while the normalized stress paths are similar to their undrained counterparts. Regarding the volumetric strains observed during drained compression (see figure 3.24c), it is evident that all samples have a clear tendency to contract

while sheared, apart from the test at $R_p = 7$ which seems to slightly dilate after an initial contraction stage; even in this case the total volumetric strains do not correspond to an overall dilatant behaviour. Overall we may say that anisotropically consolidated soils sheared under drained conditions, exhibit a contractant behaviour with volumetric strains reducing for increasing $R_p$ and increasing initial anisotropy. According to Gens (1982) similar values for the ultimate angle of friction for drained and undrained tests have also been reported by various authors (Amerasinghe 1973; Henkel 1956; Henkel 1959; Parry 1960).

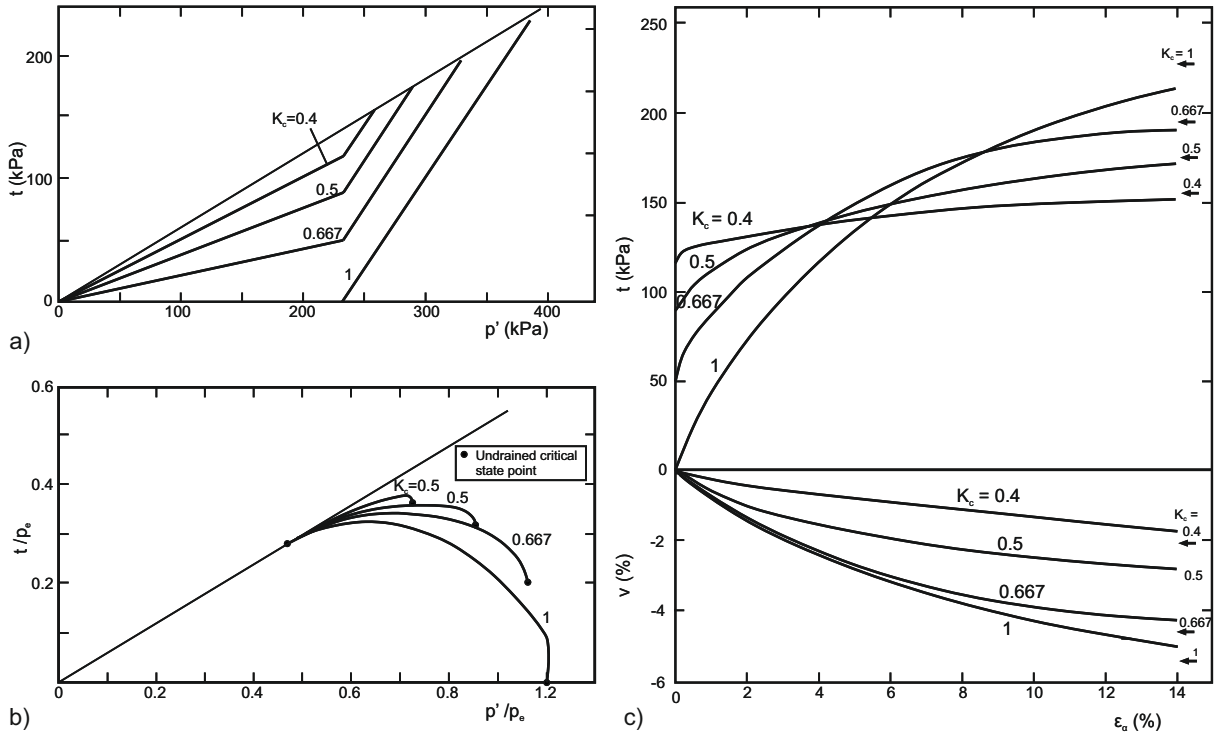


**Figure 3.24:** Drained triaxial compression on LCT samples initially normally consolidated under various $K$ ratios; a) effective stress paths in $t$ vs $p$; b) normalized stress paths and; c) the corresponding deviatoric stress - axial strain and volumetric strain - axial strain curves. (Gens 1982)

### 3.2.2.3 Behaviour in extension

Finally, Gens (1982) also investigated the behaviour of Lower Cromer Till in triaxial extension based mainly on undrained tests of both isotropically and anisotropically consolidated samples, sheared from either normally or overconsolidated initial conditions. For the isotropically consolidated tests the study indicates that the same angle of internal friction derived during undrained compression ($\phi = 30^o$) applies also for

extension. Note that this finding contradicts the predictions of the Modified Cam Clay, according to which the same slope M for the critical state line applies to both compression and extension, leading to a higher value for the friction angle in extension. Thus, according to the LCT results, the slope of the critical state line should be lower in extension and thus dependant on the direction of loading through the third invariant of the stress tensor. This difference is also reflected on the critical state line in the $w/c - \log p$ plane, where different but parallel lines seem representative of the ultimate states in extension and compression (see figure 3.25).

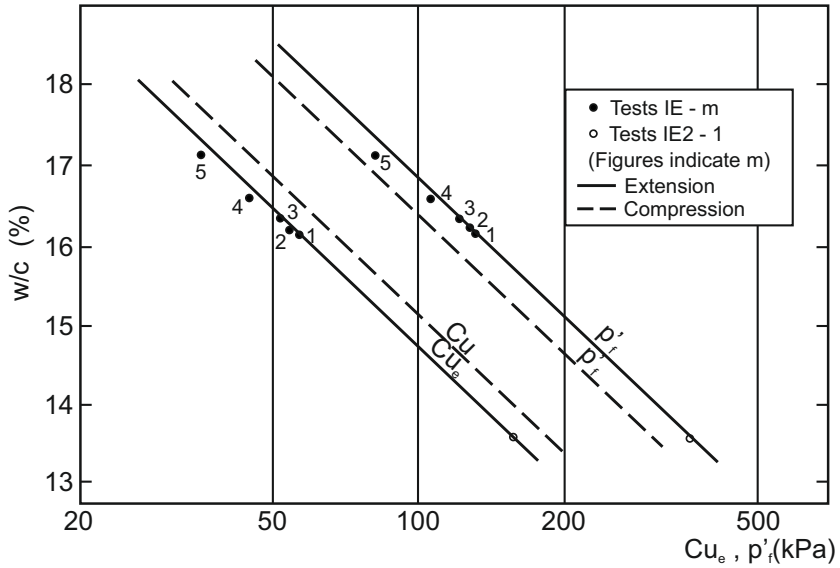


**Figure 3.25:** Peak and ultimate states in the $w/c - logp_f, C_u$ plane, corresponding to undrained triaxial compression and extension tests on isotropically consolidated LCT samples. (Gens 1982)

As far as tests on anisotropically consolidated soils are concerned, in a similar fashion to what was done for compression, the author studied the behaviour in undrained extension for various OCRs using soils samples consolidated with $K = 0.5$ and for normally consolidates soils in various $K$. The results are given in figures 3.26 and 3.27 respectively. The reported results reveal a clear dependency of the stress paths on both the applied anisotropy and overconsolidation. All paths are strain hardening, with no evidence of brittle behaviour. Regarding the ultimate points, we may observe that they plot quite close to a common strength envelope, corresponding to $\phi = 30^o$, which is equal to the extension friction angle of isotropically consolidated soils; This observation supports the assumption of a common critical state for isotropically and anisotropically consolidated soils also under extension.

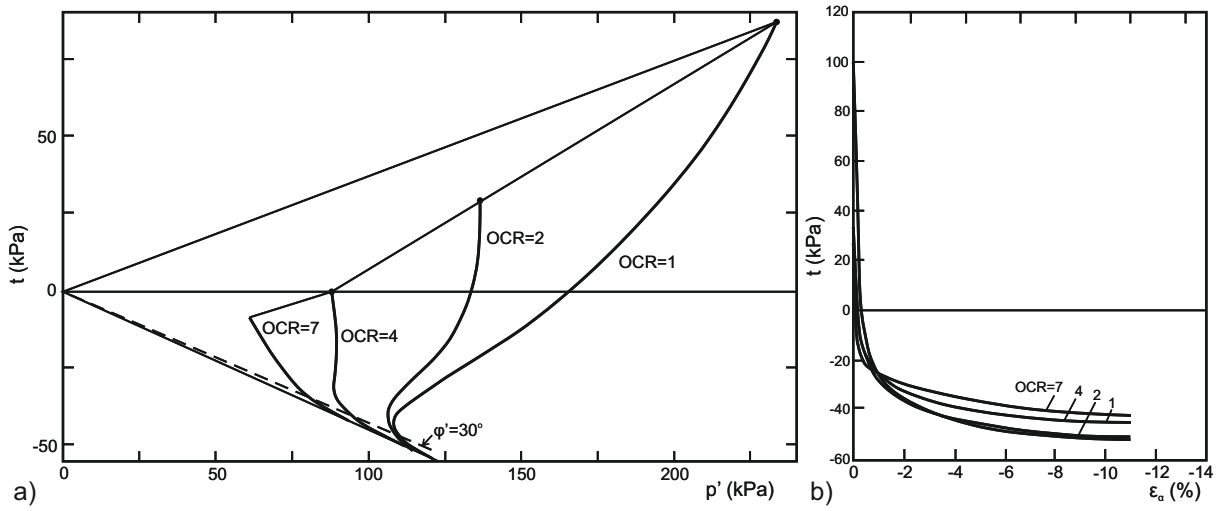


**Figure 3.26:** Undrained triaxial extension on anisotropically ($K = 0.5$) consolidated LCT samples under various overconsolidation ratios $OCR$; a) effective stress paths ($t$ vs $p$) and; b) the corresponding deviatoric stress - axial strain curves. (Gens 1982)

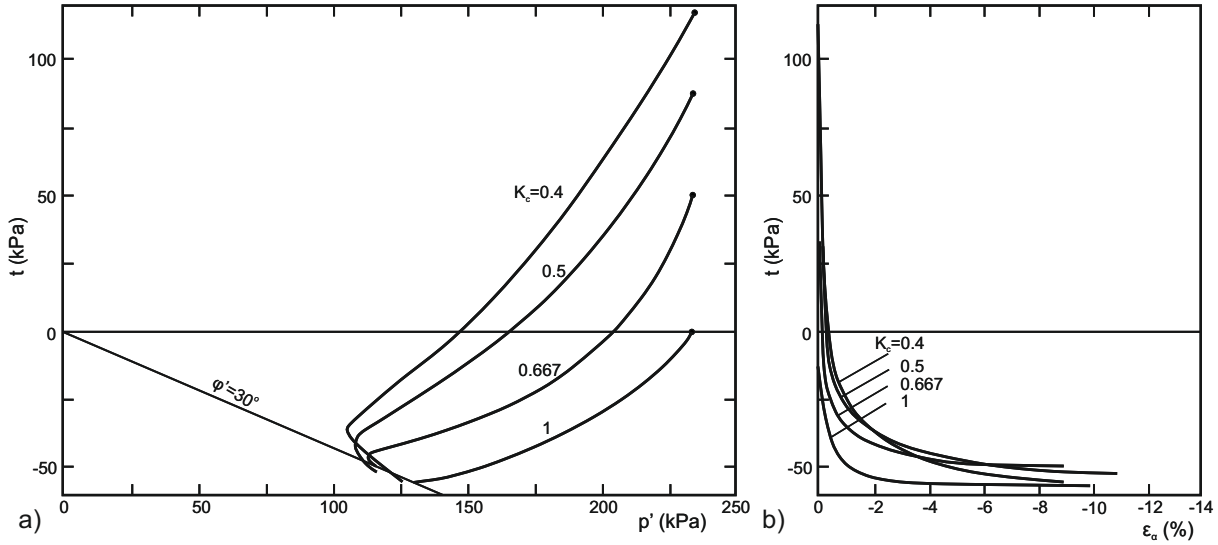


**Figure 3.27:** Undrained triaxial extension on LCT samples initially normally consolidated under various $K$ ratios; a) effective stress paths ($t$ vs $p$) and; b) the corresponding deviatoric stress - axial strain curves. (Gens 1982)

Nevertheless, we shall note that for LCT, a more thorough examination of the results raises a friction angle $\phi = 31.6^o$ in extension for the anisotropically consolidated samples. On discussing the obtained results, Gens (1982) refers to an ensemble of available preexisting experimental studies that have dealt with undrained extension. The author mentions that although the majority of these studies are in accordance

with LCT results still it is far more difficult to conclude in a general pattern of behaviour for extension compared to compression. For instance, regarding the friction angle in extension for isotropically consolidated soils there exist results in favor of a common friction angle for extension and compression (Henkel 1959; Parry 1960; Parry & Nadarajah 1974; Wu et al. 1963; Shibata & Karube 1965), while others indicate a higher friction angle in extension compared to compression (Mitachi & Kitago 1979; Broms & Casbarian 1965; Leon & Alberro 1972).

Regarding the relationship between the friction angle in extension of isotropically and anisotropically consolidated soils there are studies where significant differences in the order of $4^o$ to $7^o$ are reported (Ladd & Varallyay 1965; Parry & Nadarajah 1974; Vaid & Campanella 1974), others with smaller differences similar to those observed for LCT (Mitachi & Kitago 1979; Koutsoftas 1981), while Andersen et al. (1980) observed the same failure envelope. It should be noted that in general the results obtained from extension tests must be handled with caution as are always subjected to a greater level of uncertainty due to geometrical bifurcations occurring during extension like necking of the specimen. This can probably be one of the reasons explaining why different and quite often contradicting results exist in the literature.

#### 3.2.2.4 Yield Locus - State Boundary Surface

Gens (1982) used the obtained results from the LCT laboratory investigation to decide on whether a State Boundary Surface (SBS) similar to the one already defined for isotropically consolidated soils apply also for anisotropically consolidated soils. He claims that although there are many evidence of common behaviour between isotropically and anisotropically consolidated soil samples (i.e., common and well defined critical state, parallel virgin consolidation lines for different consolidation stress ratios) the shape of the undrained stress paths changes with $K$ and are not part of a single curve as predicted from Critical State Soil Mechanics and the Modified Cam Clay constitutive model. Gens (1982) plotted normalized stress paths for drained and undrained triaxial tests of isotropically consolidated samples together with the points corresponding to virgin $K$-consolidated soils. It is evident from figure 3.28 that the obtained curves do not coincide.

To describe the LCT behaviour in a unified way, the author postulated a new framework presented in figure 3.29. The SBS on the wet side is defined as the locus of the points corresponding to virgin constant $K$ consolidated samples. On the dry

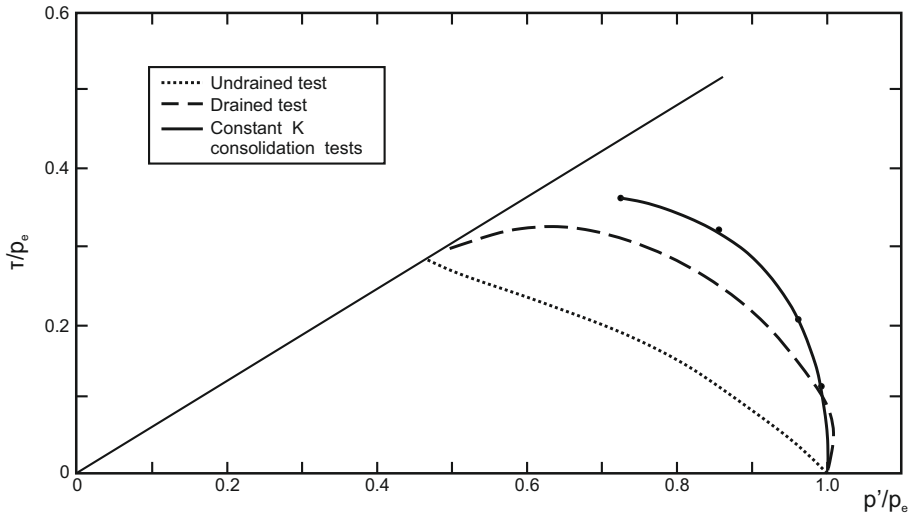


**Figure 3.28:** Locus of constant $K$ consolidation test normalized stress paths points, together with the normalized stress paths for a drained and an undrained test on isotropically normally consolidated LCT samples. (Gens 1982)

side the assumed SBS is a usual Hvorslev surface defined from the behaviour of over-consolidated samples, while a tension cut off is also assumed as there are no evidence of tension strength in LCT. Within the assumed SBS, the author defined a quasi-elastic zone similar to the one of the CSSM framework bounded to the right from the normalized undrained stress paths of isotropically consolidated samples. In-between the aforementioned bounding surface and the state boundary surface, a plastic zone is defined, within which undrained stress paths of anisotropically consolidated samples are supposed to plot.

The latter is better understood if the assumed SBS is plotted together with all the normalized undrained stress paths corresponding to different stress ratios, as proposed in Jardine et al. (2004) (see figure 3.30). From that perspective the proposed SBS is seen as the common envelope of the undrained stress paths obtained from anisotropically consolidated samples (Belokas 2008).

Although Gens (1982) work is the most comprehensive and complete investigation of the behaviour of anisotropically consolidated soils available, other worth mentioning studies also exist. Atkinson et al. (1987) carried out tests on reconstituted and $K_0$ consolidated Speshwhite Kaolin clay (see figure 3.31). They found that the strength and the stress-strain behaviour were significantly affected by the consolidation stress history. By comparing their results with available results from isotropically reconstituted Kaolin clay samples, they claim that the virgin compression lines are parallel in

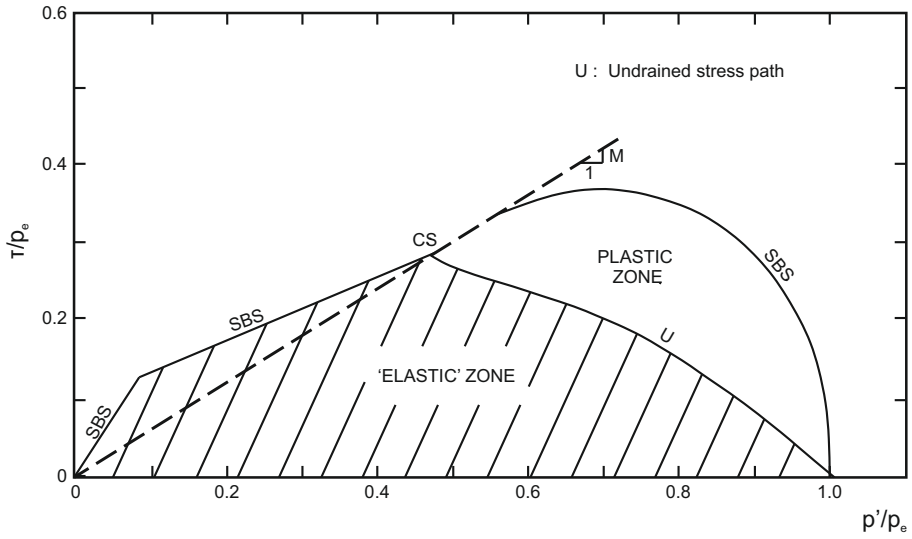


**Figure 3.29:** The Gens (1982) assumed SBS and zones of elastic and plastic behaviour.

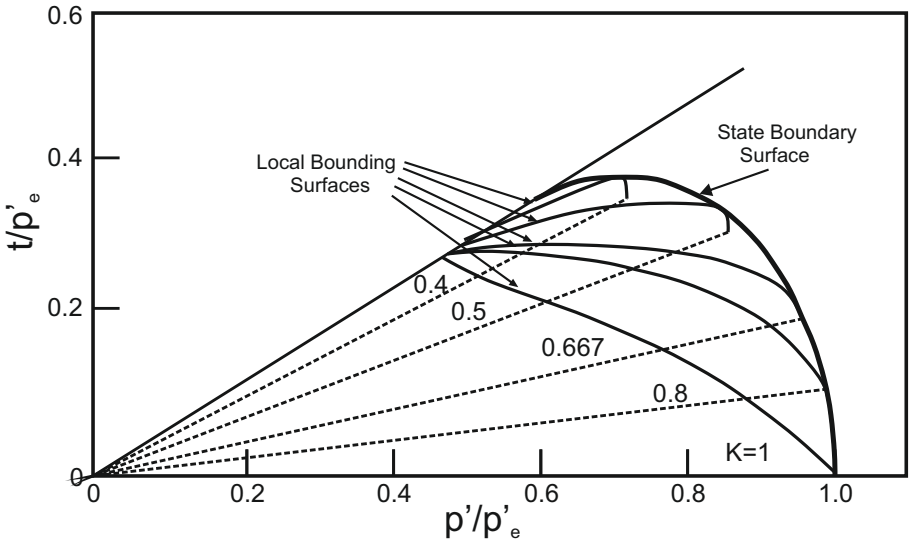


**Figure 3.30:** Normalized stress paths of triaxial compression tests on anisotropically consolidated LCT samples, plotted together with the (Gens 1982) SBS. (Jardine et al. 2004)

the $v-\ln p$ plane and the $K_0$ line plots to the left of the corresponding isotropic. They also found a common critical state line on the $v-\ln p$ independent of the consolidation history and the direction of loading (compression vs extension). Regarding the slope of the CSL in the $p-q$ space they report a common slope for both compression and extension when anisotropically consolidated samples are of concern, contrary to the isotropically consolidated samples where different slopes seem applicable. They also proposed a State Boundary Surface to describe the behaviour of the $K_0$ consolidated

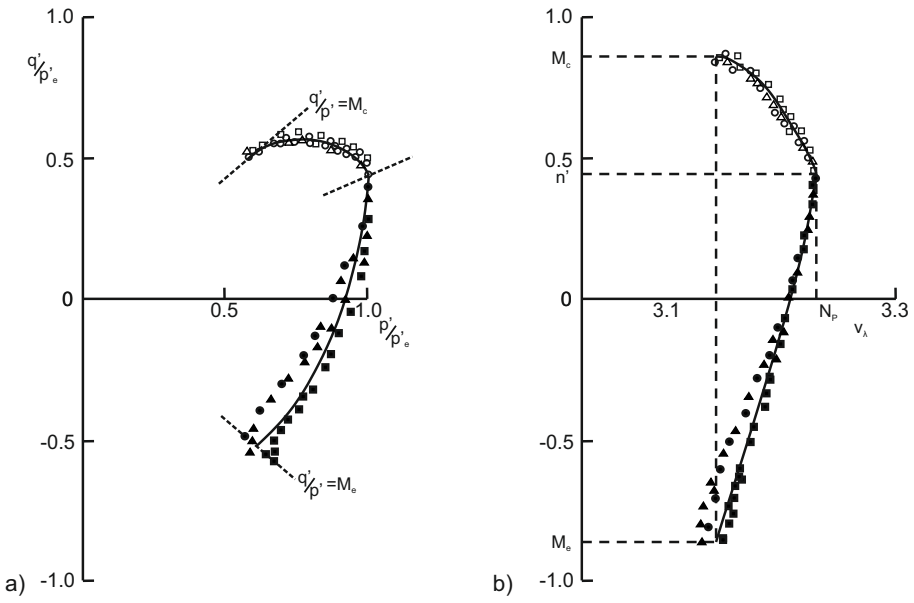


**Figure 3.31:** a) Normalized stress paths of undrained triaxial stress paths on anisotropically consolidated Speswhite Kaolin samples and; b) the corresponding normalized "volumetric" response. (Atkinson et al. 1987)

samples.

In doing so, they started from the MCC yield surface (coincides with the SBS) and reoriented it towards the stress path of the consolidation, resulting to an inclined state boundary surface also playing the role of the yield surface. Such an approach implies that the SBS assumed for anisotropically consolidated soils does not need to account for multiple degrees of anisotropy, like the one proposed by Gens (1982), but can be consolidation stress path dependant, not symmetrical about the isotropic axis.

Adoption of such an inclined Yield Surface for anisotropically consolidated soils is supported by quite many laboratory results on anisotropically consolidated samples of both reconstituted and natural soils, and as will be discussed in the next section this is an approach that has been widely utilized in the formulation of anisotropic constitutive models.

Figure 3.32 shows characteristic effective undrained stress paths followed by samples of normally consolidated $K_0$, isotropic and passively consolidated samples of natural Bothkennar Clay together with the yielding characteristics of the same material (Hight et al. 1992; Smith et al. 1992). In figure 3.32a we may notice how reminiscent the undrained stress paths are of the reconstituted LCT stress paths under similar stress conditions, indicating that there are common behavioural aspects between reconstituted and natural soils. Figure 3.32b is also in favour of an inclined yield surface

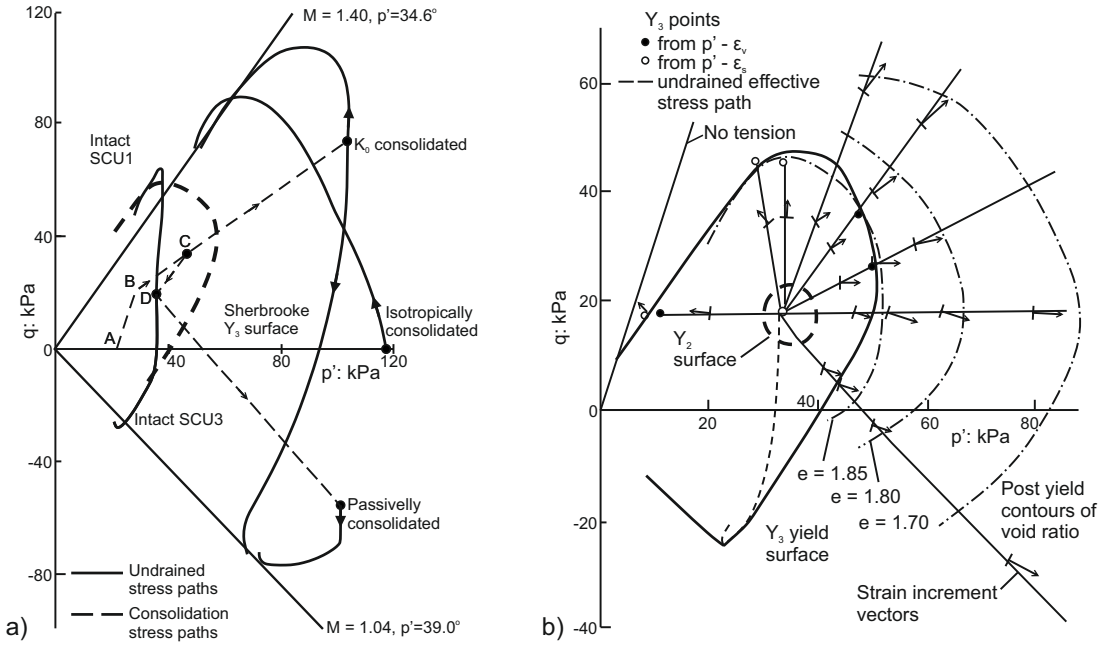


**Figure 3.32:** a) Undrained triaxial compression and extension tests on normally consolidated natural samples of Bothkennar clay and; b) a characteristic yield locus. (Smith et al. 1992)

for the anisotropically consolidated samples. Similar results can be found in Graham & Houlsby (1983), Leroueil & Vaughan (1990), Diaz-Rodriguez et al. (1992), Callisto & Calabresi (1998), Sivakumar et al. (2001) and Gao (2013). Finally, figure 3.33a and b, presents characteristic plots of inclined yield loci corresponding to the Pisa Clay (Callisto & Calabresi 1998) and to the Shanghai Clay (Gao 2013) respectively.

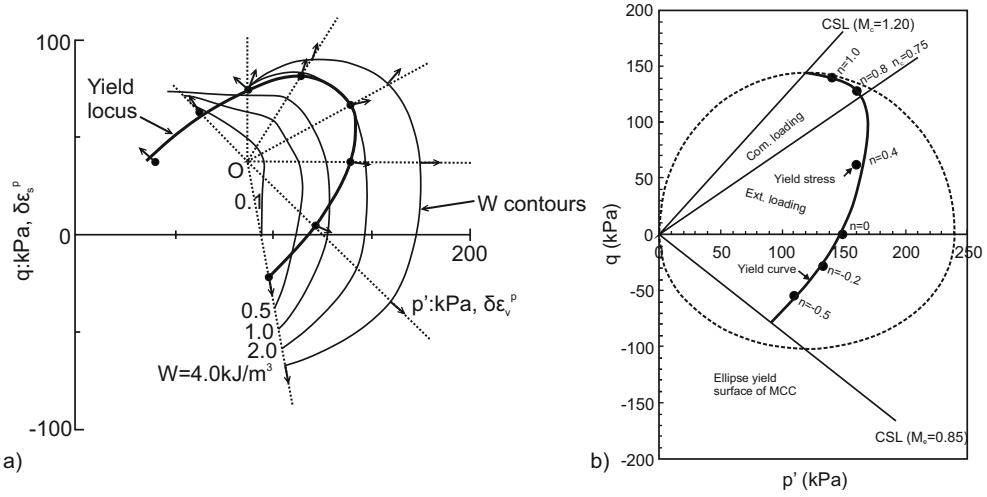


**Figure 3.33:** Characteristic Yield loci for the: a) Pisa clay (Callisto & Calabresi 1998) and; b) Shanghai clay (Gao 2013).

## 3.3 Constitutive Modelling of Soil Anisotropy

This section, describes and discusses the most popular constitutive models for anisotropic soils existing in the relevant literature. Their common characteristics is an included (or/and in some cases translated) yield surface, incorporating an additional deviatoric tensor to introduce preferred directions, different than the principal stress directions. In the following lines, we focus on the work of Kavvadas and his co-workers (i.e, Kavvadas (1982), Kavvadas & Amorosi (2000)), of Dafalias and his co-workers (i.e., Dafalias (1986), Dafalias et al. (2006)), of Newson & Davies (1996) and Wheeler et al. (2003)..

### 3.3.1 The Kavvadas (1982) model and enhancements

Kavvadas (1982) proposed a new constitutive model (MIT-E1) to overcome the main limitations of the Modified Cam - Clay, namely (according to the author): a) the model's incapability to predict strain softening for normally consolidated and lightly overconsolidated clays ($R_p < 2$); b) the model's tendency to over predict the value of the coefficient of earth pressure at rest $K_0$ and; c) it's restricted ability to describe the anisotropic stress - strain behaviour of most natural clays coming from its yield surface dependency exclusively on the first and second invariants of the effective stress tensor.

The MIT-E1 model is based on the following working hypothesis: "Soil elements consolidated along a radial stress path can be described by a model with a yield surface oriented (in the effective stress space) along the (radial) stress path of the consolidation". The proposed yield surface by Kavvadas (1982) is a distorted ellipsoid in the $(\sigma, \boldsymbol{s})$ space with its main axis along the direction of the imposed radial stress path in accordance with the ideas proposed by Tavenas & Leroueil (1977), Ko & Sture (1980) and Wood (1980).

The yield function proposed in Kavvadas (1982) to describe the assumed distorted ellipsoid is:

$$f(\sigma, \boldsymbol{s}, \alpha, \boldsymbol{b}) = \frac{1}{c^2}(\boldsymbol{s} - \sigma\boldsymbol{b}) : (\boldsymbol{s} - \sigma\boldsymbol{b}) - \sigma(2\alpha - \sigma) = 0 \tag{3.5}$$

where $\sigma$ is the mean effective stress, $\boldsymbol{s}$ is the deviatoric stress tensor, $\alpha$ is the isotropic hardening variable controlling the size of the yield surface, $\boldsymbol{b}$ is the kinematic hardening variables tensor controlling the orientation of the yield surface in all deviatoric

planes, and finally $c$ a material constant defining the ratio of the axes of the yield surface (see also eq. 2.55). Figure 3.34 presents the adopted yield surface. To describe

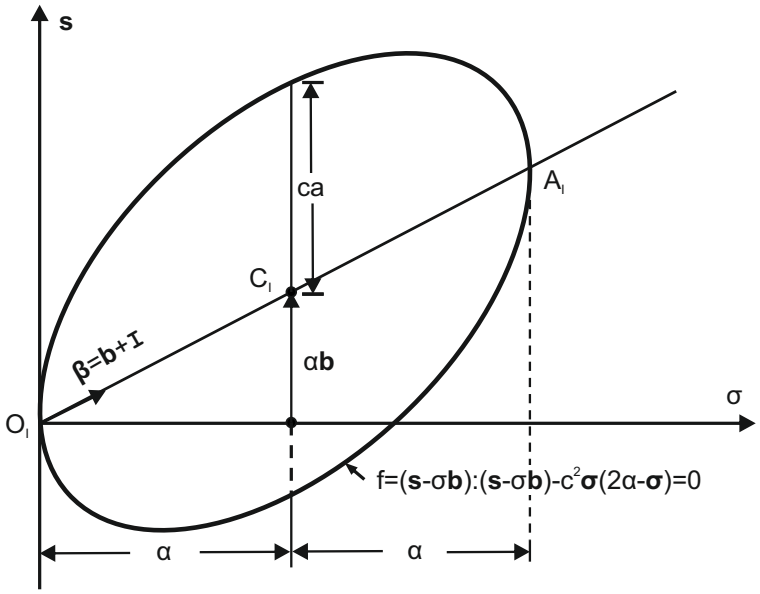


**Figure 3.34:** The yield surface of the MIT-E1 constitutive model. (Kavvadas 1982)

the evolution of anisotropy the author proposed a kinematic hardening rule (eq. 3.6) where the magnitude of anisotropy changes proportionally to the plastic volumetric strain increment ($\dot{\varepsilon_p}$), while the direction of the change in anisotropy is assumed parallel to the direction of the $(\boldsymbol{s} - \sigma\boldsymbol{b})$ vector. The mathematical form of the assumed hardening rule is:

$$\dot{\boldsymbol{b}} = \frac{1}{a}\psi(\boldsymbol{s} - \sigma\boldsymbol{b})\dot{\varepsilon}^p \tag{3.6}$$

where $\psi$ a scalar parameter controlling the rate of evolution. It is evident that with the proposed kinematic rule anisotropy evolves always when a stress path different than radial is imposed, causing the yield surface to distort. Distortion is freezed when the yield surface gets orientated towards the direction of the imposed radial stress path.

To describe the evolution of the size of the yield surface the isotropic hardening rule of the MCC (see eq. 2.63) is utilized. In an attempt to reproduce realistic $K_0$ values the author utilized a non-associated flow rule by directly postulating the mathematical form of the plastic potential tensor. Strain softening is reproduced through a failure criterion which can distinguish between peak and critical states. It is realized through two nested cones, one for the peak strength and the other for the critical state condition; the peak and critical state friction angles where used as

an input (see figure 3.35). Undertaking quite complicated geometrical calculations, regions of strain softening and stain hardening behaviour can be distinguished based on the relative position of the current stress state with respect to the position of the aforementioned conical strength envelopes. Kavvadas (1982) calibrated and validated MIT-E1 predictions using experimental results of reconstituted Boston Blue Clay (see figure 3.36).

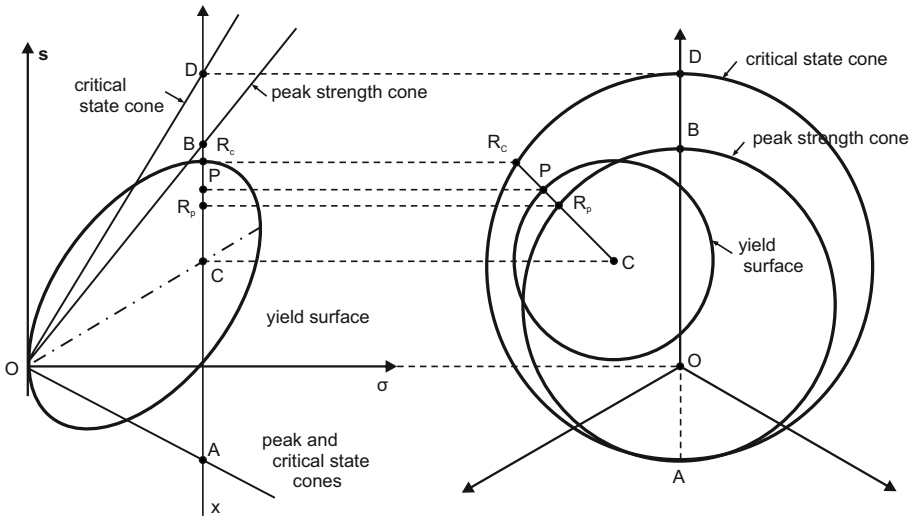


**Figure 3.35:** Geometrical representation of the yield surface and of the failure cones incorporated in the MIT-E1 constitutive model. (Kavvadas 1982)

Whittle & Kavvadas (1994) presented a model (MIT-E3) that was developed to study the performance of offshore piles supporting tension leg platforms (Whittle 1987). The critical aspect of the foundation performance of offshore platform piles is the response of the foundation soil in cyclic loading. In that respect, the authors extended MIT-E1 model by incorporating equations to account for small strain non-linearity. The porous elasticity equations (see section 2.3.2.3) are enhanced using a dimensionless distance parameter that reflects the distance between the current stress state and the load reversal point and thus the bulk modulus is not any more dependant only on the current stress level and void ratio (classical porous elasticity), but also on the distance of the current stress point from the load reversal point. The authors worked with some really highly overconsolidated soils ($OCR > 8$) and in order to improve the MIT-E1 model's predictions in the dry side, they incorporated the principles of bounding surface plasticity (see figure 3.37). In their model, the yield function proposed by Kavvadas (see eq. 3.5) is not only used as a yield surface but it also plays the role of a bounding surface. Using a proper mapping rule, the authors

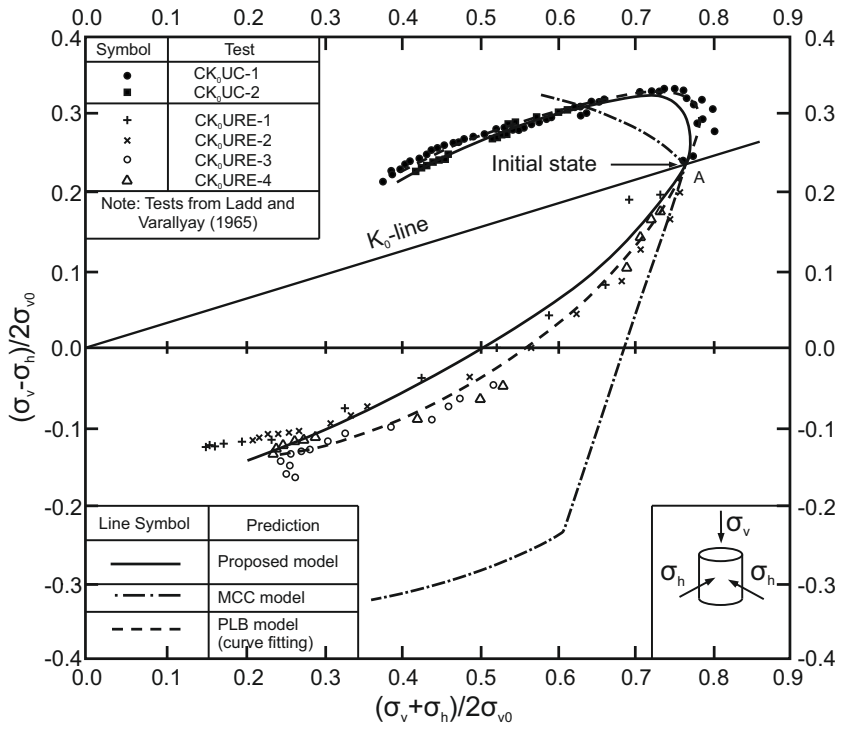


**Figure 3.36:** MIT-E1 constitutive model's simulations of undrained triaxial compression and extension tests on $K_0$ normally consolidated reconstituted Boston Blue Clay samples. (Kavvadas 1982)

reproduced plastic (irrecoverable) strains even for stress states inside the yield surface that correspond to overconsolidated soil states. They also slightly modified the kinematic hardening rule of MIT-E1 by adding a scalar variable ($r_x$) which accounts for the relative orientation of the yield surface with respect to the critical state cone. The enhanced hardening rule takes the following form:

$$\dot{\boldsymbol{b}} = \frac{1}{a}\psi\langle r_x\rangle(\boldsymbol{s} - \sigma\boldsymbol{b})\dot{\varepsilon}^p \tag{3.7}$$

Equation 3.7 imposes limits on the principal directions of anisotropy and also reproduces an anisotropy evolution rate dependant on the imposed stress path and on the initial anisotropic state.

The MIT-E3 model was further enhanced by Pestana & Whittle (1999) introducing the MIT-S1 with an eye towards the mechanical behaviour of freshly deposited and over-consolidated soils. Pestana's model follows the main principles of the MIT-E3 model, additionally incorporating significant changes in the form of the bounding surface and of the hardening laws. A new framework for the compression behaviour

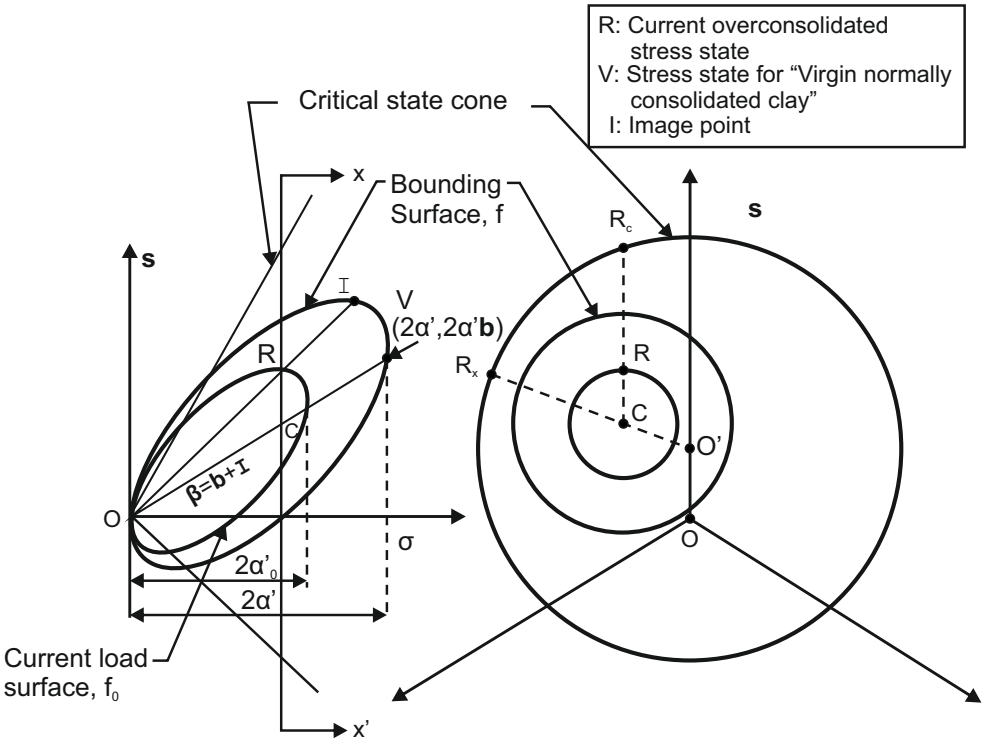


**Figure 3.37:** The yield, failure and sub-loading surfaces incorporated in the MIT-E3 constitutive model. (Whittle & Kavvadas 1994)

was also incorporated and used in an attempt to unify the modelling of clays and sands.

### 3.3.2 The Kavvadas & Amorosi (2000) model

Kavvadas & Amorosi (2000) introduced and evaluated a bounding surface plasticity constitutive model for structured soils (MSS) which combines: a) small strain response characteristics; b) stress history material memory and; c) structure degradation mechanisms. MSS has two characteristic surfaces: a) an internal Plastic Yield Envelope (PYE) that plays the role of the classical yield surface and an external Bond Strength Envelope (BSE) corresponding to material states associated with appreciable rates of structure degradation. The aforementioned envelopes are portrayed in figure 3.38 and the corresponding functions are given in equations 3.8 and 3.9 respectively. The behaviour is plastic for material states on the PYE while either

poroelasticity or hyperelasticity[4] can be used for stress paths inside the PYE.

$$\text{BSE: } F(\boldsymbol{\sigma}, \boldsymbol{\sigma}_K, \alpha) = \frac{1}{c^2}(\boldsymbol{s} - \boldsymbol{s}_K) : (\boldsymbol{s} - \boldsymbol{s}_K) + (\sigma - \sigma_K)^2 - \alpha^2 = 0 \tag{3.8}$$

$$\text{PYE: } f(\boldsymbol{\sigma}, \boldsymbol{\sigma}_L, \alpha) = \frac{1}{c^2}(\boldsymbol{s} - \boldsymbol{s}_L) : (\boldsymbol{s} - \boldsymbol{s}_L) + (\sigma - \sigma_L)^2 - (\xi\alpha)^2 = 0 \tag{3.9}$$

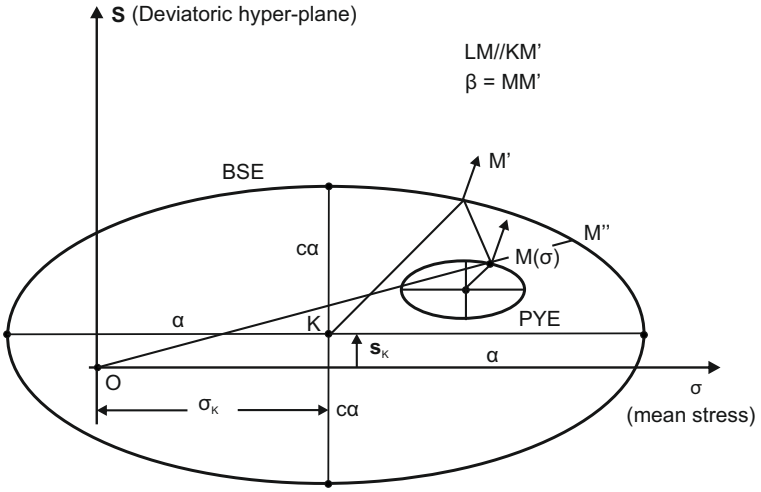


**Figure 3.38:** Characteristic surfaces of the MSS constitutive model. (Kavvadas & Amorosi 2000)

Regarding anisotropic behaviour, the authors used an isotropic ellipse identical to MCC but with its center translating in the stress space. Such a selection was rather forced by the complicated mathematical formulations of bounding surface plasticity combined with a distorted ellipse, rather than the preferable choice. Evolution of anisotropy is described through a kinematic hardening rule which translates the characteristic surfaces in the stress space, controlling the position of their centers. MSS model can describe two types of anisotropy, namely: a) primary anisotropy which is related to the offset of the center of the BSE from the isotropic axis, and; b) secondary anisotropy which is related to the position of the PYE.

Primary anisotropy represents the bond-strength anisotropy; it changes only during plastic loading from material states on the BSE. Primary anisotropy does not change during loading inside the BSE (the center of the BSE moves along a radial stress path) and also does not change even for loading on the BSE along stabilized

[4]Hyperelasticity is a conservative elasticity and thus more appropriate when cyclic loading is of concern.

radial stress paths. Equations 3.10 a and b describe the movement of the center ($\boldsymbol{\sigma}_K$) of the BSE for material states:

$$\text{on the BSE:} \quad \dot{\boldsymbol{\sigma}}_K = \frac{\dot{\alpha}}{\alpha}\boldsymbol{\sigma}_K + \psi\frac{\dot{\alpha}}{\alpha}\left(\boldsymbol{s} - \chi\frac{\sigma}{\sigma_K}\boldsymbol{s}_K\right) \tag{3.10a}$$

$$\text{inside the BSE:} \quad \dot{\boldsymbol{\sigma}}_K = \frac{\dot{\alpha}}{\alpha}\boldsymbol{\sigma}_K \tag{3.10b}$$

where $\chi$, $\psi$ model parameters and $\dot{a}$ the change of the size of the BSE described by the isotropic part of the hardening rule that is given below (see equation 3.13).

Secondary anisotropy associated with the position of the plastic yield envelope, is controlled by the requirement that PYE should move towards the BSE and attach at conjugate points for states inside the BSE, while a homothetic transformation rule ensures that PYE and BSE move together and remain attached at their conjugate points for loading states on the BSE. Thus for the movement of the PYE we have:

$$\text{on the BSE:} \quad \boldsymbol{\sigma}_L = (1-\xi)\boldsymbol{\sigma} + \xi\boldsymbol{\sigma}_K \tag{3.11a}$$

$$\text{inside the BSE:} \quad \dot{\boldsymbol{\sigma}}_L = \frac{\dot{\alpha}}{\alpha}\boldsymbol{\sigma}_L + \dot{\mu}\boldsymbol{\beta} \tag{3.11b}$$

where $\boldsymbol{\beta}$ defines the direction of the movement of the PYE towards its conjugate point on the BSE and $\dot{\mu}$ is derived from the consistency condition at the conjugate point; they are calculated through expressions:

$$\boldsymbol{\beta} = \frac{1}{\xi}(\boldsymbol{\sigma} - \boldsymbol{\sigma}_L) - (\boldsymbol{\sigma} - \boldsymbol{\sigma}_K) \tag{3.12a}$$

$$\dot{\mu} = \frac{(1/c^2)(\boldsymbol{s} - \boldsymbol{s}_L) : (\dot{\boldsymbol{s}} - (\dot{\alpha}/\alpha)\boldsymbol{s}) + (\sigma - \sigma_L)(\dot{\sigma} - (\dot{\alpha}/\alpha)\sigma)}{\xi\alpha^2 - [(1/c^2)(\boldsymbol{s} - \boldsymbol{s}_L) : (\boldsymbol{s} - \boldsymbol{s}_K) + (\sigma - \sigma_L)(\sigma - \sigma_K)]} \tag{3.12b}$$

MSS model also incorporates an isotropic hardening rule which describes the evolution of the size of the BSE, reflecting the evolution of material structure. The adopted rule includes a volumetric part, identical to the one proposed in MCC, which describes the intrinsic material (structureless) properties. It also includes two structure degradation components, one volumetric and one deviatoric, to account for structure degradation (bond damage mechanism). An exponential formula is adopted, analogous to that proposed by Wilde (1977), Kavvadas (1995), Wood (1995) and Lagioia & Nova (1995). The deviatoric component includes a non-zero parameter ($\theta_q$), uncoupled from the exponential term, to describe permanent structure degradation.

Equation 3.13 comprises the isotropic part of the hardening rule:

$$\dot{\alpha} = \alpha \left[ \left\{ \left( \frac{1+e}{\lambda - \kappa} \right) - \zeta_v exp(-n_v, \varepsilon_v^p) \right\} \dot{\varepsilon_v^p} + \left\{ \theta_q - \zeta_q exp(-n_q, \varepsilon_q^p) \right\} \dot{\varepsilon_q^p} \right] \tag{3.13}$$

where $\zeta_v$, $n_v$ are the volumetric destructuring parameters and $\theta_q$, $\zeta_q$ and $n_q$ the deviatoric destructuring parameters.

MSS model adopts an associated flow rule. The plastic modulus is derived from the consistency condition on the BSE, while for material states inside the BSE plastic modulus evolves following a suitable interpolation rule to ensure a continuous variation of its magnitude as PYE approaches the BSE. Kavvadas & Amorosi (2000) compared their model's prediction with the response of Vallerica Clay under undrained triaxial tests of $K_0$-consolidated samples. A characteristic comparison is given in figure 3.39.

### 3.3.3 The Belokas & Kavvadas (2010) model

Belokas & Kavvadas (2010) presented a new anisotropic model for structured soil (MSS-2). It is a twin-surface elastoplastic model that follows the principles introduced in MSS. Similar to MSS it employs a Plastic Yield Envelope (PYE) which holds as the yield surface and a Structure Strength Envelope (SSE) to describe the interparticle resistance due to structure. Hyperelasticity instead of porous elasticity is used for the behaviour inside the PYE. The main enhancements introduced in MSS-2 with respect to the MSS can be summarized as follows: a) distorted elliptical SSE and PYE surfaces; b) intrinsic strength envelope representing the reference structureless locus based on an Intrinsic Compressibility Framework (ICF); c) an improved structure degradation mechanism and finally; d) a non-associated flow rule.

The yield and structure envelope functions used by the authors are those initially proposed by Kavvadas & Belokas (2001). In fact the SSE incorporated is a combination of the distorted ellipsoid introduced by Kavvadas (1982) and of the translated MCC ellipse of Kavvadas & Amorosi (2000). This combination leads to a rotated distorted ellipsoid with its center mathematically described as $\boldsymbol{\sigma}_K = \sigma_K \boldsymbol{I} + \boldsymbol{s}_K$, allowing the SSE to move even to the left of the deviatoric axis to account for some tensile strength. The PYE has a shape similar to the SSE. Its axis follows the orientation of the SSE, while its size is defined relatively to the size of the SSE through a scaling down proportionality factor $\xi$. Figure 3.40 presents the characteristic surfaces of the

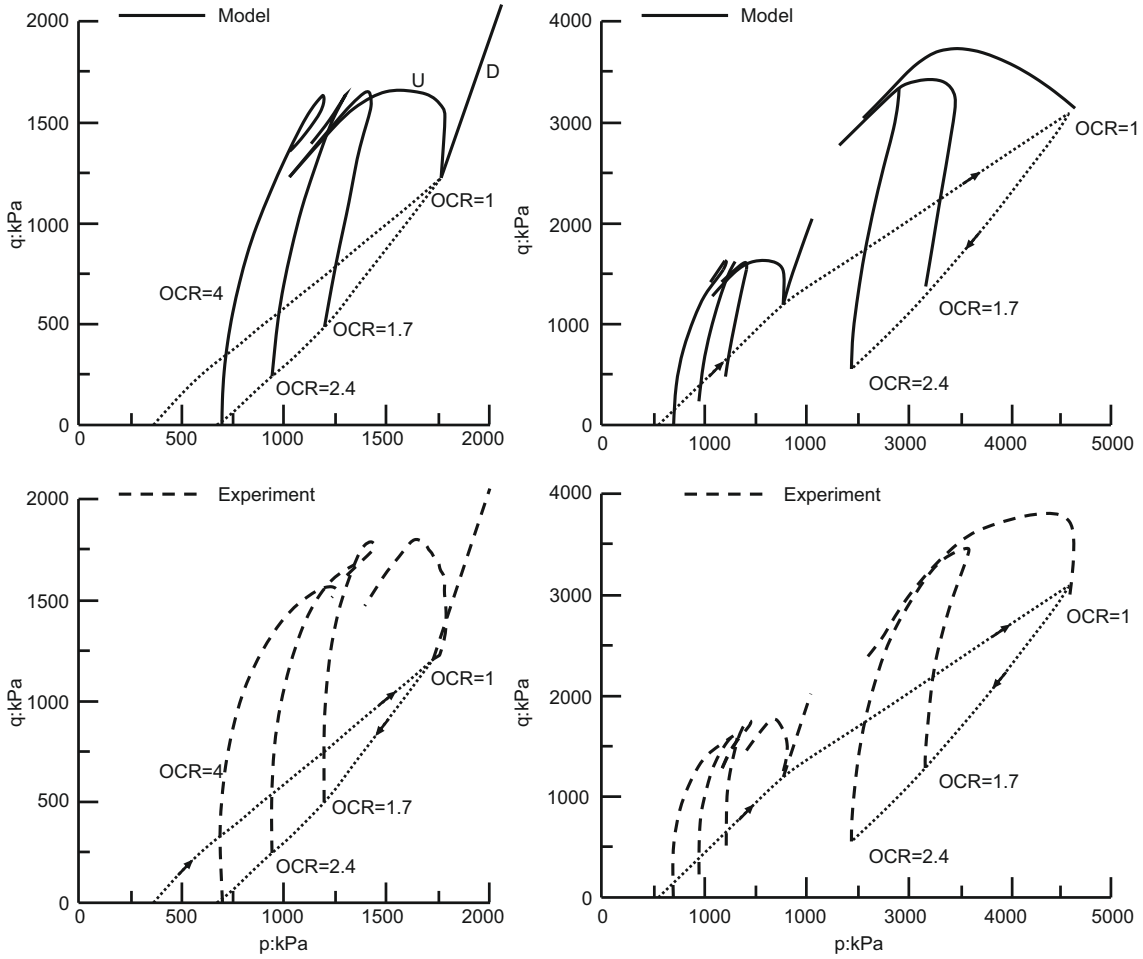


**Figure 3.39:** Comparison of MSS model's predictions with experimental results of anisotropically consolidated Vallericca clay samples undergoing undrained triaxial compression. (Kavvadas & Amorosi 2000)

MSS-2 model. They are mathematical described through:

$$\text{SSE: } F(\boldsymbol{\sigma}, \boldsymbol{\sigma}_K, \alpha) = \frac{1}{c^2}(\boldsymbol{s} - \frac{\sigma}{\sigma_K}\boldsymbol{s}_K) : (\boldsymbol{s} - \frac{\sigma}{\sigma_K}\boldsymbol{s}_K) + (\sigma - \sigma_K)^2 - \alpha^2 = 0 \qquad (3.14)$$

$$\text{PYE: } f(\boldsymbol{\sigma}, \boldsymbol{\sigma}_L, \alpha) = \frac{1}{c^2}(\boldsymbol{s} - \frac{\sigma - \sigma_L}{\sigma_K}\boldsymbol{\sigma}_K - \boldsymbol{s}_L) : (\boldsymbol{s} - \frac{\sigma - \sigma_L}{\sigma_K}\boldsymbol{\sigma}_K - \boldsymbol{s}_L) + (\sigma - \sigma_L)^2 - (\xi\alpha)^2 = 0 \qquad (3.15)$$

Regarding, the Intrinsic Strength Envelope (ISE), it plays the role of a threshold, representing the lower bound of the SSE. It defines the envelope of structureless material states, where an initially structured material state should finally lie on af-

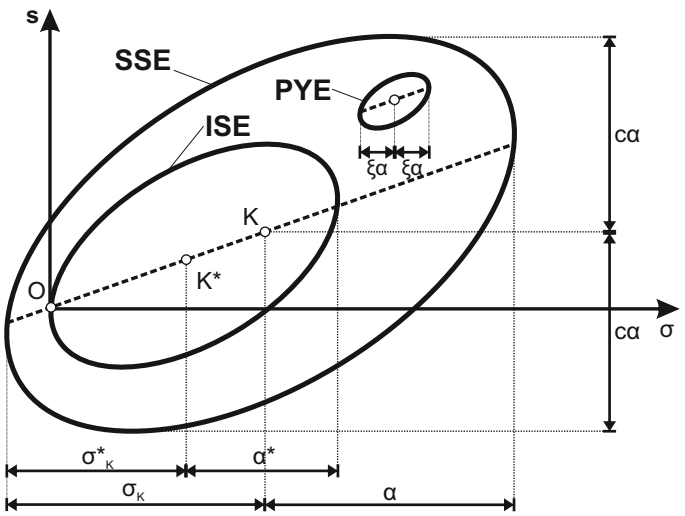


**Figure 3.40:** Characteristic surfaces of the MSS-2 constitutive model. (Belokas & Kavvadas 2010)

ter substantial structure degradation. The size difference between the SSE and the ISE is a direct measure of the magnitude of the structure. The behaviour size and orientation of the ISE is controlled through an intrinsic compressibility framework described in Belokas et al. (2005) as well as in Belokas & Kavvadas (2011) (see also section 3.2.1.2 and figure 3.9).

Alike MSS model, the MSS-2 model can account for both primary and secondary anisotropy. Primary, bond-strength anisotropy is controlled by the orientation vector $\boldsymbol{b} = \boldsymbol{s}_K/\sigma_K$; PYE describes the secondary anisotropy. Its kinematic hardening rule is similar to the MSS model (equations 3.10 and 3.11). Slight differences lie on the elimination of parameter $\chi$ in equation 3.10a and also in the different expression for $\dot{\mu}$ due to the different yield functions assumed.

The isotropic part of the hardening rule is slightly modified to account for the intrinsic strength envelope. It takes the following form:

$$\dot{\alpha} = \alpha^* \left( \frac{1+e}{\lambda - \kappa} \right) - \zeta_v exp(-n_v, \varepsilon_v^p) \dot{\varepsilon_v^p} + (\alpha - \alpha^*) \left\{ \theta_q - \zeta_q exp(-n_q, \varepsilon_q^p) \right\} \dot{\varepsilon_q^p} \qquad (3.16)$$

Volumetric hardening is now controlled by the size of the intrinsic strength envelope $\alpha^*$, while structure degradation is associated with the term $\alpha - \alpha^*$, describing the difference in size between the SSE and the ISE.

Plastic stains are described through a non-associated flow rule, following the concept of Kavvadas (1982) where zones of contractant and dilatant behaviour can be

distinguished based on the distance of the current state from the assumed phase transformation line and failure envelope (see fig 3.41). Model predictions were validated against experimental results of both reconstituted and natural Vallerica clay samples. Figure 3.42 presents characteristic results.

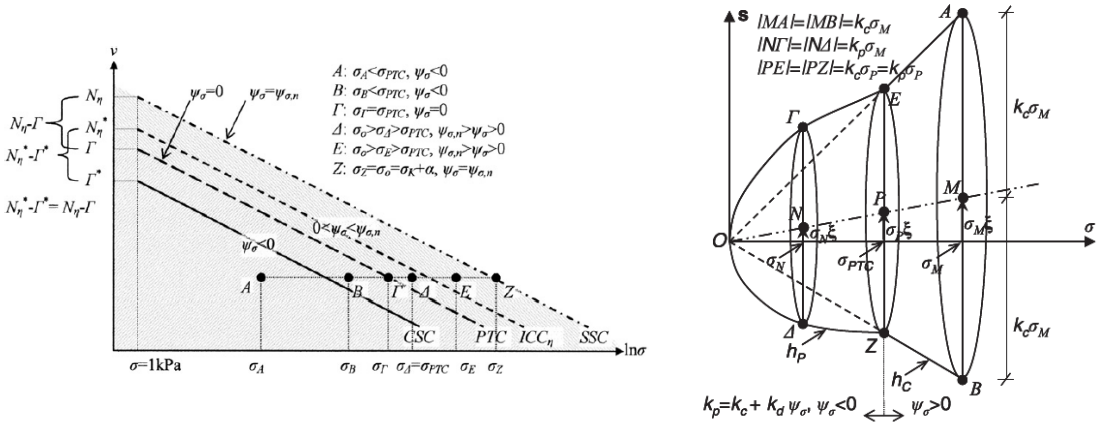


**Figure 3.41:** a) The Phase Transformation Curve and; b) the failure envelope of the MSS-2 constitutive model. (Belokas & Kavvadas 2010)

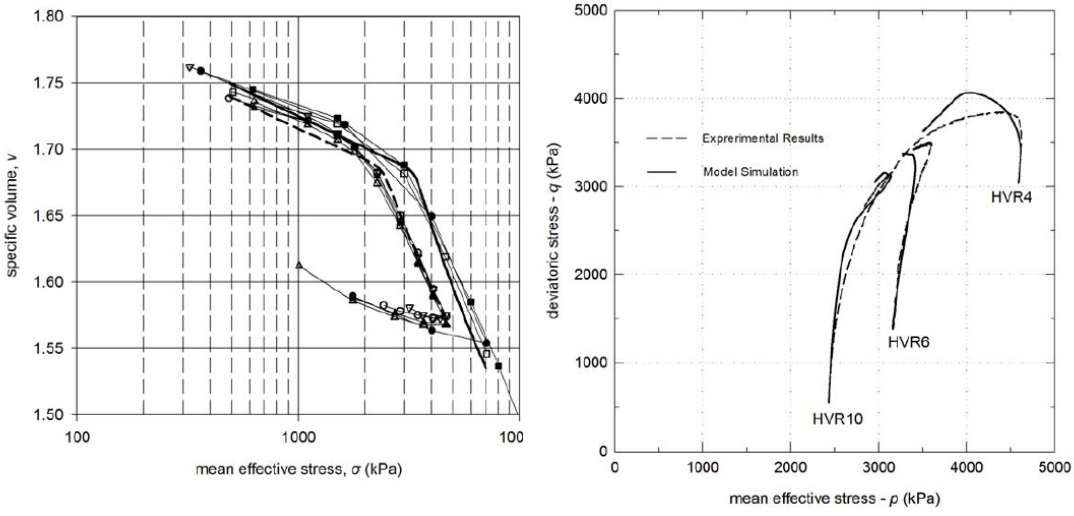


**Figure 3.42:** Comparison of the MSS-2 model's predictions with experimental results in a) consolidation tests and b) triaxial undrained tests on natural Vallerica clay samples. (Belokas & Kavvadas 2010)

### 3.3.4 The Dafalias (1986) model

Dafalias (1986) introduced an anisotropic critical state plasticity model for clays. Instead of directly postulating on the mathematical form of the yield surface he started by assuming a rate of the plastic work dissipation equation, including an anisotropic variable. Integrating the corresponding differential equation he ended up with an expression of a rotated and distorted ellipse. The derived equation represents the plastic potential function, while assuming an associated flow rule, the same function describes the yield surface. Dafalias (1986) ellipse is described by the following equation:

$$f \equiv g(\sigma, \boldsymbol{s}, \alpha, \boldsymbol{b}) = \frac{1}{c^2}\left[(\boldsymbol{s} - \sigma\boldsymbol{b}) : (\boldsymbol{s} - \sigma\boldsymbol{b}) + \sigma(2\alpha - \sigma)(\boldsymbol{b} : \boldsymbol{b})\right] - \sigma(2\alpha - \sigma) = 0 \quad (3.17)$$

where $2\alpha$ the preconsolidation pressure, representing the tip of the ellipse, and $\boldsymbol{b}$ the anisotropy tensor[5]. For $\boldsymbol{b} = 0$ in equation 3.17 the MCC yield surface is retrieved, while the inclination of the yield surface must be properly restricted to $\frac{1}{c^2}\boldsymbol{b} : \boldsymbol{b} < 1$ for eq. 3.17 to obtain real values. Figure 3.43 presents the derived anisotropic yield surface.

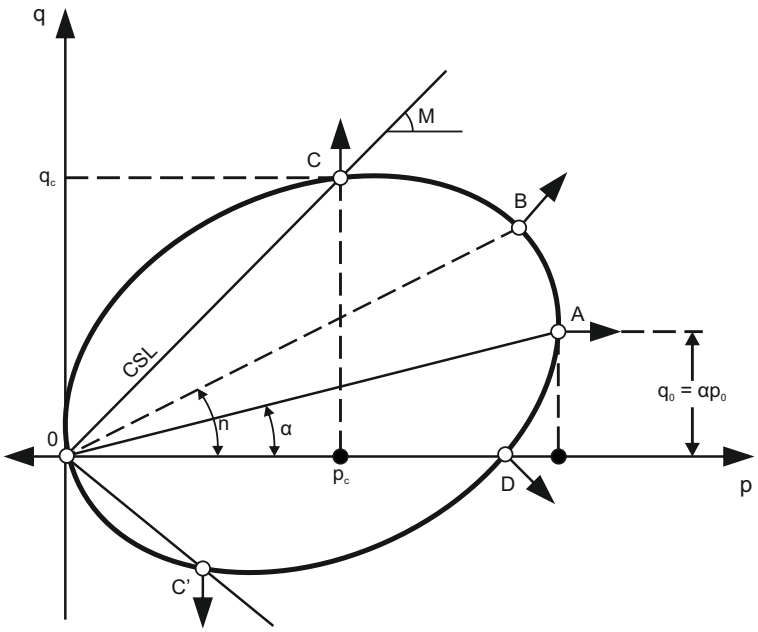


**Figure 3.43:** The anisotropic yield surface incorporated in the Dafalias (1986) constitutive model.

[5]The notation used differs from the one used by the authors. Equations are re-written using the Kavvadas (1982) notation, adopted throughout this Doctoral dissertation.

The MCC model's volumetric hardening rule (see equation 2.63) describes changes in the size of the yield function during plastic loading. The rotation of the yield surface, reflecting the evolution of anisotropy is described by the following kinematic hardening rule:

$$\dot{\boldsymbol{b}} = \frac{1}{a}\frac{v}{(\lambda-\kappa)}\frac{\psi}{2}(\boldsymbol{s}-\chi\sigma\boldsymbol{b})\dot{\varepsilon}^{p} \tag{3.18}$$

where $\psi, \chi$ material constants. Comparing equations 3.18 and 3.6 we may observe that they both describe an evolution of anisotropy which is proportional to the increment of plastic volumetric stains ($\dot{\varepsilon}^{p}$). Their main difference lies on the utilized stress attractor. In the Dafalias model, parameter $\chi$ is introduced in the term $(\boldsymbol{s}-\chi\sigma\boldsymbol{b})$ to control the orientation of the yield surface and thus the described preferred directions during a radial stress path. The reason underlying such a selection is quite simple. If the yield surface was allowed to distort until its main axis aligns with the applied stress path (as assumed in MIT-E1) then, the associated flow rule adopted would reproduce an unrealistic plastic dilation. In that respect, parameter $\chi$ is used to bound the rotation of the yield surface; it can be suitably calibrated to allow for a realistic reproduction of the plastic strains increment.

### 3.3.5 The SANICLAY (Dafalias et al. 2006) model and enhancements

Dafalias et al. (2006) enhanced the Dafalias (1986) model, to propose an improved anisotropic clay plasticity model, named the SANICLAY model. The authors' main objective was to simulate strain softening response in triaxial undrained compression following $K_0$ consolidation. Following the work of Dafalias et al. (2002), they adopt a non-associated flow rule. The proposed flow rule adopts the plastic potential function of Dafalias (1986), derived from the equation describing the rate of plastic work dissipation. For the yield envelope, a similar expression is utilized, nevertheless a different set of hardening variables control its size and position, resulting with a non-associated flow rule. The yield and the plastic potential functions take the following form:

$$f(\sigma,\boldsymbol{s},\alpha,\boldsymbol{b}) = \frac{1}{k^2}\left[(\boldsymbol{s}-\sigma\boldsymbol{b}):(\boldsymbol{s}-\sigma\boldsymbol{b})+\sigma(2\alpha-\sigma)(\boldsymbol{b}:\boldsymbol{b})\right]-\sigma(2\alpha-\sigma)=0 \tag{3.19}$$

and

$$g(\sigma, \boldsymbol{s}, \theta, \boldsymbol{d}) = \frac{1}{c^2}\left[(\boldsymbol{s} - \sigma\boldsymbol{d}) : (\boldsymbol{s} - \sigma\boldsymbol{d}) + \sigma(2\theta - \sigma)(\boldsymbol{d} : \boldsymbol{d})\right] - \sigma(2\theta - \sigma) = 0 \quad (3.20)$$

where $\boldsymbol{d}$ the tensor describing the orientation of the plastic potential surface and $2\theta$ its size; $\theta$ is properly calculated to ensure that $g(\sigma, \boldsymbol{s}, \theta, \boldsymbol{d}) = 0$ condition is satisfied at the current stress point. Figure 3.44 presents the characteristic surfaces of the SANICLAY model.

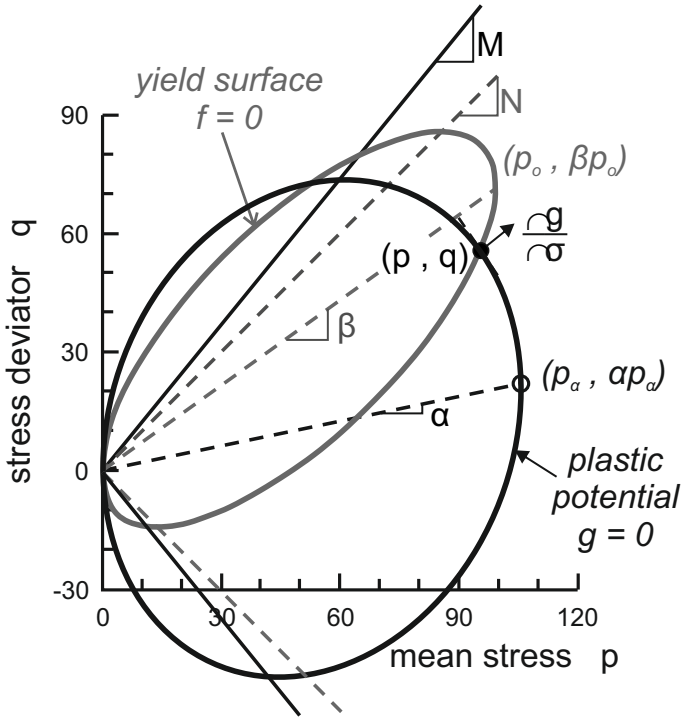


**Figure 3.44:** The characteristic surfaces of the SANICLAY constitutive model. (Dafalias et al. 2006)

The MCC model's isotropic volumetric hardening rule controls the evolution of the size of the yield surface, while the rotation-distortion of the yield and of the plastic potential surface is described through:

$$\text{Yield Surface:} \quad \dot{\boldsymbol{b}} = \frac{v}{(\lambda - \kappa)}\psi\left(\frac{\sigma}{2\alpha}\right)^2 (\boldsymbol{s} - \sigma\boldsymbol{b})(\boldsymbol{b}^b - \boldsymbol{b})\dot{\varepsilon}^p \quad (3.21)$$

$$\text{Plastic Potential Surface:} \quad \dot{\boldsymbol{d}} = \frac{v}{(\lambda - \kappa)}\psi\left(\frac{\sigma}{2\alpha}\right)^2 (\boldsymbol{s} - \chi\sigma\boldsymbol{d})(\boldsymbol{d}^b - \boldsymbol{d})\dot{\varepsilon}^p \quad (3.22)$$

Both equations resemble the hardening rule of Dafalias (1986) (see eq. 3.18) and include the same parameter $\psi$ to control the anisotropy's rate of evolution. On the

other hand, significant modifications exist which are summarized below:

- The term $\left(\frac{\sigma}{2\alpha}\right)^2$ is introduced in both equations to describe a reduced rate of anisotropy evolution with the increase of the overconsolidation ratio.

- Different attractors describe the rotation of the yield and of the plastic potential surface; rotation of the latter is controlled through parameter $\chi$, similar to Dafalias (1986), once again properly calibrated to reproduce the desired plastic dilation. On the contrary, term $\chi$ does not affect the rotation of the yield surface anymore. Instead, the Kavvadas (1982) stress attractor is used, dragging the orientation of the yield surface towards the direction of the imposed stress path.

- Terms $(\boldsymbol{b}^b - \boldsymbol{b})$ and $(\boldsymbol{d}^b - \boldsymbol{d})$ are added to prevent the corresponding functions from taking non-real values. They bound the rotation of the yield and of the plastic potential surface, as required for inequalities $\frac{1}{c^2}\boldsymbol{b} : \boldsymbol{b} < 1$ and $\frac{1}{k^2}\boldsymbol{d} : \boldsymbol{d} < 1$ to hold true.

SANICLAY model's predictions were compared with Gens (1982) experimental results. Figure 3.45 presents characteristic comparisons.

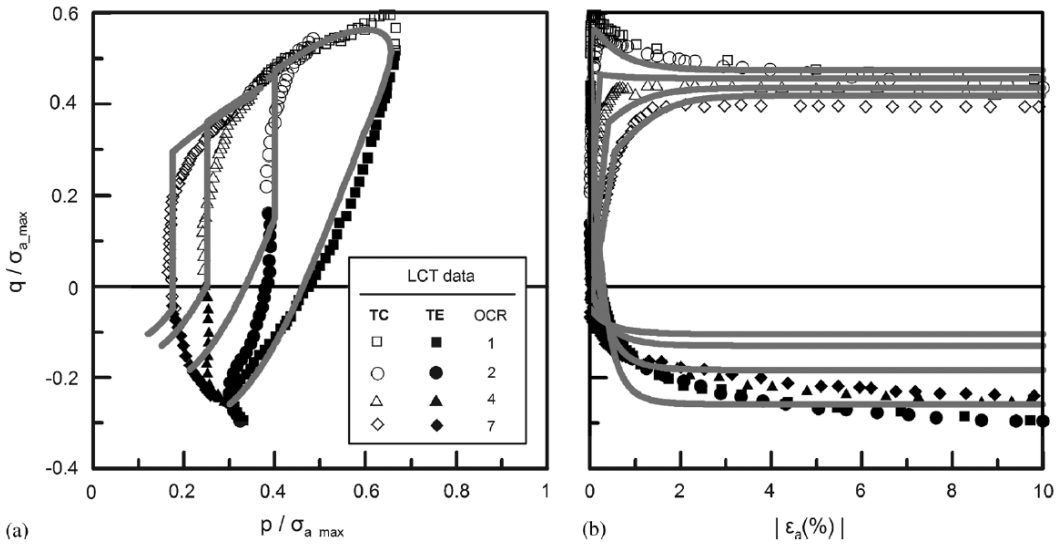


**Figure 3.45:** Comparison between SANICLAY model's simulations and experimental results regarding undrained triaxial tests on $K_0$ consolidated LCT samples under various $OCR$ values. (Dafalias et al. 2006)

Papadimitriou & Agapoylaki (2013) enhanced the SANICLAY model, with an eye towards improving the model predictions at the dry side, corresponding to the

mechanical behaviour of heavily overconsolidated soils. They introduced an extra kinematic - distortional hardening law which describes a continuous alteration of the yield surface aspect ratio with evolving anisotropy. The main idea is that parameter $k$ of equation 3.19 must continuously increase, initiating from a minimum value $k_I$ corresponding to the aspect ratio of the yield surface under isotropic conditions (coincides with the MCC value) towards a maximum value $k_K$ associated with the yield surface aspect ratio under stabilized anisotropy.

During a radial stress path with slope $n = (q/p) = \sqrt{\frac{3}{2}\frac{\boldsymbol{s}:\boldsymbol{s}}{\sigma^2}}$, the orientation of the yield surface follows the aforementioned inclination of the applied stress path, and thus we may write that $k_K$ value corresponds to $b_K = n = \sqrt{\frac{3}{2}\boldsymbol{b}_K : \boldsymbol{b}_k}$, while intermediate $K$ values are calculated through:

$$k = k_I + \frac{\sqrt{\boldsymbol{b} : \boldsymbol{b}}}{\sqrt{\boldsymbol{b}_K : \boldsymbol{b}_K}}(k_K - k_I) \tag{3.23}$$

where $\boldsymbol{b}$ represents the current anisotropy tensor. Starting from equation 3.23 and after some algebra a suitable hardening rule equation can be derived, in the form of $\dot{k} = \dot{\Lambda}\overline{k}$, where $\overline{k}$ depends on $\overline{b}$ and thus explicitly on the evolution rule of hardening variable $\boldsymbol{b}$.

Taiebat & Dafalias (2013) deal with the issue of uniqueness of the critical state line in clay plasticity. They mention that models incorporating a rotated or distorted anisotropic yield surface are vulnerable as they fail to reproduce a unique critical state in the specific volume $v$ - mean effective stress $p$ plane. To highlight the problem, the authors compared the results form two analyses (see figure 3.46a); an undrained triaxial compression and an undrained triaxial extension test, both starting from the same initial conditions representative of a $K_0$ normally consolidated soil element, while the same slope for the critical state line in compression and extension was assumed. Simulation were performed with the Dafalias (1986) model.

Since both stress paths involve undrained loading, volumetric strain is zero and the specific volume remains constant. They observed that at the end of the test, corresponding to critical state conditions, the mean effective stress reproduced is different in compression and extension, meaning that the results correspond to different critical state lines in the $v - \ln p$ plane. To avoid misunderstandings, we should mention that there exist experimental evidence indicating different critical state lines in compression and extension for anisotropically consolidated soils, nevertheless in most

cases they are also related to different critical state lines slopes in the stress space for compression and extension (i.e, different $M_c$ and $M_e$ in the $p-q$ space).

The authors attributed this behaviour to the rotational hardening law selected (see eq. 3.18), were changes in anisotropy are proportional to $\dot{\varepsilon}^p$. Equation 3.18 using the associated flow rule of Dafalias (1986) can be re-written as:

$$\dot{\boldsymbol{b}} = \frac{1}{a}\frac{v}{(\lambda-\kappa)}\frac{\psi}{2}(\boldsymbol{s}-\chi\sigma\boldsymbol{b})\dot{\Lambda}\frac{\partial f}{\partial \sigma} \tag{3.24}$$

The authors claim that the existence of the term $\frac{\partial f}{\partial \sigma}$ in equation 3.24 results in the freezing of the rotation of the yield function once at an intersection with the critical state line. They propose that, eliminating the $\frac{\partial f}{\partial \sigma}$ term from the equation and simultaneously substituting it with the atmospheric pressure $p_{atm}$ just for dimensional consistency can overcome the aforementioned freezing. They finally propose the following hardening rule equation:

$$\dot{\boldsymbol{b}} = \frac{1}{a}\frac{v}{(\lambda-\kappa)}\frac{\psi}{2}(\boldsymbol{s}-\chi\sigma\boldsymbol{b})\dot{\Lambda}p_{atm} \tag{3.25}$$

Although the proposed modification indeed solves the problem of the uniqueness of critical state (see figure 3.46) and also is consistent with theory of plasticity (quantity $\boldsymbol{h}$ in equation 2.33 can be arbitrarily selected), it is really difficult to see the physical meaning underlying the derived hardening rule in the sense that it is not anymore connected to the plastic strains induced in a soil element undergoing plastic loading.

### 3.3.6 Newson & Davies (1996) - The CARMEL Model

Newson & Davies (1996) proposed a constitutive model for anisotropically consolidated clays, named CARMEL. The authors use an experimentally derived yield surface initially proposed by Bondok (1989), mathematically represented as:

$$f(\sigma,\boldsymbol{s},\alpha,\boldsymbol{b}) = \frac{1}{c^2}\left[\xi(\boldsymbol{s}-\sigma\boldsymbol{b}):(\boldsymbol{s}-\sigma\boldsymbol{b})+\sigma(2\alpha-\sigma)(\boldsymbol{b}:\boldsymbol{b})\right]-\sigma(2\alpha-\sigma)=0 \tag{3.26}$$

The aforementioned expression is similar to Dafalias (1986) proposal (see eq. 3.17), with the addition of the extra variable $\xi$[6], which depends on the magnitude of the

[6] $\xi$ should not be confused with the PYE - SSE size proportionality parameter

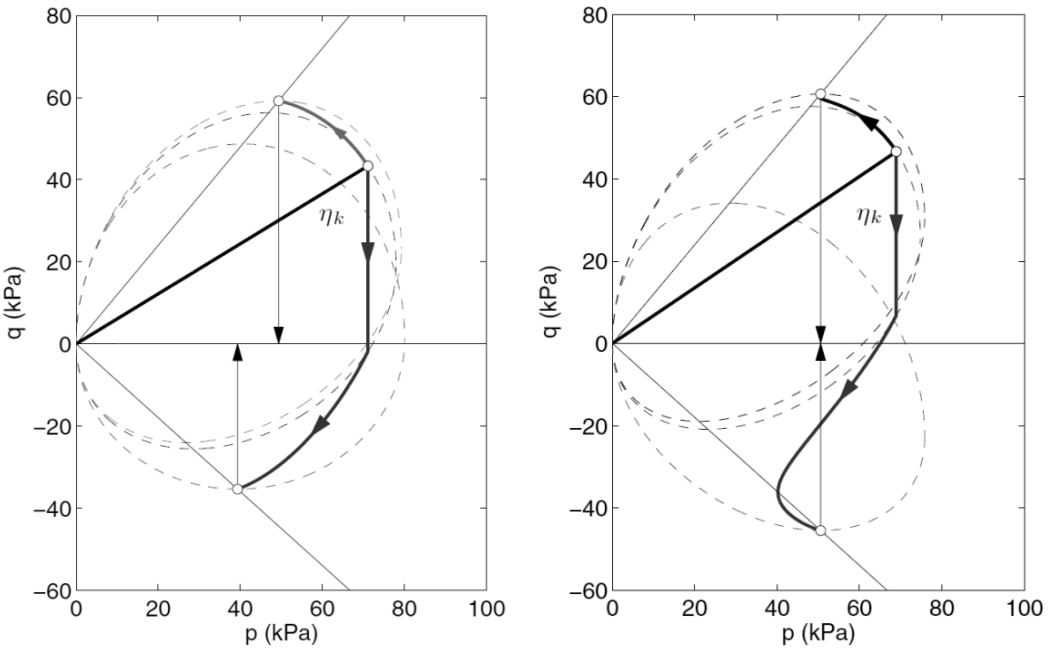


**Figure 3.46:** Simulation of undrained triaxial compression and extension tests on $K_0$ consolidated soil elements, using the kinematic hardening rules of: a) equation 3.24 and; b) equation 3.25. (Taiebat & Dafalias 2013)

developed anisotropy through the following equation:

$$\xi = 1 - \left(\frac{1}{c}\sqrt{\boldsymbol{b} : \boldsymbol{b}}\right)^3 \tag{3.27}$$

We may observe, that in fact term $\xi$ changes the aspect ratio of the yield surface with the evolution of anisotropy, an idea later also employed by Papadimitriou & Agapoylaki (2013).

CARMEL model adopts a non-associated flow rule based on the plastic potential surface of Dafalias (1986) and represented by the following plastic potential function:

$$g(\sigma, \boldsymbol{s}, \theta, \boldsymbol{d}) = \frac{1}{c^2}\left[(\boldsymbol{s} - \sigma\boldsymbol{d}) : (\boldsymbol{s} - \sigma\boldsymbol{d}) + \sigma(2\theta - \sigma)(\boldsymbol{d} : \boldsymbol{d})\right] - \sigma(2\theta - \sigma) \tag{3.28}$$

Its orientation tensor $\boldsymbol{d}$ follows a constant analogy with the orientation of the yield surface, $\boldsymbol{d} = \frac{1}{2}\boldsymbol{b}$ is proposed, implying that the inclination of the plastic potential surface is always half that of the yield surface. Figure 3.47 presents the CARMEL model's characteristic surfaces.

Regarding the model's hardening rule, unfortunately the authors do not provide detailed information. They report an incremental expression for the evolution of

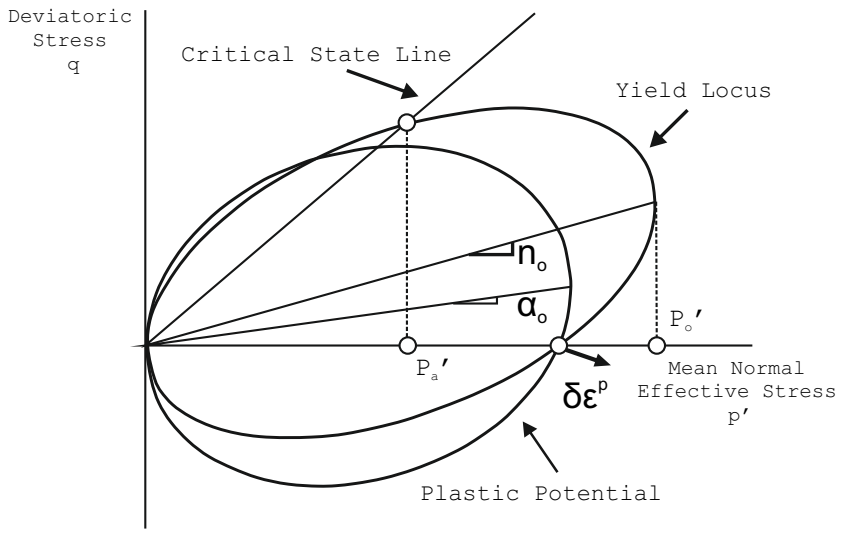


**Figure 3.47:** The yield and plastic potential surfaces of the CARMEL constitutive model. (Newson & Davies 1996)

anisotropy, which is based on the increment of the mean effective stress instead of the increment of plastic volumetric strains; an obvious shortcoming of such an assumption is the difficulty to formulate the hardening rule within the classical theory of plasticity framework. Nevertheless, the main idea is similar to the one initially proposed by Kavvadas (1982) where the main axis of the yield surface rotates until it aligns with the imposed radial stress path. Regarding the rate of anisotropy evolution it is assumed dependant on the compressibility and strength parameters of the material. In the isotropic component of the hardening rule the authors tried to simulate unique virgin compression lines dependant on the consolidation stress path followed, an idea similar to the intrinsic compressibility framework later introduced in Belokas & Kavvadas (2010).

They propose that the reproduced virgin compression line under stabilized anisotropy should depend on the level of the stress induced anisotropy through parameter $\xi$, as follows:

$$N_n = \Gamma + (\lambda - \kappa) \ln (1 + \xi) \tag{3.29}$$

Unfortunately, no further information is provided on whether and how this dependance can be incorporated in the model's hardening rules. Figure 3.48 compares the CARMEL model's predictions with experimental results, corresponding to $K_0$ normally consolidated Speswhite Kaolin samples.

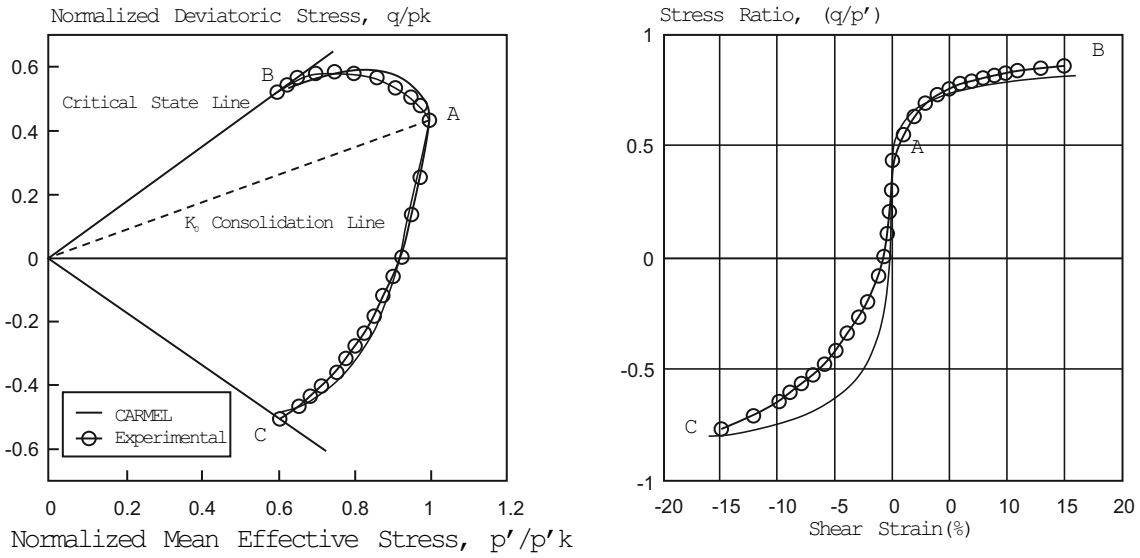


**Figure 3.48:** Triaxial undrained compression and extension experimental results of Atkinson et al. (1987) compared with the KARMEL model's predictions. (Newson & Davies 1996)

### 3.3.7 Wheeler et al. (2003) - The S-CLAY1 model

Wheeler et al. (2003) presented a soil model for anisotropic soft clays, named the S-CLAY1. Their work focused on the proposal of a new rotational hardening law. It is the first model to introduce a dependency of the kinematic part of the hardening rule on the deviatoric plastic strains, along with the volumetric plastic strains. The proposed hardening rule has been based upon an extensive laboratory investigation on the relationship between plastic straining and the evolution of the inclination of the yield surface.

The authors incorporate the yield function of Dafalias (1986) (see eq. 3.17) that is here repeated for clarity as equation 3.30:

$$f(\sigma, \boldsymbol{s}, \alpha, \boldsymbol{b}) = \frac{1}{c^2}\left[(\boldsymbol{s} - \sigma\boldsymbol{b}) : (\boldsymbol{s} - \sigma\boldsymbol{b}) + \sigma(2\alpha - \sigma)(\boldsymbol{b} : \boldsymbol{b})\right] - \sigma(2\alpha - \sigma) = 0 \quad (3.30)$$

The adopted yield surface is compared with the yield locus of anisotropically consolidated soils determined through a series of experimental results; as stated by the authors the comparison revealed that the adopted yield surface holds as "a reasonable approximation" (see figure 3.49).

Wheeler et al. (2003) also raise an interesting discussion on the necessity of a non-associated flow rule. They argue on the accuracy of laboratory test results showing

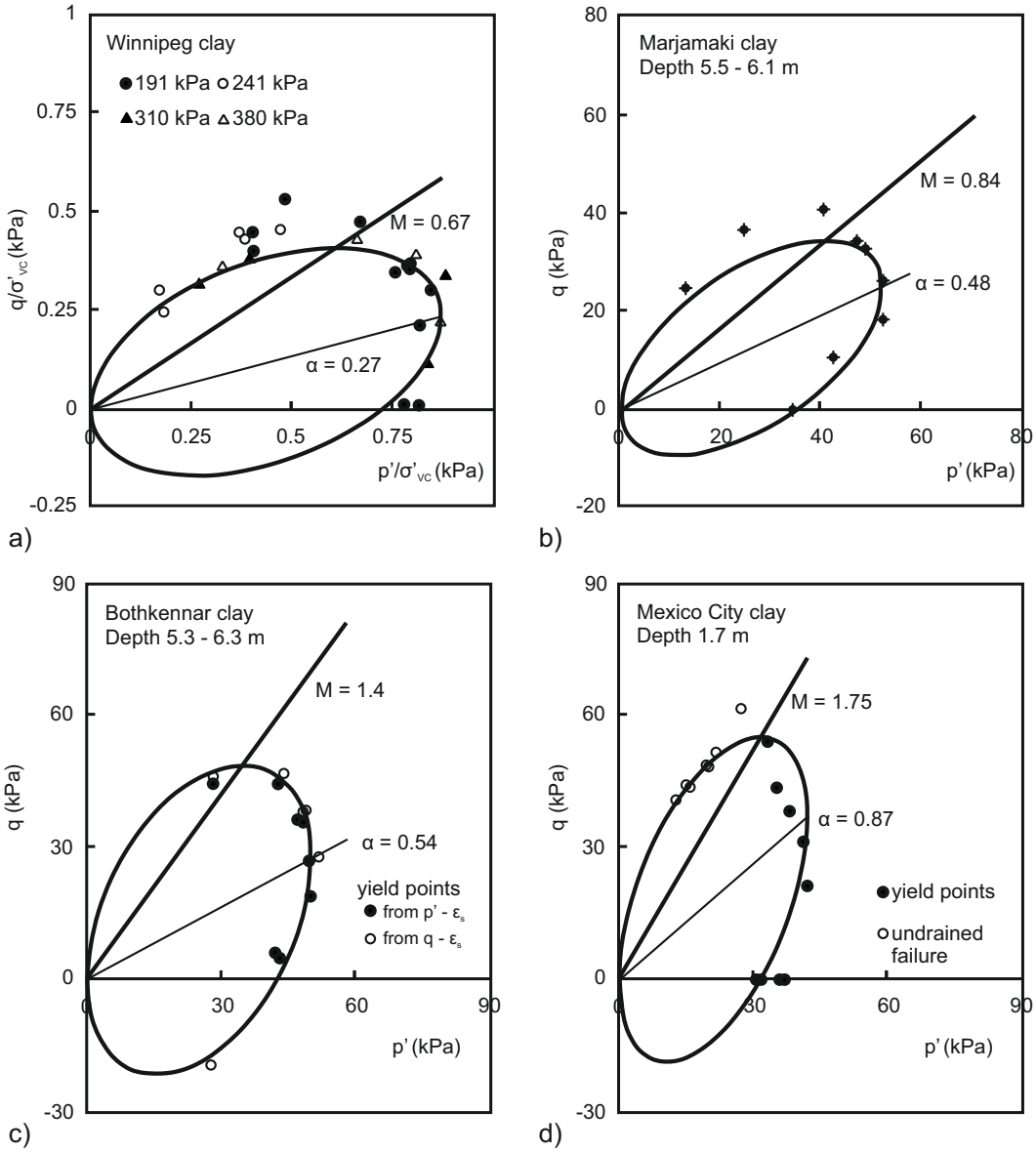


**Figure 3.49:** The S-CLAY1 model's yield surface fitted into experimentally determined yield points; a) Winnipeg clay (Graham & Houlsby 1983); b) Marjamaki clay (Länsivaara 1996); c) Bothkennar clay (Smith et al. 1992) and; d) Mexico City clay Diaz-Rodriguez et al. (1992). (Wheeler et al. 2003)

experimental plastic strain increment vectors superimposed on inclined yield surfaces due to the fact that significant rotation of the yield surface may have occurred during the deformation required to acquire the aforementioned vectors. At the end they adopt an associated flow rule, stating that such a selection is preferred due to "the absence of conclusive evidence to the contrary and in the interests of simplicity".

The size of the yield surface is controlled through the MCC models volumetric

hardening rule. The most interesting part of Wheeler et al. (2003) contribution is no doubt the novel kinematic hardening rule proposed for the rotation-distortion of their yield surface. The proposed hardening rule has the following form:

$$\dot{\boldsymbol{b}} = \mu \left[ \{ \boldsymbol{\chi}_v - \boldsymbol{b} \} < \dot{\varepsilon} > + \beta \{ \boldsymbol{\chi}_d - \boldsymbol{b} \} \dot{\varepsilon_q} \right] \tag{3.31}$$

where $\dot{\varepsilon_q}$ the increment of the plastic deviator strain defined as $\dot{\varepsilon_q} = \sqrt{\frac{2}{3} \dot{\boldsymbol{e}^p} : \dot{\boldsymbol{e}^p}}$.

Equation 3.31 reflects the authors' conceptual idea that plastic volumetric strains and plastic deviatoric strains have different effect on the fabric rearrangement occurring within a soil element subjected to an anisotropic stress path. They assumed that plastic volumetric strains drug the anisotropy tensor $\boldsymbol{b}$ towards a target value $\boldsymbol{\chi}_v$ while simultaneously, plastic deviatoric strains drag $\boldsymbol{b}$ towards a target value $\boldsymbol{\chi}_d$; both targeted orientations are assumed a function of the slope of the imposed stress path.

The major advantage of the proposed rule is its ability to represent uniqueness of critical state. The dependence on the plastic deviatoric strains ensure that anisotropy will continue evolving even if the increment of the plastic volumetric strain becomes zero. According to the authors, uniqueness of critical state appears physically sensible, because critical state corresponds to a condition where fabric is being continuously destroyed and recreated. In that respect, they claim that the inclination of the yield curve at critical state should be solely dependent on stress conditions at the critical state and be independent both of the initial yield curve inclination and of the followed stress path.

To evaluate their hardening rule's parameters, they performed an extensive laboratory investigation on Otaniemy Clay samples. The soil samples were initially radially compressed under different stress ratios. Radial compression involved substantial plastic straining to ensure stabilization of the fabric anisotropy to the principle directions of the applied stress path. A second loading stage followed, where the loading direction was changed, to determine the material's yield locus. To do so, a suitable loading path was selected, to ensure that initially the stress path moves inside the yield surface (elastic unloading), until it crosses again the yield surface, assumed constant during the elastic unloading stage. From the obtained results, the authors could correlate the stress paths imposed at the first loading stage with the orientation of the yield surface identified during the second loading stage. Figure 3.50 presents some of the results of the aforementioned tests.

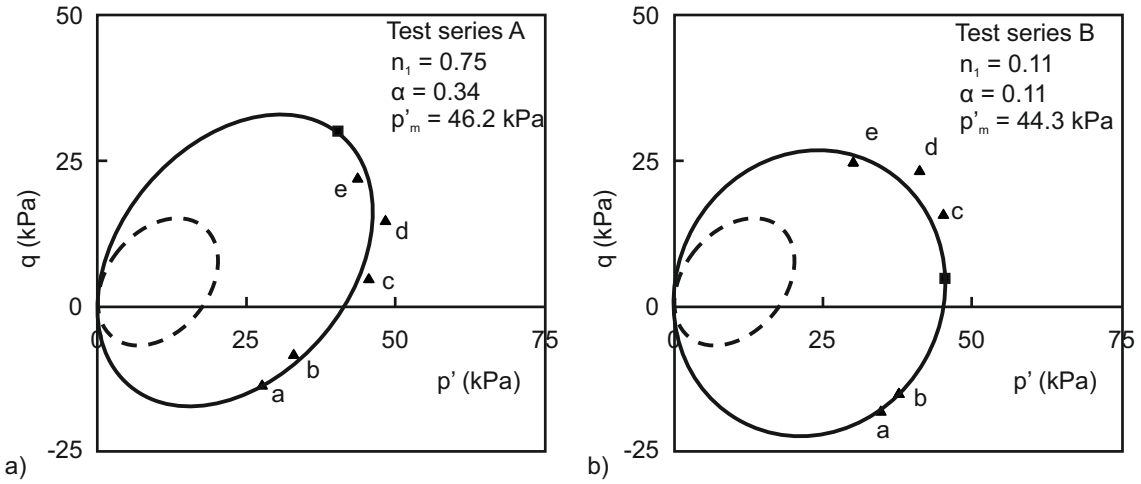


**Figure 3.50:** Expanded and rotated yield surfaces corresponding to Otaniemi clay results. (Wheeler et al. 2003)

Based on the Otaniemy clay results, the authors propose that parameter $\chi_v \equiv \frac{3n}{4}$ and parameter $\chi_d \equiv \frac{n}{3}$, where $n$ the ratio of the imposed stress path in the triaxial stress space $(p, q)$. Finally they propose the following mathematical form for their hardening rule:

$$\dot{\boldsymbol{b}} = \mu \left[ \left\{ \frac{3}{4\sigma}\boldsymbol{s} - \boldsymbol{b} \right\} < \dot{\varepsilon} > + \beta \left\{ \frac{1}{3\sigma}\boldsymbol{s} - \boldsymbol{b} \right\} \dot{\varepsilon}_q \right] \tag{3.32}$$

Regarding the rest of the parameters they propose that parameter $\beta$ can be explicitly calculated from a $K_0$ test where the yield surface should get oriented properly for the reproduced plastic dilatancy from the normality rule to correspond to zero radial strains. Finally, for parameter $\mu$, they suggest a trial and error procedure to fit the available experimental results.

## 3.4 Concluding Remarks

Natural soils are usually sedimentary soils, deposited under one-dimensional compression conditions, with the resulting anisotropic fabric influencing their mechanical behaviour. A significant number of experimental studies focusing on the mechanical behaviour of anisotropically consolidated soil elements exist and have also motivated the development of an appreciable number of anisotropic constitutive models. This chapter presented the main behavioural aspects of anisotropic soils and also the most important contributions regarding constitutive modelling. The key points are sum-

marized in the next few lines.

We should emphasize the fact that the presented review focuses on stress induced anisotropy associated with either structureless material states or structured due to over-consolidation material states, excluding bond-strength anisotropy related with other structure inducing mechanisms (i.e., cementation). In the laboratory two are the main loading paths which can result in a controllable amount of anisotropy in a soil sample, namely the radial consolidation tests realized in a triaxial cell and the one-dimensional consolidation performed in the oedometer. The behaviour of soil samples imposed to anisotropic compression is summarized below:

- In radial compression, a soil element is subjected to a constant stress ratio $n = \dot{q}/\dot{p}$ imposing certain preferred directions in the stress domain. After substantial plastic straining, soil fabric adjusts to the imposed level of anisotropy, and a linear compression curve is reproduced in the $v - \ln p$ plane; a constant dilatancy $d_q = \dot{\varepsilon_q}/\dot{\varepsilon_p}$ is reproduced.

- Oedometric compression imposes a constant dilatancy $d_q = 2/3$ as horizontal deformation is restrained ($\dot{\varepsilon_h} = 0$). Soil anisotropy is profound in the value of the ratio of the horizontal to the vertical effective stress $K_0 = \sigma_h/\sigma_v$, called the coefficient of lateral earth pressure at rest or the geostatic stress ratio. A linear compression curve is reproduced in the $v - \ln p$ plane as well. One dimensional conditions can be also indirectly imposed through a radial consolidation test where the stress ratio is incremental adjusted to maintain zero horizontal strains.

- Compression tests under different stress ratio reproduce distinct but parallel compression lines in the $v - \ln p$ plane, with their position depending on the level of the imposed stress path; their slope is described by the MCC compressibility parameter $\lambda$. The derived compression lines plot inside the domain defined by the isotropic compression line and the Critical State Line (CSL), reflecting the beneficial effect of shear strains on fabric rearrangement. The higher the stress ratio the closer the reproduced compression line plots to the CSL, with $n = M$ corresponding to the maximum theoretical stress ratio that can be imposed and reproduce a continuously hardening behaviour which does not lead to failure.

- Dilatancy increases with increasing stress induced anisotropy, approaching infinity as $n$ approaches $M$, a reasonable behaviour if we consider that critical state conditions are associated with infinite deviatoric strains.

Laboratory tests that can lead to failure (i.e., triaxial loading tests, direct simple shear tests, etc.) conducted on anisotropically consolidates samples reveal:

- In undrained compression, after an initial strain hardening response, a peak strength is reached, followed by strain softening towards an ultimate strength. Both peak strength and the obtained brittleness reduce with reducing initial anisotropy (increase in K) and with increasing over-consolidation ratio (OCR) (i.e., isotropically consolidated soil samples or anisotropically heavily over-consolidated samples exhibit a continuously strain hardening response).

- In drained compression there are no evidence of brittle behaviour as all samples systematically strain harden towards their peak ultimate strength. A systematically contracting behaviour is measured, with volumetric strains reducing with increasing over-consolidation and increasing initial anisotropy.

- All results agree on a common and well defined ultimate state (critical state) which is independent of: a) the initial anisotropy; b) the degree of overconsolidation, and; c) the imposed stress path.

- Regarding the behaviour during extension, the most interesting observation is the hook-type behaviour associated with the stress path of anisotropically consolidated samples when sheared under undrained conditions; Regarding the ultimate strength, again the results agree on a common critical state, independent of the initial anisotropy, of the degree of overconsolidation and of the imposed stress path. Nevertheless, with respect to the friction angle in extension and the position of the critical state line in the $v - \ln p$ plane contradicting results exist. They either suggest a common friction angle and thus different critical state between compression and extension or an increased friction angle in extension which may support a common critical state between compression and extension.

- Experimentally defined yield points agree on a non-isotropic yield locus.

Finally, with respect to constitutive modelling, we may summarize:

- Anisotropic soil behaviour calls for an inclined yield surface, usually oriented towards the stress path of consolidation.

- A non-associated flow rule is required.

- A mixed hardening rule is necessary. In most of the cases the MCC hardening rule is adopted for the isotropic part of the hardening rule and a volumetric kinematic component accounts for the inclination of the yield surface, with the exception of the Wheeler et al. (2003) where the evolution of anisotropy is associated with plastic deviatoric strains as well.

According to the author, the definition of the hardening laws, consists the main subject where significant room for improvement exists, mainly towards; a) a more accurate simulation of the dependency of the compression curves on the level of stress induced anisotropy, and; b) a more rigourous simulation of degradation of anisotropy with plastic straining together with uniqueness of critical state.

# Chapter 4

# Unsaturated Soils: Mechanical behaviour and Constitutive Modelling

This chapter deals with the mechanical behaviour of unsaturated soils. A brief introduction to the nature of unsaturated soils is given, followed by the definitions of suction and water retention curve. Presentation of their main mechanical behaviour characteristics follows, focusing on compressibility and shear strength. The chapter ends with the presentation and discussion of the most significant contributions regarding constitutive modelling.

It is mentioned from the beginning that the behaviour of unsaturated soils is far more complicated, compared to their saturated counterparts, and a new branch of the geotechnical discipline, the unsaturated soil mechanics discipline, has appeared and evolved the last few decades. This chapter at no means serves as a complete presentation of the theory of unsaturated soils mechanics. Instead, its main purpose is to familiarize the reader with the most important behavioural aspects of unsaturated soils, while the most interested reader shall go through the various literature references mentioned in the text, for a dipper understanding of the associated phenomena.

## 4.1 Introduction - Nature of Unsaturated Soils

An unsaturated soil is practically any soil with a degree of saturation $S_r$ less than unity and greater than zero ($0 < S_r < 100\%$). In other words, the main characteristic

of an unsaturated soil is the co-existence of three individual phases; the solid particles, the liquid and the gas phase. Unsaturated soils are also very often characterised as partially saturated soils. In recent years both terms are widely used in characterising the same material. Nevertheless, according to Delage & Graham (1996), the term unsaturated should be used to describe soils with a homogeneous degree of saturation, while on the contrary partial saturation refers to soils that do have an overall degree of saturation less than unity and greater than zero but at the same time the water content is not evenly distributed within their mass. In that end, a sample of a partially saturated soil may have areas that are fully saturated (i.e. micro - porosity within the clay aggregates) together with areas that are relatively dry (i.e. macro - porosity between the clay aggregates).

Gens et al. (2006) mentions that an unsaturated soil is not a special soil but a specific state of a soil. Any soil can be potentially unsaturated under the proper hydraulic and atmospheric boundary conditions. For instance, soils in the vicinity of the water table, in the vadose zone, can be either saturated or unsaturated depending on the fluctuations of the phreatic surface around the year. Another very common category of unsaturated soils is compacted soils. Compacted soils are used in embankments construction for railways and highways, as well as in earth dams (i.e., clay core). Compacted soils are by definition unsaturated or in many cases partially saturated soils as the water content required for optimum compaction conditions (maximum relative density) is far below the saturated water content.

A very common problem in either natural or compacted unsaturated soils, especially when compacted at the dry of optimum, is volumetric collapse (irreversible volume reduction) due to wetting. Damage in building foundations (Gens 2010), road embankments (Lloret 2012; Alonso 2012) and dams (Naylor et al. 1986; Naylor et al. 1997; Alonso et al. 2005) can be attributed to wetting of unsaturated soils. Volumetric collapse is profound to common clayey soils of low activity.

To the contrary, soils containing highly active soil minerals, like montmorillonite, smectite, vermiculite (Mitchell & Soga 2005) can swell upon wetting and cause structural failures due to heave (Lloret et al. 1988; Alonso & Lloret 1996). Such soils are called expansive soils and their behaviour is also studied within the unsaturated soil mechanics theory. Nevertheless, a detailed and accurate representation of their mechanical behaviour requires special theoretical frameworks (i.e., (Gens & Alonso 1992)).

Another application of the unsaturated soil mechanics' principles is related to the disposal of highly radioactive waste. Canisters containing high level radioactive waste materials from the reactor core of nuclear power plants must be safely stored in deep geological repositories. Bentonite backfills are used to surround the canisters and isolate them from the adjacent rock. Complicated thermo - hydro - mechanical phenomena take place, associated with the hydration process of the highly expansive bentonite backfill. More information about the role of unsaturated soil mechanics in radioactive waste disposal can be found in Cui et al. (2009), Gens et al. (2009) and Gens (2010).

Slope stability and landslides is another predominant field of application of unsaturated soils mechanics. It is very common, slopes either natural or even artificial, after periods of heavy rainfall to fail and fall due to the reduction of their shear strength caused by an increase in the degree of saturation. There are many examples, especially in regions with residual and tropical soils, where massive rainfall induced landslides have severe consequences in infrastructures, and sometimes are even connected to human losses. Studding the stability of such natural or artificial slopes requires a deep knowledge of the unsaturated soil mechanics principles and has received considerable attention by the research community worldwide (Shi 2003; Collins & Znidarcic 2004; Rahardjo et al. 2007; Springman et al. 2012).

For many years the mechanical behaviour of unsaturated soils could not be easily explained and interpreted by the classical soil mechanics theories. For instance, the irreversible reduction in volume associated with wetting of an initially unsaturated soil (collapse behaviour) could not be accommodated within the effective stress principle. Such a strange soil behaviour was for many years characterized as problematic and the associated soils as problematic soils. Nevertheless, as pointed out in Gens (2010), Vaughan (1999) mentioned that it is the classical soil mechanics theory which fails to fit the behaviour of such soils that is problematic and not the soils themselves.

Nowadays, advances in both experimental techniques but also in the theoretical framework allow for a comprehensive description of the behaviour of unsaturated soils. Moreover, advancements in numerical tools for multi - phase porous materials (Olivella et al. 1994; Olivella et al. 1996; Loret & Khalili 2000) as well as in thermo - hydro - chemical - mechanical coupling, initially developed to describe and analyze the behaviour of unsaturated soils, have proved very useful in studding new engineering problems, like tunnelling in sulfate - bearing materials; dissolution,

degradation and weathering of soils and rocks; permafrost evolution; tunnelling using ground freezing techniques; settlements induced by oil and gas extraction; $CO_2$ sequestration; and hydraulic fracturing (Gens 2010).

The most fundamental ideas of unsaturated soil mechanics are those of suction and of the water retention curve. Next section deals exclusively with the definition of suction and with the properties of the water retention curve.

## 4.2 Suction and the Water Retention Curve

### 4.2.1 Suction

**Suction** is the most fundamental idea in unsaturated soil mechanics. Soil suction can be either seen as a stress variable, from an engineering point of view, or as a potential from a thermodynamic point of view. Many factors contribute to suction development within a soil system and different components of soil suction exist. In the following lines, the capillary, the absorptive and the osmotic components of suction are introduced. In doing so, information from various sources are utilized (Fredlund & Rahardjo 1993; Lu & Likos 2004; Lloret 2012; Alonso 2012; Bardanis 2016). Basic knowledge of thermodynamic principles is required to follow.

#### 4.2.1.1 Matric Suction. Capillary and absorptive phenomena

Instead of directly postulating on the definitions of the various soil suction components it is attempted to derive their definitions, one by one, through a series of simple, illustrative examples. Such an approach offers a better understanding of the physical processes underlying each suction component.

Starting with capillary phenomena, let's assume that a capillary tube is inserted in a bowl filled with pure water as illustrated in figure 4.1a. It is well known that water within the capillary tube will rise above the surface of the water in the bowl, similar to how water rises in a straw inside a glass of water. The water within the tube has a weight equal to:

$$W_c = \gamma_w \pi r^2 h \tag{4.1}$$

where $\gamma_w$ the water unit weight, $r$ the radius of the capillary tube and $h$ the height of water rise. Equilibrium of this water column requires a force which counterbalances the weight of the water. This force comes from a pressure deficit between the air

pressure $u_a$ and the water pressure $u_w$ developing at the top of the column (point C), so that:

$$(u_a - u_w)\pi r^2 = \gamma_w \pi r^2 h \Rightarrow u_a - u_w = \gamma_w h \tag{4.2}$$

We call this pressure deficit suction and is symbolized as:

$$s = u_a - u_w \tag{4.3}$$

If we assume that the air pressure is equal to zero, a negative water pressure is required for the water column equilibrium. In this case suction coincides with the negative water pressure.

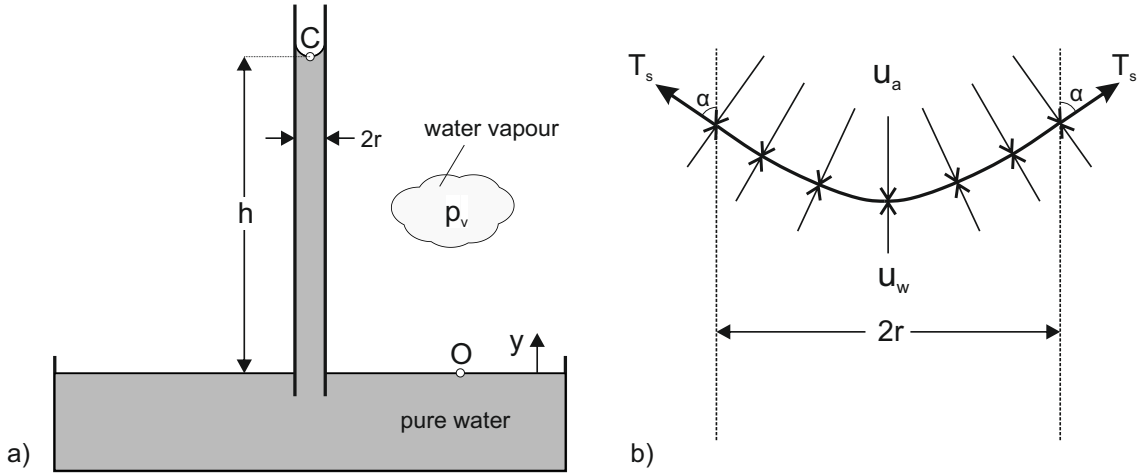


**Figure 4.1:** a) The capillary tube model and; b) a detail of the curved water - air interface.

A closer look at the top of the water column in the capillary tube (see figure 4.1b), reveals that the excess of the air pressure over the water pressure results to the curvature of the air-water interface. Equilibrium of the curved interface requires a tensile force $T_s$. This force is called surface tension and in a gas-liquid interface, as case examined hear, it arises from imbalanced intermolecular forces acting on the molecules of the liquid phase (Lu & Likos 2004), in our case pure water. For the equilibrium of the water-air interface at the vertical direction we may write:

$$(u_a - u_w)\pi r^2 = T_s \cdot 2\pi r \cdot \cos a \tag{4.4}$$

where $a$ the contact angle of the water-air-solid (tube's material) system. Solving

equation 4.4 for suction we derive:

$$s = u_a - u_w = 2T_s \frac{1}{r} \cos a \tag{4.5}$$

Equation 4.5 dictates that the suction developed in a capillary system is proportional to the surface tension but inversely proportional to the radius of the capillary tube. Assuming a really poorly graded soil where just a single diameter of solid grains exists, the voids forming between the solid particles will have a single radius $r$. Further considering that this soil is above the water table then water will rise inside the soil pores to a height equal to $h_c$ which can be calculated through the capillary tube model. This height $h_c$ is the height of capillary rise and equation 4.5 explains why capillary rise is higher in fine-grained soils compared to coarser granular materials.

In any closed liquid-gas system, molecules from the liquid phase move towards the gas phase in the form of vapour. This exchange continues until vapour pressure establishes an equilibrium with the liquid phase. Let's consider a point O located in the gas phase at the interface with the free water[1] surface. The vapour pressure at point O is in equilibrium with the free water and its vapour pressure is called the saturated water vapour pressure $P_{v,sat}$. In an analogy, at point C, in the gas phase over the forming meniscus, water vapour exist and is in equilibrium with the water phase at the meniscus. This vapour pressure at point C is symbolised as $P_v(s)$, where $s$ is the corresponding suction. In fact, vapour pressure additionally depends on temperature ($T$) and on the concentration of salts ($w$) within the water. For this reason we shall better symbolize it as $P_v(s, T, w)$, as a reminder of its dependency on the aforementioned quantities. Adopting such a notation, the saturation vapour pressure is $P_{v,sat} = P_v(0, T, 0)$ and vapour pressure at point C can be rewritten as $P_v = P_v(s, T, 0)$.

Considering the equilibrium of vapour pressure between points O and C, the change in the vapour pressure $dp_v$ with altitude is calculated as:

$$dp_v = -\rho_v g dy \tag{4.6}$$

where $\rho_v$ the density of the water vapour. The water vapour density is calculated

[1] As free water, pure water that does not interact with other phases and that is subjected only to gravitational forces is defined (Lu & Likos 2004).

according to the ideal gas law as:

$$\rho_v = p_v \frac{M_w}{RT} \tag{4.7}$$

where $T$ temperature in $^oK$, $M_w$ the molecular mass of water (in $kgr/mol$) and $R$ the universal gas constant equal to $R = 8.314N \cdot m/molK$. Combining equations 4.6 and 4.7 we may write:

$$dy = -\frac{dp_v}{p_v}\frac{RT}{M_w g} \tag{4.8}$$

Integrating equation 4.8 from $y = 0$ to $y = h$ we have:

$$h = \int_o^h dy = -\frac{RT}{M_w g}\int_{P_v(0,T,0)}^{P_v(s,T,0)} \frac{1}{p_v} dp_v = -\frac{RT}{M_w g} \ln \frac{P_v(s,T,0)}{P_v(0,T,0)} \tag{4.9}$$

The height of water rise $h$ is related to suction through equations 4.3 and 4.4, while substituting both quantities in equation 4.9 we derive:

$$s = hg = -\frac{RT}{M_w} \ln \frac{P_v(s,T,0)}{P_v(0,T,0)} \tag{4.10}$$

Finally, the ratio of the vapour pressure at any given point with respect to the saturated vapour pressure is the well known Relative Humidity $RH$:

$$RH = \frac{P_v(s,T,0)}{P_v(0,T,0)} \tag{4.11}$$

and by further elaborating equation 4.10 we may conclude that:

$$s = -\frac{RT}{M_w} \ln RH \tag{4.12}$$

Equation 4.12 is called the psychrometric equation; it relates the suction in a system (at this point at a capillary system with pure water) with the relative humidity $RH$ at the gas phase. It plays a key role in unsaturated soil mechanics as it is utilized in the description of soil-atmosphere interactions and it underlies methods for suction measurement and control.

Figure 4.2 utilizes equation 4.12, to plot suction ($s$) vs relative humidity ($RH$) at a reference temperature equal to $T = 20^oC = 293.1^oK$. We may observe the rapid suction increase with a drop in relative humidity. For instance, at a $RH$ equal to 60%, which is a very common value for temperate climates, the corresponding

suction is almost $75MPa$, indicating that usually anticipated climatic conditions have a significant potential to drain water from a soil system.

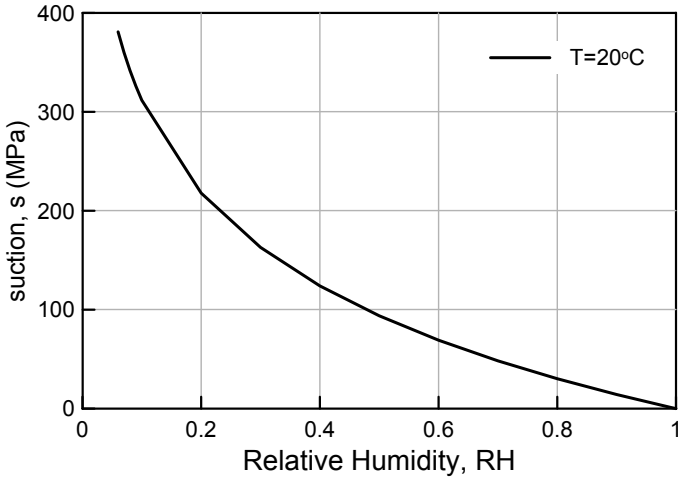


**Figure 4.2:** Suction vs Relative Humidity for a pure water-air system at T=20$^o$C.

Using the psychrometric equation, Relative Humidity, can be correlated with the radius of the capillary tube (eq. 4.5). We may write:

$$2T_s\frac{1}{r}\cos a = s = -\frac{RT}{M_w}\ln RH \tag{4.13}$$

Assuming once again that the capillary system represents a poorly graded soil, as explained previously, then a water-air-soil grains interface is of concern and it is very common to assume that in such a system the contact angle $a$ (at least under wetting condition) equals to zero. Moreover, the tensile force at an interface of pure water with atmospheric air equals to $T_s = 0.07275N/m$ at $20^oC$. Table 4.1 presents the calculated radius of the capillary tube corresponding to various RH values. All quantities are rounded within the closest order of magnitude.

We observe that even suction values in the order of $100kPa$ correspond to a really tiny radius for the forming menisci. It is really doubtful whether such a small radius can practically exist in nature. In addition to that, the required curvature at $1MPa$ is of the order of magnitude of $0.1\mu m$, smaller than the $2\mu m$ that is the assumed grain diameter corresponding to the transition from silts to clays. The aforementioned discussion indicates that the capillary model has strong limitations as from a practical point of view it can only explain soil suction in sands and marginally in some coarse silts.

In cohesive soils, suction is attributed to complicated physicochemical short-range

**Table 4.1:** Approximate suction and capillary radius values corresponding to various Relative Humidities.

| Relative Humidity | Suction | Radius (m) |
|---|---|---|
| 1.0 | 0 kPa | $\infty$ |
| 0.99999 | 1 kPa | $10^-4$ |
| 0.9999 | 100kPa | $10^-6$ |
| 0.999 | 1 MPa | $10^-7$ |
| 0.9 | 10 MPa | $10^-8$ |
| 0.5 | 100 MPa | $10^-9$ |

adsorptive phenomena taking place in the thin water layers surrounding the clay particles. Short-range adsorptive phenomena arise from electrical and Van der Walls force fields occurring within the vicinity of solid particles-water interface. Suction attributed to adsorptive phenomena does not correspond to an equal negative water pressure[2] and is better described through the thermodynamic potential.

At this point, we may state that soil suction has two different components, namely the **capillary suction** ($s_c$) and the **absorptive component of suction** ($s_a$). Their sum comprises the so called **matric suction** $s_m$:

$$s_m = s_c + s_a \tag{4.14}$$

Soils in nature are usually mixtures containing a wide variety of grain diameters and thus, both components of matric suction usually co-exist. The coarser a soil is the more important the capillary phenomena are, while on the contrary the more clayey a soil is the more dominant the absorptive phenomena become.

As already mentioned, suction can be also seen from a thermodynamic point of view as a potential. Thermodynamic potential $\psi$ represents the amount of work that must be done per unit mass of pure water in order to transport reversibly and isothermally an infinitesimal quantity of water from a reservoir of pure water at a specified elevation and gas pressure to the soil point under consideration (Gens 2010).

[2]Free water cannot withstand negative pressures higher than 100kPa as cavitation occurs.

In terms of thermodynamic potential, matric suction can be expressed as:

$$\psi_m = \psi_c + \psi_a \tag{4.15}$$

Thermodynamic potential controls water flow in any given soil system, with water flowing from regions of high water potential towards regions of low water potential.

#### 4.2.1.2 Osmotic phenomena and suction

In the discussed capillary tube model, pure water was assumed for the water-air-solid system. Nevertheless, natural soils scarcely contain pure water in their pores. Usually, impurities and dissolved solutes exist in the pore water phase. In such cases, an additional component of suction rises which is attributed to the salt concentration in the water phase. The water vapour in equilibrium with the pore water will have a partial vapour pressure that is affected both from capillary suction and from the salt concentration $w$; thus, it will be equal to $P_v(s,T,w)$.

We state from the beginning that when dissolved solutes exist in the pore water phase, soil suction has an additional component attributed to osmotic phenomena. It is called the osmotic suction $s_o$ (or osmotic component of suction) and we may write:

$$s_t = s_m + s_o \tag{4.16}$$

where $s_t$ the so called total suction, $s_m$ the matric suction and $s_o$ the osmotic suction. Using the psychrometric equation in the form of expression 4.10 we can rewrite equation 4.16 as:

$$\begin{aligned} s_t = s_m + s_o \Rightarrow \\ -\frac{RT}{M_w}\ln\frac{P_v(s,T,w)}{P_v(0,T,0)} = -\frac{RT}{M_w}\ln\frac{P_v(s,T,0)}{P_v(0,T,0)} - \frac{RT}{M_w}\ln\frac{P_v(0,T,w)}{P_v(0,T,0)} \end{aligned} \tag{4.17}$$

From equation 4.17, the definition of osmotic suction comes very naturally as the part of total suction controlled from the ratio of the water vapour pressure in a gas phase in equilibrium with a liquid containing a given concentration of dissolved salts to the saturated vapour pressure of the pure water. At this stage we shall recall the definition of relative humidity. Relative humidity is in fact the ratio of the absolute humidity in any given point in equilibrium with any solution to the absolute humidity in equilibrium with free water, at the same temperature. Thus, relative humidity in

the aforementioned expression corresponds to the vapour pressure ratio at the left part of equation 4.17. In simple words, relative humidity controls the total suction and the psychrometric equation is written as:

$$s_t = -\frac{RT}{M_w} \ln RH \tag{4.18}$$

Equation 4.18 was first derived in terms of thermodynamic potential in 1871 from William Thomson (also known as Lord Kelvin) and is called Kelvin's Equation.

In terms of thermodynamic potential, equation 4.16 can be simply written as[3]:

$$\psi_t = \psi_m + \psi_o \tag{4.19}$$

The role of osmotic suction in a soil system is better explained in terms of thermodynamic potential. In the previous section we discussed that potential represents energy per unit mass. From a practical point of view, equation 4.19 dictates that in order to dry a soil by extracting a molecule of pure water from its pore water (assumed to contain some concentration of salts), we need an increased amount of energy because apart from capillary or/and absorptive phenomena it is necessary to additionally overcome the osmotic potential which tries to resist in the imposed increase in its salt concentration.

It is obvious that in the aforementioned drying process, the existence of a semipermeable membrane is implied. When a soil is dried through relative humidity control, water is extracted in the form of water vapour and the water-air interface acts as a semipermeable membrane. On the other hand, when the soil is drained through direct water extraction, a solution and not pure water is extracted. Hence, the osmotic potential does not oppose to the water outflow and only the matric potential must be exceeded. The aforementioned difference is very important when it comes to methods for controlling or measuring the soil suction as depending on the method, either the total or the matric suction is measured/controlled.

Bardanis (2016) raises a very interesting discussion on whether the osmotic, capillary and absorptive suction are independent components of soil suction or not. He claims that in fact all the mechanisms contributing to soil suction have coupled effects. For instance, in a soil system where osmotic phenomena exist, the soil particles

[3]Total potential has also gravitational and inertia components, but in the current analyses have been neglected for brevity.

tend to come closer one to another. When adjacent soil particles come closer, the absorptive phenomena get stronger and thus matric suction rises.

In that respect, whenever soil suction is mentioned, the total soil suction should be implied. Total suction arises from different mechanisms which usually co-exist and interact, while in most of the cases the effect of each component cannot be totally separated. To that end, the terms capillary component, absorptive component and osmotic component of the total suction should be used instead of capillary, absorptive and osmotic suction.

#### 4.2.1.3 Suction measurement and control

Several methods for measuring soil suction have been developed. The most widely utilized are: the axis-translation technique (Richards 1941); the high air-entry tensiometers (Ridley & Burland 1993); the psychrometeres (Richards 1965); the porous blocks (Bouyoucos & Mick 1940), and; the filter paper technique (Chandler 1986).

Regarding suction control, suction can be imposed to a soil sample through various methods. Soil suction control is very important for measuring the water retention curve but also for common oedometer and triaxial testing under controlled suction conditions. The most common methods are: the axis translation technique; the osmotic method (Kassiff & Shalom 1971), and; the water solutions or relative humidity control method (Esteban 1990).

Suction measurement and control require specialized and usually expensive laboratory equipment, while they also involve time consuming processes. A detailed presentation and discussion of the various existing methods goes far beyond the scope of this Doctoral thesis and is not offered. The interested reader can refer to various related review papers and books (Fredlund & Rahardjo 1993; Lu & Likos 2004; Tarantino et al. 2009).

### 4.2.2 The Water Retention Curve

The **Water Retention Curve** (WRC) is the most fundamental relation in unsaturated soil mechanics. It links soil suction with the quantity of water existing in a soil system. Different entities can be used in describing the amount of water contained in a soil system. The gravimetric water content $w$, the degree of saturation $S_r$ and the

volumetric water content $\theta$[4] are usually utilized.

In the international literature, the water retention curve can be also answered as the Soil-Water Characteristic Curve (SWCC), with the name issue being still nowadays open to debate. Both terms have advantages and disadvantages. The term soil-water characteristic curve implies that the described relation is a characteristic of the soil. As explained in the following lines, the amount of water contained in a soil system under a given suction level additionally depends on the state of the soil (i.e., stress state and void ratio); thus, we cannot assume it as a characteristic. On the other side of the coin, the term water retention implies a relation describing the drying process of a soil, while both the drying and the wetting processes are important in soil mechanics and also differ. In the present dissertation, the WRC term is preferred as it is the prevailing term in the associated literature the last few years.

#### 4.2.2.1 Introducing the Water Retention Curve

To discuss the water retention curve of a material and its properties, the capillary tube model is utilized again. Instead of examining a single capillary tube, we now assume that a real soil is represented by a number of interconnected capillary tubes with different radius. In this case, water in each tube will rise to a different height above the free water surface (see figure 4.3), with the height of water rise depending on the radius of each tube.

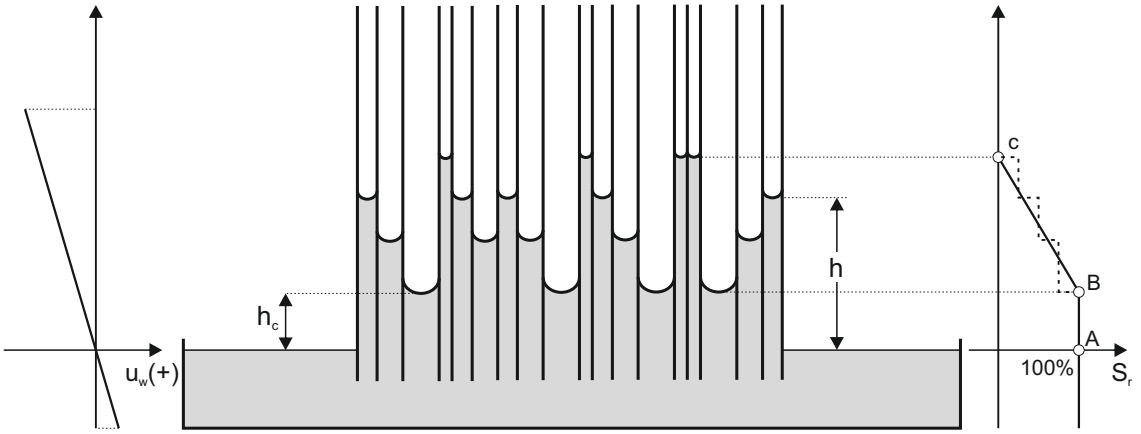


**Figure 4.3:** The capillary tube model and the effect of different capillary tube diameters on the water rise.

[4]The volumetric water content is defined as the ratio of the volume of water contained in a soil element to the total volume of the soil element, $\theta = \frac{V_w}{V} = S_r n = S_r \frac{e}{1+e}$, where $n$ the porosity and $e$ the void ratio.

On the left and the right part of figure 4.3 the variation of water pressure and of the degree of saturation corresponding to the presented capillary model are shown. We observe that the minimum water rise corresponds to the tubes (soil pores) with the larger diameter. Up to this level (point B), all tubes remain full with water (saturated) and this suction level corresponds to the maximum suction that the system can withstand before air enters the tubes with the larger diameter; thus, Point B corresponds to the so called Air Entry Value (AEV) of the material. For higher suction values degree of saturation gradually drops until the suction corresponding to the minimum tube diameter is reached where according to the capillary tube model the system gets completely dry (Point C).

Figure 4.4 plots the variation of degree of saturation ($S_r$) vs suction ($s$) corresponding to the simple capillary model examined. The thick two linear curve ABC corresponds to the water retention curve (WRC) of the idealized capillary tubes model[5]. We may distinguish two different Regimes. Regime I, extending from point A to point B where the soil remains saturated, with point B representing the air entry value mentioned above. It is evident that the smaller the radius of the bigger soil pore is (the finer the soil is) the higher its air entry value is and thus point B moves towards a higher suction.

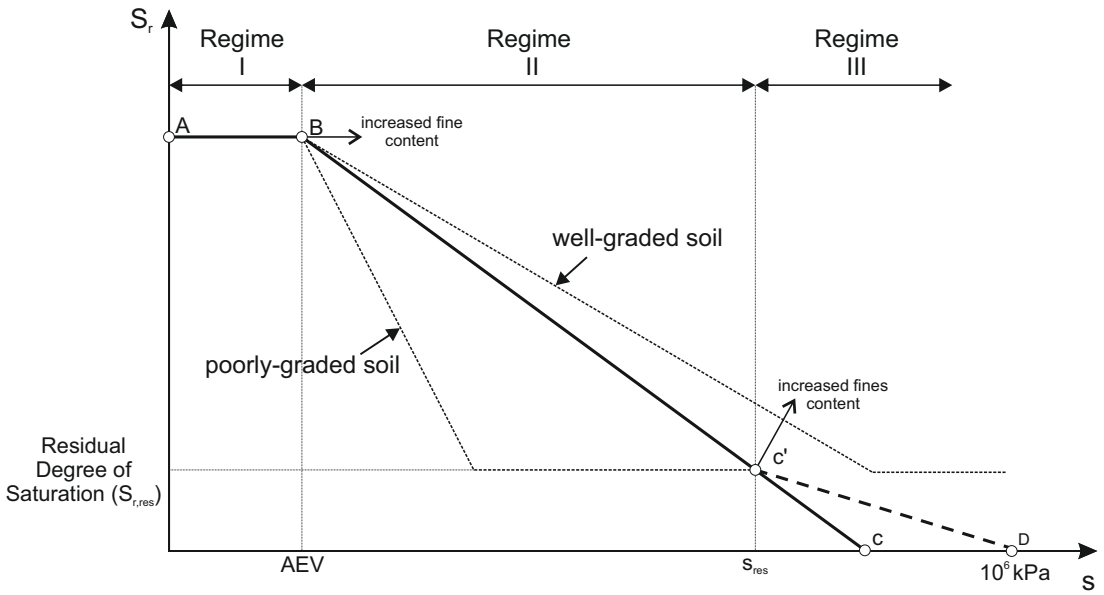


**Figure 4.4:** A simplified three-linear Water Retention Curve (WRC).

[5]It is assumed that the examined capillary tubes model contains a variety of different tube diameters, equally distributed.

When the soil starts to desaturate we enter the second regime (Regime II), where water content drops following the increasing suction. The more well-graded a soil is, the less intense the aforementioned water content decrease is. In other words, a poorly-graded soil will exhibit a sudden drop in its water content, reflected by a steeper curve in Regime II. For the capillary tubes model, Regime II extends up to point C where the system gets completely dry. Nevertheless, in reality soils retain a certain amount of water even when the suction corresponding to their smaller pore diameter is reached. This water content is usually attributed to water in the form of thin layers surrounding the finer grains or clay particles and is mainly associated with absorptive phenomena.

Thus, a rigorous representation of the water retention curve calls for a three linear model ABC′D, where point C′ represents the so called residual degree of saturation $S_{r,res}$ and the associated suction is called the residual degree of saturation suction $s_{res}$. The term residual implies that a quantity of water remains in the soil system despite the fact that suction is still increased. This statement is both true and false at the same time. For practical applications, the residual water content usually describes the maximum water content that can be extracted from a soil system if it is left to air dry (atmospheric conditions) and it is of great importance in common geotechnical applications.

On the other hand, from a thermodynamic point of view, water can still be extracted from the soil system provided that a total potential corresponding to a suction level higher than $s_{res}$ is applied. Practically, this is realized through the application of huge thermal loads[6]. Applying the laws of thermodynamics, it is proved that any soil specimen gets completely dry for a total potential corresponding to a suction level equal to $s = 10^6 kPa$. (Fredlund 2006).

In that respect, at the idealized three-linear WRC model, for the third regime (Regime III), we may assume either a constant water content or a gradual decrease towards zero water content at a suction value of $10^6 kPa$. Regarding the position of point C′ experimental observation suggest that finer a soil is, the higher both the residual water content and the corresponding suction will be. This is reflected in the WRC as an offset of point C′ towards a higher suction and a higher water content. For instance, Lu & Likos (2004) report that the residual water content in terms of gravimetric water content can range from as low as 2% for sands up to 25% for

[6]Wet clay, when exposed to a huge thermal load in a furnace, it solidifies, as is the case in pottery or in the brick construction industry.

expansive clays.

The three linear model discussed hereinbefore is an idealized water retention curve useful in clarifying the various mechanisms associated with water retention in a soil system. In real life though, the experimentally determined WRC usually obtains the shape of a continuous reverse sigmoidal curve, as the one depicted in figure 4.5 We

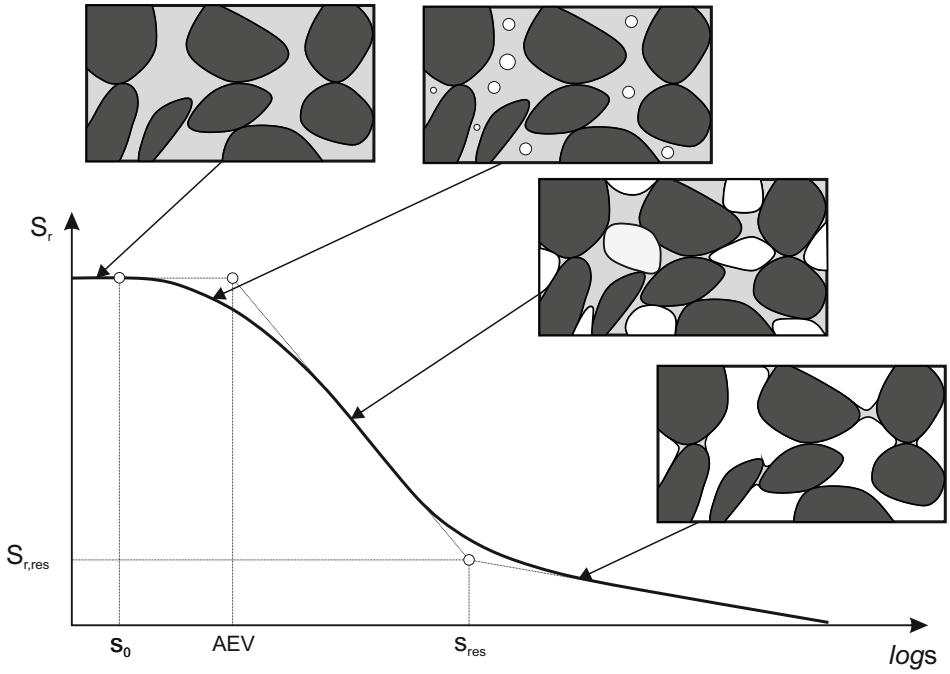


**Figure 4.5:** A typical reverse sigmoidal WRC in the $S_r - \log s$ together with a schematic representation of the coexistence of the water, air and solid phases.

observe that both the transition between Regimes I and II as well as the transition between Regimes II and III happens gradually. This is attributed to an ensemble of reasons. For the transition between Regimes I and II, the gradual drop of degree of saturation is attributed to the gradual appearance of air in the water phase in the form of occluded air, even for suction values lower than the AEV of the material. Two characteristic points are identified in this transition. The first one corresponds to the suction level where degree of saturation starts to reduce and it is usually mentioned as the desaturation suction $s_0$. The second point corresponds to the intersection of the linear branches of the WRC in Regimes I and II and it is usually assumed representative of the AEV of the material[7]. Regarding the transition between Regimes II and III, the smooth shape of the WRC is attributed to the gradual fade out of the capillary phenomena in favour of the absorptive phenomena. In a similar fashion to

[7]In the idealized capillary model the desaturation suction and the AEV coincide.

the AEV, a residual water content point is identified by the intersection of the WRC's linear branches in Regimes II and III.

Figure 4.5 also includes a schematic representation of the co-existence of the various phases in the soil skeleton. These simple sketches are quite illustrative of the link between the various parts of the WRC and the hydromechanical behaviour of unsaturated soils. The following areas of common behaviour can be identified.

- For suction levels below the desaturation suction $s_o$, the soil remains practically saturated and classical soil mechanics theories describe the soil behaviour (i.e., Terzaghi effective stress principle is valid).

- In the transition between Regime I and II, the soil is unsaturated. Air is present in the voids, but the air phase is discontinuous. Water flows through the water phase following Darcy's law.

- In Regime II, both the air and the water phase are continuous and water flows preferably through the water phase, although some transfer of water in the form of water vapour also occurs, especially as suction approaches $s_{res}$. The mechanical behaviour cannot be explained using classical soil mechanics. As discussed in a following section, the effective stress principle does not apply and two stress variables are needed for a rigorous description of the soil behaviour.

- When the water content drops below the residual water content, the water phase loses its continuity and water transfer takes place exclusively through the air phase in the form of water vapours. Fick's law describes this water vapour flow.

In the previous lines, the degree of saturation $S_r$ was mainly used as the water content representative. An almost similar WRC is obtained even if the gravimetric ($w$) or the volumetric water content ($\theta$) are plotted with suction. Small differences in the shape of the WRC derive from the fact that $w$ and $\theta$ depend on the void ratio. For instance, if we examine a WRC in terms of the gravimetric water content the initial part of the curve (Regime I) will not be horizontal. This is due to the fact that an increase in suction, in a saturated soil element, corresponds to an increase in the effective stress and produces a decrease in the void ratio. In this case, the gravimetric water content reduces despite the constant $S_r$. Nevertheless, such small differences do not alter the basic characteristics of the WRC as these where discussed hereinbefore.

The soil suction used in plotting the WRC corresponds always to the total suction. Nevertheless, regarding common laboratory practise, the WRC is usually measured

by utilizing the axis-translation technique to impose suction up to $1500kPa$ and relative humidity control techniques for higher suction levels. In the axis-translation technique water is directly extracted from the water pores and thus matric suction is controlled. On the other hand, through relative humidity control a total suction is imposed as water transfer is realized through water vapour. This difference in the utilized methods may raise doubt on the validity and consistence of the obtained data.

Fredlund (2006) mentions that such an inconsistency in the measurement techniques not only is not problematic but in fact favours proper simulation of practical geotechnical problems. This is due to the fact that usually suction levels up to $1500kPa$ are associated with Regime I and the lower suction parts of Regime II where practically water flow takes place through the water phase and is thus controlled by the matric suction, while on the other hand through relative humidity control, the part of the WRC close to the residual water content is usually obtained, resembling the water transfer mechanics prevailing in practical applications as well.

#### 4.2.2.2 Drying vs Wetting - Hysteresis of the WRC

In the previous paragraph, water retention curve was introduced by implying and discussing a drying process, where the soil water content is gradually reduced by applying an increasing suction. In common geotechnical applications though both drying and wetting of soils are important, while usually the WRCs corresponding to drying and wetting differ. This difference is called the hysteresis of the WRC.

Hysteresis is mainly reflected in the relevant position of the wetting and the drying branches of the WRC, with the drying branch plotting above and to the right of the wetting branch, representing the increased capacity of a given soil to retain water under a given suction level when dried. Fredlund (2006) reports the drying and wetting WRC branches of a sandy soil, the Beaver Creek sand (fig. 4.6a) and of a processed silt (fig. 4.6b). Apart from the apparent hysteresis in the behaviour it is also interesting to observe the increased values of the AEV and of the residual water content that the silty soil exhibits compared to the Beaver Creek sand, in accordance to what was described in the previous section.

Figure 4.7 presents the main characteristics of a hysteretic WRC. We shall focus on the thick black lines. Curve 1 corresponds to the initial drying of a fully saturated soil sample. We observe that, if we subsequently gradually wet this soil sample,

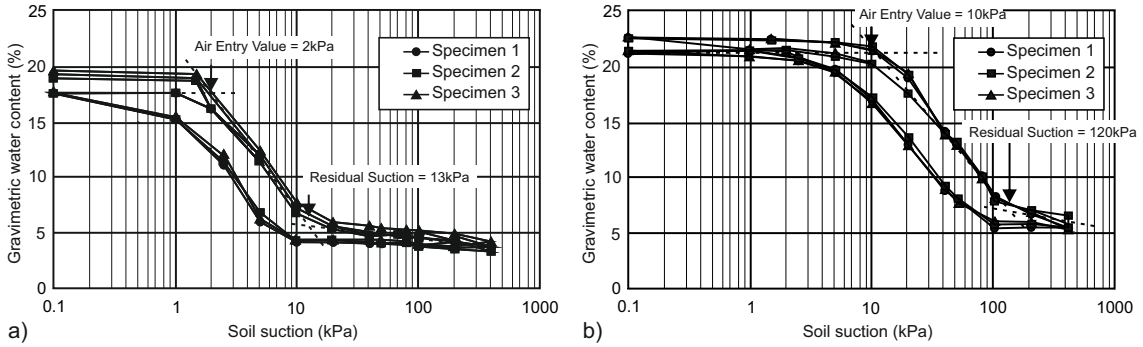


**Figure 4.6:** Measured drying and wetting WRCs from; a) Beaver Creek sand samples and b) Processed Silt's samples after Pham (2002). (Fredlund 2006)

another curve is obtained (curve 2), the so called main wetting curve, which reveals the soil's decreased ability to acquire water as it is gradually wetted.

If the soil is subsequently once again dried, then another wetting curve will be obtained (curve 3), the so called main drying curve. If the soil is then continuously subjected to subsequent wetting and drying paths and additionally; a) the imposed suction within the cycles ranges from zero to maximum and vice versa, and; b) no irreversible (plastic) volumetric deformation occurs, then theoretically the same WRC's branches will be obtained. On the other hand, if we suppose that wetting is stopped at a suction value $s_1$ corresponding to a volumetric water content equal to $\theta_1$ and then the soil is dried again, the water content variation will follow a WRC sub-branch, until the main drying branch is reached and then for further drying it will again follow the main drying branch. A similar behaviour is observed during wetting from an intermediate suction level. These intermediate drying-wetting branches are called scanning curves.

The hysteresis observed between the main branches of the WRC can be attributed to the following two mechanisms, both associated with the capillary component of suction.

1. The so called "ink-bottle" effect. The ink-bottle effect rises from irregularities in the cross-sections of the void passages. In more detail, if we examine once again the capillary model used in the previous section, in a real soil system pores of different radius can be interconnected in many different ways. Thus, a more detailed capillary model should include capillary tubes with a varying diameter instead of just tubes with different but constant diameters. Such a capillary tube is portrayed in figure 4.8a. It is observed that as water rises in

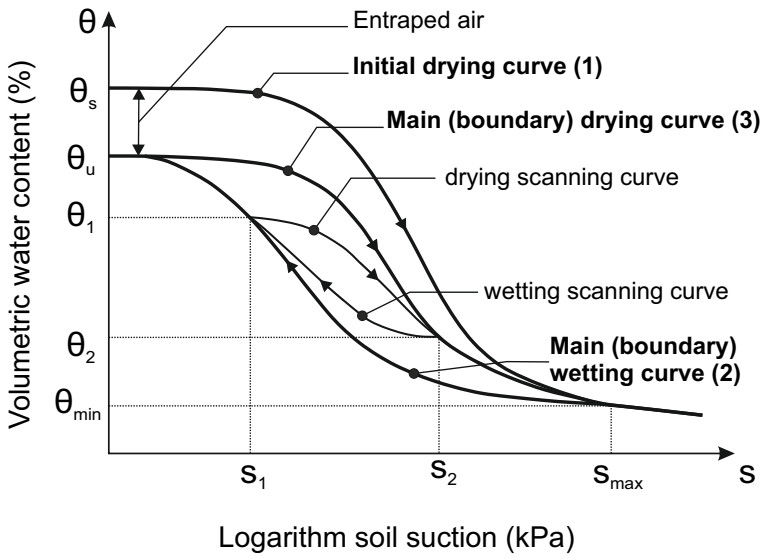


**Figure 4.7:** A hysteretic WRC model. (Pham et al. 2005)

the capillary tube (wetting process), the height of capillary rise is controlled by the radius of the wider part of the tube, while pores which theoretically should be filled with water (they correspond to a smaller diameter) remail dry. On the contrary, if the tube was initially filled with water and left to dry (drying process), the wider part of the tube can still remain filled with water as in this case, the capillary height is controlled by the radius of the narrower, upper part of the tube.

2. The difference in the contact angle $a$ of the air-water-solid interface between drying and wetting conditions. To understand this mechanism we need to recall the shape that a water drop usually obtains when it moves on any given hydrophilic surface[8]. As depicted in figure 4.8b, the contact angle at the drop's tail is almost approaching zero, while at the wetting front a significantly higher contact angle exists. Lu & Likos (2004) mention contact angles as high as $65^o$ for the wetting front. If we recall that according to equation 4.5, suction and the corresponding height of capillary rise are proportional to the $\cos a$, it is apparent that the capillary rise and the corresponding amount of water will be different.

The fact that the aforementioned mechanisms are linked to capillary phenomena explains also why hysteresis is mainly profound in the WRC's Regime II.

[8]Soil grains and clay particles are in most of the cases hydrophilic.

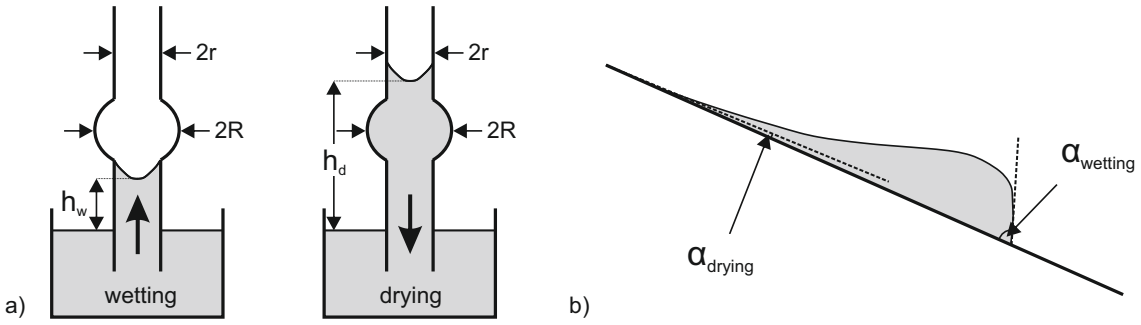


**Figure 4.8:** a) The "ink-bottle" effect and; b) the wetting front and the drying tail of a typical water drop. (Bardanis 2016)

Regarding the hysteresis observed between the initial drying curve and subsequent wetting curves, the following two additional factors contribute.

1. Entrapped air in the form of occluded air. As already mentioned, in a soil system that is gradually dried, at some point and for relatively low suction values, occluded air will appear in the water phase. Air bubbles cannot fully dissolve in the water phase when the soil is just wetted (suction reduces to zero), unless a relatively high positive water pressure is applied (i.e., the back-pressure in common triaxial laboratory tests).

2. Absorptive phenomena. In clayey soils, during the virgin drying of an initially saturated soil sample, some of the water that exists in the vicinity of clay particles, mainly in the form of free water but also to some extend as absorbed water, will be extracted. The clay particles will come closer and the short-range electrical and Van der Walls forces will become stronger. During a subsequent wetting water cannot anymore enter in-between these particles, resulting to an overall reduced water content. This mechanism is reflected only when the WRC is plotted in terms of the gravimetric or the volumetric water content.

#### 4.2.2.3 The effect of soil structure on the WRC

Preconsolidation, dynamic compaction, ageing, cementation, thixotropy are some of the most common soil structure inducing mechanisms. The effect of structure is usually profound in the water retention characteristics of a soil as well. We may say that structured soils exhibit an increased water retention capacity compared to their structureless (intrinsic) counterparts. This is mainly attributed to the fact that structured soils, under a given stress and suction state maintain a reduced void ratio,

with respect to their intrinsic void ratio at the same state. Recalling the capillary tubes model we may easily understand that the smaller the void ratio (smaller pores), the higher the water content retained in a soil system, as capillary phenomena become more intense. Nevertheless, the way in which the WRC is affected by structure, depends also on the structure inducing mechanism. For this reason the effect of preconsolidation, compaction as well as the behaviour of natural soil are separately examined in the following paragraphs.

### Effect of preconsolidation

Figure 4.9 presents the WRCs of reconstituted silt samples compressed at different stress levels. The results indicate that the higher the preconsolidation pressure, the higher the degree of saturation $S_r$ measured under a given suction value. The water retention curve is usually measured under zero total stress on zero applied stress samples, unloaded from the maximum applied stress. The void ratio of such unloaded samples depends on the applied preconsolidation pressure, while the higher the preconsolidation pressure the smaller the void ratio during unloading. The results of figure 4.9 clearly indicate that the increase in the preconsolidation pressure and the corresponding decrease in void ratio, leads to an increased water retention. When degree of saturation is used to represent the water content, this effect is reflected in the offset of the WRC towards higher suction levels.

A more thorough investigation of the results reveals that the air entry value clearly increases with the decrease in void ratio while the slope of the WRC in Regime II seems almost unaffected. The residual water content is also slightly affected but the effect of a void ratio increase seems to fade out as we move towards higher suction values. The aforementioned behaviour is mainly attributed to the fact that the pore volume (void ratio) governs the intensity of capillary phenomena will absorptive phenomena appear rather independent.

It is important to mention that the effect of an evolving void ratio on the shape of the WRC depends on the water content parameter used. For instance, both the volumetric and the gravimetric water content are functions of the void ratio and thus a simultaneous evolution of degree of saturation and void ratio has coupled effect on the calculated values of $w$ and $theta$. To give an example, if the gravimetric water content is examined, it turns out that under a given suction level, a decreasing void ratio corresponds to an increasing degree of saturation $S_r$. Whether this increase results

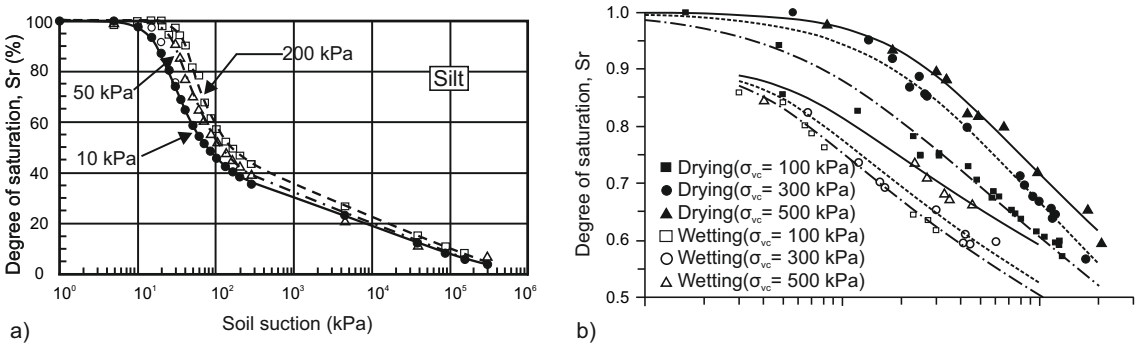


**Figure 4.9:** The effect of preconsolidation on the WRC of; a) a silty soil after Huang (1994), as reported in Barbour (1998) and b) of Barcelona Silt after Tarantino et al. (2009).

to an increasing, decreasing or even constant gravimetric water content depends on the initial value and the applied increment of the aforementioned quantities.

In other words we may say that we cannot a priory define the effect of an evolving void ratio in the relative position of the WRC when the latter is described in terms of $w$ or $\theta$. Figure 4.10a presents the WRCs under different vertical preconsolidation stress in terms of the gravimetric water content $w$ for Regina clay samples and figure 4.10b in terms of the water ratio $e_w$ for Barcelona Clay Silt samples. The water ratio $e_w$ is defined as $e_w = \frac{V_w}{V_w} = wG_s$ and thus, due to the $G_s$ being a constant, it also represents changes of the gravimetric water content. We may observe that in the first case $w$ significantly reduces with compression and thus with a decrease in void ratio, while in the second case the WRC seems practically unaffected from the applied preconsolidation pressure.

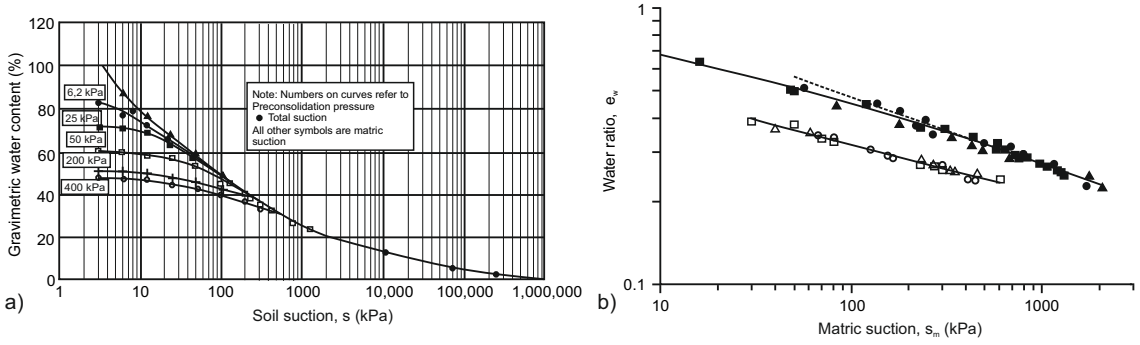


**Figure 4.10:** a) Gravimetric water content vs suction for reconstituted Regina clay, after Fredlund (2006) and; b) water ratio vs suction for the Barcelona silt of figure 4.9b, after Tarantino et al. (2009).

The dependance of the WRCs on void ratio, as described hereinbefore, is in fact

the dependance on the initial void ratio of the sample after unloading and before being progressively dried to measure the WRC. In fact, void ratio also changes during suction application (decreases in most of the times). Hence, the aforementioned water retention curves do not comprise constant void ratio WRCs but instead they are constant total stress WRCs. Various researchers have tried to reconstruct actual constant void ratio WRCs. They usually utilize available results from constant total stress measurements to define the void ratio corresponding to various $S_r - s$ combinations, and then correlate similar void ratio values to reproduce a theoretical constant volume WRCs[9]. Figure 4.11 presents such theoretical constant void ratio WRCs together with the actual WRC of the deformable soil as measured under a constant zero total stress.

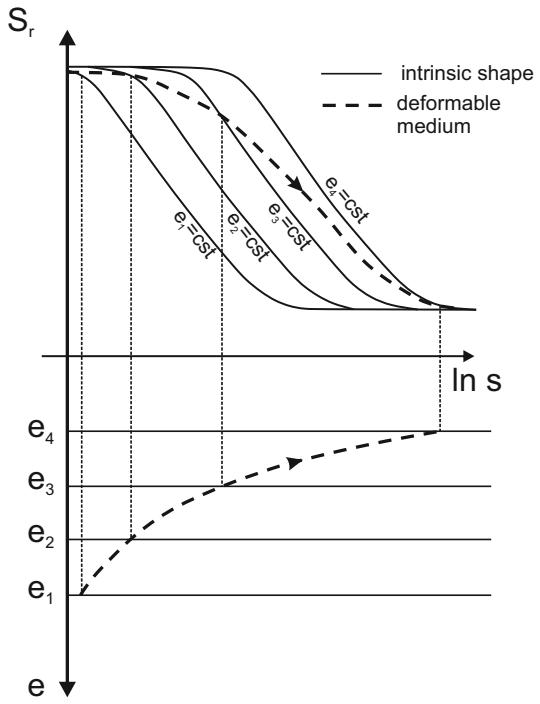


**Figure 4.11:** A schematic comparison of the WRC of a deformable porous medium together with constant void ratio contours. (Nuth & Laloui 2008a)

### Effect of compaction

Compacted soils are usually formed through static or dynamic compaction of an initially remolded soil. Compactions takes place under a constant water which is far

[9]Such constant void ratio WRCs are sometimes called intrinsic, nevertheless this term will not be used in the present dissertation to avoid confusion with intrinsic material states.

below the saturated water content, otherwise the soil skeleton would be incompressible. The standard Proctor Test is used in the laboratory to define the optimum water content that corresponds to the higher dry density that can be obtained under a given compaction energy. Soils containing a significant amount of clay obtain different fabrics depending on whether compaction takes place at a water content higher (wet of optimum) or lower (dry of optimum) compared to the optimum water content. This difference in soil fabric plays a significant role in their water retention properties.

Delage et al. (1996) were amongst the first to study in a systematic manner the fabric obtain by compacted soils using Mercury Intrusion Porosimetry (MIP) techniques together with images obtained through Electron Scanning Microscopes (ESM). Figure 4.12 presents MIP results which show the distribution (population) of different pore sizes in compacted Jossigny Silt samples. We can observe that the soil sample initially compacted at the wet of optimum has a single pore size distribution depicted as a single peak in the relevant curve. On the other hand, the sample compacted at the the wet of optimum has exhibits a clear bi-modal distribution as a second peak appears. Finally, regarding the sample compacted at the optimum water content, it practically exhibits a similar distribution with its wet of optimum counterpart. Similar results have been reported by various authors (i.e., Vanapalli et al. (1999) Romero et al. (1999) Monroy et al. (2009) Casini et al. (2012)).

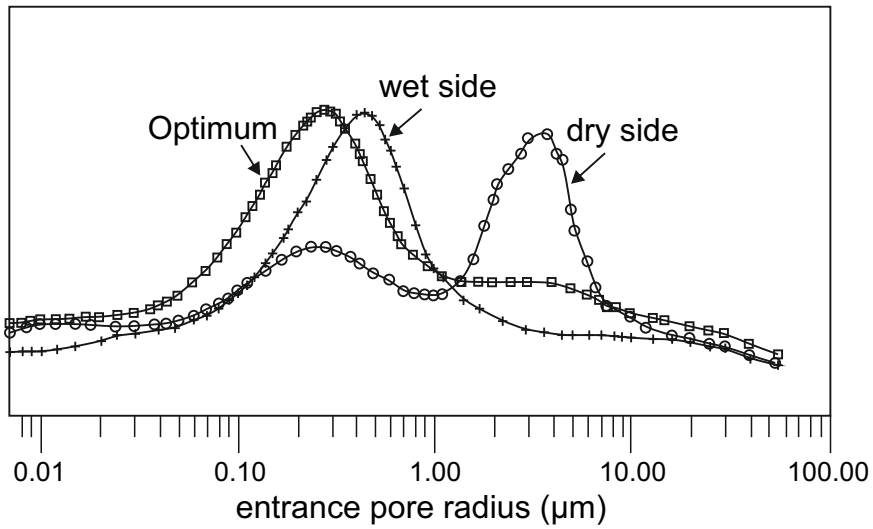


**Figure 4.12:** Porous size distribution curves for soil samples compacted at the dry of the optimum, optimum and wet of optimum water content. (Delage et al. 1996)

The observed differences in soil fabric are mainly attributed to the forming clay aggregates during initial remolding. In more detail, Delage et al. (1996) attribute

the observed difference in the inter-particle forces arising from capillary phenomena. When a soil is compacted at the dry of optimum the water content is low and the corresponding suction high. The associated strong inter-particles forces prevent the clay particles from breaking with compaction. Thus, a double porosity fabric appears with smaller voids within the aggregates (micro-structure) and larger voids between the soil aggregates (macro-structure). As water content increases and the corresponding suction decreases the aforementioned interparticle forces become weaker; in this case, the compaction energy is large enough to crash the soil aggregates, resulting to a single distribution with prevailing smaller micro-pores. As expected, soils compacted at the optimum water content are located somewhere in between and usually closer to the fabric of the wet of optimum samples.

Casini et al. (2012) doubt that the different pore distributions arise during compaction. Instead, they claim that the different fabric forms during remolding when the soil is mixed with water. They propose that in samples remoulded at an increased water content they clay aggregates tend to swell, as there is more water to be absorbed, and this process squeezes the larger macro-pores. They also report that the use of saline water is in favour of a double porosity.

Fabric differences may raise some phenomenologically bizarre results regarding the water retention behaviour. Vanapalli et al. (1999) measured the WRCs for a statically compacted sandy clay till from Canada. Figure 4.13a presents the WRCs of samples compacted at the wet of optimum, optimum and dry of optimum water content, all under the same compaction stress. If we assume that the void ratio is the only factor influencing the water retention capability of a given soil, then according to what was described in the previous paragraph we should expect the soil sample at the optimum to exhibit the higher water retention as it corresponds to the minimum void ratio (maximum density). Nevertheless, experimental results indicate that under a specific compaction energy and a given suction level, the sample compacted at the wet of optimum retains more water followed by the one compacted under the optimum water content, while the sample compacted at the dry of optimum exhibits the lowest degree of saturation.

Figures 4.13 b, c and d present the WRCs for samples compacted at different stress levels grouped for the corresponding compaction water content. We may clearly notice that while the “dry of optimum” and “optimum” soil samples exhibit a significant dependance of the WRC properties on the compaction stress and thus at the obtained

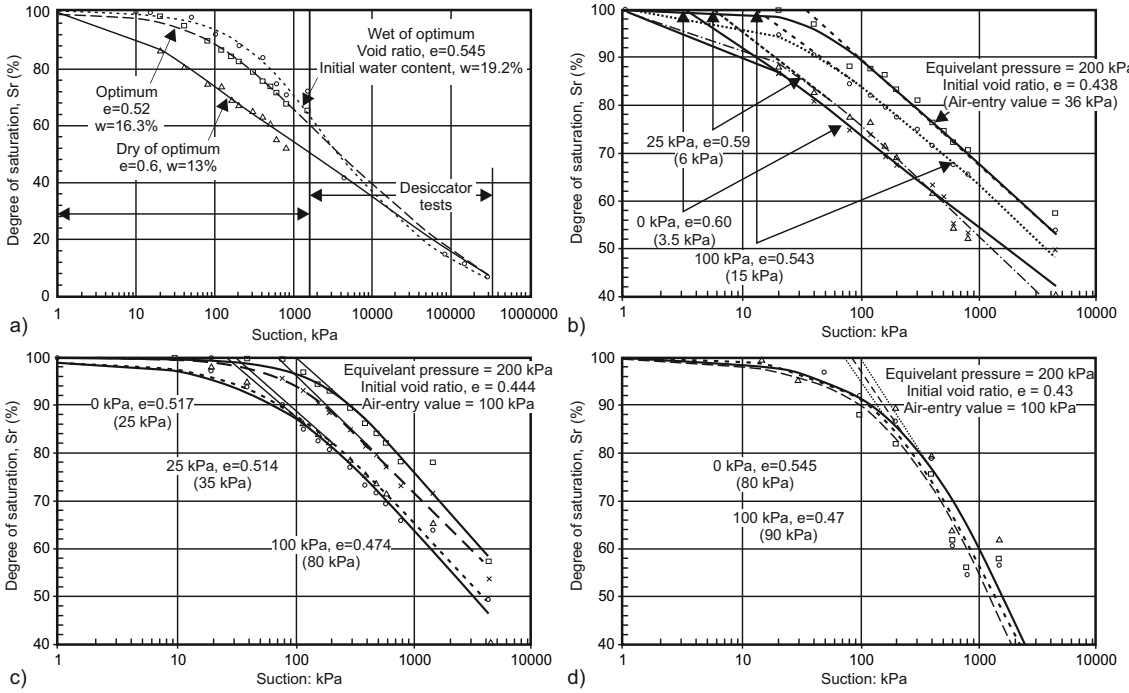


**Figure 4.13:** WRCs for a compacted sandy clay till from Canada. The effect of different; a) compaction water contents, together with the effect of different compaction stress level for samples compacted at the dry of optimum in (b), optimum water content in (c) and wet of optimum in (d). (Vanapalli et al. 1999)

void ratio, to the contrary the "wet of optimum" samples exhibit a negligible dependence on the compaction stress. This is easily explained by the difference in fabric. As already mentioned, the void ratio WRC dependence is mainly due to evolving capillarity. Capillary phenomena are primarily linked with the water of the larger macro-pores formed between the clay clods, mainly profound at soils compacted at the dry of optimum, while additionally compaction has a limited influence on the reduction of micro-porosity but it significantly reduces the larger macro-pores.

Romero et al. (1999) studied the water retention properties of compacted Boom Clay samples. They compared the WRCs corresponding to two different samples, remoulded at the same water content (dry of optimum), but compacted under two different stress levels. Figure 4.14 presents the main drying and wetting paths as measured for the two different samples. Note that the gravimetric water content $w$ reduces with increased compaction stress upon reaching a suction level equal to approximately $2MPa$, while for higher suction the same curve is practically obtained. They distinguished between two different suction regimes: a) the intra-aggregate gov-

erning suction regime, where mainly absorption phenomena in the micro-pores of clay aggregates dominate and are not influenced from the compaction level, and; b) the inter-aggregate governing suction regime where capillary phenomena in the larger macro-pores prevail and are severally affected from the compaction level. We shall mention that the aforementioned different regimes are quite clear when results in terms of $w$ or $\theta$ are examined, while to the contrary they cannot be easily identified when WRCs are plotted in terms of degree of saturation $S_r$ (see fig. 4.14b). The reduction of the larger macro-pores with compaction is also clearly depicted in the MIP results corresponding to the two examined compaction levels (see fig. 4.15).

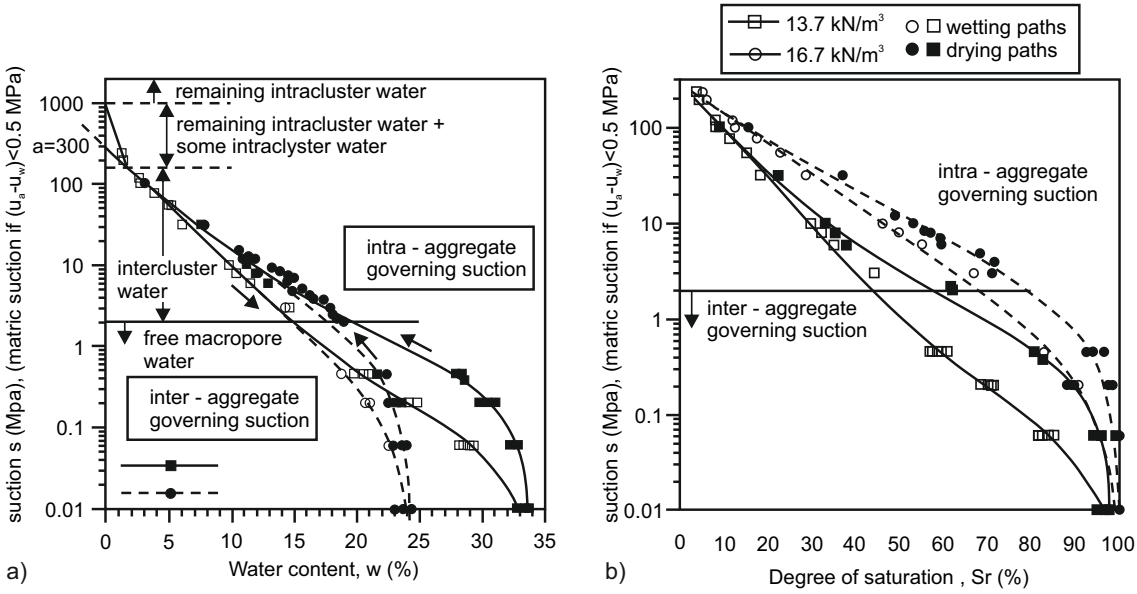


**Figure 4.14:** Effect of different soil fabric on the WRC of compacted Boom clay; a) in terms of the gravimetric water content ($w$), and in; b) in terms of the degree of saturation ($S_r$). (Romero et al. 1999)

### Natural soils

In the previous lines, we mainly emphasized on how water retention properties are influenced by compression and compaction of reconstituted and remoulded soils respectively. However, natural soils may posses structure also due to other agents like cementation, thixotropy, ageing etc. Bardanis & Kavvadas (2005) and Bardanis & Grifiza (2011) measured the WRCs of two clayey soils from Greece. The Corinth Marl, a low plasticity clayey silt, and the Chalkoytsi Marl, a low plasticity clay, both soils having a high calcite content (over 60%) which is in favor of cementation

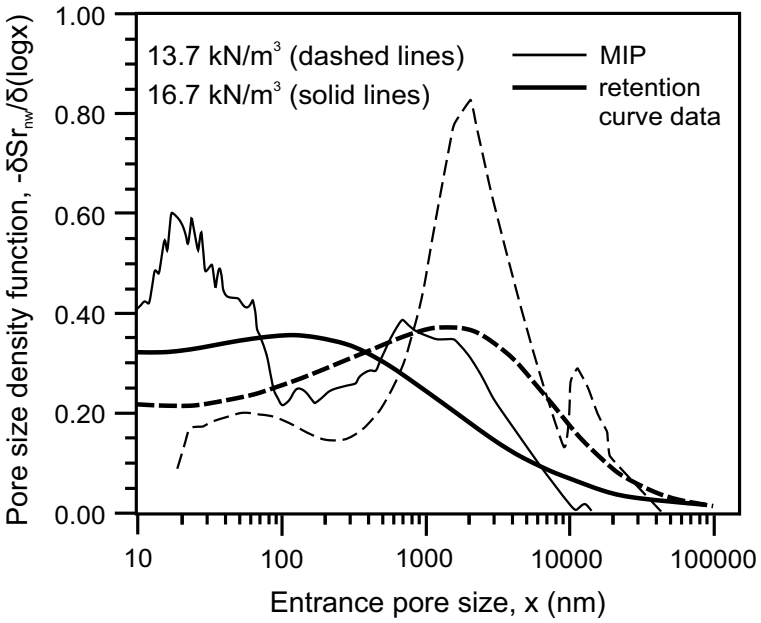


**Figure 4.15:** The pore size distribution, regarding the different soil fabrics of the compacted Boom clay of fig 4.14. (Romero et al. 1999)

bonding. The obtained WRCs corresponding to both natural and recomposed samples are compared, with recomposed samples referring to soil specimens that have been initially reconstituted in slurry, then consolidated to their in-situ void ratio or stress level and finally unloaded prior to drying. Figure 4.16 presents the obtained results in terms of both the gravimetric water content $w$ and the degree of saturation $S_r$. The corresponding variation of void ratio with suction, the so called shrinkage curve, is also included.

We observe that in the case of the Corinth Marl, despite the appreciable scatter of the results, a clear tendency for an increased water retention is profound for the natural material compared with its recomposed partner. It should be mentioned that the compared samples have similar void ratios almost at every suction level. On the other hand, the natural Chalkoutsi Marl samples at first sight seem incapable of retaining a higher water content under a given suction level, as the results of the recomposed and the natural samples coincide. Nevertheless a more detailed study of the results reveals that the void ratio of the recomposed samples is significantly lower. Thus, the results are not fully comparable and it is quite reasonable to assume that the WRC of the recomposed material would be sifted towards lower suction values if samples under the same void ratio were examined. At this point, based on the limited available results, we may state that there exist strong evidence indicating that natural

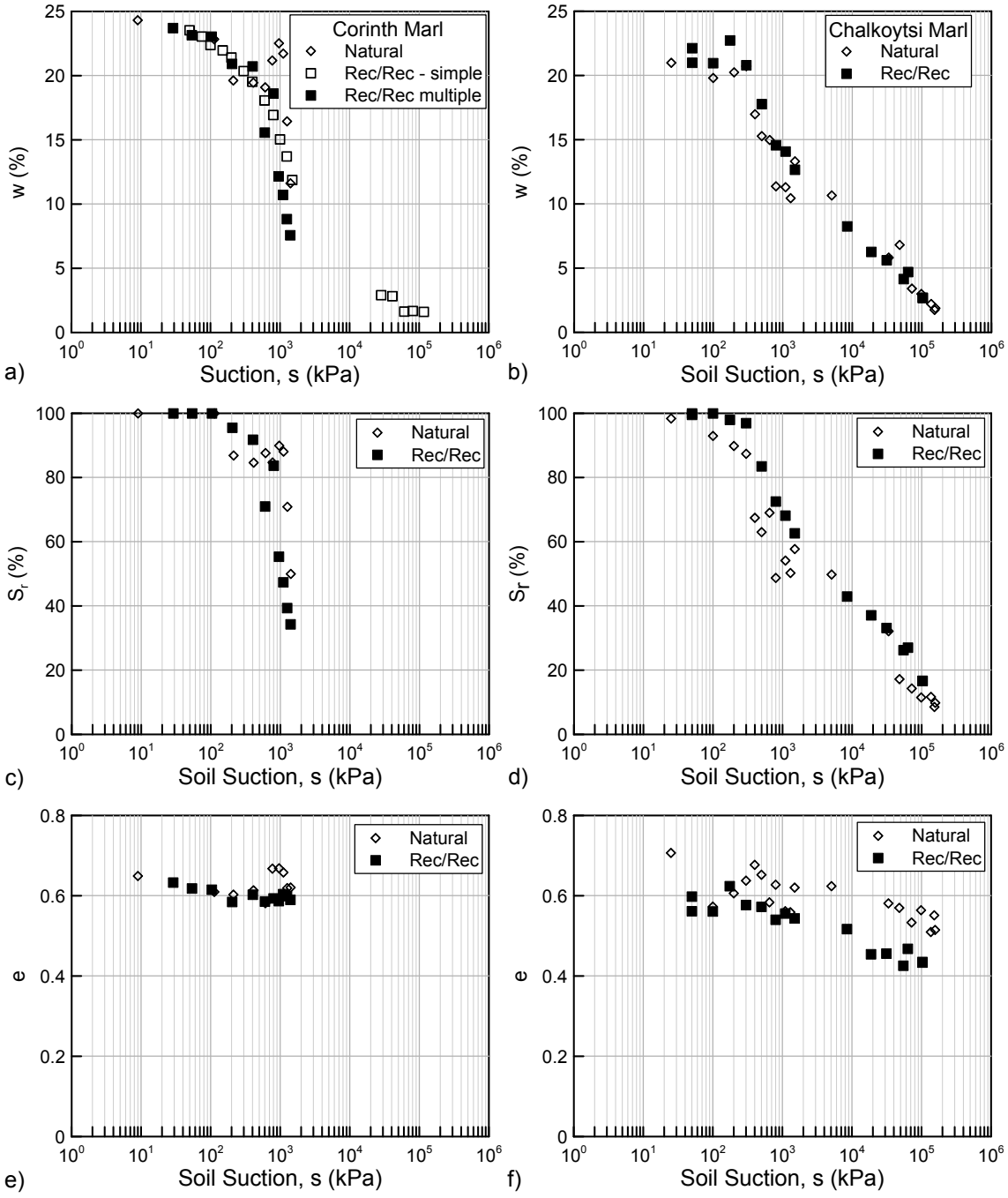


**Figure 4.16:** WRCs of recomposed and natural Corinth Marl (a,c) and Chalkoutsi Marl (b,d) soil samples, together with the corresponding evolution of the void ratio with suction in plots (e) and (f) respectively. Data from Bardanis & Grifiza (2011).

soils can retain an increased amount of water compared with recomposed samples under the same void ratio and suction level. Nevertheless more well documented results are necessary, before solid conclusions can be drawn.

#### 4.2.2.4 Water Retention Mathematical Models

As already mentioned, the WRC is the most fundamental relation in unsaturated soil mechanics. Even nowadays undertaking extensive laboratory tests to define the WRC is an expensive and time-consuming process. Laboratory measurement of the WRC usually requires the utilization of more than one techniques, as different methods apply for different suction levels. Even when such results are available they are usually consisting of a series of discrete data points limited over a small portion of the whole suction range or several portions with large gaps in between depending on the number and type of the utilized suction control methods.

At the same time, knowledge of the WRC is necessary to study the shear strength, deformation and water flow in unsaturated porous media. For numerical applications it is essential to describe the WRC through suitable mathematical equations which provide the relation between water content and suction, while preferably their equations should be continuous and continuously differentiable as well.

Various researchers have proposed suitable mathematical expressions to reproduce a reverse sigmoidal curve in the water content - suction plane. Such mathematical expressions are usually called Water Retention Models (WRMs). The minimum number of parameters (unknowns) needed to mathematically describe a reverse sigmoidal curve is three (3). Nevertheless, some researches reduce the required parameters by correlating two of their parameters, assuming a constant relationship. Some of the most recently proposed WRMs can take into account the dependance of the WRC on void ratio and hysteretic effects as well.

Table 4.2 presents some of the most popular simple (no void ratio dependance or hysterisis) WRMs. These models were initially proposed mainly to describe the relation between the volumetric water content $\theta$ and suction $s$. Nevertheless, from a mathematical point of view they are simply suitable mathematical expressions which describe a reverse sigmoidal curve. In that respect, their use can be generalized to any suitable dimensionless variable representing water content ($WC$), as far as this variable is suitably normalized to correspond to unity when the material is fully saturated and to zero when the material is totally dried. Only models that incorporate a continuous and continuously differentiable equation are included in the present review.

The Fredlund & Xing (F&X) and the Van Genuchten models include three parameters: $a$; $n$; and; $m$, while the rest of the models only two: $a$ snd; $n$. Parameter $a$

**Table 4.2:** Simple Water Retention Models (WRMs), including continuous and continuously differentiable equations.

| Equation | Reference |
|---|---|
| $WC = C(s)\frac{1}{\left[\ln\left(e+\left(\frac{s}{a}\right)^n\right)\right]^m}$ [*1] | Fredlund & Xing (1994) |
| $WC = \frac{1}{[1+(as)^n]^m}$ | Van Genuchten (1980) |
| $WC = \frac{1}{[1+(as)^n]^{\left(1-\frac{2}{n}\right)}}$ | Burdine et al. (1953) |
| $WC = \frac{1}{[1+(as)^n]}$ | Brutsaert (1966) |
| $WC = \frac{1}{[1+(as)^n]^{\left(1-\frac{1}{n}\right)}}$ | Mualem (1976) |

[*1] $e$ is the base of the natural logarithm and should not be confused with void ratio.

(or its inverse $1/a$ in the F&X model) controls the first inflection point of the WRC close to the air entry value. Parameter $n$ controls the slope of the WRC in Regime II, between the AEV and the residual water content, while parameter $m$ controls the shape of the WRC at the second inflection point near the residual water content.

In the Burdine, Brutsaert and Mualem equations, the third parameter is emitted. Comparing them with the Van Genuchten equation we may observe that in fact the same expression is adopted, while different assumptions are made with respect to the third parameter $m$. Van-Genuchted equation includes parameter $m$ as an individual additional curve fitting parameter; Burdine and Mualem correlated it with parameter $n$, while Brutsaert emitted it (in fact he assumes that it is equal to unity).

The factor $C(s)$ appearing in the F&X model is given by the following expression:

$$C(s) = 1 - \frac{\ln 1 + \frac{s}{s_r}}{\ln 1 + \frac{1{,}000{,}0000}{s_r}} \tag{4.20}$$

where $s_r$ the suction corresponding to the residual water content. It is used to enforce the WRC through zero water content at $1,000,000kPa$ for thermodynamic consistency. Leong & Rahardjo (1997) suggest that $C(s)$ can be neglected because it does not significantly affect the shape of the WRC in the lower suction values usually of interest in common engineering applications. They also performed a sensitivity

analyses which revealed that the F&X equation performs better without the $C(s)$ factor.

Table 4.3 presents four (4) advanced WRMs, all including some kind of dependency on the void ratio value. The first two models are used to interpret data in terms of

**Table 4.3:** Void ratio dependant WRMs.

| Equation | Reference |
|---|---|
| $S_r = \frac{1}{\left[1+\left(\left(\phi(v-1)^{\psi}\right)s\right)^n\right]^m}$ *1 | Gallipoli et al. (2003) |
| $S_r = \frac{1}{\left[1+\left(\left(\frac{e}{a}\right)^{1/b}s\right)^n\right]^{-b/n}}$ *2 | Tarantino et al. (2009) |
| $\frac{e_w}{e} = S_r = C(s)\frac{1}{[1+(as)^n]^m}$ | Romero & Vaunat (2000) |
| $E_w = \frac{e_w - e_{wres}}{e - e_{wres}} = \sum_{i=1}^{k} w_i \left[1+(as)^n\right]^m$ *4 | Casini et al. (2012) |

*1 $v$ the initial specific volume.
*2 $e$ the initial void ratio.
*3 $C(s)$ a correction factor similar to F&X modified to give $e_w = 0$ for $s = 300MPa$.
*4 $w_i$ the weighting factor of each sub-curve.

degree of saturation $S_r$. They should not be generalized because the effect of different initial void ratio values on the WRC is not similarly reflected in terms of $w$ or $\theta$. Both models are in fact enchantments of the van Genuchten equation, where parameter $a$ depends on the initial void ratio. Gallipoli et al. (2003) assumed that $a = \phi(v-1)^{\psi}$ and Tarantino et al. (2009) that $a = \left(\frac{e}{a}\right)^{1/b}$, while parameters $\phi$ and $\psi$ or $b$ are regarded as material constants. Tarantino et al. (2009) model takes advantage of the experimental results suggesting that different void ratio WRCs coincide when plotted in terms of the water ratio $e_w$ (see also fig. 4.10b). This observation allowed them to correlate parameters $b, m, n$, and thus eliminate parameter $m$ from their formulation. Both models have been evaluated against experimental data concerning both reconstituted and compacted materials, rasing satisfactory results.

Romero & Vaunat (2000) used the Van Genuchten expression where $S_r$ was expressed through the water ratio as $S_r = e_w/e$ and thus introduced a direct dependance on the initial void ratio. They simulated results of $e_w$ vs $s$ corresponding to different

initial void ratios concluding that similarly to Gallipoli and Tarantino models, void ratio seems to mainly affect parameter $a$, while parameters $m$ and $n$ can be assumed constants. Moreover, they proposed that the effect of void ratio should be limited to the macrostructural degree of saturation defined as $S_{r,M} = \frac{e_w - e_{wm}}{e - e_{wm}}$ where $e_{wm}$ corresponds to the micro-structural water ratio.

Casini et al. (2012) focused exclusively on the water retention properties of compacted soils. An approach similar to Romero & Vaunat (2000) was used, while a linear superposition of more than one (usually two) van Genuchten type sub-curves, one for the inter-aggregate suction regime and another for the intra-aggregate suction regime are suggested to account for the different effect of an evolving void ratio on the macro- and micro-porosity.

Water Retention Models are of great importance in engineering practice. They are utilized either as curve fitting equations to interpolate available experimental results or in combination with empirical or statistical tools in the absence of experimental data. Different techniques have been proposed towards that direction.

Arya & Paris (1981), Fredlund et al. (1997b), Fredlund et al. (2002) propose the use of statistical methods to estimate the WRC of a given soil through its grain size distribution. They are based on the assumption that the grain size distribution reflects the distribution of various pore sizes in the soil system and further utilizing the capillary tubes model, the water retention characteristics of the soil is forecasted. As mentioned in Leong & Rahardjo (1997), such methods are more suitable for coarse grained materials like sands and marginally for some silts, but they cannot raise satisfactory results for plastic soils which usually contain a significant amount of clay. Fredlund et al. (1997a), in an attempt to overcome this limitation, developed a knowledge based system which incorporates a database of a large number of measured WRCs for various soils, together with information on their grain size distribution and other physical properties (i.e., Atterberg limits). Using neural network techniques the WRC of any given soil can be estimated provided that its main physical properties are known to serve as an input.

Zapata et al. (2000) and Ganjian et al. (2007) proposed empirical correlations to link the parameters of the F&X and the Van Genuchten WRMs with characteristic soil indexes. Tables 4.4 and 4.5 present the proposed correlations. We may observe that in the case of plastic soils ($PI > 0\%$) the weighted Plastic Index ($wPI$) is used.

It is defined as:

$$wPI = \text{Passing\#200} \cdot PI \tag{4.21}$$

where passing#200 the soil fraction passing the #200 U.S. Standard Sieve expressed as a decimal and $PI$, the well known Plasticity Index. For non-plastic soils, Zapata et al. (2000) proposed additional correlations which utilize the $D_{60}$[10] as the correlating parameter.

**Table 4.4:** Empirical equations for the Fredlund & Xing (1994) equation in terms of the volumetric water content $\theta_w$ , for plastic and not plastic soils after Zapata et al. (2000).

| Plastic Soils, $PI > 0\%$ | Non-Plastic Soils, $PI = 0\%$ |
|---|---|
| $a = 0.00364(wPI)^{3.35} + 4(wPI) + 11$ | $a = 0.8627(D_{60})^{-0.751}$ |
| $\frac{n}{m} = -2.313(wPI)^{0.14} + 5$ | $\overline{n} = 7.5$ |
| $m = 0.0514(wPI)^{0.465} + 0.5$ | $m = 0.1772 \ln(D_{60}) + 0.7734$ |
| $\frac{s_r}{a} = 32.44 \exp(0.0186 wPI)$ | $\frac{s_r}{a} = \frac{1}{D_{60}+9.7e^{-4}}$ *1 |

*1 The correction factor $C(s)$ has been used and $s_r$ has been handled as an extra curve fitting parameter. Regarding $\theta_{sat}$, the empirical equation $\theta_{sat} = 0.0143(wPI)^{0.75} + 0.36$ can be used, in the absence of experimental results.

**Table 4.5:** Empirical equations for the Van Genuchten (1980) equation in terms of the degree of saturation $S_r$ , for plastic soils, after Ganjian et al. (2007).

| Plastic Soils, $PI > 0\%$ |
|---|
| $a = (0.0015(wPI)^3 + 0.1028(wPI)^2 + 0.5871(wPI) + 11.813)^{-1}$ |
| $n = 0.00011(wPI)^2 - 0.01358(wPI) + 1.76987$ |
| $m = -5x10^{-6}(wPI)^2 - 0.00014(wPI) + 0.14745$ |

#### 4.2.2.5 Water retention properties of Typical Greek Soils

Inspired by the work of Zapata et al. (2000) and Ganjian et al. (2007), a similar attempt was made[11] to calculate the curve fitting parameters of various plastic soils from

[10] Grain diameter corresponding to 60% passing, derived from the grain size distribution curve.
[11] The work described in this paragraph is the outcome of a joined research with Bardanis (2016).

Greece and correlate them with suitable soil parameters. Seven soils are examined. The main drying branch of initially saturated, recomposed soil samples was measured and the experimental results are reported in Bardanis & Kavvadas (2005), Bardanis & Kavvadas (2008b) and Bardanis & Grifiza (2011). The axis translation technique for controlling matric suction up to $1500kPa$ and the salt solutions method (relative humidity control) for controlling total suction between 4 and $150MPa$ were employed (Bardanis & Kavvadas 2008b; Bardanis & Grifiza 2011). Table 4.6 summarizes the index properties of the examined soils, ranging from the marginally plastic Ioannina Lake Silt to high plasticity soils such as the Chalkoutsi Marl.

**Table 4.6:** Index properties of the examined soils.

| Soil Name | Abr. | Grain Distr. (%) | | | Atterb. Lim. (%) | | | $Gs$ | USCS |
|---|---|---|---|---|---|---|---|---|---|
| | | Sand | Silt | Clay | $w_L$ | $w_P$ | $PI$ | | |
| Ioannina Lake Silt | ILS | 64.8 | 26.9 | 8.4 | 24.0 | 23.0 | 1.0 | 2.67 | SM |
| Corinth Marl | CM | 8.8 | 84.7 | 6.5 | 30.5 | 25.0 | 5.5 | 2.67 | ML |
| Tempi Silt | TEM | 45.6 | 54.4 [*1] | | 49.5 | 42.0 | 7.5 | 2.56 | ML |
| Chania Silty Clay | CSC | 32.1 | 49.8 | 18.1 | 24.0 | 15.0 | 9.0 | 2.68 | CL |
| Kifissia Marl | KM | 7.0 | 68.1 | 24.9 | 31.5 | 16.0 | 15.5 | 2.66 | CL |
| Kifissia Clay | KC | 3.0 | 64.0 | 33.0 | 40.5 | 20.0 | 20.5 | 2.67 | CL |
| Chalkoutsi Marl | CHM | 15.0 | 64.2 | 20.5 | 50.8 | 20.7 | 30.1 | 2.69 | CH |

[*1] For TEM it is the percentage passing #200 U.S. Standard Sieve. Organic content equal to 13.2%.

The available experimental results are simulated using the non-void ratio dependant WRMs of table 4.2. Water content is analyzed in terms of the normalized gravimetric water content $W = w/w_0$; where $w$ and $w_0$ are the gravimetric water content at each suction level and at full saturation respectively. The normalized gravimetric water content mathematically corresponds to $W = S_r \frac{e}{e_0}$; thus, if void ratio is assumed constant during drying the obtained $W$ values follow the evolution of degree of saturation $S_r$.

A regression analysis was performed to estimate the $a$, $m$ and $n$ parameters utilizing the root-mean-square technique. Thus, the optimum set of parameters is this combination of parameters $a$, $m$ and $n$ which minimizes the sum of the squared devia-

tions of the measured data from the calculated data. The following objective function is used:

$$f_0 = \sum_{i=1}^{n} (W_i^m - W_i^c) \tag{4.22}$$

where $W_i^m$ the measured normalized water content for each suction level, $W_i^c$ the calculated one and $n$ the number of the available data points. The high nonlinearity of the WRC equations is reflected in the above objective function as local minima or maxima. In such cases, traditional search techniques (i.e., the steepest descent method) usually fails to identify the optimum solutions, especially if the assigned initial parameters are too far from the global minimum. Note that, especially in the case of WRMs, the estimation of a proper set of initial values is a quite demanding task due to the fact that different combinations of parameters may produce similar curves (Leong & Rahardjo 1997).

In the present study a stochastic search technique was selected and realized with the Matlab programming code. It uses a genetic algorithm to identify promising areas in the search space where the global minimum of the objective function may lie. The proposed optimization scheme involves 100 individuals (set of parameters) in the first parental generation, randomly selected in between the deterministic boundaries of an initially selected appropriate search space. Each individual searches for local minima in its neighbourhood, while an appreciable number of individuals from each generation migrate to search for other potential local minima away from its initial location. Three successive generations are used. The reliability of each one of the calculated set of best-fit parameters is quantified through the coefficient of determination ($R^2$):

$$R^2 = 1 - \frac{f_0}{\left(\sum_{i=1}^{n} W_i^m\right)^2 - \left(\sum_{i=1}^{n} W_i^m\right)^2 / n} \tag{4.23}$$

where $f_o$ (see eq. 4.22) and $W_i^m$, $n$ as defined above. The set of parameters corresponding to the higher $R^2$ (in fact closer to unity) corresponds to the global minimum and is finally adopted.

Tables 4.7 and 4.8 report the obtain best fit values together with the corresponding coefficient of determination values. The obtained curves are presented in figures 4.17a and 4.17b respectively.

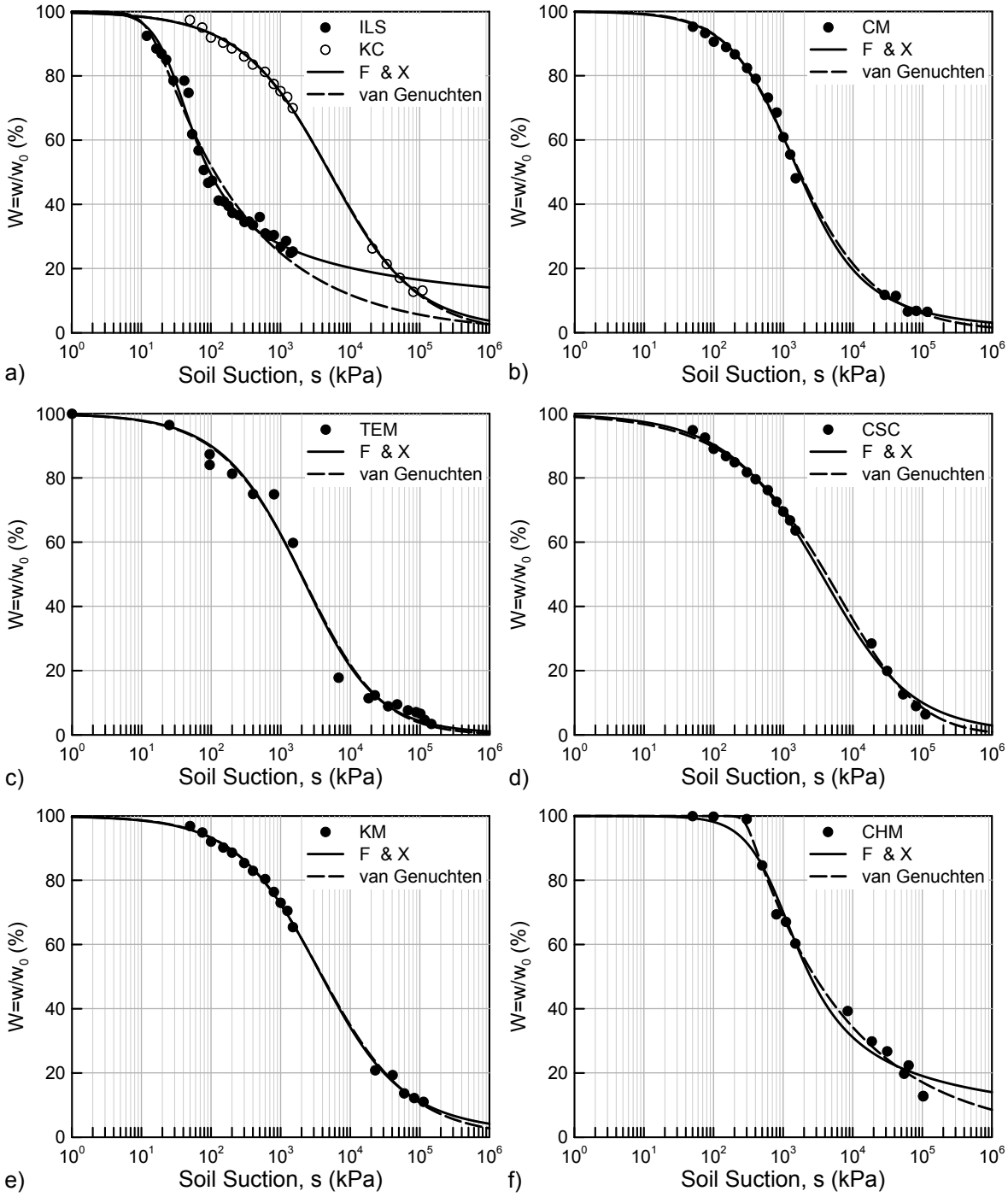


**Figure 4.17:** Experimental data and fitted curves using the Fredlund & Xing and van Genuchten equations for the: a) recomposed Ioannina Lake Silt and recomposed Kifisia Clay; b) recomposed Corinth Marl; c) Tempi silt; d) recomposed Chania Silty Clay; e) Kifisia Marl and; f) recomposed Chalkoytsi Marl.

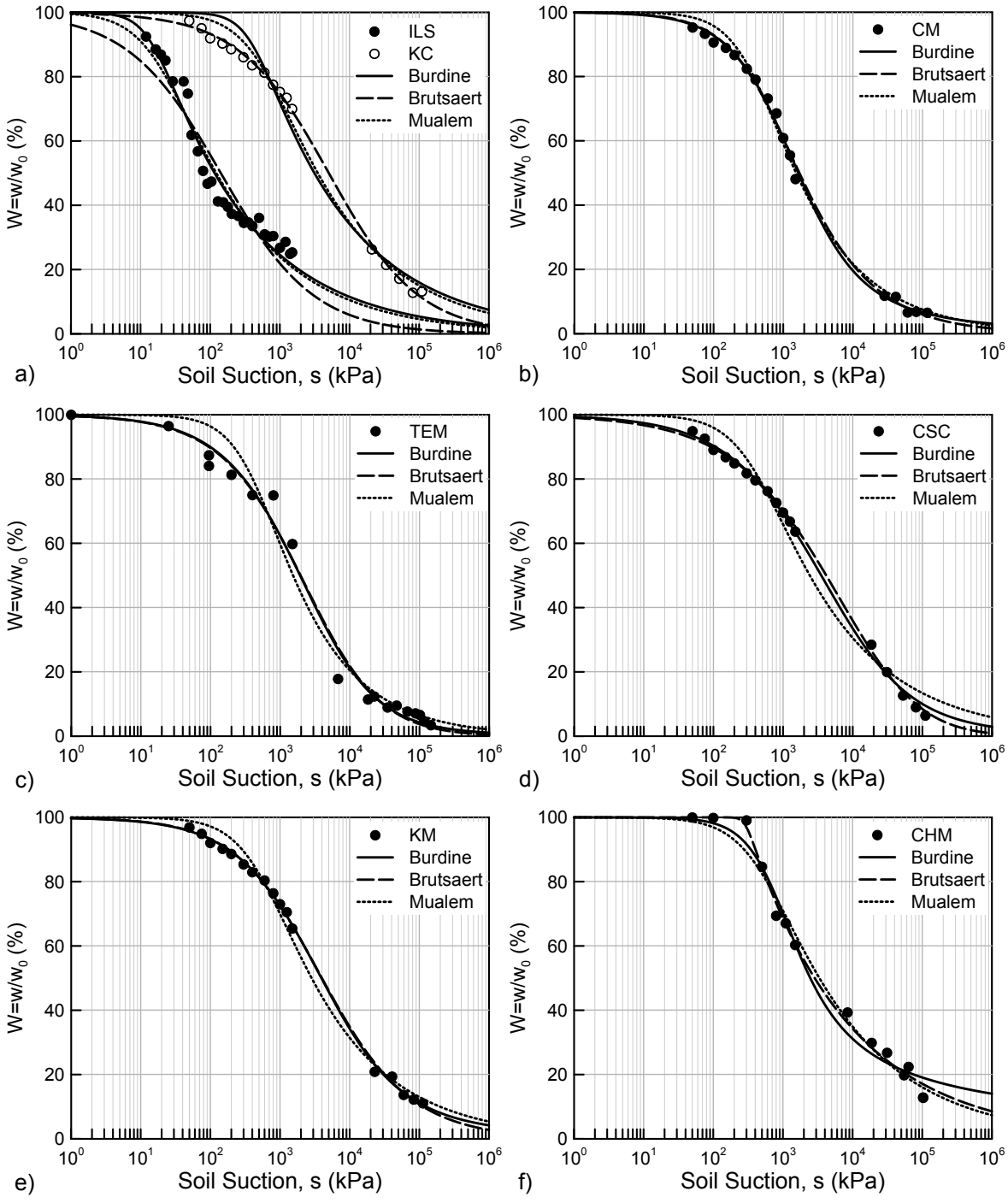


**Figure 4.18:** Experimental data and fitted curves using the Burdine, Brutsaert and Mualem WRMs for the: a) recomposed Ioannina Lake Silt and recomposed Kifisia Clay; b) recomposed Corinth Marl; c) Tempi silt; d) recomposed Chania Silty Clay; e) Kifisia Marl and; f) recomposed Chalkoytsi Marl.

**Table 4.7:** Calculated best-fit parameters and the associated $R^2$ for the Fredlund & Xing and van Genuchten equations.

| Soil | Fredlund & Xing | | | | van Genuchten | | | |
|---|---|---|---|---|---|---|---|---|
| | a | n | m | $R^2$ | a | n | m | $R^2$ |
| ILS | 24.5 | 2.071 | 0.633 | 0.997197 | 0.0763 | 3.386 | 0.095 | 0.993716 |
| CM | 1033.8 | 0.929 | 1.867 | 0.999461 | 0.014 | 1.005 | 0.567 | 0.999346 |
| TEM | 2913.2 | 0.702 | 3.181 | 0.995000 | $2.87 \cdot 10^{-4}$ | 0.6965 | 1.3507 | 0.994554 |
| CSC | 4890.0 | 0.600 | 2.954 | 0.999553 | $2.89 \cdot 10^{-5}$ | 0.527 | 2.447 | 0.999754 |
| KM | 3044.6 | 0.709 | 2.227 | 0.999786 | $3.65 \cdot 10^{-4}$ | 0.735 | 0.824 | 0.999750 |
| KC | 5380.3 | 0.650 | 2.623 | 0.999819 | $1.80 \cdot 10^{-4}$ | 0.664 | 1.043 | 0.999793 |
| CHM | 638.5 | 1.4982 | 0.818 | 0.995421 | 0.0035 | 9.2076 | 0.0327 | 0.998437 |

**Table 4.8:** Calculated best-fit parameters and the associated $R^2$ for the Burdine, Brutsaert and Mualem equations.

| Soil | Burdine | | | Brutsaert | | | Mualem | | |
|---|---|---|---|---|---|---|---|---|---|
| | a | n | $R^2$ | a | n | $R^2$ | a | n | $R^2$ |
| ILS | 0.0706 | 2.329 | 0.9942 | 142.18 | 0.651 | 0.9849 | 0.0534 | 1.359 | 0.9932 |
| CM | 0.0038 | 2.409 | 0.9960 | 1882.3 | 0.787 | 0.9989 | 0.0027 | 1.462 | 0.9984 |
| TEM | 0.0031 | 2.467 | 0.9829 | 1867.8 | 0.770 | 0.9945 | 0.0024 | 1.498 | 0.9882 |
| CSC | 0.0039 | 2.320 | 0.9921 | 3439.5 | 0.650 | 0.9995 | 0.0027 | 1.359 | 0.9956 |
| KM | 0.0028 | 2.347 | 0.9955 | 4209.4 | 0.685 | 0.9997 | 0.0020 | 1.385 | 0.9980 |
| KC | 0.0026 | 2.330 | 0.9952 | 5048.1 | 0.673 | 0.9998 | 0.0018 | 1.365 | 0.9977 |
| CHM | 0.0031 | 2.312 | 0.9974 | 4997.6 | 0.634 | 0.9912 | 0.0022 | 1.339 | 0.9959 |

Based on the obtained curve fitting results we may make the following observations:

- Three-parameter(s) models provide more adequate representations of the experimental results. It is reflected in the values of the coefficient of determination $R^2$ which are systematically higher for the three-parameter equations.

- From an engineering point of view the WRCs obtained with the two-parameter(s) models are also quite satisfactory. Among them, the Brutsaert model seems more capable of providing adequate fits, while the Burdine and Mualem equations are perhaps more suitable for experimental results exhibiting a rapid desaturation and a steeper curve in Regime II.

- Focusing on the three-parameter models, results of figure 4.17 indicate that in five (5) out of the seven (7) simulations, the obtained curves practically coincide. Exceptions are the simulation of the Ioannina Lake Silt (see fig. 4.17a) and that of the Kifisia Marl (KM) (see fig 4.17f). In the first case the F&X WRM retains a significant amount of water content for suction levels higher than the residual suction. This can be attributed to non-utilization of the correction factor $C(s)$. Regarding the Kifisia Marl (KM), the van Genuchten model provides a better representation of the material's increased air entry value and of the corresponding sudden water content reduction, with the F&X WRM proving incapable of accommodate such a response.

- The non-utilization of the correction factor $C(s)$ (F&X equation) does not seem to affect the results, with the exception of the previously mentioned Ioannina Lake Silt. The ILS is the less plastic and more coarse-grained of the available soils. The WRC data points are limited to $1500kPa$ as obtained with the axis translation technique. It turns out that under these circumstances the F&X equation tends to over-predict the water content for suction levels higher than the residual suction if the $C(s)$ factor is neglected. To the contrary, when results for higher suction levels are available the simulation curve is dragged towards zero water content by the interpolated results.

In an attempt to correlate the obtained curve fitting parameters with the characteristics of the soils, different parameters where tried and the $wPI$ turned out to systematically provide the best results. Figures 4.19 and 4.20 plot the obtained parameters versus the weighted plastic index $wPI$. Figure 4.19 concentrates on the results regarding the three-parameter(s) equations. In figure 4.19a, the inverse of the van Genuchten parameter $a$ is plotted to be comparable with the F&X parameter $a$. We observe that both models provide almost identical $a$, $1/a$ and $n$ values, while some differences are observed in the $m$ values. The latter explains the different shape of the simulation curves after the second inflection point. The significant scatter of the

results do not allow for any obvious and reliable correlation with $wPI$. An additional attempt was made ignoring the "inconsistent" Chania Silty Clay and recomposed Chalkoutsi Marl data points. Although at this case some trends were observed, we still could not identify any statistically reliable correlation.

To the contrary, a similar examination of the curve-fitting results of the two-parameter(s) raised more promising results. In figure 4.20 we may identify a trend, suggesting that parameters $a$ of the Brutsaert model and $1/a$ of the Burdine and Mualem models are a logarithmic function of $wPI$. The same applies to the $a/n$ and $(1/a)/n$ parameters respectively. The derived empirical correlations are summarized in table 4.9, with the corresponding coefficients of determinations $R_2$ included in the associated graphs.

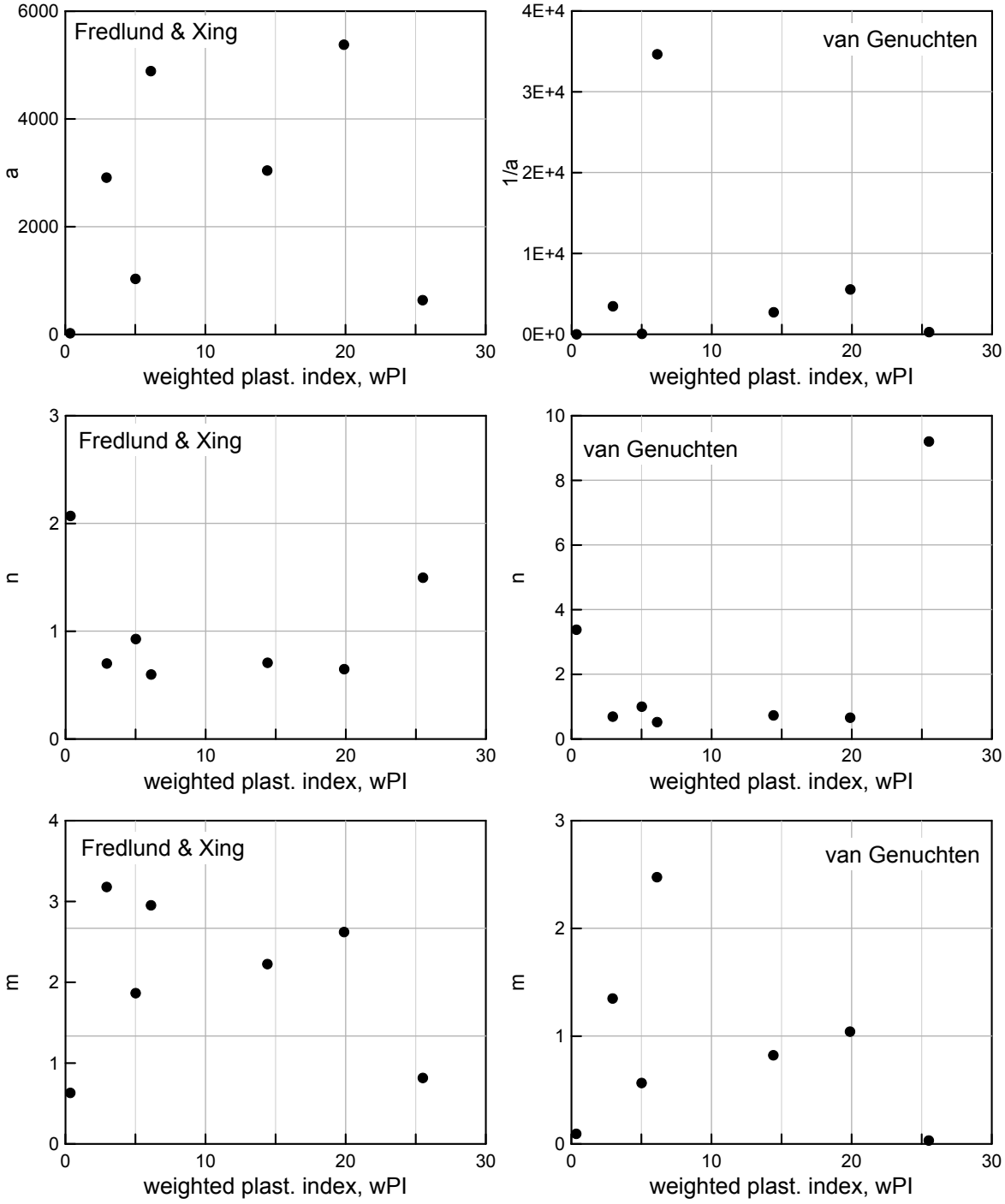


**Figure 4.19:** Fitting parameters of the: a) Fredlund & Xing and; b) van Genuchten WRMs, plotted versus the $wPI$, as defined through the performed regression analyses.

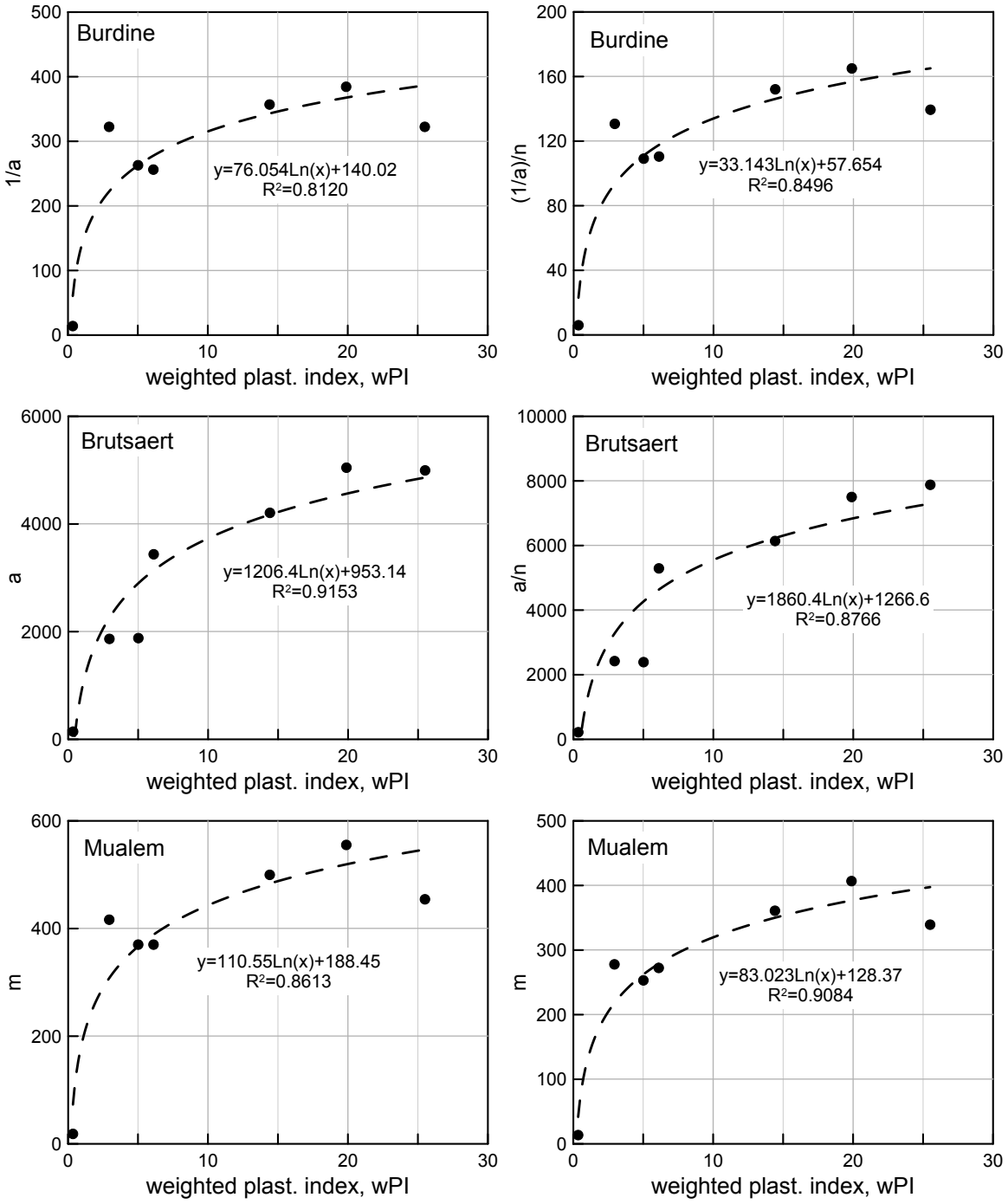


**Figure 4.20:** Correlation curves for the fitting parameters of the: a) Burdine; b) Brutsaert and c) Mualem WRMs, as defined through the performed regression analyses.

**Table 4.9:** The proposed correlations for the fitting parameters of the Burdine, Brutsaert and Mualem WRMs.

| WRM used | First parameter | Second parameter |
|---|---|---|
| Burdine (1953) | $\frac{1}{a} = 76 \cdot \ln wPI + 140$ | $\frac{1/a}{n} = 33 \cdot \ln wPI + 58$ |
| Brutsaert (1966) | $a = 1206 \cdot \ln wPI + 953$ [*1] | $\frac{a}{n} = 1860 \cdot \ln wPI + 1267$ [*1] |
| Mualem (1976) | $\frac{1}{a} = 110 \cdot \ln wPI + 189$ | $\frac{1/a}{n} = 83 \cdot \ln wPI + 128$ |

[*1] The proposed correlations for the Brutsaert model parameters are not valid for $wPI$ values less than 1 as they yield extremely low or even negative values.

Finally, as an indirect validation of the proposed correlations, we calculate parameters $a$, $n$ from the proposed correlations with the $wPI$ as an input, and the corresponding WRCs are compared with the experimental data in figure 4.21. We may observe that, in practical terms, the predicted WRCs provide fair representations of the actual data, with the marginally plastic Ioannina Lake Silt being a slight exception to the rule.

We may conclude that the two-parameter models are generally less capable of providing adequate fits compared to their three-parameter counterparts due to their limited curve shape flexibility arising from the lack of the third parameter to independently adjust the curve shape near the residual water content. Nevertheless, the aforementioned disadvantage in terms of simulation proves in favour of correlation seeking. As a result of their limited flexibility, the two-parameter WRC models are less sensitive to scatter of the experimental data and thus result in best-fit curves which mainly describe the general trend of the WRC. This allows the two-parameter equations to yield more reliable correlations between the curve-fitting parameters and soil index properties. Finally, we must emphasize that due to the limited experimental data examined, the proposed correlations are of limited practical applicability. They should only serve as an approximate estimation of the drying branch of the WRC of fine-grained soils, in the absence of experimental results, while more experimental data are needed, especially for $wPI$ values between 2 and 10. The presented simulation and correlation exercise has been already published in Sitarenios et al. (2011) and Sitarenios et al. (2012).

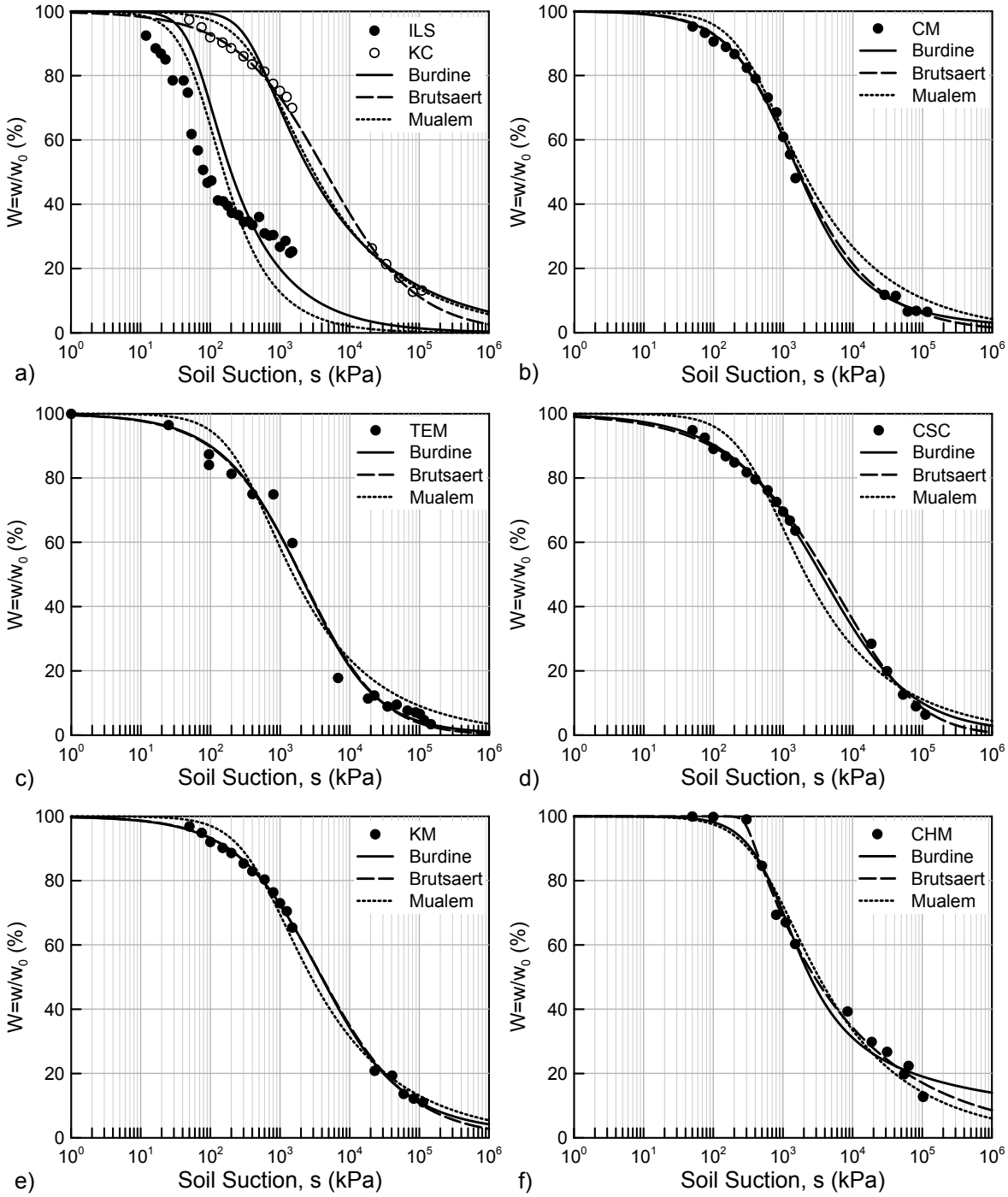


**Figure 4.21:** Comparison of the predicted WRCs using the Burdine, Brutsaert and Mualem proposed correlations with the experimental data for the: a) recomposed Ioannina Lake Silt and recomposed Kifisia Clay; b) recomposed Corinth Marl; c) Tempi silt; d) recomposed Chania Silty Clay; e) Kifisia Marl and; f) recomposed Chalkoytsi Marl.

## 4.3 Mechanical Behaviour

This section deals with the mechanical behaviour of unsaturated and partially saturated soils. It begins with a brief discussion on the stress variables required to adequately describe the mechanical behaviour of unsaturated soils, followed by the presentation of their yield, compressibility and shear strength characteristics. It is based on well documented experimental results from the international literature.

### 4.3.1 Stress variables in unsaturated soils

The development of modern soil mechanics has been based on the principle of effective stress (Terzaghi 1925). Terzaghi defined the effective stress $\sigma$[12] in a soil element as the excess of total applied stress ($\overline{\sigma}$) over the pore water pressure ($u_w$):

$$\sigma = \overline{\sigma} - u_w \tag{4.24}$$

Terzaghi stated that in a saturated soil element, all measurable effects of a change of stress, such as compression, distortion and a change of shearing resistance are exclusively attributed to changes in the effective stress[13]. The validity of the effective stress principle was soon verified by the work of many researchers (Rendulic 1936; Bishop & Eldin 1950; Henkel 1959; Henkel 1960) and even nowadays it comprises the most fundamental idea of soil mechanics.

Given the success of Terzaghi's effective stress principle, it sounds reasonable that the first attempts to describe the behaviour of unsaturated soils where concentrated on the attempt to find a proper effective stress definition for unsaturated soils as well. Aitchison & Donald (1956) demonstrated that as far as a soil element remains saturated, even under a negative water pressure, the effective stress principle is still valid, with negative water pressure increasing the effective stress. Nevertheless as far as air starts to appear in the soil pores then the water phase no longer acts over the whole cross sectional area of a soil element, differentiating equilibrium conditions.

Various researchers proposed modified versions of the effective stress equation to account for the appearance of the air phase in the soil skeleton (Hilf 1956; Jennings 1957; Croney et al. 1958; Bishop 1959; Lambe 1960; Aitchison 1960; Jennings 1961;

[12] It is reminded that throughout the present Doctoral Thesis the primes indicating effective stress have been dropped for simplicity.

[13] Soil grains and pore water are considered practically incompressible when compared to the compressibility of the soil skeleton.

Richards 1966); amongst them the one of Bishop (1959) has proved the most successful. Bishop's stress is given as:

$$\sigma = (\overline{\sigma} - u_a) + \chi\,(u_a - u_w) \tag{4.25}$$

where $\overline{\sigma}$ the total stress, $u_a$ and $u_w$ the pressure of the air and water phase respectively, while $\chi$ a parameter scaling the effect of suction. Parameter $\chi$ must be suitably selected to correspond to one ($\chi = 1.0$) for a fully saturated soil and to zero ($\chi = 0.0$) for a completely dry soil. It is evident that if such an approach is used, while simultaneously the air pressure is assumed equal to zero[14], Bishop's stress recalls Terzaghi's effective stress for $\chi = 1.0$. It comes without saying that for parameter $\chi$ to fulfill the aforementioned conditions a relation with degree of saturation ($\chi = f(S_r)$) seems the most suitable, while just assuming $\chi = S_r$ is the simplest possible form.

Unfortunately, it was very soon realized that although Bishop's stress could offer a quite comprehensive description of the evolution of shear strength with suction and degree of saturation, it could not account as an effective stress because:

a) it cannot explain the volumetric behaviour of unsaturated soils, where wetting an initially unsaturated soil and thus, decreasing Bishop's stress, its void ratio decreases (volumetric collapse). According to classical soil mechanics swelling should accompany a decreasing effective stress;

b) changes in suction and/or the applied total stress, corresponding to an identical evolution of Bishop's stress value, produce a different soil response.

Amongst the first to criticize the validity of Bishop's stress as an effective stress parameter were Jennings & Burland (1962). They measured the values that parameter $\chi$ should obtain to represent the shear strength and void ratio changes of various soils, concluding that its value is both material and stress path dependent. Additionally, they performed tests where suction and total stress increments were applied so as to correspond to identical Bishop's stress alterations ending up with different soil response. Even Bishop himself, in Bishop & Blight (1963), constrained the validity of his proposal to the interpretation of shear strength evolution. More evidence in favour of the non-validity of Bishop's stress as an effective quantity are included in Burland (1965), Matyas & Radhakrishna (1968), Barden et al. (1969) and more

[14] In practical engineering problems, atmospheric pressure is considered as the reference pressure.

recently in Wheeler & Sivakumar (1995). In fact, as stated in Jommi (2000), no single stress variable has been ever found to allow for a unified description of every aspect of the unsaturated soil's mechanical behaviour.

Nowadays, it is widely accepted that a comprehensive description of the mechanical behaviour of unsaturated soils requires the use of two independent stress variables. Evidence towards such an assumption can be found in most of the aforementioned contributions related to the criticism of Bishop's "effective" stress, with the most significant being this of Matyas & Radhakrishna (1968) where soil behaviour was interpreted using the: a) net stress and; b) suction. Fredlund & Morgenstern (1977), proposed that the required stress variables can be any suitable combination of total stress $\overline{\sigma}$, air pressure $u_a$ and water pressure $u_w$. The combination that has finally prevailed in the associated literature and is more usually utilized is this of net stress $\overline{\sigma}$[15]:

$$\overline{\sigma} = \overline{\sigma} - u_a \tag{4.26}$$

and suction $s$:

$$s = u_a - u_w \tag{4.27}$$

Net stress and suction allow for a rigorous representation of experimental results as both can be independently controlled and measured in the laboratory. Common stress paths are also easier represented (i.e., constant suction, constant total stress). On the other hand, the net stress and suction combination has strong limitations when it comes to numerical analysis of practical geotechnical problems, as net stress does not recall Terzaghi's effective stress upon saturation.

### 4.3.2 Yield - The apparent preconsolidation pressure

In the previous chapters we discussed how a soil compressed under either isotropic or anisotropic conditions exhibits an nonlinear decrease in its void ratio ($e$) or specific volume ($v$) with the increase of the applied effective stress. It was demonstrated how this nonlinear behaviour is usually approximated by two straight lines in the $v - \ln p$ plane, the virgin compression line and the swelling line, with their intercept defining the yield stress of the material. This paragraph extends the aforemention discussion to the behaviour of unsaturated soils.

[15] In the present dissertation, total and net stress coincide because $u_a$ is assumed equal to zero; thus a common symbol is used.

Figure 4.22a presents the compression curves of a silty soil under both saturated and unsaturated conditions, with the latter corresponding to air dried samples. Figure 4.22b presents the compression curves of an unsaturated low plasticity loess under two different water contents and various initial void ratios. Both results indicate that unsaturated soil specimens exhibit an increased yield stress when unsaturated. It also seems that the lower the water content, the higher the exhibited yield stress is.

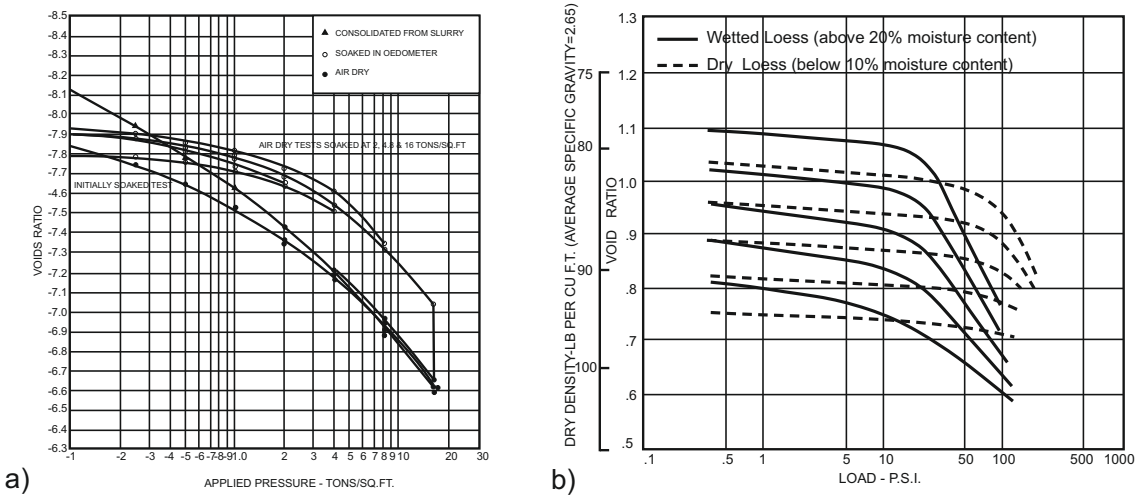


**Figure 4.22:** a) Saturated and unsaturated (air dried) compression curves of a silty soil after Jennings & Burland (1962) and; b) unsaturated compression curves of a low plasticity Loess under two different water contents and five different initial void ratios Dudley (1970) after Alonso et al. (1987).

The aforementioned tests are constant water content tests and thus both suction and degree of saturation evolve during compression. Figures 4.23 to 4.26 present the compression curves derived from constant suction, isotropic and anisotropic consolidation tests for various soils. We may observe a systematic shift of the unsaturated compression curves to the right of their saturated companions, indicating once again that partial saturation increases the material's yield stress. The increased yield stress of an unsaturated soil element is usually called apparent preconsolidation pressure. We may additionally observe that in most of the cases, the higher the applied suction, the higher the exhibited apparent preconsolidation pressure is.

Regarding the post-yield compressibility of the unsaturated samples, it seems difficult to draw solid conclusions, as different types of behaviour are observed. For instance, the results reported in Rampino et al. (2000) (see fig. 4.26) are in favour of an increased soil stiffness with increasing suction; in the results of Maâtouk et al. (1995) (see fig. 4.24) the obtained compression curves seem parallel, while in Wheeler

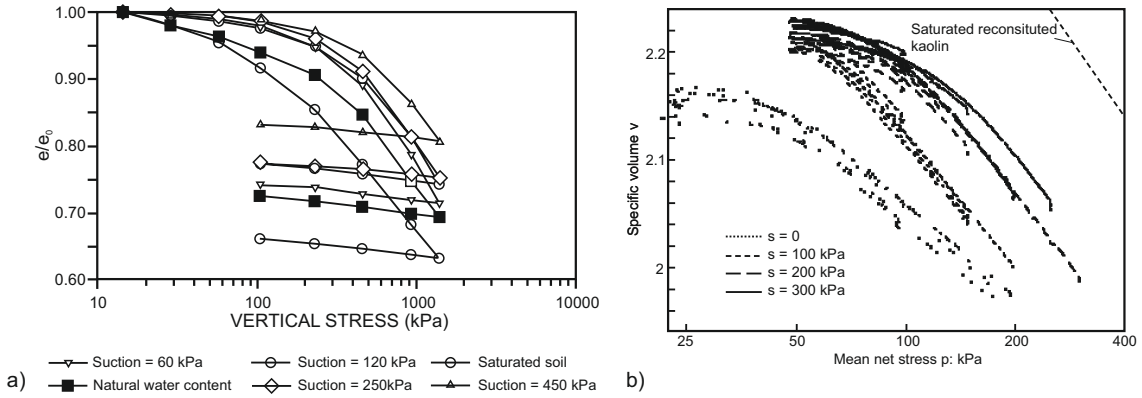


**Figure 4.23:** Constant suction compression tests under: a) oedometric conditions, for a residual Brazilian soil (Lemos 1998) and; b) isotropic conditions, for a compacted speswhite Kaolin (Wheeler & Sivakumar 1995).

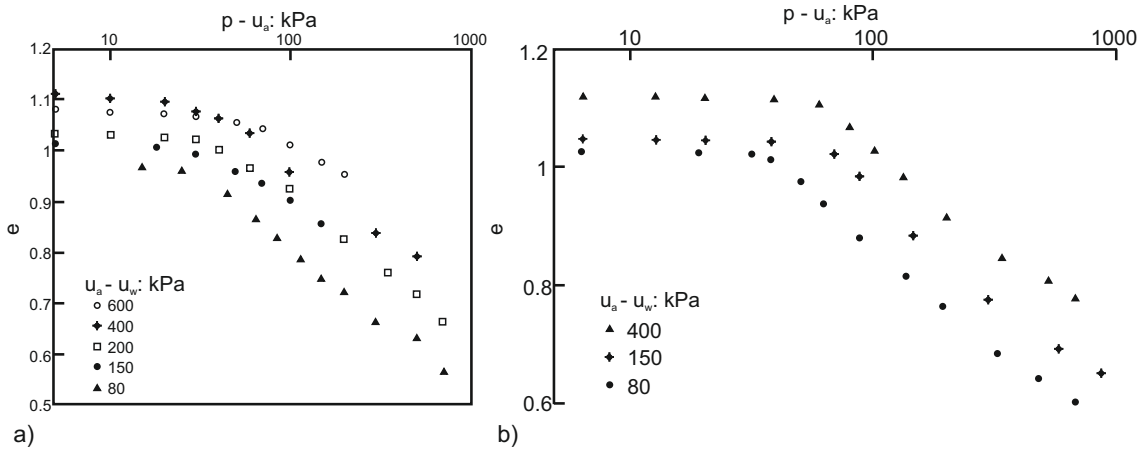


**Figure 4.24:** Compression curves under different constant suction levels for a silty soil from Canada under: a) isotropic and b) radial ($K = 0.54$) conditions both after Maâtouk et al. (1995).

& Sivakumar (1995) (see fig. 4.23b) a clear decreased soil compressibility with partial saturation is observed. Although such a behaviour seems bizarre, it is in fact reasonable and can be attributed to the effect of water content (i.e., degree of saturation) on the compressibility behaviour. This is further analyzed in the following paragraph.

## 4.3.3 Volumetric Behaviour - Swelling vs Collapse

### 4.3.3.1 Drying under constant net stress

Let's examine the behaviour of an initially saturated soil sample which is progressively dried. Initially, as far as the soil remains saturated, the decrease in void ratio is

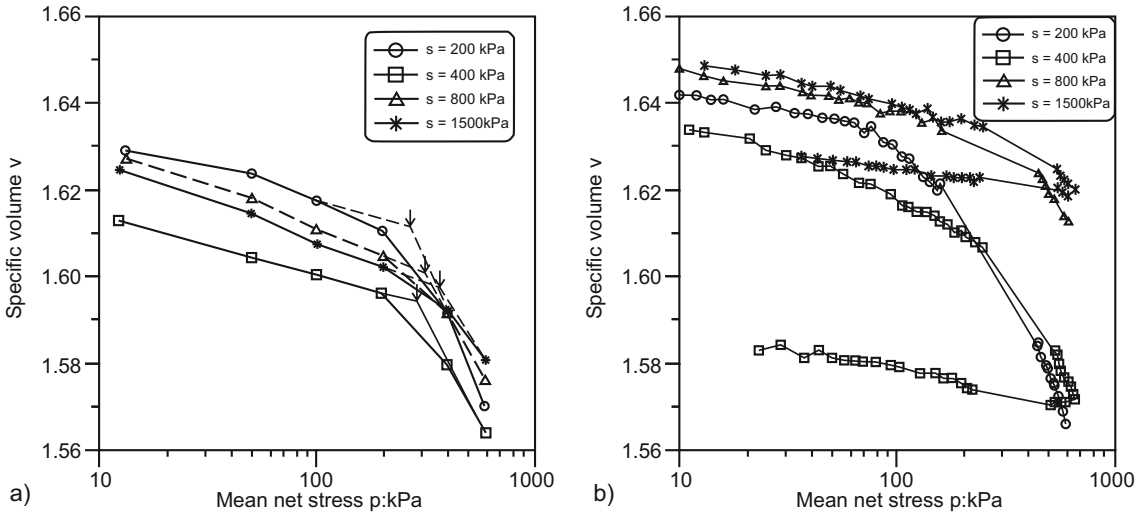


**Figure 4.25:** Isotropic compression curves under different constant suction levels, regarding Josigny silt specimens subjected to: a) ramped loading and ; b) continuous loading. Cui & Delage (1996)

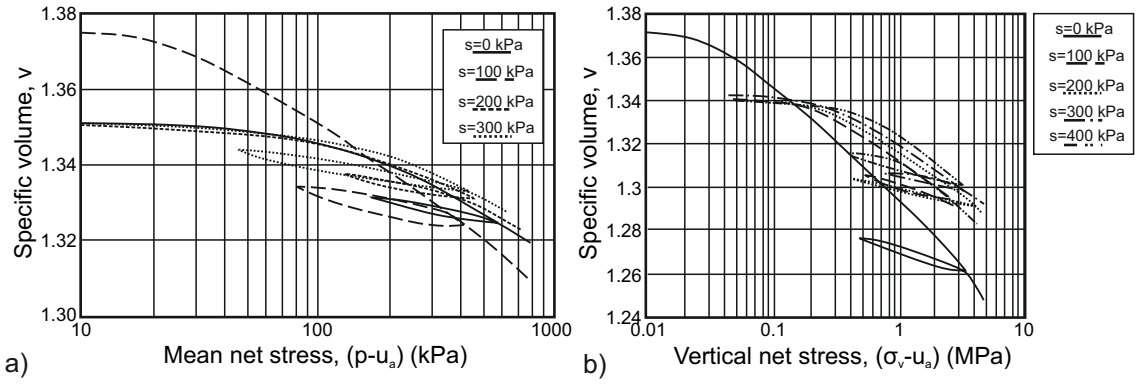


**Figure 4.26:** a) Isotropic and b) oedometric compression curves under different constant suction levels for a Loose silty soil from Italy. (Rampino et al. 2000)

controlled by Terzaghi's effective stress. Nevertheless, for suction values higher than the desaturation suction ($s_0$), the response gets stiffer with void ratio and water content reduction following a different path (see figure 4.27).

Bardanis (2016) presents a very interesting graph (figure 4.28) where the evolution of void ratio with suction, the so called "shrinkage curve", is linked to the characteristic regimes of the water retention curve of the material. We observe that in Regime I the void ratio follows the compressibility of the saturated material, while at the transition between regime I and II the response gets stiffer; a suction yield stress can be identified in the transition. The response up to the suction yield stress is assumed elastic (reversible). The existence of such a suction yield point is sup-

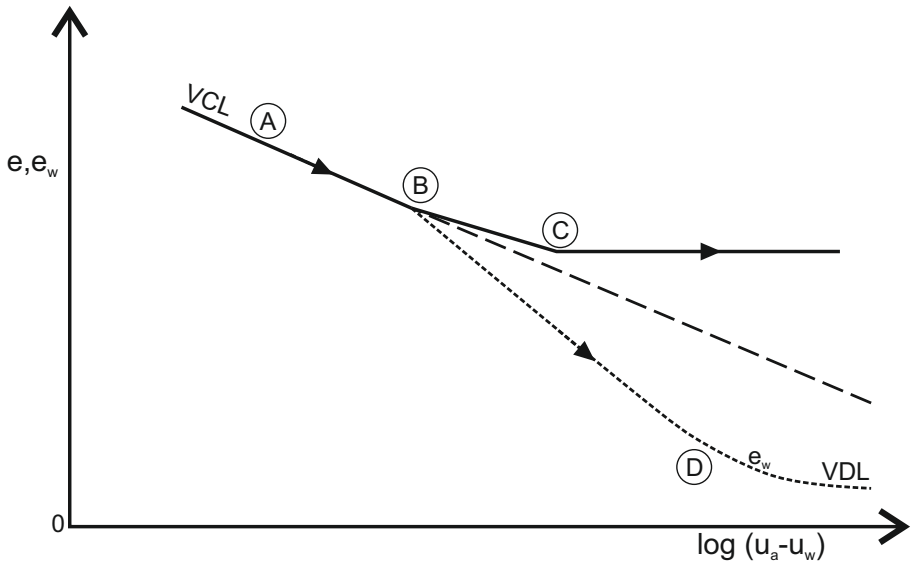


**Figure 4.27:** Volume and water content change during drying. (Toll 1995)

ported by many experimental results and has also been incorporated in conceptual frameworks addressing the behaviour of unsaturated soils (Alonso et al. 1987). Figure 4.29 presents the results of Chen et al. (1999) from drying tests on a low plasticity loess, where a distinct suction yield stress is also identified.

Examining again figure 4.28a, we observe that for further drying void ratio starts to stabilize around a minimum value. Higher suction values seem practically incapable of further compressing the soil skeleton. This minimum value of the void ratio is called the residual void ratio. Figure 4.30 presents the measured shrinkage curves corresponding to reconstituted Josigny Silt specimens and to air-dried samples of a clayey soil from Greece; both results are in favour of a stabilization of the void ratio around a minimum-residual value. Bardanis (2016) elaborating an ensemble of similar results from various soils, states that the residual void ratio depends on the type of the soil examined as well as on its loading history and structure.

#### 4.3.3.2 Wetting under constant net stress

In the previous paragraph we discussed how an initially saturated soil sample that is progressively dried shrinks, a behaviour easily understandable if we consider that the forming water menisci exert tension forces between the soil grains, particles or aggregates and in a sense increase the inter-particle forces. In an analogy, it is expected that the wetting of an initially unsaturated soil will be accompanied with volume in-

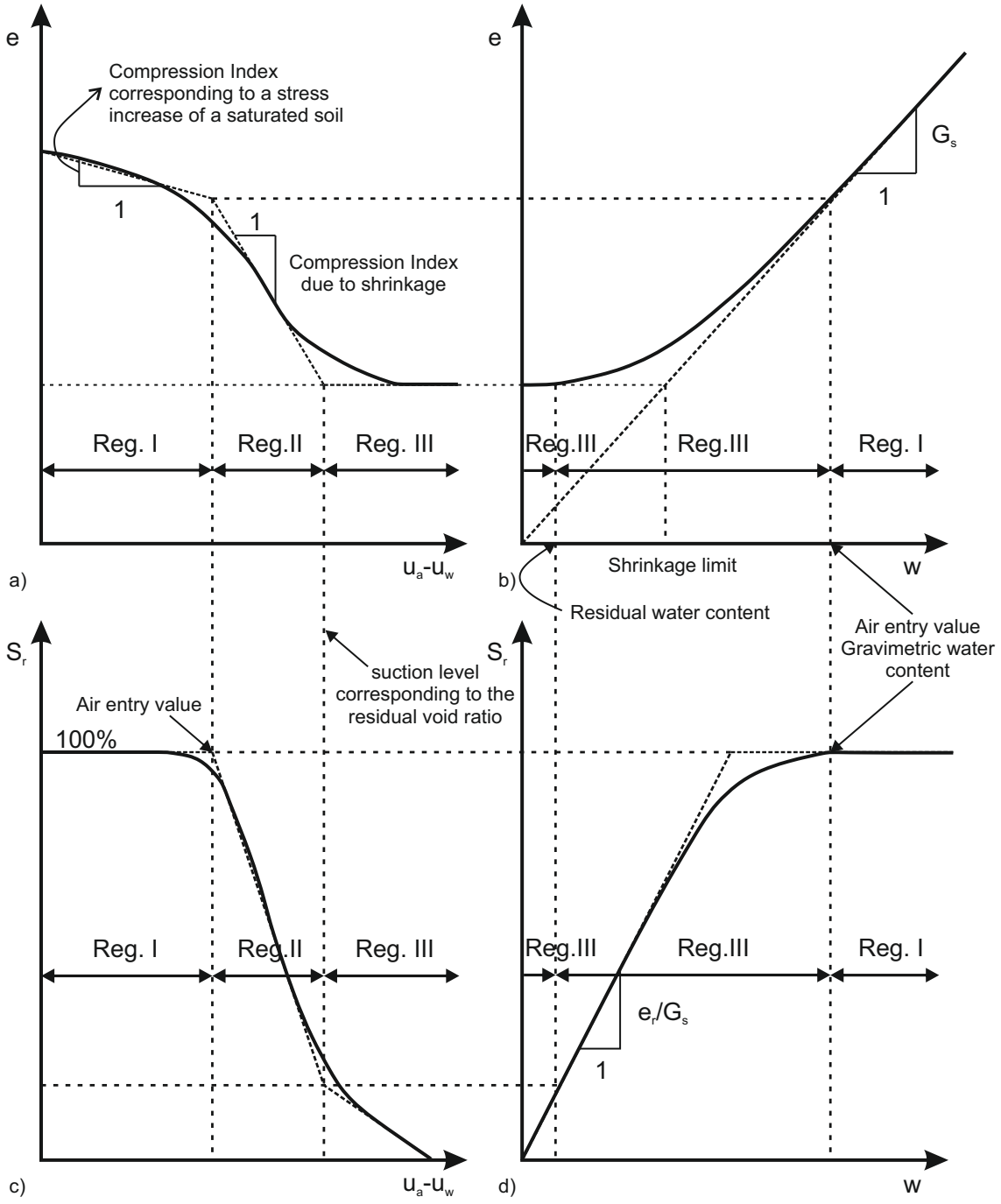


**Figure 4.28:** a) Void ratio vs suction; b) void ratio vs gravimetric water content; c) degree of saturation vs suction and; d) degree of saturation vs gravimetric water content for an initially saturated material that is progressively dried. (Bardanis 2016)

crease due to the reducing inter-particle menisci forces. Nevertheless, it was very soon realized that unsaturated soils (with the exception of highly expansive soils) either

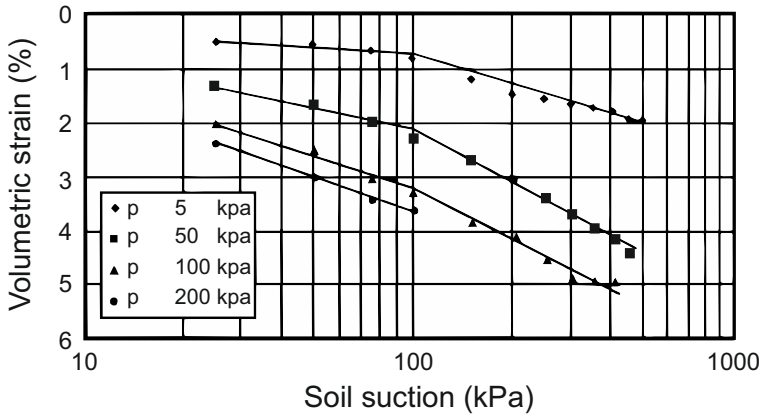


**Figure 4.29:** Volumetric strains during drying of a low plasticity compacted Loess (Chen et al. 1999), after Georgiadis (2003).

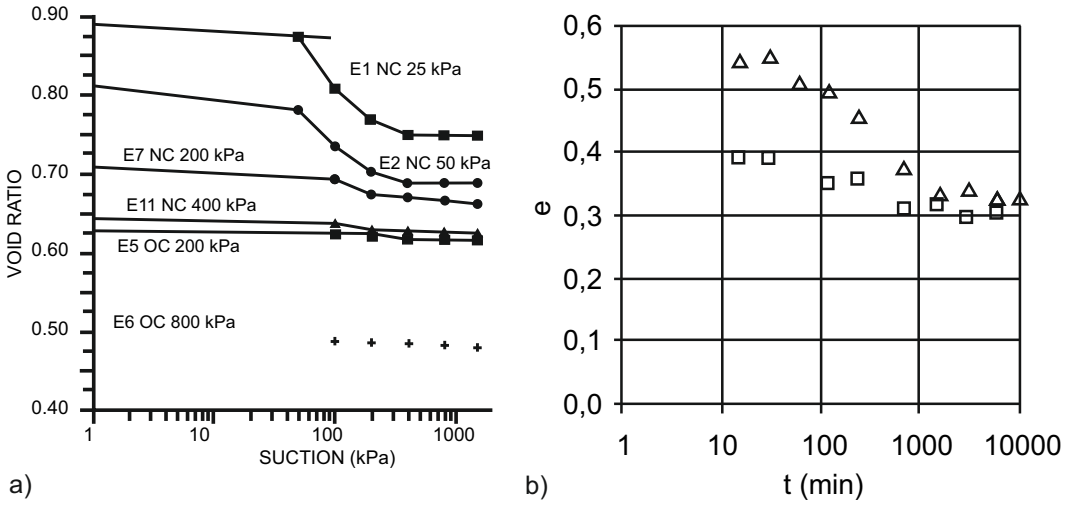


**Figure 4.30:** Shrinkage curves of recomposed: a) Josigny Silt (VICOL 1990), after Delage & Graham (1996); and b) Chania clay after Bardanis & Kavvadas (2006).

swell or shrink upon wetting depending on the level of the net stress applied during wetting. We already discussed how this eccentric mechanical behaviour contradicts the principle of effective stress.

Figure 4.31 presents the results of wetting tests on compacted, initially unsaturated soil samples. Both figures indicate that when the examined soil specimens are soaked under a relatively low vertical stress, an increase in void ratio is observed (swelling). This behaviour progressively reverses as the applied vertical stress increases, leading to a volume reduction with wetting. This irreversible volume decrease with wetting is called collapse[16]. Many experimental results indicate that as

[16]It should not be confused with an overall shear failure. (Gens 1996)

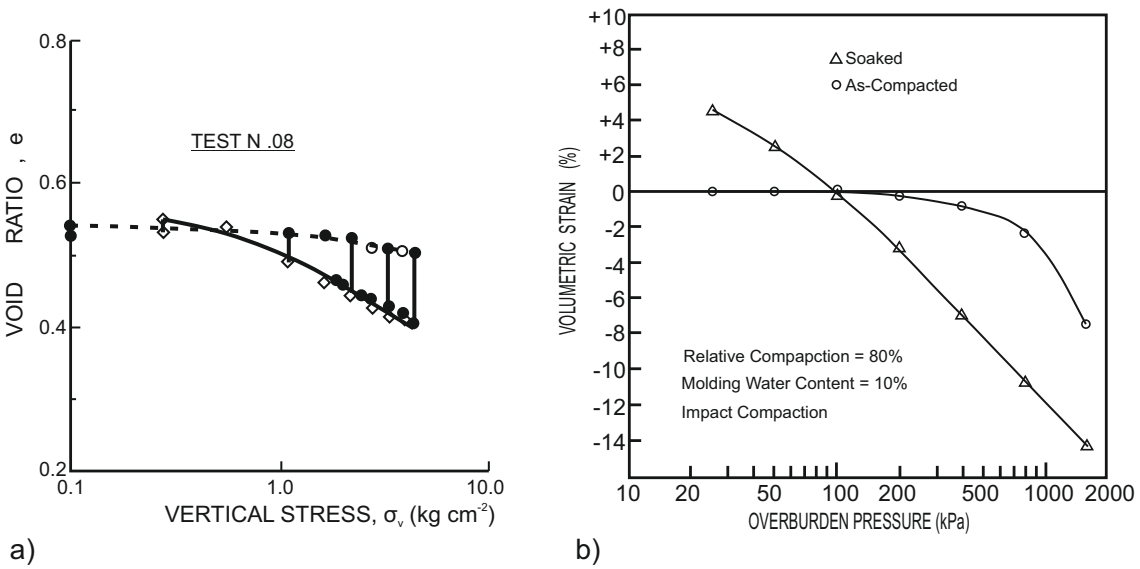


**Figure 4.31:** a) Void ratio evolution during wetting for initially unsaturated samples of compacted Lower Cromer Till, water soaked under different vertical stress levels (Maswoswe 1985) and; b) similar results in terms of volumetric strains (solid mechanics sign convention) for a compacted, slightly expansive, clayey sand (Lawton et al. 1989).

the confining stress under which wetting takes place increases, collapse reaches a maximum, and may even reduce at significant high stresses. Such a behaviour is clearly depicted in the results of Lawton et al. (1989) (see fig. 4.32).

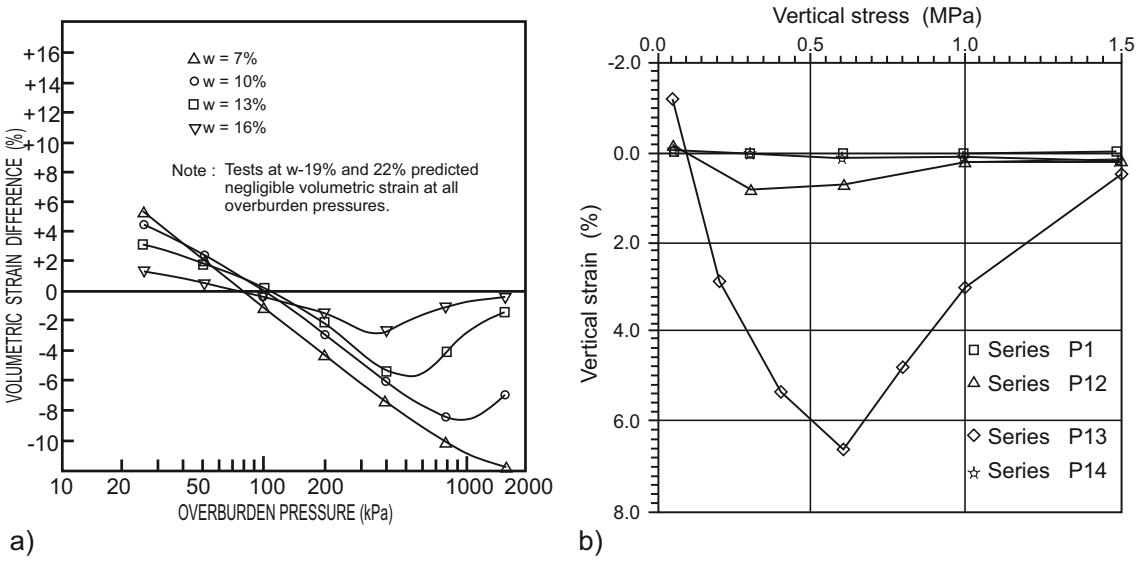


**Figure 4.32:** Evolution of the wetting induced volumetric deformation with the applied confining stress for a) compacted clayey sand samples (Lawton et al. 1989) and; b) Barcelona Clayey Silt samples (Gens et al. 1995).

Lawton et al. (1989), combining information from different sources, summarizes the following four (4) necessary conditions for a soil element to collapse upon wetting; they are:

a) an open, partially unstable, partially saturated fabric;

b) a high enough total stress so that soil structure is metastable;

c) a sufficient large soil suction or the presence of a bonding or cementing agent which stabilizes the soil in the partly-saturated condition;

d) the addition of water to the soil which reduces the soil suction or softens or destroys the bonding agent, thereby causing shear failures at the inter-aggregate or inter-granular contacts.

The results presented in figures 4.31 and 4.32 correspond to laboratory tests where an initially unsaturated soil elements is soaked at once and the overall volumetric response is reported based on the final state. Alternatively, a soil sample can be progressively wetted by gradually decreasing the imposed soil suction, utilizing one of the available techniques for suction control. Such tests additionally provide the evolution of the volumetric strains during wetting (see fig. 4.33). Note that the measured volumetric deformation may change sign even during the test, with the soil initially swelling, while at some point the behaviour reverses to volume reduction. Depending on the level of the applied stress, the final state may either correspond to an overall swelling behaviour or to an overall collapse.

Experimental results suggest that the final material state after collapse usually lies on the compression line of the saturated material (or so close as to practically assume that they coincide). Figure 4.34 includes the compression curves corresponding to compression under saturated and unsaturated conditions. We may observe that the void ratio evolution during wetting, is in fact represented from the vertical distance between the compression line corresponding to the initial water content (or suction) and to the saturated one. The latter observation allows for a unified representation of the compressibility of a given unsaturated soil with its volumetric response during wetting.

In that respect, figure 4.34 presents a typical compressibility framework which can accommodate: a) the increase in the yield stress; b) the volumetric behaviour reverse from swelling to collapse with increasing applied confining stress, and; c) a maximum

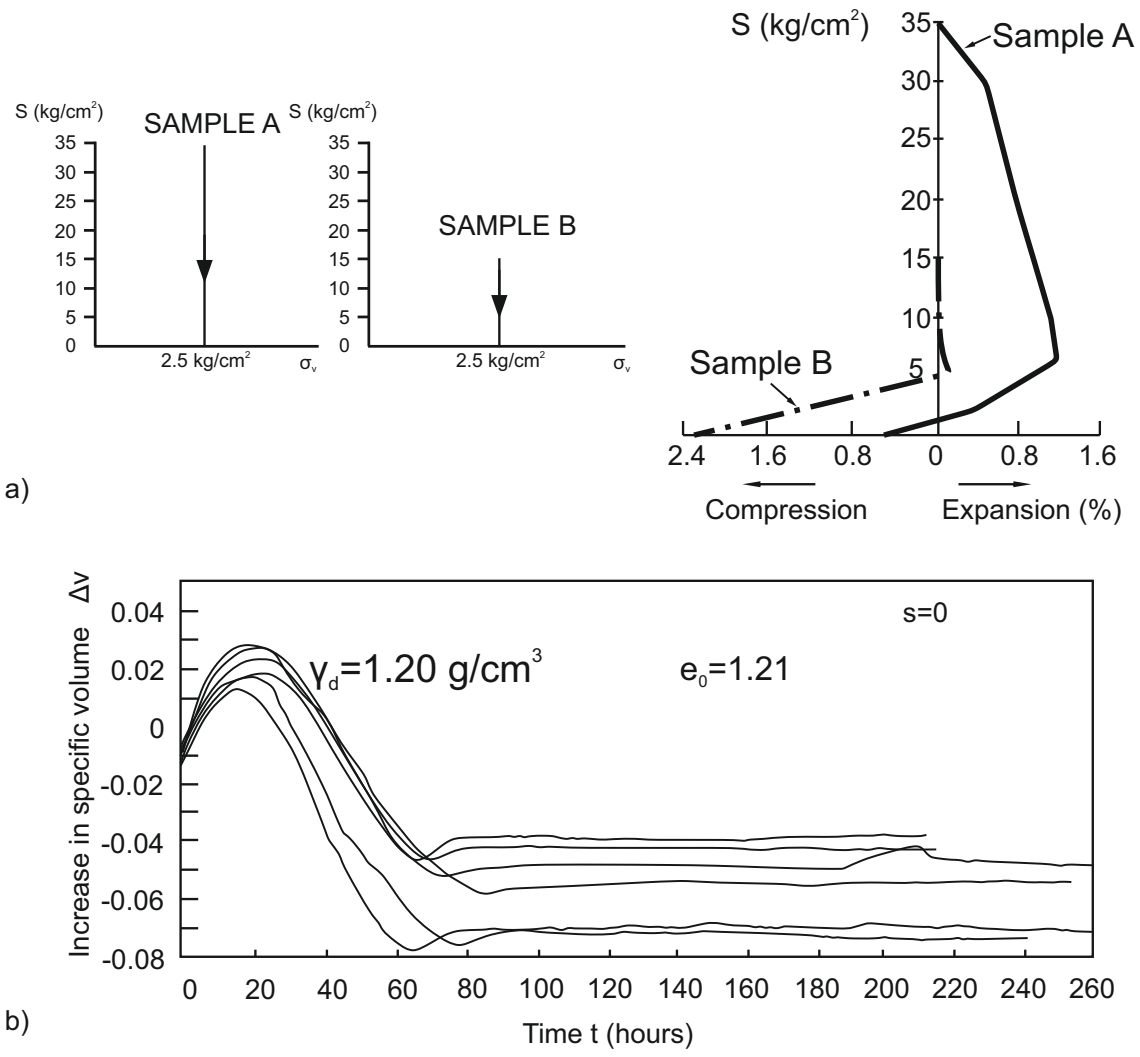


**Figure 4.33:** a) Evolution of the volumetric strains during suction controlled wetting test on an unsaturated compacted clay under two different initial water contents (Escario & Saez 1973) and b) evolution of the specific volume with time corresponding to several water soaked specimens of a compacted kaolinite (Sivakumar & Wheeler 1993).

of collapse. Moreover, the post yield compressibility of the unsaturated material under a given suction is not constant but constantly evolves with compression, explaining why controversial results appear in the associated literature when the experimentally determined behaviour is idealized through linear post yield compression curves.

Before concluding this paragraph, it is worth devoting some lines to the volumetric behaviour of compacted soils and mainly to the effect that different compaction conditions, the post-compaction density and the soaking confining stress have on the volumetric response upon wetting. Figure 4.35a plots curves of equal volumetric de-

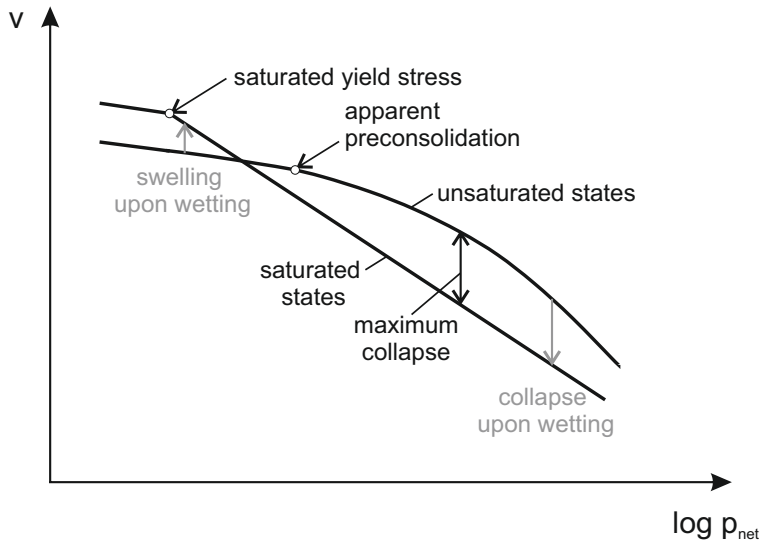


**Figure 4.34:** The main characteristics of a compressibility framework for unsaturated soils.

formation for a compacted clayey sand on the dry density - molding water content plane. The results indicate that there exists a critical relative compaction line (or area) for which an initially unsaturated compacted sample exhibits negligible volumetric deformation when soaked. Samples compacted at a dry density greater than the critical one swell upon wetting. The amount of swelling increases as the molding water content decreases, with the samples prepared to the wet of optimum exhibiting the lower swelling potential. On the other hand, soil samples with initial conditions below the critical compaction level collapse upon wetting. The collapse potential seems to increase with the decrease of the initial water content and with a decreasing initial dry density.

As already discussed, compaction at the dry of optimum favours the formation of large macro-pores between soil aggregates. It is clear that the observed volumetric behaviour is mainly attributed to volume changes in the macro-pores. In high relative compaction levels (higher initial dry densities) the larger macro-pores are initially quite small and thus there is no room for contraction with wetting, resulting to an overall volumetric behaviour which is primarily controlled by the swelling of the soil aggregates. The behaviour progressively reverses as the dry density of the sample reduces. A decreased dry density corresponds to an open fabric where bigger macro-pores can collapse upon wetting.

Regarding the effect of the confining stress under which the soil is wetted, we may

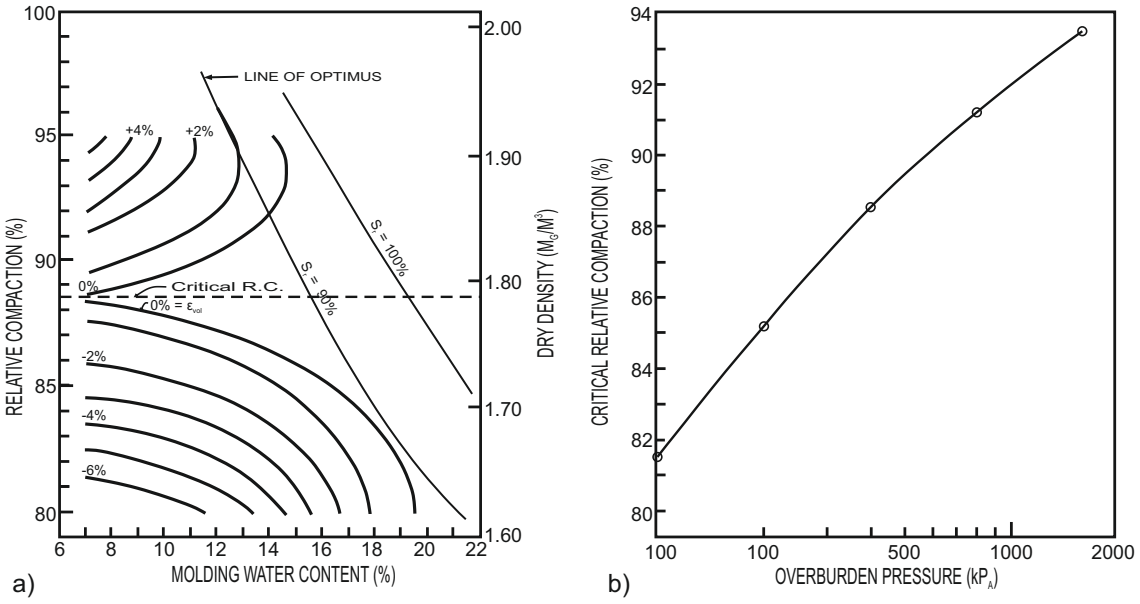


**Figure 4.35:** a) Contours of equal wetting induced volumetric deformation plotted in the initial dry density vs moulding water content plane and; b) the dependance of the critical compaction level on the vertical applied stress during wetting (Lawton et al. 1989).

observe that its increase produces an increasing potential for collapse. In figure 4.35a this would be translated to an offset of the critical compaction line towards higher initial dry densities, as indicated in figure 4.35b. It is better portrayed in figure 4.36, which plots the contours of equal volumetric deformation, for statically compacted Barcelona Clayey Silt samples soaked at two different vertical stress levels ($0.1MPa$ and $0.3MPa$). A clear swift of the iso-volumetric curves towards higher dry densities is observed.

Finally we should comment on the negligible volumetric response of the soil samples compacted at the wet of optimum. Gens et al. (1995) present a very interesting study where soil specimens compacted at the wet of optimum are progressively dried to a water content similar to their dry of optimum counterparts and then water soaked. Their results (see figure 4.37) reveal that the wet of optimum compacted specimens can also collapse upon wetting, provided that their initial water content is relatively small. Nevertheless, their collapse potential is significantly reduced compared with their dry of optimum prepared counterparts (compared under the same vertical stress and suction level). Hence, results similar to those of figures 4.35 and 4.36 must be handled with caution as the wet of optimum compacted soils do have a significant potential for collapse which is simply not identified when soaked at their post-compaction

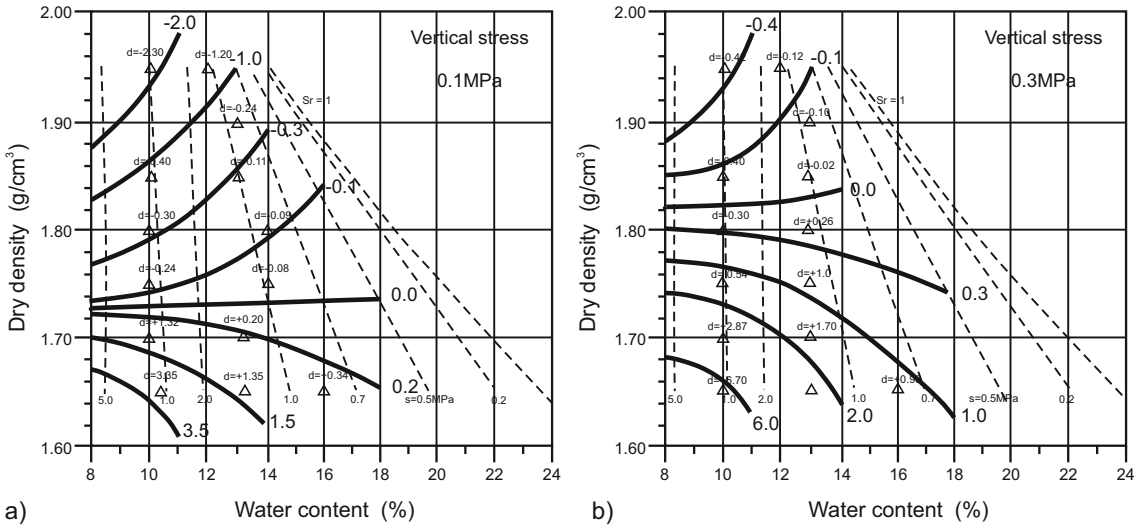


**Figure 4.36:** Contours of equal wetting induced volumetric deformation plotted in the initial dry density vs initial water content plane for statically compacted Barcelona Clayey Silt, soaked under a vertical net stress equal to: a) $0.1MPa$ and b) $0.3MPa$. (Suriol et al. 2002)

state.

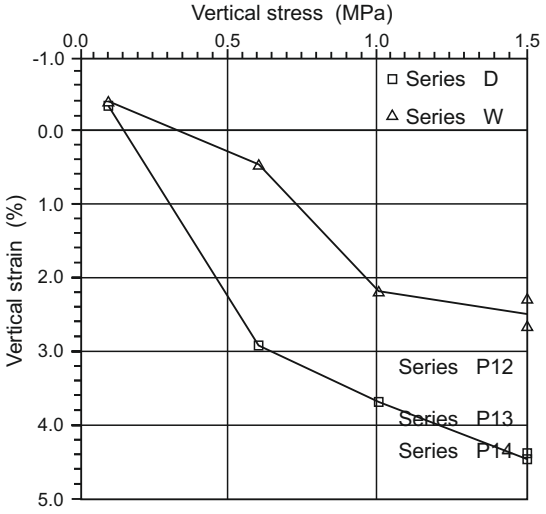


**Figure 4.37:** Volumetric collapse during wetting under different vertical stresses for samples compacted at the wet (W) and at the dry (D) of optimum, both dried to the same initial water content prior to wetting. (Gens et al. 1995)

### 4.3.4 Shear Strength and Critical State

The shear strength of unsaturated soils has been extensively studied the last several decades. It is widely accepted, that partial saturation increases the shear strength

of any given soil. As already mentioned, even from the first studies dealing with the mechanical behaviour of unsaturated soils, there were strong evidence that the shear strength of unsaturated soils can be interpreted through Bishop's stress. Bishop et al. (1960) extended the Mohr-Coulomb failure criterion, utilizing Bishop's stress (eq. 4.25), resulting to the following expression:

$$\tau = c + (\overline{\sigma} - u_a)\tan\phi + \chi\,(u_a - u_w)\tan\phi \tag{4.28}$$

Following the criticism of Bishop' stress and the utilization of two independent stress variables, Fredlund et al. (1978) proposed a generalized Mohr - Coulomb criterion where the effect of net stress and suction on the shear strength are decoupled. Shear strength is calculated as:

$$\tau = c + (\overline{\sigma} - u_a)\tan\phi + (u_a - u_w)\tan\phi_b \tag{4.29}$$

where the increase in shear strength with suction is controlled by the suction related angle of internal friction $\phi_b$. The strong limitations of such an approach where very soon realized. It implies that the increase in shear strength with suction is linear. Soils can remain fully saturated even under negative water pressures especially if they contain a high clay portion. The strength of a saturated soil element, even under a negative water pressure, is described by the classical Mohr-Coulomb failure criterion through Terzaghi's effective stress. It comes without saying that for equation 4.29 to be capable of reproducing such a behaviour,a $\phi = \phi_b$ assumption is necessary. To the contrary, there are plenty of experimental evidence suggesting that although $\phi = \phi_b$ holds true for soils which remain saturated under a relatively small suction, for higher suction values the appearance of air within the soil limits the beneficial effect of suction in shear strength, mathematically reflected in a lower $\phi_b$ ($\phi_b < \phi$).

Figure 4.38 presents the results of Escario & Saez (1986) for direct shear tests performed on various reconstituted soils from Madrid under different vertical stress and suction combinations. It is clear that even if $\phi$ can be assumed to be linear and independent of the applied vertical stress, the evolution of $\phi_b$ with suction is nonlinear and reduces with increasing suction. A similar trend was also confirmed by Fredlund et al. (1987), while Escario & Juca (1989) additionally suggested that the increase in shear strength with suction can reach a maximum ($\phi_b = 0$) and then start degrade ($\phi_b < 0$) for relatively high suction values. Nowadays there exist conclusive

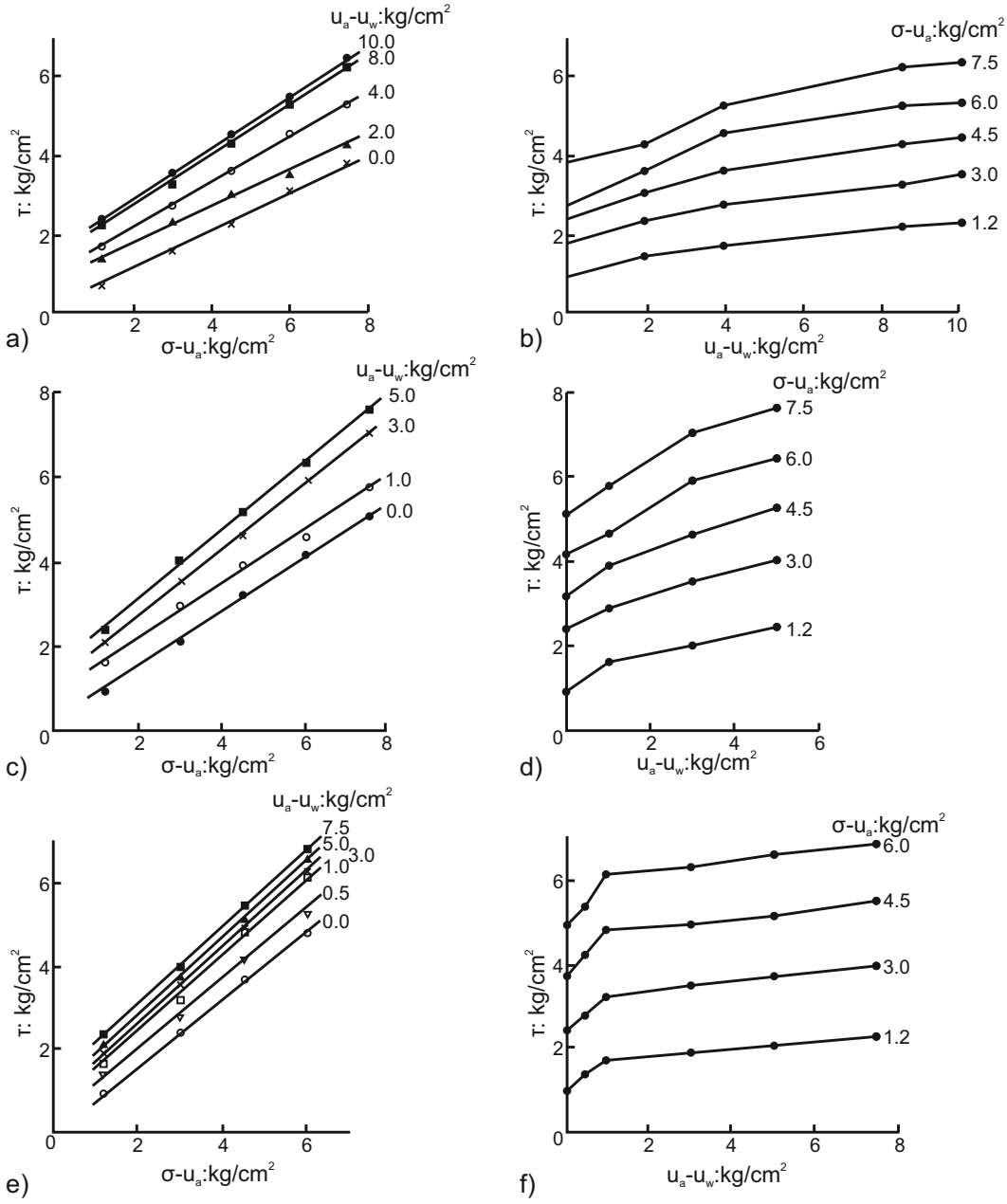


**Figure 4.38:** Direct shear tests under constant suction for Madrid gray clay "Penuela" (a,b), red clay of Guadalix de la Sierra (c, d) and Madrid clay sand (e, f). In a, c and e shear stress versus normal net stress for different values of suction and in b, d and f shear stress versus suction for different values of normal net stress. (Escario & Saez 1986)

evidence towards such an approach, which also indicate a strong relation between the nonlinearity of angle $\phi_b$ with the type of the soil and especially with its plasticity. Figure 4.39 presents the evolution of shear strength with suction for various fine-grained soils all suggesting a significant nonlinearity. Figure 4.40 summarizes similar

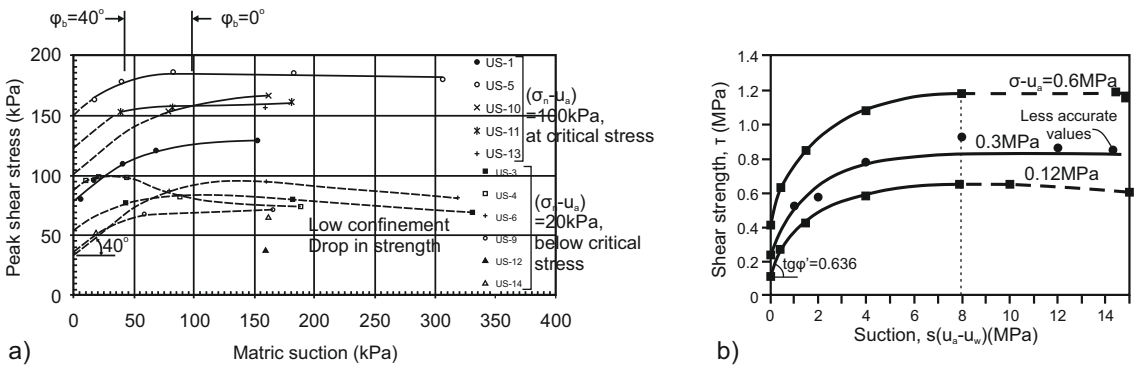


**Figure 4.39:** Evolution of shear strength with suction for: a) reconstituted Fine Ash Tuff (Gan & Fredlund 1996), and; b) Guadalix red clay (Escario & Juca 1989) after Lloret (2012)).

results for a sandy soil (Donald 1956) where a clear decrease in shear strength with increasing suction after a critical suction value is observed, calling for a negative $\phi_b$ value.

Recently, Sheng et al. (2011) summarized the following key aspects regarding the shear strength of unsaturated soils:

- under the same vertical pressure (or confining pressure), higher matric suctions result in higher shear strengths;
- under the same suction, higher vertical pressures (or confining pressures) result in higher shear strengths;
- the relationship between shear strength and the matric suction is nonlinear. The shear strength increases most rapidly at low matric suction levels, and then gradually flattens (or even decreases) at high suctions.
- it is generally more effective to increase the shear strength by increasing vertical stress (or confining pressure) than by increasing matric suction.

Regarding the nonlinearity of the relationship between shear strength and suction, Bardanis (2016), based on the soil type and plasticity, identifies the following five types of behaviour:

Type A: Steady, continuous increase in shear strength with suction. Corresponds to pure clayey soils of very high plasticity.

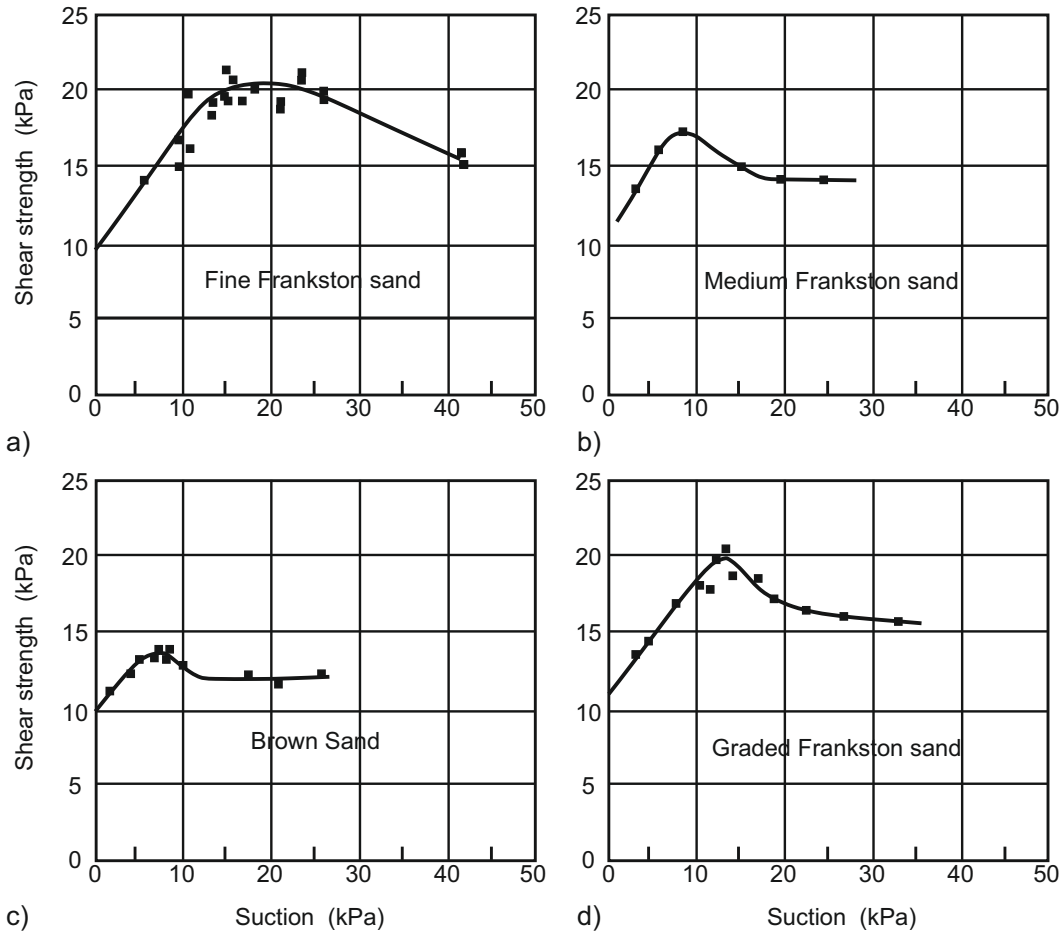


**Figure 4.40:** Evolution of shear strength with suction for: a) Fine Frankston sand; b) Medium Frankston sand; c) Brown sand and; d) Graded Frankston sand. (Donald 1956)

Type B: Continuous increase in shear strength with suction, but with a decreasing rate after a given suction level, usually related to the desaturation suction. Corresponds to clayey soils of medium to high plasticity.

Type C: Increasing shear strength with suction up to the desaturation suction level and subsequent shear strength stabilization for higher suction values. Corresponds to fine grained silts and to clayey soils of low plasticity.

Type D: Increasing shear strength with suction up to the desaturation suction level and then subsequent decrease in shear strength until a stabilization level. Corresponds to silty sands and to non-plastic silts.

Type E: Increasing shear strength with suction up to the desaturation suction level and then sudden and rapid decrease until the effect of suction in shear

strength completely vanishes. Corresponds to gravels and sands with negligible amount of fines.

The nonlinear evolution of shear strength with suction supported the recovery of Bishop's stress in unsaturated soil mechanics. Comparing equations 4.29 and 4.28 we observe that $\tan\phi_b = \chi \tan\phi_b$. Thus, using Bishop's stress in the classical Mohr-Coulomb criterion allows for a natural description of a nonlinear shear strength evolution, provided that parameter $\chi$ has been suitably selected.

As already mentioned, the simplest and most profound choice for parameter $\chi$ is degree of saturation ($\chi = S_r$). Many authors have used this approach to interpret the shear strength behaviour of unsaturated soils (i.e., Öberg & Sällfors (1997), Sheng et al. (2003), Nuth & Laloui (2008b)). Khalili & Khabbaz (1998) suggested that $\chi$ must be a function of suction, equal to unity for suction levels up to the desaturation suction and then reducing for increasing suction using a power law. Tarantino & Tombolato (2005), Tarantino (2007) and more recently Alonso et al. (2010) suggested that the shear strength of an unsaturated soil can be adequately described if parameter $\chi$ is properly related to the macrostructural degree of saturation $S_{r,M}$. The Alonso et al. (2010) power law is the simpler mathematical expression to scale down degree of saturation. It takes the following form:

$$S_{r,M} = S_r^a \tag{4.30}$$

where $a$ is a material property. Figure 4.41 presents comparisons of the predicted shear strength evolution with suction using Bishop's stress and the macrostructural degree of saturation with the experimental results of two different soils (Alonso et al. 2010). Using Bishop's stress with $\chi$ selected as a proper function of degree of saturation is also in line with the idea that the shear strength of an unsaturated soil must be fundamentally connected to its water retention properties, as suggested by Fredlund et al. (1996), Vanapalli et al. (1996) and Mohamad et al. (2006), amongst others.

Hereinbefore, the effect of partial saturation in shear strength was mainly examined in terms of the peak strength, being the one usually described through a failure criterion like the Mohr-Coulomb. Nevertheless, advances in experimental techniques allow for a more detailed examination of the mechanical behaviour, through triaxial loading tests under different states of partial saturation and different confining levels. Such tests facilitate the investigation of the effect of the consolidation history (i.e., isotropic, anisotropic, normally or over consolidated) and additionally provide

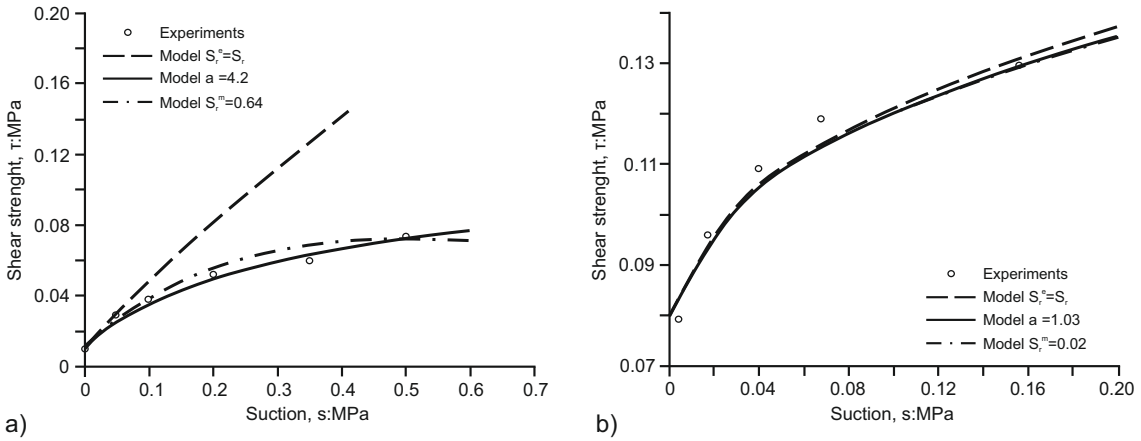


**Figure 4.41:** Comparison of the predicted evolution of shear strength with suction using Bishop's stress with $\chi = S_{r,M}$ in the Mohr-Coloumb failure criterion with experimental results of: a) a glacial till (Vanapalli et al. 1996) and b) a decomposed tuff from Hong Kong (Fredlund et al. 1996), after Alonso et al. (2010).

information on the deformational behaviour during loading. Various well documented experimental studies exist in the associated literature (Wheeler & Sivakumar 1995; Maâtouk et al. 1995; Cui & Delage 1996; Rampino et al. 2000; Cunningham et al. 2003; Thu et al. 2007; Kayadelen et al. 2007; Casini 2008; Casini et al. 2012).

The majority of the aforementioned contributions includes constant suction triaxial tests employing the axis-translation technique. Exceptions are the work of Cui & Delage (1996) who utilized the osmotic techniques to control matric suction and the work of Cunningham et al. (2003) where total suction was imposed through relative humidity control. Various types of soils are including, mostly plastic soils containing a significant amount of clay portion. Regarding sample preparation, results obtained on differently prepared soil samples can be found, including statically or dynamically soil samples, reconstituted soil samples or even natural undisturbed soil samples. With respect to the consolidation stage, most of the reported results involve isotropic consolidation, whit a limited number of anisotropically consolidated samples. Presenting in detail the results of all the available studies goes beyond the scope of this thesis. Nevertheless, based on the available results the most common behavioural aspects are identified and briefly discussed in the following lines.

We already discussed how partial saturation increases the yield stress of isotropically or anisotropically compressed soils. Results from triaxial tests allow for a generalization of this observation to say that partial saturation is in favour of an increased

elastic domain, reflected in an increased yield locus (see figure 4.42). Additionally, results from anisotropically consolidated soils suggest a non-isotropic yield locus, similar to what was discussed in chapter 3 for anisotropically consolidated saturated soils. Contradicting results exist on the effect of partial saturation on anisotropy though. For instance, Cui & Delage (1996) report that suction is profound in an isotropic way in their yield locus as it only increases its size and does not affect its orientation in the stress space. On the other hand, (Maâtouk et al. 1995) provide evidence towards an evolving yield locus orientation with suction changes.

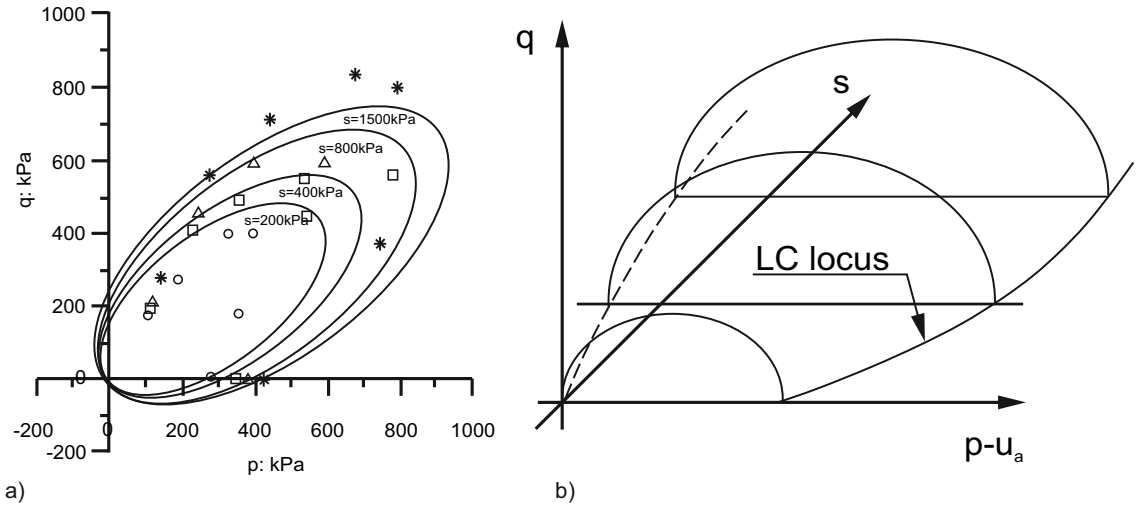


**Figure 4.42:** a) Projections of the yield surface in the $\overline{p} - q$ space for different suction values Cui & Delage (1996) and; b) the Rampino et al. (2000) adopted yield envelope in the $\overline{p} - q - s$

Figure 4.43 presents the stress-strain curves corresponding to Jossigny Silt samples (Cui & Delage 1996) triaxial loaded under four different suction levels and two different confining stress levels, while figure 4.44 compares the saturated and unsaturated stress-strain behaviour of a reconstituted silty clay (Cunningham et al. 2003).

Based on the observed behaviour we may summarize that an increase in suction (comparing results under the same confining net stress) results to:

- an increased stiffness, reflected in the initial "elastic" branch of the stress-strain curves;
- an increase in the obtained peak strength;
- an increased brittleness as softening is usually observed after reaching the peak strength;

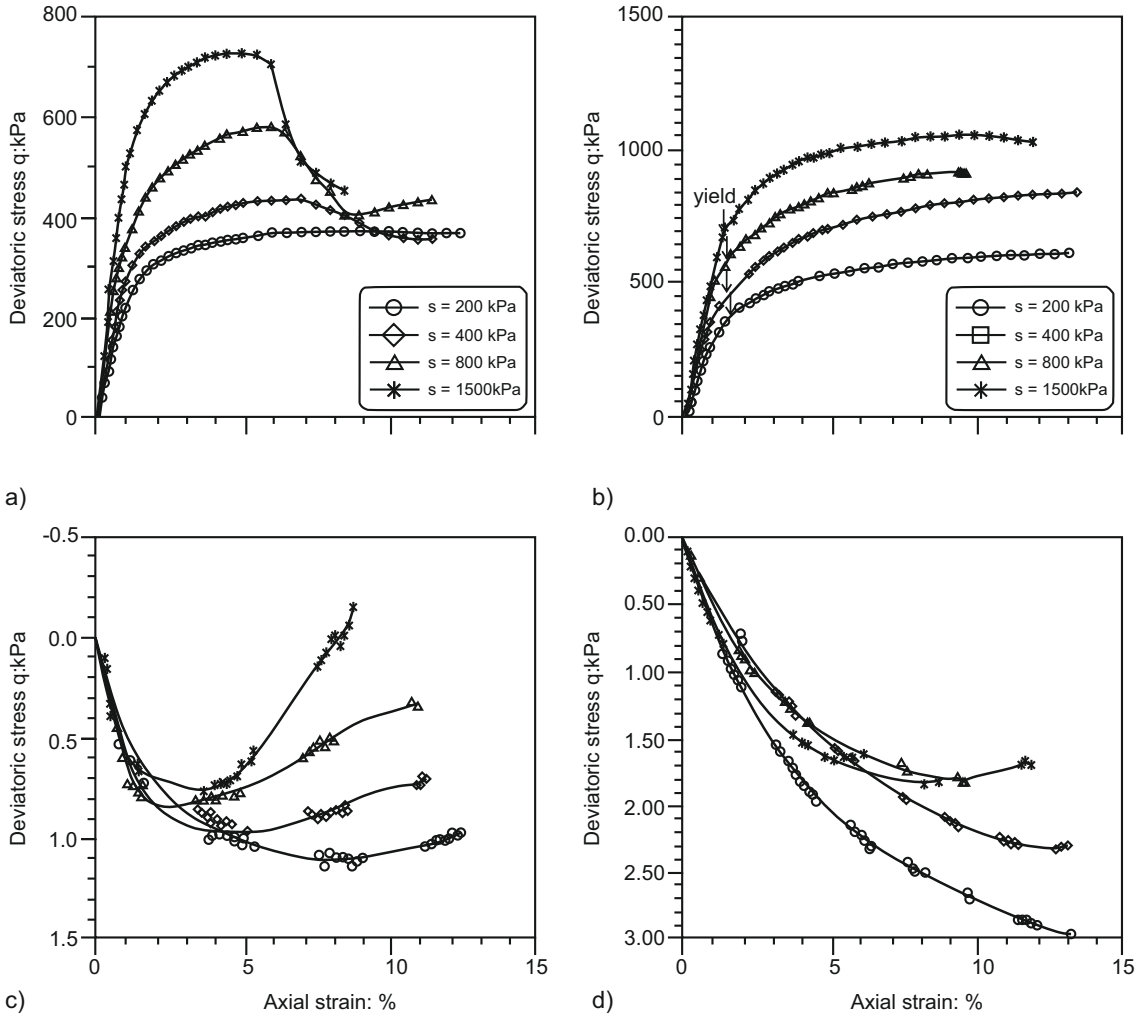


**Figure 4.43:** In (a),(b) deviatoric stress vs axial strain curves and in (c),(d) volumetric strain vs axial strain curves corresponding to triaxial compression tests on unsaturated, statically compacted Jossigny Silt samples, under four different suction levels and two different confining mean net stress levels equal to $50kPa$ in (a),(c) and to $200kPa$ in (b),(d). (Cui & Delage 1996)

- an increased tendency for dilation.

Nevertheless, the behaviour, is mainly dependant on the level of the applied net stress, with an increasing confining stress resulting to reduced brittleness, increasing initial stiffness and dilation.

In chapters 2 and 3 we discussed how the mechanical behaviour of saturated soils is suitably accommodated within the Critical State Mechanics framework. Most of the examined studies agree that the CSSM principles apply to the behaviour of partially saturated soils as well. Figure 4.45 presents indicative results from Rampino et al. (2000) experimental work. We observe that during constant suction compression,

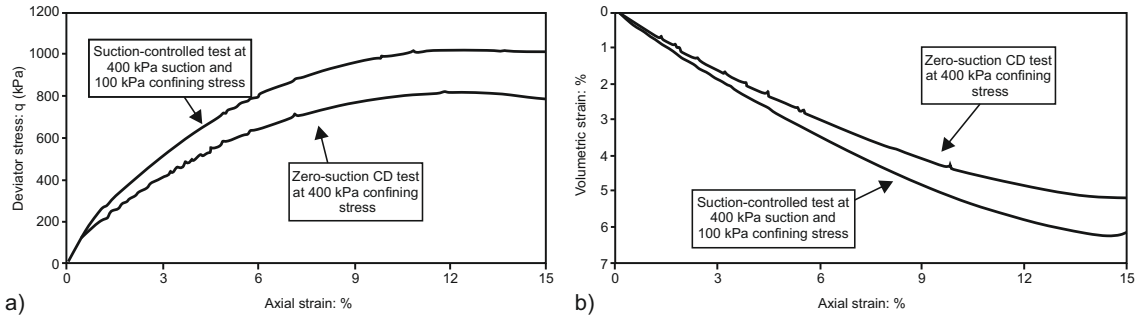


**Figure 4.44:** a) Deviatoric stress vs axial strain and; b) volumetric strain vs axial strain of a saturated and an unsaturated silty clay sample. (Cunningham et al. 2003)

degree of saturation evolves, following the volumetric deformation of the examined soil element, while it also reaches a kind of a critical state. This is reasonable if we recall that the ability of a soil to retain water, under a given suction level, depends on its void ratio. In that respect, a soil that is contracting exhibits an increase in its degree of saturation even under constant suction due to its constantly reducing void ratio. At this point we should clarify that constant suction tests are drained tests. Water is allowed to enter or leave the specimen for suction to remain in equilibrium, and thus, the aforementioned evolution of degree of saturation is solely attributed to the dependance of the WRC on the void ratio. On the contrary, during an undrained test, a contracting soil will increase its saturation even if a no void ratio dependant WRC is assumed. This is due to the fact that a constant quantity of water (constant water content) is occupying a continuously decreasing volume of voids. Results of figure 4.45 also indicate that degree of saturation stops evolving when the critical state is reached, as a result of zero volumetric deformation.

The critical state of a saturated soil is described through expressions 2.51 and 2.52, that are repeated here for the shake of brevity:

$$q = M \cdot p \tag{4.31}$$

and

$$v_{cs} = \Gamma - \lambda \ln p \tag{4.32}$$

The inclination and position of the CSL in the $p - q$ space is closely linked to the failure envelope of any given soil. In that respect, the first attempts to describe the critical state of unsaturated soils followed the generalized Mohr-Coulomb criterion

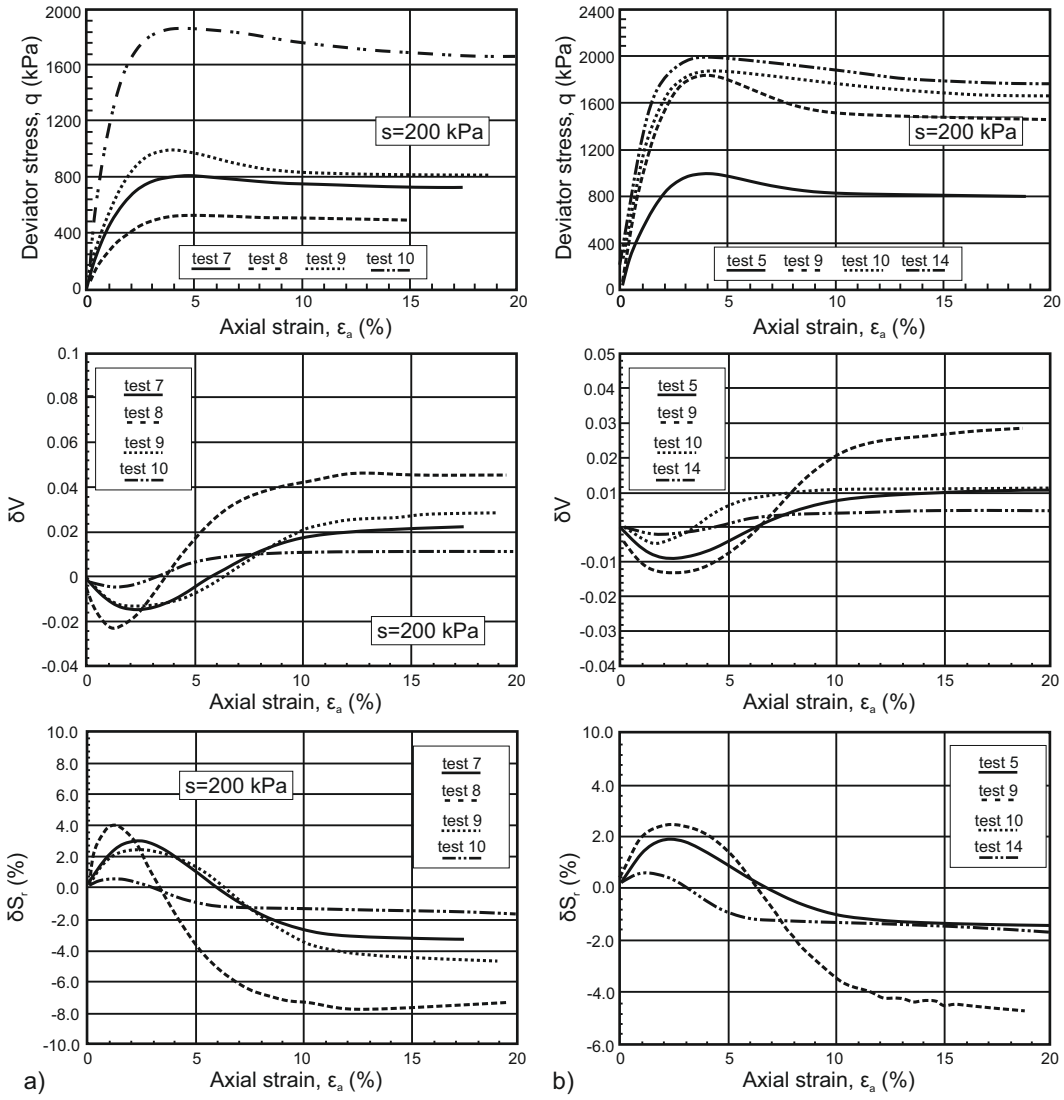


**Figure 4.45:** Results from triaxial compression tests of an unsaturated compacted silty sand from Italy, under: a) constant suction ($s = 200kPa$) and various confining stress levels and; b) different suction levels and constant mean net stress($\overline{p} = 400kPa$). Rampino et al. (2000)

(see eq. 4.29). Toll (1990), in line with the concept of the two independent variables, proposed the following equation:

$$q = M_a \left(\overline{\sigma} - u_a\right) + M_b \left(u_a - u_w\right) \tag{4.33}$$

where $M_a$ and $M_b$ the net stress and suction related slopes of the critical state line

respectively. For the $v - \ln \overline{p}$ plane he proposed:

$$v_{cs} = \Gamma_{ab} - \lambda_a \ln (\overline{\sigma} - u_a) - \lambda_b \ln (u_a - u_w) \tag{4.34}$$

where $\Gamma_{ab}$ defines the position of the CSL line and $\lambda_a, \lambda_b$ its shape in the $v-\overline{p}-\overline{q}$ space. The author presented experimental results suggesting that a comprehensive description of the critical state requires additional dependance of the material parameters on suction or/and degree of saturation. Following Toll's work, various researchers proposed similar expressions (i.e., Wheeler & Sivakumar (1995), Maâtouk et al. (1995)).

The necessity for a dependance of the critical state parameters on the state of partial saturation is a common denominator in most of the related studies. Attempts to exclusively correlate them with the level of the applied suction raise contradicting results. Figure 4.46a presents the critical state lines defined from unsaturated silty sand specimens ((Maâtouk et al. 1995)) where the slope and position of the CSLs in both the $\overline{p} - q$ and $v - \ln \overline{p}$ planes appears significantly dependant on the level of the applied suction. Kayadelen et al. (2007), based on their results of an unsaturated residual soil from Turkey, suggest that the slope of the CSL remains practical constant while its position changes significantly towards an increased shear strength in the $\overline{p}-q$ space and an increased void ratio in the $v - \ln \overline{p}$ plane, both with increasing suction.

Following the revoke of Bishop's stress, Jommi (2000) proposed that in a similar manner to equation 4.28 the critical state of an unsaturated soil element can be described though the following expression:

$$q = M (\overline{\sigma} - u_a) + \chi \cdot M (u_a - u_w) \tag{4.35}$$

where M the slope of the critical state line under saturated conditions. Such an approach allows for a unified representation of the critical state of both saturated and unsaturated material states. Selection of parameter $\chi$ follows the previous discussion on a suitable $\chi$ values for the shear strength evolution and thus, $\chi = S_r^M$ seems the most proper option.

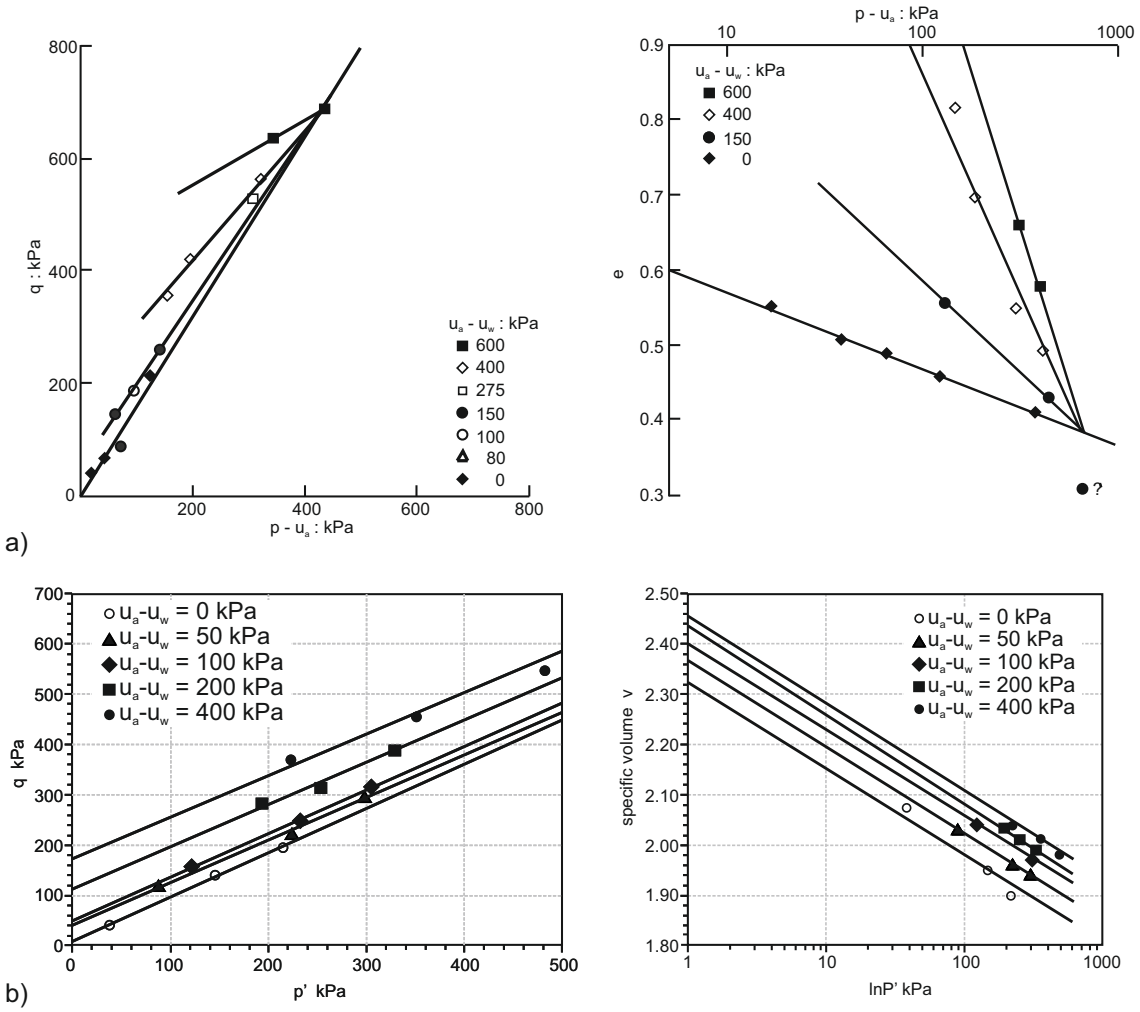


**Figure 4.46:** Critical state lines in the $\overline{p} - q$ space and in the $v$ or $e - \ln \overline{p}$ plane corresponding to different suctions. Results from: a) (Rampino et al. 2000) and b) Kayadelen et al. (2007).

## 4.4 Constitutive Modelling

Since 1990, when the first complete constitutive model for unsaturated soils the Barcelona Basic Model (BBM) (Alonso et al. 1990) was proposed, several constitutive models have been developed. Most of the available contributions are founded on the classical framework of plasticity as has been introduced in chapter 2. Contributions using the hypoplasticity framework also exist (i.e., Mašín & Khalili (2008)), but they will not be included in the present review. Moreover, discussion is limited to non-expansive soils, as their modelling requires sophisticated modelling techniques to take into account the different effects of microstructure and macrostructure in the volumetric behaviour. For the interested reader, probably the most significant con-

tribution in the constitutive modelling of expansive soils is the BExM model (Alonso et al. 1999), based on a modified BBM framework.

Several review papers regarding constitutive modelling of unsaturated soils are available and they can serve as good references to study the topic (Arairo et al. 2014; Sheng 2011; Gens 2010; Gens et al. 2006; Sheng & Fredlund 2008; Leong et al. 2003; Wheeler & Karube 1996). They offer different approaches in categorizing, comparing and discussing the modelling capabilities. For instance, constitutive modelling contributions are grouped according to their assumed characteristic surfaces, compressibility framework, critical state assumptions and on whether they include some kind of hydromechanical coupling or not. In this section we follow an alternative approach, initially proposed by Gens et al. (2006) and also elaborated in Gens (2010), where existing constitutive models are grouped according to the utilized constitutive variables.

As already mentioned, a comprehensive description of the mechanical behaviour of unsaturated soils calls for the use of two stress variables. Regarding constitutive modelling, Gens et al. (2006) propose the use of term "Constitutive Variables" instead of stress variables, to account for the fact that some of the available frameworks incorporate constitutive parameters which do not comprise a stress quantity. The most obvious example is degree of saturation, employed in Bishop's stress definition or even as an extra variable. This terminology is adopted for the rest of the present Doctoral dissertation.

Several different combinations regarding the two necessary Constitutive Variables (CVs) are available. For the First Constitutive Variable (FCV) two are the most commonly adopted approaches, namely: a) net stress and; b) Bishop's stress. As far as the Second Constitutive Variable (SCV) is concerned, suction is the most common selection with degree of saturation gaining increasing popularity the last few years as an alternative option. Also combinations of suction and degree of saturation, such as the modified suction proposed by Gallipoli et al. (2003) exist. In the following paragraphes, a brief discussion of the most important contributions is offered and the available models are grouped based on their FCV.

### 4.4.1 Net Stress Models

#### 4.4.1.1 The Barcelona Basic Model (BBM)

Alonso et al. (1987) proposed a conceptual framework to describe the behaviour of unsaturated soils, that was later formulated as the Barcelona Basic Model (BBM) (Alonso et al. 1990). BBM is the most influential contribution and has dominated subsequent development in the field. Almost any model proposed after the BBM can be seen as a modification and enhancement of the BBM.

The Barcelona Basic Model is based on the well established CSSM framework to extend the Modified Cam Clay model in the unsaturated regime. Net stress ($\overline{p}$) and suction ($s$) are used as the first and the second CVs respectively. The Loading-Collapse (LC) Surface comprises the most fundamental idea of the BBM. The Loading-Collapse curve together with the Suction Increase (SI) line bound the elastic domain in the $\overline{p} - s$ plane (see figure 4.47); thus, states on the LC or the SI are assumed plastic. In fact, both curves are an outcome of the adopted volumetric compressibility framework as the latter is depicted in figure 4.48.

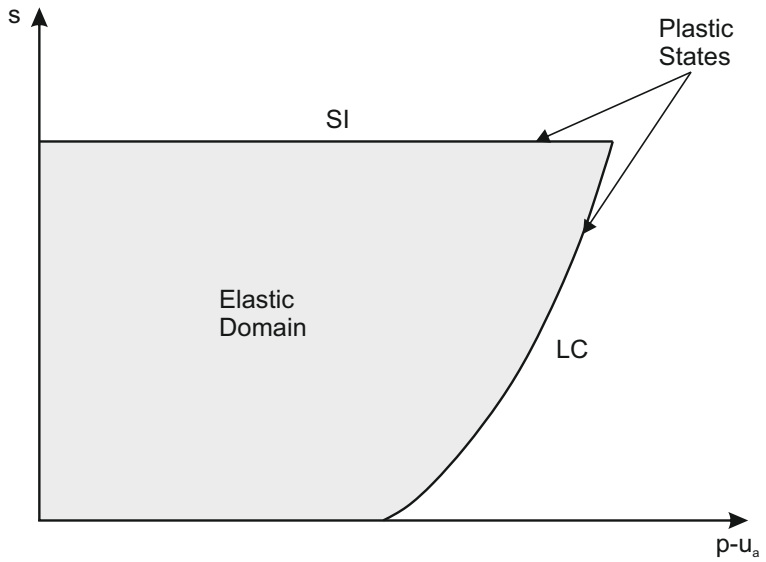


**Figure 4.47:** The Loading Collapse (LC) and the Suction Increase (SI) yield curves, bounding the elastic domain of the Barcelona Basic Model (BBM) in the $\overline{p} - s$ plane. (Alonso et al. 1990)

In figure 4.48a we may observe the assumed compressibility behaviour in the $v - \ln \overline{p}$ plane. The suction value $s_0$ corresponds to the maximum suction level ever imposed in the soil element under concern. Soil states past this "yield suction"

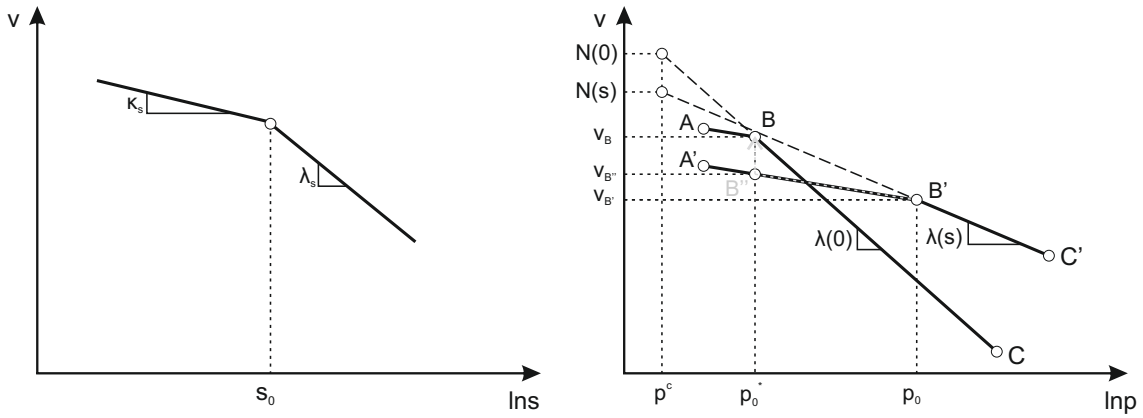


**Figure 4.48:** The compressibility framework of the BBM in the; a) $v - \ln s$ and b) $v - \ln \overline{p}$ plane. Alonso et al. (1990)

are assumed plastic and move on the virgin, suction related, compression line with slope $\lambda_s$, while a suction reduction path is assumed elastic and is represented by propoer swelling lines with a slope $\kappa_s$. Following these assumptions, the volumetric deformations related to suction changes can are described as:

$$\text{for elastic states: } \dot{v} = -\kappa_s \frac{\dot{s}}{s - p_{at}} \tag{4.36a}$$

$$\text{for plastic states: } \dot{v} = \lambda_s \frac{\dot{s}}{s - p_{at}} \tag{4.36b}$$

where $p_{at}$ the atmospheric pressure, preventing the denominator from acquiring a zero value when suction tends to zero.

Figure 4.48b presents the adopted volumetric behaviour with respect to net stress changes. Examining the compressibility behaviour of the saturated material we observe that the classical bi-linear law (ABC) of the CSSM is adopted. Swelling lines have a slope equal to $\kappa$, $p_0^*$ denotes the preconsolidation pressure of the saturated material and parameter $\lambda(0)$ corresponds to the slope of the saturated virgin compression line. Its position is defined by the specific volume value $N(0)$ under a reference mean net stress equal to $p^c$.

An initially saturated soil (point A) that is gradually dried under a relative small constant net stress, will shrink and its state moves towards point A′. Loading (net stress increase), under a constant suction level, results in further volume decrease, described by a swelling line with slope $\kappa$[17], until its apparent preconsolidation pressure

[17]BBM assumes that the slope of the swelling lines $\kappa$ in the $v - \ln \overline{p}$ plane is independent of suction.

$p_0$ is reached. The exhibited apparent preconsolidation pressure $p_0$ is higher compered to the preconsolidation pressure of the saturated material $p_0^*$, reflecting the beneficial effect of partial saturation in increasing the elastic domain. Further loading, to net stress levels higher than $p_0$, moves the soil state along a compression line with slope $\lambda(s)$. BBM assumes that partial saturation results to a decreased post yield compressibility (an increased stiffness) with $\lambda(s) < \lambda(0)$. To describe the evolution of the slope of the compression lines with suction, BBM assumes:

$$\lambda(s) = \lambda(0) \left[ (1 - r)\, e^{-\beta s} + r \right] \tag{4.37}$$

where $\lambda(0)$ the slope of the saturated compression line and $\beta$, $r$ material constants related to the stiffness increase with suction. Equation 4.37 describes an asymptotic increase towards a maximum stiffness with increasing suction. Regarding the position of any given unsaturated compression line in the $v - \ln \overline{p}$ plane it is controlled through the void ratio value $N(s)$ under the reference pressure $p^c$.

Following the assumed compressibility behaviour, the variation of the apparent preconsolidation pressure ($p_0$) with suction can be easily calculated. The apparent preconsolidation pressure of an unsaturated material under a given suction ($s$) lies on a compression curve with slope $\lambda(s)$ (i.e., point B′) with the corresponding specific volume $v_{B'}$ equal to:

$$v_{B'} = N(s) - \lambda(s) \ln \left( \frac{p_0}{p^c} \right) \tag{4.38}$$

In a similar manner, the preconsolidation pressure of the saturated material (point B) corresponds to a void ratio $v_B$ equal to:

$$v_B = N(0) - \lambda(0) \ln \left( \frac{p_0^*}{p^c} \right) \tag{4.39}$$

The specific volume values corresponding to the apparent and to the saturated preconsolidation pressure can be connected through a proper swelling line (in the examined case B′B″) additionally accounting for the volume change corresponding during suction increase. We may write:

$$v_{B'} = v_{B''} - \kappa \ln \left( \frac{p_0}{p_0^*} \right) \tag{4.40}$$

for the swelling line (B'B") and further calculate the volume change due to suction

change through equation 4.36b as:

$$\Delta v_s = N(0) - N(s) = v_{B''} - v_{B'} = -\kappa_s \ln \frac{s}{s + p_{at}} \tag{4.41}$$

Finally, combining equations 4.38 to 4.41, after some algebra we end up with:

$$\frac{p_0}{p^c} = \left( \frac{p_0^*}{p^c} \right)^{\frac{\lambda(0)-\kappa}{\lambda(s)-\kappa}} \tag{4.42}$$

Equation 4.42 describes the evolution of the apparent preconsolidation pressure with suction and thus describes the shape of the Loading - Collapse curve.

To understand the key role of the Loading - Collapse surface in modelling the mechanical behaviour we will examine a set of illustrative Loading Paths (LP) with the help of figure 4.49:

LP.1: An initially unsaturated soil element is wetted (suction reduction) under a constant, relatively small mean net stress. Such a loading path is represented by a vertical line in the $v - \ln \overline{p}$ plane, with the soil state moving towards Point A. It is an elastic loading path and reproduces an increase in the void ratio (swelling);

LP.2: From the previous initial unsaturated state (Point A), the soil element is subjected to a mean net stress increase under constant suction. The soil element will compress elastically until the apparent preconsolidation pressure $p_0$ is reached (point B), while elastoplastic strains accumulation will accompany further loading. Yield at Point B corresponds to the intersection of the imposed loading path with the LC surface and for further loading the LC surface will harden following the increase of the apparent preconsolidation pressure. Let's assume that loading stops after appreciable plastic loading (Point C) and with Point C acting as an initial state we wet the examined soil element under constant mean net stress. Similarly to LP1, the wetting (loading) path is represented by a vertical line in the $\overline{p} - s$ plane, while in this case it is obvious that the soil state tends to move outside of the LC curve. With the LC surface acting as a yield surface, plastic loading is reproduced and the LC curve hardens again. Hence, the imposed wetting path is "equivalent" to an increase in the applied stress field, both leading to a volume reduction. As already mentioned, the irreversible (plastic) volume reduction during wetting of an initially

unsaturated soil element is called collapse;

LP.3: Wetting at an intermediate stress level (i.e., point D), corresponding to a confining net stress smaller that the apparent preconsolidation pressure of the material, a reverse in the volumetric behaviour is reproduced, with swelling (elastic behaviour) until the wetting path reaches the LC curve at point D′, followed by compressive elastoplastic strains and associated hardening of the LC curve for further suction reduction until point D″ is reached.

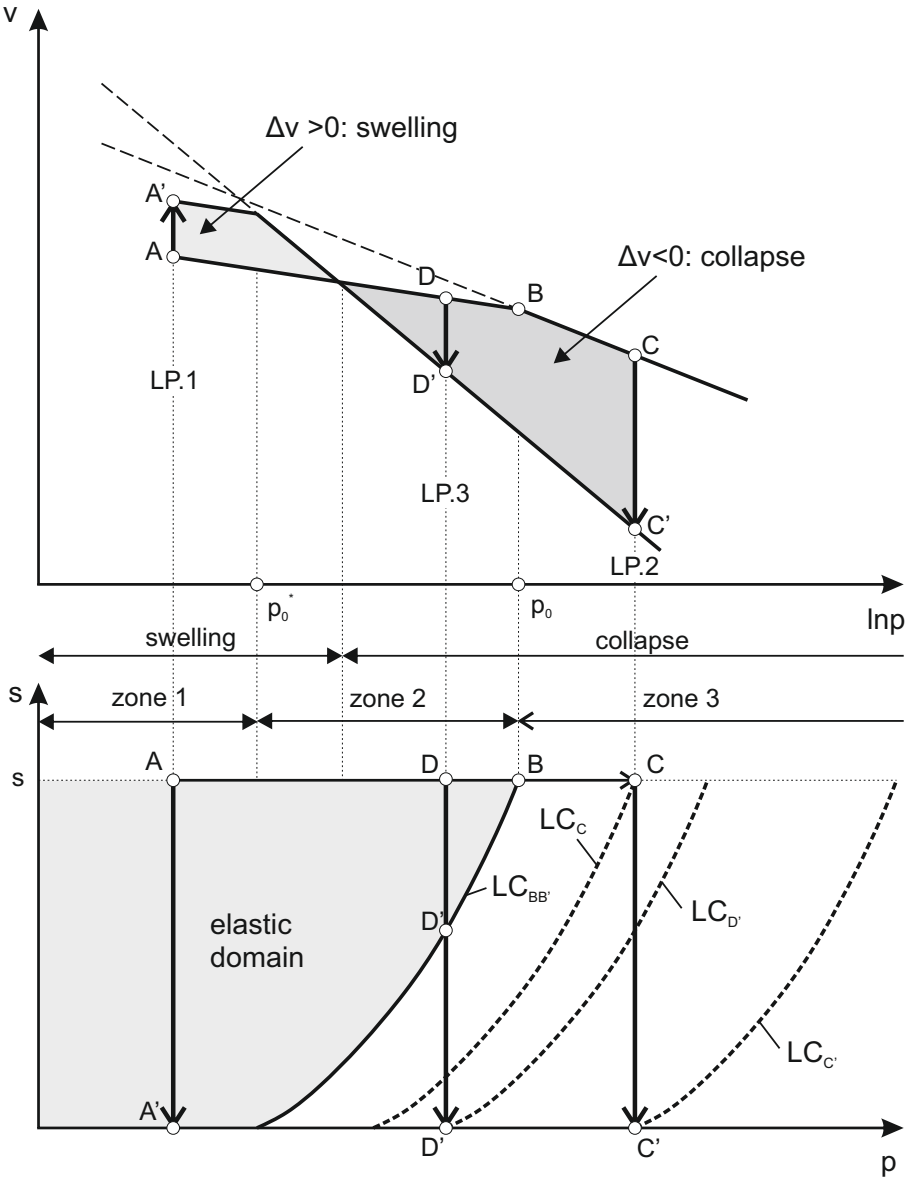


**Figure 4.49:** The BBM compressibility framework in the $v - \ln \overline{p}$ plane and the correspondence with the LC curve in the $p - s$ plane.

The aforementioned framework allows for a quantification of the net stress values for which each type of behaviour will be addressed. From the previous discussion it is clear that saturating a sample at a stress level $\overline{p} < p_0^*$ is associated with a purely elastic swelling behaviour. To the contrary, saturating a sample from an initially plastic state $\overline{p} > p_0^*$ on the LC curve is associated with purely plastic behaviour and thus leads to collapse. For intermediate net stress values, a reverse in the volumetric behaviour is reproduced, while whether the net deformation corresponds to swelling or collapse depends on the projection of the stress path on the $v - \ln \overline{p}$ plane.

To extend the proposed framework in the triaxial stress space Alonso et al. (1990), used the isotropic elliptical yield surface of the MCC model and thus, the complete yield envelope of figure 4.50 is obtained in the $\overline{p}-q-s$ space. We may observe that the right apex of the MCC's yield surface follows the variation of the apparent preconsolidation pressure with suction, or in other words it follows the LC curve (equation 4.42). The preconsolidation pressure under zero suction $p_0^*$ serves as an isotropic hardening variable and its evolution is described through the classical volumetric hardening rule of the Modified Cam Clay model (see equation 2.63).

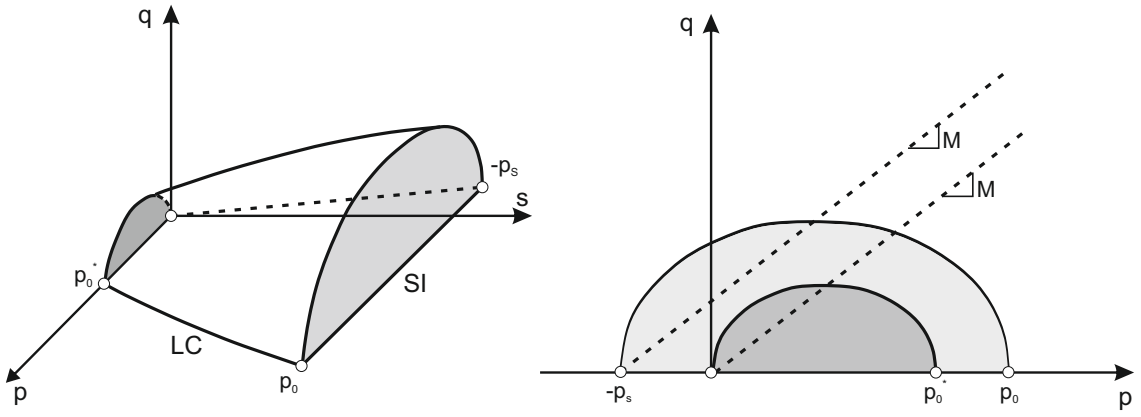


**Figure 4.50:** a) The BBM yield envelope in the $\overline{p} - q - s$ space and; b) projections of the yield envelope in the $\overline{p} - s$ plane for unsaturated and saturated material states. (Alonso et al. 1990)

Regarding the left apex of the yield surface, we observe that it moves towards negative net stress values (tension). This tension stress reflects the increase in shear strength with partial saturation and the corresponding ability of unsaturated soil elements to resist tensile stresses due to developing apparent cohesion. For the aforementioned evolution of the tensile strength with suction, Alonso et al. (1990) suggested

a simple linear law of the following form:

$$p_s = k \cdot s \tag{4.43}$$

where $k$ a material constant. Through simple mathematical calculations, it is proved that the CSL corresponding to such an assumption is described as:

$$q = M(\overline{p} + p_s) = M(\overline{p} + ks) \tag{4.44}$$

BBM included a primitive form of hydromechanical coupling as the movement of the SI curve was linked to the hardening of the LC curve. Finally, it also incorporates a slightly enhanced MCC flow rule which can reproduce realistic values of $K_0$ under 1D compression. The BBM's flow rule is a non-associated flow rule.

Barcelona Basic Model's wide success is mainly attributed to its volumetric compressibility framework which can consistently reproduce all the fundamental behavioural characteristics of unsaturated soils in a unified way. Moreover, the proposed framework builds on the critical state soil mechanics principles and follows the classical theory of plasticity, extending a well established constitutive model for saturated soils in the unsaturated regime. Thus BBM highlights the idea that partial saturation should be handled as a specific state of a soil and not as a special soil.

Nevertheless, being the first attempt for a systematic modelling of unsaturated soils, it is reasonable to have some limitations. The three most important are:

a) It reproduces a continuous linear increase in shear strength with suction while, as was demonstrated in the previous section, experimental evidence suggest a highly nonlinear behaviour.

b) The reproduced collapse increases continuously with an increasing net stress, contrary to experimental evidence which suggest that collapse potential stabilizes and may even reduce with increasing confining. In other words, the BBM cannot reproduce a maximum in collapse.

c) During drying it reproduces a continuously decreasing void ratio with increasing suction, contrary to experimental evidence indicating a void ratio stabilization.

#### 4.4.1.2 Other Significant Contributions

Numerous constitutive models (or framework modifications) founded upon the conceptual framework of the BBM exist in the international literature, with most of the researchers trying to address the three previously mentioned shortcomings.

Josa et al. (1992), in an attempt to address the issue of maximum of collapse, proposed a new formula to describe the increase in preconsolidation pressure with suction by additionally taking into account the level of the applied stress. The adopted formula is:

$$p_0 = (p_0^* - p^c) + p^c \left[ e^{(1-m)-as} + m \right] \tag{4.45}$$

where parameter $a$ controls the shape of the LC curve and parameter $m$ controls the confining level under which the maximum of collapse appears. The latter is computed through:

$$m = +1 \frac{\zeta_\psi - 1}{\zeta_\chi - p^c} \left( P_0^* - p^c \right) e^{\frac{\zeta_\chi - P_0^*}{\zeta_\chi - p^c}} \tag{4.46}$$

where $\zeta_\chi$, $\zeta_\psi$ variables related to the maximum volumetric strains during wetting. The obtained LC is always convex describing a continuous increase of the apparent preconsolidation pressure towards an asymptotic value. Figure 4.51 presents predictions of volumetric collapse, where a maximum of collapse is observed at an intermediate level of confinement.

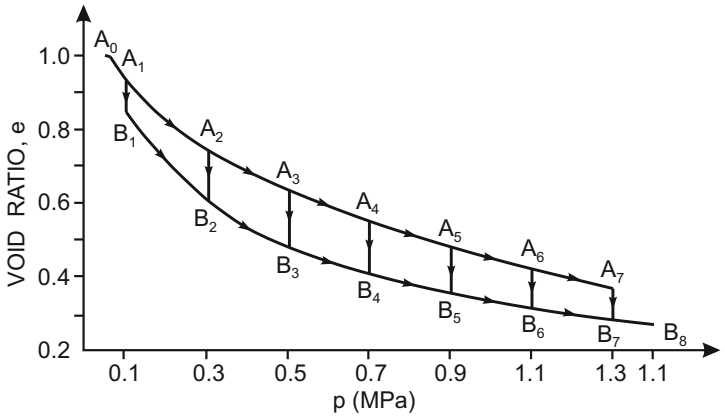


**Figure 4.51:** Volumetric collapse predictions of the Josa et al. (1992) constitutive model.

Wheeler & Sivakumar (1995), based on their experimental results on compacted kaolinite samples (see fig. 4.23b), questioned the validity of equation 4.37. They suggest that the post yield compressibility of an unsaturated soil element should not be de facto assumed to decrease with increasing suction but instead, that $\lambda(s)$ must be

suitably modelled for any given soil under consideration. Suitable modifications are proposed in the compressibility framework to ensure that the LC curve will always predict an increasing elastic domain with suction. Their approach allows the simulation of a continuously decreasing amount of collapse potential with increasing net stress. Furthermore, following Toll (1990) and Wheeler (1991), they claim that the slope and position of the critical state line in both the $\overline{p}-q$ space and the $v-\ln\overline{p}$ plane is suction dependant, proposing the following expressions towards that direction:

$$q = M(s)\cdot\overline{p} + \mu(s) \tag{4.47a}$$

$$v = \Gamma(s) - \psi(s)\ln\frac{\overline{p}}{p_{at}} \tag{4.47b}$$

$$\tag{4.47c}$$

Figure 4.52 summarizes the main modifications of Wheeler & Sivakumar (1995) in the BBM framework.

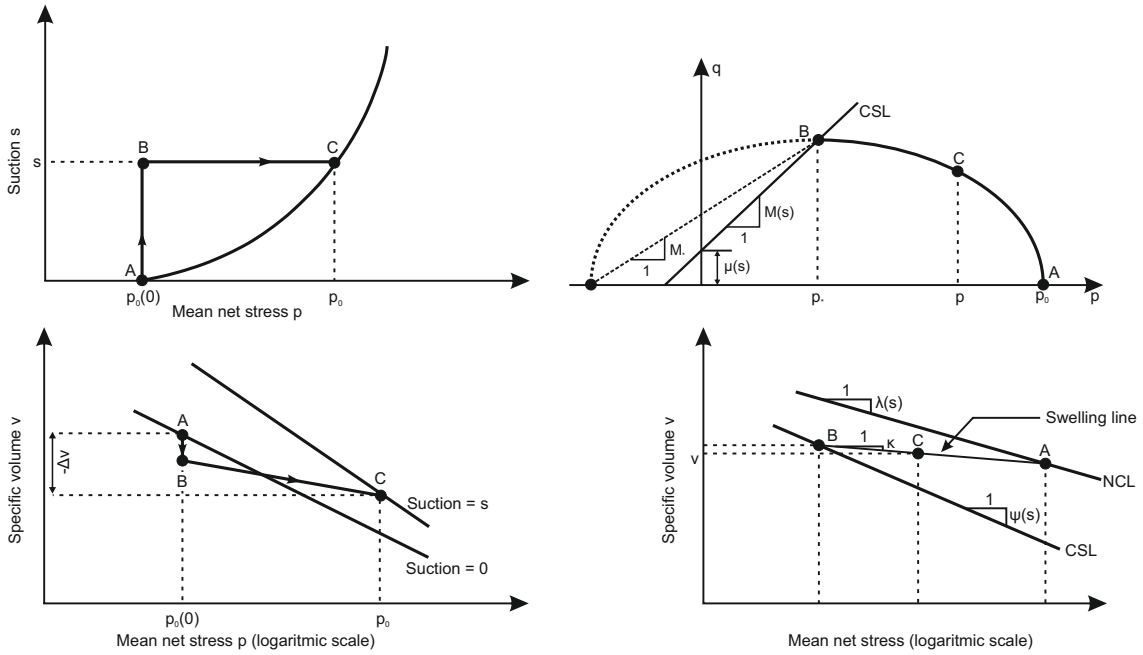


**Figure 4.52:** a) The LC curve; b) the yield surface in the $\overline{p}-q$ space; c) the compressibility framework and; d) the critical state lines in the $v-\ln\overline{p}$ plane, as assumed in the Wheeler & Sivakumar (1995) constitutive model.

Wheeler (1996) further enhanced the Wheeler & Sivakumar (1995) model to describe the variation of water content within a soil element, using the specific water volume $v_w$. The role of soil fabric was also recognised and especially the different effects

of micro- and macro-structure in the behaviour of compacted soils. Finally, Sivakumar & Doran (2000) included a smooth transition between the SI and the LC curves in the $\overline{p} - s$ plane which lead to a continuous and continuously differentiable curve.

Cui & Delage (1996) present an extensive experimental investigation regarding the unsaturated behaviour of Jossigny Silt, including both isotropically and anisotropically consolidated samples. Their results confirm the validity of BBM's compressibility framework, while they suggest that an anisotropic soil model must be used as the reference saturated model in order to better capture the yield locus of anisotropically consolidated samples (see fig 4.43). They additionally suggest that the yield surface shall be inclined along the $K_0$ line and also symmetrical with respect to the same line. To that end, they adopt a general mathematical expression which describes a symmetrical ellipse rotated at an angle $\theta$ with respect to the isotropic axis and its extension in the unsaturated regime is realized through the volumetric compressibility framework of the BBM. Regarding the effect of anisotropy, they claim that according to their experimental results, partial saturation is reflected in a rather isotropic way without affecting the yield surface's shape or orientation. They conclude by suggesting the selection of a non-associated flow rule.

Following Cui & Delage (1996), Stropeit et al. (2008) presented an anisotropic constitutive model for unsaturated soils using as a reference model the S-CLAY1 model (see section 3.3.7). The latter was extended it in the $\overline{p} - q - s$ stress space using BBM's LC curve (eq. 4.42) to account for the evolution of the apex of the distorted yield surface of the S-CLAY1 model with suction. The derived model was named the Anisotropic Barcelona Basic Model (ABBM). D'Onza et al. (2010) slightly enhanced the ABBM, with an eye towards more accurate shear strength predictions. They claim that the enhanced model, named the ABBM1, can better fit the experimental results of Barrera (2002) used in their modelling exercise. Figure 4.53 presents the yield surfaces of ABBM and ABBM1 models.

Vaunat et al. (2000) was amongst the first to present a complete hydromechanical model for unsaturated soils. They coupled the mechanical framework of the BBM with a hysteretic, void ratio dependant water retention model to reproduce irreversible strains within drying-wetting cycles. In doing so, the main wetting and main drying branches of the WRC are considered as yield surfaces, while the scanning curves describe the elastic domain. The WRM used accounts for the micro- and macro-structural degree of saturation, with the authors suggesting that the me-

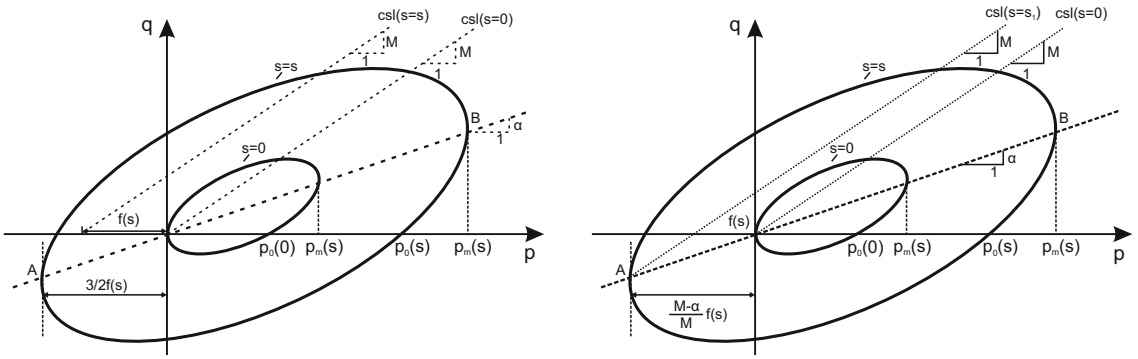


**Figure 4.53:** Saturated and unsaturated yield surfaces of: a) the ABBM (Stropeit et al. 2008) and; b)the ABBM1 (D'Onza et al. 2010) constitutive models .

chanical behaviour shall be primary linked to the evolution of the macro-structure as usually only larger macro-pores are affected by mechanical loading. Their mathematical formulation is very interesting, nevertheless it is quite extended and complicated to be included in the present review. Simultaneously, Buisson & Wheeler (2000) proposed a general hydromechanical framework, which can be incorporated in any given constitutive model for unsaturated soils provided that net stress and suction are used as the FCV and SCV respectively. The proposed framework is conceptually similar with the Vaunat et al. (2000) proposal and can also reproduce plastic irreversible strains within a drying-wetting cycle.

Rampino et al. (2000) investigated experimentally the mechanical response of a quite plastic silty sand. They claim that the BBM's compressibility framework can adequately describe the mechanical behaviour of the examined soil. Their material resembled the behaviour of typically saturated sands and in that respect, they adopted a reference model for sands, the Nor-Sand model (Jefferies 1993). The BBM's volumetric framework was used for the extension in partially saturated material states; an additional suction dependency regarding the slope of the swelling lines on the $v-ln\overline{p}$ is incorporated, while for the critical state they adopt the Wheeler & Sivakumar (1995) proposal. The Rampino et al. (2000) model is probably the first one and also one of the very few attempts to extend a saturated model for sands in the unsaturated regime.

Tang & Graham (2002) presented one of the most serious attempts to unify the effects of net stress and suction through an equivalent stress. The proposed equivalent stress is computed as:

$$p_{eq} = \sqrt{\overline{p}^2 + s^2} \tag{4.48}$$

Equivalent stress allows for a unified description of the mechanical behaviour in the $\overline{p} - q - s$ space, while the SI and LC curves are naturally linked to one hyper-surface that is continuous and continuously differentiable. The proposed equivalent stress probably comprises the most successful attempt to derive a real effective stress for unsaturated soils, in the sense that every aspect of the mechanical behaviour, even wetting induced volumetric collapse could be reproduced. Nevertheless an obvious shortcoming of their proposal is its inability to recall Terzaghi's effective stress upon saturation.

Georgiadis (2003) proposed a constitutive model for unsaturated soils and implemented it in the Imperial College Finite Element Program (ICFEP). The proposed model follows the framework of BBM, with suitable modifications to address most of its shortcomings. An "equivalent suction" $s_{eq}$ is utilized as the SCV, defined as the excess of soil suction ($s$) over the desaturation suction ($s_0$) and mathematically described as:

$$s_{eq} = \begin{cases} 0 & \text{if } s \leq s_0 \\ s - s_0 & \text{if } s > s_0 \end{cases} \tag{4.49}$$

Equivalent suction ensures a consistent transition between saturated and unsaturated material states, nevertheless the derived constitutive equations are discontinuous and thus complicate numerical implementation. To reproduce a decreasing collapse potential with increasing net stress Georgiadis (2003) followed an approach similar to Josa et al. (1992). In fact, in low confining stress levels the BBM compressibility framework (eq. 4.42, with $s = s_{eq}$) is used, while for higher confining stresses a modified LC curve expression was proposed; it has the following form:

$$P_0 = P_0^* \cdot \alpha_c^{\frac{\lambda(0)-\lambda(s_{eq})}{\lambda(s_{eq}-\kappa)}} \tag{4.50}$$

where parameter $\alpha_c$ can be calibrated to reproduce a maximum of collapse at the desired confining level.

Georgiadis (2003) additionally proposed an alternative option, where instead of modifying the BBM's compressibility framework, a new equation was used to describe the virgin compression line of an isotropic material at a given suction level; it has the following form:

$$v = N(s_{eq}) - \lambda(0) - \lambda_m \left(\frac{p_0}{P^c}\right)^{-b} \left(1 - b \ln \frac{p_0}{p^c}\right) \tag{4.51}$$

where again all parameters can be suitably linked with the confining stress level for which the maximum of collapse is observed.

Regarding the behaviour in the triaxial stress space, the yield surface of Lagioia et al. (1996) was extended in the unsaturated regime using $s_{eq}$, the slope of the CSL in the $\overline{p} - q$ space was assumed independent of suction while moreover, in order to describe a nonlinear increase in shear strength with suction increase he proposed a new expression for the translation of the left apex ($f(s_{eq})$) of his yield surface towards the tensile regime:

$$f(s_{eq}) = S_r \cdot s_{eq} + s_(0) \tag{4.52}$$

It is apparent that the model needs to be coupled with a proper WRM to give the $S_r$ value at each suction level. Figure 4.54 summarizes schematically the assumed and reproduced behaviour of the proposed constitutive model in the $\overline{p}-q-s_{eq}$ stress space. The Georgiadis (2003) constitutive model is one of the most complete attempts to propose an unsaturated model formulated in terms of net stress, addressing successfully most of the BBM's shortcomings. At the same time, the model was implemented in a FEM code and an extended numerical investigation was performed to highlight the importance of unsaturated behaviour in common engineering problems.

Tsiampousi et al. (2013a) enhanced the Georgiadis (2003) model by incorporating a curved Hvorslev state surface (see fig. 4.55a) to improve the model predictions on the dry side. Moreover, in Tsiampousi et al. (2013b) an advanced hysteretic WRM, with void ratio dependency (see fig. 4.55b), was proposed and implemented in ICFEP to improve the reproduced hydromechanical behaviour.

Bardanis & Kavvadas (2008a) modified the BBM model to account for the residual void ratio during shrinkage and to increase the versatility of the model's prediction of shear strength with suction increase. In more detail, they proposed that the volumetric behaviour of BBM in the $v - \ln s$ plane needs a proper modification to take into account that soils do not shrink continuously with increasing suction. A simple trilinear behaviour in the $v - \ln s$ plane, as depicted in figure 4.56a, was proposed as the simplest possible modification, where the residual void ratio $e_r$ is used as an extra parameter. Expressions that link the residual void ratio with different physical characteristics for structured and structureless soils are also proposed. As far as the increase in shear strength with suction is concerned, the authors propose that BBM's parameter $k$ (see eq. 4.43) should be nonlinear. To that end, in a similar fashion to (Georgiadis 2003), the degree of saturation was used while two additional

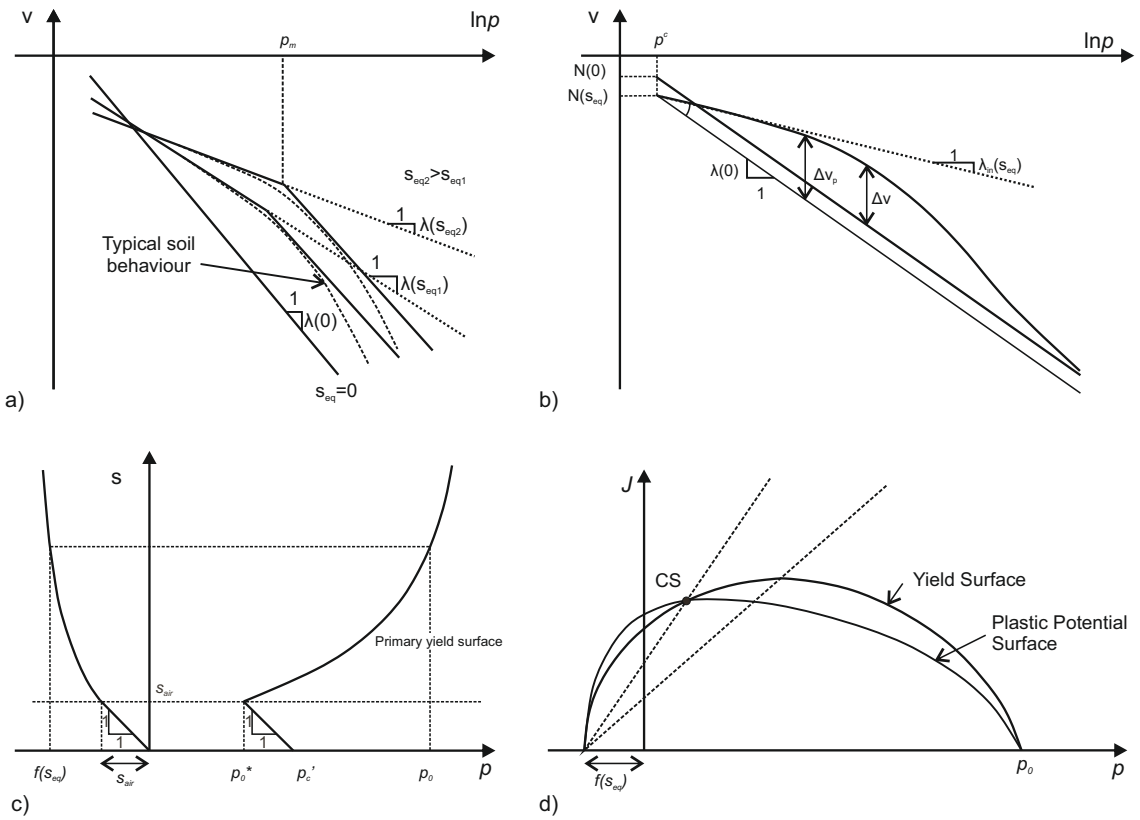


**Figure 4.54:** The Georgiadis (2003) constitutive model's a) modified BBM compressibility framework; b) alternative compressibility framework; c) yield envelope in the $\overline{p}-s$ plane and; d) yield and plastic potential surfaces in the deviatoric stress plane.

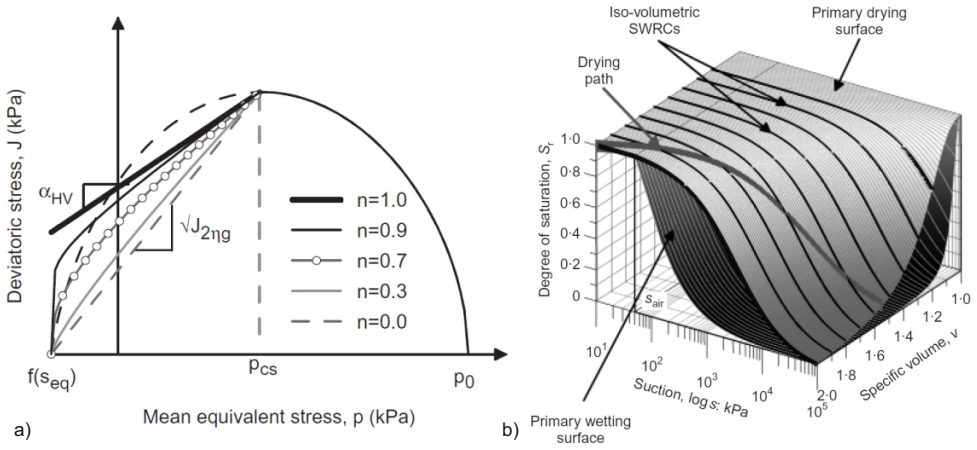


**Figure 4.55:** a) The Tsiampousi et al. (2013a) curved Hvorslev state surface and; b) the Tsiampousi et al. (2013b) hysteretic, void ratio dependant WRM.

empirical parameters, $\zeta_k$ and $n_k$ where added to allow for increased versatility. The

proposed expression is:

$$k = \zeta_k \cdot S_r^{n_k} \tag{4.53}$$

and allows for different types of behaviour to be simulated like continuous but nonlinear increase, stabilization or even decrease after an initial increase up to the air-entry value (see figure 4.56b). Recently, in Bardanis (2016) more experimental evidence in

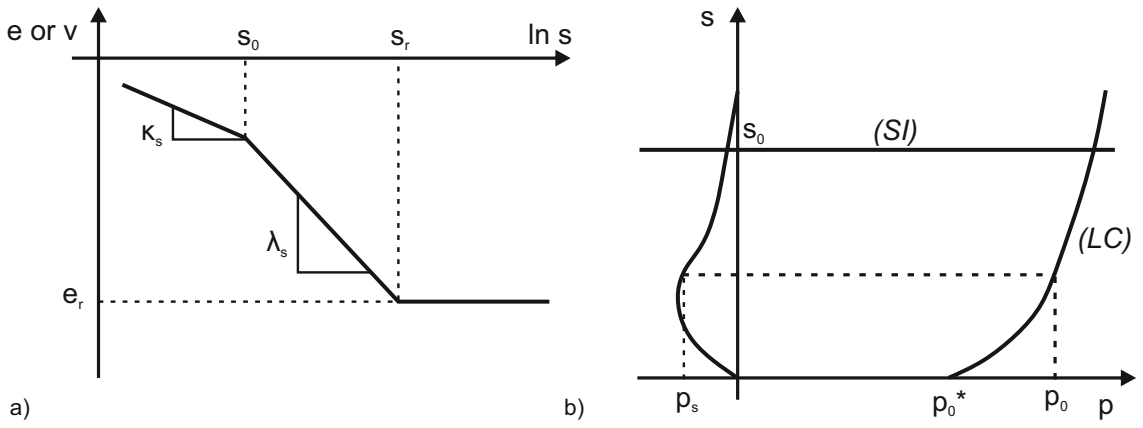


**Figure 4.56:** The Bardanis & Kavvadas (2008a) proposed BBM modifications; a) the modified volumetric framework in the $v - \ln s$ plane and; b) the modified yield envelope in the $\overline{p} - s$ plane.

favour of the proposed modifications where presented.

Somewhere in between the net stress and Bishop stress models, the SFG model, proposed by Sheng et al. (2008) is located. The authors tried to address most of the shortcomings of the net stress models by introducing a new modelling concept based on the use of two independent stress variables. They started from the behaviour of a reconstituted soil element which is progressively dried, emphasizing on the fact that until the soil becomes unsaturated, even for positive suction values (negative water pressures) the volumetric behaviour cannot differ from the behaviour of a saturated soil element, as the latter is represented through the principle of effective stresses. Their fundamental idea is that an increment of the applied net stress ($\dot{\overline{p}}$) and/or of the applied suction ($\dot{s}$), under an initial level of net stress ($\overline{p}$) and suction ($s$) reproduces the following increment of the volumetric deformation:

$$\dot{\varepsilon_v} = \lambda_{vp} \frac{\dot{\overline{p}}}{\overline{p} + s} + \lambda_{vs} \frac{\dot{s}}{\overline{p} + s} \tag{4.54}$$

while for the corresponding suction compressibility parameter the next function is

proposed:

$$\lambda_{vs} = \begin{cases} \lambda_{vp} & \text{if } s \leq s_0 \\ \lambda_{vp}\frac{s_0+1}{s+1} & \text{if } s > s_0 \end{cases} \tag{4.55}$$

allowing for a smooth transition between saturated and unsaturated conditions. Moreover, a gradual decrease in soil compressibility with drying is described. Regarding the net stress related compressibility, it is ensured that as far as the material remains saturated the slope $\lambda_{vp}$ equals the compressibility of the saturated material, while for higher suction values the compressibility decreases with increasing suction and increases with increasing net stress. Figure 4.57 presents characteristic predictions of the SFG model.

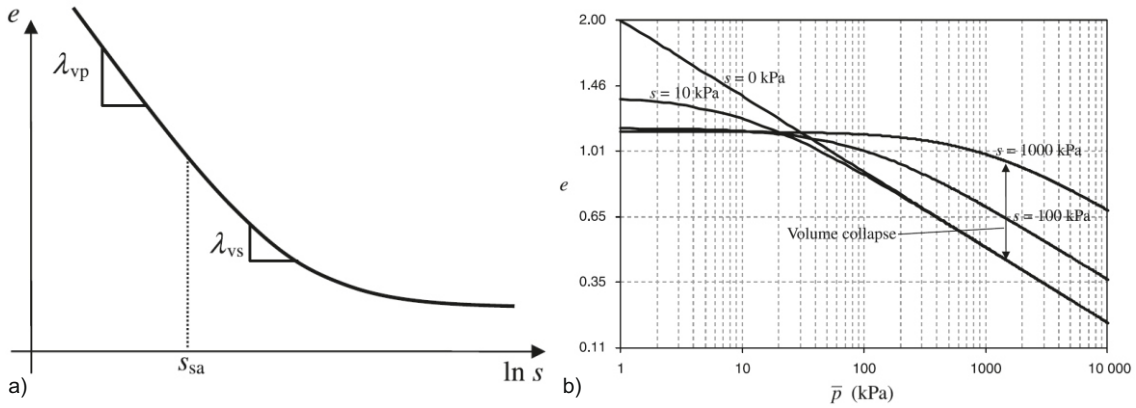


**Figure 4.57:** Characteristic predictions of the SFG model on the: a) $e - \ln s$ and b) $e - \ln p_{eq}$. (Sheng et al. 2008)

The initial model was coupled with a hysteretic WRM similar to Wheeler et al. (2003). In Sheng & Zhou (2011) an advanced hydromechanical coupling for the SFG model was proposed, based on the idea that the experimentally obtained WRCs are usually constant net stress curves and not constant void ratio curves. The SFG model is one of the most complete attempts to represent in a consistent way the mechanical behaviour of unsaturated soils, using net stress and suction as independent stress variables. Nevertheless, the last few years it has been surpassed by the revival of Bishop's stress in constitutive modelling of unsaturated soils.

### 4.4.2 Bishop's stress models

The main advantage of the net stress and suction approach is the simplicity and perspicuity offered in the representation of common laboratory results and of common

stress paths corresponding to typical loading conditions. On the other hand, the transition between saturated and unsaturated conditions cannot be efficiently handled, especially in numerical analyses, as net stress does not recover the Terzaghi's effective stress upon saturation.

Kohgo et al. (1993) were amongst the first to address the aforementioned issue by incorporating Bishop's stress in their constitutive formulation. The authors selected parameter $\chi$ based on a micro-mechanical analyses of the inter-particle menisci forces that develop between the soil grains in an unsaturated porous medium. They resulted in the following proposal which associated parameter $\chi$ exclusively with suction:

$$\chi = \begin{cases} 1 & \text{if } s \leq s_0 \\ \frac{s_c - s_0}{(s^* + \alpha^e)^2} & \text{if } s > s_0 \end{cases} \tag{4.56}$$

where $s_0$ the desaturation suction, $s_c$ the critical suction and $\alpha$ a material parameter, while $s^*$ represents an equivalent suction calculated as: $s^* = s - s_0$. We may observe that if degree of saturation is not somehow related to parameter $\chi$, a discontinues definition is required to reduce Bishop's stress to Terzaghi's effective stress upon saturation. They also utilized a volumetric framework where the virgin compression lines depend on the equivalent suction through a hyperbolic function to reproduce a volumetric behaviour similar to BBM, namely an increased stiffness with increasing suction. The MCC was used as the reference model. The significance of their contribution lies on the fact that being probably the first to utilize Bishop's stress in constitute modelling, they still realized and also emphasized on the fact that an additional constitutive variable is necessary (they selected the equivalent suction) to consistently describe wetting induced volume reduction.

Bolzon et al. (1996) also used Bishop's stress and suction to extend the Pastor et al. (1990) model for saturated soils in the unsaturated regime. They assumed that parameter $\chi$ is equal to the degree of saturation $S_r$, thus describing a smooth and natural transition between saturated and unsaturated soils. Alike Kohgo et al. (1993) they emphasized on the need for a SCV, while in their case soil suction ($s$) was selected and incorporated in their definition of the Plastic modulus $H$. They also tried to address the problem of a maximum of collapse by further elaborating on the definition of the Plastic Modulus $H$ to include an additional dependence on the level of confinement. Then, they derived their hardening rule by employing the consistency condition, resulting with an LC curve equation which is identical with the

BBM's equation 4.42 with net stress simply substituted by Bishop's stress. Regarding the post yield compressibility, the proposed $\lambda(s)$ was both suction and pressure dependant, following their assumed Plastic Modulus definition.

Probably the most significant contribution in constitutive modelling of unsaturated soils using Bishop's stress is this of Jommi (2000), mainly due to the fact that her contribution was the one triggering the systematic use of Bishop's stress. The author started from the MCC model and just substituted Terzaghi's stress with Bishop's stress. Then, the author compared the derived behaviour in terms of net stress, with the BBM framework. The performed comparison identified those aspects of the unsaturated soils' mechanical behaviour which are naturally reproduced through Bishop's stress implementation and those aspects that require additional assumptions.

Starting from equation 2.54 the Yield Function of the MCC model in the triaxial stress space is represented by:

$$f\left(p,q,P_0\right)=q^2-Mp\left(p_0-p\right)=0 \tag{4.57}$$

where $p_0$ that preconsolidation pressure. Substituting $p$ with Bishop's stress (eq. 4.25) we derive:

$$f\left(p,q,P_0\right)=q^2-M\left(\overline{p}+\chi\cdot s\right)\left(p_0-\overline{p}-\chi\cdot s\right)=0 \tag{4.58}$$

while for $\chi=S_r$ we further obtain:

$$f\left(p,q,P_0\right)=q^2-M\left(\overline{p}+S_r\cdot s\right)\left(p_0^*-\overline{p}-S_r\cdot s\right)=0 \tag{4.59}$$

where $\overline{p}$ the net mean stress, $S_r$ the degree of saturation, $s$ suction and $p_0^*$ the preconsolidation pressure of the saturated material. Using equation 4.59, projections of the yield surface on the $q-\overline{p}$ and $\overline{p}-s$ planes can be plotted for a saturated ($s=0$ and $S_r=1$) and an unsaturated soil state ($s>0$ and $S_r<1.0$), as depicted in figure 4.58.

We observe that unsaturated material states correspond to a yield surface where its projection on the $\overline{p}-q$ space is translated to the left of the saturated yield envelope. Comparing it with the BBM's yield surface in the same plane we observe:

a) The transition of the left apex of the yield surface towards negative $\overline{p}$ is consistent with BBM's predictions reflecting the increase in shear strength with suction. Moreover, the reproduced strength increase, if interpreted in terms of the BBM's

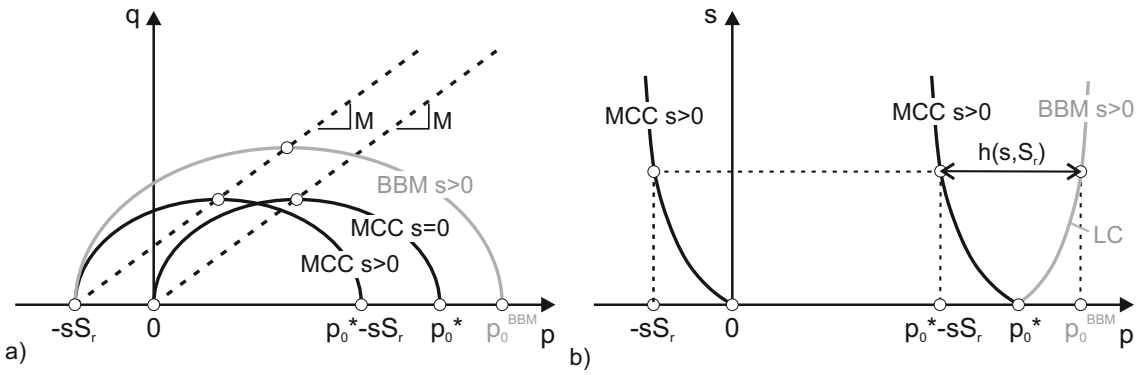


**Figure 4.58:** Comparison between the yield surface of the MCC model (Bishop's stress instead of Terzaghi's stress) and the BBM yield surface; a) the $q-\overline{p}$ space and the $\overline{p}-s$ plane.

parameters, correspond to $p_s = s \cdot S_r$ and thus $k = S_r$. It is obvious that the derived increase is nonlinear and also its nonlinearity depends on the $s - S_r$ relation, thus on the soil's WRC. At this point we shall recall that many researches how tried to enchase the BBM in order to reproduce a nonlinear shear strength evolution with suction (i.e., Georgiadis (2003), Bardanis & Kavvadas (2008a)) incorporated the $S_r$ in their formulations, while in the examined case this dependance arises naturally through the Bishop's stress implementation.

b) On the contrary, regarding the right apex of the yield surface, the reproduced transition of the yield surface towards reduced net stress values, implies that the apparent preconsolidation pressure decreases with increasing suction, contradicting the BBM's framework and of course the usually anticipated experimental behaviour.

With respect to the volumetric compressibility framework, in a similar fashion to the yield surface, we may substitute effective stress for Bishop's stress, in the well known equation of critical state plasticity to end up with:

$$v = N(0) - \lambda \ln \frac{p}{p^c} \Rightarrow \tag{4.60a}$$

$$v = N(0) - \lambda \ln \frac{\overline{p} + s \cdot S_r}{p^c} \tag{4.60b}$$

where $N(0)$ the specific volume of the saturated material at a reference pressure equal to $p^c$ and; $\lambda$ the slope of the virgin compression line of the saturated material.

Let's examine the behaviour of a soil element that is progressively dried under a constant net stress, with the help of equation 4.60b and figure 4.59. We observe

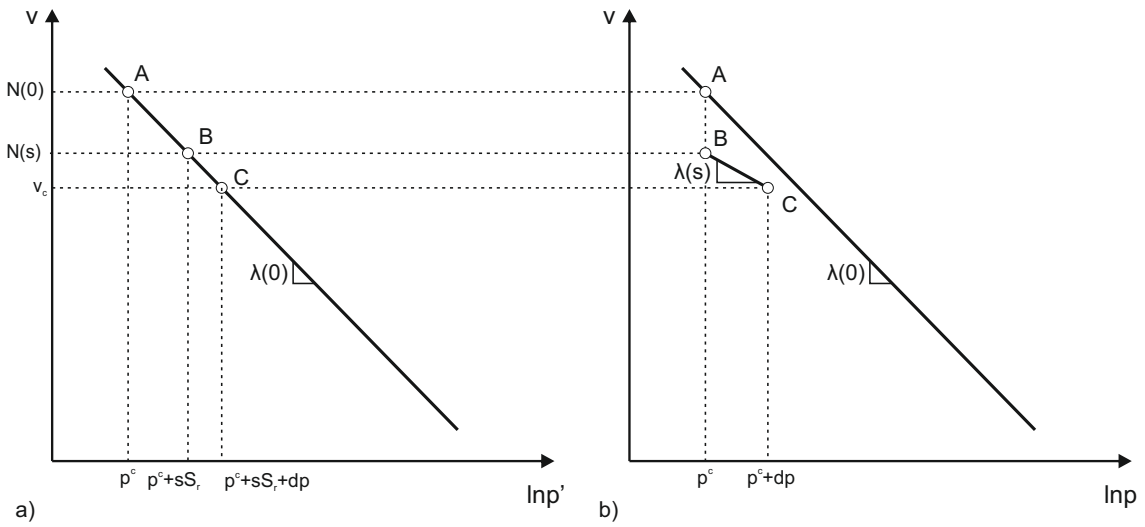


**Figure 4.59:** The MMC model's compressibility behaviour for Bishop stress implementation; a) the $v - \ln p$ and b) the $v - \ln \overline{p}$ planes.

that the corresponding volume change AB follows the virgin compression line of the material in the $v - \ln p$ plane, due to the fact that an increase in suction is equivalent to an increase in Bishop's stress. In the $v - \ln \overline{p}$ plane though, such a suction increase corresponds to a vertical stress path as net stress remains constant. We may calculate:

$$v_B = N(s) = N(0) - \lambda \ln \frac{p^c + s \cdot S_r}{p^c} \tag{4.61}$$

The corresponding volumetric strains can be simply calculated through differentiation of equation 4.60a to obtain:

$$\dot{v} = -\lambda(0) \frac{p^c}{p} \frac{1}{p^c} \dot{p} = -\lambda(0) \frac{\dot{p}}{p} \tag{4.62}$$

If we further assume that the soil sample is compressed under constant suction (Point $B \rightarrow C$) and constant degree of saturation[18], we can calculate the corresponding evolution of the specific volume by differentiating equation 4.60b to obtain an incremental relation in terms of net stress changes;

$$\dot{v} = -\lambda(0) \frac{p^c}{\overline{p} + s \cdot S_r} \frac{1}{p^c} \dot{p} = -\lambda(0) \frac{\dot{p}}{\overline{p} + s \cdot S_r} \frac{\dot{p}}{p} \tag{4.63}$$

Comparing equations 4.62 and 4.63 we may derive that an increment of net stress, under a constant suction level, corresponds to a compressibility $\lambda(s)$ which is equal

[18] A non-void ratio dependant WRM is assumed.

to:

$$\lambda(s) = -\lambda(0)\frac{\dot{\overline{p}}}{\overline{p} + s \cdot S_r} \tag{4.64}$$

Equation 4.65 reveals that stiffness increases with increasing suction and decreases with increasing net stress, both being consistent with the compressibility behaviour usually observed in experimental tests. It is also obvious that although the response in the $v - \ln p$ plane is linear (alike MCC), the corresponding response in the $v - \ln \overline{p}$ plane is nonlinear.[19]

A similar calculation can be performed for the elastic domain, to calculate the slope of the swelling lines $\kappa(s)$ in the $v - \ln \overline{p}$ plane. We end up with:

$$\kappa(s) = -\kappa(0)\frac{\dot{\overline{p}}}{\overline{p} + s \cdot S_r} \tag{4.65}$$

In this case we observe that contrary to BBM's framework, the slope of the swelling lines depend on suction, in line with various experimental results.

Up to this point, we may state that every aspect of the mechanical behaviour of unsaturated soils can be represented by simple using Bishop's stress in any effective stress constitutive model, with the exception of the variation of the preconsolidation pressure with partial saturation. To overcome this limitation, Jommi (2000) proposed that if $p'_0$ is the "effective" preconsolidation pressure of the saturated reference model, an additional term $h$ (see figure 4.58b) can be included to account for an increase in the preconsolidation pressure with suction and/or degree of saturation ($h(s, S_r)$)[20].

The modified "effective" preconsolidation pressure can take the following form:

$$p'_{0,mod} = p_0 + h(s, S_r) = p^*_0 - s \cdot S_r + h(s, S_r) \tag{4.66}$$

It becomes apparent that the term $h(s, S_r)$ calls for the use of extra constitutive variables to consistently represent unsaturated mechanical behaviour. For instance,

[19] A net stress increment $\dot{\overline{p}}$ under a constant suction in the $v - lnp$ plane is represented by a smaller horizontal distance compared to the $v - ln\overline{p}$ plane plot, as it initiates from a higher initial $p$ value and the stress axis is logarithmic.

[20] In the original publication the author suggests that term h needs to be exclusively dependent on degree of saturation $h(S_r)$, nevertheless it is preferable to consider term $h$ as a function of both suction and degree of saturation.

to simply enforce the BBM's LC curve equation (see eq. 4.42), we may write:

$$p_0' = p_0 + s \cdot S_r = p^c \left( \frac{p_0^*}{p^c} \right)^{\frac{\lambda(0)-\kappa}{\lambda(s)-\kappa}} + s \cdot S_r \tag{4.67}$$

Combining equations 4.66 and 4.67 we may calculate $h(s, S_r)$ as:

$$h(s, S_r) = p^c \left( \frac{p_0^*}{p^c} \right)^{\frac{\lambda(0)-\kappa}{\lambda(s)-\kappa}} + 2 \cdot s \cdot S_r - p_0^* \tag{4.68}$$

Summarizing, Jommi (2000) through a hierarchical approach demonstrated that, by substituting Terzaghi effective stress with Bishop's stress, the increase of shear strength with suction comes naturally together with the variation in stiffness with confinement and suction. On the other hand, should no other variables be introduced in the calculation, Bishop's stress formulation cannot naturally describe the increase in the apparent preconsolidation pressure.

Karube & Kawai (2001) formulated a simple constitutive model emphasizing on the effect of the suction induced inter-particle forces. They mention that although Bishop's stress can serve as a constitutive variable, the obvious assumption of parameter $\chi$ being equal to the degree of saturation $S_r$ is rather simplistic. Instead, they suggest that under different degrees of saturation, different types of water can be identified in the soil pores, namely: a) the bulk water; b) the meniscus water and; c) the absorbed water. Different water states result to a different intensity for the inter-particle forces, even when soil states under a common suction are examined. They tried to address these different micro-mechanical effects by incorporating a new quantity, named the "suction stress".

Loret & Khalili (2000) proposed a constitutive model for unsaturated soils based on the MCC model and further utilizing Bishop's stress and suction as their FCV and SCV respectively. The authors where probably the first to highlight that as far as suction remains below the desaturation suction $s_0$ the constitutive formulations should not deviate from the saturated base framework. In their case they used a $\chi$ definition which is a discontinues function of suction, to enforce $\chi = 1.0$ for $s \leq s_0$. According to the authors, assuming $\chi$ a function of suction eliminates the need for a WRM to describe the $s - S_r$ relationship and thus their model can be used even when the WRC of the simulated material is not available. Nevertheless, nowadays with advances in the experimental techniques, defining the WRC of a material is not

such a demanding task and should be considered a prerequisite for any attempt to simulate the mechanical behaviour of unsaturated soils.

The model proposed by Gallipoli et al. (2003) can be definitely placed near the top of the list of the most significant contributions in constitute modelling of unsaturated soils. The authors used Bishop's stress as the FCV with $\chi = S_r$. They highlighted that the SCV, necessary to describe the increase in the apparent preconsolidation pressure with partial saturation, must be related to the bonding effect of suction induced inter-particle forces, in a sense subscribing to Kavvadas (2000) idea that from the perspective of constitutive modelling unsaturated soils can be regarded structured soils. They also suggest that the number and intensity of inter-particle forces in partially saturated soils depend on both: a) the level of the applied suction and; b) the relative area over which this effect acts, with the latter depending directly on the degree of saturation. In that respect, they used a bonding factor $\xi$ equal to $\xi = (1 - S_r) \cdot f(s)$ as their SCV, where $f(s)$ a suction dependant function representing the intensity of the inter-particle forces. Their constitutive model was also coupled with the void ratio dependant Gallipoli et al. (2003) WRM.

Wheeler et al. (2003) presented a coupled hydromechanical constitutive model for unsaturated soils, by extending the ideas of Buisson & Wheeler (2000) in the Bishop's stress domain. The selection of their SCV was done with eye towards thermodynamic consistency. According to Houlsby (1997), the development of any constitutive relationships shall be based on properly selected work conjugate stress and strain variables, as such a selection ensures that the rate of input work per unit mass to a soil element is equal to the sum of the products of the stresses with their corresponding strain variables. With respect to unsaturated soil states, they mathematically proved and proposed the stress and strain combinations of table 4.10.

**Table 4.10:** The work conjugate stress and strain variables for unsaturated soils according to Houlsby (1997).

| Formulation | Stress variable | Strain variable rate |
|---|---|---|
| Net Stress | $\overline{\boldsymbol{\sigma}}$ | $\dot{\boldsymbol{\varepsilon}}$ |
| | $s$ | $-n \cdot \dot{S}_r + S_r \dot{\boldsymbol{\varepsilon}}^{*1}$ |
| Bishop Stress | $\boldsymbol{\sigma} = \overline{\boldsymbol{\sigma}} + s \cdot S_r$ | $\dot{\boldsymbol{\varepsilon}}$ |
| | $n \cdot s^{*1}$ | $- \cdot \dot{S}_r$ |

$^{*1}$ $n$ is the porosity.

Following Houlsby (1997)'s work, Wheeler et al. (2003) utilized the so called "modified suction" $(n \cdot s)$ as his SCV. His model is capable of reproducing a coupled hysteretic hydraulic and mechanical behaviour, by incorporating a Suction Increase (SI) and a Suction Decrease (SD) yield surface. An example of hydraulic hysteresis is the irreversible volume change within wetting-drying cycles, while an example of the mechanical coupling is the yield stress reduction accompanying such wetting-drying cycles. According to the authors the "modified suction", together with the coupled movement of the SI, SD and LC yield surfaces allow for a "reverse" coupling (mechanical to hydraulic), in the sense that a strain increment can reproduce a reduction in the degree of saturation under constant suction, without the need to incorporate a void ratio dependant WRM.

Following Wheeler et al. (2003), Sheng et al. (2004) proposed a similar hydromechanical constitutive model. Although, they recognise that from a thermodynamical point of view the CVs adopted by Wheeler et al. (2003) are the appropriate ones, they argue on the physical meaning of the "modified suction" emphasizing on the fact that it cannot be experimentally controlled. In that respect, they formulated their model using suction as their SCV, while they additionally proposed independent hardening rules for the SI, SD and LC constitutive surfaces. They adopt the BBM's equations following the formulation proposed in Jommi (2000), while hyper-elasticity was implemented to describe a conservative elastic rule (linear volumetric response in the $\ln v - \ln p$). A similar constitutive model was later proposed by Sun et al. (2007) as well.

In recent years, various researchers have suggested that the compressibility behaviour of unsaturated soils on the $v - \ln p$ can be better reproduced in terms of degree of saturation rather than suction, in fact proposing that degree of saturation can serve as the SCV. Zhang & Ikariya (2011) and Kikumoto et al. (2011) are amongst the first to try to represent soil compressibility through such an approach. They both suggest that the normal compression lines and the critical state line of an unsaturated soil element translates towards higher void ratio values under a given effective stress level (see fig. 4.60), always with respect to the CLs of the saturated material. Moreover, Kikumoto et al. (2011) claim that the experimental results of Cui & Delage (1996) are in favour of such an approach, provided that these are re-plotted in terms of Bishop's stress and degree of saturation.

Zhou et al. (2012a) and Zhou et al. (2012b) offered an extensive discussion on

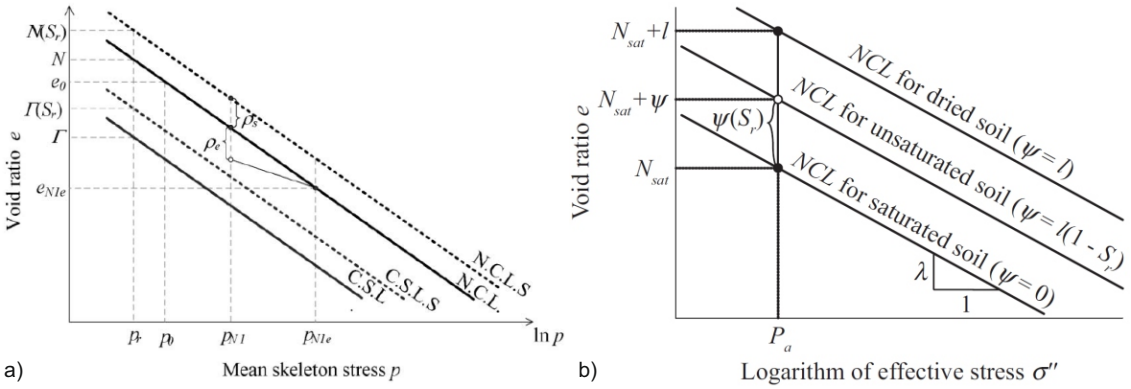


**Figure 4.60:** The assumed volumetric behaviour in $e - \ln p$ plane for the: a) Zhang & Ikariya (2011) and; b) Kikumoto et al. (2011) models.

the advantages that the interpretation of unsaturated soils behaviour in the stress - saturation space has over the conventional approach where suction is usually used as the SCV. They mainly emphasize on the fact that saturation dependant compression lines ensure that the soil state will not deviate from the saturated compression line as far as the soil remains saturated, and that during compression under constant suction the evolving degree of saturation (usually increasing) will affect the compressibility of the material. For their constitutive model they adopt Bishop's stress with $x = S_{r,M} = S_{r,e}$ in fact subscribing to Alonso et al. (2010) idea for the effective degree of saturation. Regarding the described compressibility behaviour they assume that an unsaturated material state should lie on compression curves that originate from a unique reference point in the $v - \ln p$ plane while their slope depends on the "effective" degree of saturation, according to:

$$\lambda(S_{r,e}) = \lambda_0 - (1 - S_{r,e})^{\alpha_1} (\lambda_0 - \lambda_d) \tag{4.69}$$

where $\lambda_0$ the compressibility of the saturated material, $\alpha_1$ a model parameter and $\lambda_d$ the theoretical compressibility of the same material when totally dried. To reduce the number of parameters, they suggest that $\lambda_d$ can be assumed equal to the slope of the swelling lines $\kappa$. The adopted framework is presented in figure 4.61a together with a typical drying-loading stress path (ABCD), while in figure 4.61b, their framework is compared with experimental results. It is proved that according to the aforementioned framework, the Loading - Collapse surface is described be the following expression:

$$p_0(S_{r,e}) = p_0^{\frac{\lambda_0 - \kappa}{\lambda(S_{r,e}) - \kappa}} \tag{4.70}$$

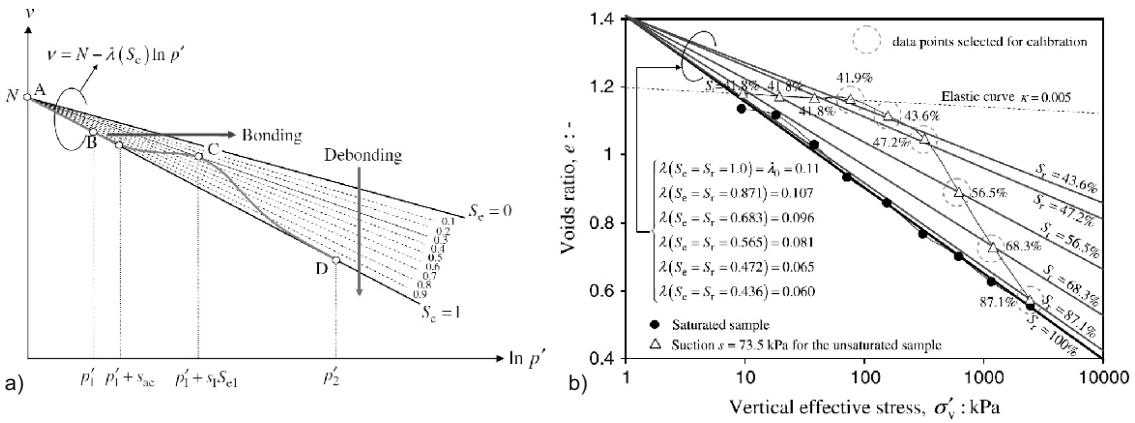


**Figure 4.61:** a) The (Zhou et al. 2012a) proposed volumetric compressibility framework and; b) its validation towards the experimental results of Honda (2000).

Equation 4.70 was used to describe the increase in preconsolidation pressure with degree of saturation on the MCC model, while for the $s - S_r$ relationship a hysteretic and void ratio dependant WRM was used. Figure 4.62 presents characteristic surfaces of the proposed model. Recently their model was further enhanced by Zhou & Sheng

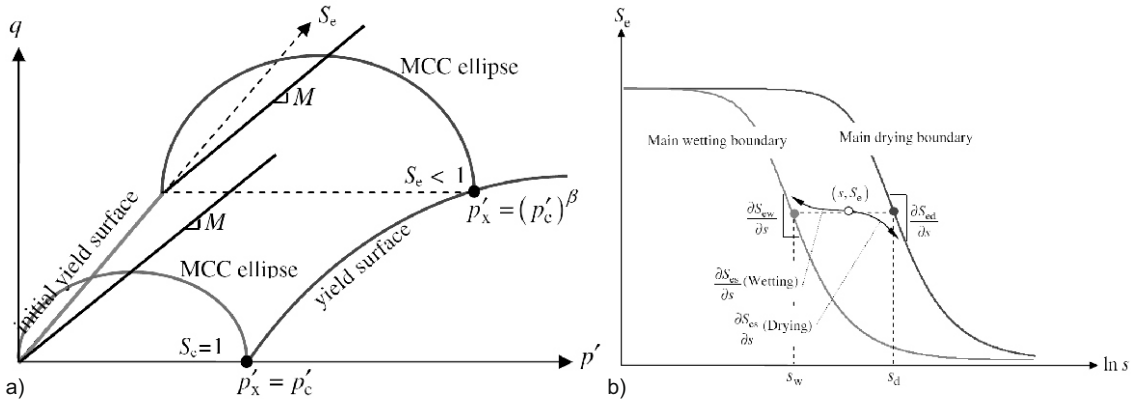


**Figure 4.62:** a) Yield surface of the Zhou et al. (2012b) constitutive model in the $p' - q - S_r$ domain; and b) characteristic curves of the WRM used.

(2015) to better capture the mechanical behaviour of compacted soils by incorporating a sub-loading surface utilizing some of the ideas of bounding surface plasticity.

Casini (2012) presented a volumetric framework for unsaturated soils, that was later extended to the triaxial stress space (Casini et al. 2012) using the MCC principles. Similar to Zhang & Ikariya (2011) and Kikumoto et al. (2011) the proposed framework assumes that the compression line of an unsaturated material state lies above the compression line of the corresponding saturated state, while the slope of the compression lines is assumed independent of the saturation state. This parallel

transition of the compression lines towards higher void ratio values (see figure 4.63) is the outcome of the assumed law for the evolution of the apparent preconsolidation pressure with degree of saturation:

$$p(\chi) = p_0 \cdot \alpha \exp(1 - \chi) \tag{4.71}$$

where $\alpha$ a material parameter and $\chi$ the same parameter used in the Bishop's stress definition. The macro-structural degree of saturation $S_{r,M} = S_r^a$, as proposed in Alonso et al. (1990), was used by the author. For the necessary description of the $s - S_r$ relationship the Casini et al. (2012) void ratio dependant WRM was utilized.

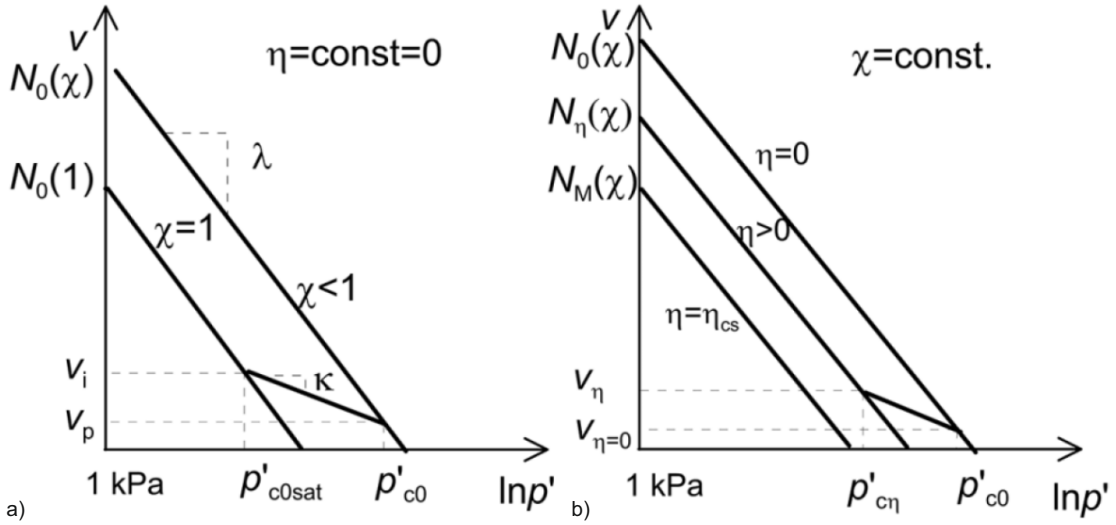


**Figure 4.63:** The volumetric compressibility framework proposed in Casini et al. (2012).

Alonso et al. (2012) proposed a constitutive model which addresses the different mechanical behaviour of compacted soils when prepared at different initial water contents. The model incorporates Bishop's stress as its FCV, with parameter $\chi$ related to the effective, macro-structural degree of saturation following the idea of Alonso et al. (2010). The product of suction with the effective degree of saturation is used as the SCV, named as the effective suction:

$$\overline{s} = s \cdot S_r^e \tag{4.72}$$

For the volumetric behaviour, an expression similar to BBM is used to describe the

evolution of the slope of the virgin compression lines:

$$\lambda(\overline{s}) = \overline{r} + (1 - \overline{r}) \left[ 1 + \left( \frac{\overline{s}}{\overline{s}_\lambda} \right)^{\frac{1}{1-\overline{\beta}}} \right]^{-\overline{\beta}} \tag{4.73}$$

where $\overline{r}$, $\overline{\beta}$ and $\overline{s}_\lambda$ material parameters. After some algebra it is proved that the increase in the apparent preconsolidation pressure with partial saturation is described through the classical BBM expression (see eq. 4.42), nevertheless with the compressibility parameter $\lambda$ being dependant on the effective suction, and thus dependant on both suction and degree of saturation. Figure 4.64 plots the variation of compressibility with partial saturation and the associated volumetric behaviour of the Alonso et al. (2012) model.

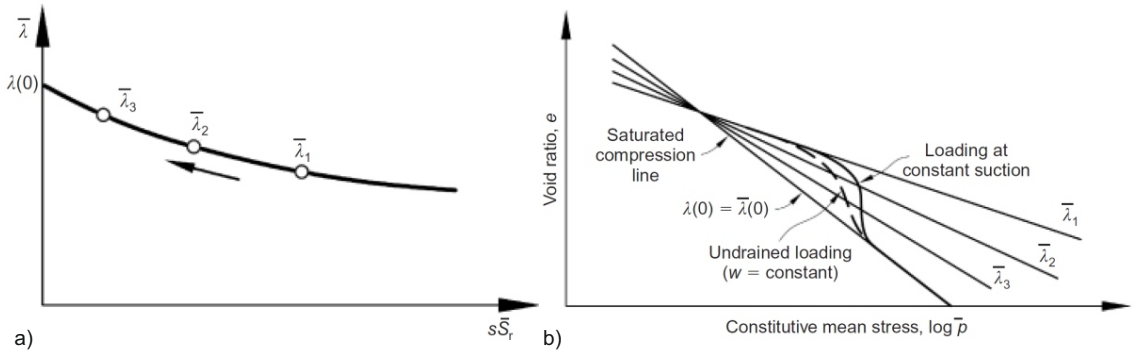


**Figure 4.64:** a) The evolution of compressibility with partial saturation and; b) simulation results for drained and undrained compression isotropic tests according to the Alonso et al. (2012) model.

## 4.5 Concluding Remarks

The present chapter focused on the nature and mechanical behaviour of unsaturated soils. The presented review is quite extended; nevertheless it was considered necessary, in order to familiarize the reader with the main features of unsaturated soils. The definitions of soil suction and of the water retention curve where introduced, before discussing the effects of partial saturation on soil behaviour. It was concluded with the presentation of the most important contributions regarding the constitutive modelling of unsaturated soils.The key points of chapter 4 are summarized hereinafter.

Soil suction is a stress variable, defined as the excess of air pressure $u_a$ over the water pressure $u_w$ in a three phase porous material. Different mechanisms contribute

to soil suction, reflected in the different suction components, namely the capillary, absorptive and osmotic components. From a thermodynamic point of view, soil suction is a potential (energy) with the latter defining water flow in unsaturated porous media. Soil suction is also connected to the presence of water vapour in the atmosphere (relative humidity) through Kelvin's law, explaining the predominant role of atmospheric conditions on the quantity of water contained in a soil system.

In any soil system, water extraction or absorption follows an increase or decrease in soil suction respectively. The water retention curve provides the fundamental relation between suction and water content, with the latter usually described through the degree of saturation $S_r$, while other alternatives include the gravimetric water content $w$ and the volumetric water content $\theta$. The WRC describes how capable a given soil is to retain water in its pores under a given suction level. The water retention capability of a given soil, under a given suction level, additionally depends on an ensemble of other factors with the most important being the void ratio and the process examined (drying vs wetting). The lower the void ratio the more capable a soil system is of retaining water, while in general during a drying process a soil system is more capable of water retention.

The water retention curve plays a fundamental role in understanding and describing unsaturated soil behaviour. It is experimentally determined in the laboratory by progressively applying different suction levels to a given soil element while simultaneously monitoring the water content. When it comes to numerical analyses, it is simulated through various available Water Retention mathematical Models (WRMs), which can interpolate the experimental data with a continuous reverse sigmoidal curve in a $S_r - \ln s$ plot.

Early attempts to study the mechanical behaviour of unsaturated soils focused on the search for an effective stress. It was soon realized that contrary to saturated soils, where Terzaghi's effective stress is the only necessary stress variable, in unsaturated soil mechanics two independent stress variables are needed. Regarding common stress path interpretation, soil testing and representation of experimental results, the excess of the total stress over the air pressure, called the net stress $\overline{\boldsymbol{\sigma}}$ and suction $s$ are utilized. Nevertheless, when it comes to numerical analyses and constitutive modelling, nowadays the combination of Bishop's average skeleton stress $\sigma = \overline{\sigma} + S_{r,M} \cdot s$ [21] with

[21] The macro-structural degree of saturation $S_{r,M}$ representing the water contained within the larger macro-pores forming between clay aggregates is the predominant choice for Bishop's parameter $\chi$.

suction is the preferable choice. This is mainly due to the fact that Bishop's stress recalls Terzaghi's effective stress upon saturation, allowing for a unified approach of the mechanical behaviour of saturated and unsaturated material states.

Partial saturation is manifested in both shear strength and volumetric behaviour of soils. The most important aspects of the mechanical behaviour of unsaturated soils are summarized as follows:

- Drying an initially saturated soil results in a decrease in its void ratio (shrinkage). A residual void ratio value is usually reached where further drying cannot produce further shrinking.

- Partial saturation is in favour of an increased yield stress, called the apparent preconsolidation pressure. In general we may say that the apparent preconsolidation pressure increases with increasing suction.

- An increasing suction favours a decreasing compressibility; unsaturated compressibility depends also on the level of the applied stress.

- Initially unsaturated soil elements may either swell or collapse (volume decrease) when water soaked, depending on the level of the applied stress. An increasing stress level favours collapse; collapse usually reaches a maximum where further increase in the applied stress level may either not affect or even reduce the potential for collapse.

- Partial saturation increases shear strength; the effect of suction in strengthening a given soil element becomes less effective as water content decreases; thus, shear strength increase with suction is highly nonlinear and mainly depends on the type of soil. Bishop's average skeleton stress, used instead of Terzaghi's effective stress in common soil strength criteria, can adequately account for the evolution of shear strength with partial saturation.

The first complete constitutive model for unsaturated soils is the Barcelona Basic Model. It is based on the concept of the two independent stress variables, with net stress and suction used by the authors. Its pioneering nature lays on the proposed volumetric compressibility framework, which combined with the principles of theory of plasticity, leads to the definition of the Loading - Collapse surface, a yield surface, bounding the elastic domain in the net stress $\overline{\boldsymbol{\sigma}}$ - suction $s$ plane. The loading collapse surface, represents both virgin compression states and volume reduction with

suction increase (collapse) through a unified single yield curve associating both conditions with plastic loading. It represents the increase in the apparent preconsolidation pressure with suction, while moreover, this is described as the natural outcome of the increased unsaturated soil stiffness. The MCC was used as the saturated reference model and thus its isotropic ellipse represents the yield surface in the deviatoric stress space.

The BBM dominated the subsequent research in constitutive modelling. Most of the post BBM models are in fact enchantments trying to address the three major shortcoming of BBM, namely: a) its inability to represent a nonlinear increase in shear strength with suction; b) the reproduction of an ever reducing void ratio with suction increase and; c) the reproduction of a constantly increasing collapse with applied stress. Moreover, other researches used the BBM's framework to extend different saturated reference models in the unsaturated regime, with the Cui & Delage (1996) a characteristic example of an anisotropic BBM and the Rampino et al. (2000) for sands.

The last few years following primary the work of Jommi (2000), modern unsaturated constitutive models incorporate Bishop's stress instead of net stress as their first constitutive variable to allow for a natural and unified description of the strength and elastic behaviour with suction and also a smooth transition between unsaturated and saturated material states. A second constitutive value is still needed to provide an adequate description of the Loading - Collapse surface, with suction (i.e., Jommi (2000), modified suction (i.e., Gallipoli et al. (2003)) or degree of saturation (i.e., Casini (2012), Zhou et al. (2012a)) being some of the choices.

# Chapter 5

# The proposed Compressibility Framework

## 5.1 Introduction

The present chapter presents the compressibility framework based on which the hardening law of the proposed constitutive model is formulated. The analysis focuses on the volumetric response of a soil element subjected to compression, with emphasis on the effects of stress-induced anisotropy and partial saturation..

The proposed framework builds on an Intrinsic Compressibility Framework (ICF) for anisotropically consolidated saturated soils, initially proposed by Belokas & Kavvadas (2011). Furthermore, for the case of unsaturated material states, Bishop's average skeleton stress substitutes the Terzaghi's effective stress, while the slope of the compression lines is described as a function of both suction and degree of saturation.

Note that, upon saturation the proposed framework reduces to an intrinsic compressibility framework for saturated materials which only accounts for an anisotropic material fabric. On the other end, following appropriate calibration of the parameters controlling anisotropy, the framework reduces to a simple isotropic compressibility framework for unsaturated materials.

## 5.2 Modified Intrinsic Compressibility Framework

Belokas & Kavvadas (2011) proposed an Intrinsic Compressibility Framework (ICF) to describe the volumetric behaviour of structureless soils subjected to radial stress

paths. It was part of the Belokas & Kavvadas (2010) constitutive model for structured soils, used in defining the structureless, reference state. Moreover, it was also employed in the formulation of the hardening rule of an early version of the proposed constitutive model in Sitarenios et al. (2013), at that time addressing only the behaviour of fully saturated soils.

Its incorporation in constitutive models provides a consistent description of the dependance of virgin Compression Lines (CLs) on the level of stress induced anisotropy, significantly improving the simulation of soil response under radial stress paths. As part of the present thesis, the Belokas & Kavvadas (2011) approach was slightly modified, and the complete mathematical formulation of the proposed scheme is presented in the next paragraph.

### 5.2.1 Intrinsic Compression Curves

The proposed ICF is established on the observation of Lewin & Burland (1970) that initially reconstituted soil elements, consolidated along radial stress paths (i.e., along a constant stress ratio $n = q/p$, where $q$ and $p$ the deviatoric and mean effective stress respectively in the triaxial stress space) move along distinct and almost parallel straight compression lines in the $v - \ln p$ plane, where $v = 1 + e$ the specific volume. In the simplest triaxial case, the stress ratio $n$ is correlated with the horizontal stress ratio $K = \sigma_h/\sigma_v$, where $\sigma_h$ and $\sigma_v$ correspond to the horizontal (radial) and vertical effective stress respectively, as follows:

$$n = \frac{q}{p} = \frac{3\,(1-K)}{1+2K} \tag{5.1}$$

A schematic representation of the ICF is given in fig. 5.1. The various intrinsic compression curves correspond to material states that initially reconstituted soils may possess when radially compressed under different stress ratios $n$. In fact, radially consolidated soil elements plot on the aforementioned ICLs only after substantial plastic straining, so that the material fabric adjusts to the applied anisotropy.

To clarify the latter, figure 5.2 presents actual compression curves of radially consolidated soil elements. Under the applied radial stress path, the initial isotropic fabric alters towards the one corresponding to the imposed anisotropy. This is reflected as a gradual transition of the compression curves towards the corresponding intrinsic curves.

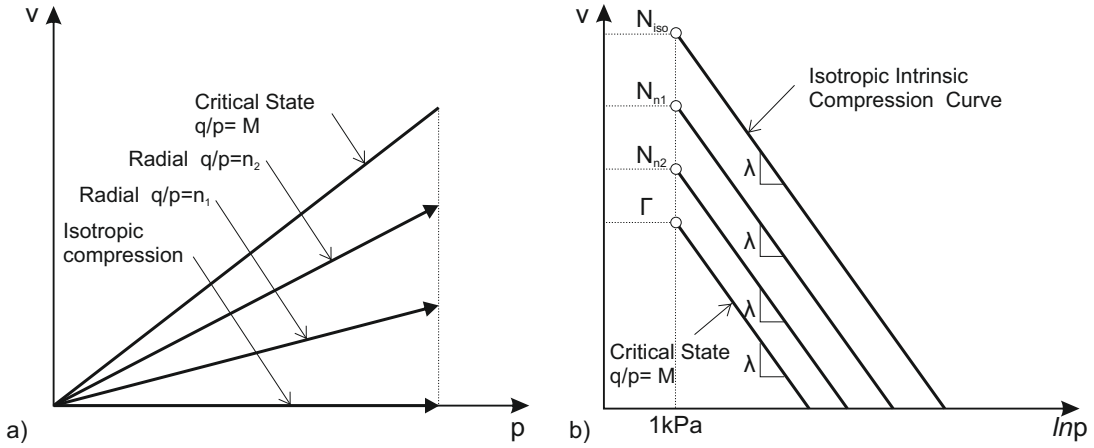


**Figure 5.1:** The Intrinsic Compressibility Framework (ICF) proposed by Belokas & Kavvadas (2011).

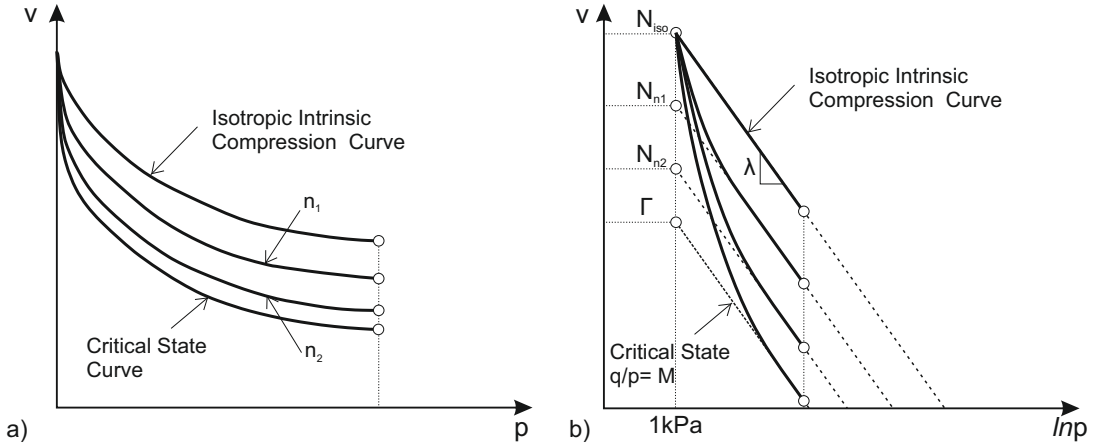


**Figure 5.2:** Compression curves of an initially isotropically consolidated soil element, subjected to radial consolidation stress path; the behaviour on the: a) $v - p$ and; b) $v - \ln p$ planes.

The intrinsic compression curves are mathematically represented by the well known MCC equation:

$$v = N_n - \lambda \ln p \tag{5.2}$$

where $\lambda$ describes the slope of the CLs and $N_n$ refers to the theoretical value of the specific volume at $p = 1kPa$, defining the position of each compression line in the $v - \ln p$ plane.

The $N_n$ value depends on the stress ratio of the imposed radial stress path. Experimental evidence suggests a decreasing $N_n$ with an increasing consolidation stress ratio (Lewin & Burland 1970; Gens 1982; Rampello et al. 1997), reflecting the beneficial effect of deviatoric stress on fabric rearrangement. The Compression Curves

depend exclusively on the current stress state ($p$, $q$) and current specific volume ($v$), implying that the proposed framework describes structureless material states (Leroueil & Vaughan 1990). Such material states, following Burland (1990), are also characterized as intrinsic.

Belokas & Kavvadas (2011) proposed a normalization procedure to describe a biunique relationship between the imposed radial stress path and the projection of the intrinsic CLs in the $v - \ln p$ plane. They assumed that: a) the upper limit of $N_n$ is the $N_{iso}$ value corresponding to the isotropic compression curve ($n = 0$) and; b) the lower limit is the $\Gamma$ value representing the position of the Critical State Line (CSL). The latter theoretically corresponds to failure, but at the same time it can be considered as the limiting case for which the compression curve corresponds to a radial stress path with slope equal to the critical state slope $M$, i.e., the maximum stress ratio of a continuously hardening stress path (Gens 1982).

According to Belokas & Kavvadas (2011), the normalized position, $N_{n,norm}$, and stress ratio, $n_{norm}$, are defined as:

$$N_{n,norm} = \frac{N_{iso} - N_n}{N_{iso} - \Gamma} \tag{5.3}$$

$$n_{norm} = \frac{q/p}{M} \tag{5.4}$$

The authors applied the above expressions (eq. 5.3, 5.4) to normalize the results from various radial consolidation tests, corresponding to seven different soils. To interpolate the data, they propose the following nonlinear equation:

$$N_{n,norm} = \frac{N_{iso} - N_n}{N_{iso} - \Gamma} = 1 - (1 - n_{norm})^r \tag{5.5}$$

where $r$ a curve fitting parameter, which depends on the soil type, thus it comprises a material constant. Figure 5.3 shows the available experimental data together with the outcome of the regression analysis. The reported $r$ values are summarized in table 5.1.

Incorporation of $N_{n,norm}$ and $n_{norm}$ in the curve fitting expression (see eq. 5.5) yields:

$$N_n = \Gamma + (N_{iso} - \Gamma)\left(1 - \frac{q/p}{M}\right)^r \tag{5.6}$$

Equation 5.6 will be used in the formulation of the hardening rule, to provide an accu-

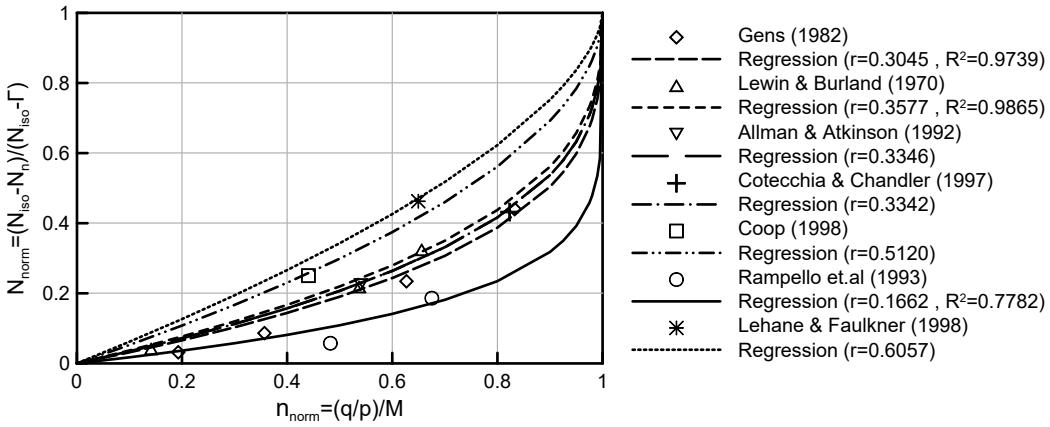


**Figure 5.3:** The normalized specific volume vs the normalized stress ratio for seven different soils (data from Belokas (2008)) and the interpolated evolution curves.

**Table 5.1:** Details regarding the data of figure 5.3.

| $r$ | Material | No Points | $R^2$ | Reference |
|---|---|---|---|---|
| 0.3045 | Lower Cromer till | 4 | 0.9739 | Gens (1982) |
| 0.3577 | Kaolin | 3 | 0.9865 | Lewin & Burland (1970) |
| 0.3346 | Bothkennar clay | 1 | - | Allman & Atkinson (1992) |
| 0.3342 | Papadai clay | 1 | - | Cotecchia & Chandler (1997) |
| 0.5120 | Sand | 1 | - | Coop (1990) |
| 0.1662 | Vallerica clay | 2 | 0.7782 | Rampello et al. (1993) |
| 0.6057 | Clay | 1 | - | Lehane & Faulkner (1998) |

rate description of the volumetric behaviour of the material with evolving anisotropy. In doing so eq. 5.6 needs to be generalized in the tensorial stress space $(\sigma,\ \boldsymbol{s})$. Starting from equation 5.4 and taking into account that $p \equiv \sigma$ and $q = \sqrt{\frac{3}{2}\boldsymbol{s} : \boldsymbol{s}}$ we may write:

$$n_{norm} = \frac{q/p}{M} = \frac{\sqrt{\frac{3}{2}\frac{\boldsymbol{s}:\boldsymbol{s}}{\sigma^2}}}{M} \tag{5.7}$$

Using $c$ to represent the slope of the critical state line in the generalized stress space, where $c = \sqrt{2/3}M$[1], we end up with the following expression for the normalized

[1]The slope of the critical state line is assumed independent of the Lode Angle.

stress ratio $n_{norm}$ in the tensorial stress space:

$$n_{norm} = \sqrt{\frac{\frac{1}{c^2}\left(\boldsymbol{s} : \boldsymbol{s}\right)}{\sigma^2}} \tag{5.8}$$

Using the generalized expression 5.8, equation 5.6 can be rewritten as:

$$N_n = \Gamma + \left(N_{iso} - \Gamma\right)\left(1 - \sqrt{\frac{\frac{1}{c^2}\left(\boldsymbol{s} : \boldsymbol{s}\right)}{\sigma^2}}\right)^r \tag{5.9}$$

Sitarenios et al. (2013) used the aforementioned expression in the formulation of an early version of the proposed constitutive model. The presence of the square route complicates the hardening rule's mathematical expressions, and can also lead to numerical problems associated with the constitutive equations' numerical solver. For this purpose the following slight modification is proposed for $n_{norm}$ in triaxial and multiaxial space::

$$n_{norm} = \frac{\left(q/p\right)^2}{M^2} \tag{5.10}$$

for the triaxial stress space, and also generalized as:

$$n_{norm} = \frac{\frac{1}{c^2}\left(\boldsymbol{s} : \boldsymbol{s}\right)}{\sigma^2} \tag{5.11}$$

The experimental results previously utilized by Belokas (2008) (see. fig 5.3) are now re-assessed using the proposed modified normalized parameter (eq. 5.10). Again equation 5.5 is used to interpolate the data. The outcome of the regression analysis is presented in figure 5.4 and table 5.2. Only experimental results including more than one data points are used.

The comparison indicates that eq. 5.5 can still accurately describe the experimental data, scoring high correlation factors. On these grounds, equations 5.10 and 5.11, are finally selected and substitute the normalized stress ratio in eq. 5.5, ending up with the following expressions for the triaxial and the generalized stress space respectively:

$$N_n = \Gamma + \left(N_{iso} - \Gamma\right)\left(1 - \frac{\left(q/p\right)^2}{M^2}\right)^{r_s} \tag{5.12a}$$

$$N_n = \Gamma + \left(N_{iso} - \Gamma\right)\left(1 - \frac{\frac{1}{c^2}\left(\boldsymbol{s} : \boldsymbol{s}\right)}{\sigma^2}\right)^{r_s} \tag{5.12b}$$

Obviously, due to the new definition of the stress ratio, the curve fitting parameter $r$ obtains different values, compared to Belokas (2008) for the same dataset. Thus, for the shake of clarity, its notation is changed to $r_s$.

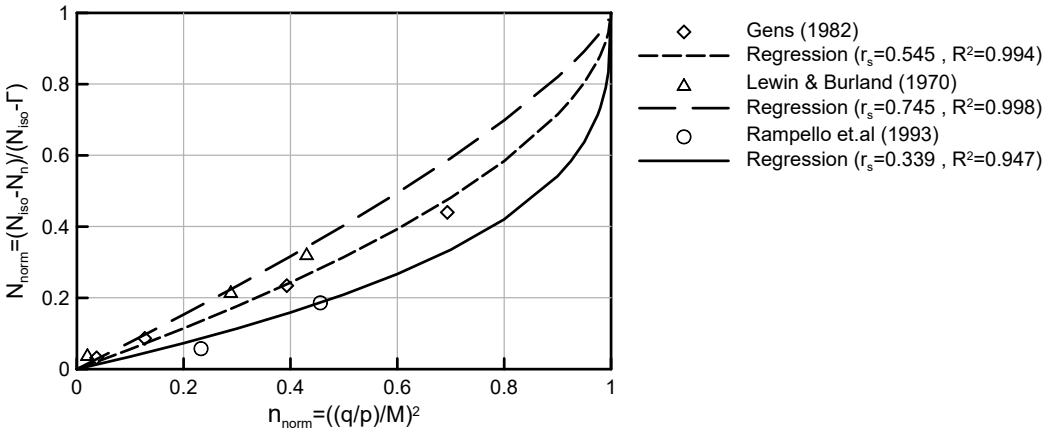


**Figure 5.4:** The normalized specific volume vs the modified normalized stress ratio for seven different soils (data from Belokas (2008)) and the interpolated evolution curves.

**Table 5.2:** The outcome of the regression analyses regarding figure 5.4.

| $r_s$ | Material | No Points | $R^2$ | Reference |
|---|---|---|---|---|
| 0.545 | Lower Cromer till | 4 | 0.994 | Gens (1982) |
| 0.745 | Kaolin | 3 | 0.998 | Lewin & Burland (1970) |
| 0.339 | Vallerica clay | 2 | 0.947 | Rampello et al. (1993) |

### 5.2.2 Intrinsic Compressibility Envelope

Application of the previously defined Intrinsic Compression Curves for material states corresponding to soil samples compressed under different stress ratios, leads to the definition of an Intrinsic Compressibility Envelope (ICE), a state boundary surface in the $v - \sigma - \boldsymbol{s}$ space, which describes the locus of all possible structureless material states.

If we assume that under stabilized anisotropic conditions, a material state corresponding to a stress path ratio $n = q/p$ lays on a compression curve with a $N_n$ value given by equation 5.12a, we may write:

$$\left.\begin{aligned} v &= N_n - \lambda \ln p \\ N_n &= \Gamma + (N_{iso} - \Gamma)\left(1 - \frac{(q/p)^2}{M^2}\right)^{r_s} \end{aligned}\right\} \Rightarrow$$

$$\begin{aligned} \frac{v + \lambda \ln p - \Gamma}{N_{iso} - \Gamma} &= \left(1 - \frac{(q/p)^2}{M^2}\right)^{r_s} \Rightarrow \\ \left(1 - \frac{(q/p)^2}{M^2}\right) &= \left(\frac{v + \lambda \ln p - \Gamma}{N_{iso} - \Gamma}\right)^{(1/r_s)} \Rightarrow \\ \frac{1}{M^2}\left(\frac{q}{p}\right)^2 &= 1 - \left(\frac{v + \lambda \ln p - \Gamma}{N_{iso} - \Gamma}\right)^{(1/r_s)} \end{aligned} \tag{5.13}$$

Similarly, in the tensorial stress space:

$$\frac{1}{c^2}\frac{\boldsymbol{s} : \boldsymbol{s}}{\sigma^2} = 1 - \left(\frac{v + \lambda \ln \sigma - \Gamma}{N_{iso} - \Gamma}\right)^{(1/r_s)} \tag{5.14}$$

To reproduce a graphical representation of the ICE in the $p - q$ space we need to normalize expression 5.13 to take into account for the difference in the specific volume and in the applied stress level between the various elements. In doing so, we assume that ICE represents material points under different levels of stress induced anisotropy which lie on a common swelling line, as depicted in figure 5.5. Then, the specific volume corresponding to any material state can be expressed as:

$$v = N_{iso} - \lambda \ln p_0^{iso} - \kappa \ln\left(\frac{p}{p_0^{iso}}\right) \tag{5.15}$$

where $p_0^{iso}$ the mean effective stress corresponding to the isotropically compressed sample. Using eq. 5.15 to substitute for the specific volume in the right hand side of eq. 5.13 we derive:

$$\frac{1}{M^2}\left(\frac{q}{p}\right)^2 = 1 - \left(\frac{N_{iso} + (\lambda - \kappa)\ln\left(\frac{p}{p_0^{iso}}\right) - \Gamma}{N_{iso} - \Gamma}\right)^{(1/r_s)} \tag{5.16}$$

Finally, multiplying both members of eq. 5.16 with $\frac{M^2 p^2}{p_0^{iso\,2}}$ we end up with:

$$\left(\frac{q}{p_0^{iso}}\right)^2 = M^2 \left(\frac{p}{p_0^{iso}}\right)^2 \left(1 - \left(\frac{N_{iso} + (\lambda - \kappa)\ln\left(\frac{p}{p_0^{iso}}\right) - \Gamma}{N_{iso} - \Gamma}\right)^{(1/r_s)}\right) \tag{5.17}$$

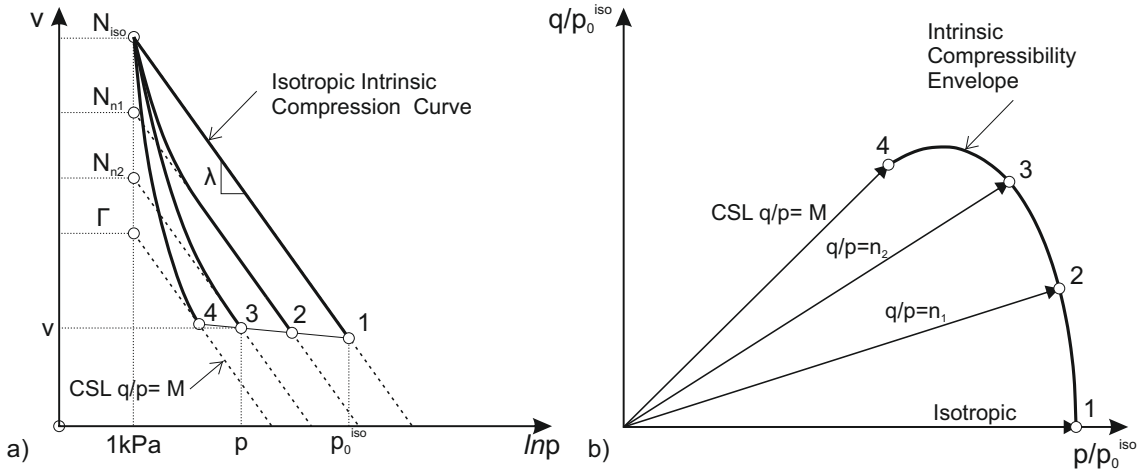


**Figure 5.5:** Graphical representation of the Intrinsic Compressibility Envelope (ICE).

The above expression is plotted in fig. 5.6 for the material constants shown in table 5.3 for different values of $r_s$, while figure 5.7 plots the corresponding intrinsic compression curves. Also plotted in figure 5.6 is the SBS of the Modified Cam Clay (Roscoe Surface). Note, however, that the presented compression envelopes, are not directly comparable with the Roscoe bounding surface, as the latter is mainly representative of the behaviour during triaxial loading, and further assumed to represent the compressibility envelope. Lewin & Burland (1970) suggest that such a common envelope does not exist for anisotropically consolidated soils. Finally, the presented ICE should not be confused with the state boundary surface proposed by Gens (1982), representing the common envelope of normalized (Hvorslev normalization) stress paths initiating from different anisotropic conditions.

**Table 5.3:** Material constant values used in plotting the Intrinsic Compressibility Envelope.

| Material constant | Value | Material constant | Value |
|---|---|---|---|
| M | 1.0 | $N_{iso}$ | 2.20 |
| $\kappa$ | 0.01 | $\Gamma$ | 2.14 |
| $\lambda$ | 0.10 | | |

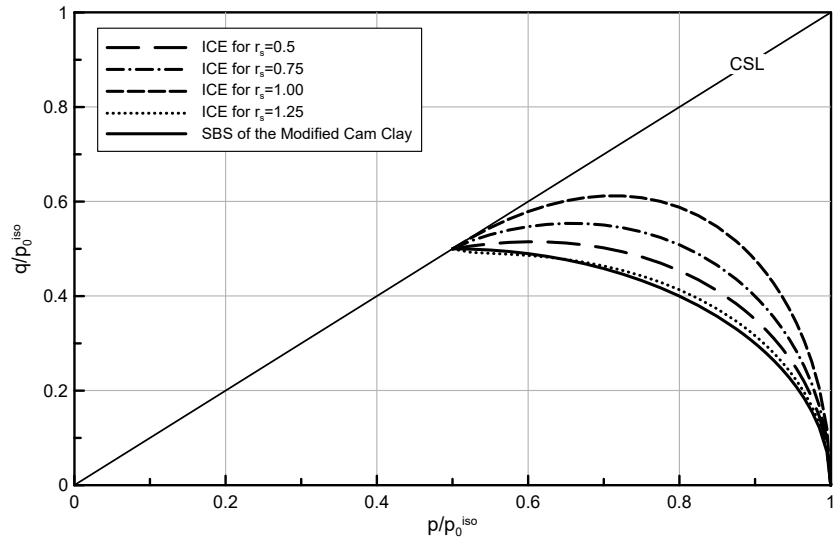


**Figure 5.6:** Normalized plots of the Intrinsic Compressibility Envelope for different $r_s$ values.

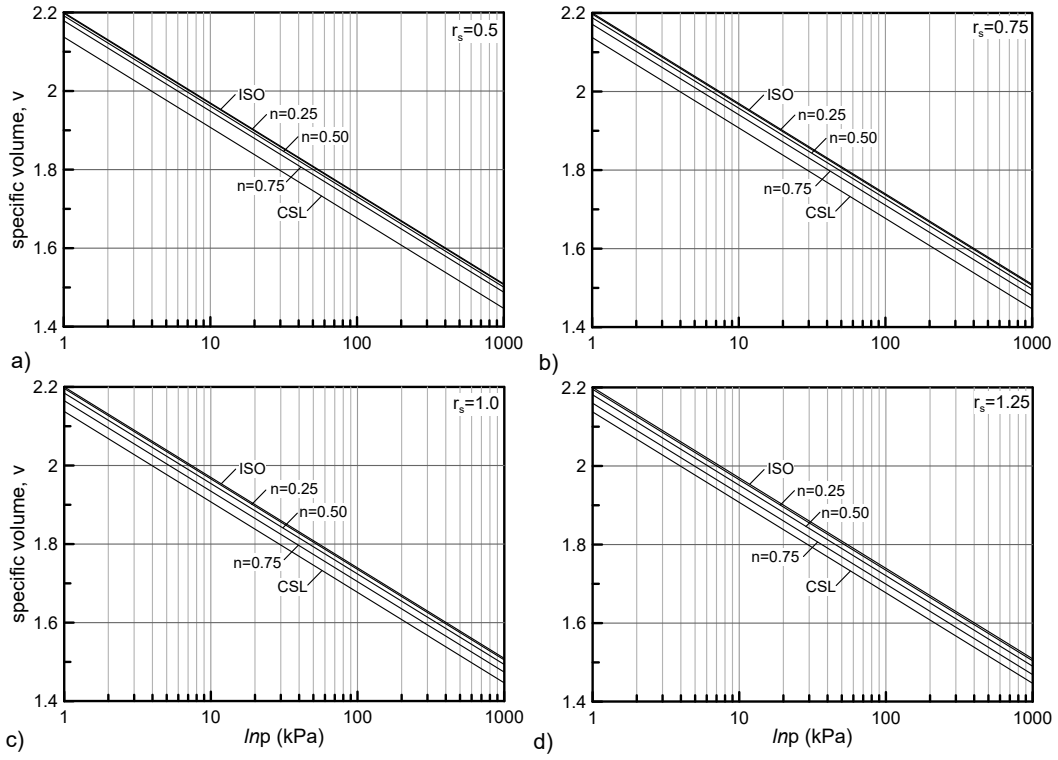


**Figure 5.7:** The effect of parameter $r_s$ on the intrinsic compression lines.

## 5.3 Extension in the Unsaturated Regime

This section, extends the modified Belokas & Kavvadas (2011) Intrinsic Compressibility Framework, introduced and described in the previous section, to account for the mechanical behaviour of unsaturated soils. The developed compressibility framework will provide a comprehensive description of the combined effects of anisotropy and partial saturation in the constitutive model developed within the present Doctoral thesis.

### 5.3.1 The utilized constitutive variables

To extend the above conceptual framework for saturated soils in the unsaturated regime, the first crucial assumption required, concerns the stress variable which will substitute the Terzaghi's effective stress. In chapter 4 we discussed the two main available options, namely: a) the net stress ($\sigma = \sigma - u_w$) and; b) Bishop's average skeleton stress (see eq. 4.25).

Bishop's average skeleton stress is the preferable option in this thesis, which in the tensorial stress space is written as:

$$\boldsymbol{\sigma'} = (\boldsymbol{\sigma} - u_a \boldsymbol{I}) + \chi \, (u_a - u_w) \, \boldsymbol{I} \tag{5.18}$$

and further simplified as:

$$\boldsymbol{\sigma'} = \boldsymbol{\sigma} + \chi \cdot s\boldsymbol{I} \tag{5.19}$$

Regarding the scaling parameter $\chi$, we subscribe to the idea proposed in Alonso et al. (2010), who suggest the use of the macrostructural degree of saturation $S_{r,M}$, also referred as the effective degree of saturation, depicted as $S_r^e$. To correlate $S_r^e$ with the overall degree of saturation $S_r$ we further utilize the power law of Alonso et al. (2010):

$$\chi = S_r^e = (S_r)^\alpha \tag{5.20}$$

where $\alpha$ a material constant. As already described in Chapter4, Bishop's average skeleton stress along with the effective degree of saturation as the First Constitutive Variable (FCV) has been extensively used in the past (i.e. Zhou et al. (2012a), Casini (2012) Alonso et al. (2012)), nevertheless, at least according to the author's knowledge, the present thesis constitutes the first attempt to incorporate Bishop's stress for unsaturated soils in the development of an anisotropic constitutive model.

Selection of Bishop's average skeleton stress, with the effective degree of saturation as the $\chi$ parameter is based on a couple of reasons, namely:

- Bishop's skeleton stress allows for a smooth transition between saturated and unsaturated soil states, and thus it is the preferable option when it comes to the implementation of constitutive models in commercial Finite Element Method (FEM) codes. In this thesis, the developed constitutive model is implemented in the FEM computer code Simulia Abaqus as a user defined material, while by default Simulia Abaqus utilizes the Bishop's average skeleton stress for analyses of geotechnical problems.

- Bishop's stress offers a natural description of the evolution of shear strength with suction, while additionally accounts for the elastic behaviour of unsaturated materials. In other words, incorporation of Bishop's stress eliminates the need for additionally assumptions regarding shear strength and elasticity, thus favouring simplicity and a reduced number of material parameters.

Despite Bishop's stress advantages, we should always keep in mind that no single constitutive variable has been ever found capable of adequately describing the entire mechanical behaviour of unsaturated soils, and hence we still need to account for extra constitutive variables. The need for extra constitutive variables emanates from Bishop's stress incapacity to describe an increasing yield stress with suction.

In the following paragraph we utilize both suction and effective degree of saturation as extra variables, to account for the evolution of the slope of the compression lines with partial saturation, and finally describe the increase in the apparent yield stress with partial saturation. Although both suction and effective degree of saturation are utilized, it is rational to consider only suction as an extra constitutive variable, as the degree of saturation is an outcome of the water retention curve and not a direct input.

### 5.3.2 Partial saturation as a structure inducing mechanism

The Loading - Collapse surface, initially proposed in the Barcelona Basic Model (BBM) by Alonso et al. (1990), comprises the most important constitutive relationship, reflecting the assumptions made in the compressibility framework and specifically in the evolution of the position and/or inclination of the CLs with partial saturation. It describes the increase in the apparent preconsolidation pressure with

partial saturation, as an outcome of the bonding inter-particle forces developing in an unsaturated soil. Moreover, in terms of constitutive modelling, it is a state boundary surface, playing the role of a yield surface, used in identifying plastic states associated with an increase in the applied net stress or a decrease in suction.

In that perspective, to derive the Loading Collapse surface of our constitutive model, we start with the formulation of the compressibility framework. In doing so, we will initially examine the mechanical behaviour of a soil element, consolidated under saturated conditions and subsequently dried under constant net stress. In chapter 4, we demonstrated, that any soil element subjected to a suction increase, as far as it remains fully saturated, its mechanical behaviour follows the Terzaghi's effective stress principle. Considering that Bishop's stress recovers Terzaghi's stress for saturated material states, it is expected that in the $v - \ln p$ plane, its volumetric response plots on the CL of the saturated material. Such a suction increase stress path is depicted in figure 5.8a where the material state moves from point O to point A, with point A corresponding to a suction level smaller than the material's desaturation suction ($s < s_0$).

For further suction increase, upon desaturation ($s > s_0$), the material starts to progressively dry and to develop suction induced structure, attributed to the bonding effect of the inter-particle forces, mainly due to the formation of water menisci. Thus, it is expected that the soil state will move to the right of the ICL in the meta-stable domain (Kavvadas 2000). Similar to classical structured soils (i.e., cemented soils), the elastic domain will increase following the increasing apparent preconsolidation pressure, also in line with common experimental observations.

Back to figure 5.8, the aforementioned suction increase (i.e., from $s_A$ to a suction value $s_B > s_0$) is assumed to produce only elastic strains, moving on a swelling line, from point A to point B. It is obvious that a major assumption is implied here. It is a priori assumed that the drying process produces an increase in the apparent preconsolidation pressure which is higher than the corresponding Bishop's stress increase, as in any other case the response would be plastic.

This increase in the elastic domain is reflected in the value of the apparent preconsolidation pressure $P^*_{0,B}$, that the material exhibits after drying, represented by point $Y_B$ in figure 5.8b. Point $Y_B$ lays on the same swelling line. The reason why is quite obvious. If we assume that the soil element is now compressed under constant suction, the behaviour shall be elastic (and thus on a swelling line) until point $Y_B$ is

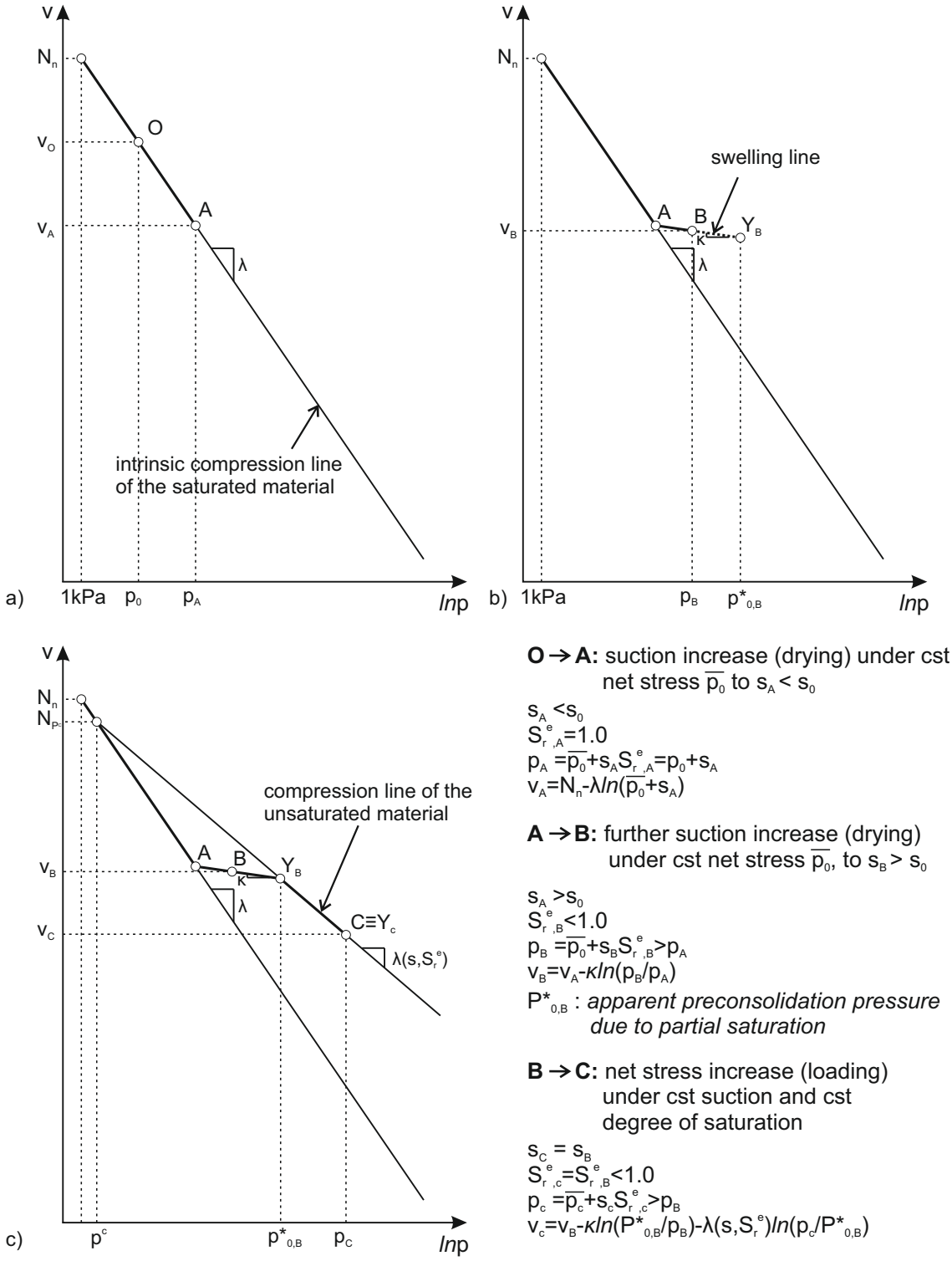


**O → A:** suction increase (drying) under cst net stress $\overline{p_0}$ to $s_A < s_0$

$s_A < s_0$
$S_{r,A}^e = 1.0$
$p_A = \overline{p_0} + s_A S_{r,A}^e = p_0 + s_A$
$v_A = N_n - \lambda ln(\overline{p_0} + s_A)$

**A → B:** further suction increase (drying) under cst net stress $\overline{p_0}$, to $s_B > s_0$

$s_A > s_0$
$S_{r,B}^e < 1.0$
$p_B = \overline{p_0} + s_B S_{r,B}^e > p_A$
$v_B = v_A - \kappa ln(p_B/p_A)$
$P^*_{0,B}$ : *apparent preconsolidation pressure due to partial saturation*

**B → C:** net stress increase (loading) under cst suction and cst degree of saturation

$s_C = s_B$
$S_{r,c}^e = S_{r,B}^e < 1.0$
$p_c = \overline{p_c} + s_c S_{r,c}^e > p_B$
$v_c = v_B - \kappa ln(P^*_{0,B}/p_B) - \lambda(s,S_r^e) ln(p_c/P^*_{0,B})$

**Figure 5.8:** Graphical representation of the assumed volumetric response for an initially saturated soil element which is subjected to a suction increase stress path followed by compression under constant suction.

reached. It follows that further loading, beyond point $Y_B$, will cause plastic yielding.

To account for plastic states, we need to define proper unsaturated compression curves, to describe the onset of plastic deformation. Towards that direction, we assume that there exists a point on the compression line of the saturated material, defined in terms of a reference pressure $p^c$ and a corresponding specific volume $N_{n,P_c}$, which serves as the origin of different compression lines, whose slope depends on the state of partial saturation. Such a compression line is shown in figure 5.8c. Having defined the unsaturated compression line, we can now plot the aforementioned loading path (i.e., from point B to C).

Until now, we examined the theoretical behaviour of an initially fully saturated soil element that was dried under a constant net stress, and subsequently loaded by increasing the net stress under a constant suction. We demonstrated how the corresponding volumetric behaviour in the $v-\ln p$ plane deviates from the compression line of the saturated material when the degree of saturation drops below unity, causing an increase in the elastic domain. Moreover, the soil state moves to the right of the intrinsic compression line of the saturated material, in the meta-stable domain, as a consequence of the partial saturation induced structure. In the following section we discuss in details the influence of partial saturation on the slope of the compression curves.

### 5.3.3 Slope of the Unsaturated Compression Lines

To start with the elastic behaviour, the slope of the swelling lines is assumed constant and equal to $\kappa$. A constant slope implies that the swelling lines are independent of the saturation state, a very common assumption in constitutive modelling of unsaturated soils. Additionally it is in line with Bishop's average skeleton stress ability to naturally represent the elastic behaviour of an unsaturated material. As demonstrated by Jommi (2000) and also described in 4, a constant $\kappa$ in the $v - \ln p$ plane, corresponds to suction dependant elastic compressibility, regarding the behaviour in terms of net stress. Hence, a constant slope $\kappa$, does not imply a volumetric behaviour independent of the level of the applied suction and of the corresponding degree of saturation, but that their effect is sufficiently represented through Bishop's stress.

For the post yield compressibility of the material, the developed framework subscribes to the idea that partial saturation favours a decreased post yield compressibility. This is also reflected in the previously discussed figure 5.8c where the slope of

the plotted unsaturated compression line is smaller compared to the saturated one. Such a selection is mainly based on the following reasons:

- It is consistent with the idea adopted in this thesis, that partial saturation can be handled in the general framework of structured soils. In structured soils, based on experimental results, it is usually assumed that soil structure favours an initially decreased post yield compressibility, which progressively increases with the onset of plastic deformation (structure degradation).

- It is the preferable choice in the associated literature and consistent with most of the available experimental results.

To mathematically represent the desired behaviour, we focus on the factors affecting the forming inter-particle forces. As pointed out by Gallipoli et al. (2003), the number and intensity of inter-particle forces depend on both the level of the applied suction and on the relative area over which this effect acts, with the latter depending directly on the degree of saturation. This statement in fact emphasizes on the need to incorporate both suction and the degree of saturation to comprehensively describe unsaturated compressibility.

Suction is the main parameter controlling the state of saturation in any given soil element. This may sound a bit controversial because unsaturated soils are characterized by their degree of saturation. Nevertheless, we should keep in mind that suction is the main stress parameter independently controlled either by technical means in a laboratory or by the prevailing atmospheric conditions in the field. To move a soil towards a more unsaturated state we increase suction, while on the other hand, to saturate it we need to reduce the imposed suction. Suction, as a stress variable controls the strength of the inter-particle forces developing between soil grains or clay particles. Hence, an increased suction in general corresponds to stronger bonding forces while at the same time water drainage a drop in degree of saturation. At this point we may think that as far as suction and degree of saturation are coupled variables, just incorporating a suction dependance on the rule describing the partial saturation induced structure, is sufficient to describe the compressibility of the relevant soil.

Such an approach, where the slope of the compression lines depends only on suction is given in figure 5.9a. In line with the previously described behaviour an increase in suction reduces the degree of saturation and simultaneously stiffness the behaviour. This increase in stiffness, results also in an increase in the apparent preconsolidation pressure of the material, reflected in the increased yield stress.

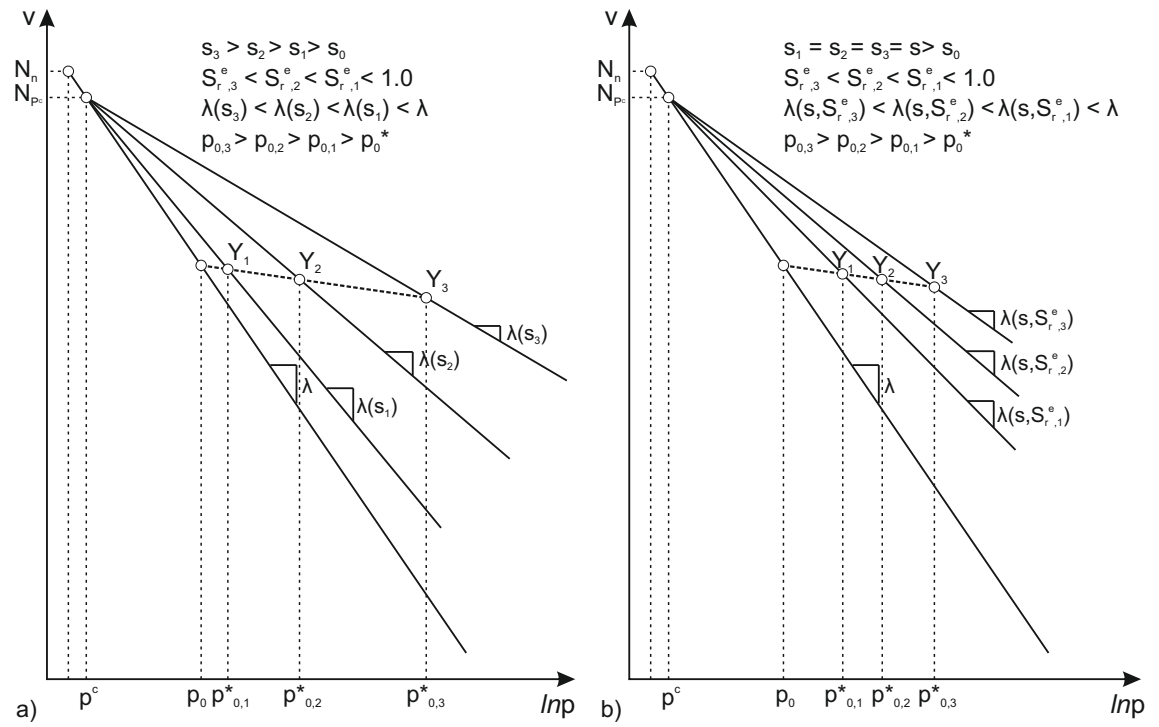


**Figure 5.9:** The effect of a) suction and; b) of effective degree of saturation on the unsaturated compressibility.

Nevertheless, there is one main shortcoming with this approach. It is implied that examining two different soils under the same suction level but different degrees of saturation will exhibit the same compression characteristics. This is fundamentally problematic as it neglects the contribution of degree of saturation in the intensity of the developed inter-particle forces. This shortcoming can be easily addressed by incorporating material constants in the proposed evolution rule. Nevertheless, a problematic behaviour still exists, if we examine the behaviour of the same soil under two different states, where for instance due to compression the void ratio has changed and thus its water retention capacity has changed as well. Then, theoretically under the same suction level, the same material can possess different degrees of saturation and consequently its acquired structure will be different.

To comprehensively understand the problematic behaviour related to solely suction dependant compression lines, we shall examine the following two simple loading cases, by intensionally assuming that the slope of the compression lines is only suction dependant ($\lambda = f(s)$).

- Firstly we may re-examine the volumetric response of a soil that is progressively imposed to increasing suction levels ($s > 0$). As an increase in suction

is in favour of a decreased compressibility, the material's behaviour will deviate from the compression line of the saturated material and move along the CLs representing unsaturated soil states. To the contrary, on reality a small increase in suction is usually not sufficient to desaturate the soil and thus its volumetric response shouldn't deviate from the compression line of the saturated material. To avoid such a paradox, the assumed evolution rule needs to be a discontinues function of suction (i.e. Sheng et al. (2003)) to ensure that for $s < s_0$, where $S_r$ remains equal to unity, the slope of the compression line remains equal to that of the saturated material. Such an approach overcomes the aforementioned issue, by preventing the evolution of the CLs as far as the material remains saturated. Nevertheless, it necessitates the incorporation of $s_0$ as an extra material parameter, which in most of the cases; a) cannot be clearly identified on the WRC of the material, and; b) it evolves with volumetric deformation and thus it is rather a variable than a material constant. Moreover, discontinuous material laws are always problematic when it comes to numerical implementation.

- The second case regards a compression test under a given constant suction level. Imagine a soil element that has been dried to a given suction level and then loaded (net stress increase) while suction is kept constant. An exclusively dependant on suction compressibility framework will predict a volumetric behaviour that lays on a constant slope compression line. Nevertheless, as discussed in chapter 4, compression under constant suction does not necessarily means compression under a constant degree of saturation. To the contrary, it is expected that a material compressed under constant suction will increase its degree of saturation, due to the decreasing void ratio and the corresponding increasing water retention capability. An increasing degree of saturation is reflected on the mechanical behaviour of the soil as an increase in its compressibility as graphically depicted in figure 5.9b.

To overcome these limitations, the degree of saturation is incorporated in the adopted evolution rule, finally resulting in unsaturated compression lines with their slope a function of both suction and of the effective degree of saturation:

$$\lambda = f(s, S_r^e) \tag{5.21}$$

Summarizing the adopted rule needs to be capable of representing:

- a decreasing compressibility with increasing suction;
- a unique saturated compressibility irrespective of the level of the applied suction;
- an increasing compressibility with increasing degree of saturation, under a constant suction level.

Such a behaviour is described by the following equation:

$$\lambda(s, S_r^e) = \lambda - (\lambda - \lambda(s))\,(1 - S_r^e)^{\gamma} \tag{5.22}$$

where $\lambda$ the compressibility of the saturated material and $\gamma$, a material constant scaling the effect of degree of saturation on the compressibility. As $\lambda(s)$ any suitable relation describing in general an increased stiffness with increasing suction can be incorporated. We select the equation proposed in the Barcelona Basic Model (Alonso et al. 1990). The BBM constitutive model was widely described in chapter 4, nevertheless its unsaturated compressibility evolution rule is repeated here for clarity:

$$\lambda(s) = \lambda\left[(1 - r)\,e^{-\beta s} + r\right] \tag{5.23}$$

It is reminded that equation 5.23, describes a decreasing compressibility with increasing suction, with a rate of decrease controlled through parameter $\beta$, asymptotically decreasing towards a minimum value, controlled by parameter $r$. Both parameters are considered material constants.

Combining equations 5.22 and 5.23 we end up with:

$$\lambda(s, S_r^e) = \lambda\left[1 - (1 - r)\,(1 - S_r^e)^{\gamma}\left(1 - e^{-\beta s}\right)\right] \tag{5.24}$$

Equation 5.24 in fact can reproduce the combined effect of suction and degree of saturation in the compressibility of an unsaturated soil as was given graphically in figure 5.9. To better understand the advantages of such an approach we shall examine two stress paths corresponding to compression tests under different but constant suction levels (see figure 5.10).

Let's suppose that two soil samples corresponding to the same material are dried, from an initially saturated state (i.e., point A), to two different suction levels $s_C$ and $s_B$, where $s_C > s_B$. The initial drying causes elastic straining, represented through a proper swelling line, while upon further loading yielding will occur at point B for

the lower suction sample and at point C for the higher suction sample. We may observe how the adopted framework describes an increase in the elastic domain or in other words in the apparent preconsolidation pressure with suction as the higher the imposed suction, the higher the apparent preconsolidation pressure. For further load-

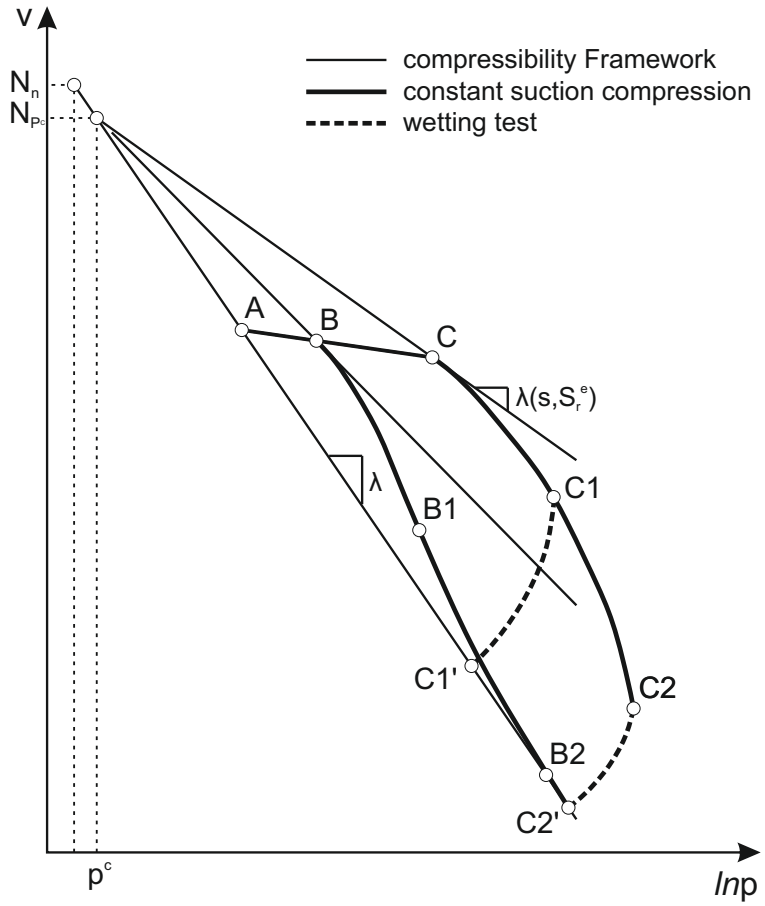


**Figure 5.10:** The proposed compressibility framework for partially saturated soils, and characteristic constant suction compression stress paths.

ing under constant suction, plastic straining occurs, and the void ratio significantly decreases. The decreasing void ratio, causes an increase in the degree of saturation and thus the corresponding path starts to progressively follow compression lines of a reduced stiffness due to the dependance of the latter on degree of saturation. In fact as degree of saturation increases the material state starts moving towards the compression line of the saturation material, resembling a structure degradation process. Assuming that compression is realized under a relatively small applied suction (i.e., $s_B$), the material may saturate and thus the material state should move on the compression line of the saturated material as indicated by point $B2$ in figure 5.10.

Moreover, figure 5.10 illustrates how the assumed compressibility behaviour can naturally represent the variation in collapse potential with the applied stress level, usually observed in wetting tests. For instance, focusing on the compression curve of the second test $C-C1-C2$ point C2 is closer to the saturated compression line compared to point C1 and thus wetting under constant net stress will result to a reduced volumetric deformation, with respect to its counterpart if wetting was initiated at point C1.

To avoid possible misunderstandings, we should mention that although an approach similar to structured soils has been used in describing the behaviour of unsaturated soils, their behaviour is not identical. The behaviour of unsaturated soils is far more complicated, while moreover, as pointed out by Gens (2010), contrary to cemented soils, their structure-like effects are reversible and depend on the applied hydraulic conditions.

### 5.3.4 Apparent preconsolidation pressure - The LC surface

Hereinbefore the main assumptions regarding the extension of the intrinsic compressibility framework for anisotropic soils in the unsaturated regime were presented. In this section we determine the evolution of the apparent preconsolidation pressure of an unsaturated material, building on the already made assumptions.

In figure 5.11 point A corresponds to the preconsolidation pressure $p_0$ of a normally consolidated material under saturated conditions ($S_r^e = 1.0$). The apparent preconsolidation pressure ($p_0(s, S_r^e)$) of the same material under unsaturated conditions described by a given level of applied suction ($s$) and the corresponding degree of saturation ($S_r^e$) is represented by point B. Point B is the intersection of the swelling line originating from point A and of the compression line whose slope corresponds to the aforementioned state of partial saturation.

Based on figure 5.11, the specific volume at point A is calculated through the compression curve of the saturated material with slope $\lambda$ as:

$$v_A = N_{p^c} - \lambda \ln\left(\frac{p_0}{p^c}\right) \tag{5.25}$$

In a similar way the specific volume at point B is calculated through the compression

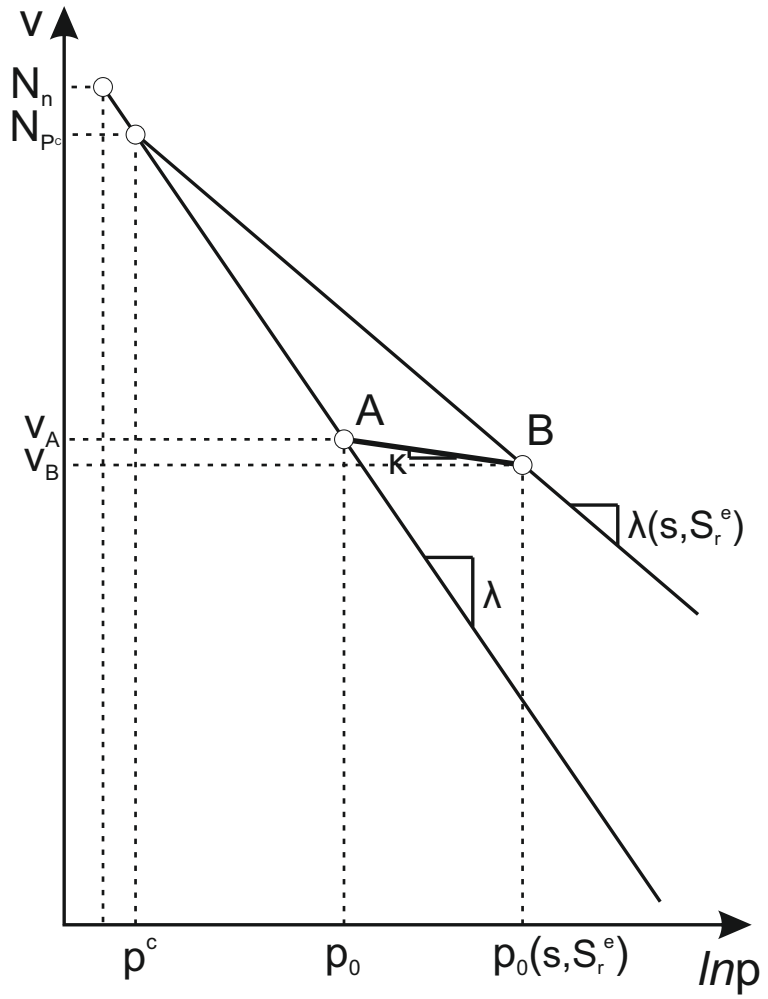


**Figure 5.11:** Calculating the apparent preconsolidation pressure.

curve corresponding to the unsaturated material state with slope $\lambda(s, S_r^e)$ as:

$$v_B = N_{p^c} - \lambda(s, S_r^e) \ln\left(\frac{p_0(s, S_r^e)}{p^c}\right) \tag{5.26}$$

Furthermore, points A and B are located on the same swelling line and thus the following relationship applies:

$$v_A = v_B - \kappa \ln\left(\frac{p_0(s, S_r^e)}{p_0}\right) \tag{5.27}$$

By substituting eq. 5.25, 5.26 in eq. 5.27, we obtain:

$$N_{p^c} - \lambda(s, S_r^e) \ln\left(\frac{p_0(s, S_r^e)}{p^c}\right) = N_{p^c} - \lambda \ln\left(\frac{p_0}{p^c}\right) - \kappa \ln\left(\frac{p_0(s, S_r^e)}{p_0}\right) \Rightarrow$$
$$\lambda(s, S_r^e) \ln p^c - \lambda(s, S_r^e) \ln p_0(s, S_r^e) = \lambda \ln p^c - \lambda \ln p_0 + \kappa \ln p_0 - \kappa \ln p_0(s, S_r^e) \quad (5.28)$$

By subtracting from both parts of equation 5.28 the term $\kappa \ln p^c$, we may further elaborate:

$$\begin{aligned}
\lambda(s, S_r^e) \ln p^c - \lambda(s, S_r^e) \ln p_0(s, S_r^e) + \kappa \ln p_0(s, S_r^e) - \kappa \ln p^c &= \lambda \ln p^c - \lambda \ln p_0 + \kappa \ln p_0 - \kappa \ln p^c \Rightarrow \\
(\lambda(s, S_r^e) - \kappa) \ln p^c - (\lambda(s, S_r^e) - \kappa) \ln p_0(s, S_r^e) &= (\lambda - \kappa) \ln p^c - (\lambda - \kappa) \ln p_0 \Rightarrow \\
(\lambda(s, S_r^e) - \kappa) (\ln p^c - \ln p_0(s, S_r^e)) &= (\lambda - \kappa) (\ln p^c - \ln p_0) \Rightarrow \\
(\lambda(s, S_r^e) - \kappa) \ln \frac{p_0(s, S_r^e)}{p^c} &= (\lambda - \kappa) \ln \frac{p_0}{p^c} \Rightarrow \\
\ln \frac{p_0(s, S_r^e)}{p^c} &= \frac{\lambda - \kappa}{\lambda(s, S_r^e) - \kappa} \ln \frac{p_0}{p^c}
\end{aligned} \quad (5.29)$$

and finally, exponentiating both terms using the base of the natural logarithm $e$ we may eliminate the natural logarithm and derive:

$$p_0(s, S_r^e) = p^c \left(\frac{p_0}{p^c}\right)^{\frac{\lambda - \kappa}{\lambda(s, S_r^e) - \kappa}} \quad (5.30)$$

It is observed that the derived equation is similar to the one proposed in BBM for the variation of the net apparent preconsolidation pressure, with the difference that in the proposed form the compressibility of the unsaturated material depends on both suction and degree of saturation (eq. 5.24).

In the next few lines, expressions 5.24 and 5.30 for the compressibility $\lambda(s, S_r^e)$ and apparent preconsolidation pressure $p_0(s, S_r^e)$ are applied parametrically both to gain insight on the effect of the various parameters as well as to provide an preliminary evaluation of the proposed framework..

To account for different degrees of saturation, the void ratio dependant Water Retention Model (WRM) proposed by Gallipoli et al. (2003) is adopted (see chapter 4),

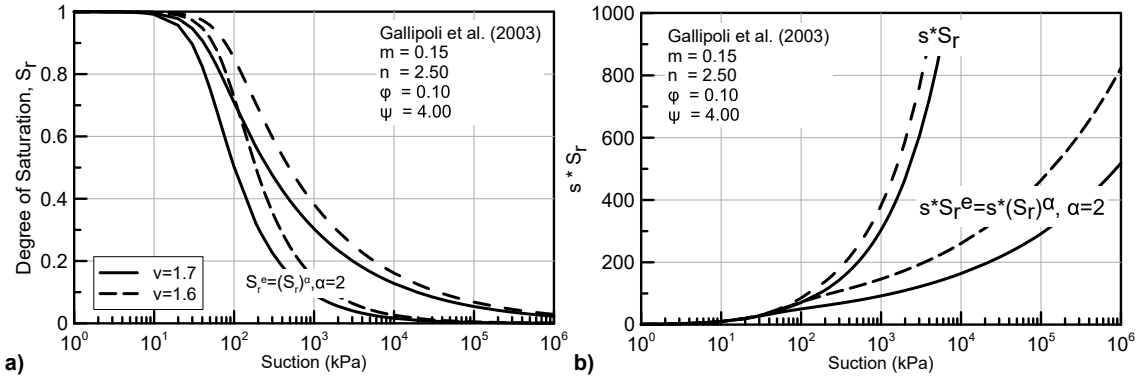


**Figure 5.12:** The assumed water retention behaviour and the corresponding variation of the $s \cdot S_r^e$ term.
a) The assumed water retention behaviour and; b) the corresponding variation of the $s \cdot S_r^e$ term.

described by the following expression:

$$S_r = \left( \frac{1}{1 + \left( \phi \, (v-1)^{\psi} \, s \right)^n} \right)^m \tag{5.31}$$

where $\phi$, $\psi$, $n$ and $m$ are soil constants and $v$ the specific volume of the material. Equation 5.31 was applied for $v = 1.6$ and 1.7, while all other parameters were kept constant. Figure 5.12a shows the variation of saturation with suction according to eq. 5.31 and according to Alonso et al. (2010) for a=2.0 (see eq. 5.20), while figure 5.12b presents the corresponding variation of Bishop's stress term $s \cdot S_r^e$.

Figures 5.13 to 5.15 include the results of the parametric study, based on the material constants shown in table 5.4. More specifically, figure 5.13 presents the variation of compressibility with suction and the corresponding increase in the apparent preconsolidation pressure, which in fact corresponds to the Loading - Collapse surface. In figure 5.14 the LC curves of figure 5.13 are repeated, this time with respect to the apparent preconsolidation pressure in terms of net stress ($\overline{p_0}(s, S_r^e)$). The latter is calculated by subtracting from $p_0(s, S_r^e)$ the Bishop's stress term $s \cdot S_r^e$.

Based on the results of the parametric study we may summarize:

- Equation 5.24 predicts a clear increase in soil stiffness with partial saturation, under various combinations of the associated parameters. The stiffness increase is also reflected on the variation of the apparent preconsolidation pressure which

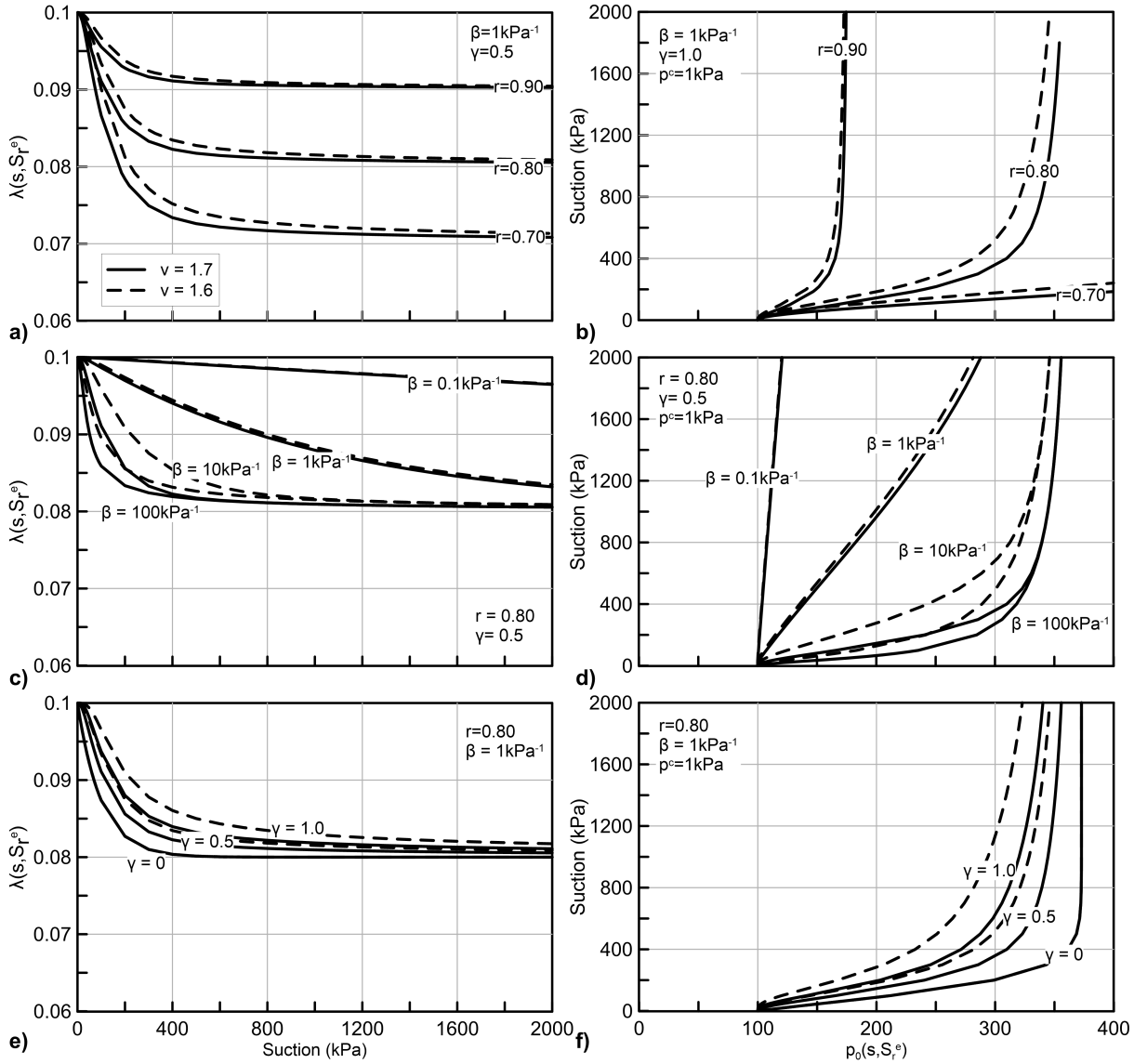


**Figure 5.13:** The effect of parameters $r$ (in (a), (b)), $\beta$ (in (c), (d)) and $\gamma$ (in (e), (f)) on the evolution with suction of the unsaturated compressibility $\lambda(s, S_r^e)$ (in (a), (c) and (e)) and of the apparent preconsolidation pressure $p_0(s, S_r^e)$ (in (b), (d) and (f)). Two different WRCs (fig. 5.12) are used to demonstrate the effect of degree of saturation.

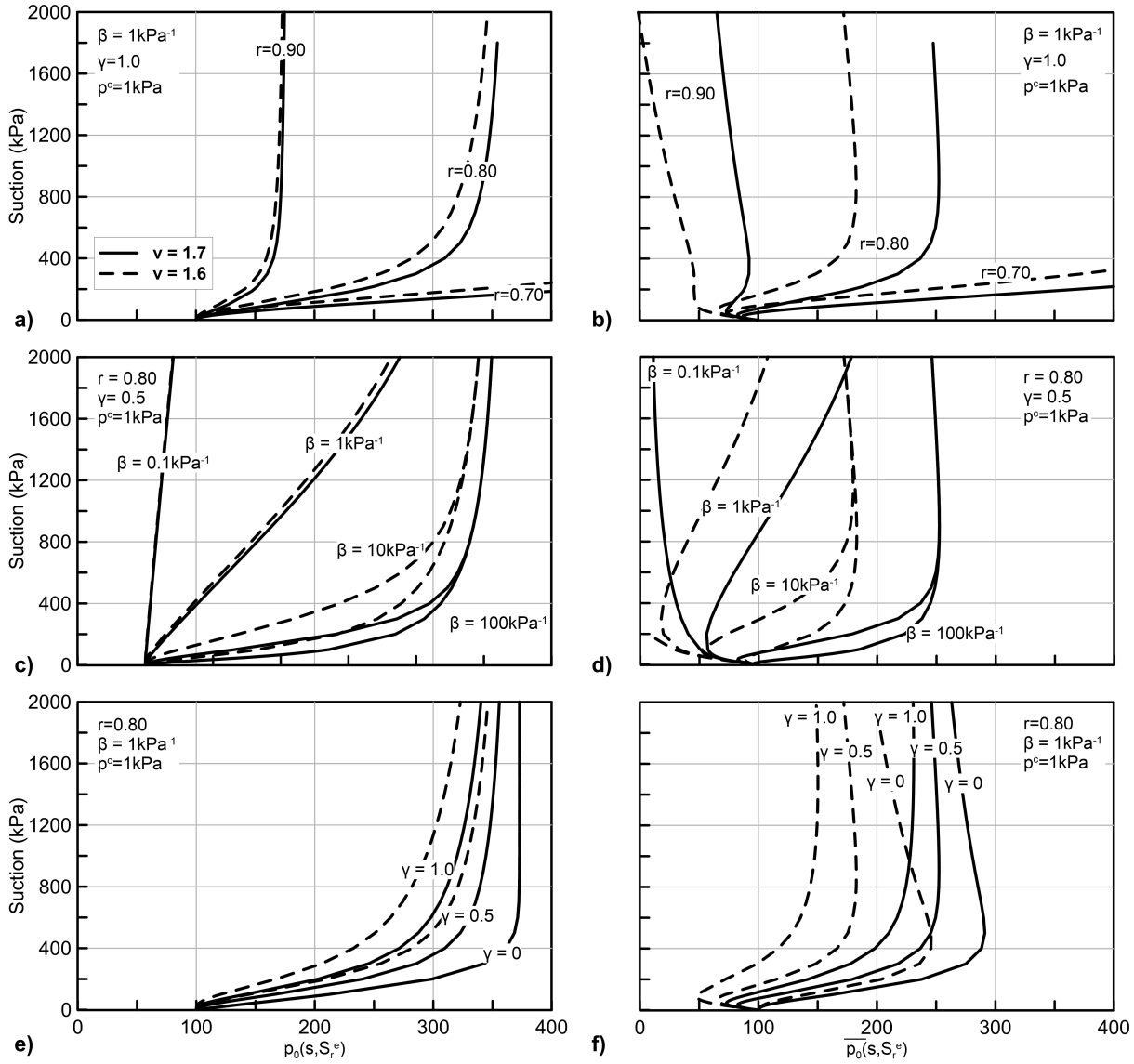


**Figure 5.14:** The effect of parameters $r$ (in (a)), $\beta$ (in (c)) and $\gamma$ (in (e)) on the evolution of the apparent preconsolidation pressure $p_0(s, S_r^e)$ with suction. The corresponding variation in terms of net stress in graphs (b),(d) and (f). Two different WRCs (fig. 5.12) are used to demonstrate the effect of degree of saturation.

**Table 5.4:** Material constant values used in the parametric study.

| Material constant | Value | Material constant | Value |
|---|---|---|---|
| $\lambda$ | 0.10 | $\beta$ $(kPa^{-1})$ | 0.1, 1.0, 10, 100 |
| $\kappa$ | 0.01 | $\gamma$ | 0, 0.5, 1.0 |
| $r$ | 0.9, 0.8, 0.7 | $p^c$ $(kPa)$ | 10, 1.0, 0.1 |

significantly increases with partial saturation.

- The effective degree of saturation has a twofold effect: a) under any given suction level the soil element under the higher degree of saturation (lower void ratio) exhibits a decreased stiffness and a decreased apparent preconsolidation pressure, and; b) it favours a more gradual increase in stiffness with suction, as identified by comparing the curves corresponding to $\gamma \neq 0$ and $\gamma = 0$.

- Parameters $r$ and $\beta$ hold, qualitatively, a role similar to their original one in BBM. Parameter $r$ mainly affects the maximum stiffness increase, while parameter $\beta$ controls the rate of this increase. Nevertheless we shall highlight that their contribution is not identical, with the exception of the $\gamma = 0$ case, where the selected stiffness variation rule falls back to the BBM's rule. Thus, even if the BBM parameters are known, re-calibration is needed to define suitable values for the proposed compressibility framework.

- Parameter $\gamma$ successfully scales the influence of degree of saturation, as clearly depicted in charts 5.13e and f, where the higher the $\gamma$ value is the more dependant on the degree of saturation the examined variation gets.

Regarding the variation of the net apparent preconsolidation pressure $\overline{p_0}(s, S_r^e)$, as depicted in the right column of figure 5.14, we may notice that:

- the shapes of the LC curves on the $p_0 - s$ and $\overline{p_0} - s$ planes differ, with $\overline{p_0}$ being smaller than $p_0$ by $s \cdot S_r^e$;

- the net apparent preconsolidation pressure initially decreases with an increase in the applied suction. This is a desirable pattern; in terms of simulation it is the outcome of the proposed framework's ability to describe unique compression curves for saturated material states, irrespectively of the level of the applied

suction. In practical terms it implies that if an initially normally consolidated saturated material is progressively subjected to an increasing suction under constant net stress, at the very begging it will cross the Loading Collapse surface. This is reasonable, because, as far as the soil remains saturated ($s < s_0$), an increase in suction causes an increase in the effective stress and thus further yielding;

- for unsaturated material states, the shape of the LC curve in the net stress - suction plane depends on the selected material constants and on the water retention characteristics of the material. Proper calibration is required in order to avoid peculiar results (i.e., continuously decreasing net yield stress with increasing suction).

Finally, figure 5.15 presents the effect of the reference pressure $p^c$ and of an evolving saturated preconsolidation pressure $p_0^*$, on the shape of the Loading - Collapse surface. The results illustrate that an increase in $p^c$ results in a decrease in the apparent preconsolidation pressure, over the entire suction range, without significantly affecting the shape of the L-C surface. The reference pressure $p^c$ offers an independent control on the evolution of the apparent preconsolidation pressure with suction, facilitating the calibration.

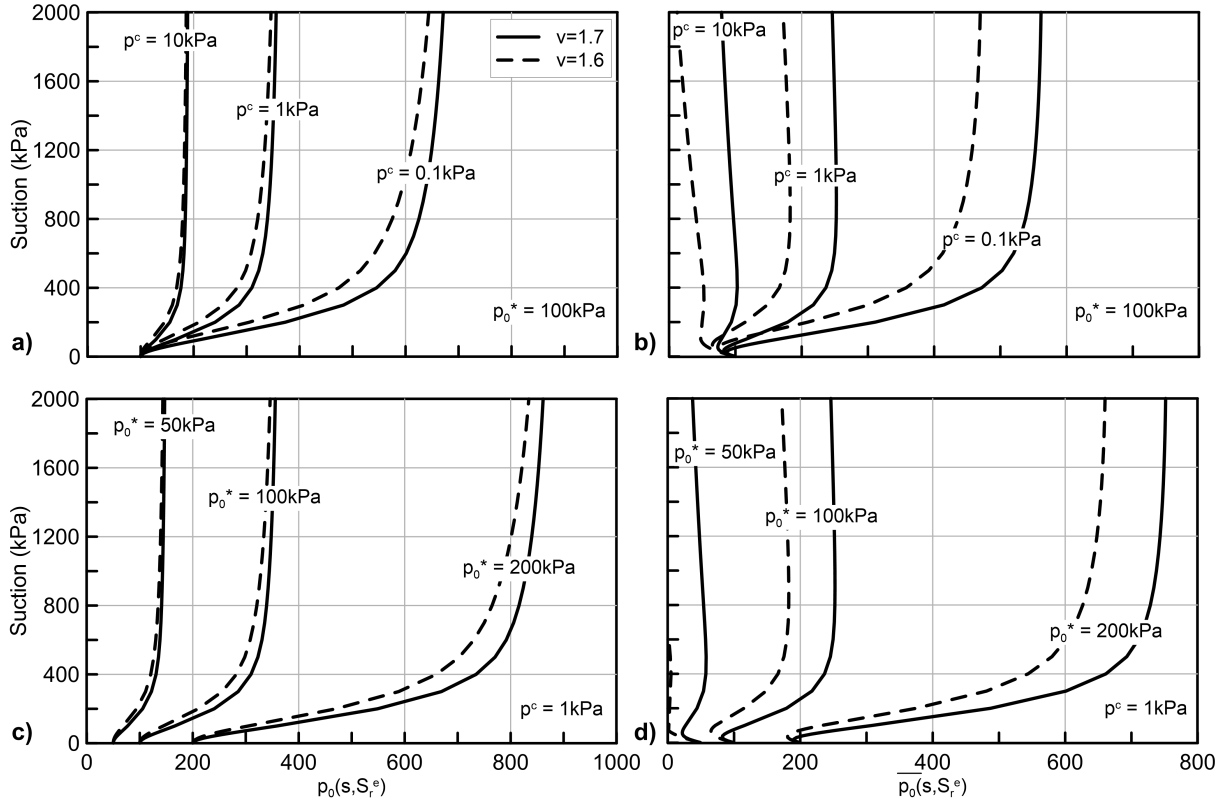


**Figure 5.15:** The effect of $p^c$ (in (c), (d)) and of $p_0^*$ (in (a), (b)) on the evolution of the apparent preconsolidation pressure $p_0(s, S_r^e)$ with suction. The corresponding variation in terms of net stress in graphs (b) and (d). Two different WRCs (fig. 5.12) are used to demonstrate the effect of degree of saturation.

## 5.4 Concluding Remarks

In this chapter the Intrinsic Compressibility Framework proposed by Belokas & Kavvadas (2011) for anisotropically consolidated clayey soils, has been slightly enhanced to favour numerical implementation, and further extended to account for the effect of partial saturation, leading to a complete volumetric compressibility framework for anisotropic, unsaturated clayey soils.

The proposed framework adopts virgin compression lines with a constant slope $\lambda$ for all saturated material states, while their position in the $v - \ln p$ plane, depends on the level of the stress induced anisotropy. It is based on experimental observations suggesting that anisotropically consolidated soils, in the $v - \ln p$ plane, move on distinct but parallel compression lines with anisotropy favouring a decreased void ratio (or specific volume). Graphically, all anisotropic compression curves are drawn in the area defined by the isotropic compression line (maximum void ratio) and the critical state line (minimum void ratio), while their relative position is controlled through a material constant $r_s$. The intrinsic compression curves, represent material states under stabilized anisotropic conditions and in that respect, the framework will be used in formulating the hardening rule of the proposed constitutive model.

The framework is extended in the unsaturated regime, by substituting Terzaghi's effective stress with Bishop's average skeleton stress. Additionally, partial saturation is assumed to influence the slope of the compression lines, in an inversely proportional way. A new unsaturated compressibility evolution rule, including three material constants, is proposed. It describes a double dependence of the compression lines on both suction and on the macrostructural degree of saturation, aiming to capture: a) unique compression lines for saturated materials irrespectively of the level of the applied suction, b) a continuously increasing compressibility for soils compressed under constant suction, and; c) a maximum of collapse. The developed framework defines the Loading - Collapse Surface of the constitutive model proposed within the present thesis.

# Chapter 6

# The Proposed Model

## 6.1 Introduction

This chapter presents the mathematical formulation of a new constitutive model for the analysis of geotechnical boundary value problems. The proposed model is based on the principles of critical state soil mechanics, while its formulation follows the framework of incremental, rate - independent, theory of plasticity. Its two main characteristics are:

- it incorporates the effect of stress induced anisotropy in the mechanical behaviour of soils by accounting for the memory of preferred directions;
- it accounts for the effects of partial saturation.

The model attempts to accommodate the most important behavioural aspects of both anisotropic and unsaturated soils as these were introduced and described in chapters 3 and 4 respectively. It builds on existing modelling ideas, while it incorporates various enchantments to improve the modelling capabilities. The main modification - enchantments focus on:

- the reproduction of compression lines which depend on the level of stress induced anisotropy;
- the simulation of the strain softening response typical of anisotropically, normally consolidated soil elements under triaxial undrained loading;
- the reproduction of unique critical state conditions, independent of the level of the initial anisotropy and of the loading path;

- the description in a consistent way of the effects of both suction and degree of saturation in the mechanical behaviour of unsaturated soils, focusing on shear strength and compressibility.

In the following sections, details regarding the utilized model variables, the selected elasticity, plastic yield envelope, flow rule and the hardening rule are included, introducing the complete mathematical formulation of the proposed constitutive model. Chapter 7 follows with the integration of the proposed formulation in suitable numerical algorithms to allow for the evaluation of the model's capabilities in later chapters.

## 6.2 Model Variables

Before proceeding to the mathematical formulation of the proposed constitutive model, the necessary external and internal variables are introduced.

### 6.2.1 External Variables

In chapter 2, we defined as external variables those variables associated with the loading conditions applied to a given material element. For common geotechnical problems, neglecting partial saturation and thermal or viscus effects, only one external variable needs to be defined, the tensor of the effective stress $\boldsymbol{\sigma}$.

The proposed model deals with the behaviour of unsaturated soils, thus a comprehensive description of the material state requires the definition of the following **external variables**:

- the tensor of Bishop's average skeleton stress, $\boldsymbol{\sigma}$;
- the suction, $s$;
- the effective (macro-structural) degree of saturation, $S_r^e$;
- the strain tensor, $\boldsymbol{\varepsilon}$;
- the specific volume $v = 1 + e$, where $e$ the void ratio;

Bishop's average skeleton stress can be written in the tensorial stress space as[1]:

$$\boldsymbol{\sigma} = \overline{\boldsymbol{\sigma}} + s \cdot S_r^e \cdot \boldsymbol{I} \tag{6.1}$$

where $\overline{\boldsymbol{\sigma}}$ is the net stress tensor, defined as the excess of total stress over the pressure of the air phase $u_a$:

$$\overline{\boldsymbol{\sigma}} = \boldsymbol{\sigma}_{tot} - u_a \cdot \boldsymbol{I} \tag{6.2}$$

Nevertheless, in typical geotechnical applications, it is common to assume that the air pressure is usually assumed equal to zero, thus the net stress and the total stress are considered equal for simplicity.

Bishop's stress tensor can be decomposed to an isotropic and a deviatoric part. The former is defined as:

$$\sigma = \frac{1}{3}\boldsymbol{\sigma} : \boldsymbol{I} = \frac{1}{3}\overline{\boldsymbol{\sigma}} : \boldsymbol{I} + s \cdot S_r^e \tag{6.3a}$$

corresponding to the octahedral stress. Subtracting the isotropic stress component from the stress tensor the deviatoric component $\boldsymbol{s}$ is defined:

$$\boldsymbol{s} = \boldsymbol{\sigma} - \sigma \boldsymbol{I} \tag{6.3b}$$

Suction $s$ is a scalar, stress quantity defined as the excess of water pressure over the air pressure ($s = u_a - u_w$), while in an analogy to net stress, if air pressure is assumed equal to zero it can be simply regarded as the opposite of water pressure. Suction comprises the Second Constitutive Variable (SCV) required for a comprehensive representation of the effects of partial saturation in the mechanical behaviour of soils. It is considered an external variable as it depends on the hydraulic boundary conditions imposed to any given material element, and in that respect, controls the loading conditions.

Finally, the third external variable, the effective degree of saturation accounts for the water content. It is reminded that the term effective is used for the macro-structural degree of saturation, referring to that portion of the larger macro-pores (larger pores forming between clay aggregates), that is filled with water. As described in chapter 5, for the relation between the effective degree of saturation and

[1]Most of the entities used in this chapter have been already introduced in the previous chapters. However, repeating some fundamental definitions is inevitable, to facilitate an independent reading of the present chapter.

the common degree of saturation $S_r$ the present study adopts the power law proposed by Alonso et al. (2010), repeated here for clarity:

$$S_r^e = (S_r)^\alpha \tag{6.4}$$

where $\alpha$, a material constant. It is well known that the degree of saturation cannot be explicitly controlled but it is the outcome of the applied hydraulic conditions, following the Water Retention Curve (WRC) of the material. From this perspective, it seems rather peculiar that the degree of saturation is considered an external and not an internal variable, however such a selection can be justified with regard to the nature of the proposed constitutive model.

Constitutive models for unsaturated soils are usually treated as hydromechanical models where both the hydraulic and the mechanical behaviour are integrated in a single model. Such models, starting from any given initial state of stress ($\boldsymbol{\sigma}$), suction ($s$) and hardening variables ($\boldsymbol{q}$), and given an imposed increment of the strain tensor ($\dot{\boldsymbol{\varepsilon}}$) and suction ($\dot{s}$), calculate the updated state of stress ($\boldsymbol{\sigma} + \dot{\boldsymbol{\sigma}}$) and the updated hardening variables ($\boldsymbol{q} + \dot{\boldsymbol{q}}$). They incorporate the Water Retention Model as an internal part of the constitutive formulations and thus suction is the only necessary external variable, while the degree of saturation is considered an internal variable.

If we examine the mechanical and the hydraulic part of the model separately, the approach is different. Fundamentally, the mechanical part of the model describes exclusively the relation between an increment of the strain tensor ($\dot{\boldsymbol{\varepsilon}}$) and the corresponding stress increment ($\dot{\boldsymbol{\sigma}}$). The mechanical behaviour of unsaturated soils, though, depends strongly on the state of partial saturation as the latter is reflected on suction and degree of saturation. Thus, both quantities are needed as an input for the mechanical constitutive law. Since, the proposed model is a mechanical constitutive model both suction and degree of saturation should be defined as external variables.

Of course, incorporation of degree of saturation, requires coupling with a proper hydraulic model to provide the variation of degree of saturation with suction and preferably with void ratio as well. Nevertheless, in the proposed model the WRM does not comprise an internal part of the formulation but it is incorporated as an external component. Two are the main reasons underlying this choice.

The first and probably the obvious one is versatility. The model's formulation is independent of the WRM used and thus any suitable, existent or even future WRM

can be coupled to the proposed model, without the need of modifying its mathematical formulation.

The second reason is related to the implementation of the proposed model in a commercial FEM computer code. Existing commercial FEM codes (e.g., Simulia Abaqus) include their own hydraulic WRM. This is quite reasonable as the WRM is involved in the solution of the water balance equation, usually solved simultaneously with the mechanical equilibrium equations. It describes the quantity of water existing in the system at any given analysis' time-step and in that sense it is a prerequisite for any FEM code which can perform analyses of unsaturated porous medium. In commercial codes, the user can usually interfere exclusively with the mechanical part of the solution, by implementing a suitably formulated mechanical constitutive model. Hence, such a user defined constitutive model must handle the output of the hydraulic problem as an external input.

### 6.2.2 Internal Variables

The ensemble of internal variables of the proposed model consists of its **hardening variables**, namely:

- the projection of the center of the yield surface ($a$) on the hydrostatic axis, under saturated conditions, and;
- the anisotropy tensor $\boldsymbol{b}$ representing the material's memory of preferred directions (memory of stress induced anisotropy).

## 6.3 Elasticity

The model follows the basic kinematic assumption of the additive decomposition of the total strain increment in an elastic $\dot{\boldsymbol{\varepsilon}}^{\mathbf{e}}$ and a plastic (irreversible) $\dot{\boldsymbol{\varepsilon}}^{\mathbf{p}}$ part:

$$\dot{\boldsymbol{\varepsilon}} = \dot{\boldsymbol{\varepsilon}}^{e} + \dot{\boldsymbol{\varepsilon}}^{p} \tag{6.5}$$

The elastic strain increment is computed through the elastic law for which the proposed model adopts the porous elastic behaviour, introduced in details in subchapter 2.3.2.3.

Poroelasticity is an isotropic linear elastic law where the Bulk Modulus $K$ and the Shear Modulus $G$ are computed as:

$$K = \frac{v\sigma}{\kappa} \tag{6.6}$$

and

$$G = \frac{1}{2}\left(\frac{2G}{K}\right)K \tag{6.7}$$

where $\kappa$ the MCC parameter representing the slope of the swelling lines in the $v - \ln\sigma$ plane. The quantity $\frac{2G}{K}$ is assumed a material constant and can be related to Poisson's ratio through the following expression:

$$\frac{2G}{K} = \frac{3\,(1-2\nu)}{1+\nu} \tag{6.8}$$

No further assumptions are required to represent the elastic behaviour due to changes in suction and/or degree of saturation, as Bishop's average skeleton stress in combination with the MCC porous elastic behaviour can sufficiently represent elastic straining in unsaturated media, without the need to modify the basic kinematic assumption. On the contrary, net stress models would require an additional decomposition of the elastic strains in a net stress and a suction stress related subcomponents.

Finally, recalling equations 2.5 and 2.8 the elastic Jacobian $\boldsymbol{C}^e$ of the proposed model is computed according to:

$$\dot{\boldsymbol{\sigma}} = \boldsymbol{C}^{\mathbf{e}} : \dot{\boldsymbol{\varepsilon}}^e \Rightarrow \begin{Bmatrix} \dot{\sigma} \\ \dot{\boldsymbol{s}} \end{Bmatrix} = \begin{pmatrix} K & \mathbf{0} \\ \mathbf{0} & 2G \end{pmatrix} : \begin{Bmatrix} \dot{\varepsilon}^e \\ \dot{\boldsymbol{e}}^e \end{Bmatrix} \tag{6.9}$$

## 6.4 Plastic Yield Envelope (PYE)

The proposed model incorporates a single yield surface, that serves as a Plastic Yield Envelope (PYE), differentiating between elastic and elastoplastic stress states. Following the fundamental principles of theory of plasticity, any stress increment inside the yield surface is assumed elastic and results to fully reversible elastic strains, while, any elastoplastic stress increment leads to an updated position on the yield surface.

The incorporated yield surface accommodates all types of soil behaviour that this thesis deals with, namely anisotropy and partial saturation. Nevertheless, for a comprehensive introduction of the underlying principles, the concept of characteristic

surfaces is used, to simplify the presentation. Characteristic surfaces represent reference states, while the yield surface coincides with these reference states under specific conditions. Two characteristic surfaces are used in this model, the Saturated Strength Envelope (SatSE) and the Unsaturated Strength Envelope (UnsSE). The former, as as implied by its name, describes all material states under saturated conditions, while it additionally accounts for stress induced anisotropy. The latter is an extension of the SatSE, associated to material states under partial saturation.

### 6.4.1 Saturated Strength Envelope

The Saturated Stress Envelope describes the elastoplastic behaviour under saturated conditions and it additionally accommodates the effect of stress induced anisotropy in the material behaviour. The yield locus of anisotropically consolidated soil elements is inclined with respect to the hydrostatic axis, while its inclination depends on the direction of the consolidation stress path.

Such an inclined yield locus has been proposed by Kavvadas (1982) and is also adopted in the proposed constitutive model to describe the Saturated Strength Envelope. Its mathematical formulation is given by the following expression:

$$F(\sigma, \boldsymbol{s}, \alpha, \boldsymbol{b}) = \frac{1}{k^2}(\boldsymbol{s} - \sigma\boldsymbol{b}) : (\boldsymbol{s} - \sigma\boldsymbol{b}) - \sigma(2\alpha - \sigma) \tag{6.10}$$

where:

- $\sigma$: Bishop's average skeleton stress; under saturated conditions it coincides with Terzaghi's effective stress,
- $\boldsymbol{s}$: the deviatoric stress tensor,
- $\alpha$: the isotropic hardening variable controlling the size of the Saturated Strength Envelope,
- $\boldsymbol{b}$: the kinematic hardening variable tensor controlling the orientation of the Saturated Strength Envelope in all deviatoric planes, and;
- $k$: a material constant defining the ratio of the axes of the Saturated Strength Envelope.

As depicted in figure 6.1, equation 6.10 represents a distorted ellipsoid with its main axis along the direction $\boldsymbol{\beta} = \boldsymbol{b} + \boldsymbol{I}$. Following Kavvadas (1982), we assume that

any soil element normally consolidated along a radial stress path with direction $\boldsymbol{\beta}$ lays on the tip of a distorted yield surface with its axis oriented along the same direction $\boldsymbol{\beta}$. Furthermore, according to the proposed compressibility framework introduced in chapter 5, the volumetric behaviour of the same soil element will plot on the intrinsic compression line corresponding to the stress ratio of the radial stress path. As a result, the projection of the tip of the yield surface on the isotropic axis ($2a$) will coincide with the preconsolidation pressure of the material $p_0$. This is a key point in the formulation of the proposed model and will be used in the development of the hardening rule.

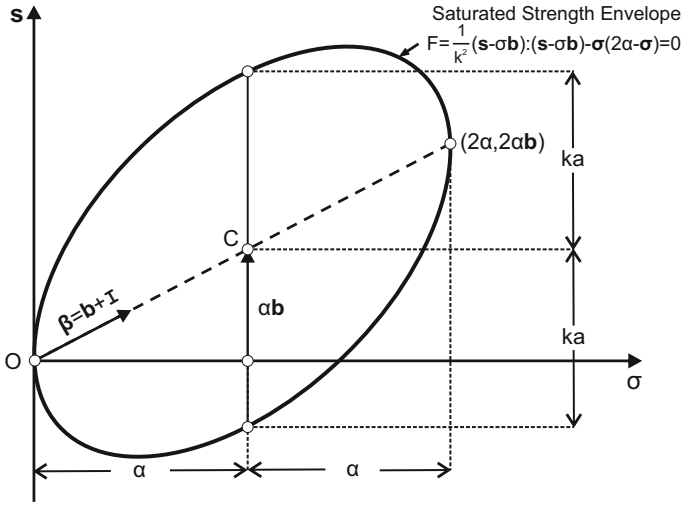


**Figure 6.1:** The adopted Saturated Strength Envelope (SSE).

The selected saturated strength envelope, reduces to the MCC yield surface when the anisotropy tensor is null ($\boldsymbol{b} = \mathbf{0}$). Thus, the yield locus of isotropically consolidated soil elements is still represented by the isotropic MCC yield surface, a common reference for any critical state models.

### 6.4.2 Unsaturated Strength Envelope

With the Saturated Strength Envelope acting as a reference level we may now project the behaviour to the unsaturated regime. We have extensively discussed that partial saturation strengthens and stiffens the behaviour of any given soil. This is mainly reflected through a substantial increase of the elastic domain as the yield locus moves towards higher yield stress values.

In chapter 5 we demonstrated how the compressibility of an unsaturated soil

element is correlated with the compressibility of its saturated counterpart through equation 5.30, which describes the evolution of the apparent preconsolidation pressure with suction and with the effective degree of saturation. Equation 5.30 is repeated below, as it describes the Loading Collapse surface of the proposed constitutive model and thus plays the role of a yield surface.

$$p_0(s, S_r^e) = p^c \left( \frac{p_0}{p^c} \right)^{\frac{\lambda-\kappa}{\lambda(s,S_r^e)-\kappa}} \tag{6.11}$$

According to equation 6.13, partial saturation increases the yield stress of the material. We assume that the increase of the preconsolidation pressure produces a homothetical enlargement of the strength envelope, under constant orientation. In other words we may say that drying a saturated soil, already exhibiting a certain level of anisotropy, does not affect its stress induced anisotropy. The enlarged strength envelope as a result of partial saturation, represents the Unsaturated Strength Envelope and is mathematically described by the following expression:

$$f\left(\sigma, \boldsymbol{s}, \alpha\left(s, S_r^e\right), \boldsymbol{b}\right) = \frac{1}{k^2}(\boldsymbol{s} - \sigma\boldsymbol{b}) : (\boldsymbol{s} - \sigma\boldsymbol{b}) - \sigma(2\alpha\left(s, S_r^e\right) - \sigma) \tag{6.12}$$

where $\sigma$, $\boldsymbol{s}$, $\boldsymbol{b}$ and $k$ identical to the SSE (equation 6.10), while $\alpha(s, S_r^e)$ can be correlated with $\alpha$ by taking into account that $p_0 = 2\alpha$ and $p_0(s, S_r^e) = 2\alpha(s, S_r^e)$ as follows:

$$\alpha(s, S_r^e) = \frac{p^c}{2} \left( \frac{2 \cdot \alpha}{p^c} \right)^{\frac{\lambda-\kappa}{\lambda(s,S_r^e)-\kappa}} \tag{6.13}$$

We may notice that the effect of suction and effective degree of saturation appear indirectly in the unsaturated strength envelope through the dependance of the apparent preconsolidation pressure on the evolution of compressibility with partial saturation, as described by equation 5.24 and repeated below:

$$\lambda(s, S_r^e) = \lambda \left[ 1 - (1 - r)\left(1 - S_r^e\right)^{\gamma} \left(1 - e^{-\beta s}\right) \right] \tag{6.14}$$

For $S_r^e = 1.0$, equation 6.14 describes the compressibility of the saturated material $\lambda$, which further results in $\alpha(s, S_r^e) = \alpha$ according to equation 6.13. Thus, the transition from saturated to unsaturated material states and vive versa, is described by continuous and thus continuously differentiable equations. In terms of constitutive

modelling, this mathematical continuity allows for both the saturated and the unsaturated strength envelope to be represented through a common equation, apparently the most general one, which is the one of the Unsaturated Strength Envelope. In that respect, equation 6.12 comprises the yield surface of the proposed constitutive model. Figure 6.2 presents the yield surface of the proposed model under the most general case where both an anisotropic and unsaturated soil fabric exists, and figure 6.3 presents the complete Yield Envelope in the stress - partial saturation hyperspace.

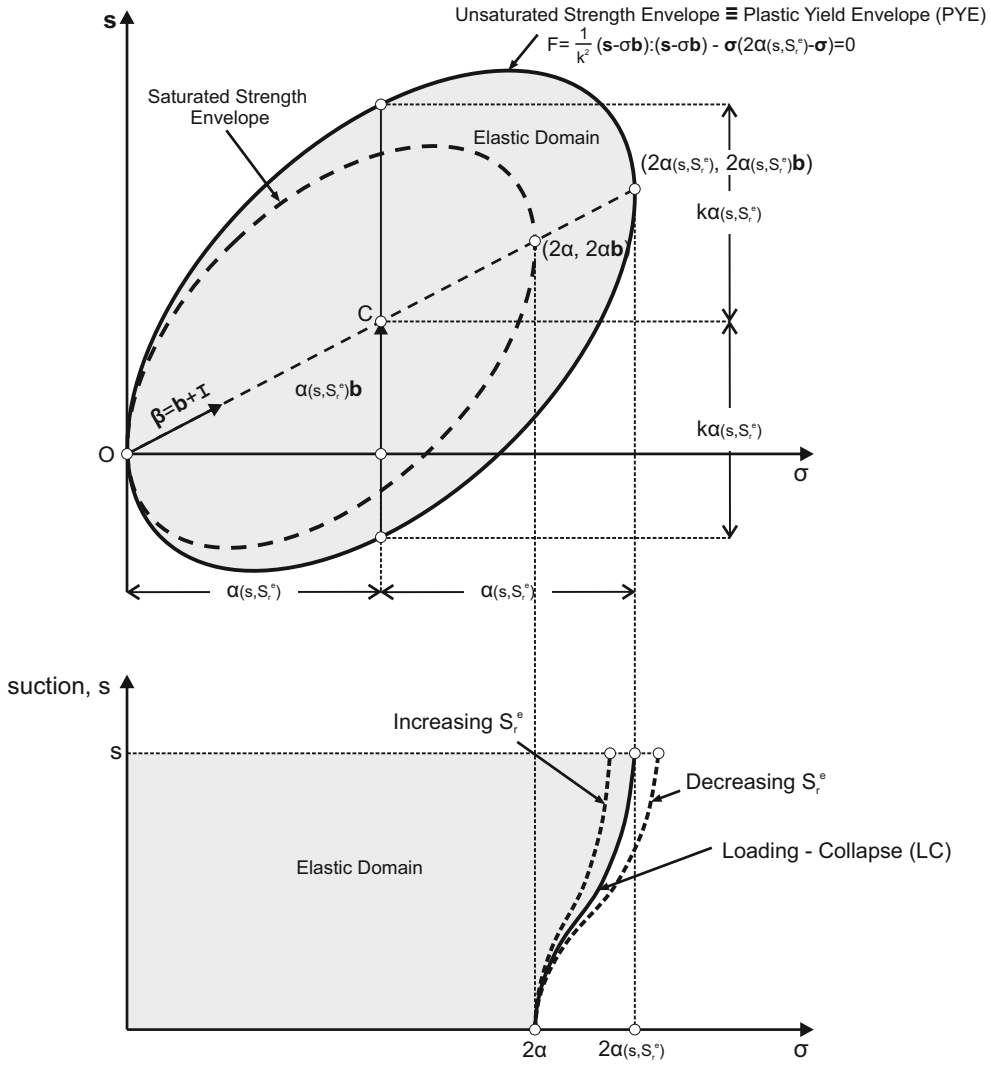


**Figure 6.2:** The adopted Unsaturated Stress Envelope and the correspondance with the Saturated Strength Envelope.

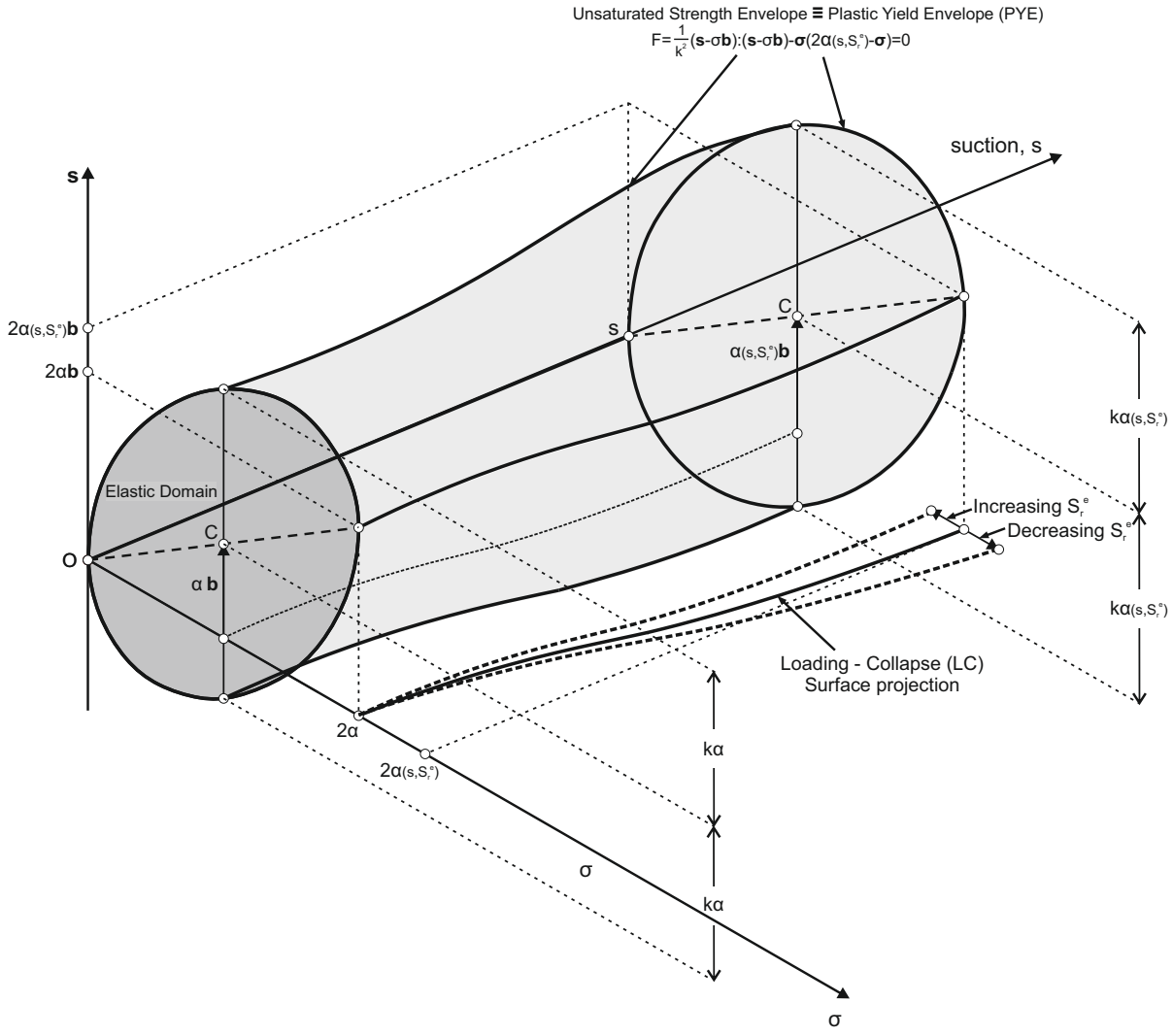


**Figure 6.3:** The complete yield envelope of the proposed constitutive model in the stress - partial saturation hyperspace.

### 6.4.3 Elastic vs Plastic Loading

The adopted yield surface (see eq. 6.12), apart from the Bishop's stress tensor $\boldsymbol{\sigma}$, includes additional dependencies on suction ($s$) and effective degree of saturation ($S_r^e$). This modifies the definition of elastic and plastic loading conditions, contrary to classical theory of plasticity in which, the only yield surface variable evolving during elastic loading is the stress tensor is the only yield surface variable evolving. In the proposed model however, both suction and degree of saturation may also evolve, as both comprise external variables. In that end, **elastic loading** is associated with:

- an elastic initial state ($f(\boldsymbol{\sigma}, s, S_r^e) < 0$) and

an elastic updated state ($f(\boldsymbol{\sigma}+\dot{\boldsymbol{\sigma}}, s+\dot{s}, S_r^e+\dot{S}_r^e)<0$);

- a plastic initial state ($f(\boldsymbol{\sigma}, s, S_r^e)=0$) and
  an elastic updated state ($f(\boldsymbol{\sigma}+\dot{\boldsymbol{\sigma}}, s+\dot{s}, S_r^e+\dot{S}_r^e)<0$).

Moreover, the yield surface equation ensures that:

- its projections in the stress subspace are convex curves, and;
- it is a bijective function of both suction and effective degree of saturation.

Thus, starting from a plastic state ($f(\boldsymbol{\sigma}, s, S_r^e)=0$), an updated elastic state ($f(\boldsymbol{\sigma}+\dot{\boldsymbol{\sigma}}, s+\dot{s}, S_r^e+\dot{S}_r^e)<0$), requires that:

$$\boldsymbol{Q}:\dot{\boldsymbol{\sigma}}+\frac{\partial f}{\partial s}\dot{s}+\frac{\partial f}{\partial S_r^e}\dot{S}_r^e<0 \tag{6.15}$$

During elastic loading, the corresponding strain increment is purely elastic ($\dot{\boldsymbol{\varepsilon}}=\dot{\boldsymbol{\varepsilon}}^e$), and following the adopted elastic law we may write:

$$\dot{\boldsymbol{\sigma}}=\boldsymbol{C}:\dot{\boldsymbol{\varepsilon}}^e=\boldsymbol{C}:\dot{\boldsymbol{\varepsilon}} \tag{6.16}$$

Further substituting the stress increment from equation 6.16 in 6.15, it proves that elastic unloading occurs when:

$$\boldsymbol{Q}:\boldsymbol{C}^{\mathbf{e}}:\dot{\boldsymbol{\varepsilon}}+\frac{\partial f}{\partial s}\dot{s}+\frac{\partial f}{\partial S_r^e}\dot{S}_r^e<0 \tag{6.17}$$

We state that **plastic loading** is associated with:

$$\boldsymbol{Q}:\boldsymbol{C}^{\mathbf{e}}:\dot{\boldsymbol{\varepsilon}}+\frac{\partial f}{\partial s}\dot{s}+\frac{\partial f}{\partial S_r^e}\dot{S}_r^e\geq 0 \tag{6.18}$$

Similarly to classical plasticity it is important to note that plastic loading does not requires $\boldsymbol{Q}:\dot{\boldsymbol{\sigma}}+\frac{\partial f}{\partial s}\dot{s}+\frac{\partial f}{\partial S_r^e}\dot{S}_r^e>0$. Instead, the following three subcases of plastic loading are defined:

- $\boldsymbol{Q}:\dot{\boldsymbol{\sigma}}+\frac{\partial f}{\partial s}\dot{s}+\frac{\partial f}{\partial S_r^e}\dot{S}_r^e>0$: **plastic hardening**;
- $\boldsymbol{Q}:\dot{\boldsymbol{\sigma}}+\frac{\partial f}{\partial s}\dot{s}+\frac{\partial f}{\partial S_r^e}\dot{S}_r^e=0$: **neutral loading**, and;
- $\boldsymbol{Q}:\dot{\boldsymbol{\sigma}}+\frac{\partial f}{\partial s}\dot{s}+\frac{\partial f}{\partial S_r^e}\dot{S}_r^e<0$: **plastic softening**.

The necessary derivatives of the yield surface with respect to the external variables are given below.

- Derivatives with respect to the stress tensor

  The tensor $\boldsymbol{Q}$ is decomposed to its isotropic and deviatoric part:

$$\boldsymbol{Q} = (Q, \boldsymbol{Q}^{'}) = (\frac{\partial f}{\partial \sigma}, \frac{\partial f}{\partial \boldsymbol{s}} - \frac{1}{3}\left(\frac{\partial f}{\partial \boldsymbol{s}} : \boldsymbol{I}\right)\boldsymbol{I}) \tag{6.19a}$$

  where the associated derivatives are equal to:

$$\frac{\partial f}{\partial \sigma} = 2(\sigma - \alpha\left(s, S_r^e\right)) - \frac{2}{k^2}\boldsymbol{b} : (\boldsymbol{s} - \sigma\boldsymbol{b}) \tag{6.19b}$$

$$\frac{\partial f}{\partial \boldsymbol{s}} = \frac{2}{k^2}(\boldsymbol{s} - \sigma\boldsymbol{b}) \tag{6.19c}$$

- Derivatives with respect to suction and effective degree of saturation

  As already mentioned, suction and effective degree of saturation appear indirectly in the yield envelope equation through equations 6.13 and 6.14, thus the chain rule can be used to define the necessary derivatives:

$$\frac{\partial f}{\partial s} = \frac{\partial f}{\partial \alpha(s, S_r^e)} \cdot \frac{\partial \alpha(s, S_r^e)}{\partial \lambda(s, S_r^e)} \cdot \frac{\partial \lambda(s, S_r^e)}{\partial s} \tag{6.20a}$$

$$\frac{\partial f}{\partial S_r^e} = \frac{\partial f}{\partial \alpha(s, S_r^e)} \cdot \frac{\partial \alpha(s, S_r^e)}{\partial \lambda(s, S_r^e)} \cdot \frac{\partial \lambda(s, S_r^e)}{\partial S_r^e} \tag{6.20b}$$

  where:

$$\frac{\partial f}{\partial \alpha(s, S_r^e)} = -2\sigma \tag{6.20c}$$

$$\frac{\partial \alpha(s, S_r^e)}{\partial \lambda(s, S_r^e)} = \alpha(s, S_r^e) \ln\left(\frac{2\alpha}{p^c}\right) \frac{\kappa - \lambda}{\left(\lambda(s, S_r^e) - \kappa\right)^2} \tag{6.20d}$$

  while finally:

$$\frac{\partial \lambda(s, S_r^e)}{\partial s} = -\lambda\beta\left(1 - r\right)\left(1 - S_r^e\right)^{\gamma} e^{-\beta s} \tag{6.20e}$$

$$\frac{\partial \lambda(s, S_r^e)}{\partial S_r^e} = \lambda\gamma\left(1 - r\right)\left(1 - e^{-\beta s}\right)\left(1 - S_r^e\right)^{\gamma - 1} \tag{6.20f}$$

## 6.5 Flow Rule

Various approaches regarding the flow rule of anisotropic constitute models exist in the international literature, both associated (i.e., Dafalias (1986), Kavvadas & Amorosi (2000), Wheeler et al. (2003)) and non-associated (i.e., Kavvadas (1982), Newson & Davies (1996), Dafalias et al. (2006), Belokas & Kavvadas (2010)). The selection usually follows the assumptions regarding the orientation of the yield surface during anisotropic consolidation tests. In more detail, if the orientation of the yield surface during a radial consolidation stress path tends towards the slope of the imposed stress path then the plastic dilatancy predicted by an associated flow rule is unrealistic, especially under $K_0$ conditions. For this reason researchers adopting an associated flow rule (Dafalias 1986; Wheeler et al. 2003) incorporate hardening rules that bound the rotation of the yield surface to a smaller inclination with regards to the imposed stress ratio. A non-associated flow rule, overcomes this restriction and thus allows for a wider versatility in the reproduced plastic dilatancy.

Following the discussion above and considering that the adopted PYE aligns to the stress path of consolidation, a non-associated flow rule is selected for the proposed model, based on a suitable Plastic Potential Function (PPF) introduced below. The flow rule determines the plastic strain increment $\dot{\boldsymbol{\varepsilon}}^p$, through an incrementally linear relation of the following form:

$$\dot{\boldsymbol{\varepsilon}}^p = \dot{\Lambda}\boldsymbol{P} \tag{6.21}$$

where $\dot{\Lambda}$ the plastic multiplier and $\boldsymbol{P}$ the plastic potential tensor.

Regarding the plastic multiplier $\dot{\Lambda}$, in the case of unsaturated plasticity, a redefined expression is needed to account for the additional external variables. The following form is adopted:

$$\dot{\Lambda} = \frac{1}{H}\left(\boldsymbol{Q} : \dot{\boldsymbol{\sigma}} + \frac{\partial f}{\partial s}\dot{s} + \frac{\partial f}{\partial S_r^e}\dot{S}_r^e\right) \tag{6.22}$$

while following the classic theory of plasticity, the plastic modulus $H$ is calculated by employing the consistency condition on a later stage.

Following the definition of the flow rule, a stress increment can be computed as:

$$\dot{\boldsymbol{\sigma}} = \boldsymbol{C}^e : \dot{\boldsymbol{\varepsilon}}^e = \boldsymbol{C}^e : (\dot{\boldsymbol{\varepsilon}} - \dot{\boldsymbol{\varepsilon}}^p) = \boldsymbol{C}^e : \left(\dot{\boldsymbol{\varepsilon}} - \dot{\Lambda}\boldsymbol{P}\right) \tag{6.23}$$

Multiplying with $\boldsymbol{Q}$ we obtain:

$$\boldsymbol{Q} : \dot{\boldsymbol{\sigma}} = \boldsymbol{Q} : \boldsymbol{C}^e : \dot{\boldsymbol{\varepsilon}} - \dot{\Lambda}\ \boldsymbol{Q} : \boldsymbol{C}^e : \boldsymbol{P} \tag{6.24}$$

while further employing equation 6.22 we get:

$$\boldsymbol{Q} : \boldsymbol{C}^e : \dot{\boldsymbol{\varepsilon}} - \dot{\Lambda}\ \boldsymbol{Q} : \boldsymbol{C}^e : \boldsymbol{P} = \dot{\Lambda} H - \frac{\partial f}{\partial s}\dot{s} - \frac{\partial f}{\partial S_r^e}\dot{S}_r^e \tag{6.25}$$

Finally, we may obtain the formula to compute $\dot{\Lambda}$ with respect to any given increment of the strain tensor ($\dot{\boldsymbol{\varepsilon}}$), suction ($\dot{s}$) and effective degree of saturation ($\dot{S}_r^e$):

$$\dot{\Lambda} = \frac{\boldsymbol{Q} : \boldsymbol{C}^e : \dot{\boldsymbol{\varepsilon}} + \frac{\partial f}{\partial s}\dot{s} + \frac{\partial f}{\partial S_r^e}\dot{S}_r^e}{H + \boldsymbol{Q} : \boldsymbol{C}^e : \boldsymbol{P}} \tag{6.26}$$

For the direction of the plastic strain, the following **Plastic Potential Function** is introduced:

$$g(\sigma, \boldsymbol{s}, \theta, \boldsymbol{d}) = \frac{1}{c^2}(\boldsymbol{s} - \sigma\boldsymbol{d}) : (\boldsymbol{s} - \sigma\boldsymbol{d}) - \sigma(2\theta - \sigma) \tag{6.27}$$

where $\sigma$ is Bishop's mean stress, $\boldsymbol{s}$ is the deviatoric stress tensor, $\theta$ is the size of the PPS, $\boldsymbol{d}$ is a tensor controlling the orientation of the PPS in all deviatoric planes, and finally $c$ a material constant defining the ratio of the axes of the proposed ellipsoid. Parameter $c$, in fact represents the slope of the critical state line in the generalized stress space and thus can be directly correlated with parameter $M$ of the Modified Cam Clay as:

$$c = \sqrt{2/3}M \tag{6.28}$$

The proposed plastic potential function, has the same mathematical form with equation 6.12 and also describes a rotated distorted ellipsoid, with a similar shape to the yield envelope. Figure 6.4 presents the plastic potential surface together with a projection of the yield envelope, under a given, random plastic state. Differentiating eq. 6.27, the partial derivatives comprising the plastic tensor can be computed:

$$P = \frac{\partial g}{\partial \sigma} = 2(\sigma - \theta) - \frac{2}{c^2}\boldsymbol{d} : (\boldsymbol{s} - \sigma\boldsymbol{d}) \tag{6.29a}$$

$$\boldsymbol{P}' = \frac{\partial g}{\partial \boldsymbol{s}} = \frac{2}{c^2}(\boldsymbol{s} - \sigma\boldsymbol{d}) \tag{6.29b}$$

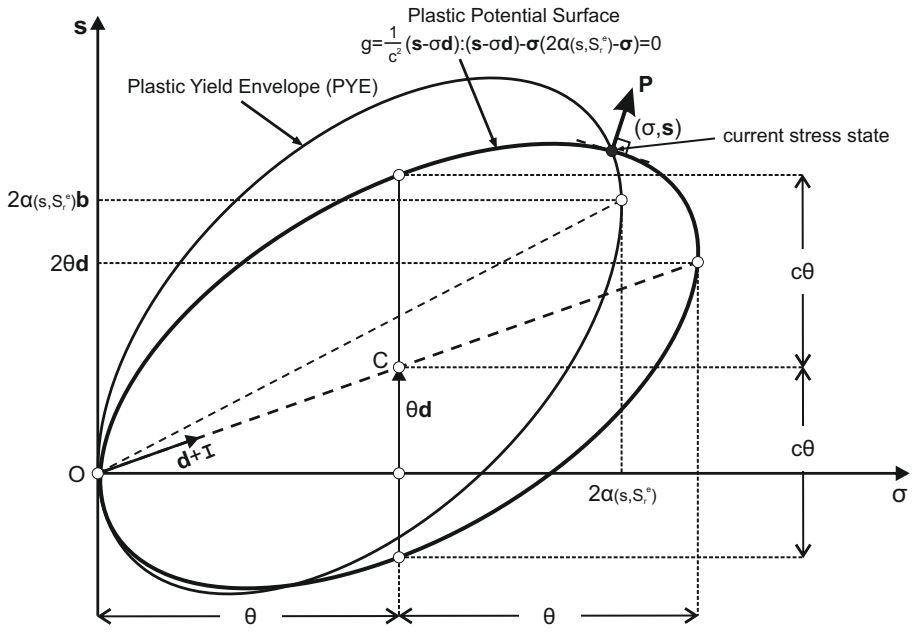


**Figure 6.4:** The adopted Plastic Potential Surface.

Regarding the orientation tensor $\boldsymbol{d}$, it is assumed to be analogous to its yield surface counterpart $\boldsymbol{b}$, through parameter $\chi$ according to:

$$\boldsymbol{d} = \chi \boldsymbol{b} \tag{6.30}$$

Parameter $\chi$ controls the analogy in the orienetation of the two surfaces, and is suitably selected to reproduce the desired dilatancy, under any given stress path. The size of the plastic potential function $\theta$ is calculated based on the requirement that under any given plastic state in the stress space $(\sigma, \boldsymbol{s})$, the plastic potential surface must pass through it. This is expressed mathematically through the $g(\sigma, \boldsymbol{s}) = 0$ condition which leads to:

$$\theta = \frac{1}{2}\left(\sigma + \frac{\frac{1}{c^2}(\boldsymbol{s} - \sigma\boldsymbol{d}) : (\boldsymbol{s} - \sigma\boldsymbol{d})}{\sigma}\right) \tag{6.31}$$

In chapter 2 we discussed how a non-associated flow rule can ensure the same level of solution's stability with an associated flow rule, as far as inequality 2.32 is fulfilled. Given the various parameters involved in both the yield surface and the plastic potential surface equations, it is almost impossible to derive mathematically the conditions under which the adopted flow rule does fulfill the aforementioned inequality. Alternatively, it is suggested that the value $\boldsymbol{Q} : \boldsymbol{C}^e : \boldsymbol{P}$ shall be continuously

monitored during numerical analyses and whenever it violates equation 2.32, the obtained results should be handled with caution as there is the possibility[2] of hidden errors due to potential numerical instabilities.

## 6.6 Hardening Rule

The proposed model incorporates two hardening variables. Parameter $\alpha$, a scalar quantity corresponding to the projection of the center of the saturated strength envelope on the hydrostatic axis and controls the size of the yield surface. The second hardening variable is the anisotropy tensor $\boldsymbol{b}$, which controls the orientation of the ellipsoid in every deviatoric sub-plane. To describe their evolution the proposed model employs a mixed hardening rule consisting of an isotropic component for the evolution of the hardening variable ($\alpha$) and a kinematic (rotational - distortional) component to control the evolution of the anisotropy tensor $\boldsymbol{b}$.

### 6.6.1 Isotropic Hardening

Most of the anisotropic models reviewed in section 3.3 adopt the MCC isotropic hardening rule. In MCC the hardening rule controls the size of a non-rotating isotropic ellipse and thus the tip of the yield surface always represents the isotropic preconsolidation pressure. However, adopting exactly the same relationship to describe the evolution of the tip of a distorted yield surface, does not allow for an accurate control of the reproduced compression lines during radial stress paths.

Exceptions to this rule are the Newson & Davies (1996) and Belokas & Kavvadas (2010) constitutive models. Newson & Davies (1996) proposed a mathematical formula to describe dependance of the position of the ICC on the level of stress induced anisotropy, but unfortunately didn't provide essential information on whether and how the proposed formula was incorporated in their constitutive model. Belokas & Kavvadas (2010) proposed and incorporated the Belokas & Kavvadas (2011) Intrinsic Compressibility Framework in the Belokas & Kavvadas (2010) constitutive model. Nevertheless, the ICF was introduced in their model's formulation in a rather approximate way, by postulating directly the incremental form of their hardening rule. Their approach cannot ensure that, under stabilized anisotropic conditions (i.e., yield surface has aligned with the imposed stress path), the volumetric behaviour in the

[2]It is reminder that this conditions is sufficient for stability and not a necessary one.

$v - \ln\sigma$ plane will plot on the corresponding compression curve. In that respect, the proposed hardening rule attempts to improve the Belokas & Kavvadas (2010) formulation, by deriving the hardening rule from the desired compressibility behaviour instead of directly postulating on its incremental form.

In chapter 5 we discussed how a structureless material subjected to a radial consolidation stress path, moves along Intrinsic Compression Curves (ICC) which are assumed to be parallel straight lines in the $v - \ln\sigma$ plane (see figures 5.1 and 5.2). Based on the proposed framework, we examine the case of a saturated soil element, initially isotropically consolidated, subjected to a radial consolidation stress path with slope $n = \sqrt{\boldsymbol{s} : \boldsymbol{s}/\sigma^2}$.

Let's suppose that the initially isotropically consolidated soil element is represented by point A in figure 6.5. From Point A it is firstly isotropically unloaded (Point A to Point B) and its stress ratio is elastically adjusted (inside the yield surface) to the desired stress ratio (Point C). If the material is then compressed under a constant stress ratio, after a small initial elastic part, the stress path will cross the yield surface, plastic strains will start to accumulate, and the hardening rules will activate leading to enlargement and distortion of the yield surface, following the imposed stress path. Examining the soil state at the end of the aforementioned radial compression and further assuming that stabilized anisotropic conditions have been reached (i.e, yield surface aligned with the stress path), then the tip of the yield surface (point D), in the $v - \ln\sigma$ plane should lie on that compression curve which corresponds to the imposed radial stress path.

The projection of the tip of the yield surface on the isotropic axis corresponds to $2\alpha$ where $\alpha$ the model's isotropic hardening variable. In the $v - \ln\sigma$ plane, point D can be projected on the Isotropic Compression Curve through a properly selected swelling line. The isotropic stress at the corresponding Point D* is denoted $2\alpha^*$ and in fact reflects the projection of the hardening variable $\alpha$ on the isotropic compression curve. We can write that the specific volume values corresponding to points D and D* are:

$$v_D = N_n - \lambda \ln 2\alpha \tag{6.32}$$

and

$$v_{D^*} = N_{iso} - \lambda \ln 2\alpha^* \tag{6.33}$$

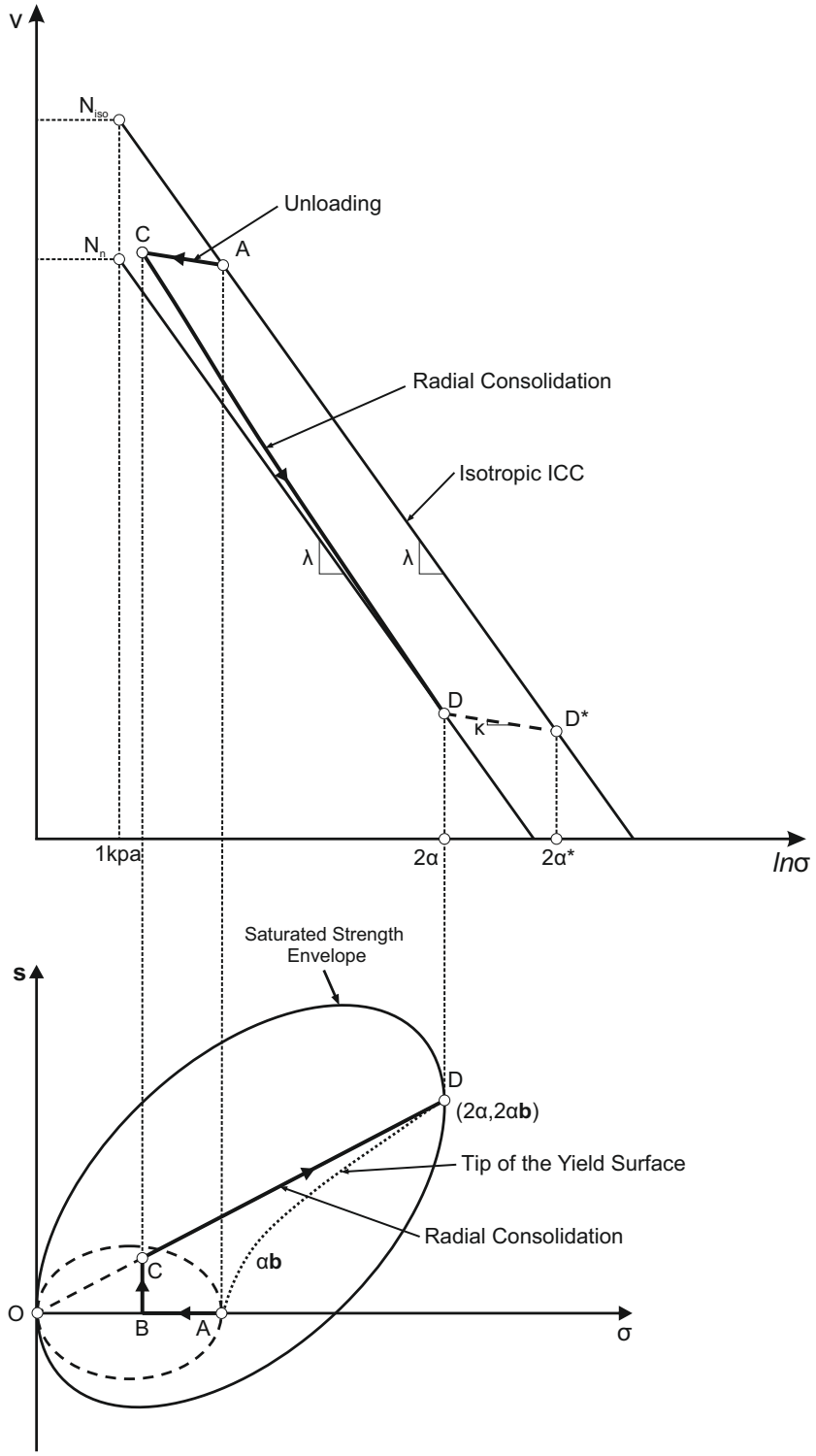


**Figure 6.5:** The desired volumetric behaviour during a radial compression test on an initially isotropically consolidated soil element, used in formulating the hardening rule.

respectively, while the swelling line DD* allows us to write that:

$$v_{D^*} = v_D - \kappa \ln \frac{2\alpha^*}{2\alpha} \tag{6.34}$$

Finally substituting $v_{D^*}$ and $v_D$ in equation 6.34 with 6.32 and 6.33 we derive:

$$\alpha = \exp\left(\frac{N_{iso} - N_n}{\kappa - \lambda}\right) \alpha^* \tag{6.35}$$

Regarding the position of the corresponding compression curve $N_n$ it depends on the applied stress path ($n = \sqrt{\boldsymbol{s} : \boldsymbol{s}/\sigma^2}$) through equation 5.12b. Furthermore, the orientation of the yield surface is identical to the imposed stress path and thus we may write that:

$$n = \sqrt{\boldsymbol{b} : \boldsymbol{b}} = \sqrt{\boldsymbol{s} : \boldsymbol{s}/\sigma^2} \tag{6.36}$$

Using equation 6.36 in 5.12b we obtain:

$$N_n = \Gamma + (N_{iso} - \Gamma)\left(1 - \frac{1}{c^2}\boldsymbol{b} : \boldsymbol{b}\right)^{r_s} \tag{6.37}$$

Combining equations 6.35 and 6.37 we can simply write that:

$$\alpha = A\alpha^* \tag{6.38}$$

where:

$$A = exp\left[\frac{\Gamma - N_{iso}}{\lambda - \kappa}\left[1 - \left(1 - \frac{1}{c^2}\boldsymbol{b} : \boldsymbol{b}\right)^{r_s}\right]\right] \tag{6.39}$$

The incremental form of the hardening rule is now simply calculated by differentiating equation 6.38:

$$\dot{a} = A\dot{a^*} + \dot{A}a^* \tag{6.40}$$

For the increment of quantity $A$ we calculate:

$$\dot{A} = \frac{2A \cdot r_s}{(\kappa - \lambda)} \frac{(N_n - \Gamma)}{\left(1 - \frac{1}{c^2}\boldsymbol{b} : \boldsymbol{b}\right)} \frac{1}{c^2}\boldsymbol{b} : \dot{\boldsymbol{b}} \tag{6.41}$$

Parameter $\alpha^*$, lays on the isotropic compression line and its value can be easily computed for any given combination of specific volume ($v$) and mean effective stress ($\sigma$) as:

$$a^* = \frac{1}{2} exp\left(\frac{N_{iso} - v - \kappa \ln \sigma}{\lambda - \kappa}\right) \tag{6.42}$$

while finally for its incremental calculation $\dot{a^*}$ the MCC hardening rule can be employed:

$$\dot{a^*} = \frac{v}{\lambda - \kappa} a^* \dot{\varepsilon^p} = \frac{v}{\lambda - \kappa} a^* \dot{\Lambda} P \tag{6.43}$$

Equations 6.39 to 6.43 comprise the isotropic hardening rule of the proposed constitutive model. It is fully compatible with the MCC hardening rule, as whenever an isotropic material state is examined $\boldsymbol{b} : \boldsymbol{b} = 0$ and thus $\alpha = \alpha^*$ and $\dot{\alpha} = \dot{\alpha^*}$, making the equations to reduce to the MCC hardening. On the other hand, for anisotropically consolidated soil elements, the size of the yield surface follows its orientation through the anisotropy tensor $\boldsymbol{b}$, with the reproduced behaviour being in line with the proposed compressibility framework through parameter $r_s$ in equation 6.39.

### 6.6.2 Kinematic Hardening

To control the orientation of the yield surface, a kinematic hardening rule is incorporated describing the evolution of the soil's memory of preferred directions, in simpler words the memory of anisotropy. We select to directly postulate on the incremental form of the associated hardening variable, the anisotropy tensor $\boldsymbol{b}$. The proposed kinematic hardening rule, consists of two subcomponents (parts) with an additive effect:

$$\dot{\boldsymbol{b}} = \dot{\boldsymbol{b}}_o + \dot{\boldsymbol{b}}_d \tag{6.44}$$

#### 6.6.2.1 Orientational part

The first part $\dot{\boldsymbol{b}_o}$ takes the following form:

$$\dot{\boldsymbol{b}}_o = \frac{1}{\alpha(s, S_r^e)} \psi (\boldsymbol{s} - \sigma \boldsymbol{b}) \dot{\varepsilon^p} \tag{6.45}$$

This subcomponent is similar to equation 3.6, corresponding to the hardening rule of the Kavvadas (1982) constitutive model. This part of the hardening rule is responsible for rotating the yield surface axis towards the slope of the imposed stress path. The magnitude of anisotropy change is assumed proportional to the plastic volumetric strain increment $\dot{\varepsilon^p}$, while $(\boldsymbol{s} - \sigma \boldsymbol{b})$ is a stress attractor dragging the yield surface axis towards the direction of the imposed stress path. Parameter $\psi$ controls the rate of evolution, while the half-size of the yield surface $(\alpha(s, S_r^e))$ is used for dimensioning. According to equation 6.45, anisotropy evolves continuously, and freezes distortion

only when a radial stress path is imposed and the yield surface is already oriented towards the same direction.

#### 6.6.2.2 De - Orientational part

The second part $\dot{\boldsymbol{b}}_{\boldsymbol{d}}$ is based on a new idea, initially introduced in Sitarenios et al. (2013) as part of the hardening rule of an early version of the proposed constitutive model. This part of the hardening rule attempts to accommodate in a unified and "natural" way the following patterns:

a) The strain softening behaviour exhibited by anisotropically consolidated soil samples when subjected to triaxial undrained loading.

b) Unique critical state conditions irrespective of the initial anisotropy and of the stress path followed.

The main idea is that the aforementioned behaviour is the outcome of an anisotropy degradation mechanism. In more detail, we suggest that the plastic straining occurring during any stress path which can lead to failure (i.e., triaxial undrained loading), produces a progressive loss in the material's memory of anisotropy. In terms of constitutive modelling this can be described as a progressive re-orientation (or de-orientation) of the yield surface towards the isotropic axis, with a common critical state associated with an isotropic yield surface.

The following expression is proposed to describe the anisotropy degradation mechanism:

$$\dot{\boldsymbol{b}}_d = -\frac{1}{a(s, S_r^e)^2}\boldsymbol{b}\,(\boldsymbol{s}-\sigma\boldsymbol{b}) : (\boldsymbol{s}-\sigma\boldsymbol{b})\,\zeta_q^p \dot{\varepsilon}_q^p \tag{6.46}$$

The de-orientation is proportional to the increment of the magnitude of the plastic deviatoric strain $\dot{\varepsilon}_q^p$, calculated as $\dot{\varepsilon}_q^p = \sqrt{\frac{2}{3}(\dot{\boldsymbol{e}}_p : \dot{\boldsymbol{e}}_p)}$. Parameter $\zeta_q^p$ controls the intensity of the distortion while the half-size of the yield surface is used for dimensioning. Equation 6.46 includes the anisotropy tensor as an attractor, that freezes the rotation when the yield surface becomes isotropic ($\boldsymbol{b} = \boldsymbol{0}$), while at the same time the attractor $(\boldsymbol{s}-\sigma\boldsymbol{b}) : (\boldsymbol{s}-\sigma\boldsymbol{b})$ is additionally included to ensure that whenever a radial stress path is imposed, the induced anisotropy stabilizes at the level of the imposed stress ratio.

In Sitarenios et al. (2013) the following far more complicated expression was proposed:

$$\dot{\boldsymbol{b}}_{\mathrm{d}} = -\frac{1}{a^2}\boldsymbol{b}\left(\boldsymbol{s}-\sigma\boldsymbol{b}\right):\left(\boldsymbol{s}-\sigma\boldsymbol{b}\right)\left(\zeta_{\mathrm{v}}^{\mathrm{p}}\left|\dot{\varepsilon}_{\mathrm{v}}^{\mathrm{p}}\right|+\zeta_{\mathrm{q}}^{\mathrm{p}}\dot{\varepsilon}_{\mathrm{q}}^{\mathrm{p}}\right)\exp\left(-\left(\mathrm{n}_{\mathrm{v}}^{\mathrm{p}}\left|\varepsilon_{\mathrm{v}}^{\mathrm{p}}\right|+\mathrm{n}_{\mathrm{q}}^{\mathrm{p}}\varepsilon_{\mathrm{q}}^{\mathrm{p}}\right)\right) \tag{6.47}$$

Theoretically, the above selection provides increased simulation versatility due to: a) its three additional parameters associated with additional terms, and; b) its dependance on the plastic volumetric strains. Nevertheless, it turned out that this increased versatility was not clearly reflected in the simulation results as they were marginally improved compared to corresponding with the simpler finally adopted. In addition, the calibration process was quite complicated as different material parameters had similar effects, i.e., various combinations (parameters sets) produced the same result. Finally, the exponential term was prone to mathematical saturation, leading to an undesirable freezing of the yield surface rotation, before critical state was reached.

On the other hand, the simplified expression, apart from easier to calibrate and almost similarly efficient, leads to a more elegant formulation of the kinematic hardening rule as the two incorporated subcomponents are decoupled, in the sense that the orientation part (eq. 6.45) is proportional to the increment of the plastic volumetric strains, while the de-orientational is proportional to the increment of the plastic deviatoric strains.

The proposed rule implies that critical state corresponds to an isotropic soil fabric. It is true that this is just an assumption and there are no conclusive experimental evidence either towards an isotropic or an anisotropic soil fabric at critical state. Thus, the proposed anisotropy degradation mechanism is mainly a tool to efficiently represent the macroscopical soil behaviour usually observed during common laboratory testing. We should further emphasize that an isotropic yield surface at critical state should not be confused with an isotropic critical state. The stress state at critical state is not isotropic and thus there are still preferred directions, those defined by the stress tensor. Instead, the adopted rule suggests that critical state conditions are independent of the soil's memory of preferred directions prior to failure.

## 6.7 Consistency Condition - Plastic Modulus

The previous sections introduced all the necessary features of the developed constitutive model. The present section employs the consistency condition to calculate the

Plastic Modulus $H$.

Based on the proposed yield surface equation (eq. 6.12) the consistency condition requires that:

$$\dot{f} = 0 \Rightarrow \dot{f} = \boldsymbol{Q} : \dot{\boldsymbol{\sigma}} + \frac{\partial f}{\partial s}\dot{s} + \frac{\partial f}{\partial S_r^e}\dot{S}_r^e + \frac{\partial f}{\partial \alpha}\dot{\alpha} + \frac{\partial f}{\partial \boldsymbol{b}} : \dot{\boldsymbol{b}} = 0 \tag{6.48}$$

and combining with equation 6.22 we may calculate the Plastic Modulus $H$:

$$H = -\left(\frac{\partial f}{\partial \alpha}\overline{\alpha} + \frac{\partial f}{\partial \boldsymbol{b}} : \overline{\boldsymbol{b}}\right) \tag{6.49}$$

where:

$$\dot{a} = \dot{\Lambda}\overline{a} \tag{6.50}$$

and

$$\dot{\boldsymbol{b}} = \dot{\Lambda}\overline{b} \tag{6.51}$$

The derivatives of the yield surface with respect to the hardening variables $\alpha$ and $\boldsymbol{b}$ are given by:

$$\frac{\partial f}{\partial \alpha} = \frac{\partial f}{\partial \alpha(s, S_r^e)} \cdot \frac{\partial \alpha(s, S_r^e)}{\partial \alpha} \tag{6.52}$$

with $\dfrac{\partial f}{\partial \alpha(s, S_r^e)}$ given by equation 6.20c, while:

$$\frac{\partial \alpha(s, S_r^e)}{\partial \alpha} = \frac{\alpha(s, S_r^e)}{\alpha}\frac{\lambda - \kappa}{\lambda(s, S_r^e) - \kappa} \tag{6.53}$$

and finally for $\boldsymbol{b}$:

$$\frac{\partial f}{\partial \boldsymbol{b}} = -\frac{2\sigma}{\mathrm{c}^2}(\boldsymbol{s} - \sigma\boldsymbol{b}) \tag{6.54}$$

To derive quantities $\overline{\alpha}$ and $\overline{\boldsymbol{b}}$ the flow rule is implemented in the incremental form of the hardening rule to describe the increments of plastic strains involved in each one of the equations. This allows for the plastic multiplier to appear as a common multiplier and accordingly we obtain:

$$\overline{a} = A\overline{a^*} + \overline{A}a^* \tag{6.55}$$

where

$$\overline{a^*} = \frac{v}{\lambda-\kappa} a^* P \tag{6.56a}$$

$$\overline{A} = \frac{2A \cdot r_s}{(\kappa-\lambda)} \frac{(N_n-\Gamma)}{\left(1-\frac{1}{c^2}\boldsymbol{b}:\boldsymbol{b}\right)} \frac{1}{c^2}\boldsymbol{b}:\overline{\boldsymbol{b}} \tag{6.56b}$$

while quantity $\overline{\boldsymbol{b}}$ is:

$$\overline{\boldsymbol{b}} = \overline{\boldsymbol{b}}_{\mathbf{o}} + \overline{\boldsymbol{b}}_{\mathbf{d}} \tag{6.57}$$

where:

$$\overline{\boldsymbol{b}}_{\mathbf{o}} = \frac{1}{a(s, S_r^e)} \psi(\boldsymbol{s}-\sigma\boldsymbol{b}) P \tag{6.58a}$$

$$\overline{\boldsymbol{b}}_{\mathbf{d}} = -\frac{1}{a(s, S_r^e)^2} \boldsymbol{b}\,(\boldsymbol{s}-\sigma\boldsymbol{b}) : (\boldsymbol{s}-\sigma\boldsymbol{b})\, \zeta_{\mathrm{q}}^{\mathrm{p}} \sqrt{\frac{2}{3}\boldsymbol{P}' : \boldsymbol{P}'} \tag{6.58b}$$

## 6.8 Elastoplastic Jacobian(s)

Following the procedure described in section 2.2.7, the elastoplastic Jacobian, correlating the total strain increment to the corresponding stress increment can be computed. Nevertheless in constitutive modelling of unsaturated soils a stress increment additionally depends on extra external variables employed, in our case suction and effective degree of saturation. The modified calculation is thoroughly demonstrated in the following.

During the definition of the flow rule we demonstrated how starting from the calculation of a stress increment through elasticity, and further employing the flow rule we end up with expression 6.26:

$$\dot{\Lambda} = \frac{\boldsymbol{Q} : \boldsymbol{C}^e : \dot{\boldsymbol{\varepsilon}} + \frac{\partial f}{\partial s}\dot{s} + \frac{\partial f}{\partial S_r^e}\dot{S}_r^e}{H + \boldsymbol{Q} : \boldsymbol{C}^e : \boldsymbol{P}}$$

It is used to substitute the plastic multiplier in equation 6.23, to calculate an increment of the stress tensor as:

$$\dot{\boldsymbol{\sigma}} = \boldsymbol{C}^e : \dot{\boldsymbol{\varepsilon}}^e - \left[\frac{1}{\Omega}\boldsymbol{Q} : \boldsymbol{C}^e : \dot{\boldsymbol{\varepsilon}} + \frac{1}{\Omega}\frac{\partial f}{\partial s}\dot{s} + \frac{1}{\Omega}\frac{\partial f}{\partial S_r^e}\dot{S}_r^e\right] \boldsymbol{C}^e : \boldsymbol{P} \tag{6.59}$$

where similarly to section 2.2.7, $\Omega$ is set equal to:

$$\Omega = H + \boldsymbol{Q} : \boldsymbol{C}^e : \boldsymbol{P} \tag{6.60}$$

Further elaborating we obtain:

$$\dot{\boldsymbol{\sigma}} = \left[\boldsymbol{C}^e - \frac{1}{\Omega}\left(\boldsymbol{C}^e : \boldsymbol{P}\right) \otimes \left(\boldsymbol{Q} : \boldsymbol{C}^e\right)\right] : \dot{\boldsymbol{\varepsilon}} - \frac{1}{\Omega}\frac{\partial f}{\partial s}\left(\boldsymbol{C}^e : \boldsymbol{P}\right)\dot{s} - \frac{1}{\Omega}\frac{\partial f}{\partial S_r^e}\left(\boldsymbol{C}^e : \boldsymbol{P}\right)\dot{S}_r^e \tag{6.61}$$

Finally, we may write that a stress increment is calculated according to:

$$\dot{\boldsymbol{\sigma}} = \boldsymbol{C}^{ep} : \dot{\boldsymbol{\varepsilon}} + \boldsymbol{W}_s \dot{s} + \boldsymbol{W}_{S_r^e} \dot{S}_r^e \tag{6.62}$$

where the classical elastoplastic Jacobian is computed as:

$$\boldsymbol{C}^{ep} = \boldsymbol{C}^e - \frac{1}{\Omega}\left(\boldsymbol{C}^e : \boldsymbol{P}\right) \otimes \left(\boldsymbol{Q} : \boldsymbol{C}^e\right) \tag{6.63}$$

while additionally the following two terms arise, correlating the stress increment with an imposed suction increment $\dot{s}$ and the corresponding increment of the effective degree of saturation $\dot{S}_r^e$.

$$\boldsymbol{W}_s = -\frac{1}{\Omega}\frac{\partial f}{\partial s}\left(\boldsymbol{C}^e : \boldsymbol{P}\right) \tag{6.64}$$

and

$$\boldsymbol{W}_{S_r^e} = -\frac{1}{\Omega}\frac{\partial f}{\partial S_r^e}\left(\boldsymbol{C}^e : \boldsymbol{P}\right) \tag{6.65}$$

These extra "Jacobian" terms, must be provided to any external code, to allow for an accurate prediction of the stress increment.

## 6.9 Model Parameters

This section summarizes the parameters involved in the proposed model. The parameters have been grouped in three categories, namely: a) Basic; b) Anisotropy and c) Partial saturation. The group of basic parameters includes the MCC parameters and it is the minimum of parameters required for the constitutive model to function as a simple Modified Cam Clay. The second group includes all the necessary parameters that the model needs to simulate anisotropic behaviour, while the third group includes the parameter associated with partial saturation.

### 6.9.1 Basic Parameters

This first group of parameters, the group of basic parameters, in fact includes the MCC parameters. In other words, it represents the minimum set of parameters required for the proposed model to function, even as a simple MCC model with neither anisotropic nor unsaturated characteristics. The following parameters are included:

$\kappa$**:** porous-elastic compressibility. Describes the slope of the swelling lines in the $v - \ln \sigma$ plane. It can be directly estimated from unloading tests (i.e., isotropic or one-dimensional). It is also associated with the swelling index ($C_r$): $\kappa = \frac{C_r}{\ln 10} \approx 0.434 C_r$;

$\nu$**:** Poisson's ratio. It controls the $2G/K$ ratio and thus can be indirectly estimated from the initial part of deviatoric stress vs deviatoric strain plots;

$\lambda$**:** intrinsic compressibility. Describes the slope of the saturated compression lines in the $v - \ln \sigma$ plane. It can be directly estimated from compression tests (i.e., isotropic or one-dimensional). It is also associated to the virgin compression index ($C_c$): $\lambda = \frac{C_c}{\ln 10} \approx 0.434 C_r$;

$c$ or $c_i$**:** projection of the critical state line on the stress space. Controls the residual shear strength in all deviatoric planes (if different $c_i$ values are used). In the simplest case it is proportional to the slope of the critical state line in the $p - q$ space $M$: $c = \sqrt{(2/3)} M$. It is estimated through laboratory tests that lead to failure (i.e., triaxial undrained loading).

$k$ or $k_i$**:** $k$ defines the ratio of the plastic yield envelope in all deviatoric planes. In the proposed constitutive model the plastic yield envelope has been associated with the structured strength envelope, thus its value can be estimated from the peak strength observed in shear tests. In the absence of suitable data it can be assumed equal to $c$ or $c_i$, or estimated indirectly from the $\Gamma$ value (see below).

$N_{iso}$**:** location of the isotropic compression line in the $v - \ln \sigma$ plane, corresponding to the specific volume value under $\sigma = 1kPa$. It is derived through isotropic compression tests.

$\Gamma$**:** the location of the CSL in the $v - \ln \sigma$ plane, corresponding to the specific volume value under $\sigma = 1kPa$. It is estimated through laboratory tests that lead to

failure (i.e., triaxial undrained loading). In the absence of suitable data, it can be derived directly from the position of the isotropic ICC as:

$$\Gamma = N_{iso} - (\lambda - \kappa) \ln (1 + \frac{c^2}{k^2}) \tag{6.66}$$

The aforementioned relationship was derived in the triaxial stress space ($p$, $q$) under saturated conditions and reflects the proposed model's assumption that critical state coincides with an isotropic yield surface. It holds true for the simplest case where $c$, $k$ are assumed independent of the examined deviatoric plane. The analytical documentation is given in Appendix A.1. It reveals that some of the model's parameters are in fact interconnected and should be selected with caution in order for the results to conform with the underlying framework. Regarding that $N_{iso}$, $\lambda$, $\kappa$, $c$ are usually easily experimentally determined, the aforementioned relationship can assist in estimating $\Gamma$ in case of a well defined $k$ or in estimating $k$ in case of a well defined $\Gamma$. Values not respecting the aforementioned relationship can be anytime selected, nevertheless the model's predictions will slightly violate the proposed compressibility framework.

The group of basic parameters includes a total of seven (7) parameters that through suitable assumptions can be reduced to five (5).

### 6.9.2 Parameters related to Anisotropy

This second group includes four (4) extra parameters, related to the anisotropic characteristics of the model, namely:

$r_s$ **:** controls the location of intermediate radial stress paths in the $v - \ln \sigma$ plane. At least two radial consolidation tests at different stress ratios are required to determine its value (i.e., isotropic compression and 1-D compression), in addition to the position and slope of the critical state line $\Gamma$ in the $v - p - q$ space.

$\psi$**:** controls the evolution rate of stress induced anisotropy. Its calibration requires at least one radial compression test that involves an evolving anisotropy (i.e., 1D consolidation initiating from an isotropic material fabric). A trial and error process is usually required.

$\zeta_q^p$**:** controls the rate of anisotropy degradation. It is estimated through laboratory tests that lead to failure, preferably including loading under undrained conditions. A trial and error procedure is usually followed.

$\chi$**:** controls the relative orientation of the plastic potential surface with respect to the yield surface. Parameter $\chi$ can be suitably selected to reproduce the desired total dilatancy under any given radial stress path. Consider a radial (triaxial) stress path under a constant $b_q = n_q = \dot{q}/\dot{p}$. After substantial straining the yield surface will get oriented across the imposed stress ratio $b_q = \sqrt{\frac{3}{2}\boldsymbol{b} : \boldsymbol{b}}$ and the PPS towards $d_q = \sqrt{\frac{3}{2}\boldsymbol{d} : \boldsymbol{d}}$ following equation 6.30. Under anisotropic stabilized conditions the model will reproduce a total dilatancy equal to $D_q = \dot{\varepsilon}_q/\dot{\varepsilon}_v = \frac{\dot{\varepsilon}_q^e + \dot{\varepsilon}_q^p}{\dot{\varepsilon}_v^e + \dot{\varepsilon}_v^p}$. Provided that total dilatancy is known, we can subtract the effect of the elastic strains to calculate a measure of the plastic deviatoric dilation $d_q^p$ through the following expression:

$$d_q^p = D_q \left( \frac{\kappa}{\lambda - \kappa} + 1 \right) - \frac{2}{9} \cdot \frac{1+\nu}{1-2\nu} \cdot \frac{\kappa}{\lambda - \kappa} \cdot b_q \tag{6.67}$$

where $D_q$ the desired total dilation and $b_q$ the imposed stress path in the triaxial stress space.

With plastic dilation $d_q^p$ calculated, the relative orientation of the plastic yield surface which reproduced the desired plastic dilatancy is computed, through the following quadratic equation ($\chi$ is the unknown parameter):

$$\left( \frac{2}{3}(b_q)^2 d_q^p \right) \chi^2 + \left( \frac{4}{3} b_q \right) \chi + \left( c^2 d_q^p - \frac{2}{3}(b_q)^2 d_q^p - \frac{4}{3} b_q \right) = 0 \tag{6.68}$$

From the two routes obtained one is usually easily rejected based on logical assumptions. The detailed mathematical formulation leading to equations 6.67 and 6.68 is given in Appendix A.2.

The simplest way to obtain parameter $\chi$ is probably through a $K_0$ consolidation test. In $K_0$ consolidation the stress ratio $b_q$ is directly derived from the coefficient of earth pressure at rest $K_0$ as $b_{q,K_0} = 3\,(1 - K_0)\,/\,(1 + 2K_0)$, while simultaneously the total dilatancy reproduced shall be $D_{q,K_0} = 2/3$, for the total horizontal stain to be zero. With $b_{q,K_0}$ and $D_{q,K_0}$ values as an input in equations 6.67 and 6.68 respectively the parameter $\chi$ is computed.

### 6.9.3 Parameters related to Partial saturation

The following set of four (4) additional parameters, is finally necessary to activate the unsaturated characteristics of the proposed model:

$r$**:** controls the evolution of compressibility with partial saturation.

$\beta$**:** controls the evolution of compressibility with partial saturation.

$\gamma$**:** controls the evolution of compressibility with partial saturation.

$p^c$**:** controls the increase in apparent preconsolidation pressure with partial saturation.

It is mentioned that this subsection deals exclusively with the parameters required for the mechanical part of the behaviour of unsaturated soils. Knowledge of the water retention characteristics of any given soil is also a prerequisite when unsaturated soil behaviour is examined.

## 6.10 Concluding Remarks

This chapter introduced the mathematical formulation of an anisotropic model for the analyses of unsaturated soils. The proposed constitutive model is established on the principles of Theory of Plasticity suitably modified to account for unsaturated soil's analyses. The compressibility framework for anisotropic and partially saturated soils previously introduced in chapter 5 was used in the formulation of the hardening rules and also to extend the behaviour in the unsaturated regime. An attempt to capture most of the mechanical aspects of both anisotropic (see chapter 3) and unsaturated soils (see chapter 4) was undertaken by keeping, at the same time, the mathematical formulation as simple and robust as possible and also by reducing the model parameters to a minimum.

The main features of the proposed constitutive model can be summarized as follows:

- it incorporates the anisotropic, distorted elliptical yield surface proposed by Kavvadas (1982) to account for the yield locus of anisotropically consolidated soils;
- plastic strains accumulation follows a non-associated flow rule, defined through a plastic potential surface with a similar shape but different orientation, with respect to the yield surface. The proposed flow rule can be calibrated to account

for the desired plastic dilatancy in radial stress paths (with emphasis on 1D compression) and further enhances the control over the position of the critical state line in the void ratio – mean effective stress plane;

- it incorporates a new mixed hardening rule consisting of three different parts:

  a) a new isotropic part based on the Intrinsic Compressibility Framework of Belokas & Kavvadas (2011), slightly modified in the previous chapter, which in combination with the kinematic part of the rule can describe the dependence of the virgin compression lines on the level of the stress induced anisotropy;

  b) the kinematic hardening rule proposed by Kavvadas (1982) to describe the evolution of the orientation of the yield surface with plastic deviatoric straining, and;

  c) a new kinematic hardening rule, which describes a progressive elimination of the soil's memory of anisotropy with the onset of plastic deviatoric strains. It aims in reproducing in a simple, natural and unified way the strain softening behaviour that anisotropically consolidated soils tend to exhibit when loaded under triaxial undrained conditions (anisotropy degradation) together with a unique critical state, independent of the initial anisotropy and of the stress path undertaken;

- the extension of the constitutive model to the unsaturated regime is realized through Bishop's average skeleton stress, using the macrostructural degree of saturation as a scaling parameter. This selection allows for a natural representation of the nonlinear increase in shear strength and the evolution of elastic compressibility with partial saturation. Bishop's average skeleton stress, also, ensures a smooth transition between saturated and unsaturated conditions, as it reduces to Terzaghi's effective stress upon saturation;

- finally, it includes a Loading – Collapse (LC) surface, derived from a new compressibility framework proposed in the previous chapter. The latter describes a double dependence of the unsaturated compressibility on suction and degree of saturation.

The proposed model requires a total of fifteen (15) parameters to simulate the behaviour of an anisotropically consolidated unsaturated soil element. It can also be

easily reduced to either an anisotropic model for saturated soils or to an isotropic model for unsaturated soils. For either case eleven (11) parameters are required. Finally through suitable assumptions and in the lack of available experimental data, the total number of parameters in all cases can be further reduced by two.

In the next chapter the proposed constitutive model is implemented in an incremental driver which solves the constitutive equations, using an explicit integration scheme. The driver is used to simulate common laboratory stress paths at a single material point, but also for the implementation in the computer code Simulia Abaqus as a user defined material. Both numerical tools will be employed in chapters 8, 9 and 10 to evaluate the model's simulation capabilities.

# Chapter 7

# Numerical Implementation

## 7.1 Introduction

Following the formulation of the proposed constitutive model in the previous chapter, the present chapter presents the numerical tools developed for the solution of the constitutive equations. **Fortran** programming language is used to develop an incremental driver responsible for the numerical solution of the constitutive equations. The developed incremental driver is tested using a single material point computer program, which can simulate common geotechnical laboratory tests, while the same driver is used for the implementation in the Simulia Abaqus Finite Element Method (FEM) computer code. The following sections deal with the developed incremental driver, the single material point testing code and with the Abaqus implementation respectively.

## 7.2 The Incremental Driver

The incremental driver is responsible for the solution of the constitutive equations. Starting from a known state (external and internal variables) and given an applied increment of the strain tensor ($\dot{\boldsymbol{\varepsilon}}$), suction ($\dot{s}$) and degree of saturation ($\dot{S}_r^e$), it computes the updated stress state, the updated internal and external variables as well as the updated Jacobian(s).

The incremental driver requires the following input:

- the model's fifteen material constants,
- the current Bishop's stress state ($\boldsymbol{\sigma}$),

- the current suction value ($s$),
- the current effective degree of saturation value ($S_r^e$),
- the current value of the hardening variables ($\boldsymbol{q}$),
- the current void ratio value,
- the maximum infinitesimal strain, suction, and degree of saturation increments,
- an increment of the strain tensor ($\dot{\boldsymbol{\varepsilon}}$),
- an increment of suction ($\dot{s}$), and
- an increment of the effective degree of saturation ($\dot{S}_r^e$).

Constitutive equations are solved using an explicit integration scheme, where calculations take place at the current state by applying infinitesimal increments of strain, suction and degree of saturation. The solution within an infinitesimal increment is linear and thus the imposed increments have to be sufficiently small to minimize potential error accumulation at highly nonlinear problems. Note that at this stage of the conducted research, the developed integration scheme is not "adaptive", in the sense that the imposed infinitesimal increment is not automatically adjusted to the nonlinearity of the constitutive equations, but instead, the latter are solved using a predefined maximum value. The corresponding values can be selected by the user, while suggested values are $10^{-5}$ to $10^{-6}$ for the strain increment and $10^{-2}$ to $10^{-3}$ for the suction and degree of saturation increments. Based on the selected infinitesimal quantities, the incremental driver splits any imposed (finite) increment to a number of smaller infinitesimal increments and solves the constitutive equations repeatedly.

Implementation follows the soil mechanics stresses and strains convention, where compressive stresses and strains are assumed positive, while the constitutive equations are formulated using a transformed stress space (Kavvadas 1982; Kavvadas & Amorosi 2000) consisting of the isotropic stress axis ($\sigma$) and five deviatoric hyperplanes ($\boldsymbol{s} = \{S_1, S_2, S_3, S_4, S_5\}$), together with the corresponding work conjugate strain measures consisting of the volumetric strain ($\varepsilon$) and the deviatoric strain vector ($\boldsymbol{e} = \{E_1, E_2, E_3, E_4, E_5\}$). Compared to the standard tensorial quantities, they have the advantage that the size of the space required to represent any loading path is the absolute minimum. For example, a triaxial test (TRX) is represented in the two-dimensional

space $(\sigma, S_1)$, a Plane Strain (PS) test in the three-dimensional space $(\sigma, S_1, S_2)$ and a Direct Simple Shear (DSS) in the four-dimensional space $(\sigma, S_1, S_2, S_3)$.

The model's numerical formulation allows for an independent control of the aspect ratio of the yield surface ($k$) and of the plastic potential surface ($c$) on each deviatoric sub-plane, and in that end parameters $k$ and $c$ are handled as vectors. By assigning different values to each of the vector components the user can independently adjust the model's prediction under different loading conditions (i.e., triaxial, simple shear, plane strain). Appendix B summarizes the transformed stress and strain quantities and further correlates them with the standard tensorial quantities.

Figure 7.1 presents a simplified flow chart of the developed incremental driver which describes the succession of the main calculation processes. Implementation focused on producing an efficient and robust algorithm, using subroutines for repeated processes and dummy variables to minimize memory allocation.

Finally, the incremental driver provides the following output:

- the updated Bishop's stress state $(\boldsymbol{\sigma} + \dot{\boldsymbol{\sigma}})$,
- the updated values of the hardening variables $(\boldsymbol{q} + \dot{\boldsymbol{q}})$,
- the updated void ratio value,
- the updated stress-strain, stress-suction and stress-degree of saturation Jacobian(s).

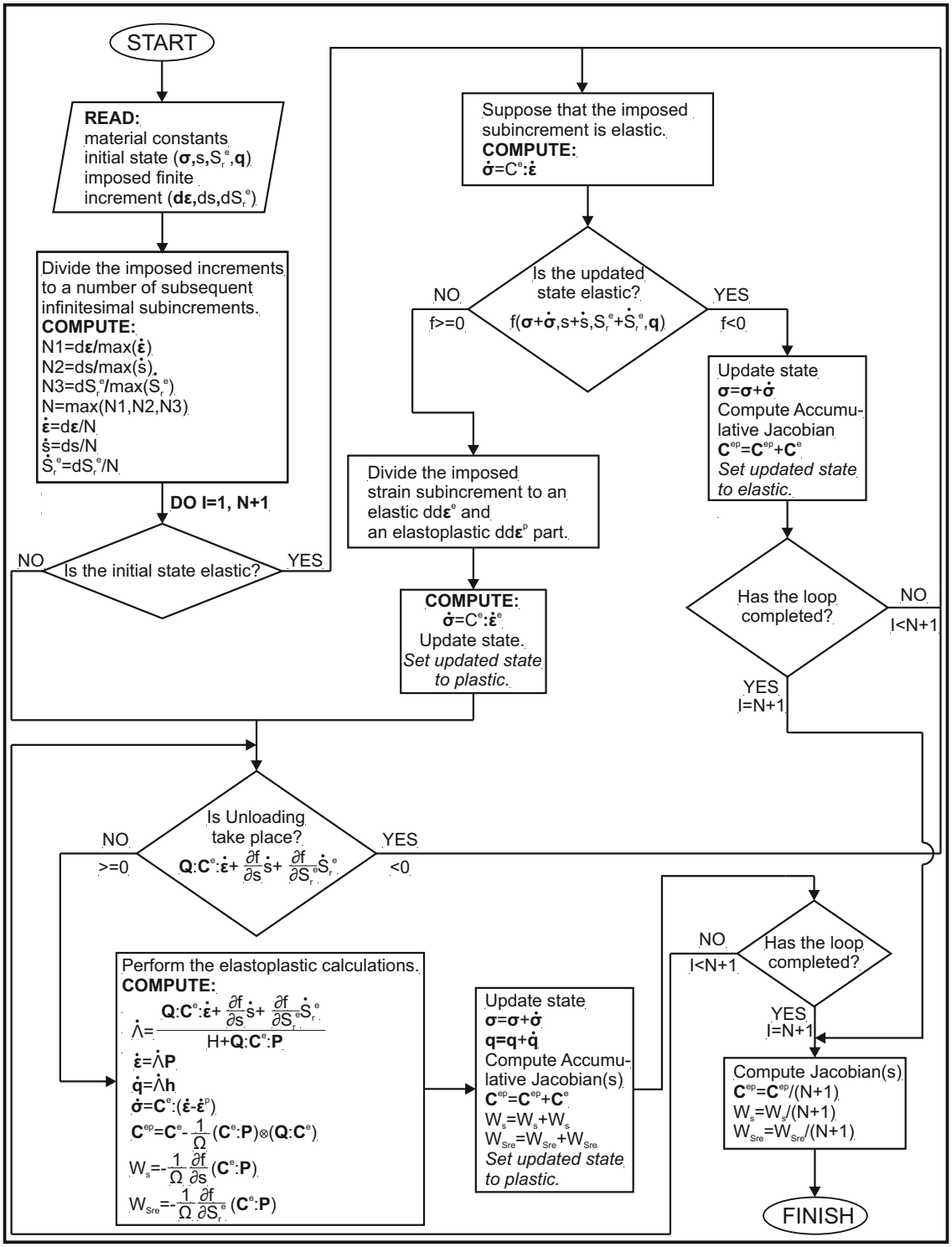


**Figure 7.1:** The flow chart of the developed incremental driver.

## 7.3 Single Material Point testing code

Performing simulations at a single material point is probably the simplest and most efficient way to evaluate the predictions of any constitutive model. In that respect, a Single Material Point (SMP) testing code is developed, suitably formulated for the proposed constitutive model, which can simulate common geotechnical laboratory tests. The developed software builds on an existing algorithm for saturated soils (Kavvadas 1982; Belokas 2008), which is extensively modified and enchanted to accommodate the analysis of unsaturated material states.

The developed numerical tool can simulate the following laboratory tests- stress paths:

a) isotropic compression,

b) 1-D compression,

c) radial compression at any given stress ratio $K$,

d) triaxial loading (compression and extension),

e) direct simple shear,

f) plane strain,

g) constant $\sigma$, and

h) drying (suction increase) or wetting (suction increase).

The aforementioned simulations can be performed under either drained or undrained conditions[1], while either a stress or a strain controlled process can be simulated with respect to the targeted value at the end of the test. Series of different stress paths can be imposed (i.e., undrained triaxial compression after drained 1D compression etc.). All simulations can be performed under either saturated or unsaturated conditions..

The code requires the initial state of all the external and internal variables, as well as of the material constants, both to be transferred to the incremental driver. Additional information includes the type of test and the desired target value (i.e, an undrained triaxial compression test until $\varepsilon_q = 20\%$). Depending on the desired

[1]It is well known that an undrained isotropic compression test or an 1D consolidation test are both meaningless under saturated conditions, nevertheless this is not the case in unsaturated material states.

simulation, the code calculates and transfers to the incremental driver suitable combinations of a finite strain increment ($\dot{\boldsymbol{\varepsilon}}$), a suction increment ($\dot{s}$) and an effective degree of saturation increment ($\dot{S}_r^e$) corresponding to the boundary conditions of the simulated test. Calculation of the aforementioned increments requires the solution of equation 6.62 and thus the code necessitates knowledge of the initial and the updated Jacobian(s), both being provided by the incremental driver. At its present version the developed SMP testing code can only handle simulations where equation 6.62 is solved analytically, a shortcoming which obviously limits the applicability of the code (i.e., drying or wetting tests require an isotropic stress field).

With respect to the modifications realized in order to facilitate the simulation of laboratory tests under unsaturated conditions we may summarize:

- The Gallipoli et al. (2003) WRM is implemented to provide the crucial $S_r = f(s, v)$ relationship, with Its four material constants ($\phi$, $\psi$, $n$, $m$) being an additional input to the code.

- The Alonso et al. (2010) power law is used to calculate the macro-structural (effective) degree of saturation and parameter $\alpha$ is considered an additional input as well.

- Drained tests under unsaturated conditions are handled as constant suction tests where $\dot{s} = 0$ and $\dot{S}_r = f(\dot{\varepsilon})$.

- Undrained tests are handled as constant water content tests where $\dot{w} = 0$.

- The imposed boundary conditions are modified to account that net stress ($\overline{\boldsymbol{\sigma}}$) and suction ($s$), are the only quantities which can be efficiently controlled in the laboratory.

- Calculation of the imposed stress increment is severely modified to account for the additional (with respect to saturated analyses) dependance of the stress increment on suction and on the effective degree of saturation.

Appendix C elaborates on the implementation of "unsaturated capabilities" in the developed numerical tool, as it provides an insight on the undertaken calculations within the algorithm.

## 7.4 Implementation in Simulia Abaqus - UMAT

One of the main objectives of the present thesis is to develop appropriate numerical tools which will allow future research efforts to focus on the analyses of large scale problems where unsaturated materials are involved (i.e., dams, landslides, slope stability, foundations). In that respect, the developed constitutive model is implemented in a general purpose numerical software for the analyses of engineering problems.

The Simulia Abaqus Finite Element computer code was selected. The main facts underlying the selection of the Simulia Abaqus FEM code are:

- It is a general purpose program which offers increased versatility to the end user, and particularly in the implementation of user defined materials.

- It utilizes Bishop's average skeleton stress for the analysis of geotechnical problems.

- It simulates water flow in unsaturated porous by incorporating the water retention characteristics into the solution of the water balance equilibrium.

- It is officially licensed to the National Technical University of Athens (author's host institution) and installed in its main computer center.

As already mentioned, the Simulia Abaqus is a general purpose finite element software. It offers two main analysis modulus, the Abaqus - Standard and the Abaqus - Explicit. Abaqus - Standard is a general purpose code for common engineering problems, which uses an implicit integration scheme to perform classical Lagrangian analyses. On the other hand, the Abaqus - Explicit is oriented to specific engineering problems where transient phenomena are of significant importance. The latter employs an explicit integration scheme, using the Eulerian analysis approach. In the present thesis we deal exclusively with the Abaqus - Standard module.

Abaqus - Standard solves highly nonlinear problems utilizing an incrementally linear additive numerical scheme. Any alteration in the loading conditions is assumed as a load step, while the succession of different load steps defines the complete loading history. Within each step, Abaqus uses an automatic incrementation technique to define the optimum loading increment which can accommodate the solution's nonlinearity. The term optimum implies the larger increment which ensures convergence

within a reasonable number of Newton-Raphson[2] iterations. Difficulties in convergence (i.e., convergence is not achived within a maximum number of iterations) are an indication that the selected increment is too large for the nonlinearity of the analyzed problem, leading to the automatic selection of a decreased increment to repeat the analysis from the latest converged state. On the other hand, if convergence is quickly achieved, within one or two Newton-Raphson iterations, the selected increment is automatically increased to reduce the computational cost and the time required for the completion of the loading step. The user can define all the parameters involved in the aforementioned incrementation technique (i.e., initial suggested increment, minimum and maximum increment, maximum number of N-R iterations, etc.).

Abaqus utilizes the constitutive model at the end of every iteration in order to calculate the updated stress state. Any calculation related to the solution of the constitutive equations takes place at the integration points, while the calculated stress state is then compared to the predicted force field to decide on whether convergence has been achieved or not (based on the defined criteria). In classical mechanical problems, convergence is judged on the bases of both residual forces and residual displacements criteria, while additional convergence criteria are involved in coupled hydromechanical analyses. Belokas (2008) summarized the Abaqus - Standard incrementation scheme in the flow chart of figure 7.2.

User defined constitutive models are implemented in Abaqus using the User Material (UMAT) subroutine[3]. UMAT is a Fortran subroutine facilitating the exchange of information between the main program (Abaqus) and any suitable external algorithm which provides the material constitutive behaviour. The main data exchanged through UMAT are:

- the material constants (PROPS array - see D),
- the increment of the strain tensor,
- the stress state at the beginning of the increment to be updated in UMAT and returned to the main program,

[2] ABAQUS/Std. uses the modified Newton - Raphson method.

[3] It is assumed that the reader and potential user of the developed user defined material subroutine is quite familiar with the analyses of geotechnical problems with the Simulia Abaqus FEM computer code and with the utilization of user defined materials through the UMAT subroutine. The Abaqus Documentation can help towards this direction.

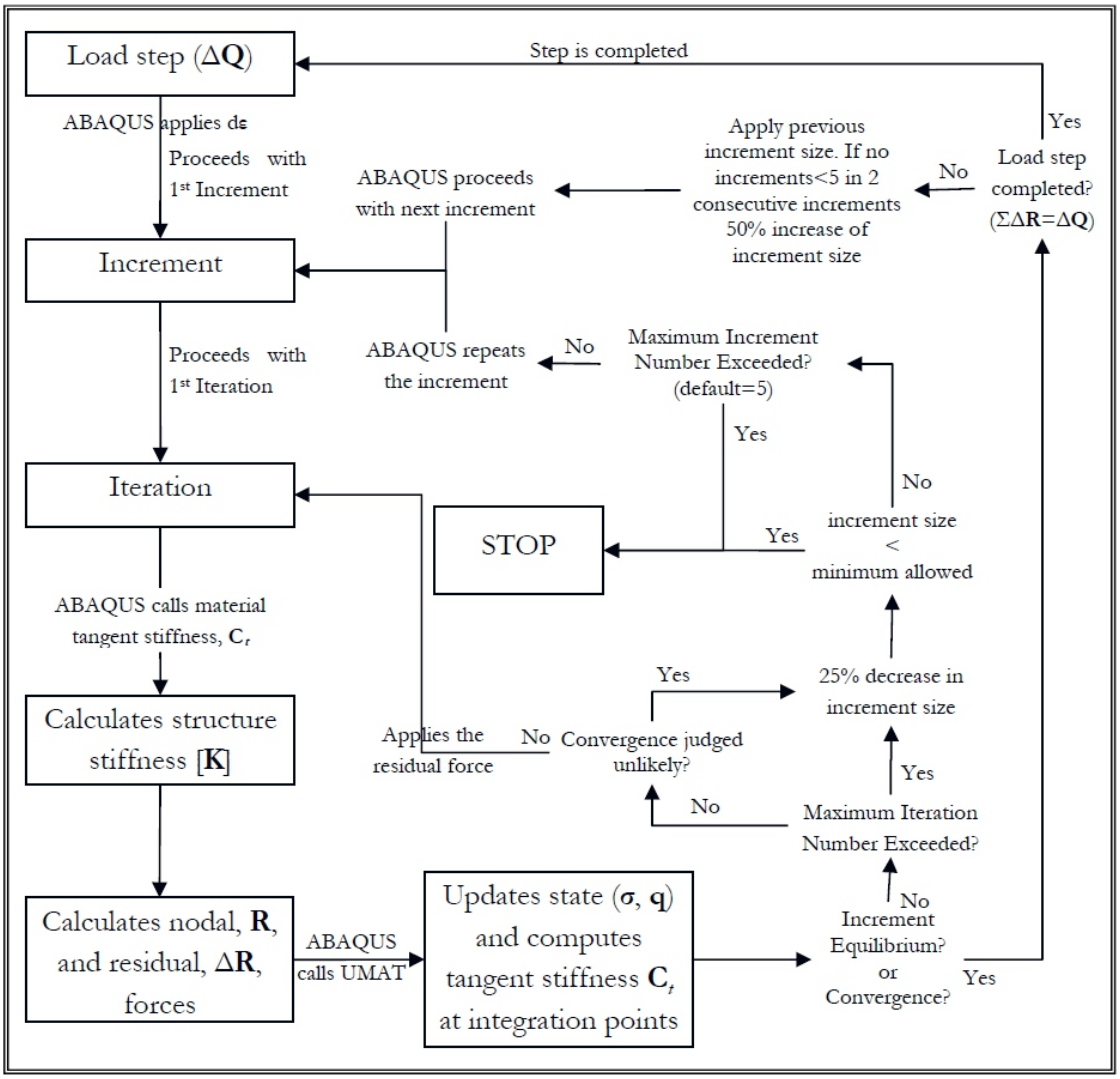


**Figure 7.2:** The flow chart of the Abaqus - Standard incrementation technique. (Belokas 2008)

- the hardening variables (STATEV array - see D) at the beginning of the increment to be updated in UMAT and returned to the main program, and;
- the updated mechanical Jacobian $\boldsymbol{C}^e$ used in the prediction of the next increment.

The Abaqus UMAT subroutine was developed with an eye towards classical elastoplastic constitutive models which calculate the updated stress state based on an imposed strain increment. In the previous chapter we discussed the in unsaturated soils analysis the elastoplastic stress increment additionally depends on the level of applied suction, on the corresponding degree of saturation and on their corresponding incre-

ments as well. Hence, the UMAT environment necessitates further enhancements to handle the exchange of suction and degree of saturation between Abaqus and the incremental driver.

To that end, we further utilize the User Defined Field Variables (USDFLD) subroutine, which enables the calculation of user defined (additional) variables as a function of the available nodal quantities. Moreover, UMAT can extract these extra user defined variables from the main program, together with their corresponding increment, through the PREDEF and DPRED arrays ( D). In that respect, we define as extra user defined field variables the pore pressure ($U_w$) and the degree of saturation ($S_r$).

Figure 7.3 presents the flow chart of the most important operations taking place inside the developed UMAT subroutine. Note that the developed UMAT builds on the incremental driver presented in section 7.2, as the latter is the main numerical tool responsible for the solution of the constitutive equations. Inside UMAT, before and after the solution of the constitutive equations, a series of suitable transformations of the necessary quantities are performed to align the different definitions and conventions used.

Regarding the analyses of unsaturated porous media with the Simulia Abaqus FEM computer code we shall emphasize on the following facts:

- Abaqus utilizes the Bishop's average skeleton for the analysis of geotechnical problems. By default, it correlates parameter $\chi$ with the degree of saturation ($S_r$), contrary to the proposed constitutive model which correlates $\chi$ with the macro-structural (effective) degree of saturation. Thus, for Abaqus calculations to be consistent with the desired behaviour the assigned WRC must be already scaled according to the Alonso et al. (2010) power law. In other words, in the Abaqus WRM definition (SORPTION command) we shall input directly the $S_r^e - s$ relationship instead of the $S_r - s$ relationship. It is evident that such a selection additionally influences the solution of the hydraulic problem as the WRM is also involved in the water mass balance equilibrium (it provides the water storage term), as well as the calculated unsaturated permeability[4]. It is reasonable to suspect that such a selection is against the accuracy of the performed simulation as the actual water content contained in any given soil system is associated with the total degree of saturation. Nevertheless, it is to the author's belief that, substituting the degree of saturation for the macrostruc-

[4]Abaqus scales the saturated permeability with degree of saturation through a power law.

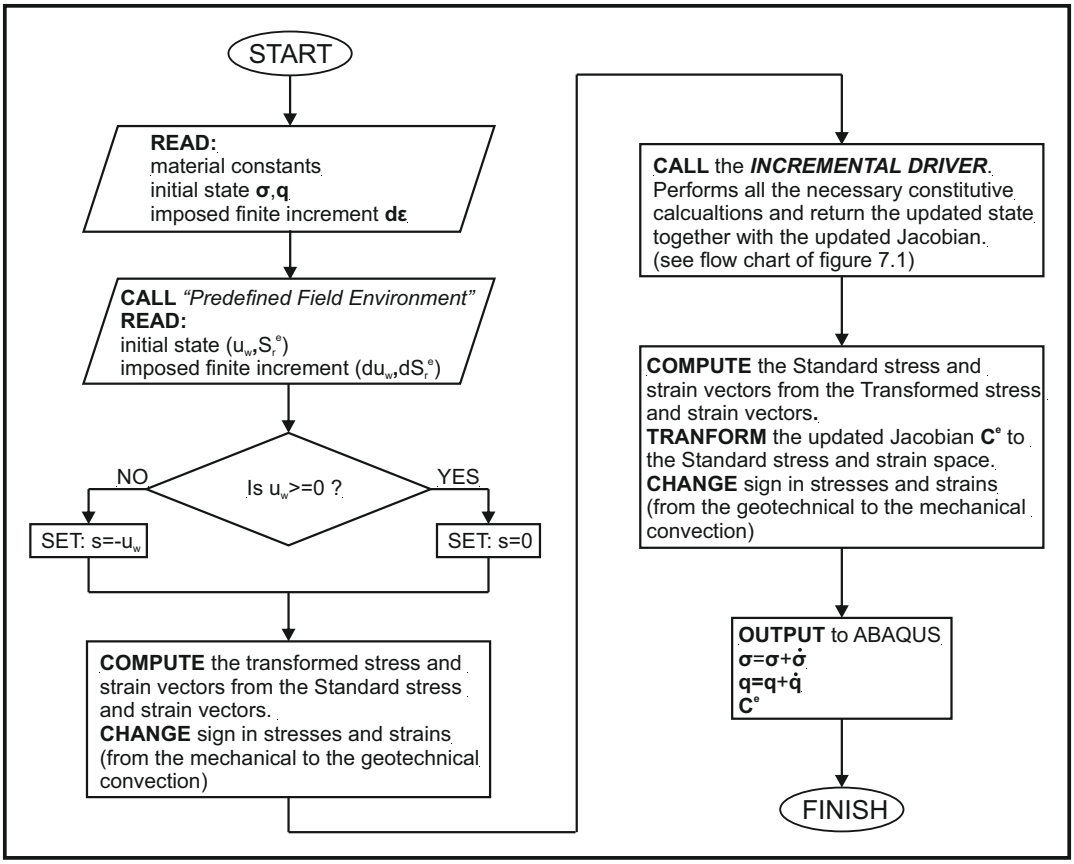


**Figure 7.3:** The flow chart of the main operations taking place inside the developed Abaqus UMAT subroutine.

tural degree of saturation does not has deleterious effects in the solution of the hydraulic problems but instead, it may even favour the accuracy of the calculations, in the sense that in common engineering problem the water of the larger-macropores governs the hydraulic problem.

- Abaqus sets by default the air pressure equal to zero ($u_a = 0$) and thus, suction always corresponds to the opposite of the pore water pressure ($s = -u_w$). Such a selection limits the Abaqus's applicability in engineering problems where the flow of the air phase is not of importance.

- Abaqus cannot account for a void ratio dependent water retention model, as the SORPTION command does not allow for dependencies with any field variable. This shortcoming is expected to have severe implications on the simulation capabilities of the proposed model, and it is further discussed in the following chapter.

- Finally, Abaqus does not account for the dependance of the stress increment on suction and degree of saturation through the related $W_s$ and $W_{S_r^e}$ Jacobian(s). Thus, although calculated within the incremental driver, these are not provided to the main program. Nevertheless, the lack of the $W_s$ and $W_{S_r^e}$ terms, does not pose any errors to the solution due to the fact that FEM codes utilize the the Jacobian terms to predict the forthcoming strain increment but not the material state. Convergence is always judged on the accuracy of the calculated updated state, with the latter precisely calculates through the constitutive equations. In that respect, this shortcoming can only affect the speed of convergence and thus increase the computational time, but it does not affect the accuracy of the obtained solution.

## 7.5 Simple Validation Tests - MCC

This sections offers a preliminary evaluation of the developed numerical tools in simple Modified Cam Clay analyses. To reduce the proposed model to the MCC both its anisotropic and unsaturated capabilities are deactivated (following a suitable selection of parameters). Such a selection enables the evaluation of the predictions of the developed numerical tools against the predictions of the Abaqus build-in MCC constitutive model (CLAY PLASTICITY). The performed simulations do not evaluate the main behavioural aspects of the proposed constitutive model (this is addressed in the following chapter), nevertheless they were deemed necessary as a first verification step of the developed tools.

The following laboratory tests are simulated:

- Drained triaxial compression following isotropic consolidation to three different stress levels ($p = 100, 300, 500$ kPa);
- Undrained triaxial compression following isotropic consolidation to three different stress levels ($p = 100, 300, 500$ kPa);
- 1D consolidation (oedometer) test up to $\sigma_v = 1000$ kPa;

A fictitious set of material parameters is assigned (see table 8.1), while with respect to the initial conditions we assume an isotropic stress field ($K = 1.0$) corresponding to an overconsolidated material state ($p = 10kPa$ and $p_0 = 30kPa$).

**Table 7.1:** Constitutive parameters involved in the presented analyses.

| Basic Parameters | | Anisotropy | | Partial Saturation | |
|---|---|---|---|---|---|
| Parameter | Value | Parameter | Value | Parameter | Value |
| $\kappa$ | 0.01 | $r_s$ | $1.0^{*3}$ | $r$ | $1.0^{*3}$ |
| $\lambda$ | 0.10 | $\psi$ | 0.0 | $\beta$ | $1.0^{*3}$ |
| $\nu$ | 1/3 | $\zeta_{\mathrm{q}}^{\mathrm{p}}$ | 0.0 | $\gamma$ | $1.0^{*3}$ |
| $k$ | $0.8165^{*1}$ | $\chi$ | $1.0^{*3}$ | $p^c$ | $1.0^{*3}$ |
| $c$ | $0.8165^{*1}$ | | | | |
| $N_{iso}$ | 2.2 | | | | |
| $\Gamma$ | $2.1376^{*2}$ | | | | |

$^{*1}$ corresponds to $M = 1.0$.
$^{*2}$ corresponds to $\Gamma = N_{iso} - (\lambda - \kappa)\ln 2$.
$^{*3}$ do not affect the analyses results due to isotropic and saturated conditions.

For each one of the simulated laboratory tests we compare the result from three different analyses each one utilizing a different numerical tool, namely:

- the Single Material Point (SPM) computer code in conjunction with the proposed models' incremental driver,
- the Simulia Abaqus FEM code in conjunction with the UMAT subroutine developed, and;
- the Simulia Abaqus FEM code in conjunction with the Abaqus build-in MCC constitutive model.

The FEM analyses are realized using two different numerical models, an axis-symmetric model which represents a typical cylindrical soil specimen (triaxial laboratory apparatus specimen), and a three-dimensional (3D) model for oedometer testing simulations, presented in figures 7.4 and 7.5 respectively. The cylindrical model is realized using eight axis-symmetric, 8-noded, second order, solid pore pressure elements (CAX8P), while the 3D model uses twenty seven (27) 3D solid, pore pressure elements with eight (8) nodes and eight (8) integration points each (C3D8P). The dimensions of the axis-symmetric model corresponds to the actual dimensions of a

triaxial apparatus soil specimen, while the 3D model is out of scale with respect to the oedometer, to investigate whether different element sizes influence the results.

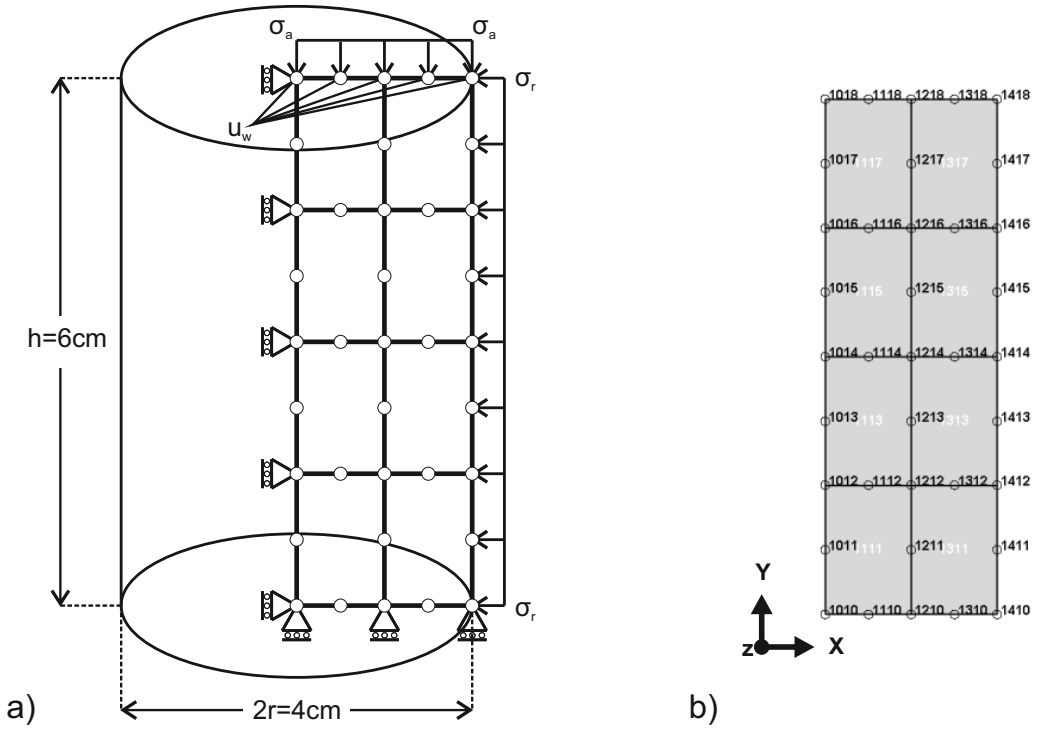


**Figure 7.4:** The axis-symmetric model used in Abaqus; in: a) a sketch of the model illustrating its dimensions and boundary conditions and; b) the actual Abaqus model.

Figures 7.6 to 7.8 present the results of the performed simulations. In more detail, figure 7.6 depicts the results of the drained triaxial compressions tests at three different mean effective stress levels ($p$ = 100, 300, and 500$kPa$). After the consolidation stage, the soil elements are triaxial loaded under drained conditions until deviatoric strains reach $\varepsilon_q = 16\%$. The performed FEM analyses are coupled hydromechanical analyses using the axis-symmetric numerical model. Loading was slow enough to ensure sufficient drainage and thus prevent pore water pressure build up.

We observe that the obtained simulation results practically coincide and are consistent with the MCC framework as well. For instance, during the consolidation stage all results lay on a swelling line until the assigned preconsolidation pressure is reached followed by plastic yield identified from the abrupt change in the slope of the compression line in the $v - \ln p$ plane. Additionally, during TRX loading we observe that the stress path follows a constant stress ratio ($\dot{q}\dot{p} = 3/1$), which is in line with the

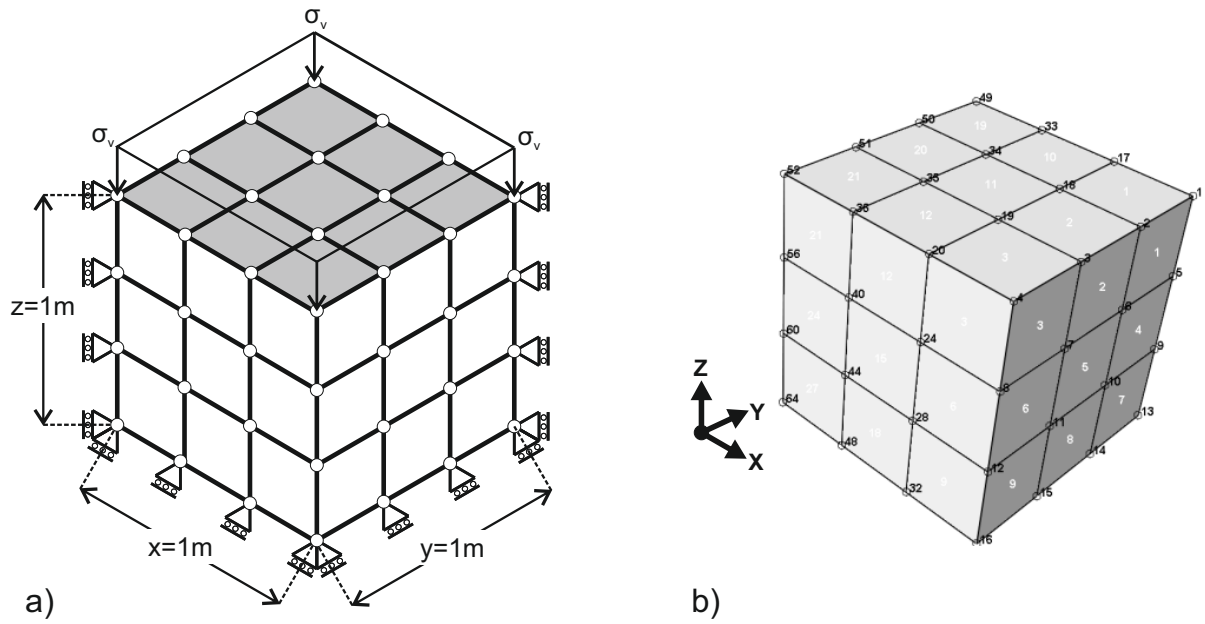


**Figure 7.5:** The 3D cubical model used in ABAQUS; In: a) a sketch of the model illustrating its dimensions and boundary conditions and; b) the actual Abaqus model.

boundary conditions of the simulated test, and the material state moves towards the critical state line[5].

A slightly different response is identified in the $v - \ln p$ plane when the Abaqus build-in MCC analyses results are compared with their SMP and UMAT counterparts, attributed to the fact that Abaqus is not constantly updating the specific volume. In more detail, specific volume $\dot{v}$ is updated following the evolution of the volumetric strain $\dot{\varepsilon}_{vol}$ (results coincide, see figure 7.6d) through the following incrementally linear relationship: $\dot{v} = -v \cdot \varepsilon_{vol}$. In the SMP code as well as in the developed UMAT, specific volume is constantly updated during every infinitesimal strain increment and is stored as a solution dependant variable. Contrary to that, Abaqus updates the specific volume at the end of every sub-step and not at the end of every iteration. A sub-step may correspond to a relatively large volumetric strain increment for the behaviour to be assumed linear, and thus a small calculation error builds up and is reflected in the obtained results.

The same simulations are repeated assuming that the TRX loading stage occurs under undrained conditions and the corresponding results are depicted in figure 7.7, while figure 7.7 presents the simulation results from the oedometer test. In both

[5]The $\varepsilon_q = 16\%$ imposed was not sufficient to reach critical state conditions.

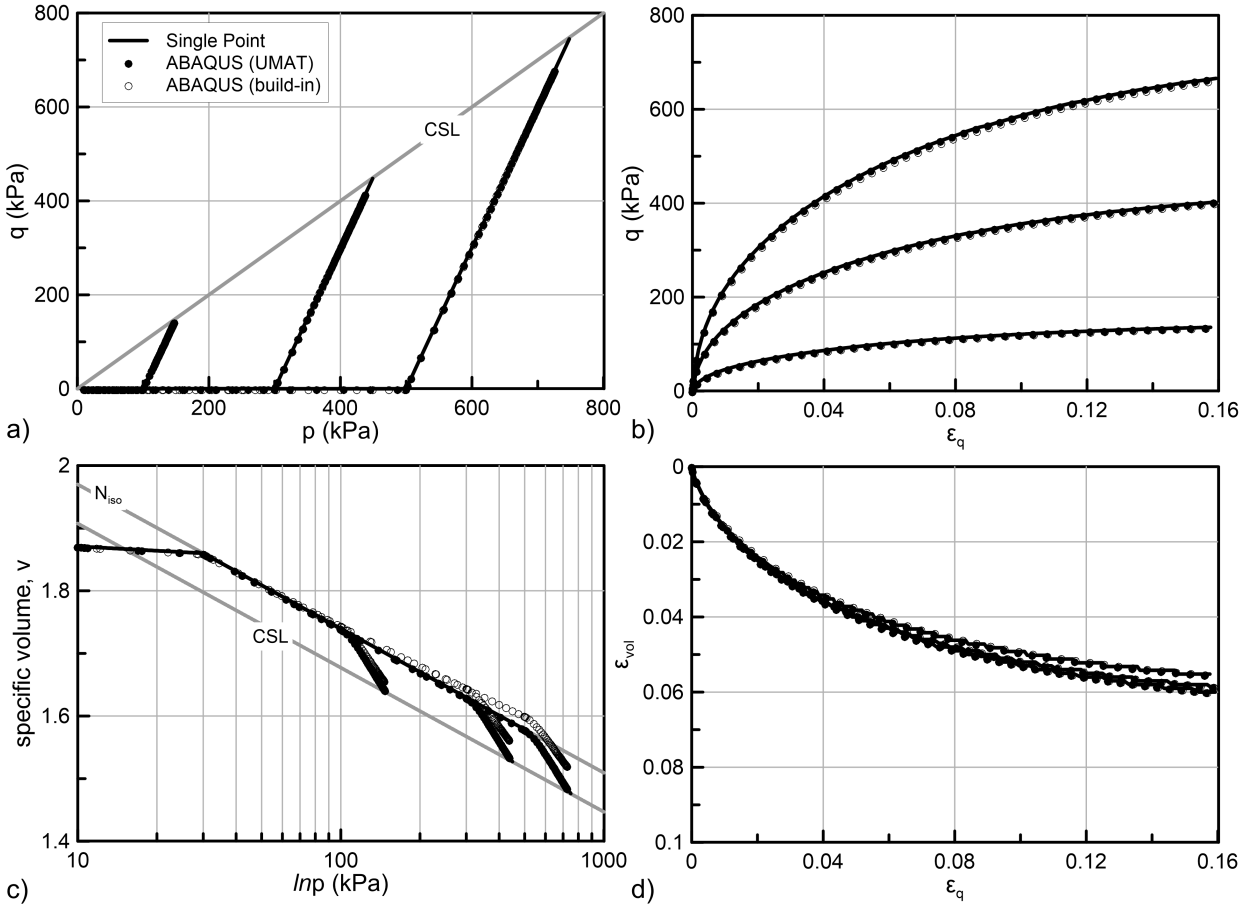


**Figure 7.6:** Drained triaxial compression tests on isotropically consolidated soil elements, under three different stress levels ($p = 100, 300, 500$kPa). a) the $p - q$ space; b) the $q - \varepsilon_q$ diagram; c) the $v - \ln p$ plane and; d) the $e_{vol} - e_q$ diagram.

cases, the three different analyses provide consistent results with the exception of the specific volume evolution for the reasons previously discussed. Note that in the undrained TRX loading, the aforementioned inconsistency has deleterious effects in the calculated pore water pressure as a result of the hydraulic solution's dependance (water mass equilibrium) on the void ratio value.

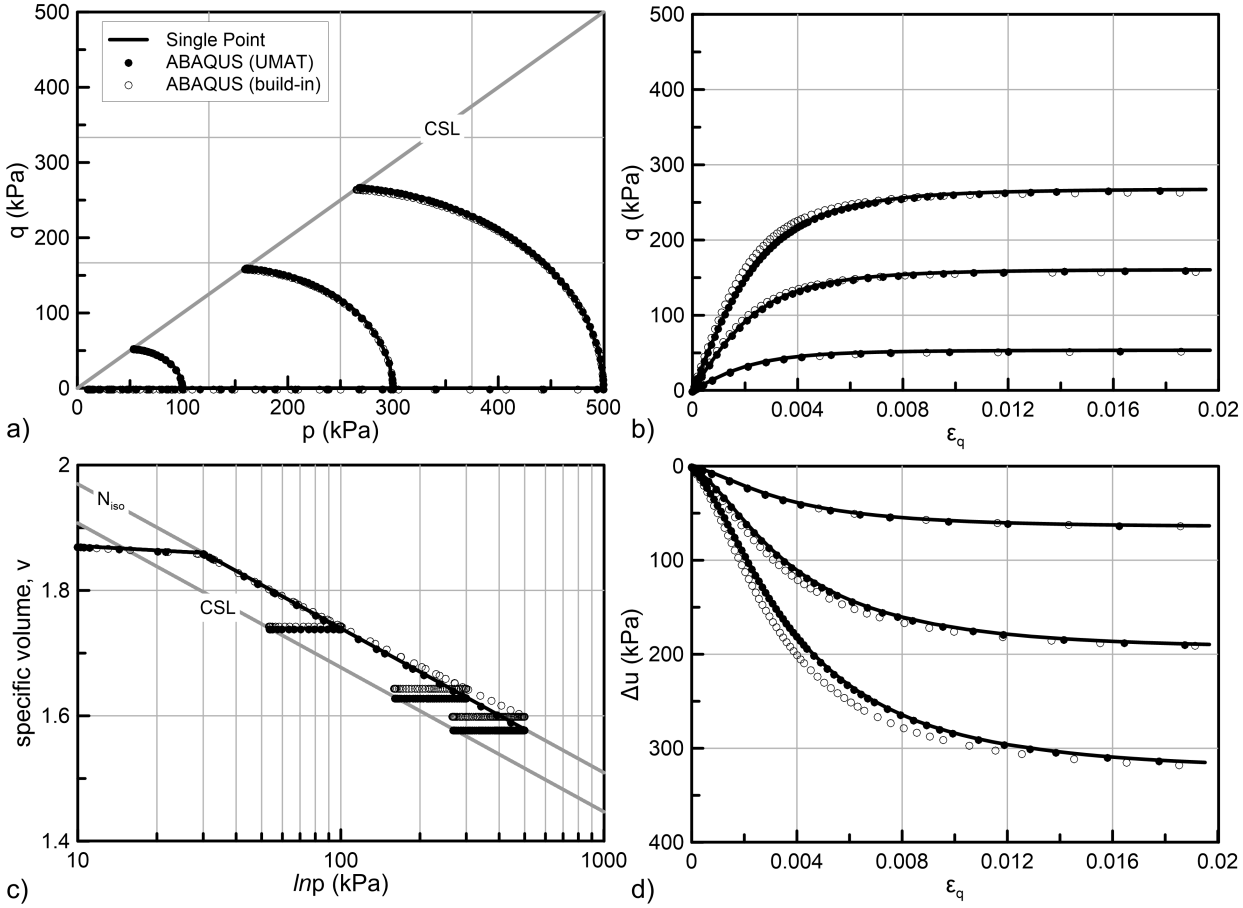


**Figure 7.7:** Undrained triaxial compression tests on isotropically consolidated soil elements, under three different stress levels ($p = 100, 300, 500$kPa). a) the $p-q$ space; b) the $q-\varepsilon_q$ diagram; c) the $v-\ln p$ plane and; d) the $e_{vol}-e_q$ diagram.

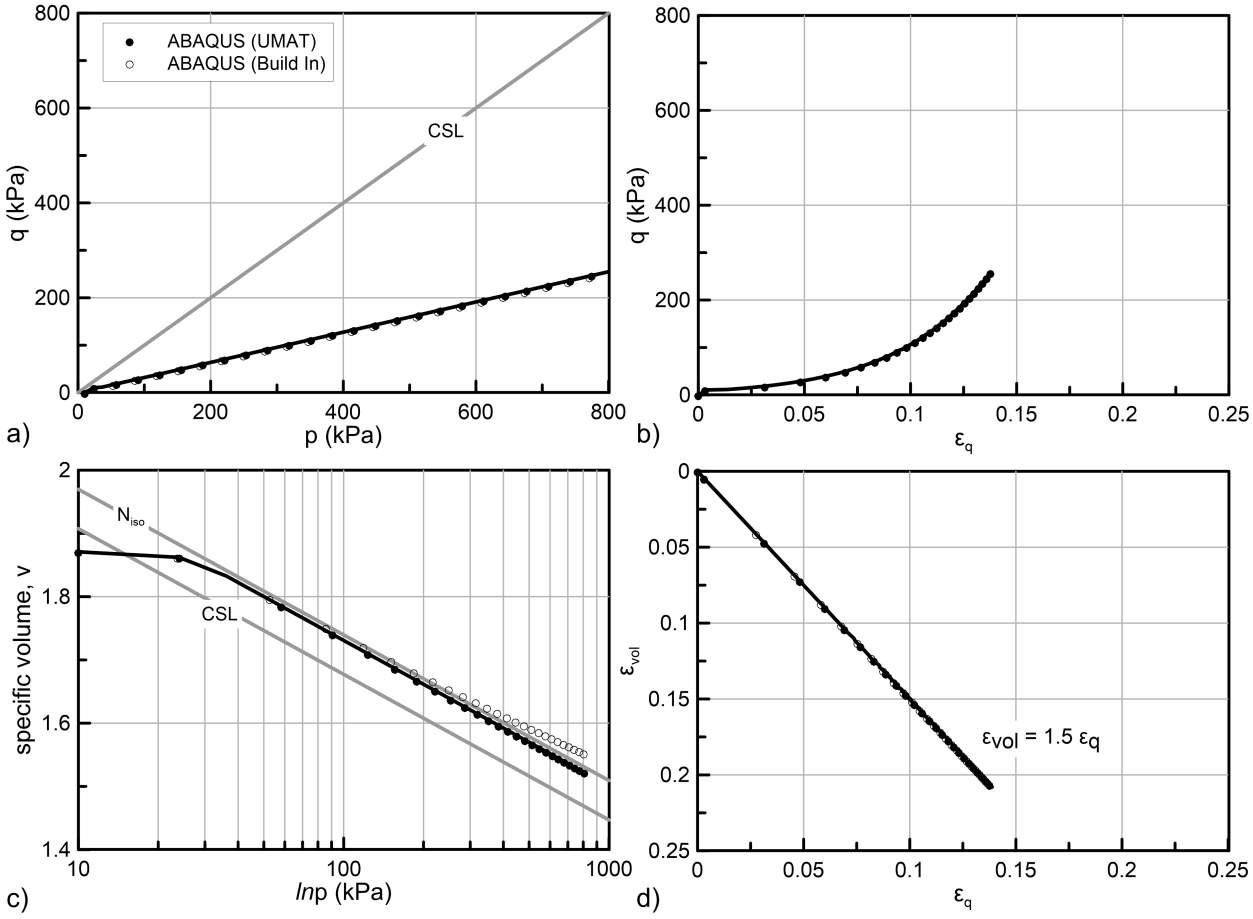


**Figure 7.8:** An 1D consolidation test. a) the $p-q$ space; b) the $q-\varepsilon_q$ diagram; c) the $v-\ln p$ plane and; d) the $e_{vol}-e_q$ diagram.

## 7.6 Concluding Remarks

This chapter offered a brief description of the numerical tools developed for the solution of the proposed model's constitutive equations. The main software developed is an incremental driver. It uses an explicit integration scheme to solve the constitutive equations by imposing a series of infinitesimal increments of strain, suction, and effective degree of saturation.

A Single Material Point (SMP) testing program was additionally developed to simulate common laboratory stress paths. It is an enhancement of existing tools for the analysis of saturated soil elements, severely modified to additionally accommodate the behaviour of unsaturated soils. Towards that direction: a) the implementation of drained and undrained tests was modified to include constant suction and constant water content tests respectively; b) suction change stress paths where implemented in order to allow for the simulation of drying and wetting tests, and; c) the Gallipoli et al. (2003) WRM was incorporated to provide the crucial link between suction and the corresponding degree of saturation.

The main incremental driver was additionally integrated in an Abaqus User Material (UMAT) subroutine to facilitate the incorporation of the proposed model in the analyses of geotechnical boundary value problems through FEM analyses. The standard Abaqus UMAT environment is enhanced using the User Defined Field (USDFLD) subroutine to additionally account for the exchange of suction and degree of saturation between the main code (Abaqus) and the developed UMAT subroutine. It was realized that Abaqus cannot account for a void ratio dependant water retention behaviour and the implication of this fact on the modelling capabilities will be exploited in the following chapter.

Finally, the developed numerical tools where applied in the analyses of three common laboratory tests. The proposed model was reduced to the Modified Cam Clay model to allow for the comparison of the obtained results bewteen the developed tools and the Abaqus build-in MCC model. Consistent results were raised, providing increased confidence on the developed algorithms, necessary prior to extending the discussion into more complicated analyses associated with the anisotropic and unsaturated features of the model.

Next, the developed numerical tools will be heavily utilized to evaluate the model's prediction: a) through an extensive parametrical study in chapter 8; b) against experimental results in chapter 9, and; c) in the analyses of large boundary value problems

in chapter 10.

# Chapter 8

# Model Evaluation

## 8.1 Introduction

This chapter discusses and evaluates the predictions of the proposed constitutive model. To this end, the constitutive model is utilized to simulate the stress paths of typical geotechnical laboratory testing. The performed simulations serve two main objectives: a) the model predictions are compared with the underlying behavioural framework to ensure that the model behaves accordingly, and; b) all the parameters involved in the model which are not a straight-forward outcome of experimental results, are parametrically investigated to familiarize the potential user with their effect.

To perform the aforementioned calculations the numerical tools developed in the previous chapter are used. Most of the presented results concern Single Material Point (SMP) testing using the developed SMP testing code. In addition to SMP analyses, some of the simulations are repeated as FEM boundary value problems with Abaqus, to evaluate the predictions of the Abaqus UMAT subroutine. For simplicity and brevity, all results are reported in the triaxial stress space $(p, q)$.

The chapter is divided in three main sections. The first one deals with the anisotropic characteristics of the model and the simulations are performed under saturated conditions. The second section focuses purely on the effects of partial saturation on the model's predictions and for simplicity the simulations regard isotropic conditions (the model is reduced to an MCC model). A third section follows which deals with the combined effects of anisotropy and partial saturation.

In section 6.9, we divided the fifteen parameters of the proposed constitutive

model in three groups. The basic MCC parameters, the anisotropy-related parameters and the unsaturated-related parameters. In the following lines, the latter two are discussed and some of them are also parametrically investigated. WIth respect to the group of basic parameters, however, constant values are assumed and their effect is not examined. Table 8.1 summarizes the selected values, which are assumed representative of a relatively stiff clayey silt and their selection has been based on experience and engineering judgment.

**Table 8.1:** Parameters used in the presented analyses.

| Basic Parameters | | Basic Parameters | |
|---|---|---|---|
| Parameter | Value | Parameter | Value |
| $\kappa$ | $0.01^{*1}$ | $c$ | $0.93897^{*3}$ |
| $\lambda$ | $0.07^{*2}$ | $N_{iso}$ | 2.1 |
| $\nu$ | 1/3 | $\Gamma$ | $2.0584^{*4}$ |
| $k$ | $0.93897^{*3}$ | $\chi$ | $0.469^{*5}$ |

$^{*1}$ corresponds to $C_r \approx 0.023$.
$^{*2}$ corresponds to $C_c \approx 0.16$.
$^{*3}$ is equivalent to $M = 1.15$ in the triaxial stress space and corresponds to a material with $\phi \approx 28^o$ in compression.
$^{*4}$ corresponds to $\Gamma = N_{iso} - (\lambda - \kappa)\ln 2$ due to $k = c$ selection.
$^{*5}$ calibrated for $K_0 = 0.55$ based on Jaky's estimation (see table 3.1) for $\phi \approx 28^o$.

## 8.2 Anisotropic Characteristics

This section deals exclusively with the anisotropic characteristics of the model and thus, the presented results correspond to saturated conditions. The model incorporates four (4) parameters that are directly associated with its anisotropic characteristics. Parameter $r_s$ is a material constant controlling the relative position of the intrinsic compression curves. In fact, through the hardening rule, parameter $r_s$ controls the trace of intermediate radial stress paths in the $v - \ln p$ plane. It is estimated utilizing experimental results from at least one anisotropic compression test, provided that the isotropic compression curve and the critical state lines are both

already known.

In chapter 5, parameter $r_s$ was parametrically investigated and characteristic plots of the derived compressions curves were given in figure 5.7. The values used ranged from $r_s = 0.5$ to $r_s = 1.25$, selected on the bases of experimental results, as representative of typical soil behaviour. For the analyses performed in this chapter a constant value $r_s = 0.75$ is assumed. Figure 8.1 plots the assumed compressibility framework in the $v - p$ and $v - \ln p$ planes for the selected $r_s$ value.

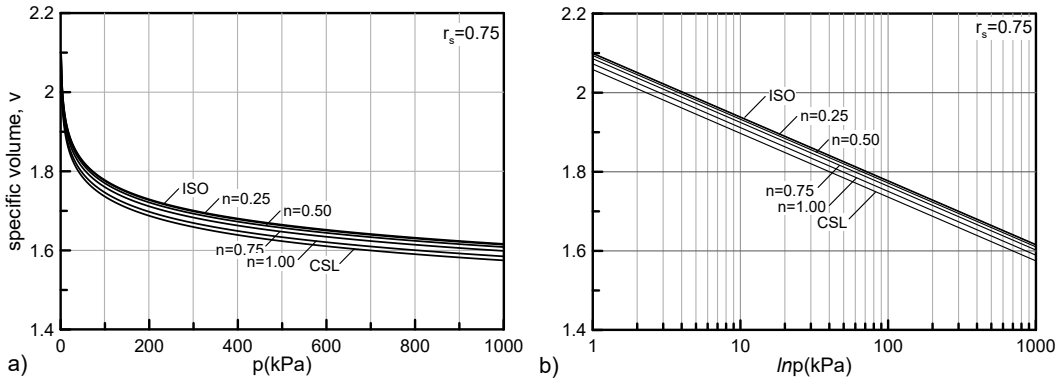


**Figure 8.1:** The intrinsic compression curves on the: a) $v-p$ and; b) $v-\ln p$ corresponding to different stress ratios $n = 0$, 0.25, 0.50, 0.75 and 1.0 for $r_s = 0.75$ combined with the parameters of table 8.1.

The following two subsections deal with the rest of the anisotropic parameters, namely with parameters $\psi$, $\zeta_q^p$ both involved in the hardening rule and with parameter $\chi$ related to the orientation of the plastic potential surface. A third subsection follows which focuses on the shear strength predictions under different initial anisotropic conditions and different stress paths.

### 8.2.1 Hardening rule parameters $\psi$, $\zeta_q^p$

The proposed model utilizes a mixed hardening rule comprising of an isotropic and a kinematic part (see section 6.6). The isotropic part of the rule incorporates the proposed compressibility framework to control the evolution of the size of the yield surface correlating it with the developing anisotropic fabric. The kinematic part is responsible for altering the orientation of the yield surface in the stress space whenever primary anisotropy changes. It consists of two components, the orientational one, and the de-orientational one.

The orientational component drags the yield surface's main axis inclination towards the one of the imposed stress path. It is mainly in charge of adjusting primary anisotropy during stress paths that alter the soil fabric and additionally do not lead to failure. Such stress paths include radial anisotropic compression or 1D compression from initially isotropic conditions, as well as isotropic compression from initially anisotropic conditions. It is a volumetric hardening component as the evolution of the anisotropy tensor $\dot{\boldsymbol{b}}$ is linearly proportional to the increment of the plastic volumetric strain $\dot{\varepsilon^p}$ (see eq 6.45), with parameter $\psi$ controlling the rate of anisotropy evolution.

The second component drags the yield surface's main axis inclination towards the isotropic axis. It reproduces an anisotropy degradation effect which attempts to accommodate the stain softening behaviour usually exhibited by anisotropically consolidated samples during undrained triaxial loading, together with a common critical state independent of the initial anisotropy and of the stress path taken to failure. Thus, Its role is mainly profound in stress paths that lead to failure (i.e., triaxial loading). In this case the evolution of the anisotropy tensor $\dot{\boldsymbol{b}}$ is linearly proportional to the increment of the plastic deviatoric strain $\dot{\varepsilon}_q^p$ (see eq 6.46), and parameter $\zeta_q^p$ controls the rate of anisotropy degradation.

Irrespectively of the examined stress path, usually volumetric and deviatoric plastic strains accumulate simultaneously and thus, both components tend to drag the inclination of the yield surface axis towards different targeted orientations. In that respect, suitable cominations of parameters $\psi$ and $\zeta_q^p$ must be selected to provide fair simulation results under any possible loading circumstances.

For such a successful selection, a suitable step by step calibration process is proposed, which includes three individual calibration steps. In the first step, parameter $\psi$ is individually calibrated to the experimental results focusing on available data from tests that alter anisotropy but do not lead to failure. During this calibration step, the de-orientational component of the hardening rule must be deactivated by selecting $\zeta_q^p = 0$.

The second calibration step concerns the individual calibration of parameter $\zeta_q^p$. In this case, experimental results from tests that lead to failure are utilized, while the orientational component of the hardening rule is deactivated by selecting $\psi = 0$. It is highly recommended to use results from undrained triaxial compression tests, as during undrained loading, the accumulated plastic volumetric strains are usually negligible and in terms of numerical analyses the simulation the results will be almost

independent of the $\psi$ value.

Finally during the third calibration step, using the previously selected values as a reference, both components are activated and the available experimental tests are simulated once again. If the results are not satisfactory a different combination of $\psi$ and $\zeta_q^p$ must be selected. A similar procedure is followed hereinafter in order to familiarize the potential user with the selection of parameters $\psi$ and $\zeta_q^p$, .

#### 8.2.1.1 Effect of parameter $\psi$

To demonstrate the effect of parameter $\psi$ on the predictions of the proposed model, the following simulations of common laboratory stress paths are performed:

- **Radial compression test on an initially isotropically consolidated soil element**;
  An initially isotropically, normally consolidated ($p_0 = 100kPa$) soil element is unloaded to $p = 60kPa$. The stress ratio is elastically adjusted by raising the deviatoric stress to $q = 38.568kPa$ and a radial stress path corresponding to $n = 0.6428$ is imposed until the isotropic stress gets equal to $p = 1000kPa$. The imposed stress ratio corresponds to the selected $K_0 = 0.55$ and thus the imposed test is a $K_0$ test. Figure 8.2 demonstrates the simulation results for five different $\psi$ values, namely $\psi = 1$, 10, 20, 30 and 50.

- **1D compression test on an initially isotropically, normally consolidated soil element**;
  An initially isotropically normally consolidated soil sample is directly 1D compressed (oedometer test) up to a vertical stress of $\sigma_v = 4MPa$. The results are given for two different simulations regarding different initial conditions. The difference in initial conditions regard two different preconsolidation pressures assumed, namely $p_0 = 100kPa$ and $p_0 = 10kPa$. The results are presented in figures 8.3 and 8.4, respectively. The two different initial preconsolidation pressures demonstrate the effect of stress level in the evolution of anisotropy. The same five $\psi$ values, are analyzed again.

- **Isotropic compression test on an initially anisotropically consolidated soil element**:
  In the previous two tests the assumed initial conditions where isotropic. In this simulation we examine how anisotropy evolves when the initial state is

anisotropic. In that respect, we assume that the examined soil element has been anisotropically normally consolidated to a stress ratio $n = 0.6428$ up to $p = 100kPa,\ q = 64.28kPa$. The yield surface is assumed aligned with the imposed stress path by imposing a $b_q = n = 0.6428$ selection. The soil element is elastically unloaded to $p = 50kPa,\ q = 0kPa$ and finally isotropically compressed to $p = 1000kPa$. Figure 8.5, demonstrates the acquired results for the five different $\psi$ values selected.

The aforementioned figures (fig. 8.2 to fig. 8.5 ) include the following six graphs:

a) the mean effective stress $p$ vs the deviatoric stress $q$, where apart from the stress paths the graph additionally includes characteristic plots of the yield surface;

b) the deviatoric stress $q$ vs the deviatoric strain $\varepsilon_q$;

c) the specific volume $v$ ($v = 1 + e$) vs the natural logarithm of the mean effective stress $\ln p$ (or $\ln \sigma_v$ in oedometer tests). The graph also includes characteristic plots of the assumed compressibility framework.

d) the volumetric strain $\varepsilon_{vol}$ vs the deviatoric strain $\varepsilon_q$;

e) the measure of the developed anisotropy $b_q$ vs the natural logarithm of the mean effective stress $\ln p$ (or $\ln \sigma_v$ in oedometer tests), and finally;

f) the measure of the developed anisotropy $b_q$ vs the plastic volumetric strain $\varepsilon^p_{vol}$.

The obtained results demonstrate the proposed constitutive model's hardening rule predictions. Note that the yield surface alters orientation following the one of the imposed stress path, while at the same time the specific volume (void ratio) evolves and moves towards the corresponding intrinsic compression line. Moreover, the results confirm the successful calibration of the flow rule's orientation parameter $\chi$. It is reminded that the imposed radial stress path $n = 0.6428$ corresponds to a $K_0$ test while the flow rule has been calibrated for the same $K_0$. In figure 8.2d, we may observe that under stabilized anisotropic conditions (test with $\psi = 50$), the reproduced total dilatancy is $\dot{\varepsilon_q}/\dot{\varepsilon_{vol}} = 2/3$ corresponding to zero horizontal (radial) strains. The efficiency of the flow rule's calibration is also manifested in the one-dimensional compression tests of figures 8.3 and 8.4 where the stress path and the yield surface orientation tend towards the stress ratio value $n = 0.6428$ corresponding to the selected $K_0$.

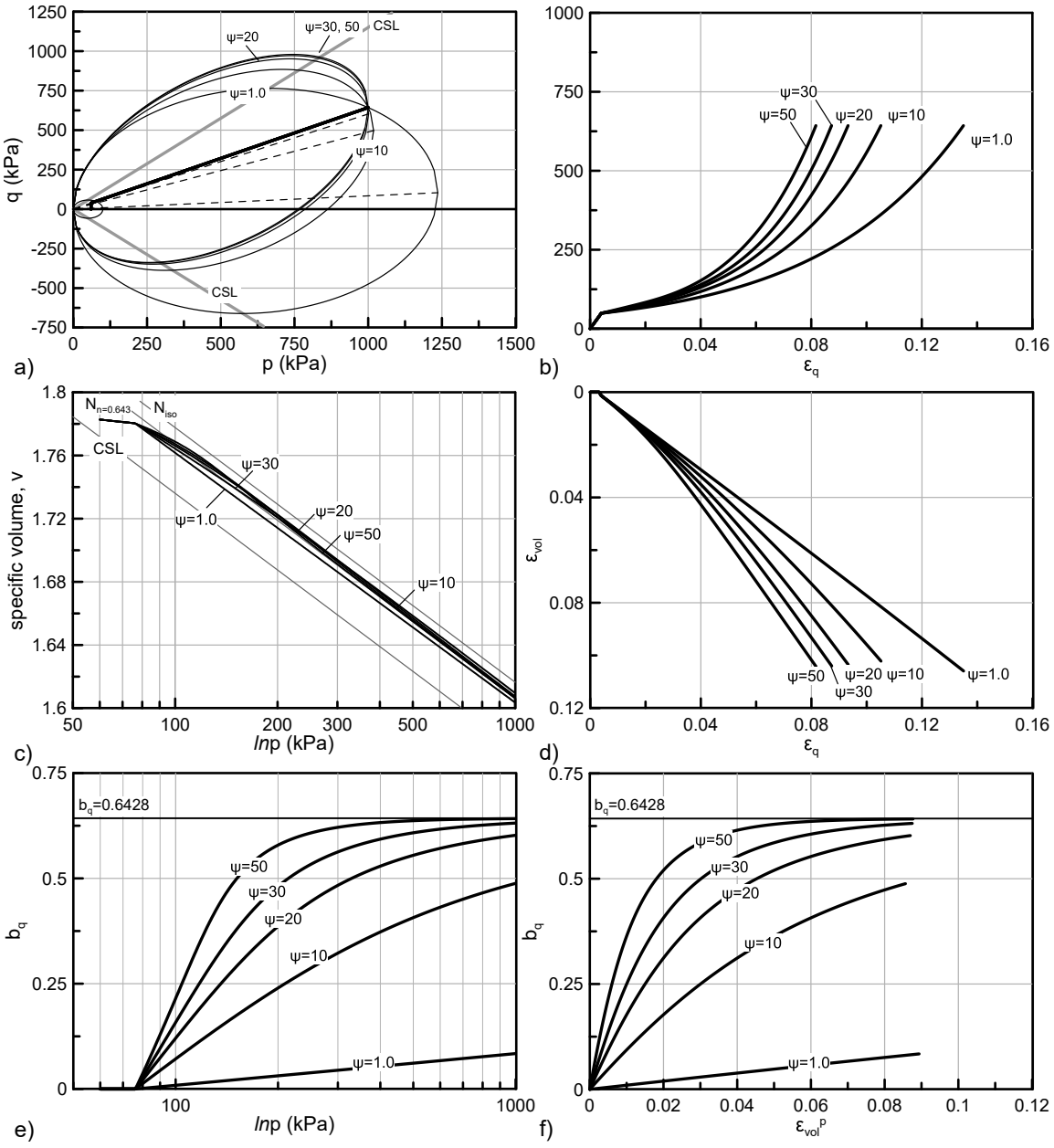


**Figure 8.2:** Radial consolidation ($n = 0.6428$) on initially isotropically consolidated soil elements. Effect of parameter $\psi$. a) the $p - q$ space; b) the $q - \varepsilon_q$ diagram; c) the $v - \ln p$ plane; d) the $\varepsilon_{vol} - \varepsilon_q$ diagram; e) the $b_q - \ln p$ diagram and; f) the $b_q - \varepsilon_{vol}^p$ diagram.

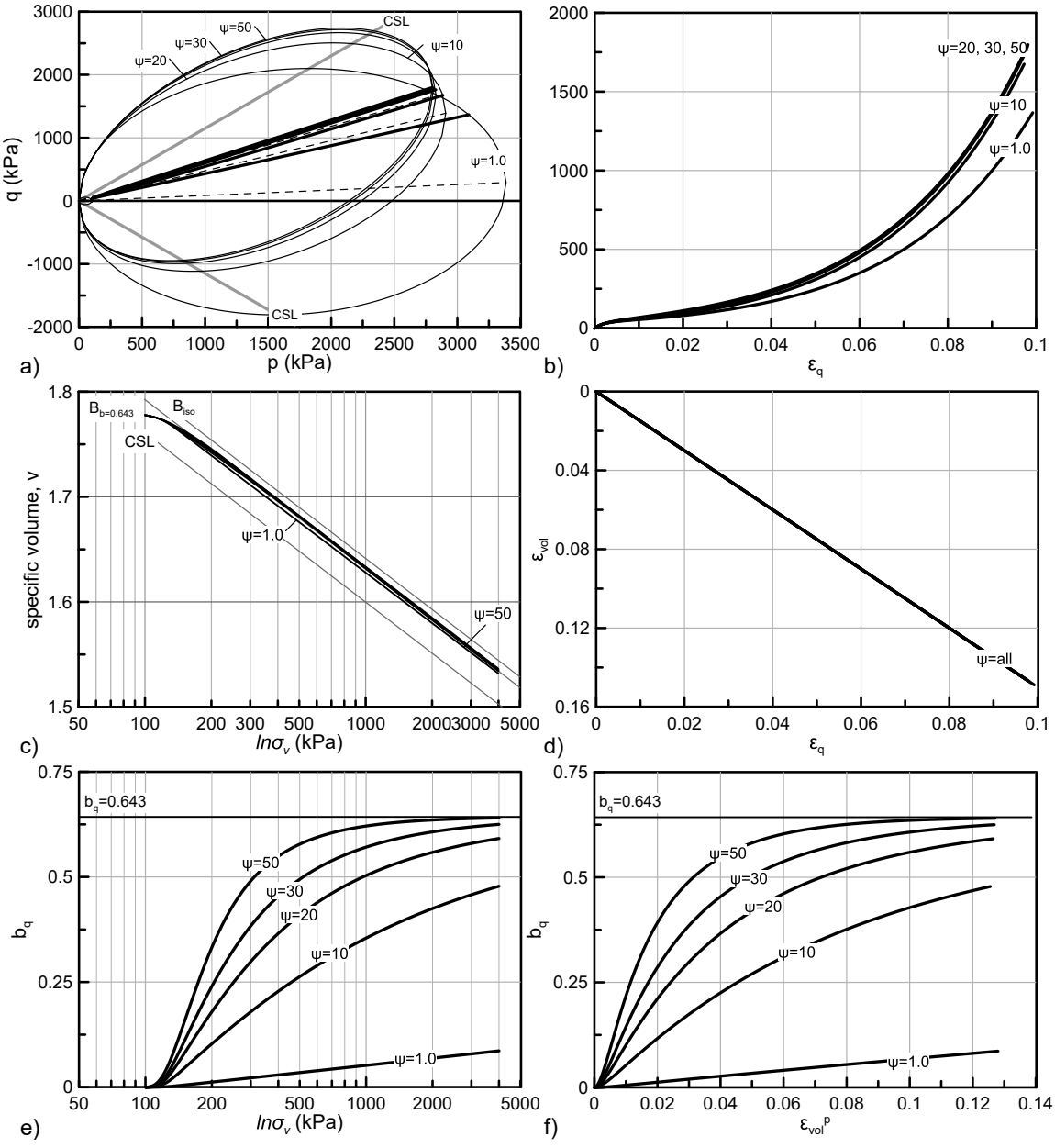


**Figure 8.3:** 1D consolidation on initially isotropically consolidated soil elements ($p_0 = 10kPa$). Effect of parameter $\psi$. a) the $p-q$ space; b) the $q-\varepsilon_q$ diagram; c) the $v-\ln\sigma_v$ plane; d) the $\varepsilon_{vol}-\varepsilon_q$ diagram; e) the $b_q-\ln\sigma_v$ diagram and; f) the $b_q-\varepsilon_{vol}^p$ diagram.

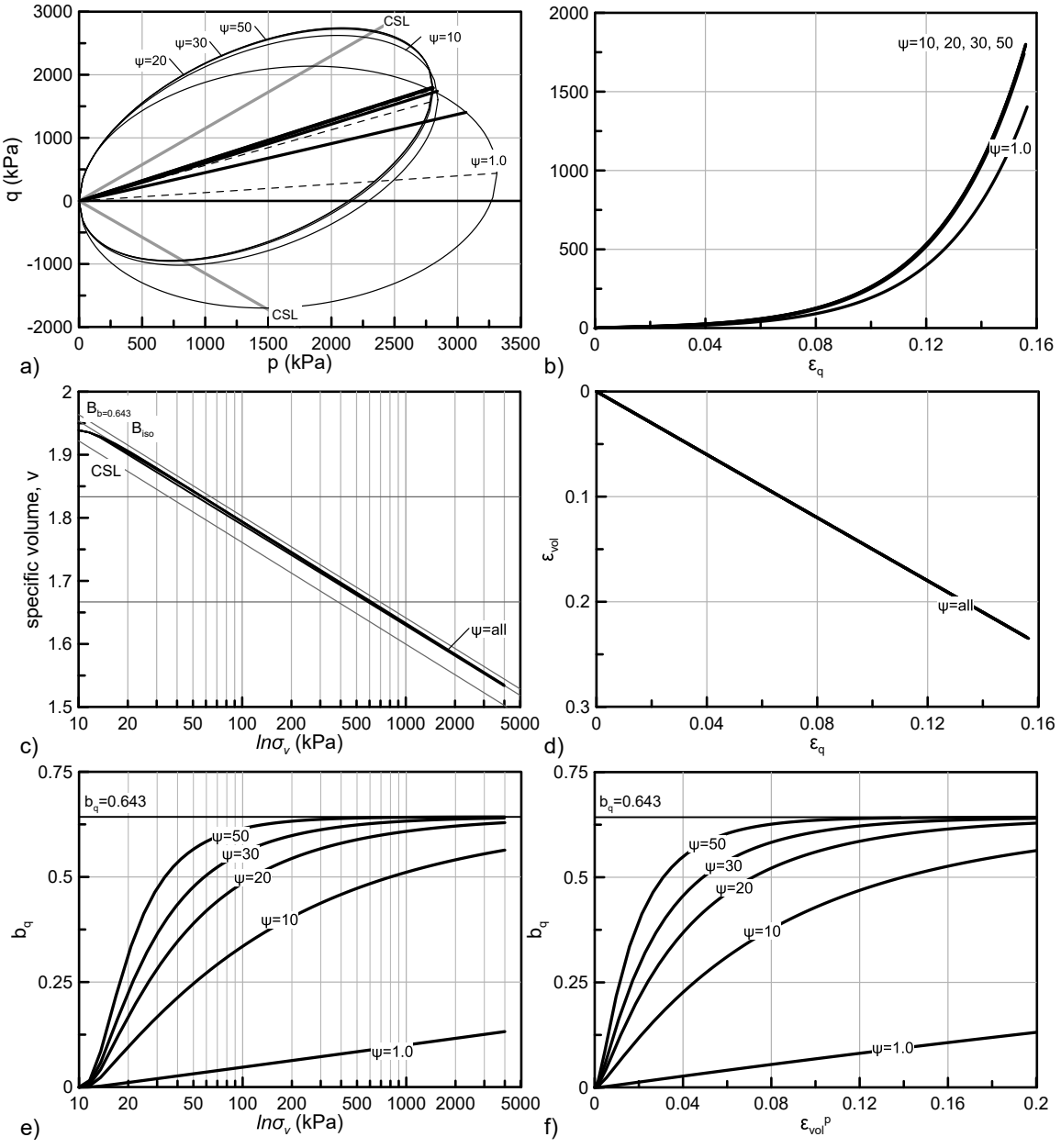


**Figure 8.4:** 1D consolidation on initially isotropically consolidated soil elements ($p_0 = 100kPa$). Effect of parameter $\psi$. a) the $p-q$ space; b) the $q-\varepsilon_q$ diagram; c) the $v-\ln\sigma_v$ plane; d) the $\varepsilon_{vol}-\varepsilon_q$ diagram; e) the $b_q-\ln\sigma_v$ diagram and; f) the $b_q-\varepsilon_{vol}^p$ diagram.

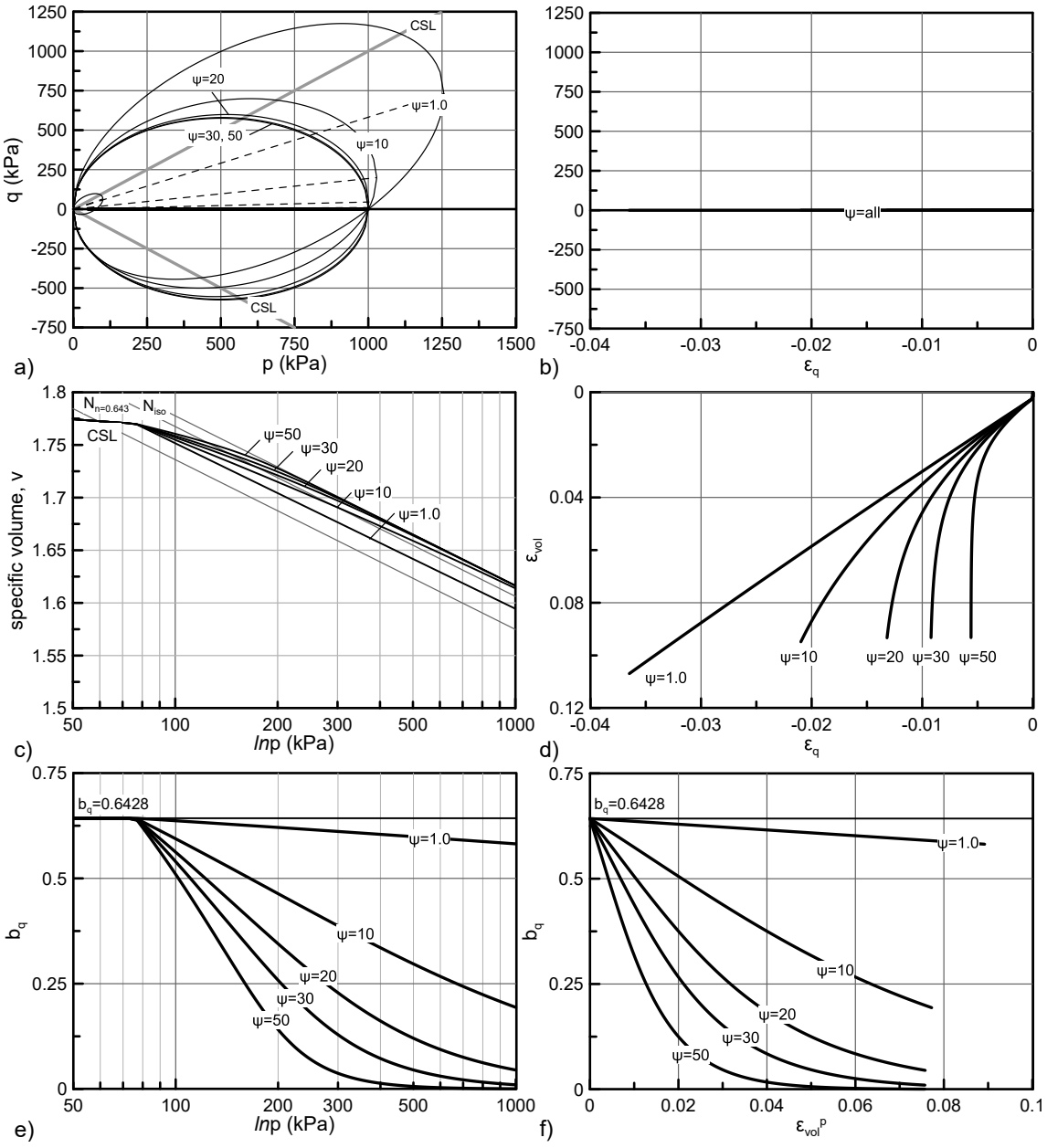


**Figure 8.5:** Isotropic compression on initially anisotropically consolidated soil elements. Effect of parameter $\psi$. a) the $p-q$ space; b) the $q-\varepsilon_q$ diagram; c) the $v-\ln p$ plane; d) the $\varepsilon_{vol}-\varepsilon_q$ diagram; e) the $b_q-\ln p$ diagram and; f) the $b_q-\varepsilon_{vol}^p$ diagram.

With respect to the evolution of anisotropy and the effect of parameter $\psi$ the following comments are made:

- The smaller tested value ($\psi = 1$) seems unrealistically small resulting to a limited evolution of the anisotropy tensor. Observe that even for accumulated plastic volumetric strains of up to 20%, the predicted anisotropy evolution is smaller than 20% of the imposed one.

- Values from $\psi = 10$ to $\psi = 50$ seem more representative of the usually anticipated soil behaviour. It is observed that for the tests where the initial anisotropy has been established at a stress level of $100kPa$, 10% of plastic volumetric straining is sufficient to alter the anisotropy to more than 50% of the imposed one, while for $\psi = 30$ and $\psi = 50$ the developed anisotropy is almost established to the imposed one.

- Comparing the results of figures 8.3 and 8.4 we observe that the initial stress level plays a significant role in the evolution of anisotropy. The tests initiating from a relatively lower stress level of $p = 10kPa$ when compared with their counterparts from the $p = 100kPa$ analysis for the same $\psi$ value, appear more capable of altering their anisotropy and adjust to the imposed one faster. This is quite reasonable as the soil elements consolidated to the lower stress level, correspond to an initial fabric that is much more "open" (i.e., higher void ratio) and thus, such soils are much more receptive to changes in their anisotropic fabric.

- The radial consolidation tests appear more efficient in altering the primary anisotropy of any given soil sample compared to 1D consolidation tests. It should be mentioned though, that this effect is a mathematical consequence of the expression selected for the kinematic component of the hardening rule. The selected hardening rule uses stress attractors to describe the changes of anisotropy and in that end imposing a stress ratio proves more efficient compared with a strain ratio application (the case of oedometer test). Nevertheless whether this is really representative of the experimental behaviour of soils is open to discussion as there are no solid experimental evidence indicating whether a stress or a strain ratio application is more efficient.

- Regarding the volumetric behaviour, we may observe that in the $v - \ln p$ plane

the effect of an evolving anisotropy is less profound compared with the evolution of the yield surface's orientation. This is clearly observed in figure 8.5c, where for the case of $\psi = 10$ the specific volume results for $p > 300kPa$ plot practically on the isotropic compression line although the yield surface has not yet get aligned with the isotropic axis. Of course the anticipated behaviour is highly dependant on the selected compressibility framework[1], nevertheless, this observation is of great importance when it comes to the calibration of parameter $\psi$ with experimental data.

In common laboratory practise, an anisotropic compression test provides the evolution of the specific volume with stress and not the orientation of the yield surface. Due to the decreased sensitivity of the $v - \ln p$ results on the evolving anisotropy, it is highly likely during a calibration exercise to overestimate the $\psi$ value by assuming that the examined experimental results suggest established anisotropic conditions, while this may not be the case.

Kavvadas (1982), based on experimental results, reports that for an initially isotropically consolidated soil element imposed to a $K_0$ or $1D$ compression test plastic volumetric strains of up to 30% are required for primary anisotropy to adjust to the imposed one. In that respect, it is believed that a realistic range of values for parameter $\psi$ is approximately from $\psi = 20$ to 30 and these values are recommended as initial reference values.

#### 8.2.1.2 Effect of parameter $\zeta_q^p$

This paragraph deals with the de-orientational component of the kinematic hardening rule, evaluating its predictions and demonstrating the effect of parameter $\zeta_q^p$ on the simulation results. It is reminded that the de-orientational part of the hardening rule is responsible for "erasing" the memory of anisotropy as failure is approached. In that end, parameter $\zeta_q^p$ is evaluated using shear tests. Figures 8.6 and 8.7 present the results of triaxial compression and extension tests under undrained and drained conditions. Regarding the initial conditions, an anisotropically, normally consolidated soil element is assumed, with $p = 200kPa$ and $q = 118.56kPa$ corresponding to the same stress ratio used in the analysis of the previous paragraph, while the initial orientation of the yield surface is assumed equal to that of the stress ratio.

[1] In the selected one stress paths with $n < 0.25$ plot very close to the isotropic compression line (see figure 8.1).

The graphs presented for each one of the tests are similar to those used in the previous subsection and offer a complete picture of the predicted soil response. The main difference is that the evolution of anisotropy in graph (f) is now plotted in terms of the plastic deviatoric strains ($\varepsilon_q^p$) as these are involved in the de-orientational component of the kinematic part of the hardening rule. Moreover, in undrained tests, graph (d) presents the excess pore pressure development $\Delta U$ versus the deviatoric strains, instead of the volumetric deformation which is null. Additionally we shall mention that the plotted deviatoric stress $q$ corresponds to $q = \sigma_a - \sigma_r$, while the plotted deviatoric strain to $\varepsilon_q = \frac{2}{3}(\sigma_a - \sigma_r)$ and thus both obtain negative values at triaxial extension tests. The latter does not apply to the ($\varepsilon_q^p$) plotted in graph (f) which corresponds to the generalized expression for deviatoric strain ($\varepsilon_q = \frac{2}{3}\sqrt{\boldsymbol{e} : \boldsymbol{e}}$) and thus, systematically obtains positive values.

Five different values of parameter $\zeta_q^p$ are examined, namely $\zeta_q^p = 1$, 20, 30, 50 and 100, while $\psi = 0$ is selected to deactivate the orientational component of the hardening rule for the analysis to focus on the pure effect of the anisotropy degradation mechanism.

A first observation of the numerical results reveals that the hardening rule successfully describes a smooth and continuous degradation of anisotropy. In more detail, based on the results of figures 8.6 and 8.7, the following comments can be made:

- The proposed hardening rule can reproduce strain softening behaviour as usually observed in the experimental results of undrained compression on anisotropically consolidated soil samples.

- In undrained extension tests the model does reproduce a hook-type behaviour in the $p-q$ space, similar to what is usually anticipated in experimental results. In drained extension tests this hook-type behaviour is observed in the evolution of specific volume with stress.

- The stress paths move towards a unique critical state for both compression and extension. This is clearly observed in figure 8.6a where for the case of $\zeta_q^p = 100$ both the extension and compression tests have reached a common critical state.

- In drained compression tests an initially strain softening behaviour is observed which, as loading progresses, reverses to a strain hardening response. With a suitable selection of parameters this strain softening response almost vanishes (i.e., for $\zeta_q^p = 10$), while still is quite profound in undrained compression. This is

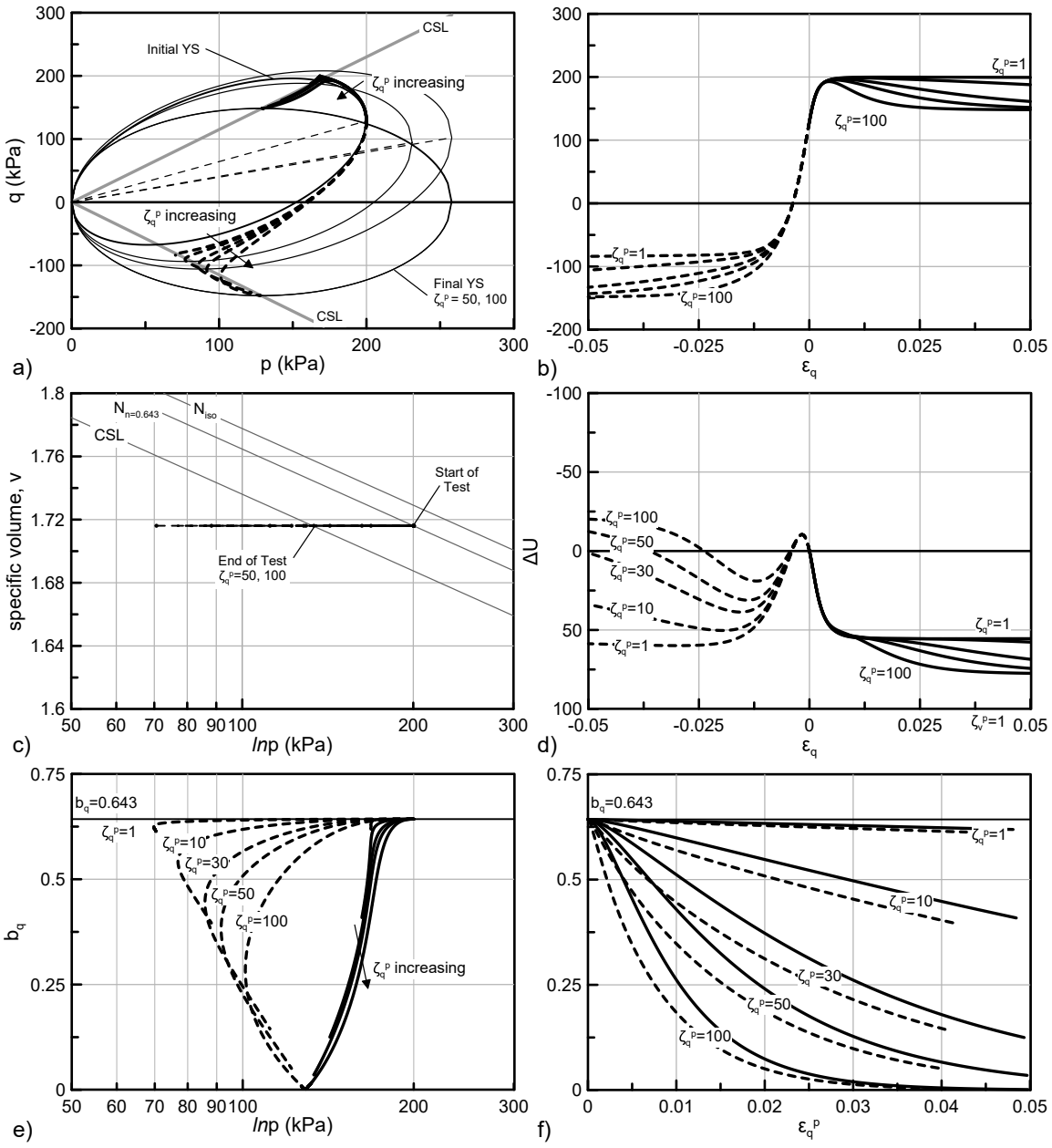


**Figure 8.6:** Undrained triaxial loading (compression and extension) of anisotropically, normally consolidated soil elements. Effect of parameter $\zeta_q^p$. a) the $p-q$ space; b) the $q-\varepsilon_q$ diagram; c) the $v-\ln p$ plane; d) the $\Delta U - e_q$ diagram; e) the $b_q - \ln p$ diagram and; f) the $b_q - \varepsilon_q^p$ diagram.

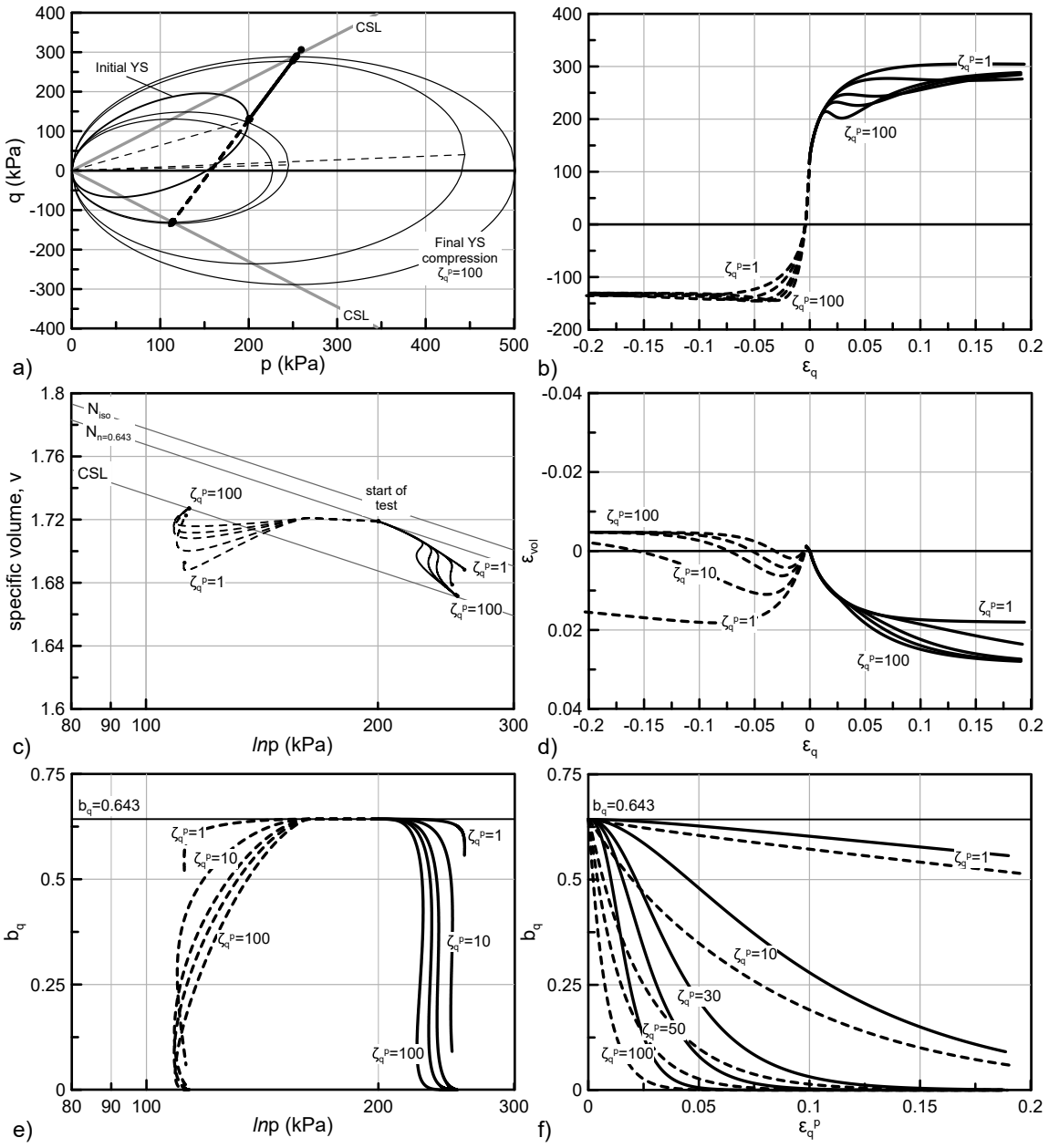


**Figure 8.7:** Drained triaxial loading (compression and extension) of anisotropically, normally consolidated soil elements. Effect of parameter $\zeta_q^p$. a) the $p-q$ space; b) the $q-\varepsilon_q$ diagram; c) the $v-\ln p$ plane; d) the $\varepsilon_{vol}-\varepsilon_q$ diagram; e) the $b_q-\ln p$ diagram and; f) the $b_q-\varepsilon_q^p$ diagram.

very important as usually experimental results of drained and undrained triaxial loading of anisotropically consolidated soil samples indicate such a behaviour.

- Parameter $\zeta_q^p$ efficiently controls the rate of anisotropy degradation. The smaller examined value ($\zeta_q^p = 1.0$) is unrealistically small and cannot reproduce strain softening behaviour in the deviatoric stress vs deviatoric strain plots. To the contrary, for $\zeta_q^p = 10$, 30, 50 and 100 the rate of anisotropy degradation progressively increases, while only in the $\zeta_q^p = 100$ analyses the element totally loses its memory of anisotropy at 4% of accumulated plastic deviatoric strains. Nevertheless $\zeta_q^p = 100$ is an extreme value that describes a very rapid change in soil's anisotropy. In fact, available experimental results, rarely indicate that critical state is truly reached under the commonly imposed levels of deviatoric strains, especially when anisotropically consolidated soil samples are examined. Usually, the end of test corresponds to a stress state close enough, but yet not at the theoretical critical state of the material. In that end values from $\zeta_q^p = 30$ to 50 are considered more realistic and are suggested as initial reference values.

#### 8.2.1.3 The combined effect of parameters $\psi$ and $\zeta_q^p$

Following the individual examination of the effect of parameter $\psi$ in describing the evolution of the model's memory of anisotropy and the individual examination of the effect of parameter $\zeta_q^p$ in eliminating the aforementioned memory, this paragraph extends the discussion to the combined effect of both parameters. Simulations regarding both tests that lead and do not lead to failure are examined. The necessity to examine the combined effect of both parameters stems from the fact that in realistic applications, both the orientational and the de-orientational components of the hardening rule will simultaneously function, irrespectively of the stress path imposed or followed. Thus, the selected combination of parameters must allow for a realistic representation of the behaviour of anisotropic effects under a variety of different loading conditions.

In that respect, the oedometric and the isotropic compression tests presented in paragraph 8.2.1.1, as well as the analyses included in paragraph 8.2.1.2 are repeated below for the following combinations of parameters $\psi$ and $\zeta_q^p$:

- $\psi = 10$ and $\zeta_q^p = 10$, 50 as well as $\psi = 50$ and $\zeta_q^p = 10$, 50 for the compression tests, and;

- $\zeta_q^p = 10$ and $\psi = 10,\ 50$ as well as $\zeta_q^p = 50$ and $\psi = 10,\ 50$ for the triaxial loading tests.

The obtained results indicate that the effect of parameters $\psi$ and $\zeta_q^p$ are quite independent, in the sense that the response in the compression tests where anisotropy evolves to follow the anisotropy induced by the applied stress path is mainly dominated by parameter $\psi$, while on the other hand during tests that lead to failure, parameter $\zeta_q^p$ is the one mainly controlling the rate at which the memory of anisotropy erases.

In more detail, in figures 8.8 and 8.9, where the results of the 1D compression of an initially anisotropically consolidated soil element and the isotropic compression of an initially anisotropically consolidated soil element are presented respectively, we may observe that the evolution of the anisotropy ( see scalar measure of anisotropy $b_q$) and the corresponding stress path and stress vs strain paths curve depend on the value of parameter $\psi$, while parameter $\zeta_q^p$ has only secondary effects. Moreover, it seems that the greater the value of parameter $\psi$ is, the less significant the effect of parameter $\zeta_q^p$ gets. This is very clearly depicted, in both the 1D and the isotropic tests examined, in the case of $\psi = 50$ where the results seem practically not affected by the selected $\zeta_q^p$ value. It should be also mentioned that in the latter case (isotropic compression) both the orientational and the de-orientational component of the hardening rule drag the yield surface inclination towards the isotropic axis.

Regarding the triaxial loading tests, the results of figure 8.10 are almost independent of the $\psi$ value selected, attributed to the limited plastic volumetric strain developing during undrained loading. On the other hand, under drained conditions, a quite significant combined effect of both parameters is observed (see fig. 8.11). The latter is quite reasonable and attributed to the fact that both volumetric and deviatoric plastic strains accumulate in a comparable manner and thus, both components of the kinematic hardening rule significantly influence the results. In that respect, it is necessary to re-calibrate parameters $\psi$ and $\zeta_q^p$ when the drained behaviour is of importance.

In the presented simulations, additional results from FEM analyses with the Simulia Abaqus are included and compared with their counterparts from the SMP algorithm. For the 1D compression the 3D cubical numerical model was used (see fig. 7.5), while for the isotropic compression test and the triaxial loading tests the axis-symmetric numerical model (see.fig 7.4). We may observe that the results co-

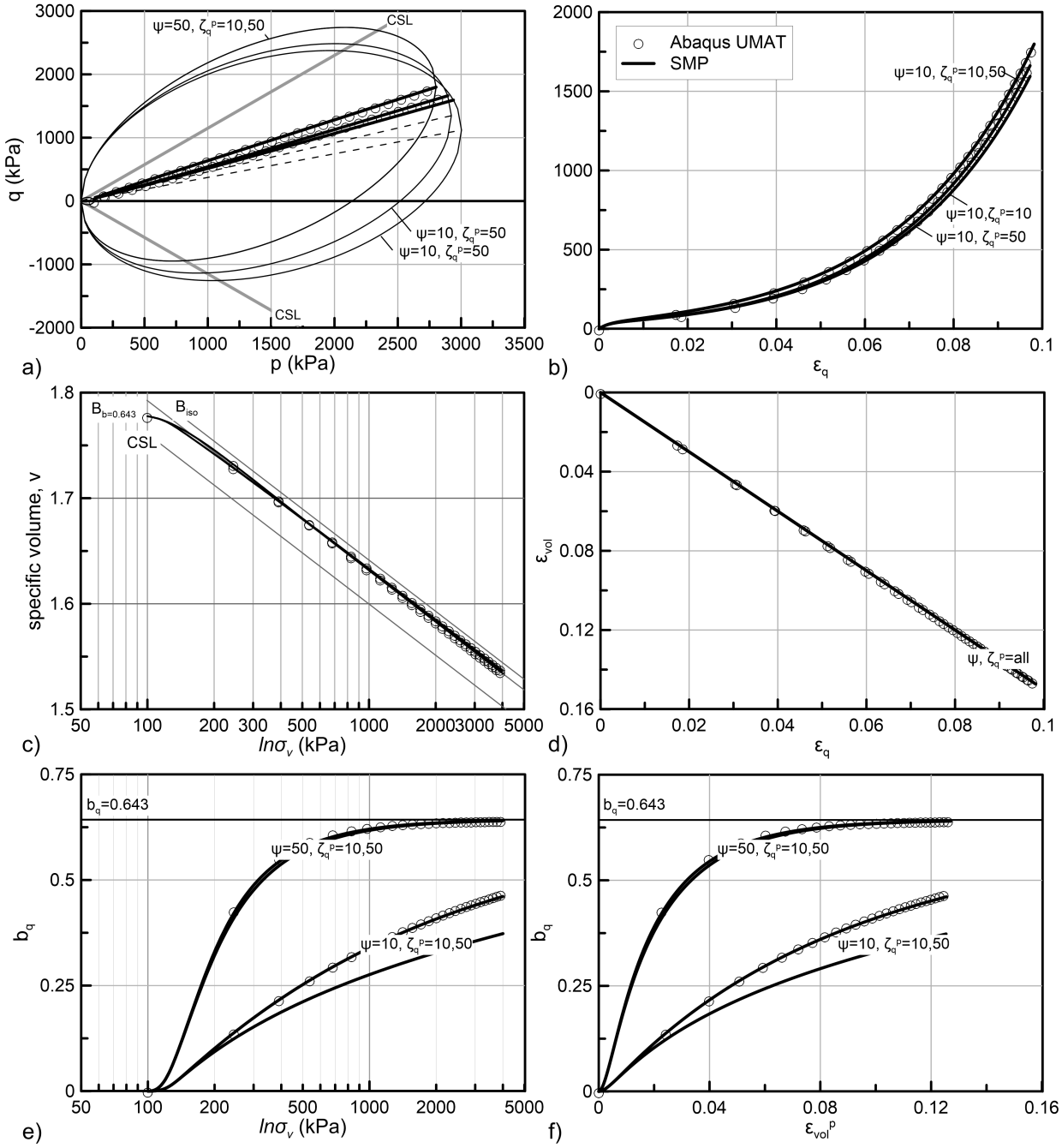


**Figure 8.8:** 1D consolidation on initially isotropically consolidated soil elements. Combined effect of parameters $\psi$ and $\zeta_q^p$. Results from both SMP and Abaqus FEM analyses. a) the $p-q$ space; b) the $q-\varepsilon_q$ diagram; c) the $v-\ln\sigma_v$ plane; d) the $\varepsilon_{vol}-\varepsilon_q$ diagram; e) the $b_q-\ln\sigma_v$ diagram and; f) the $b_q-\varepsilon_{vol}^p$ diagram.

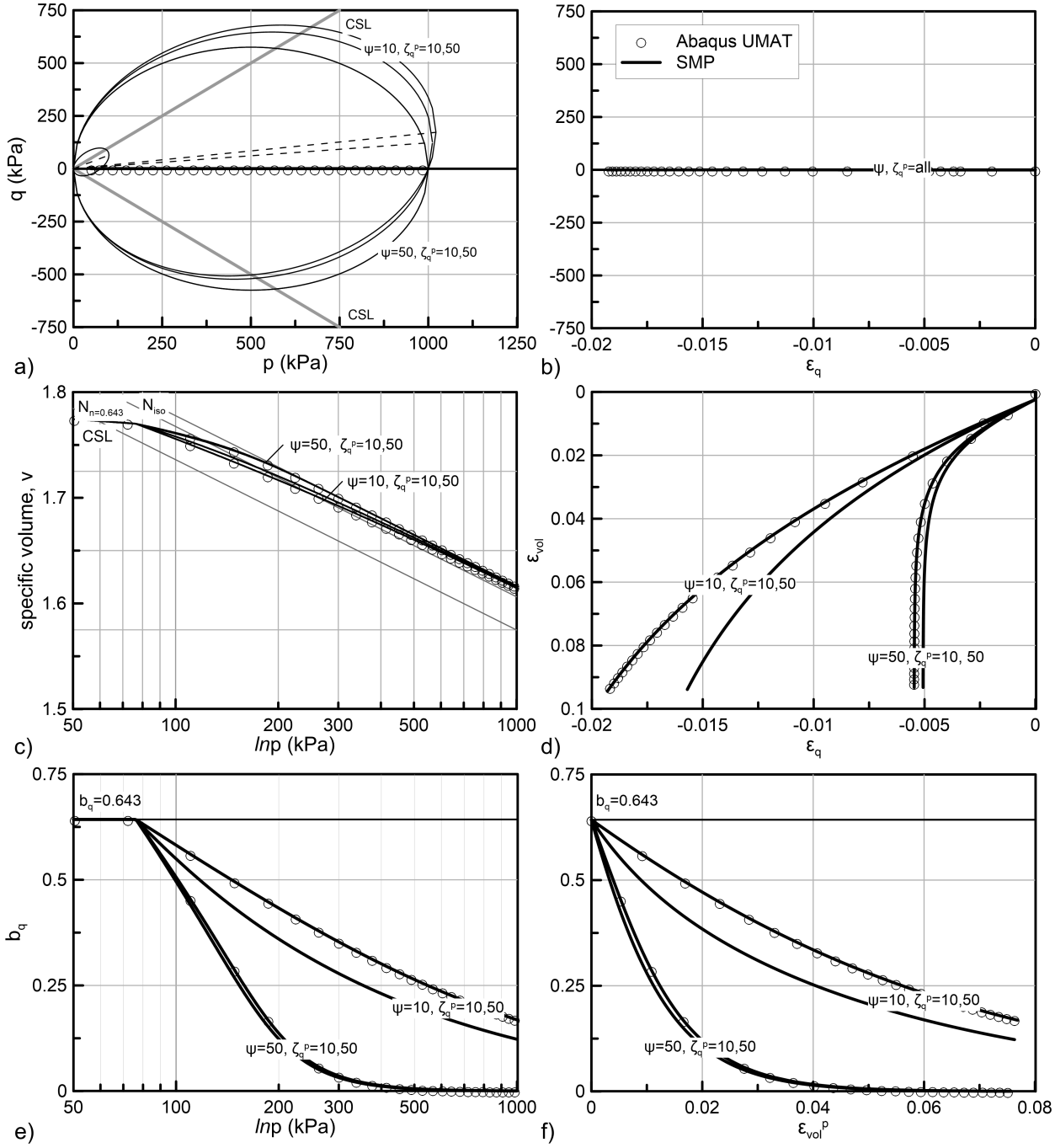


**Figure 8.9:** Isotropic compression on initially anisotropically consolidated soil elements. Combined effect of parameters $\psi$ and $\zeta_q^p$. Results from both SMP and Abaqus FEM analyses. a) the $p-q$ space; b) the $q-\varepsilon_q$ diagram; c) the $v-\ln p$ plane; d) the $\varepsilon_{vol}-\varepsilon_q$ diagram; e) the $b_q-\ln p$ diagram and; f) the $b_q-\varepsilon_{vol}^p$ diagram.

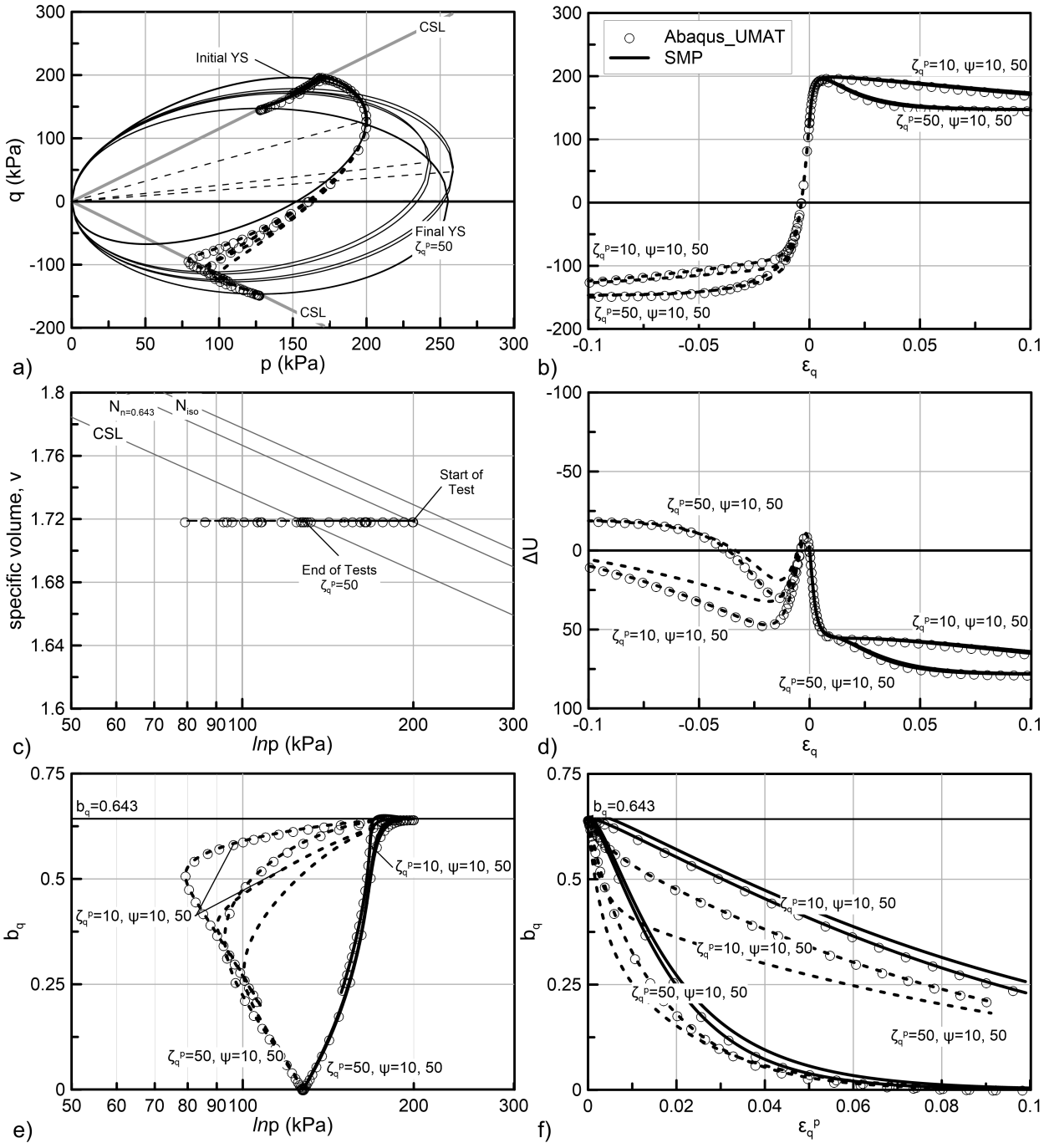


**Figure 8.10:** Undrained triaxial loading (compression and extension) of anisotropically, normally consolidated soil elements. Combined effect of parameters $\psi$ and $\zeta_q^p$. Results from both SMP and Abaqus FEM analyses. a) the $p-q$ space; b) the $q-\varepsilon_q$ diagram; c) the $v-\ln p$ plane; d) the $\Delta U-\varepsilon_q$ diagram; e) the $b_q-\ln p$ diagram and; f) the $b_q-\varepsilon_q^p$ diagram.

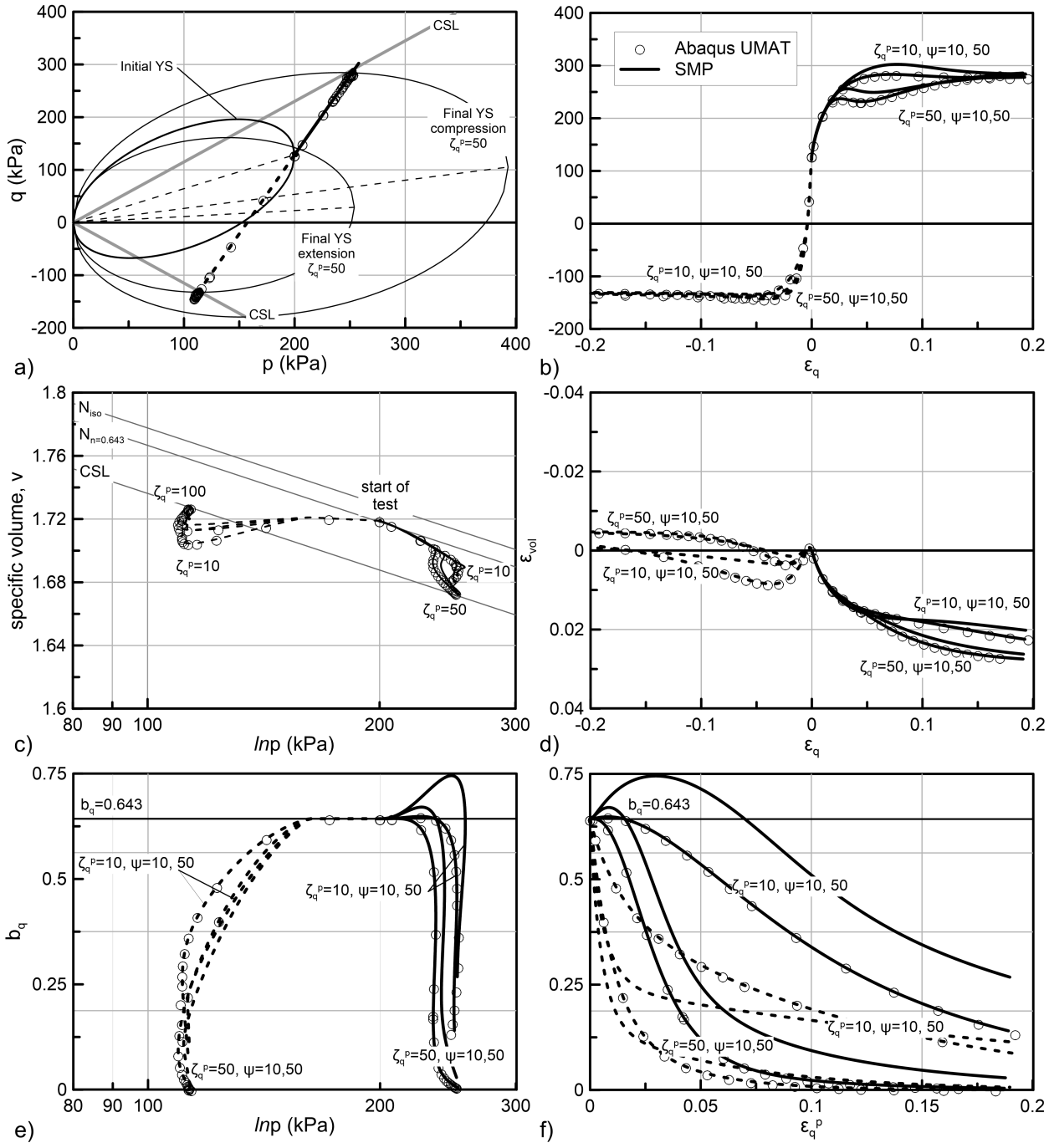


**Figure 8.11:** Drained triaxial loading (compression and extension) of anisotropically, normally consolidated soil elements. Combined effect of parameters $\psi$ and $\zeta_q^p$. Results from both SMP and Abaqus FEM analyses. a) the $p-q$ space; b) the $q-\varepsilon_q$ diagram; c) the $v-\ln p$ plane; d) the $\varepsilon_{vol}-\varepsilon_q$ diagram; e) the $b_q-\ln p$ diagram and; f) the $b_q-\varepsilon_q^p$ diagram.

incide, ensuring that both numerical tools can provide sound simulations. It should be mentioned though that for the Simulia Abaqus to efficiently handle the strong non-symmetric Jacobian deriving from the non-associated flow rule of the proposed constitutive model, the unsymmetric solver needs to be used[2], while additionally in the material definition the unsymmetric option must be activated for the program to allocate sufficient computer memory to store an unsymmetric Jacobian[3].

### 8.2.2 Flow rule parameter $\chi$

The proposed constitutive model incorporates a non-associated flow rule. It is based on a Plastic Potential Surface (PPS) mathematically described by equation 6.27, which corresponds to a distorted ellipsoid with a shape similar to that of the yield surface. Regarding the orientation of the PPS it was assumed to follow that of the yield surface through the proportionality rule of equation 6.30 with the scalar parameter $\chi$ defining the proportionality ratio.

In chapter 6, a calibration procedure was proposed to obtain suitable values of parameter $\chi$ depending on the geostatic stress ratio ($K_0$) of any given soil. The analyses of the previous two paragraphs assumed a constant $\chi$ value corresponding to the arbitrarily selected $K_0 = 0.55$ value. The efficiency of the proposed calibration procedure was discussed based on the derived results where, it was demonstrated how a suitably calibrated flow rule can reproduce: a) zero total horizontal tests during $K_0$ radial stress paths, and; b) the desired $K_0$ under oedometric conditions.

In this paragraph, we examine the dilatancy $\dot{\varepsilon}_q/\dot{\varepsilon}_{vol}$ reproduced by the selected flow rule under various radial stress paths for different $\chi$ values. Table 8.2 summarizes the $\chi$ values used in this parametric investigation.

The selected $\chi$ values correspond to the calibration's results for various $K_0$ values associated with $n = 0.25$, 0.5, 0.75 and 1.0, while two extra values, the $\chi = 1.0$ corresponding to an associated flow rule and the $\chi = 0.0$, corresponding to a non-rotating isotropic PPS have been additionally selected. We shall mention that for $K_0 > 0.68$ the proposed calibration raises negative $\chi$ values, indicating a PPS with its main axis inclined towards the extension domain.

For each one of the selected $\chi$ values, four (4) different radial stress paths, at stress ratios $n = 0.25$, 0.5 ,0.75 and 1.0 are simulated. The parameters of table 8.1

[2]This is the default option in ABAQUS when the UMAT environment is used.
[3]This is not a default option.

**Table 8.2:** The selected parameter $\chi$ values and the corresponding stress rations $n$ and $K$.

| $\chi$ | stress ratio $n$ | corresponding $K_0$ |
|---|---|---|
| -0.9542 | 0.25 | 0.786 |
| 0.0[*1] | 0.41 | 0.672 |
| 0.2355 | 0.50 | 0.625 |
| 0.5785 | 0.75 | 0.50 |
| 0.7305 | 1.00 | 0.40 |
| 1.00 | Associate flow rule | |

[*1] Isotropic plastic potential surface.

are used, while the initial conditions are similar to those adopted for the radial stress paths presented in figure 8.2. Regarding the hardening rule parameters, a relatively large $\psi = 100$ value is used, while the de-orientational component is deactivated by selecting $\zeta_q^p = 0.0$. The selected parameters ensure a rapid evolution of anisotropy and a sufficient accumulation of strains under stabilized anisotropic conditions, necessary for a clear imprint of the reproduced dilatancy at the deviatoric strains vs volumetric strains plots.

In more detail, figure 8.12 presents the analytical results of the performed analyses for the case of $\chi = 0.5785$. In graph (d) the corresponding relation between the deviatoric strain increment ($\dot{\varepsilon}_{vol}$) and the volumetric strain increment ($\dot{\varepsilon}_q$) reproduced for each one of the radial stress paths under stabilized anisotropic conditions are depicted. The presented relation is an outcome of curve fitting of a simple linear expression on the linear part of each one of the $\varepsilon_{vol}$ vs the $\varepsilon_q$ plots and represents the reproduced total (elastic and plastic) dilatancy.

Figure 8.13 summarizes similar results from the various $\chi$ values analyzed. Similar to common experimental observations, the adopted flow rule predicts an increased accumulation of plastic deviatoric strains over volumetric strains as the stress ratio of consolidation increases. Moreover, when examined under a constant stress ratio, dilation increases for decreasing $\chi$ values. One of the shortcomings of the proposed calibration procedure is that the rate at which dilatancy increases with increasing stress ratio seems to abruptly change when the analyses corresponding to negative

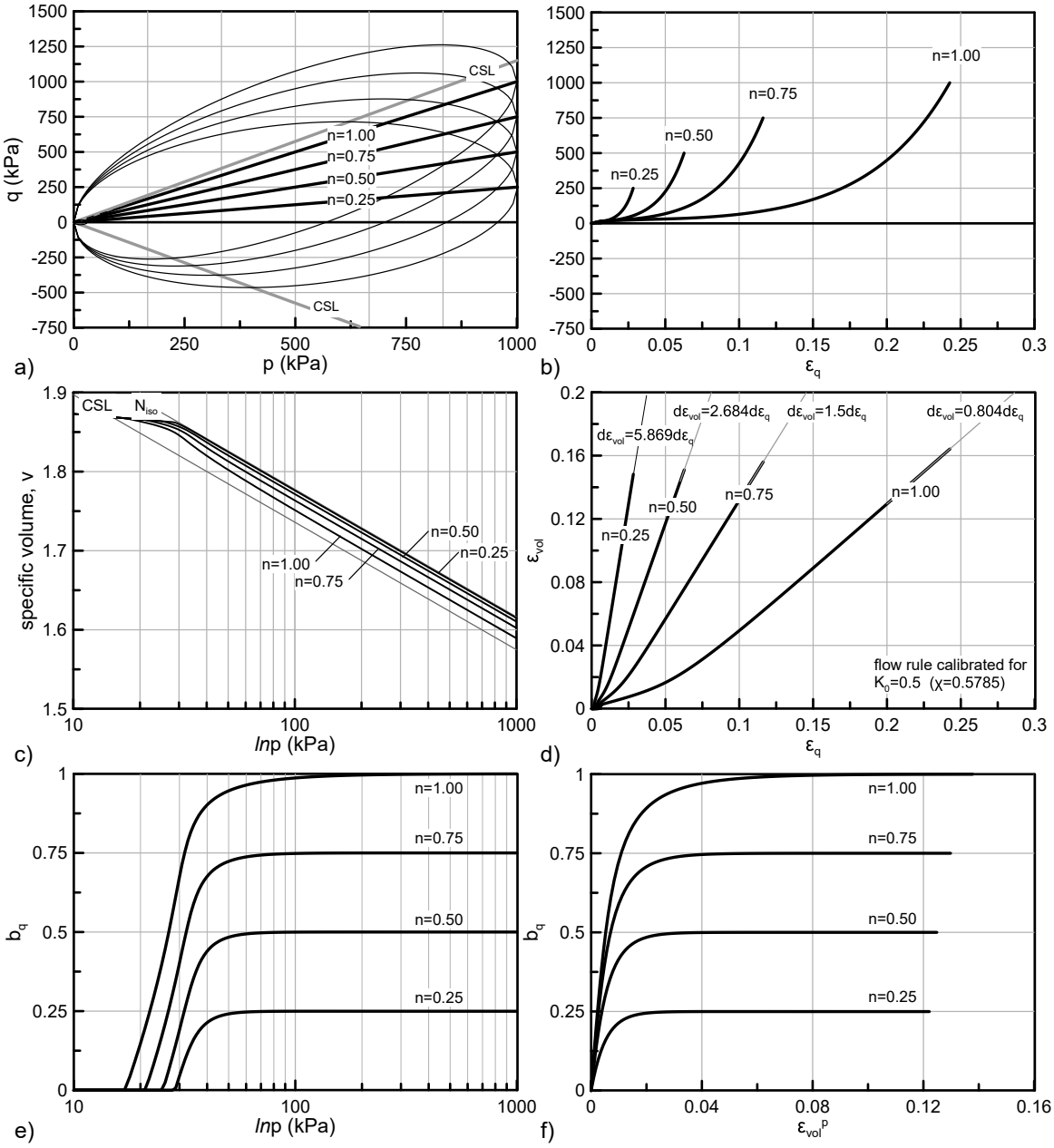


**Figure 8.12:** Radial consolidation (various $n$) on initially isotropically consolidated soil elements. Defining the reproduced total dilatancy. a) the $p-q$ space; b) the $q-\varepsilon_q$ diagram; c) the $v-\ln p$ plane; d) the $\varepsilon_{vol}-\varepsilon_q$ diagram; e) the $b_q-\ln p$ diagram and; f) the $b_q-\varepsilon_{vol}^p$ diagram..

$\chi$ values is examined. For instance, the results regarding a stress ratio $n < 0.8$ seem consistent, in the sense that the $\chi < 0$ case still describes an increased dilatancy compared with the $\chi \geq 0$ case, nevertheless this trend reverses for higher stress ratios.

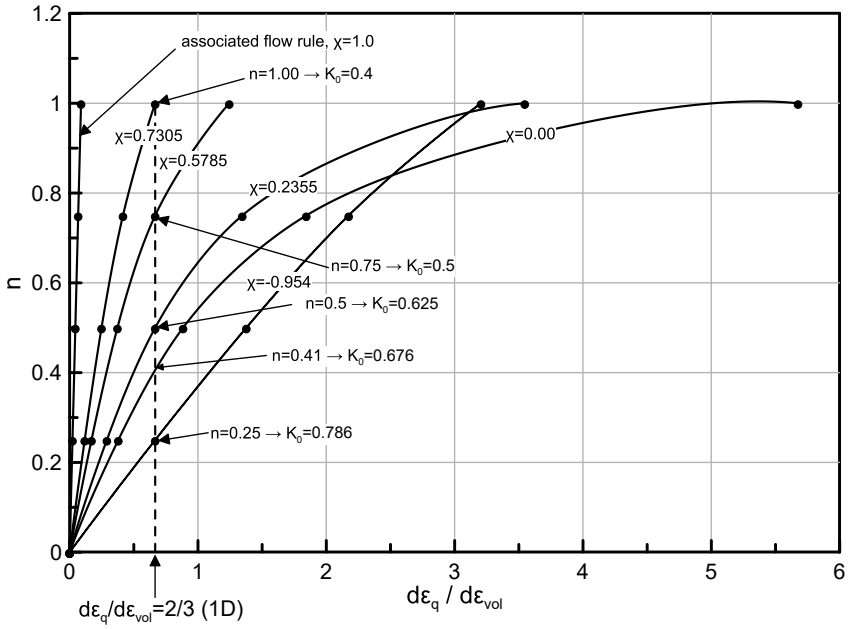


**Figure 8.13:** Effect of the flow rule parameter $\chi$ on the reproduced total dilatancy during radial consolidation.

Gens (1982) reports the dilation measured during consolidation tests from various studies, including his own results of the Lower Cromer Till. The aforementioned results were presented in chapter 5 (see fig. 3.11 and table 3.3). Figure 8.14 re-plots the aforementioned results and compares them with the predictions of the adopted flow rule. It should be mentioned that this is a qualitative comparison as the flow rule has not been calibrated for the experimental results used in the comparison. Nevertheless, the presented comparison indicates that the flow rule's predictions, when calibrated for realistic $K_0$ values can successfully predict realistic strain ratios, in close agreement with the range of values determined in laboratory tests.

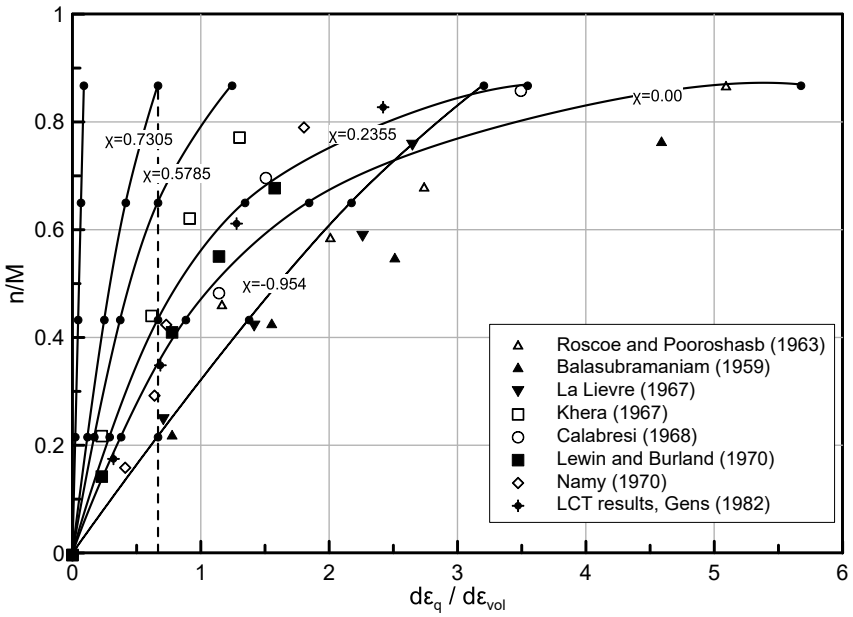


**Figure 8.14:** A qualitative comparison of the model's predicted total dilatancy with experimental results.

### 8.2.3 Shear strength predictions under different anisotropic states and stress paths

The already presented and discussed analyses focused on the effect of various constitutive parameters on the model's predictions, demonstrating some of the anisotropic capabilities of the developed model. Nevertheless, the behaviour of the proposed constitutive model under different levels of initial anisotropy and different stress paths (loading directions) has not been extensively covered.

To address this issue, a set of additional analyses is performed. Figure 8.15 presents the results from numerical simulations where, anisotropically consolidated soil element are subjected to undrained triaxial compression and extension tests, initiating from different levels of stress induced anisotropy ($n$ = 0.25, 0.5, 0.643, 0.75 and 1.0). The results corresponding on an isotropically consolidated soil element ($n$ = 0.0) are additionally included for comparison. The soil elements are loaded from normally consolidated initial conditions, corresponding to $p = p_0 = 200kPa$, while the deviatoric stress ($q$) follows the corresponding stress ratio. The model parameters of table 8.1 are used, while for the hardening rule $\psi = 30$ and $\zeta_q^p = 50.0$ are

selected.

We observe (see fig. 8.15) that all elements exhibit a strain softening response in undrained compression (with the exception of the isotropically consolidated one) with clearly defined peak and residual states. Both peak and residual strength increase with the stress ratio of the consolidation. The $n = 1.0$ analysis produced a peculiar hook-type behaviour, in the $p - q$ space, also reflected in the $q$ vs $\varepsilon_q$ and $\Delta U$ vs $\varepsilon_q$ plots. This behaviour is considered rather unrealistic and can be attributed to the increased consolidation stress ratio, locating the initial stress state very close to the critical state line.

With respect to the volumetric behaviour, as this is reflected in the developed excess pore pressures, all compression tests develop positive excess pore pressures, indicating a tendency for contraction, with the latter decreasing as the initial anisotropy increases.

Regarding the triaxial extension tests, all elements exhibit a continuously strain hardening response, with the exhibited strength increasing with an increasing initial anisotropy. Figure 8.16 presents normalized graphs of the anticipated behaviour, allowing for a qualitative assessment of the obtained results. Results from another set of similar simulations, corresponding to an increased preconsolidation pressure of $p_0 = 500kPa$ are also included, while their detailed results are not presented.

Graph 8.16a plots the ratio of the deviatoric stress at peak ($q_{peak}$) over the deviatoric stress at the ultimate state ($q_{ult}$). The results from triaxial compression tests indicate an increased "brittleness" with increasing anisotropy. For the triaxial extension tests, there is no difference between the peak and the ultimate state as the soil samples continuously strain harden.

In graph 8.16b we may observe the stress ratio $q/p$, corresponding to the ultimate state and to the peak deviatoric strain. In all cases, the stress ratio at the ultimate state coincides with the critical state slope assumed, clearly demonstrating the proposed model's ability to reproduce unique critical state conditions, irrespectively of the initial state of anisotropy. Regarding the stress ratio at peak, for the compression tests, it seems that it initially decreases with an increasing initial anisotropy, reaching a minimum for $n = 0.25$ and then progressively increases. It gets almost equal to that of the ultimate state for $n = 0.6428$ (corresponding to $K_0$ in the presented case).

The results corresponding to different preconsolidation pressures ($p_0 = 200kPa$ and $p_0 = 500kPa$) coincide, a reflection of the critical state soil mechanics' principle

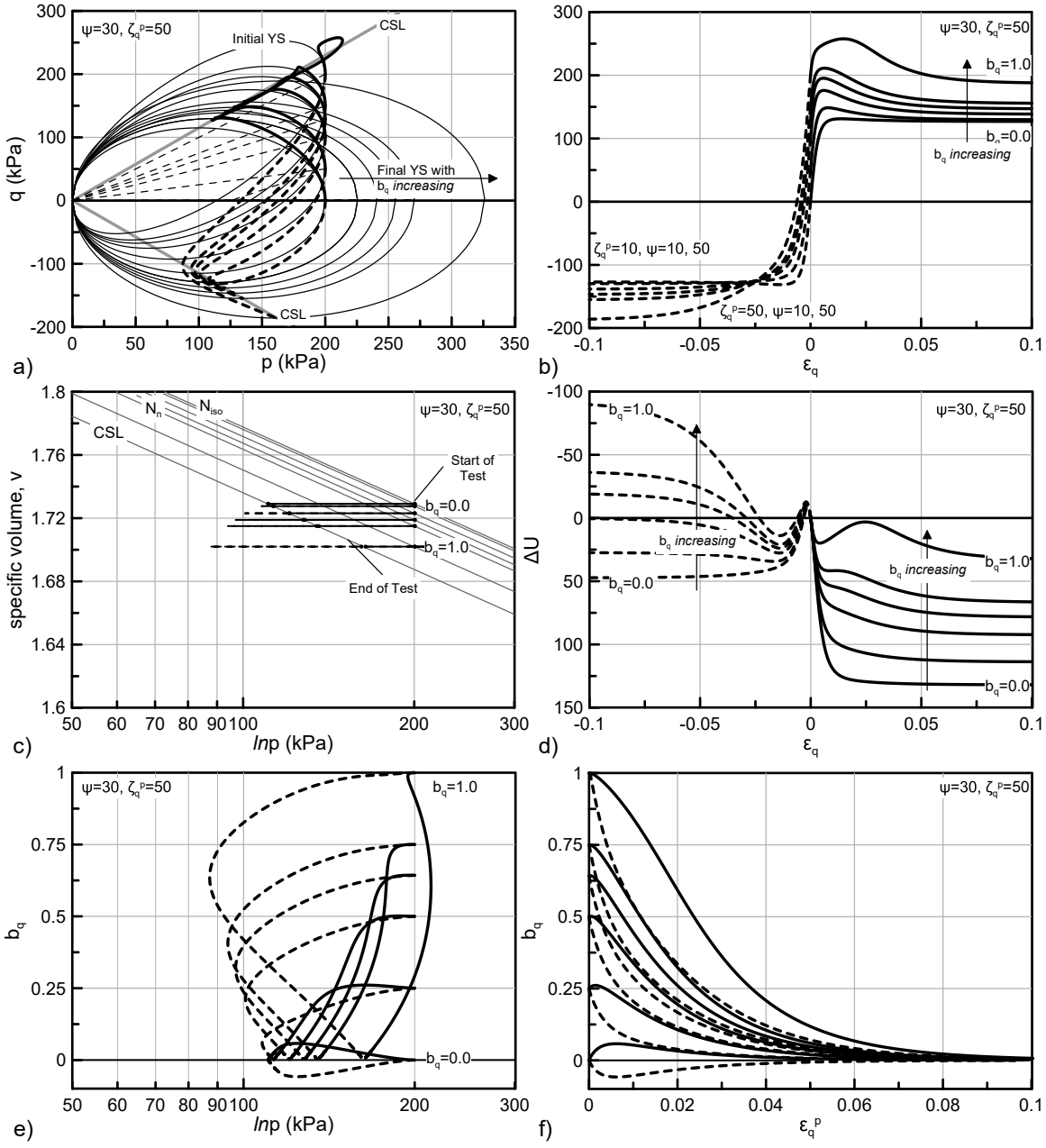


**Figure 8.15:** Undrained triaxial loading (compression and extension) of anisotropically, normally consolidated soil elements. The effect of different initial anisotropic conditions. a) the $p-q$ space; b) the $q-\varepsilon_q$ diagram; c) the $v-\ln p$ plane; d) the $\Delta U-\varepsilon_q$ diagram; e) the $b_q-\ln p$ diagram and; f) the $b_q-\varepsilon_q^p$ diagram.

that the behaviour is normalizable in terms of the preconsolidation pressure.

Comparing the anticipated simulation results with the usually observed experimental behaviour, as the latter has been discussed in chapter 3, it seems that at least in a qualitative manner, the proposed model is capable of capturing most of the behavioural trends of anisotropically consolidated soils. The similarity in response between figure 8.16 and figure 3.22 of Gens (1982) is quite indicative.

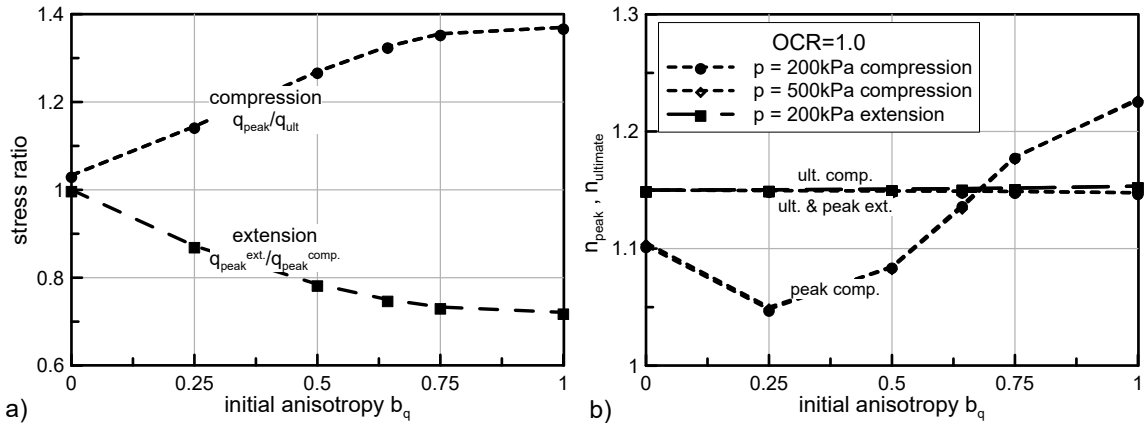


**Figure 8.16:** Normalized results of the evolution of the peak and residual strength with initial anisotropy.

The analyses presented hereinbefore focused on the usually called "wet side", as only normally consolidated soil elements have been considered. To evaluate the model predictions on the "dry side", figure 8.17 reports the results of simulations on overconsolidated soil samples with $OCR = 4.0$. The initial consolidation conditions are assumed identical to those of figure 8.15, but the soil elements are elastically unloaded to $p = 50kPa$, $q = 0kPa$[4], prior to triaxial loading.

It is observed that the anisotropically consolidated soil elements subjected to undrained triaxial compression still exhibit a significant strain softening with a well defined peak and a common ultimate state, contrary to common experimental results, which indicate that overconsolidated soil samples continuously strain harden. We may attribute the aforementioned inability of the model to capture well the behaviour, to its large elastic region. Such a handicap is typical of single yield surface models when the initial conditions of the simulated stress path lie well inside the yield surface.

[4]A $K_0 = 1.0$ is assumed for $OCR = 4.0$

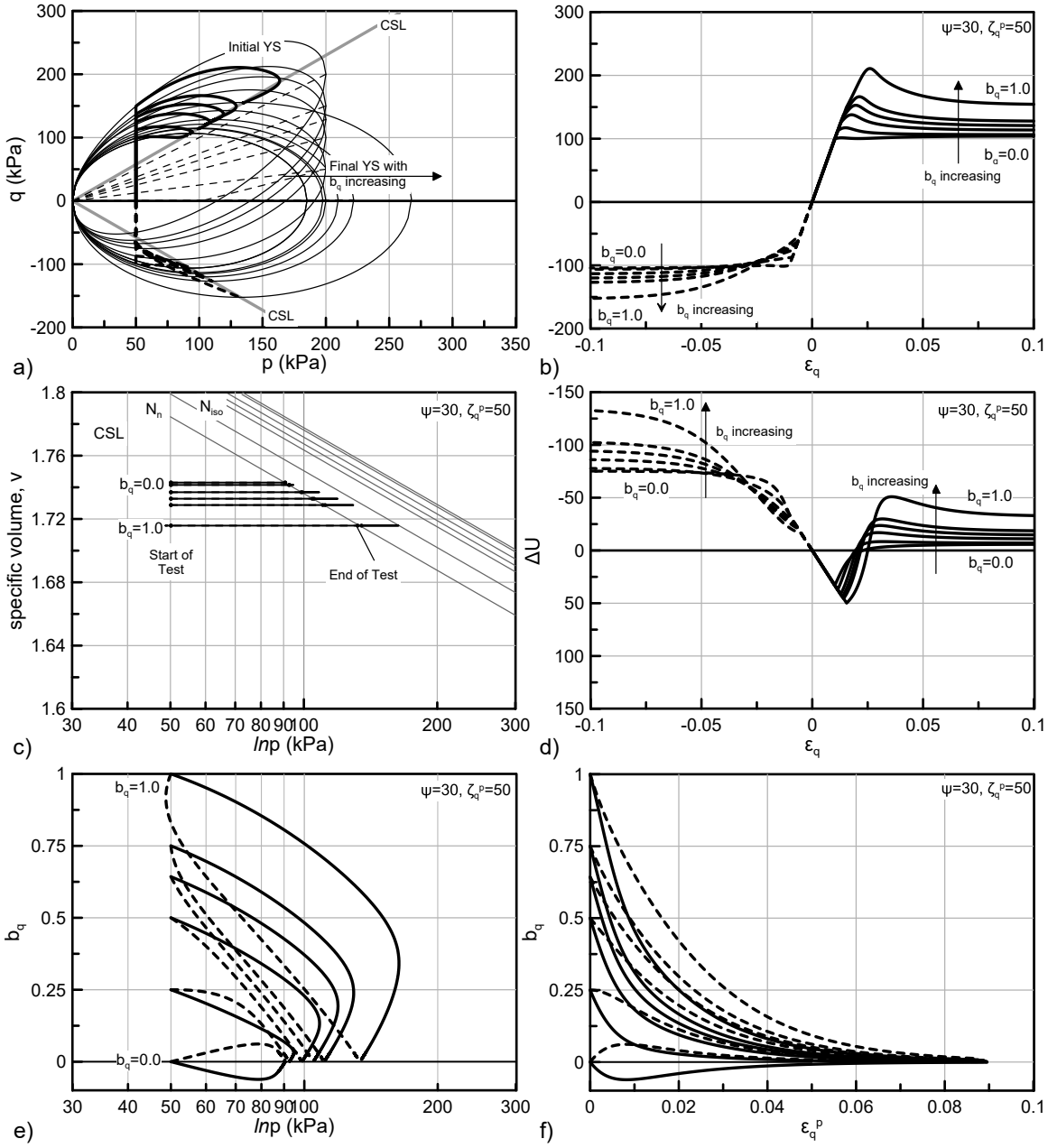


**Figure 8.17:** Undrained triaxial loading (compression and extension) of anisotropically, overconsolidated ($OCR = 4.0$) soil elements. The effect of different initial anisotropic conditions. a) the $p - q$ space; b) the $q - \varepsilon_q$ diagram; c) the $v - \ln p$ plane; d) the $\Delta U - \varepsilon_q$ diagram; e) the $b_q - \ln p$ diagram and; f) the $b_q - \varepsilon_q^p$ diagram.

In reality, usually soils exhibit a very limited elastic (reversible) behaviour. As briefly discussed in chapter 2, in soil plasticity, such a behaviour can be captured by bubble models, utilizing the principles of bounding surface plasticity. Bubble models incorporate a very limited elastic region enclosed by the PYE which kinematically hardens towards the bounding surface. Incorporating such a small elastic region in the proposed model would significantly improve the predictions regarding overconsolidated soil samples. The accumulated plastic strains inside the saturated strength envelope would activate the de-orientational component of the hardening rule to gradually erase the memory of anisotropy and thus significantly reduce the observed peak.

Nevertheless, including an inner yield surface to the proposed model is not an easy task. The fact that the yield surface is a distorted ellipsoid with a constantly evolving orientation due to changes in primary anisotropy and an evolving size due to changes in the state of partial saturation, makes the formulation of the necessary interpolation rules quite demanding and it was deliberately selected not to include such small-strain stiffness characteristics at the current version of the proposed constitutive model. This decision inevitable comes with a sacrifice of the model's capabilities to realistically capture the behaviour of overconsolidated soils.

Finally, in figure 8.18, the model's predictions under different stress paths are presented. In more detail, an anisotropically normally consolidated soil sample, is subjected to four different loading conditions, all of them performed under undrained conditions. The tests include a triaxial compression and a triaxial extension test, a direct simple shear test and a plane strain test. The initial anisotropy has been established on the triaxial stress space, corresponding to the conditions usually anticipated in the field (geostatic conditions of a sedimentary soil).

The results are also compared with the predictions of the Modified Cam Clay. For a fair comparison, the initial conditions in both sets of tests are identical, and thus the anisotropy of the stress tensor is there, hence the only difference in behaviour arises from the fact that the proposed model accounts for the memory of preferred directions.

We may observe that the MCC model predicts a common peak irrespective of the examined test. On the other hand, the results of the proposed model differ significantly. It can reproduce a clear peak strength, followed by a strain softening response in the triaxial compression and plane strain tests, with the peak observed

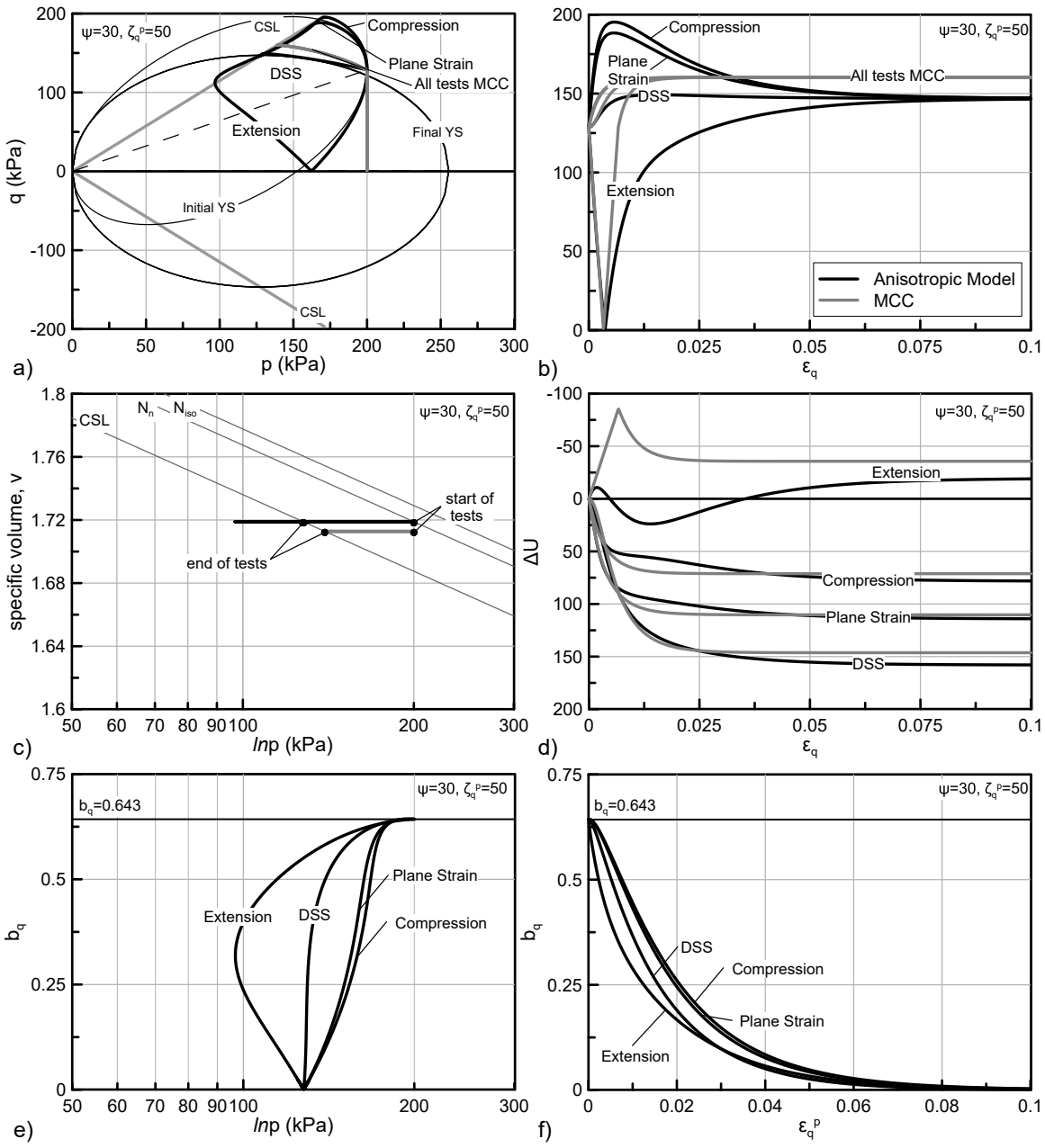


**Figure 8.18:** Undrained triaxial loading (compression and extension), plane strain and direct simple shear tests on anisotropically, normally consolidated soil elements. Comparison between the Modified Cam Clay and the proposed model's predictions. a) the $p-q$ space; b) the $q-\varepsilon_q$ diagram; c) the $v-\ln p$ plane; d) the $\Delta U-\varepsilon_q$ diagram; e) the $b_q-\ln p$ diagram and; f) the $b_q-\varepsilon_q^p$ diagram.

during triaxial loading, slightly higher than this of the plane strain test. The Direct Simple Shear (DSS) test exhibits a slight initial strain hardening behaviour, followed by an almost negligible strain softening and thus, its peak and residual states almost coincide. Finally the extension test continuously strain hardens up to its residual state.

This difference in the observed peak strength is attributed to the different principal directions corresponding to the simulated stress paths and to the models capability to account for the effect of different principal directions. Additionally for the case of the DSS, the plane strain and the triaxial extension tests the corresponding principal directions differ with respect to the principal directions of the initially imposed anisotropy. Note that the initial anisotropy and the loading direction do not influence the residual state, as all tests result at a unique residual state.

## 8.3 Unsaturated Characteristics

Following the discussion on the model's anisotropic capabilities, this section deals with its unsaturated characteristics. In chapters 5 and 6 it was explained how the proposed model predicts a decreasing compressibility and increasing elastic domain with an increase in suction, as well as how the unsaturated compressibility evolves with the degree of saturation even under constant suction. The model's unsaturated compressibility is reflected in the slope ($\lambda(s, S_r^e)$) of the virgin compression lines through equation 5.24.

Equation 5.24 includes three material constants, namely, parameters $r$, $\beta$ and $\gamma$. Regarding the increase in the elastic domain, it is described by equation 5.30, defining the variation of the apparent preconsolidation pressure with partial saturation, as an outcome of the reduced unsaturated compressibility. An extra parameter, the reference pressure $p^c$ is involved in the definition of the apparent preconsolidation pressure.

As discussed, the aforementioned parameters can be derived on the bases of experimental results under different suction levels. Usually, provided that laboratory tests under at least two (2) different suction levels are available, no trial and error simulations are required. For that reason, none of the aforementioned parameters is parametrically investigated in this section. Instead, their calibration is further discussed in the following chapter based on actual experimental results.

Thus, in this section constant values are assumed and the study focuses on the model's performance under different suction levels. Table 8.3 summarizes the selected parameters, assumed representative of the typical behaviour of a silty soil. Apart from the "unsaturated parameters", table 8.3 additionally includes the assumed Gallipoli et al. (2003) WRM's parameters. Finally, to calculate the effective degree of saturation, the Alonso et al. (2010) power law is used, while parameter $\alpha$ is selected equal to 2.5 ($\alpha = 2.5$), assumed representative of a silty soil as well. Figures 8.19 and 8.20, present the assumed evolution of: a) the degree of saturation $S_r$ and of the term $s \cdot S_r^e$ and; b) compressibility ($\lambda(s, S_r^e)$), with suction ($s$).

**Table 8.3:** The assumed parameters for the presented analyses. Used in combination with the parameters of table 8.1. The anisotropic characteristics of the model are deactivated.

| Unsaturated Parameters | | WRM Parameters | |
|---|---|---|---|
| Parameter | Value | Parameter | Value |
| $r$ | 0.8 | $\phi$ | 0.011 |
| $\beta$ | 100.0 $kPa^{-1}$ | $n$ | 1.005 |
| $\gamma$ | 0.8 | $m$ | 0.567 |
| $p^c$ | 1 $kPa$ | $\psi$ | 4.0 |
| Alonso et. al. (2005) power law | | | |
| $\alpha$ | 2.5 | | |

In this section we deal exclusively with the predictions of the model regarding partial saturation effects, while the effects of primary anisotropy are neglected. In other words, the presented analyses correspond to a simple isotropic constitutive model, similar to the MCC, with the addition of unsaturated characteristics. The following two subsections deal with constant suctions tests. The first one with simple isotropic compression tests under different suction levels, while the second one with triaxial loading tests. A third subsection follows, where wetting tests are performed to evaluate the model's capability to simulate volumetric collapse.

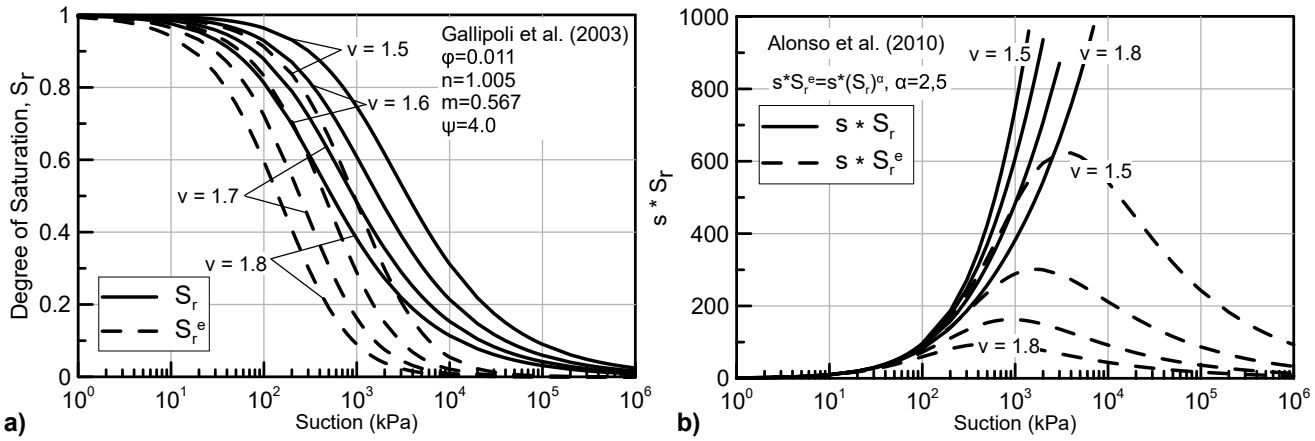


**Figure 8.19:** a) The assumed Water Retention Behaviour and; b) the corresponding evolution of the $s \cdot S_r^e$.

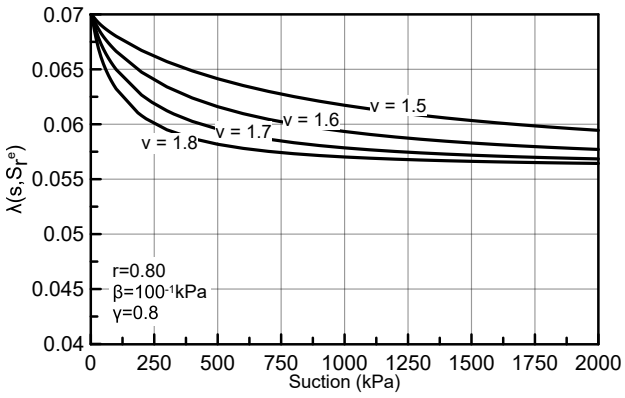


**Figure 8.20:** The variation of the unsaturated compressibility $\lambda(s, S_r^e)$ with suction, corresponding to different WRCs of fig. 8.19.

### 8.3.1 Isotropic compression tests at different suction levels

Constant suction tests are widely utilized in studying the mechanical behaviour of unsaturated soils. Suction control requires specialized laboratory equipment (i.e., the Bishop's double cell for triaxial testing, suction control oedometer), incorporating one of the available techniques for suction application and control (i.e., axis-translation technique, osmotic method, relative humidity control etc.) .

Constant suction tests provide useful information regarding the evolution of the mechanical characteristics of the tested soil like compressibility, yielding and shear strength with suction. They usually include an initial compression stage under saturated conditions, followed by a drying stage where suction is progressively increased to the desired level. Afterwards, upon reaching hydraulic equilibrium, the soil specimen is loaded under drained conditions by imposing either stress or displacement increments, depending on the type of the test.

Performing isotropic compression tests under different suction levels is probably the most appropriate type of test to define the evolution of yield stress and compressibility with partial saturation. Contrary to oedometer tests, which are usually easier to perform and thus preferred in laboratory practice, isotropic compression tests draw solid conclusions on the unsaturated behaviour of soils, independent of the effects of anisotropy.

Figure 8.21 presents the simulation results of isotropic compression tests on initially overconsolidated saturated soil elements. Prior to compression they are dried to seven (7) different suction levels ranging from $s = 50kPa$ to $s = 5MPa$. The selected suction values provide a complete evaluation of the model's predictions along an extended portion of the assumed WRC.

The initial saturated conditions correspond to a preconsolidation pressure of $P_0^* = 100kPa$ and an initial mean effective stress of $p = 50kPa$, while suction is assumed equal to zero ($s = 0kPa$) and thus net and Bishop's stress coincide. A drying stage, under constant net stress, is simulated for the soil element to reach the desired suction level. Finally, the soil elements are isotropically compressed by raising the mean net stress up to $\overline{p} = 5.0MPa$. Figure 8.21 presents the results of the performed simulations, including graphs for the behaviour in the mean stress vs deviatoric stress space with characteristic plots of the yield surface, the stress -strain behaviour (in triaxial loading tests), the volumetric response in terms of the specific volume and additionally the behaviour on the suction - mean stress and the water retention behaviour

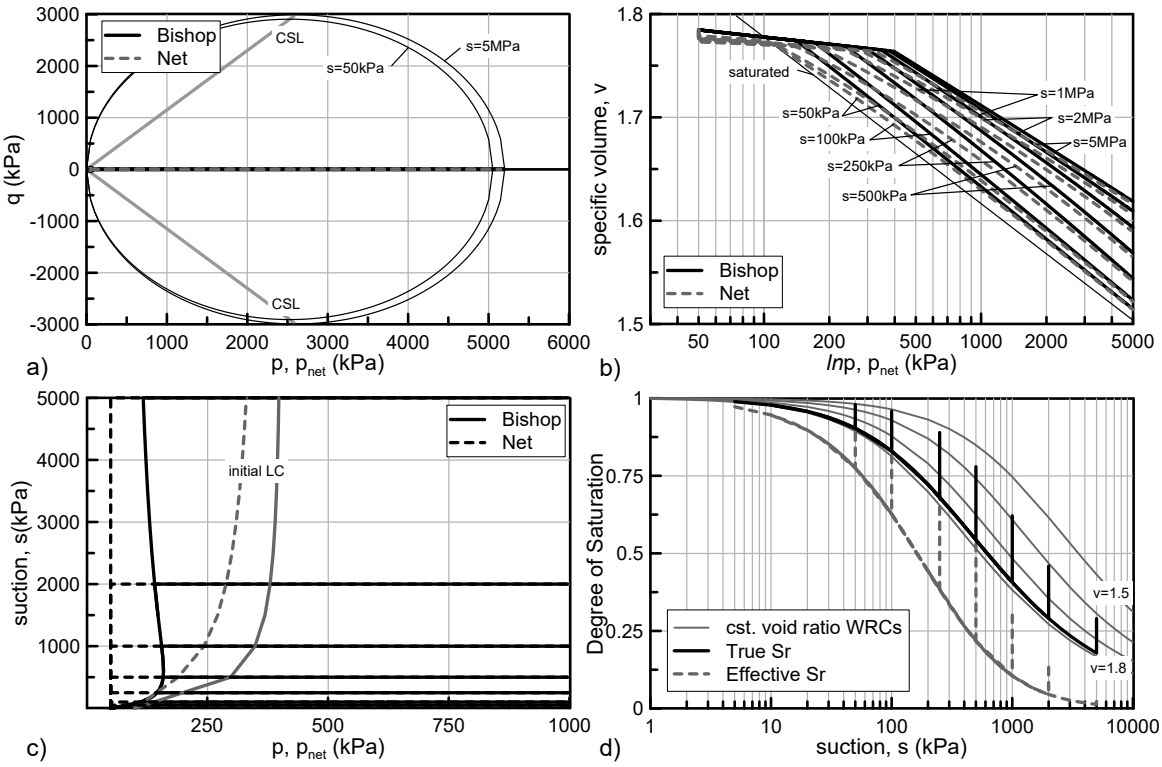


**Figure 8.21:** Isotropic compression under seven different constant suction levels. a) the $p, \overline{p} - q$ planes; b) the $v - \ln p, \overline{p}$ planes; c) the $p, \overline{p} - s$ planes and; d) the $S_r, S_r^e - s$ plots.

during the simulations. All stress paths are plotted both in terms of Bishop's and in terms of net stress.

In figure 8.21b the results of the isotropic compression tests in the $v - \ln p$ and $v - \ln \overline{p}$ planes are depicted. We may observe that, the proposed constitutive model can successfully reproduce an nonlinear increase in the yield stress with suction, both in the Bishop stress and in the net stress domain (see LC curve in graph 8.21c).

In the elastic domain, it is evident that when plotted in terms of Bishop's stress all test results lie on the same swelling line, a direct consequence of the assumption that the elastic behaviour is not influenced by partial saturation apart from the implicit influence of Bishop's stress. Nevertheless, when the same behaviour is plotted in terms of net stress, we observe the reduction in the specific volume due to suction increase under constant net stress, followed by an elastic non-linear response, as the slope of the swelling lines on the $v - \ln \overline{p}$ is not constant but reduces with an increase in suction. At this point we shall recall that net stress models, usually assume a constant elastic

compressibility (i.e., Barcelona Basic Model) mainly due to simplicity, although there are experimental evidence in favour of suction dependant swelling lines (i.e., Rampino et al. (2000)). In our case, the aforementioned dependence stems naturally from Bishop's stress formulation, as has been also widely discussed in Jommi (2000).

With respect to the post yield compressibility, note that the model can sufficiently represent the desired volumetric behaviour as introduced in chapter 5, predicting a continuously evolving compressibility for compression under constant suction. In more detail, comparing the slope of the compression lines under the same net stress but different suction levels, we may observe that an increased suction is in favour of a decreased post yield compressibility, reflecting the beneficial effect that partial saturation has in stiffening the soil behaviour. Moreover, the volumetric behaviour depends also on the level of the applied net stress with the compression curves under constant suction indicating an initially decreased compressibility, compared to a saturated state, which progressively increases as net stress increases. The shape of the reproduced compression lines is very reminiscent of the compression lines assumed in constitutive models which try to address the issue of a maximum in collapse (i.e., Josa et al. (1992), Georgiadis (2003)), while in the proposed model is a direct and natural outcome of the double dependance of the compression lines on the suction and the degree of saturation.

In figure 8.22 the results of the SMP algorithm for three suction levels ($s = 100$, 500kPa and 2.0 MPa) are compared with their counterparts obtained through Abaqus FEM analyses with the developed UMAT subroutine. The results regard coupled hydromechanical analyses, while the axis-symmetric numerical model presented in chapter 7 is used. The results confirm that the developed UMAT can successfully handle unsaturated analyses. It is reminded that the original UMAT subroutine available in ABAQUS cannot account for the exchange of the pore pressure (suction) and degree of saturation, as it is oriented towards saturated soil's analyses. In that respect, the results demonstrate that the undertaken modification (utilization of the User Defined Field Variables) successfully address this inherent UMAT shortcoming.

On the other hand, unfortunately the results are highly influenced from the Abaqus' inability to account for a void ratio dependant water retention behaviour. In fact any constant suction stress path, in Abaqus corresponds to a constant degree of saturation stress path as well. This is no doubt an important deficit which inevitably alters the results and to some extend cancels significant characteristics of

the developed model.

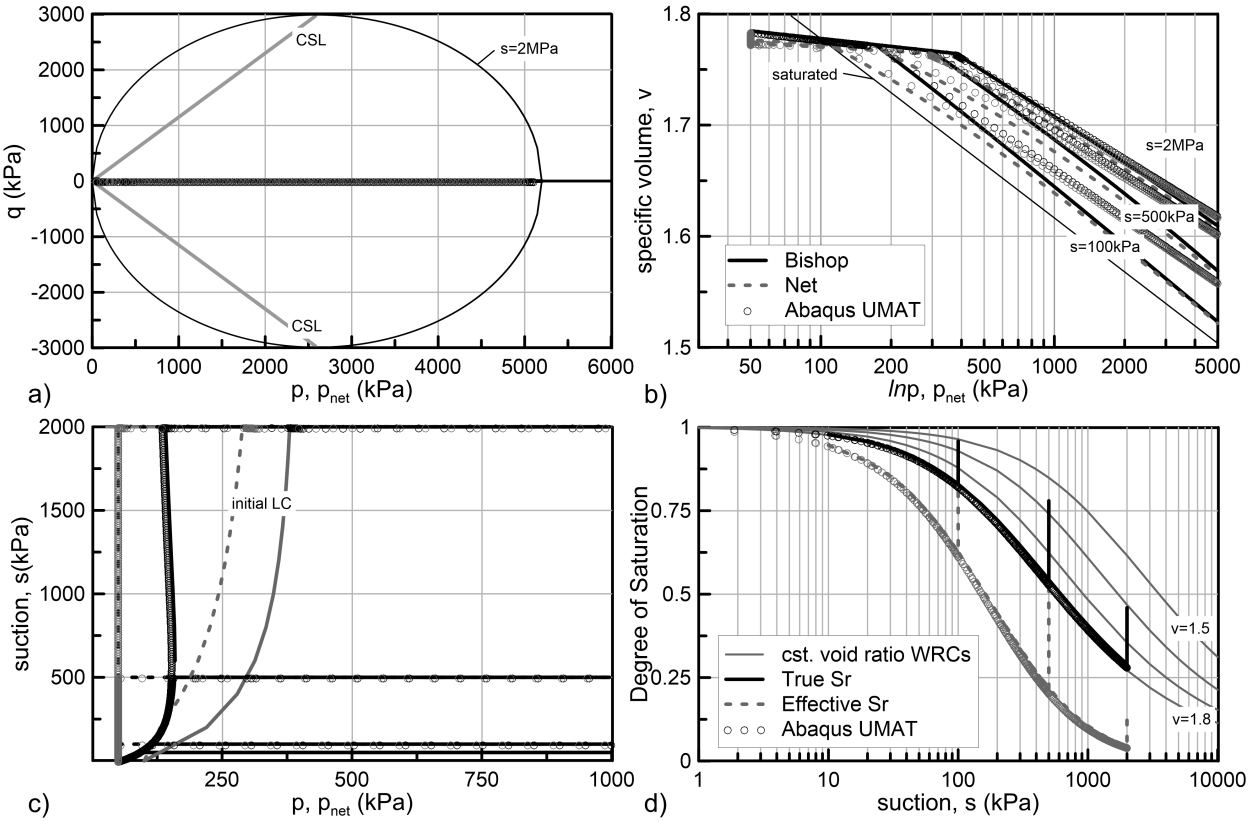


**Figure 8.22:** Isotropic compression tests under three different constant suction levels. Results from both SMP and Abaqus FEM (cst. WRC) analyses. a) the $p, \overline{p} - q$ planes; b) the $v - \ln p, \overline{p}$ planes; c) the $p, \overline{p} - s$ planes and; d) the $S_r, S_r^e - s$ plots.

The results of figure 8.22 indicate that a constant WRC primary affects the post yield compressibility, reproducing a constant compressibility in the Bishop's stress domain (linear on the $v - \ln p$), also reflected on the anticipated behaviour in the $v - \ln \overline{p}$ plane. The latter is expected to affect significantly the reproduced wetting induced collapse and is further analyzed in a following paragraph. On the other hand, the evolution of the apparent preconsolidation pressure, developed during the initial drying stage, is not significantly affected. This is reasonable if we consider that during drying, only elastic volumetric strains accumulate, corresponding to a limited volume change which cannot alter the water retention characteristics significantly.

### 8.3.2 Triaxial loading (compression) tests under constant suction

It is well known that partial saturation is in favour of an increased shear strength (see chapter 4). Moreover, this increase in strength is a nonlinear function of suction. For instance, clays in general are expected to exhibit a continuously increasing shear strength with suction, with a continuously decreasing rate of increase though. On the other hand, sandy soils, although at relatively low suction values demonstrate an increase in their shear strength, this increase usually reaches a maximum after which, further drying leads to a drop of their shear strength.

The present subsection evaluates the proposed model's ability to describe a non-linear evolution of the shear strength with suction and additionally discusses the critical state conditions reproduced. It is reminded that the parameters selected for this ongoing evaluation of the model's characteristics are representative of a silty soil, and thus, the shear strength predictions are expected to lie somewhere in-between the two extremes mentioned above.

Evaluation is based on a series of simulations of triaxial loading (compression) tests under different suction levels, ranging from $s = 50kPa$ to $s = 5MPa$. The soil elements are initially isotropically consolidated under saturated conditions up to $p_0^* = 100kPa$ and then dried under constant mean net stress to the desired suction level. Then they are isotropically compressed under constant suction, up to three different mean net stress levels, namely $\overline{p} = 500,\ 1000,$ and $1500kPa$. Finally they are subjected to triaxial loading under a constant suction and constant net confining stress. Constant suction tests are in fact drained tests and thus, the soil elements excibit significant strain hardening. For that reason a relatively high $\varepsilon_q$ is selected, for all tests to reach critical state conditions.

Figure 8.23 presents results regarding different suction levels and a common confining stress of $\overline{p} = 500kPa$. We may observe that the stress state at which the triaxial compression stage initiates, lies well above the apparent preconsolidation pressure that the material develops during drying, and thus all results regard normally consolidated soil elements. All elements exhibit a strain hardening response and a contractant behaviour. The final states of the various Bishop's stress paths are located on a common CSL, while on the contrary in the $v - \ln \overline{p}$ plane different CSLs apply to each suction level. Regarding the ultimate deviatoric stress reached, the lower strength is exhibited by the saturated soil sample (sheared under zero suction), while

a maximum is exhibited by the analysis under $s = 1000kPa$. Regarding dilatancy, the anticipated volumetric strains seem to increase, with respect to the saturated one, until the $s = 250kPa$ analysis and then decrease significantly for further suction increase. In fact the volumetric strains accumulated, reflect the compressibility of the soil elements during the triaxial compression.

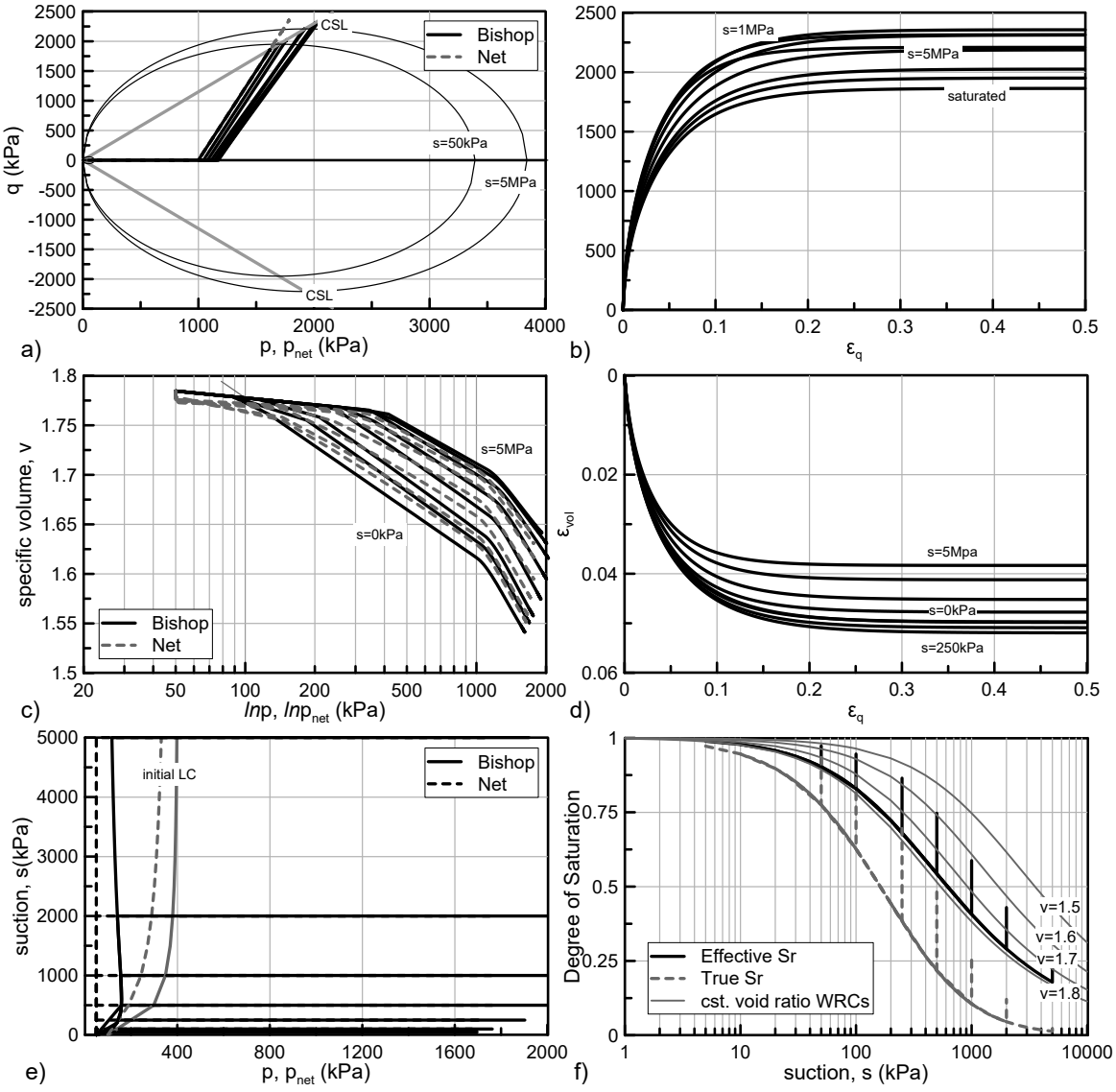


**Figure 8.23:** Drained (cst. suction) triaxial loading of isotropically, normally consolidated ($\overline{p} = 500kPa$) unsaturated soil elements under seven different constant suction levels. a) the $p, \overline{p} - q$ planes; b) the $q - \varepsilon_q$ diagram; c) the $v - \ln p, \overline{p}$ planes; d) the $\varepsilon_{vol} - \varepsilon_q$ diagram; e) the $p, \overline{p} - s$ planes and; f) the $S_r, S_r^e - s$ plots.

The plots presented in figures 8.24 and 8.25 summarize the predicted evolution of shear strength with suction. In figure 8.24a the evolution of the ultimate deviatoric stress reached ($q_u$) with suction for the three different net stress levels is given, while, figure 8.24b plots the same results in terms of the normalized term ($q_{u,s}/q_{u,s=0}$) corresponding to the ultimate deviatoric stress of each tests with respect to the ultimate deviatoric stress of the same material when saturated (with $s = 0$) at the same confining net stress level.

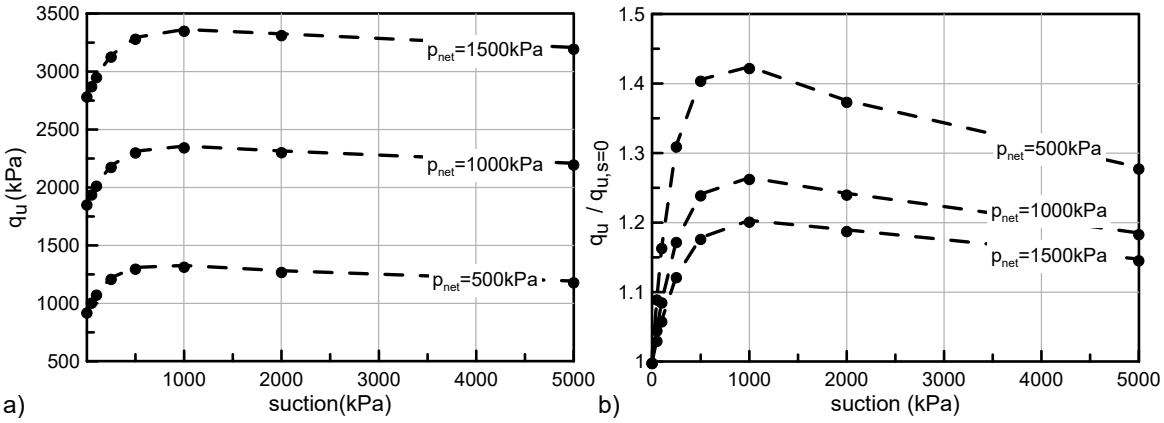


**Figure 8.24:** Evolution of the ultimate strength with suction. a) the $q_u$ vs suction and; b) the $q_{u,s}/q_{u,s=0}$; both for three different levels of net confining pressure $\overline{p}$.

The results clearly demonstrate the proposed constitutive model's ability to represent a nonlinear evolution in shear strength with suction. For the selected material parameters, shear strength increases significantly until a peak is observed for $s = 1000kPa$ and then decreases for further suction increase, still remaining higher than the corresponding saturated one. Additionally, it turns out that beneficial effect of partial saturation in shear strength, decreases as net stress increases. In more detail, both partial saturation and an increased net stress favour an increased shear strength, as clearly depicted in figure 8.24a. Nevertheless, the normalized results of figure 8.24b demonstrate that as net stress increases the effect of confining stress becomes more dominant and thus, comparatively reduces the effect of partial saturation.

Figures 8.25 and 8.26 extend the discussion to the predicted critical state conditions. In figure 8.25a the final stress states are plotted in terms of Bishop's and

in terms of net stress. As expected, in the Bishop's stress domain all states plot on a common critical state line with $M = 1.15$, corresponding to the one selected for the analyses. Nevertheless, when plotted in terms of net stress an individual critical state line can be identified for each suction level. The critical state lines do not pass through the axis origin, while moreover, they are not parallel, with their inclination dependent on the level of the applied suction. Jommi (2000) highlighted that different but parallel CSLs turn out in the $v - \ln \overline{p}$ plane whenever Bishop's stress is used in any critical state effective stress model, while additionally the tensorial translation $(-P_s)$ follows the evolution of the $s \cdot S_r^e$ term.

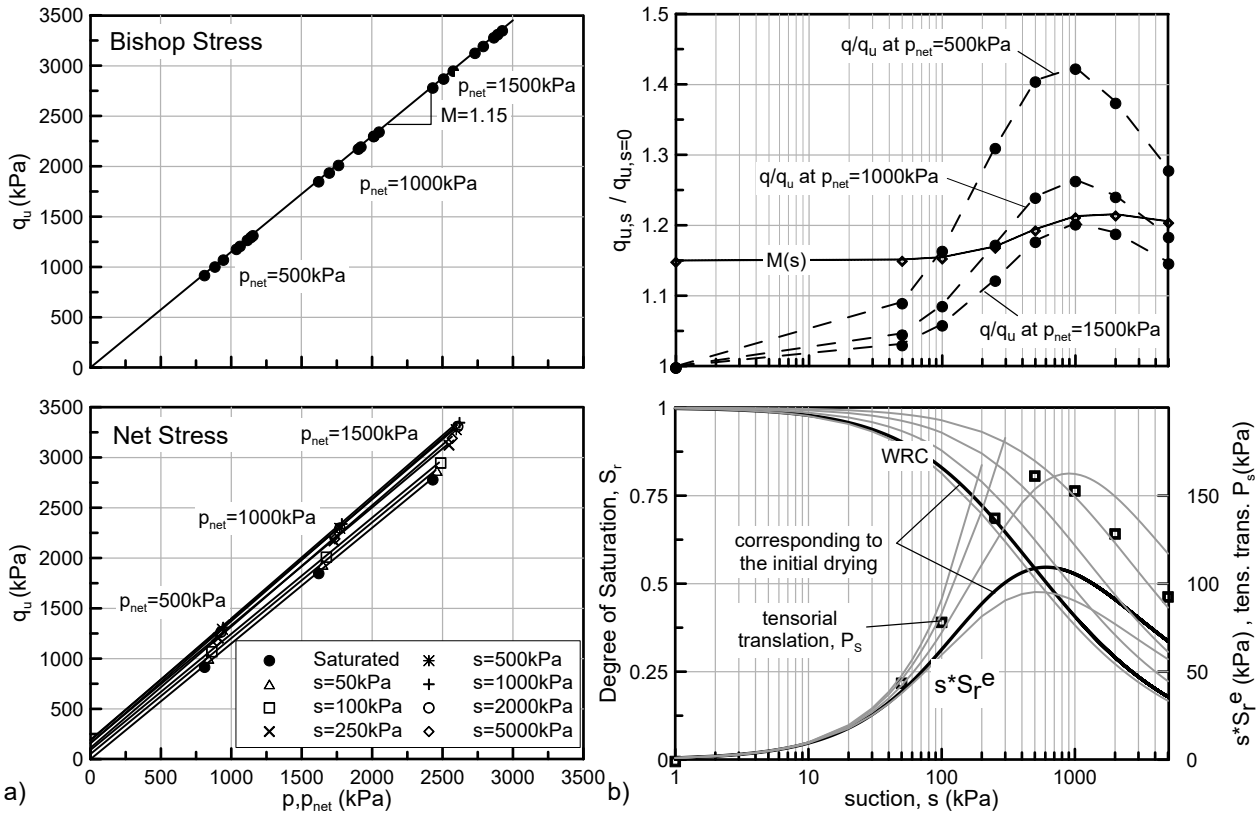


**Figure 8.25:** a) The critical state lines in the $p-q$ space (top) and $\overline{p}-q$ space (bottom), and; b) the evolution of the $q_{u,s}/q_{u,s=0}$ ratio, of the critical state slope M(s) (net stress domain) and of the tensorial translation $P_s$ with suction (top), together with the WRC and the evolution of the $s \cdot S_r^e$ term with suction (bottom).

The obtained results confirm both Jommi (2000)'s observations. The tensorial translation $(-P_s)$ follows the evolution of the $s \cdot S_r^e$ term, as the latter is influenced

from the constantly evolving degree of saturation. The slop of the net stress CSLs though is not constant but changes with suction, another outcome of the model;s constantly evolving compressibility under constant suction. In more detail, figure 8.25b plots the evolution of M(s), $-P_s$, as well as of the normalized shear strength ratio $q_{u,s}/q_{u,s=0}$ with suction and additionally compares it with the $s \cdot S_r^e$ values, where from a qualitative point of view all quantities seem to follow the evolution of the $s \cdot S_r^e$ term.

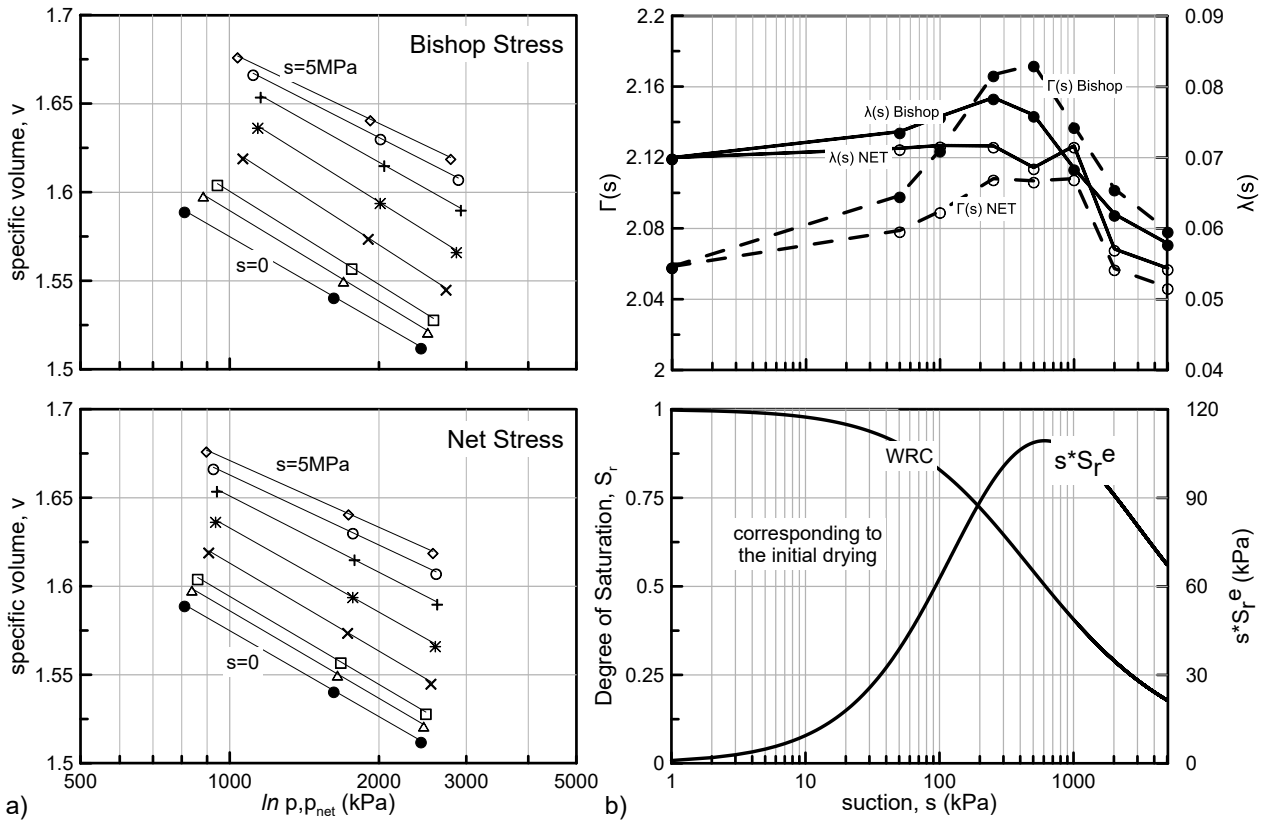


**Figure 8.26:** a) The critical state lines in the $v - \ln p$ plane (top) and $v - \ln \overline{p}$ plane (bottom), and; b) the evolution of $\Gamma$ and $\lambda$ with suction (top), together with the WRC and the evolution of the $s \cdot S_r^e$ term with suction (bottom).

In figure 8.26a, the specific volume values corresponding to critical state conditions are plotted in terms of Bishop's and in terms of net stress, to identify the CSLs on the $v - \ln p$ and $v - \ln \overline{p}$ planes. Note that the corresponding critical state void ratio increases with increasing suction, an additional reflection of the partial saturation induced "structure", also highlighting a fundamental difference between partial

saturation and other structure inducing mechanisms. The state of partial saturation is controlled by the hydraulic conditions applied and does not degrade as failure is approached. Thus, an unsaturated soil can reach a critical state without necessarily recalling its intrinsic properties.

Figure 8.26b plots the $\Gamma(s)$ and $\lambda(s)$ values corresponding to each one of the critical state lines of figure 8.26a. The obtained values do not obey to a specific pattern although their values seem to evolve following a trend similar to the $s \cdot S_r^e$ term. To understand this behaviour, we shall recall that in fact critical state constitutive models, reproduce CSLs which are parallel to the virgin compression lines. In the examined case, the slope of the virgin compression lines constantly evolve and thus, any attempt to represent the CSLs with a constant compressibility is by definition problematic.

Figures 8.27 to 8.29 repeat the previous discussion, this time based on Abaqus FEM analyses with the developed UMAT, with figure 8.30 presenting indicative simulation outputs. These analyses, apart from identifying the limitations imposed by the constant Abaqus WRC they will additionally provide a better insight into the evolution of shear strength with suction and especially on the critical state behaviour without the effect of the evolving post-yield compressibility.

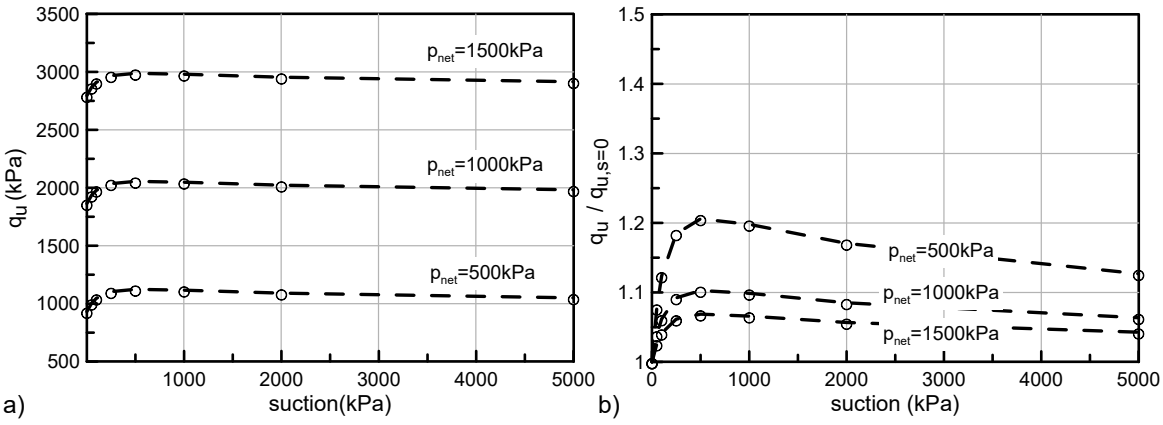


**Figure 8.27:** Evolution of the ultimate strength with suction. Results from Abaqus FEM (cst. WRC) analyses. a) the $q_u$ vs suction and; b) the $q_{u,s}/q_{u,s=0}$; both for three different levels of net confining pressure $\overline{p}$.

Comparing figure 8.27 with figure 8.24, we may observe that the model can still reproduce a nonlinear variation of shear strength with suction, while in terms of the

normalized ratio $q_{u,s}/q_{u,s=0}$, the constant WRC analyses indicate a reduced increase of shear strength with suction. This is a direct consequence of the fact that shear strength depends on Bishop's average skeleton stress. With compression under constant suction but increasing degree of saturation, shear strength increases due to the fact that the $s \cdot S_r^e$ term increases, while in the present case it is not.

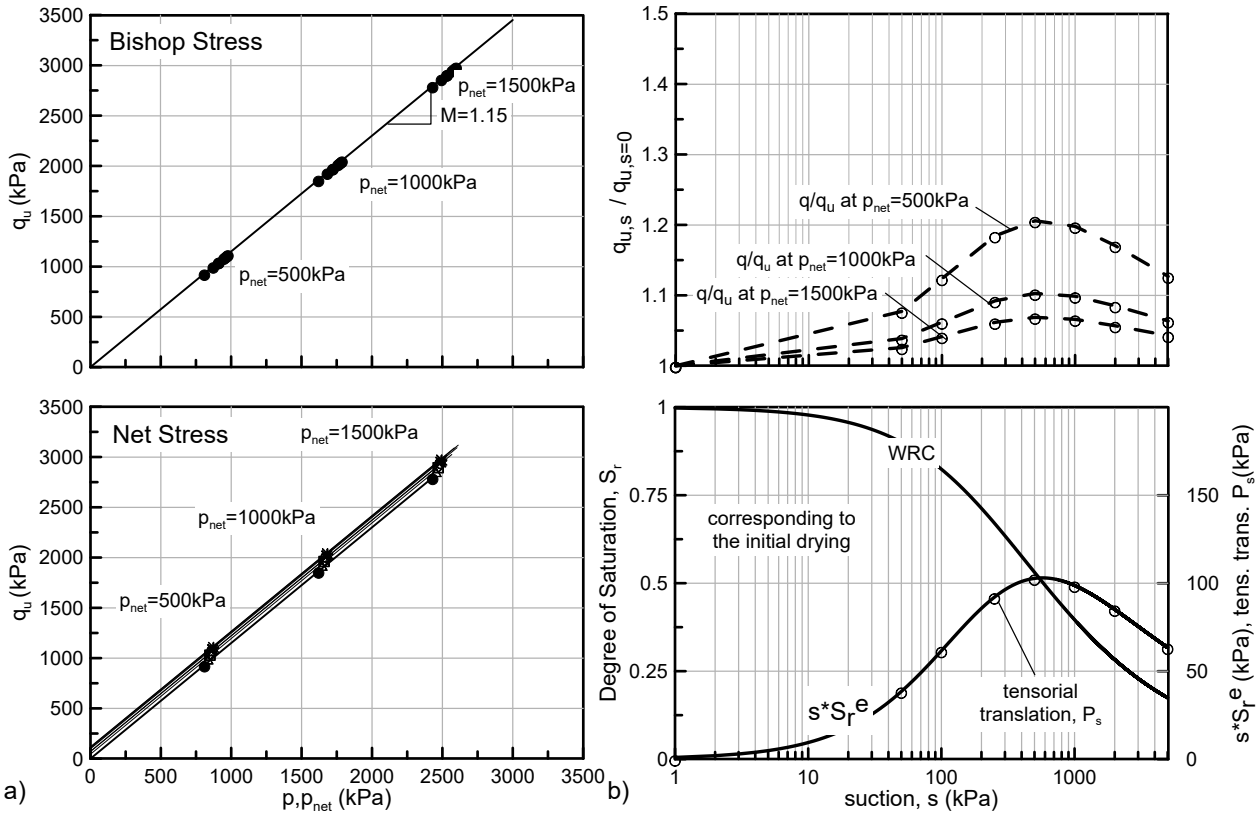


**Figure 8.28:** a) The critical state lines in the $p-q$ space (top) and $\overline{p}-q$ space (bottom), and; b) the evolution of the $q_{u,s}/q_{u,s=0}$ ratio, of the critical state slope M(s) (net stress domain) and of the tensorial translation $P_s$ with suction (top), together with the WRC and the evolution of the $s \cdot S_r^e$ term with suction (bottom). Results from Abaqus FEM (cst. WRC) analyses.

Regarding the reflections of the constant compressibility on the predicted unsaturated critical state conditions, the results of figures 8.28 and 8.29 are quite illustrative. We may observe that the obtained critical state line in the $p-q$ space is common, while in the $\overline{p}-q$ space parallel compression lines apply. The latter confirms the hypothesis that the suction dependance observed in the net stress CLSs is attributed to the evolving compressibility. Additionally, with respect to the tensorial translation

$(-P_s)$ we may observe that it precisely follows the $s \cdot S_r^e$ term.

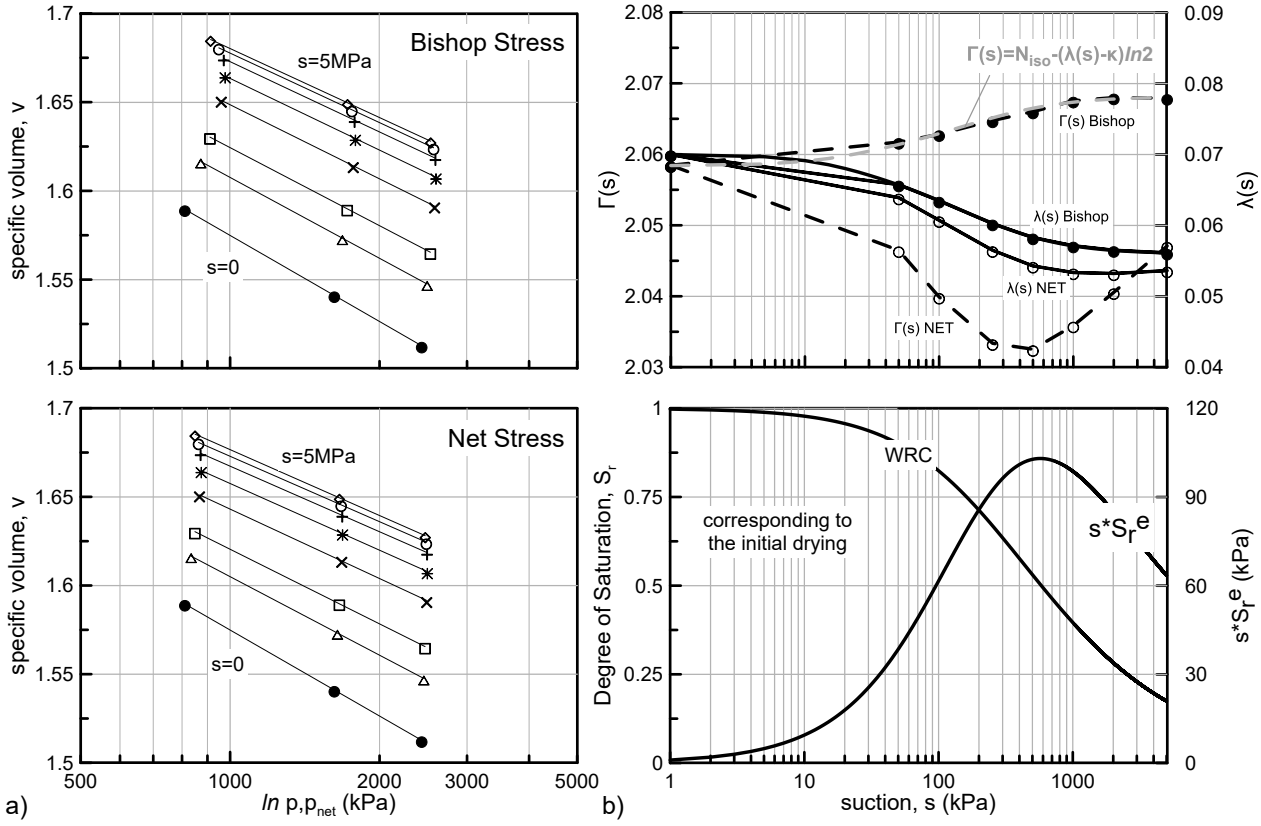


**Figure 8.29:** a) The critical state lines in the $v - \ln p$ plane (top) and $v - \ln \overline{p}$ plane (bottom), and; b) the evolution of $\Gamma$ and $\lambda$ with suction (top), together with the WRC and the evolution of the $s \cdot S_r^e$ term with suction (bottom). Results from Abaqus FEM (cst. WRC) analyses.

The critical state lines in the $v - \ln p$ plane are parallel to the corresponding compression lines as the evolution of their slope with suction is identical to the prediction of the model's framework. Moreover, if we now examine the evolution of the obtained parameters $\Gamma(s)$ with suction, we further conclude that the position of the CSLs follows the Modified Cam Clay critical state prediction through the well known equation $\Gamma(S) = N_{iso} - (\lambda(s) - \kappa) ln(2)$, elaborated to account for the unsaturated compressibility.

Regarding the critical state lines in terms of net stress ($v - \ln \overline{p}$ plane), the results are still "problematic" in their interpretation, due to the nonlinear volumetric response. Nevertheless, a clear trend towards a shift of the critical state line position ($\Gamma(s)$) towards smaller specific volume values and a reduced compressibility can be

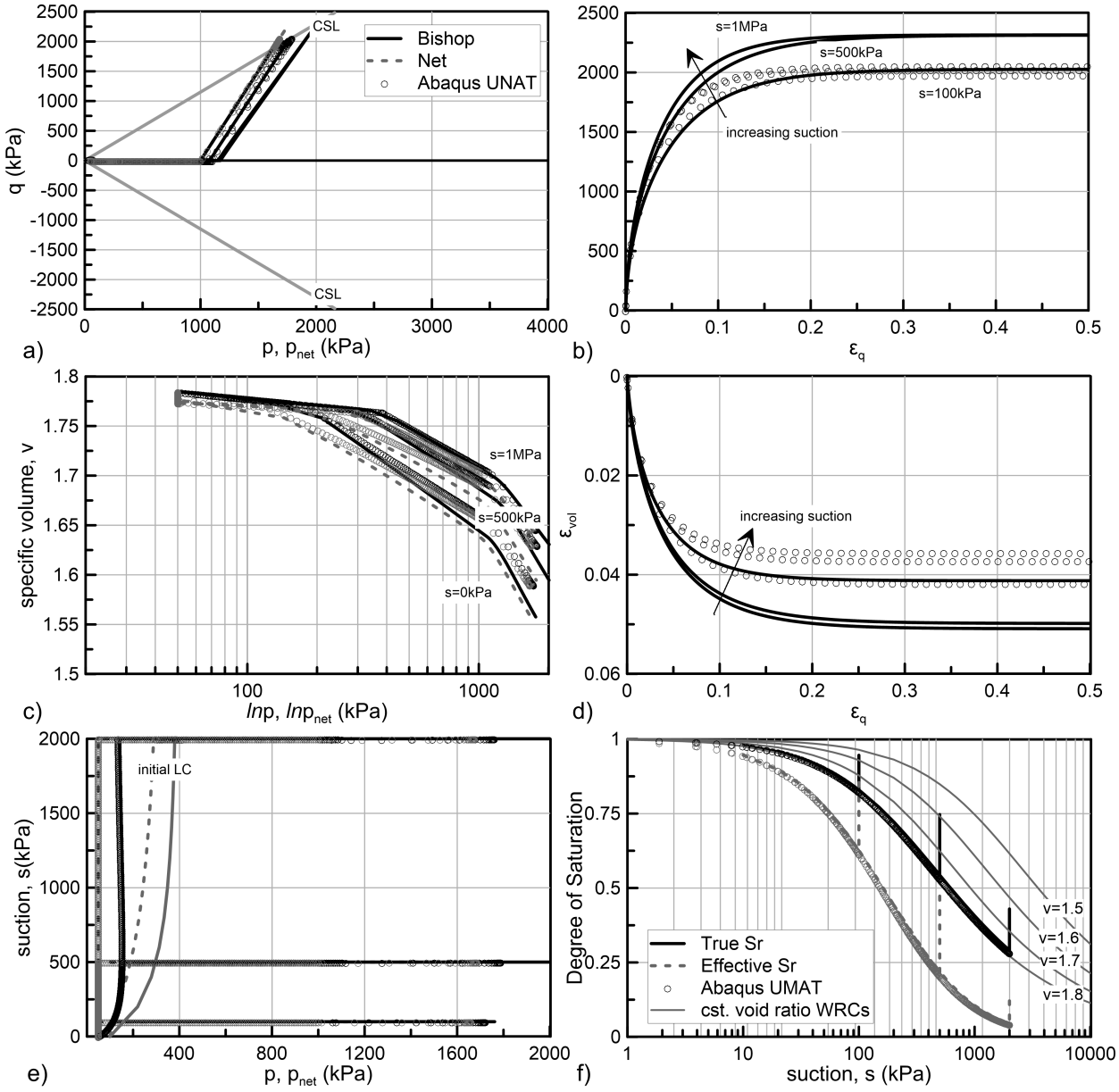


**Figure 8.30:** Drained (cst. suction) triaxial loading of isotropically, normally consolidated ($\overline{p} = 500kPa$) unsaturated soil elements under three different constant suction levels. Results from both SMP and Abaqus FEM (cst. WRC) analyses. a) the $p, \overline{p} - q$ planes; b) the $q - \varepsilon_q$ diagram; c) the $v - \ln p, \overline{p}$ planes; d) the $\varepsilon_{vol} - \varepsilon_q$ diagram; e) the $p, \overline{p} - s$ planes and; f) the $S_r, S_r^e - s$ plots.

identified. In fact the $\Gamma(s)$ response follows the evolution of the specific volume with drying, while $\lambda(s)$ reflects the average compressibility of a curve with continuously increasing slope as net stress increases.

The results from the Abaqus analyses (constant WRC) reveal that the model can

still adequately represent the shear strength of unsaturated soils, even if its double dependence of the compression lines on suction and degree of saturation is "cancelled", as is the case with Abaqus. This is due to the fact that at least for normally consolidated soils, shear strength is mainly controlled by the evolution of Bishop's average skeleton stress and especially from the value of the $s \cdot S_r^e$ term. Nevertheless, a different calibration is suggested for Abaqus analyses, taking into account the same constant WRC that will be used as an input.

### 8.3.3 Wetting Tests - Volumetric collapse predictions

This paragraph investigates the proposed model's capability to reproduce wetting induced collapse. As discussed in chapter 4, unsaturated soils tend to either swell or collapse when wetted from an initially unsaturated state, while the anticipated volumetric behaviour depends on the level of the applied net stress. Generally, collapse increases with increasing suction and also with increasing net stress. Nevertheless, with respect to the stress levelthis increase is not continuous. Instead, it usually reaches a maximum for a given level of applied net stress (depending on the type of the soil), after which further compression leads to a reduction in the anticipated collapse strain.

The proposed model tries to address the issue of the maximum of collapse, through the double dependance of the compression lines on suction and effective degree of saturation. In section 8.3.1 we discussed how the proposed compressibility framework reproduces convex compression lines in the $v - ln\overline{p}$ plane which can justify the modelling of a maximum collapse.

To provide solid evidence towards this direction, figure 8.31 presents the simulation results of wetting tests under constant mean net stress. A soil element is initially dried to $s = 100kPa$, and then isotropically compressed to seven different net stress levels ranging from $\overline{p} = 50$kPa to $\overline{p} = 5$MPa. Wetting tests are simulated as a suction decrease test, under constant net stress. Seven different net stress levels, depicted in figure 8.31a, are examined.

We may observe that with the exception of the analyses under $p = 50$kPa and $p = 100kPa$, which produce swelling due to a corresponding elastic stress path, the rest of the tests initiate from normally consolidated condition, with the stress state lying on the LC surface and thus, plastic compressive volumetric strains are reproduced with wetting. Moreover, the collapse strains continuously increase until

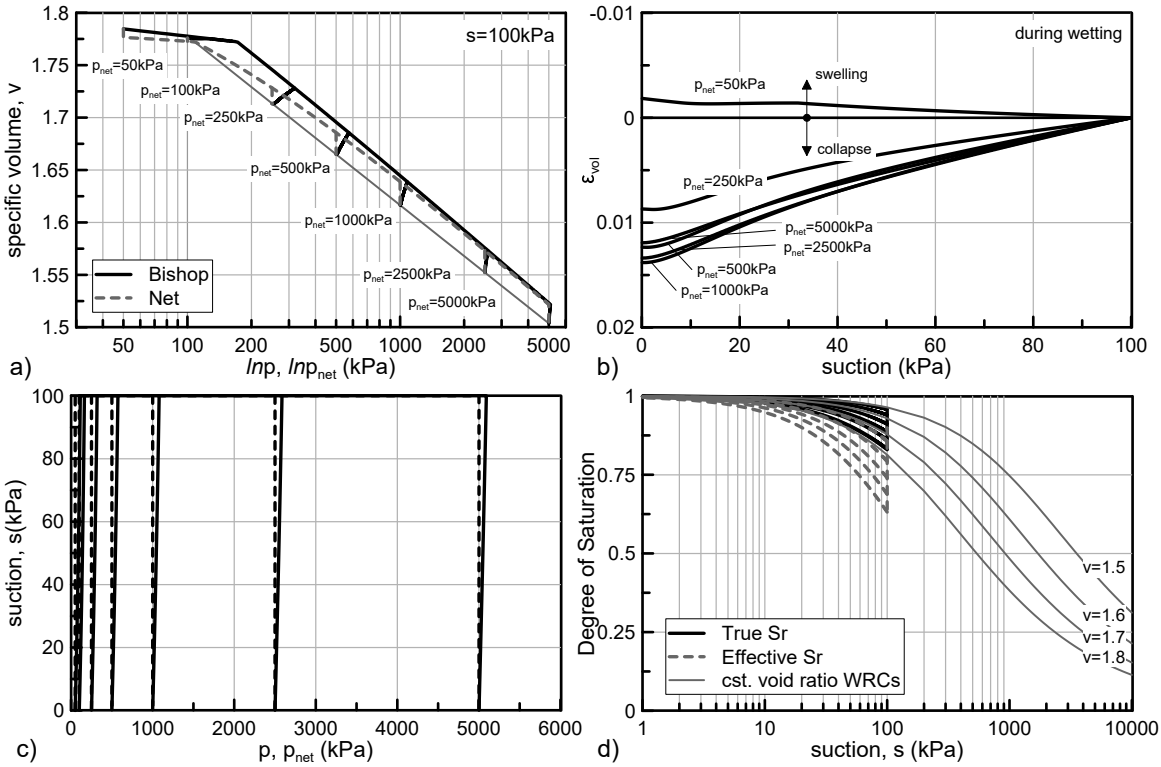


**Figure 8.31:** Wetting (suction decrease) tests on initially isotropically consolidated, unsaturated ($s = 100$kPa) soil elements under seven different constant net stress levels. a) the $v - \ln p, \overline{p}$ planes; d) the $\varepsilon_{vol}$ vs suction during the wetting stage; c) the $p, \overline{p} - s$ planes and; f) the $S_r, S_r^e - s$ plots.

reaching a maximum for $p = 1MPa$ and then slightly reduce as higher stress levels are examined.

The aforementioned simulations are repeated for another six suction levels and the volumetric strains accumulated during the wetting phase are summarized in figure 8.32. The obtained results reveal that, at least qualitatively, the proposed model can adequately represent the commonly observed experimental behaviour. Swelling or collapse strains are reproduced depending on the level of the applied net stress, while they also increase with increasing suction under a constant net stress level. Regarding the variation in collapse strains with the level of the applied net stress, it is confirmed that the model can clearly reproduce a maximum of collapse.

For the assumed parameters, the maximum volumetric collapse appears at a net stress level of $\overline{p} = 1MPa$, for the elements with an initial suction up to $s = 250kPa$, while in general increases with increasing suction. This is attributed to the increasing

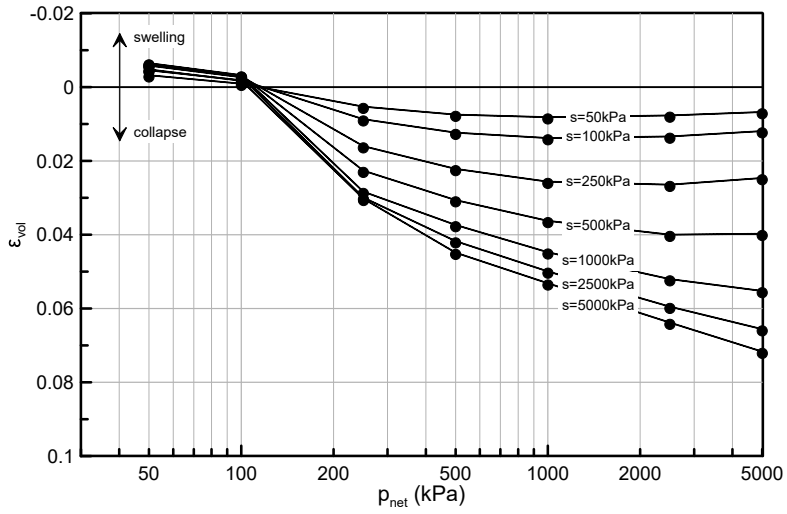


**Figure 8.32:** Wetting induced volumetric strains for initially unsaturated soil elements under different suction and net stress levels.

stiffness with suction resulting to a soil which is more capable of retaining increased void ratio values compared to the same element under the same net stress when fully saturated.

Thus, both the collapse strains and also the net stress at which the maximum of collapse is observed are expected to increase with increasing suction. It is reminded, that the soil parameters assumed for the ongoing analyses, correspond to a relatively stiff silty soil ($C_c = 0.16$), and thus compression to relatively high net stress levels is necessary for a maximum of collapse to appear as suction increases.

Once again the discussion is repeated including Abaqus FEM analyses with a constant WRC. Figure 8.33 presents the obtained results associated with unsaturated soil elements initial dried to a suction level equal to $s = 100kPa$. Their SMP counterparts of figure 8.31 are also included for comparison.

As expected, the lack of the dependance of the WRC on void ratio, highly alters the results. Under constant suction and degree of saturation, constant slope compression lines apply, and thus, alike BBM a continuously increasing collapse potential is reproduced. This is clearly depicted in the summarizing graph of figure 8.34 which compares the predicted volumetric strains accumulated during wetting from the SMP simulations with their Abaqus FEM counterparts.

Finally, we shall mention that the simulation of wetting tests with FEM codes,

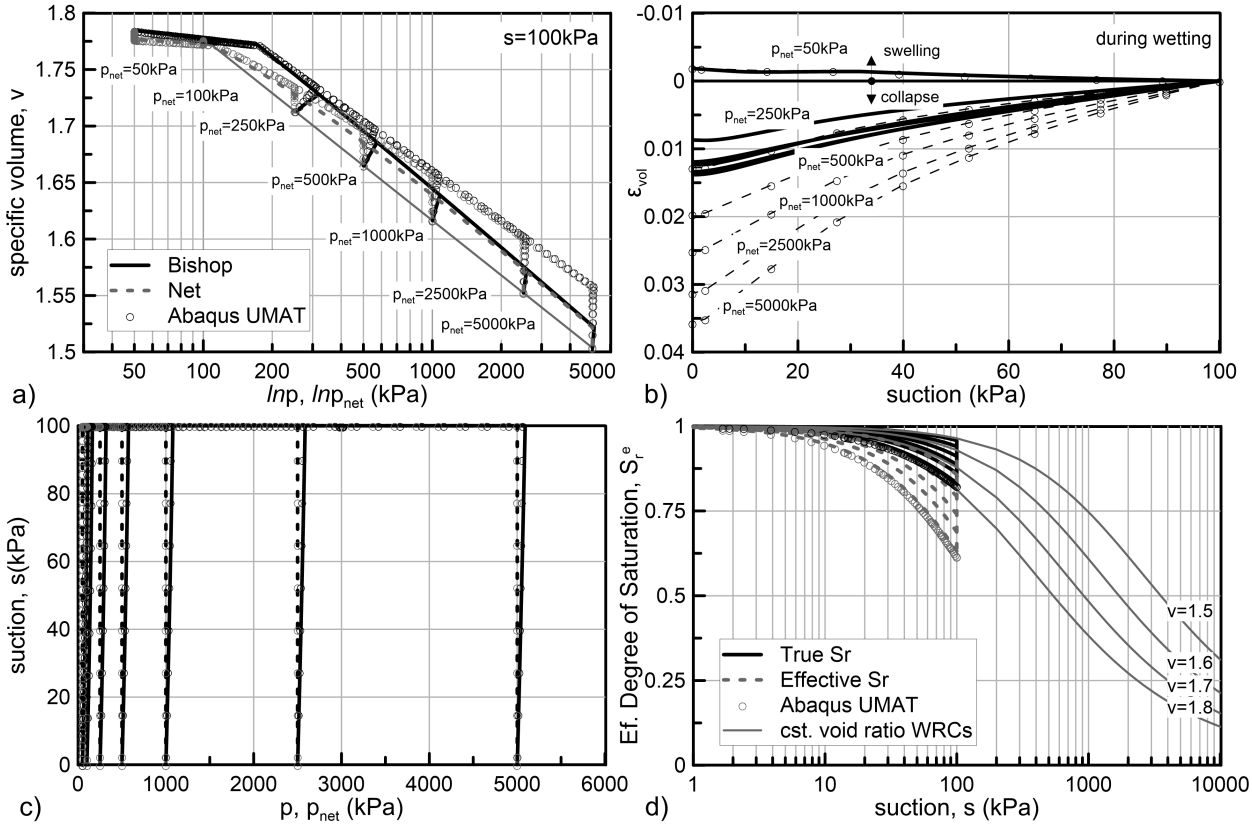


**Figure 8.33:** Wetting (suction decrease) tests on initially isotropically consolidated, unsaturated ($s$ = 100kPa) soil elements under seven different constant net stress levels. Results from both SMP and Abaqus FEM (cst. WRC) analyses. a) the $v - \ln p, \overline{p}$ planes; d) the $\varepsilon_{vol}$ vs suction during the wetting stage; c) the $p, \overline{p} - s$ planes and; f) the $S_r, S_r^e - s$ plots.

proves significantly demanding in terms of computational time, because relatively small sub-increments, are needed for the analyses to converge successfully, while additionally an increased number of N-R iterations is required for each incrementation. This latter is due to the fact that commercial, general purpose FEM codes like Abaqus, cannot account for the suction and degree of saturation Jacobian(s), describing the relationship between increments of suction and/or degree of saturation with the corresponding increment of the stress tensor. Thus, as usually wetting tests are performed under a constant stress level, the initially predicted strain increment is not representative of the finally anticipated results, making convergence a demanding task. Nevertheless, as far as convergence is achieved, the results are accurate.

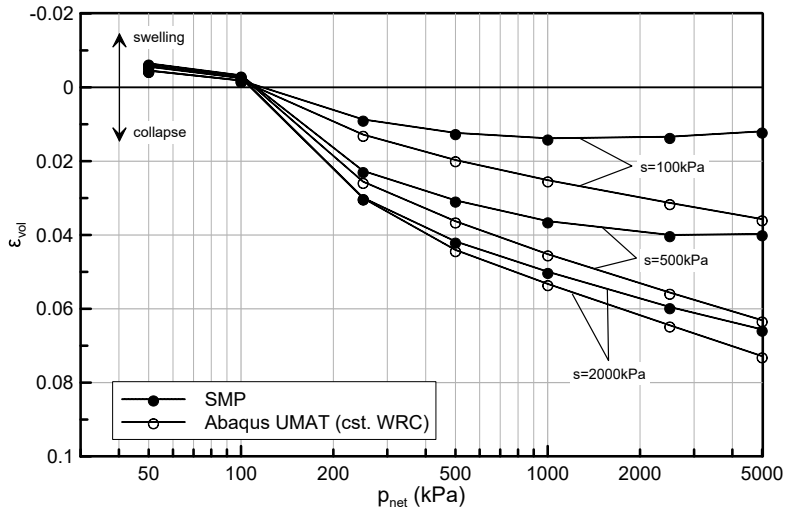


**Figure 8.34:** Wetting induced volumetric strains for initially unsaturated soil elements under different suction and net stress levels. Comparison between the SMP and Abaqus FEM (cst. WRC) results.

## 8.4 Combined effects of Primary Anisotropy and Partial Saturation

Following the individual examination of the anisotropic and unsaturated characteristics of the proposed model, this section evaluates the model's ability to represent the combined effects of partial saturation and anisotropy. In that respect, in the following paragraph, unsaturated soil elements are subjected to anisotropic consolidation under different stress paths and suction levels. The section is concluded with the predictions of the model regarding triaxial loading tests under constant and different suction levels, initiating from different levels of stress induced anisotropy.

### 8.4.1 Anisotropic compression tests under different suction levels

Figure 8.35 presents the simulation results of oedometric tests under different suction levels. The same set of parameters, already introduced in tables 8.1 and 8.3 are used for consistency. The results regard an initially isotropically consolidated soil element, with a preconsolidation pressure $p_0^* = 100kPa$, that has been elastically unloaded to $p = 50kPa$. A drying stage follows where suction is progressively raised to the

desired level (seven different suction levels are selected) and then the soil elements are compressed under 1D conditions until the vertical net stress reaches $\overline{\sigma_v} = 4000kPa$.

To allow for a rapid orientation of the primary anisotropy to the imposed one, a relatively high $\psi = 50$ value is selected while, the de-orientational part of the hardening rule is deactivated ($\zeta_q^p = 0.0$). The obtained behaviour is in fact a combination of partial saturation and an evolving anisotropy. The compression lines obtained (see fig. 8.35) reflect the beneficial effect of partial saturation in stiffening the behaviour and increasing the elastic domain, while additionally, the evolving post yield compressibility is the combined effect of the increasing degree of saturation with compression together with an adjustment of the compression line towards the intrinsic compression line corresponding to the imposed stress induced anisotropy.

To clarify the latter, figure 8.36 plots the compression curves derived from the present analyses together with the results from the isotropic compression tests on unsaturated soil elements of figure 8.21. Both analyses where performed using the same set of parameters as well as identical initial conditions and thus, the results are fully comparable. The behaviour at four out of the seven analyzed suction levels is examined for the plots to be more legible.

Back to the results of figure 8.35, another interesting observation is that suction affects significantly the rate of anisotropy's evolution, with an increase in suction favouring a decreased rate. In terms of modelling, this is the combined effect of two different factors. First of all, an increase in suction is in favour of an increased elastic domain. Thus, when comparing soil elements at the same level of net stress but different suction levels it is expected that the one compressed under a higher suction level has undergone a smaller amount of plastic straining. Additionally, its response is much more stiffer, implying that even under a similar (in terms of net stress) compression the accumulated plastic strains under unsaturated conditions are reduced. In practical terms, this is absolutely desired and sensible as the stiffer a soil is the less deceptive to fabric alteration is expected to be.

Regarding the orientation of the yield surface at the end of compression, we may observe that irrespectively of the level of the applied suction, the yield surface axis is dragged towards the corresponding $K_0$ conditions (according to the flow rule calibration). This is expected as 1D compression imposes a defined constant dilatancy. The flow rule can represent such a dilatancy only under a specific orientation of the plastic potential surface, which inevitably drags the Bishop's stress path and also the

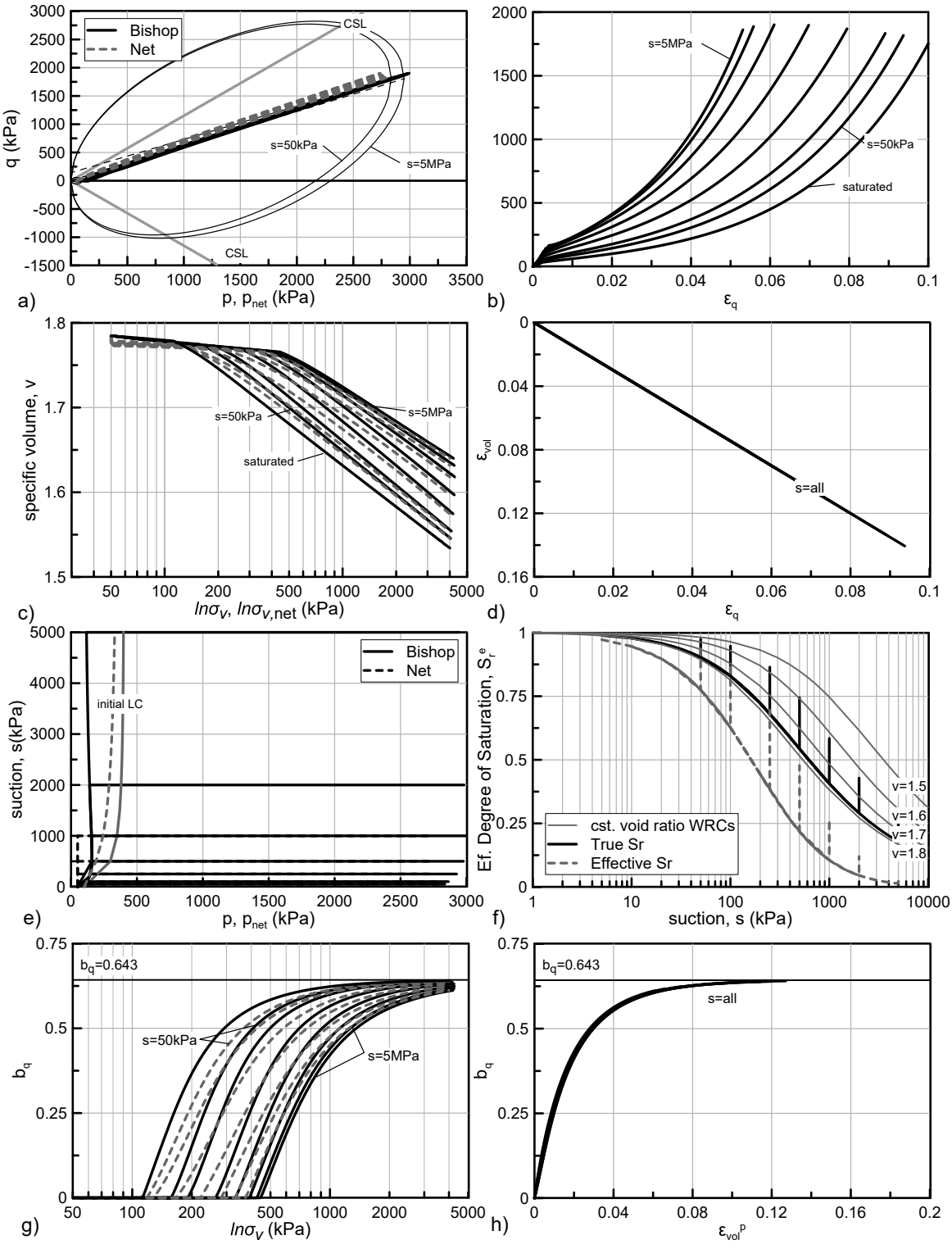


**Figure 8.35:** 1D compression under seven different constant suction levels. a) the $p, \overline{p} - q$ planes; b) the $q - \varepsilon_q$ diagram; c) the $v - \ln \sigma_v, \overline{\sigma_v}$ planes; d) the $\varepsilon_{vol} - \varepsilon_q$ diagram; e) the $p, \overline{p} - s$ planes; f) the $S_r, S_r^e - s$ plots; g) the $b_q - \ln \sigma_v, \ln \overline{\sigma_v}$ and; h) the $b_q - \varepsilon_{vol}^p$ diagram.

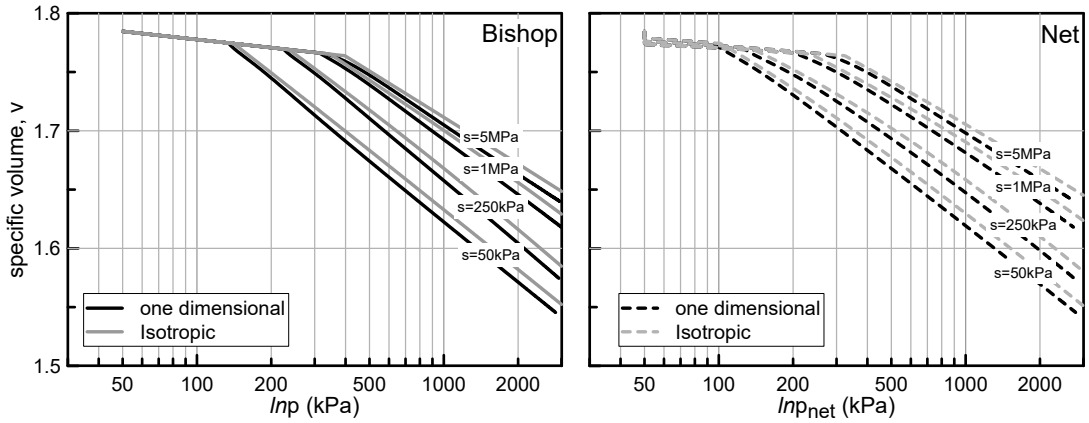


**Figure 8.36:** Comparison of the model's predictions in isotropic and 1D compression under four different suction levels. a) the $v - \ln p$ and; b) the $v - \ln \overline{p}$ planes.

orientation of the yield surface to a specific value of $b_q$, namely the one corresponding to the $K_0$ calibrated for. In the present analyses where a $K_0 = 0.55$ has been assumed the corresponding stress ratio is $n = b_q = 0.6428$. Such a behaviour is clearly depicted in figure 8.37a.

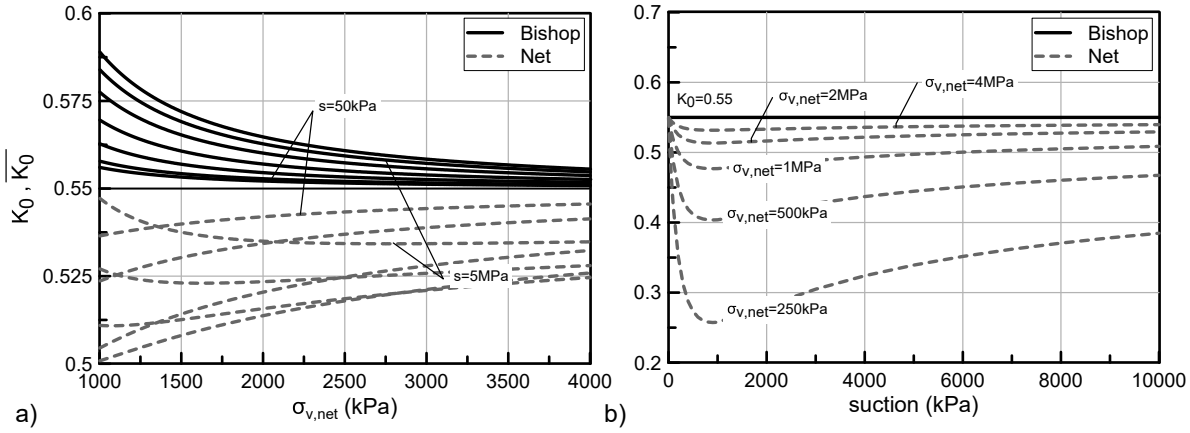


**Figure 8.37:** Variation of the coefficient of earth pressure at rest both in terms of net stress ($\overline{K_0}$) and in terms of Bishop's stress ($K_0$), in: a) with the vertical net stress under different suction levels (simulation results) and in; b) with suction under different vertical net stress levels based on eq. 8.1.

However, in the same graph, we may also observe that partial saturation affects the $\overline{K_0}$ reproduced in terms of net stress, which systematically obtains lower values.

This is also quite expected. For any given $K_0 = \sigma_h/\sigma_v$ that the flow rule has been calibrated for, the net stress path reproduces a different coefficient of earth pressure at rest $\overline{K_0}$. After some algebra, we may derive the following expression to relate the $\overline{K_0}$ with the $K_0$:

$$\overline{K_0} = K_0 + (K_0 - 1) \cdot \frac{s \cdot S_r^e}{\overline{\sigma_v}} \tag{8.1}$$

Equation 8.1 reveals that the net stress $\overline{K_0}$ reproduced, depends on the value of the selected $K_0$, on the level of the vertical net stress $\overline{\sigma_v}$ and on the state of partial saturation as the letter is reflected by the $s \cdot S_r^e$ term. Figure 8.37b presents an indicative plot of the variation of $\overline{K_0}$ value with suction, for various vertical net stress levels. The presented curves correspond to stabilized anisotropic conditions and a constant $K_0 = 0.55$. To calculate the $s \cdot S_r^e$ term, the constant $v = 1.7$ WRC of figure 8.19 is used. We may observe that a suction increase favours a decreased $K_0$, with the rate of decrease becoming less intense as the stress level increases. Equation 8.1 as well as plots similar to figure 8.37 may assist in estimating the $K_0$ value that the flow rule must be calibrated for, to reproduce any desired $\overline{K_0}$ under unsaturated conditions.

In figure 8.38 the results of radial compression tests under unsaturated conditions are given. In more detail, initiating from the exact same conditions with the previously presented simulations, four soil elements are subjected to radial compression tests under $\overline{n} = 0.25$, 0.5, 0.75 and 1.0. Prior to compression the soil elements are dried by imposing $s = 1000$kPa and the net stress ratio is adjusted to the desired $\overline{n}$. We shall once again mention that in practice only net stress is controlled in the laboratory and for that reason, radial stress path are simulated as constant net stress ratio tests.

The obtained results demonstrate the effect of suction in the developing memory of primary anisotropy, as the latter is reflected in the orientation of the yield surface at the end of compression. Any stress ratio imposed under net stress conditions in fact corresponds to a smaller stress ratio in terms of Bishop's stress. Thus the hardening rule, which drags the orientation of the yield surface towards the Bishop's stress path, limits the rotation to a smaller stress ratio compared to the imposed one. In practical terms, this means that partial saturation tends to reduce the memory of preferred directions at any given soil element subjected to anisotropic consolidation.

The reason why such a behaviour is observed is quite profound. Suction is a scalar quantity and thus it is by definition isotropic. Using an isotropic quantity to describe

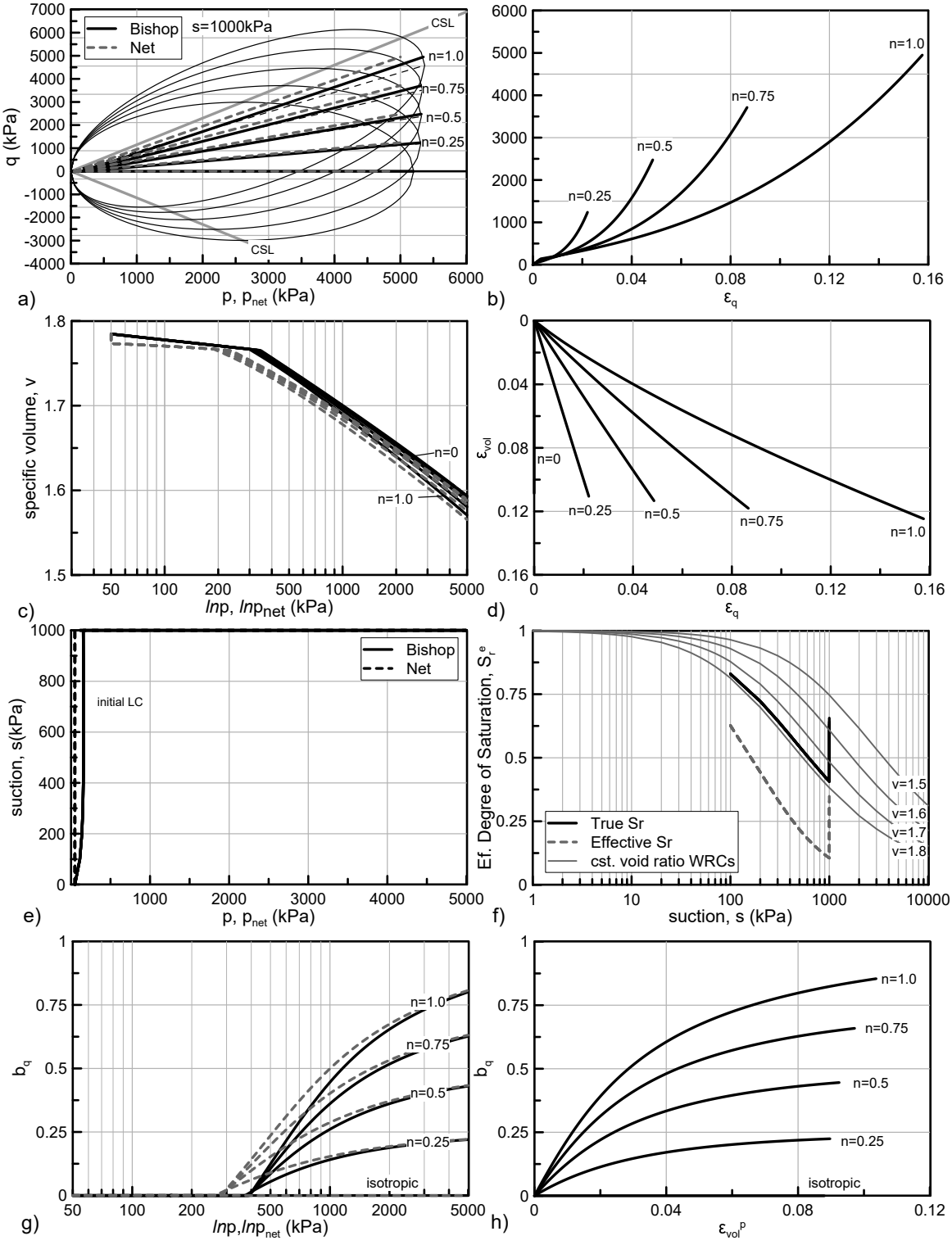


**Figure 8.38:** Radial compression (four different stress ratios $\overline{n}$) on an unsaturated ($s = 1000kPa$) soil element. a) the $p, \overline{p} - q$ planes; b) the $q - \varepsilon_q$ diagram; c) the $v - \ln p, \overline{p}$ planes; d) the $\varepsilon_{vol} - \varepsilon_q$ diagram; e) the $p, \overline{p} - s$ planes; f) the $S_r, S_r^e - s$ plots; g) the $b_q - \ln p, \ln \overline{p}$ and; h) the $b_q - \varepsilon_{vol}^p$ diagram.

the effects of partial saturation a priory implies that any effect attributed to suction will be isotropic as well.

Nevertheless, whether such an isotropic effect of suction is realistic or not is still an open debate, with the most profound answer being probably not. An isotropic effect of partial saturation requires that the inter-particle forces developed in an unsaturated soil, mainly due to the forming water meniscus, are randomly distributed and also randomly orientated for the induced structure to be isotropic. Although this may be the case when an isotropic soil fabric exists, it is highly doubtful whether it holds trues for an anisotropic soil fabric.

Just a few researchers have raised the discussion on whether the effect of partial saturation in soil behaviour is isotropic or anisotropic, with the most important and complete discussion being probably this of Li (2003). The author suggested that the effects of suction in soil behaviour should be represented through a suction-associated tensor, acting in fact as a fabric tensor which represents the orientation of the inter-particle forces in the soil skeleton.

Although fundamentally correct and probably closer to reality, the obvious reason why such an approach is extremely difficult to find practical applications springs from the fact that such a suction tensor can neither by defined nor be controlled either in the laboratory or in the field. Thus, unfortunately, assuming that partial saturation has isotropic effects in the soil behaviour is still nowadays the only practically available option, nevertheless it should be always kept in mind that probably this is not the reality, at least in soils with an anisotropic soil fabric.

### 8.4.2 Triaxial shear tests on Anisotropic soil samples under constant suction

Simulation results from an ensemble of triaxial loading tests under different suction levels and different initial anisotropic conditions are utilized to investigate how unsaturated shear strength predictions alter with anisotropy. The analyses include tests originating from five different states of initial anisotropy, namely ($b_q = 0.25$, 0.50, 0.75 and $b = 1.0$), which are loaded under seven different suction levels, similar to the previous analyses. Results concerning initially isotropic, as well as initially anisotropic but saturated soil elements are included to serve as a reference for comparisons.

The simulated loading sequence includes four (4) stages. In the first one, the soil element is dried to the desired suction level. The stress state is assumed isotropic with

$p = 50kPa$, while the initial size of the yield surface corresponds to a preconsolidation pressure equal to $p_0^* = 100kPa$. Regarding its initial orientation, it is assumed that this coincides with the primary anisotropy selected. In other words, it is assumed that initially the soil elements have been compressed under saturated conditions to $p = 100kPa$ and $q = 100 \cdot b_q$, where $b_q$ the desired orientation. It is obvious that a silent assumption has been made here. It is assumed that compression to $p = 100kPa$, a relatively low stress level, is sufficient to alter the fabric of a given soil and stabilize it towards the one corresponding to the desired anisotropy. Although this is not the case for natural soils, perhaps with the exception of highly plastic recomposed clays, the aforementioned assumption is made to allow for solid conclusions regarding the effect of anisotropy without the additional effect of the rate of anisotropy evolution.

In the second stage, the stress state is adjusted to the desired net stress ratio $\overline{n}$, to coincide with the initial anisotropy and then in the third stage the soil element is radially compressed up to $\overline{p} = 500kPa$ under the given constant net stress ratio. Finally in the fourth stage, the soil element is sheared under constant suction, thus under drained conditions, until critical state is reached.

Figure 8.39 presents the obtained results corresponding to an initial yield surface orientation of $b_q = 0.5$. We may observe that a continuously hardening behaviour is reproduced with the ultimate strength depending on the imposed suction level. It is interesting to notice that during the compression stage, the orientation of the yield surface slightly changes (for the unsaturated soil elements). It slightly reduces in order to adjust to the corresponding Bishop's stress path, according to what was discussed in the previous paragraph. Thus, the orientation of the yield surface at the begging of the triaxial loading is slightly lower compared to the one imposed in terms of net stress, nevertheless this is neglected in the discussion offered in the following lines for the sake of simplicity.

Figure 8.40 plots the evolution of the ultimate strength with suction for the four different levels of stress induced anisotropy examined together with results from initially isotropically consolidated soil samples. We may observe that an increase in the initial anisotropy results to a reduced ultimate deviatoric stress, irrespective of the level of the applied suction. Such a behaviour is in accordance with available experimental results (Gens 1982) on saturated soil samples. In fact this increase in the ultimate strength with decreasing anisotropy derives from the fact that the stress state at the beginning of the shearing stage is located closer to the critical state line

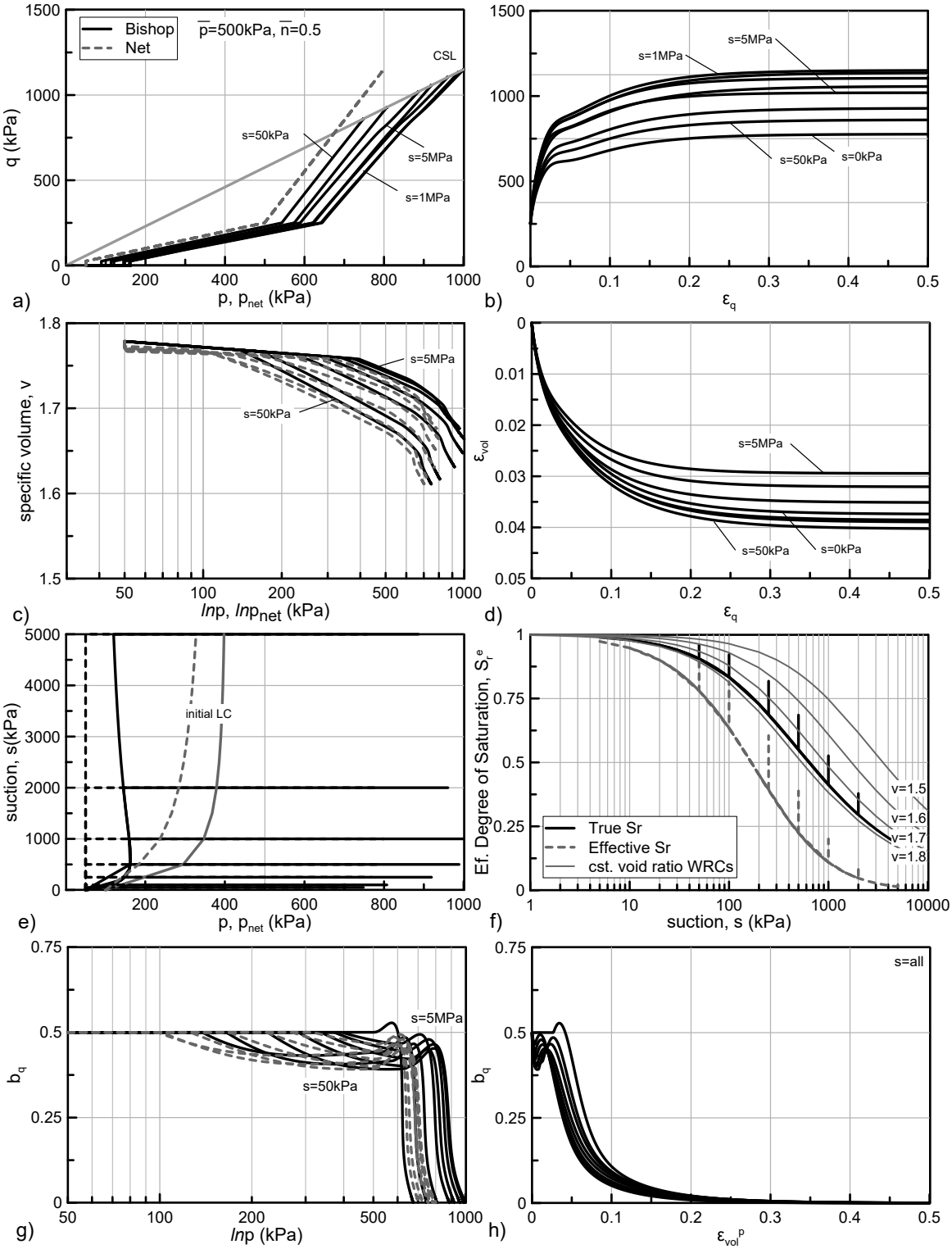


**Figure 8.39:** Drained triaxial loading of anisotropically consolidated ($\overline{p} = 500kPa$, $\overline{n} = 0.5$), unsaturated soil elements under seven different constant suction levels. a) the $p, \overline{p} - q$ planes; b) the $q - \varepsilon_q$ diagram; c) the $v - \ln p, \overline{p}$ planes; d) the $\varepsilon_{vol} - \varepsilon_q$ diagram; e) the $p, \overline{p} - s$ planes; f) the $S_r, S_r^e - s$ plots; g) the $b_q - \ln p, \ln \overline{p}$ and; h) the $b_q - \varepsilon_q^p$ diagram.

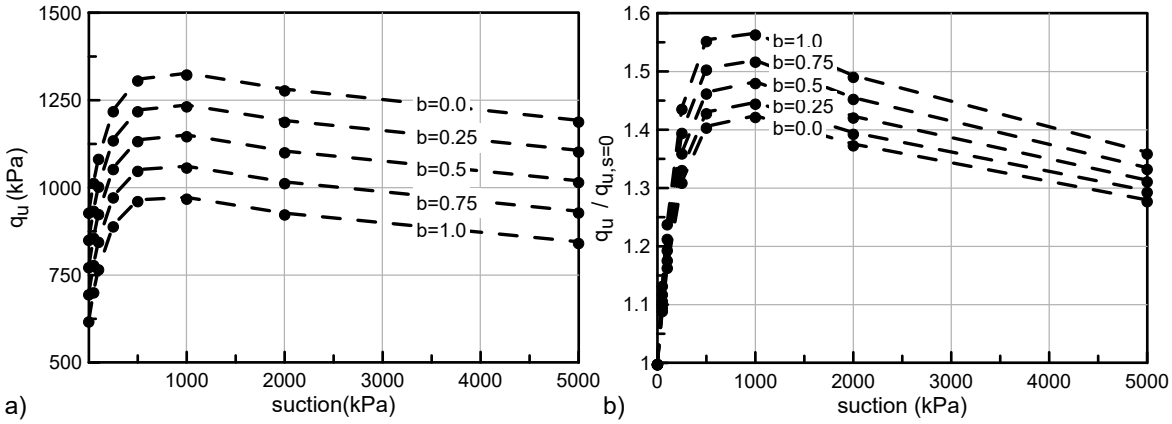


**Figure 8.40:** Evolution of the ultimate strength with suction under different initial anisotropic states. a) the $q_u$ vs suction and; b) the $q_{u,s}/q_{u,s=0}$.

as anisotropy increases. Considering that the imposed stress path during a drained triaxial compression test is $(\dot{q}/\dot{p} = 3.0)$[5] the lower the initial deviatoric stress is, the higher the mean effective stress and the corresponding critical state deviatoric stress will be (i.e., see figure 3.24).

Regarding the evolution of shear strength with suction, under a given initial anisotropy, we may observe that it follows the same trend observed in isotropically consolidated soil elements as has been extensively discussed in paragraph 8.3.2. Nevertheless it is interesting to notice that when plotted in terms of the normalised ratio $q_{u,s}/q_{u,s=0}$, it turns out that the effect of partial saturation in increasing the soil strength gets more profound as initial anisotropy increases. This is also a consequence of the fact that failure occurs under a higher mean stress with decreasing anisotropy, while as discussed in paragraph 8.3.2 the higher the net mean stress is, the less efficient partial saturation becomes in increasing shear strength.

Finally in figure 8.41 the critical state lines corresponding to the performed analyses are plotted both in the stress space and in terms of specific volume vs stress. The results indicate that common critical state conditions apply to elements initiating from different anisotropic conditions under a given suction level, while as far as the position and slope of the critical state lines is concerned the behaviour is identical to the one obtained form isotropically consolidated samples (see figures 8.25 and 8.26),

[5] When degree of saturation alters under constant suction the stress path slightly deviates from $\dot{q}/\dot{p} = 3.0$, nevertheless the aforementioned deviation is negligible and does not alter the overall response.

as extensively described in the previous section.

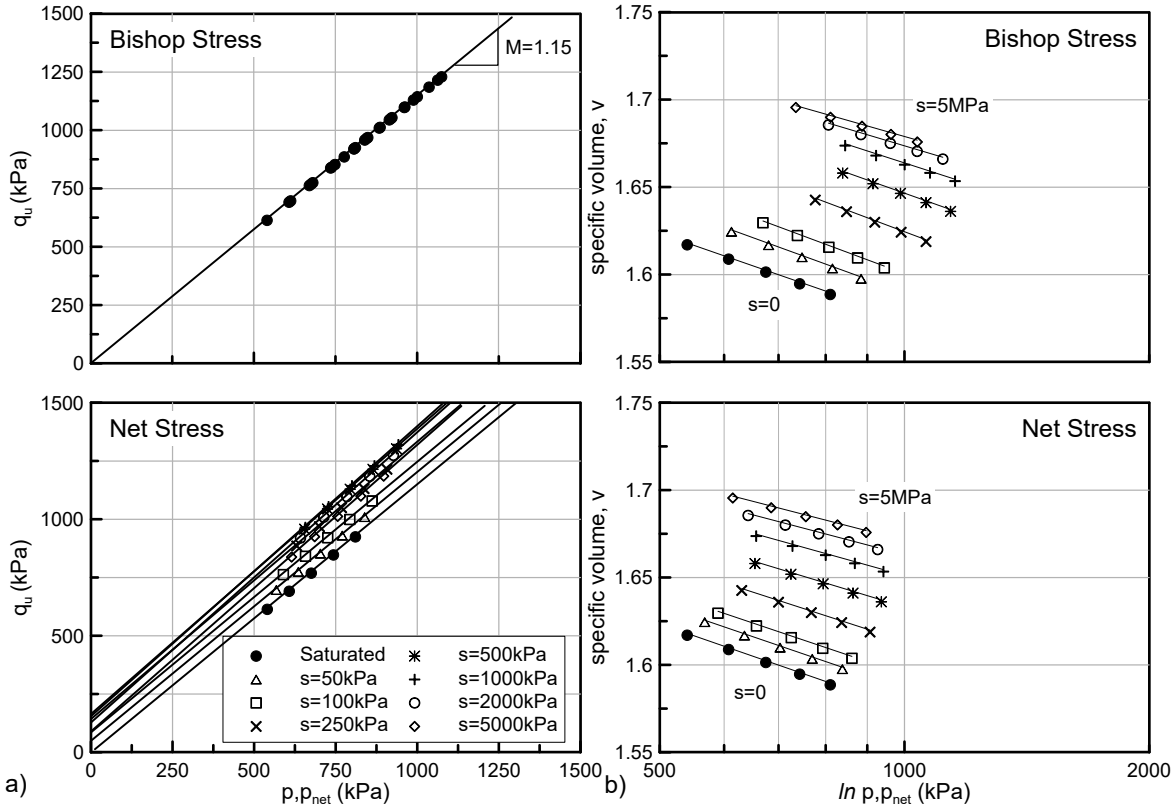


**Figure 8.41:** The critical state lines on the; a) $p-q$ space (top) and $\overline{p}-q$ space (bottom), and; b) in the $v-\ln p$ plane (top) and $v-\ln \overline{p}$ plane (bottom), corresponding to different suction levels and different initial anisotropic conditions.

## 8.5 Concluding Remarks

This chapter evaluated the proposed constitutive model through an ensemble of simple numerical analyses simulating common laboratory tests. A constant set of parameters has been selected for the presented analyses. The selected parameters are fictitious, nevertheless coherent and assumed to correspond to a common silty soil. A parametric study was conducted focusing on the predicted behaviour under different stress path, different levels of stress induced anisotropy and different states of partial saturation. Additionally the effect of the hardening rule parameters $\psi$, $\zeta_q^p$ and of the flow rule parameter $\chi$ was parametrically studied.

The main objectives of the conducted analyses was to:

a) validate the model predictions against the underlying mechanical framework,

b) offer a qualitative comparison of the model's predictions against common experimental observations,

c) investigate the effect of various model parameters, and

d) compare the simulation results obtained from SMP analyses with the results of Abaqus FEM analyses.

In doing so, the present study included three individual steps (groups of analyses) including analyses of progressively increasing complexity in order to allow for a step by step evaluation of the model's predictions. The following set of analyses where performed:

- **anisotropic analyses**, focusing on the model's predictions related to stress induced anisotropy. They were performed under saturated conditions. Radial compression, oedometric compression and isotropic compression tests were included, as well as drained and undrained triaxial loading (both compression and extension) tests under different levels of initial anisotropy;

- **unsaturated analyses**, focusing on the model's predictions related to partial saturation phenomena. They were performed under isotropic conditions with the anisotropic features of the model deactivated. Isotropic compression and drained triaxial loading tests under different constant suction levels, as well as wetting tests (suction decrease) where included;

- finally the **combined effects of anisotropy and partial saturation** were evaluated through anisotropic compression under different constant suction levels and drained triaxial loading under different suction levels and different levels of initial stress induced anisotropy.

The main outcome of the performed study is summarized in the following points. Regarding the anisotropic features of the proposed model we may highlight:

- The proposed model can efficiently represent an evolving fabric anisotropy during stress paths which alter the material's anisotropy. Distinct compression curves are precisely reproduced in line with the proposed compressibility framework. The hardening rule's parameter $\psi$ can sufficiently accommodate different

rates of anisotropy's evolution with suggested values in the order of $\psi = 20$ to 40.

- The proposed model's new de-orientational kinematic hardening rule, succeeds in describing a strain softening response together with a unique and common critical state conditions independent of the initial anisotropy and of the stress path followed, as an outcome of an anisotropy degradation mechanism associated with the onset of plastic deviatoric strains. Parameter $\zeta_q^p$ efficiently controls the intensity of the described anisotropy degradation, with suggested values ranging from $\zeta_q^p = 20$ to 50.

- With a proper selection of parameters $\psi$ and $\zeta_q^p$ the model can simultaneously simulate a strain softening response during undrained triaxial loading and a continuous strain hardening response during drained triaxial loading, in agreement with common experimental observations.

- The selected flow rule can accurately reproduce the desired plastic dilatancy provided that parameter $\chi$ has been properly calibrated. In general it accounts for an increasing dilatancy with an increasing anisotropy.

- The model's predictions during triaxial loading of overconsolidated soil elements are severally affected by its relatively large elastic region. It predicts a strain softening response during undrained triaxial loading, contradicting experimental evidence which suggests a continuously strain hardening response.

- The model's ability to account for the preferred stress directions due to an anisotropic soil fabric is reflected on the predictions during loading tests to different loading directions (i.e, plane strain, direct simple shear), where contrary to isotropic constitutive models the proposed model can accommodate a loading direction dependent behaviour within a common set of parameters.

Regarding the unsaturated features of the proposed model we may highlight:

- The proposed model reproduces a nonlinear increase of the post-yield compressibility with suction and also an increasing elastic domain, both representing the beneficial effect of partial saturation in strengthening and stiffening soil response, in agrement with the proposed framework and with common experimental observations.

- During constant suction compression tests the model adequately represents a constantly increasing compressibility following an increasing degree of saturation; it results in convex compression lines in the net stress domain.

- A nonlinear increase in shear strength with suction is reproduced as an outcome of Bishop's stress formulation, while its evolution follows the nonlinearity of the $s \cdot S_r^e$ term.

- The beneficial effect of suction in shear strength gets less profound as the confining stress increases.

- Critical state conditions are represented by a unique critical state line in terms of Bishop's stress and by suction dependant critical state lines in terms of net stress. Additionally, partial saturation favours an increased void ratio under critical state conditions.

- Wetting tests reveal that the model can adequately reproduce a maximum in the volume reduction during wetting. The collapse potential depends on both the applied suction and on the level of the applied net stress in agrement with common experimental observations.

With respect to anisotropic and unsaturated material states, the model's predictions are in fact the resultant of the two different behavioural aspects as previously summarized. We may highlight that:

- Partial saturation decreases the rate of anisotropy's evolution.

- Any radial stress path imposed in terms of net stress corresponds to a smaller stress ratio in terms of Bishop's stress.

- The model predicts a decreasing coefficient of lateral earth pressure at rest with partial saturation.

Finally regarding the developed numerical tools we shall mention that:

- both the SMP algorithm and the Abaqus UMAT reproduce sound results;

- the Simulia Abaqus' lack of a void ratio dependent WRM severely limits the model's unsaturated capabilities and especially the constantly evolving post yield compressibility and the model's natural representation of a maximum of

collapse. On the other hand the reproduced, apparent preconsolidation pressure and initial post yield compressibility as well as the behaviour in the elastic domain and shear strength predictions are not severely affected.

In the following chapter the proposed constitutive model is further evaluated against specific experimental results.

# Chapter 9

# Comparison with Experimental Measurements

## 9.1 Introduction

The present chapter addresses the necessity to evaluate the proposed model's simulation capabilities against experimental results, while it additionally elaborates on the calibration procedure required to estimate the model parameters.

It is divided in three main sections. The first section deals exclusively with the anisotropic characteristics of the model, utilizing data from the Lower Cromer Till (LCT) experimental investigation presented by Gens (1982). The second section deals with unsaturated soil behaviour, based on the experimental investigation of Casini (2008) on the Jossigny silt behaviour. Finally, in the third section, results from the Barrera (2002) experimental investigation on the hydromechanical behaviour of Barcelona Clayey Silt (BCS) are used to evaluate the model's ability to simulate collapse.

The presented simulations have been performed with the Single Material Point (SMP) testing code, presented in chapter 7 and evaluated in chapter 8. Both the experimental and the simulation data are presented in the triaxial stress space $(p, q)$. It is reminded that deviatoric stress $q$ and the corresponding strain $\varepsilon_q$ are systematically calculated as $q = \sigma_v - \sigma_h$ and $\varepsilon_q = \frac{2}{3}(\sigma_v - \sigma_h)$. Hence, in triaxial extension they obtain negative values facilitating an easy representation of the results.

## 9.2 Evaluation of the Anisotropic Characteristics of the proposed model based on Gens (1982) experimental results

### 9.2.1 General - The tested soil

Gens (1982) presented one of the most complete and well documented experimental studies on the effect of stress induced anisotropy on shear strength and on compressibility of structureless soils. The soil used is a glacial till of low plasticity, named the Lower Cromer Till (LCT). Table 9.1 summarizes its main physical properties. The author originally classified the soil as a sandy clay of low plasticity (CLS), based on the British Soil Classification System, while according to the Unified Soils Classification System (USCS) it is classified as a Clayey Sand (SC).

**Table 9.1:** Index properties of the Lower Cromer Till (LCT). (Gens 1982)

| Grain Size Distribution | | Atterberg Limits | | Other | |
|---|---|---|---|---|---|
| Gravel | 0% | LL | 25% | $G_s$ | 2.65 |
| Sand | 58%[*1] | PL | 13% | Activity | 0.71 |
| Silt | 25% | PI | 12% | | |
| Clay | 17% | | | | |

[*1] mainly fine sand.

The available experimental results comprise of a significant number of consolidation tests under different boundary conditions as well as triaxial compression and extension tests on both isotropically and anisotropically consolidated soil samples. Laboratory tests where conducted on reconstituted samples.

Focusing on the effects of stress induced anisotropy, Gens (1982) paid special attention to the sample preparation method and three different technics where used. Soil samples intended for isotropic testing where prepared by isotropically consolidating the slurry in a large diameter ($152mm$) triaxial cell. A maximum mean effective stress equal to $p = 120kPa$ was applied and after consolidation the sample was unloaded to form smaller samples suitable for conventional triaxial testing in a $38mm$

apparatus. The selected preparation method ensured that soil specimens tested under isotropic conditions had never been subjected to an anisotropic stress field during their post-reconstitution stress history.

For $K_0$ testing, soil specimens where prepared by initially consolidating the slurry soil in a large oedometer ($229mm$ diameter) to ensure an 1D consolidation background. The maximum vertical effective stress applied was $\sigma_v = 200kPa$. After sufficient time, to allow for excess pore pressure dissipation, the sample was unloaded and typical $38mm$ diameter specimens where formed for triaxial testing.

Finally, a third procedure was used to directly obtain small cylindrical samples ($38mm$ in diameter) for anisotropic radial compression under different stress ratios. The samples where prepared directly from a slurry state, by imposing an initial suction of $s = 7kPa$. Suction applications increases the effective stress in the sample and thus they become sufficiently self supported to be set up for the triaxial test. Such specimens are not expected to posses any memory of initial anisotropy.

### 9.2.2 Compressibility and Critical State parameters

This paragraph describes the calibration procedure performed in order to estimate representative values for the compressibility and critical state parameters. Figure 9.1 presents results from consolidation tests under different stress paths. Graphs (a) and (b) refer to isotropically consolidated soil samples, while graphs (c) and (d) to anisotropically ($K_0 = 0.5$) consolidated soil samples.

Data of figure 9.1 are used to derive the slope and the position of the virgin compression lines corresponding to isotropic and $K_0$ conditions. For that reason only compression tests at a relatively high stress level are included, as such tests ensure deformation under a practically constant compressibility. The estimated intrinsic compression lines are also included in the figure, with their properties derived through a two stage regression analyses.

Initially the typical $v = N - \lambda \ln p$ expression is fitted in the experimental results, by assuming both $\lambda$ and $N$ as unknowns. Data points corresponding to a relatively high mean stress where used ($p > 300kPa$), to ensure a linear behaviour in the $v - \ln p$ plane. Table 9.2 summarizes the outcome of the performed regression analyses, which indicate that practically parallel intrinsic compression lines, with an averaged slope of $\lambda = 0.067$, apply for both isotropically and $K_0$ consolidated specimens.

With a representative $\lambda$ value, the regression analyses is repeated to fit the $v =$

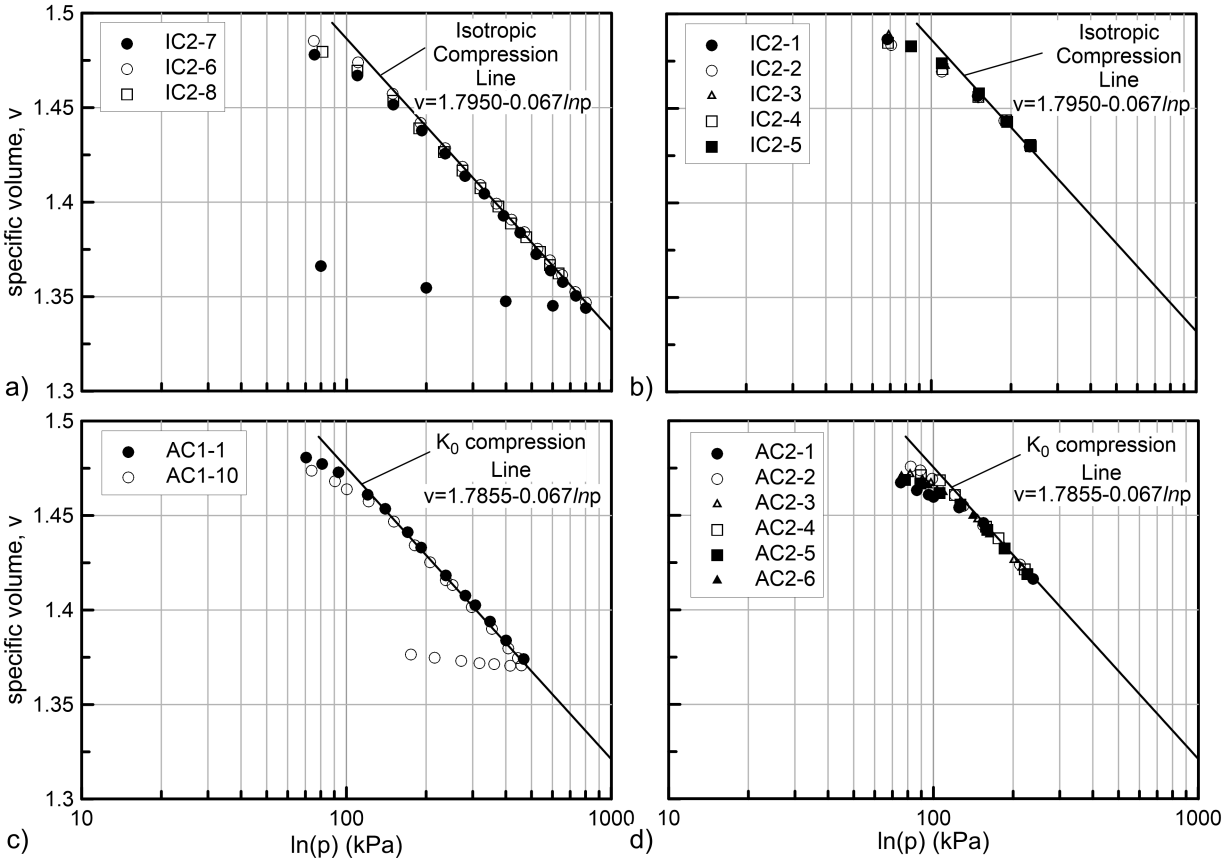


**Figure 9.1:** Gens (1982) experimental results in: a, b) from isotropic compression tests, while: c, d) from $K_0 = 0.5$ radial compression tests, together with the calibrated intrinsic compression lines.

**Table 9.2:** Regression analysis results. Fitted equation $v = N - \lambda \ln p$

| Test | N | $\lambda$ |
|---|---|---|
| IC2-6 | 1.806 | 0.066 |
| IC2-7 | 1.799 | 0.068 |
| IC2-8 | 1.778 | 0.065 |
| AC1-1 | 1.788 | 0.068 |
| AC1-10 | 1.791 | 0.068 |
| Average | | 0.067 |

$N - 0.067 \ln p$ equation. Thus, new $N$ values are raised, mathematically enforced to be parallel, according to the compressibility framework underlying the proposed

model. Such a double stage curve fitting approach is necessary due to the fact that even the slightest difference in the slope of the compression lines, produces significant variations in the calculated $N$ values. Table 9.3 summarizes the results of the latest regression analyses.

**Table 9.3:** Regression analysis results. Fitted equation: $v = N - 0.067 \ln p$

| Test | $N_{iso}$ | Test | $N_{0.75}$ |
|---|---|---|---|
| IC2-6 | 1.7964 | AC1-1 | 1.7835 |
| IC2-7 | 1.7932 | AC1-10 | 1.7876 |
| IC2-8 | 1.7951 | | |
| Average | 1.7950 | | 1.7855 |

Finally, the isotropic and the $K_0$ intrinsic compression lines are described by the following expressions:

$$v_{iso} = 1.7950 - 0.067 \ln p \tag{9.1a}$$

$$v_{K_0} = 1.7855 - 0.067 \ln p \tag{9.1b}$$

Figure 9.1 also includes the results from unloading tests. They are used to estimate the slope of the swelling line by fitting a logarithmic expression. The IC2-7 data raise a $\kappa = 0.1$ value, while the AC2-10 data raise a $\kappa = 0.06$ value. Hence, an average value of $\kappa = 0.08$ is selected on the absence of additional data.

The next calibration step deals with the slope of the Critical State Line (CSL) in the $p - q$ space as well as with its position in the $v - \ln p$ plane. The examined experimental data agree on a common critical state which is independent of the initial stress induced anisotropy and from the stress path taken to critical state (drained or undrained). Nevertheless, different critical state conditions apply to compression and extension. Given that the proposed model does not account for a different behaviour in extension and compression, the performed calibration will initially focus on triaxial compression tests.

Figure 9.2 plots the ultimate states corresponding to drained and undrained triaxial compression tests, both from isotropically and anisotropically consolidated soil

samples. Moreover, results from both normally and overconsolidated soil samples are included.

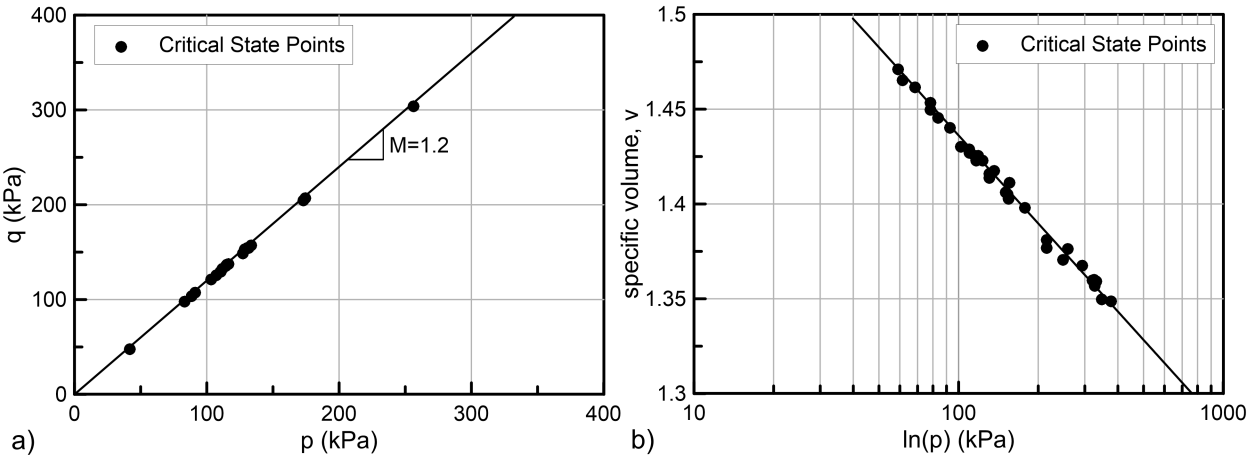


**Figure 9.2:** Gens (1982) critical state points on: a) the $p-q$ and b) the $v-\ln p$ planes together with the calibrated CSL. Data correspond to drained and undrained triaxial loading tests under various initial anisotropic states and overconsolidation ratios.

The ultimate stress points reveal a well defined critical state surface on the $v-p-q$ space. Its projection on the $p-q$ space is described by a line with a slope $M=1.2$ ($c=0.9798$, in the transformed stress space) passing through the axes origin (typical CSL), while in the $v-\ln p$ plane, the $v=\Gamma-0.067\ln p$ equation is fitted to the available results a priory assuming that it is parallel to the previously defined ICLs. The $\Gamma=1.7450$ value is raised by the regression analyses, while the excellent fitting achieved confirms the hypothesis of parallel lines.

Based on the already defined parameters, we may further calculate a representative value for parameter $r_s$, describing the relative position of different compression curves in the proposed compressibility framework. Equation 5.12a, repeated here as equation 9.2 for clarity, is used:

$$N_n=\Gamma+(N_{iso}-\Gamma)\left(1-\frac{(q/p)^2}{M^2}\right)^{r_s} \tag{9.2}$$

Utilizing the previously estimated $N_{iso}$, $N_{K_0}$, $\Gamma$ and $M$ values, we may solve for the unknown parameter $r_s$:

$$1.7855=1.7450+(1.7950-1.7450)\left(1-\frac{(0.75)^2}{1.2^2}\right)^{r_s}\Rightarrow r_s=0.425 \tag{9.3}$$

The calculation contains a silent assumption; that the coefficient of lateral earth pressure at rest is $K_0 = 0.5$, in order for the corresponding stress ratio to equal $n = q/p = 0.75$. The $K_0 = 0.5$ value is the one suggested by Gens (1982), based on the results of $K_0$ consolidation tests in the triaxial apparatus where the stress ratio was adjusted to maintain zero horizontal strains.

Furthermore, based on the estimated parameters, the yield surface aspect ratio parameter $k$ is calculated using equation 6.66, also repeated below as equation 9.4 for clarity.

$$\Gamma = N_{iso} - (\lambda - \kappa) \ln (1 + \frac{c^2}{k^2}) \tag{9.4}$$

In eq. 9.4, the only unknown parameter is $k$, resulting to:

$$1.7450 = 1.7950 - (0.067 - 0.008) \ln (1 + \frac{0.9798^2}{k^2}) \Rightarrow k = 0.84841 \tag{9.5}$$

which in the triaxial stress space ($p$, $q$) corresponds to a yield surface aspect ratio $N = 1.039 \approx 1.05$.

Table 9.4 summarizes the derived parameters for the Lower Cromer Till (LCT), while the hardening rule parameters $\psi$ and $\zeta_q^p$ will be estimated on the basis of consolidation and triaxial loading tests.

**Table 9.4:** The calibrated model parameters corresponding to the LCT behaviour.

| Parameter | Value | Parameter | Value |
|---|---|---|---|
| $\kappa$ | 0.008 | $N_{iso}$ | 1.7950 |
| $\lambda$ | 0.067 | $\Gamma$ | 1.7450 |
| $\nu$ | $1/3^{*1}$ | $r_s$ | 0.47 |
| $k$ | 0.79046 | $\chi^{*2}$ | 0.49444 |
| $c$ | 0.91287 | | |

$^{*1}$ assumed value.
$^{*2}$ based on the proposed calibration procedure (see eq. 6.68) for $K_0 = 0.5$.

Finally, before concluding this paragraph, the compressibility framework's equation 9.2 is used in combination with the parameters of table 9.4 to compare the predicted position of intrinsic compression lines corresponding to intermediate stress

ratios $n$ with actual LCT data. It is reminded that with the exception of the isotropic and the $K_0$ ICLs the rest of the data corresponding to different stress ratios have not been raised in the performed calibration. Thus, the presented comparison is regarded a blind prediction. Figure 9.3 presents the comparison, revealing a good agreement between the predicted ICLs and the available experimental results.

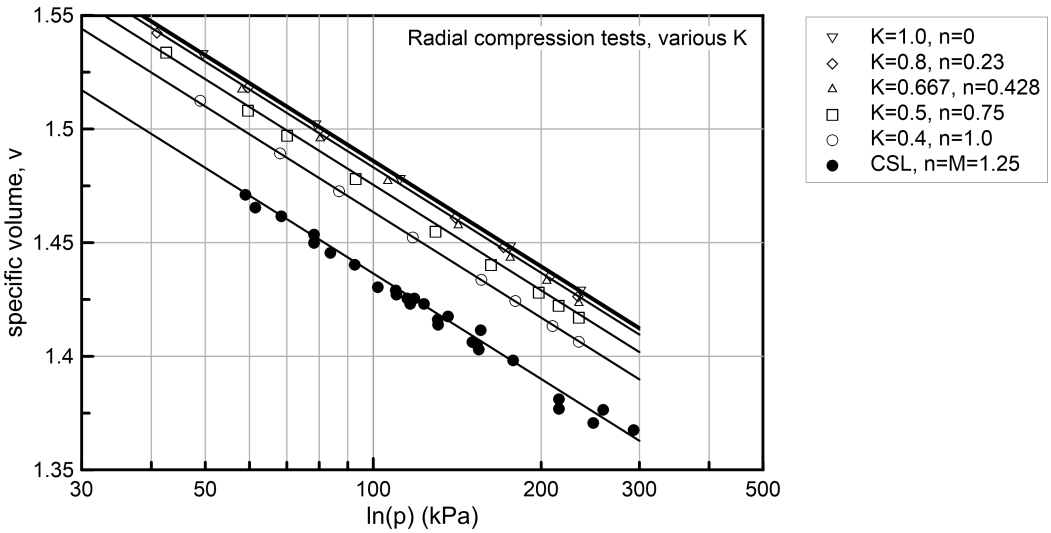


**Figure 9.3:** Gens (1982) experimental results from various K consolidation tests and the ICLs predicted by the proposed compressibility framework.

### 9.2.3 Simulation of Consolidation Tests

Based on the derived parameters, the proposed constitutive model is used to simulate various consolidation tests reported in Gens (1982). Figure 9.1a, presents the experimentally determined compressibility behaviour of the LCT under isotropic conditions. The results regard three initially overconsolidated soil samples with a $p_0 = 120kPa$, corresponding to the maximum cell pressure applied in the large triaxial cell during sample preparation. The isotropic nature of the preparation method also justifies the assumption of $\boldsymbol{b} = \mathbf{0}$ for the initial anisotropy tensor.

Figure 9.4 compares the simulation (SMP) results with their laboratory counterparts. The unloading stage of test $IC2-7$ is also modelled. A satisfactory agreement is achieved, attributed primarily on the good prediction of the initial void ratio value, which is an outcome of the compressibility framework using the assumed initial state. The good representation of the post yield compressibility was expected due to the fact that the simulation data where also used during calibration. The results are

independent of the hardening rule parameters $\psi$ and $\zeta_q^p$ as no evolution of the stress induced anisotropy occurs.

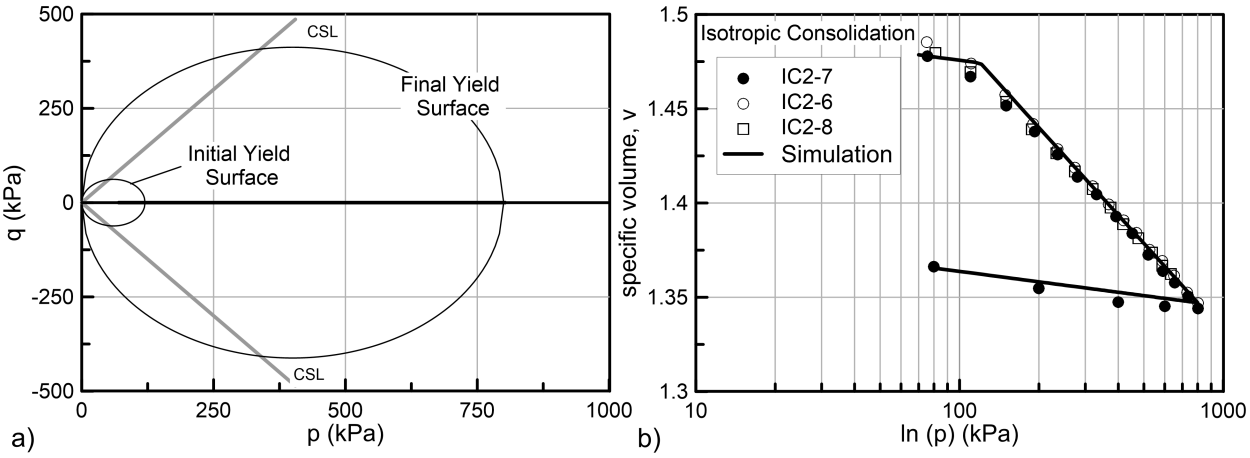


**Figure 9.4:** Simulation of LCT isotropic compression tests; a) the $p-q$ space; b) the $v-\ln p$ plot.

Figure 9.5 extends the discussion to anisotropic compression, comparing simulation results with the experimental results of figure 9.1c (corresponding to $K_0$ consolidation). The preparation method involved ($1D$) consolidation in a large oedometer and thus, the tested specimens had already been subjected to an anisotropic stress field prior to the examined $K_0$ radial consolidation. Therefore, we select to simulate the complete loading history of the material starting from a slurry state, with the latter assumed related to an isotropic stress state with a mean effective stress of $p = 1kPa$, normally consolidated and without any memory of stress induced anisotropy ($\boldsymbol{b} = \mathbf{0}$).

Initiating from the aforementioned conditions, an $1D$ compression tests, up to a vertical effective stress of $\sigma_v = 200kPa$, is simulated to account for the preparation method. The soil is then unloaded and reloaded by imposing a radial stress path with $K_0 = 0.5$. Various $\psi$ values were tried, while simultaneously the anisotropy degradation mechanism was deactivated ($\zeta_q^p = 0.0$), as suggested in Chapter 8. A value of $\psi = 30$ turns out as a reasonable selection with the simulation results depicted in figure 9.5.

Regarding the evolution of primary anisotropy during the aforementioned loading sequence, we may observe that the initial oedometric compression seems sufficient to adjust the soil's anisotropy to the loading direction. This is reflected in the orientation of the yield surface at the end of the $1D$ compression which is practically aligned with

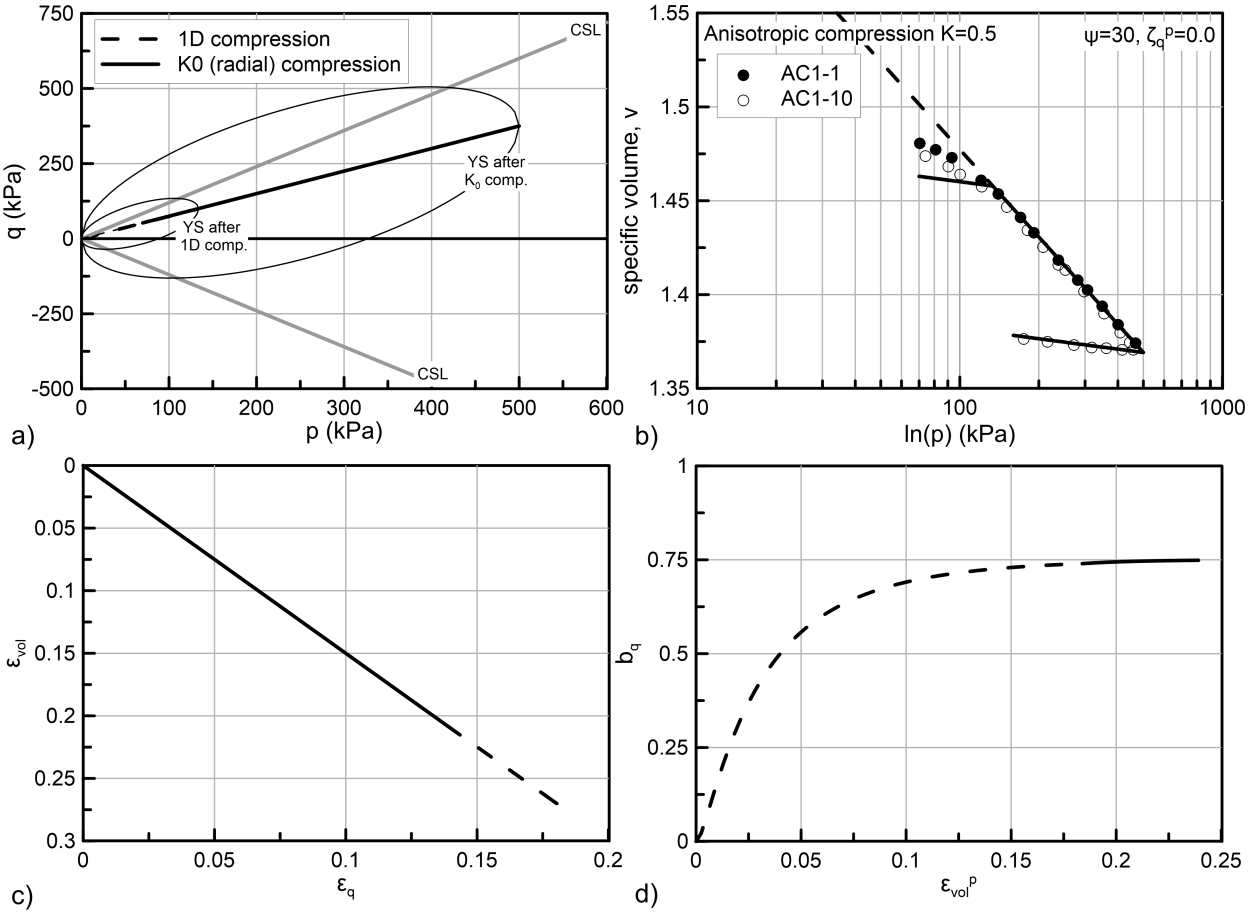


**Figure 9.5:** Simulation of LCT anisotropic ($1D$ & $K_0$) compression tests; a) the $p-q$ space; b) the $v-\ln p$ plot; c) the $\varepsilon_q - \varepsilon_{vol}$ and; d) the $b_q - \varepsilon_{vol}^p$ plot.

the corresponding stress path, as well as in the constant dilatancy reproduced during the $K_0$ consolidation stage. It is also interesting to notice that anisotropy stabilizes after 20% of plastic volumetric straining, which is similar to what Kavvadas (1982) reports for the Boston Blue Clay.

With the selected $\psi$ parameter, the proposed constitutive model is used to simulate the radial compression tests under various stress ratios $K$ (see figure 9.3). Samples were prepared by applying a small amount of suction ($s = 7kPa$) to the reconstituted LCT. We assume that these samples were initially isotropically consolidated with $p_0 = 10kPa$, due to the increase in the mean effective stress caused by the applied negative water pressure, with no stress induced anisotropy[1] ($\boldsymbol{b} = \mathbf{0}$).

Figure 9.6 presents the simulation results and compares them with the experimental data. The model provides an accurate prediction of the obtained compress-

[1]The effect of suction is assumed isotropic.

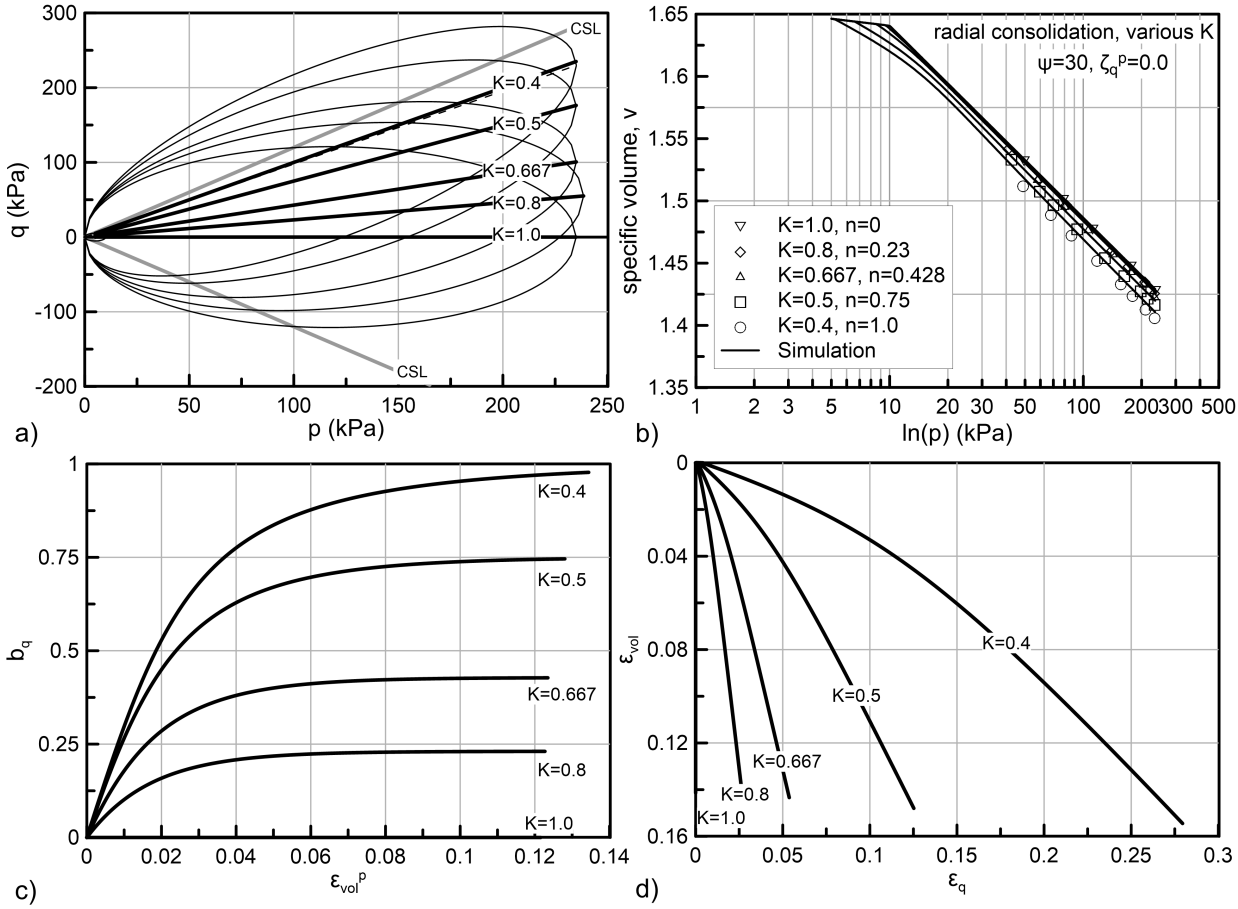


**Figure 9.6:** Simulation of LCT anisotropic (various K) compression tests; a) the $p-q$ space; b) the $v-\ln p$ plot; c) the $\varepsilon_q-\varepsilon_{vol}$ and; d) the $b_q-\varepsilon_{vol}^p$ plot.

ibility behaviour, considering that the presented simulation corresponds to a blind prediction. Additionally, the results indicate that initial loading up to $p=233kPa$ sufficiently adjusts primary anisotropy to the applied stress path. This is of great importance, as the $p=233kPa$ is the preconsolidation pressure used by Gens in the triaxial loading tests discussed in the following paragraphs. The required plastic volumetric strains corresponding to stabilized anisotropic conditions is approximately 12%. This is below the 20% observed in the case of $1D$ compression, indicating that radial compression tests (stress controlled) are more efficient in altering soil anisotropy.

### 9.2.4 Simulation of Triaxial Compression Tests

This paragraph focuses on the evaluation of the model's predictions against experimental results of drained and undrained triaxial loading. Emphasis is given in the

simulation of anisotropically consolidated LCT specimens. Parameters of table 9.4 are used and with respect to the hardening rule parameters, a value of $\psi = 30$ is selected according to what discussed in the previous paragraph, while through a trial and error simulation approach on the available experimental results (mainly undrained loading), a $\zeta_q^p = 40$ value was found to be the most representative of the anticipated behaviour.

The applied initial stress conditions are identical to those reported by Gens (1982) and the initial yield surface inclination is assumed identical to the one imposed during consolidation ($b_q = n$). Such a selection is supported by the simulation results of the previous paragraph, indicating that the selected consolidation stress level of $p = 233kPa$ involves sufficient plastic straining for the material to fully adjust to the preferred directions of the imposed stress path. Finally the initial void ratio is an outcome of the compressibility framework, based on the assumed initial state and the selected parameters.

Figure 9.7 presents and compares the simulation with the laboratory data regarding normally consolidated soil specimens subjected to undrained triaxial loading under different initial anisotropic states. Figure 9.8 extends the comparison to overconsolidated LCT samples focusing exclusively on $K_0$ consolidated soil samples.

The comparison indicates that the model successfully predicts the residual state for increased deviatoric strains $\varepsilon_q \geq 4\%$. The ultimate deviatoric stress, the ultimate states in the $p-q$ and in the $v-lnp$ planes are well represented for all tests, irrespective of the initial anisotropy or the initial overconsolidation ratio. Thus, the results favour the model's anisotropy degradation mechanism based on the assumption of a common critical state, with the latter corresponding to an isotropic yield surface.

Unfortunately, on the other hand the model's predictions at smaller strains ($\varepsilon_q < 4\%$) lack precision, indicating that the proposed model significantly overestimates the peak strength. Moreover, in overconsolidated samples the increased peak strength predicted is also accompanied by a peculiar hook type behaviour of the stress path in the $p - q$ space.

The unsuccessful prediction of the initial part of the tests, indicates that the selected initial orientation of the yield surface ($b_q = n$) is to high. To check whether a reduced initial orientation can sufficiently improve the predictions, the anisotropy tensor $\boldsymbol{b}$ is calibrated on the experimental results, leaving aside, for the moment, the idea that the orientation of the yield surface should match the direction of the

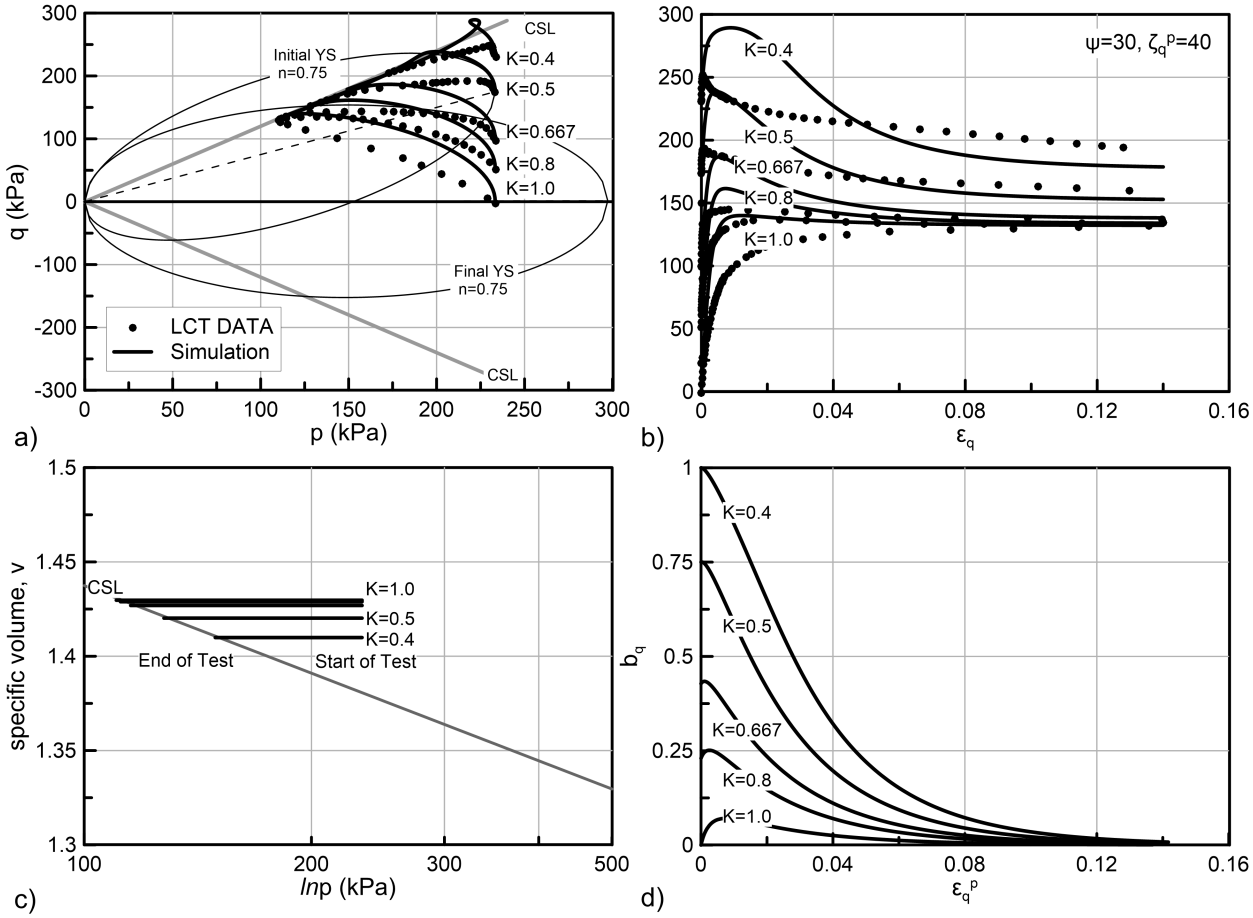


**Figure 9.7:** Simulation of LCT undrained behaviour for K-consolidated soils specimens (initial yield surface inclination coincides with the consolidation stress path); a) the $p - q$ space; b) the $q - \varepsilon_q$ graph; c) the $v - \ln p$ plot; and; d) the $b_q - \varepsilon_q^p$ plot.

consolidation stress path.

To estimate a representative initial $b_q$ value, the experimental results regarding the $K_0$ consolidated sample ($K = 0.5$) from figure 9.7 are used to perform a trial and error simulation exercise, testing different initial yield surface orientations as a portion of the stress path of the consolidation. It turned out that a reduced initial yield surface inclination corresponding to $b_q = 0.30$ is required for an adequate representation of the experimentally determined behaviour. The derived value is reduced by 60% with respect to the stress ratio of the consolidation ($n = 0.75$ for the examined $K_0 = 0.5$).

Following the calibration of the model on the $K_0$ consolidation test, we make the assumption that the observed reduction of 60% percent applies also to the rest of the examined laboratory tests. Thus, the undrained triaxial loading tests are simulated again by applying an initial yield surface orientation according to $b_q =$

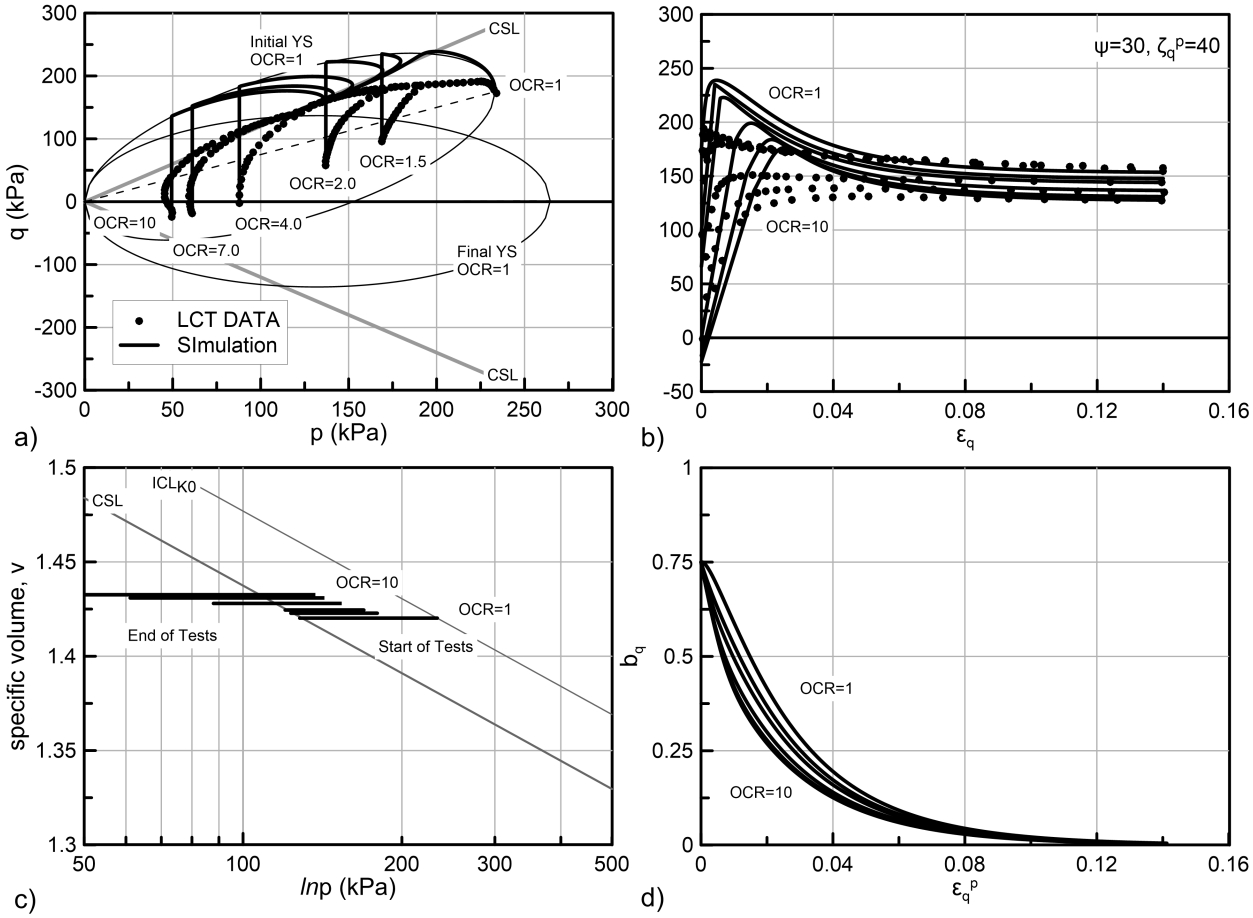


**Figure 9.8:** Simulation of LCT undrained behaviour for $K_0$ consolidated soils specimens at various OCR (initial yield surface inclination coincides with the consolidation stress path); a) the $p-q$ space; b) the $q-\varepsilon_q$ graph; c) the $v-\ln p$ plot; and; d) the $b_q-\varepsilon_q^p$ plot.

$0.4\cdot n$. Figures 9.9 and 9.10 present the results of this second simulation attempt.

It is clearly observed that the assumed reduced inclination improves significantly the simulation results. Especially for the case of the normally $K_0$ consolidated sample, used as a reference for the performed re-calibration, the predicted behaviour is practically identical to the one observed in the laboratory. For the rest of the tests, shear strength overestimation is drastically reduced, making the predictions more than satisfactory for practical applications. The already good representation of the residual state is practically not affected.

The aforementioned results are a strong indication that the idea of orienting the yield surface towards the stress path of consolidation requires reconsideration. It seems that such an assumption is very strict and although there may be evidence that it holds true for some soils it should not be generalized, as this may not be the

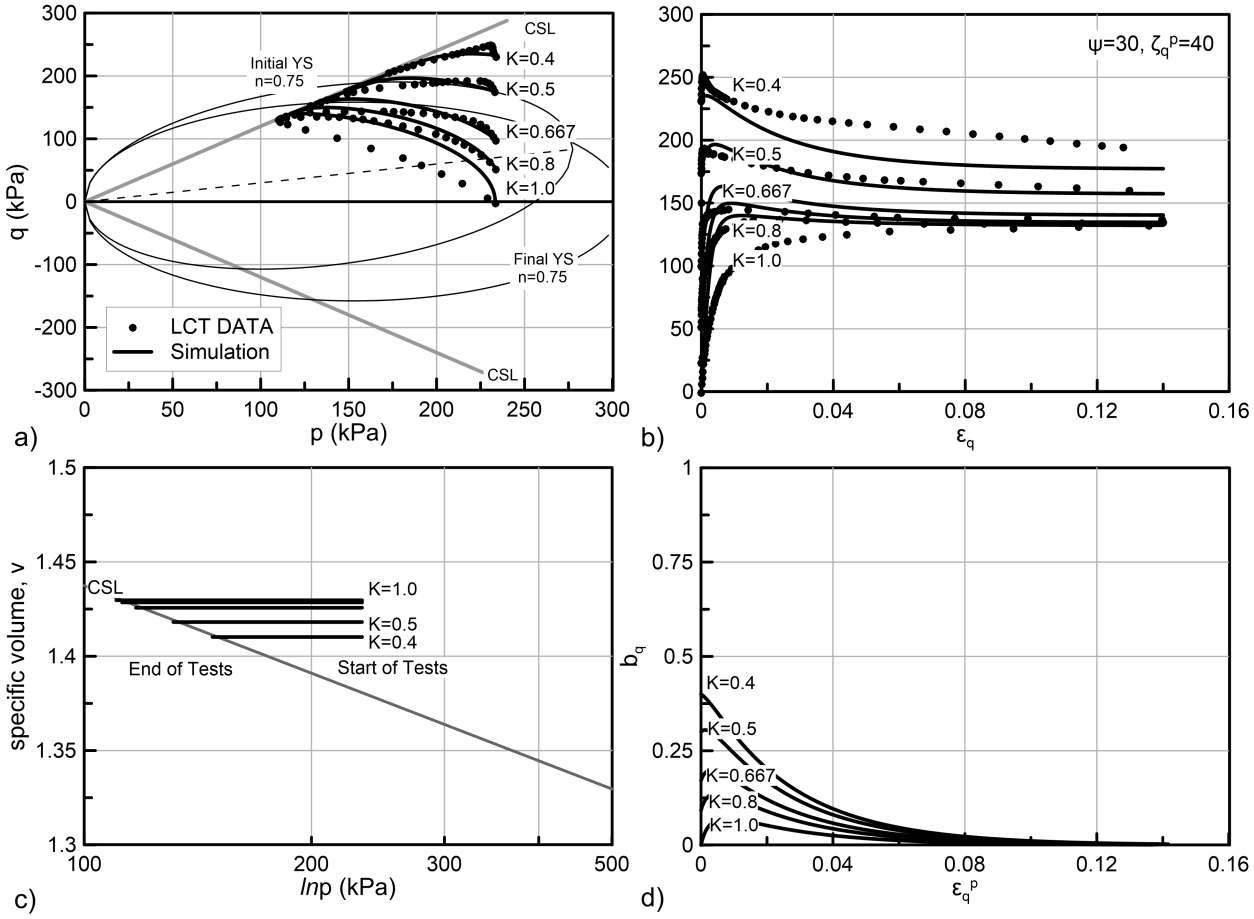


**Figure 9.9:** Simulation of LCT undrained behaviour for K-consolidated soils specimens (reduced yield surface inclination); a) the $p-q$ space; b) the $q-\varepsilon_q$ graph; c) the $v-\ln p$ plot; and; d) the $b_q-\varepsilon_q^p$ plot.

case for all soils. To improve the model towards this direction, the orientational part of the hardening rule needs enhancement towards increased versatility. Such an enhancement requires additional parameters to describe the desired relative orientation between the yield surface and the consolidation stress path.

Nevertheless, even without such a modification, the model can be efficiently used by handling the initial inclination of the yield surface as an extra "parameter", instead of a strict outcome of the consolidation process. In practical terms, when only shear strength predictions are of importance, the initial inclination of the yield surface can be fine tuned to the available experimental results, while when the behaviour during consolidation is also significant to the simulated problem, a reduced $\psi$ value can be selected to delay the rotation - distortion of the yield surface. Of course, in both cases the model's predictions will violate the underlying compressibility framework

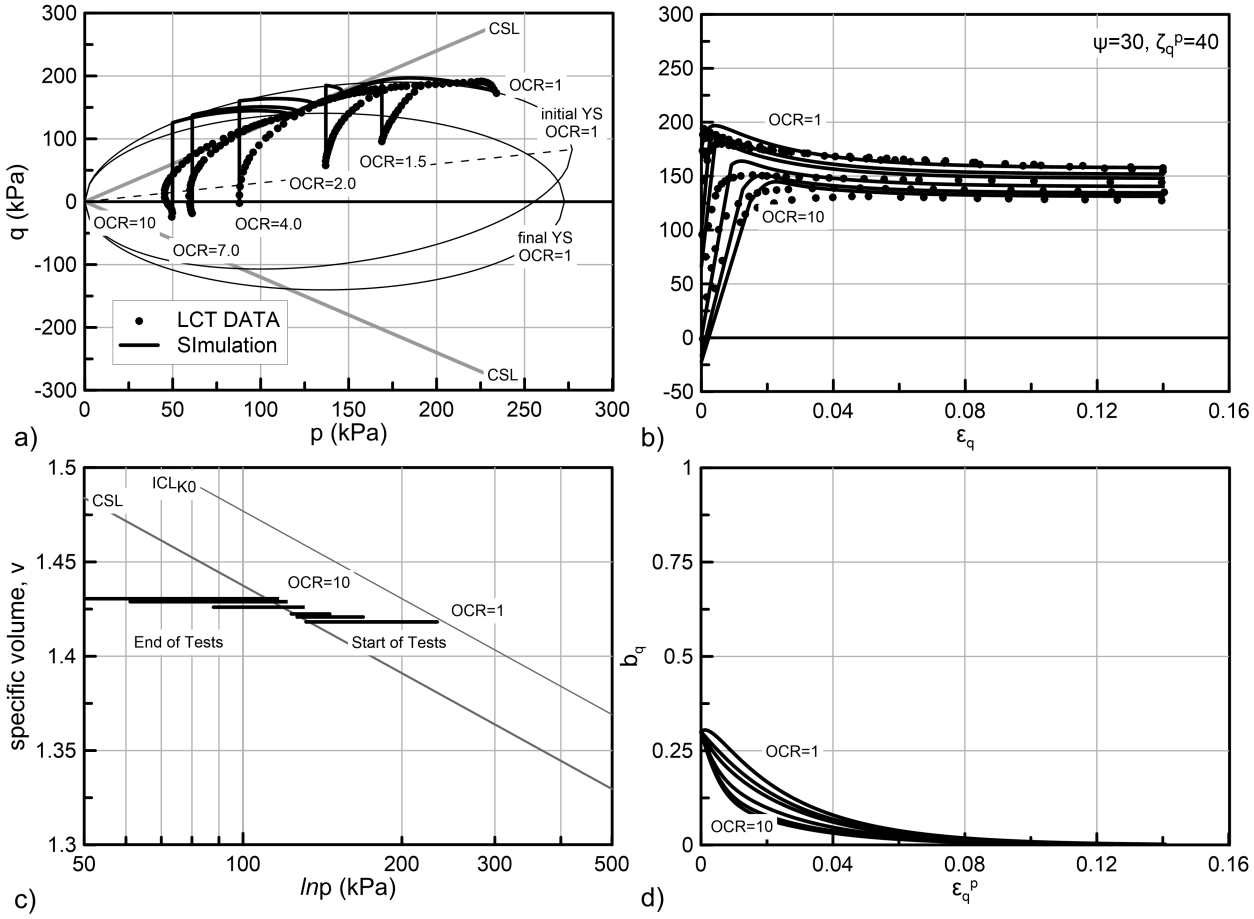


**Figure 9.10:** Simulation of LCT undrained behaviour for $K_0$ consolidated soils specimens at various OCR (reduced yield surface inclination); a) the $p-q$ space; b) the $q-\varepsilon_q$ graph; c) the $v-\ln p$ plot; and; d) the $b_q-\varepsilon_q^p$ plot.

and especially the void ratio prediction.

Regarding the simulation of the overconsolidated samples, the predicted behaviour still lacks accuracy. Nevertheless, this was expected and it is a common problem of single surface models. Single surface models, inevitable include an unrealistically extended elastic domain. Thus, in overconsolidated material states, where the initial stress state lies well inside the elastic region, it is inevitable that a significant portion of any applied loading will produce only elastic, reversible strains. On the contrary, experimentally determined data rarely indicate an extensive elastic region. The lack of an elastic region is very profound on the LCT results, especially on the $p-q$ stress path which completely lacks any evidence of an initial constant $p$ loading, typical of elastic undrained loading. To improve the results, the proposed model need to evolve to a bounding surface plasticity model.

Figure 9.11 presents and compares with experimental results, the model's predictions during drained triaxial loading on anisotropically, normally consolidated soil specimens. The same set of parameters used for the undrained tests of figure 9.9 are used, including the assumption of the reduced yield surface orientation. The model provides fair representations of the experimentally determined behaviour, both in terms of the stress strain behaviour and in terms of the reproduced dilatancy, especially if we consider that the examined data have not been used during calibration. The simulation results can be further improved if the model is recalibrated, taking into account the drained behaviour as well.

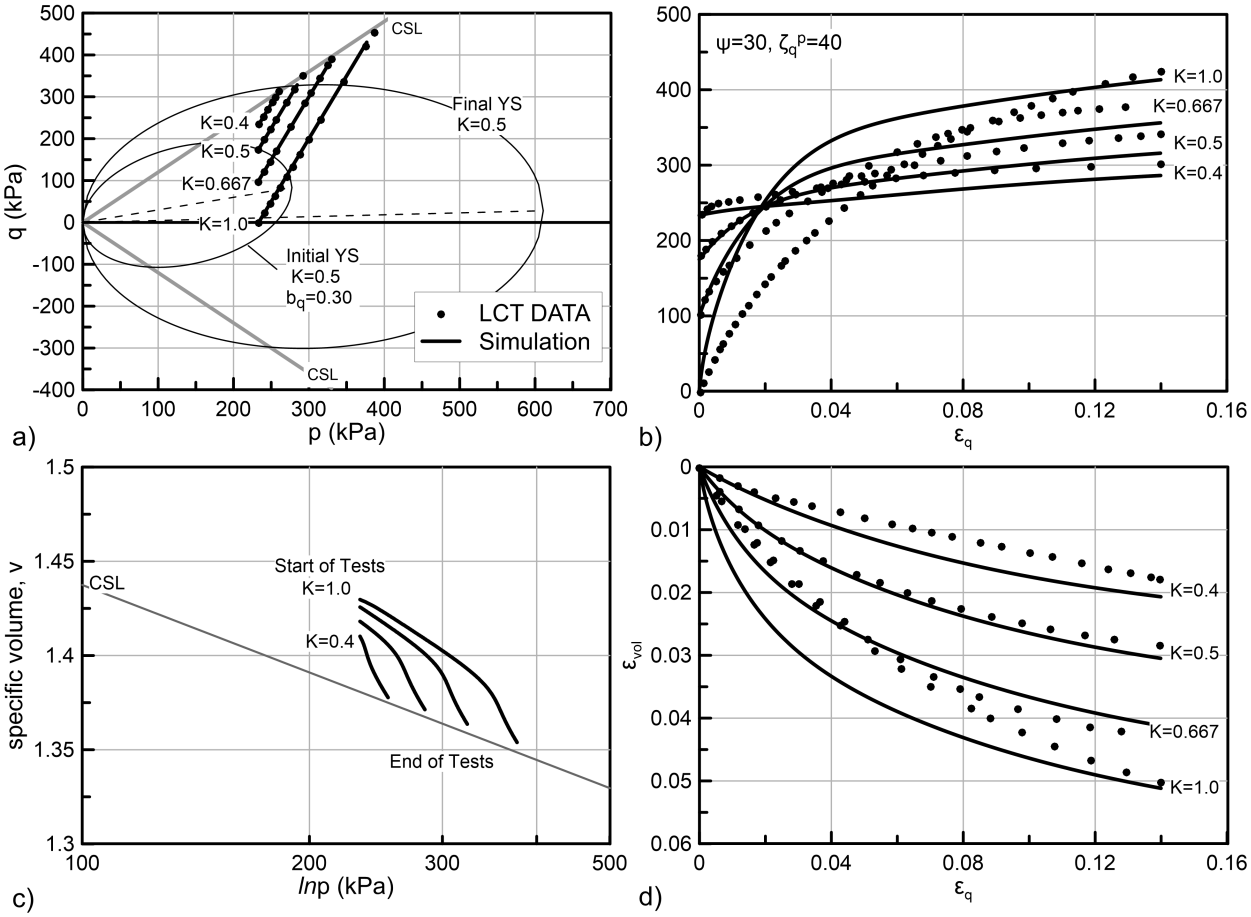


**Figure 9.11:** Simulation of LCT drained behaviour for K-consolidated soils specimens (reduced yield surface inclination); a) the $p-q$ space; b) the $q-\varepsilon_q$ graph; c) the $v-\ln p$ plot; and; d) the $\varepsilon_q-\varepsilon_{vol}$ plot.

### 9.2.5 Simulation of Triaxial Extension Tests

Gens (1982) investigated the LCT behaviour under triaxial extension loading as well. The author concluded that the material exhibits the same angle of internal friction (at the ultimate state) both in compression and extension ($\phi = 30^o$), thus indicating different critical state slopes. The proposed model lacks dependance of its critical state envelope on the Lode Angle and thus, cannot account for a unique angle of internal friction within a common set of parameters.

In order to comprehensively simulate the LCT behaviour under triaxial extension recalibration of the model's parameters is required, involving:

- the slope of the critical state line in the $p-q$ space. In triaxial conditions for $\phi = 30^o$ in extension the corresponding value is $M_e = 0.86$, which in the generalized stress space corresponds to $c_e = 0.7022$;
- the aspect ratio of the yield surface. It is recalculated according to equation 9.4 to provide a $\Gamma_e = 1.7296$, with the latter corresponding to the position of the critical state line in the $v - \ln p$ space, as proposed in Gens (1982) for extension. The calculation raises $k_e = 0.49$.

Figure 9.12 compares the model's predictions with experimental results regarding undrained triaxial extension tests on anisotropically normally consolidated soil specimens. To be in accordance with the assumptions made for the behaviour under triaxial loading, the initial yield surface inclination was assumed to be reduced with respect to the consolidation stress path ratio, using the same analogy ratio $b_q = 0.4 \cdot n$. The same set of hardening rule parameters, namely $\psi = 30$ and $\zeta_q^p = 40$ is used.

The results of figure 9.12 reveal that in terms of the stress - strain behaviour, the simulation outcome is quite satisfactory. Nevertheless the behaviour in the $p-q$ space is not well represented. Experimental data indicate that plastic loading takes place from the beginning of the test, while on the other hand the simulation predicts a significant initial elastic part. This is due to the reduced inclination of the yield surface, which moves the initial stress state away from the tip of the yield surface. Thus, undrained extension moves the stress state inside the yield surface in the elastic domain (elastic loading). Similar to what was discussed for simulations regarding overconsolidated material states the results can be significantly improved if the model evolves to a bounding surface plasticity model with a reduced elastic region.

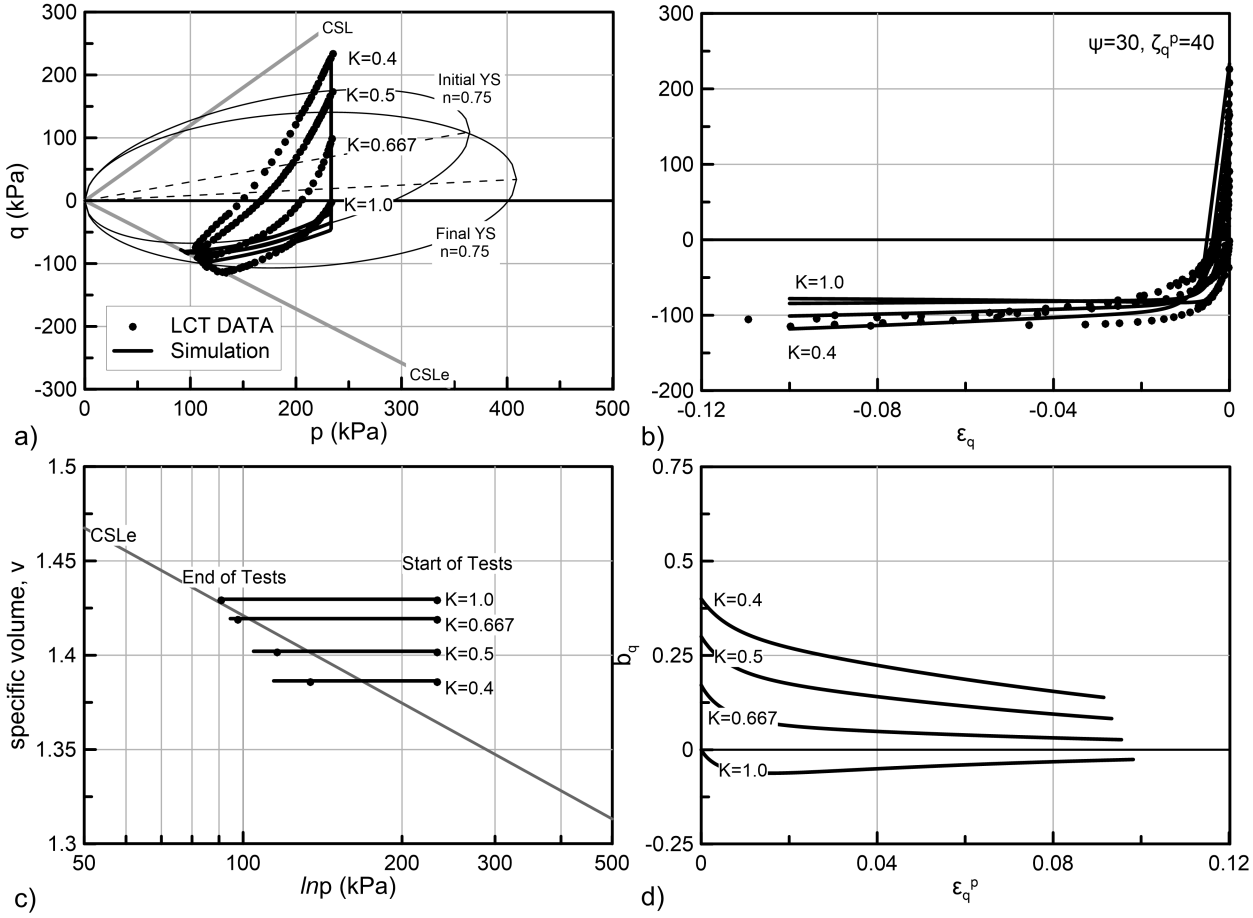


**Figure 9.12:** Simulation of LCT undrained triaxial extension behaviour for K-consolidated soils specimens (reduced yield surface inclination); a) the $p-q$ space; b) the $q-\varepsilon_q$ graph; c) the $v-\ln p$ plot; and; d) the $\varepsilon_q-\varepsilon_{vol}$ plot.

## 9.3 Evaluation of the Unsaturated Characteristics of the proposed model based on Casini (2008) experimental results

### 9.3.1 General - The tested soil

In this section the proposed constitutive model is evaluated against the experimental data of Casini (2008) on the unsaturated behaviour of a Silty Clay, namely the Jossigny Silt. The results include $1D$ consolidation tests under different suction levels, radial compression tests at different stress ratios and triaxial loading tests as well. Thus, they provide an excellent reference to evaluate both the anisotropic and unsaturated features of the proposed model.

Table 9.5 summarizes the main properties of Jossigny Silt. According to the USCS classification system, it is classified as a Silty Clay of low plasticity (ML).

**Table 9.5:** Index properties of the Jossigny Silt (JS) (Casini 2008)

| Grain Size Distribution | | Atterberg Limits | | Other | |
|---|---|---|---|---|---|
| Gravel | 0% | LL | 32% | $G_s$ | 2.69 |
| Sand | 5%[*1] | PL | 17% | | |
| Silt | 70% | PI | 15% | | |
| Clay | 25% | | | | |

[*1] exclusively fine sand.

To prepare specimens for laboratory testing, (Casini 2008) reports that loose soil was mixed at a water content equal to 13%, and then statically compacted under $1D$ conditions. For the triaxial cell, samples of $7cm$ in diameter and $14cm$ in height were formed. Compaction was performed in four layers to achieve homogenous initial conditions. For the oedometer samples, of $5cm$ in diameter and $2cm$ in height, compaction at a single layer was sufficient. In both cases, samples were compacted until a dry density of $14.5kN/m^3$ was reached. Casini (2008) reports that the required vertical stress to achieve the aforementioned dry density was ranging from 150kPa to 200kPa for each layer.

Table 9.6 summarizes the laboratory tests considered in the calibration of the proposed constitutive model. Triaxial testing involved continuous loading under a relatively small strain rate, ensuring hydraulic equilibrium and thus, the examined tests correspond to drained constant suction tests. In the oedometer, step loading was used and the available data correspond to the end of each loading step, at sufficient time after the load application, allowing for consolidation to complete. A Bishop's double cell and a suction controlled oedometer were used, both incorporating the axis-translation technique.

**Table 9.6:** The Jossigny Silt (JS) laboratory tests examined.

| Test | Stress path | Initial state (after equalization) |
|---|---|---|
| Radial Compression @ $s = 200kPa$ | | |
| TX03 | $\overline{n} = 0$ to $\overline{p} = 250kPa$ | $\overline{p} = 20kPa,\ q = 0\ \ kPa,\ e = 0.84,\ S_r = 0.44$ |
| TX04 | $\overline{n} = 0.375$ to $\overline{p} = 285kPa$ | $\overline{p} = 20kPa,\ q = 7.5kPa,\ e = 0.83,\ S_r = 0.42$ |
| TX08 | $\overline{n} = 0.750$ to $\overline{p} = 370kPa$ | $\overline{p} = 27kPa,\ q = 20kPa,\ e = 0.84,\ S_r = 0.46$ |
| TX09 | $\overline{n} = 0.875$ to $\overline{p} = 370kPa$ | $\overline{p} = 22kPa,\ q = 19kPa,\ e = 0.81,,\ S_r = 0.41$ |
| Radial Compression followed by triaxial loading (compression) @ $s = 200kPa$ | | |
| TX01 | No compression | $\overline{p} = \ 9kPa,\ q = \ 0kPa,\ e = 0.85,\ S_r = 0.44$ |
| TX02 | $\overline{n} = 0.0\ \ \ $ to $\overline{p} = 20kPa$ | $\overline{p} = 11kPa,\ q = \ 0kPa,\ e = 0.84,\ S_r = 0.44$ |
| TX06 | $\overline{n} = 0.750$ to $\overline{p} = 100kPa$ | $\overline{p} = 20kPa,\ q = 15kPa,\ e = 0.84,\ S_r = 0.39$ |
| TX07 | $\overline{n} = 0.750$ to $\overline{p} = 200kPa$ | $\overline{p} = 20kPa,\ q = 15kPa,\ e = 0.81,\ S_r = 0.41$ |
| Oedometric Compression at various suction levels | | |
| EDO-sat | to $\overline{\sigma_v} = 1600kPa$ | $\overline{\sigma_v} = \ 1kPa,\ e = 0.84,\ s = 0kPa,\ S_r = 1.00$ |
| EDO-10 | to $\overline{\sigma_v} = 1200kPa$ | $\overline{\sigma_v} = 20kPa,\ e = 0.82,\ s = 10kPa,\ S_r = 0.76$ |
| EDO-50 | to $\overline{\sigma_v} = 1200kPa$ | $\overline{\sigma_v} = 20kPa,\ e = 0.82,\ s = 50kPa,\ S_r = 0.54$ |
| EDO-100 | to $\overline{\sigma_v} = 1080kPa$ | $\overline{\sigma_v} = 20kPa,\ e = 0.76,\ s = 100kPa,\ S_r = 0.53$ |
| EDO-200 | to $\overline{\sigma_v} = 800kPa$ | $\overline{\sigma_v} = 20kPa,\ e = 0.81,\ s = 200kPa,\ S_r = 0.42$ |

### 9.3.2 Calibrating the Water Retention Model

For a successful simulation of experimental results, regarding unsaturated soil behaviour, the first calibration step should concern the estimation of a proper set of parameters for the Water Retention Model (WRM). This will provide the vital link between, suction, void ratio and degree of saturation. An accurate prediction of the degree of saturation is of a major importance, especially in Bishop's stress analysis, as it affects the accuracy of the rest of the calibration.

To proper calibrate the Gallipoli et al. (2003) WRM, data from the radial compression tests, at a constant suction $s = 200kPa$, are mainly used to calibrate the WRM for the evolution of degree of saturation with void ratio under constant suction, while data from the oedometer tests at different suction values are used to calibrate the suction vs degree of saturation relation. Figure 9.13 summarizes the experimental data considered and additionally a comparison to the predicted by the Gallipoli et al. (2003) WRM, the latter corresponding to the parameters of table 9.7.

**Table 9.7:** The Gallipoli et al. (2003) WRM parameters representative of the Jossigny Silt water retention behaviour.

| Parameter | Value | Parameter | Value |
|---|---|---|---|
| $\phi$ | 1.318 | $n$ | 1.34 |
| $\psi$ | 6.04 | $m$ | 0.15 |

It should be mentioned that the Casini (2008) study includes additional results from two wetting - drying cycles, performed at different initial void ratio values. Nevertheless these are not consistent with the rest of the available data and thus they are neglected.

The selected parameters of table 9.7 follow the values proposed in a similar calibration exercise presented by D'Onza et al. (2011). The aforementioned work presents a benchmark exercise to model the Casini (2008) results using different constitutive and different water retention models. Researches who utilized the Gallipoli et al. (2003) WRM, suggested the values of table 9.7. Figure 9.13 reveals that the proposed parameters provide an adequate modelling of the experimentally determined water retention behaviour, both in terms of $S_r$ vs $v$ and in terms of $S_r$ vs $s$ and thus, are adopted in the present study as well.

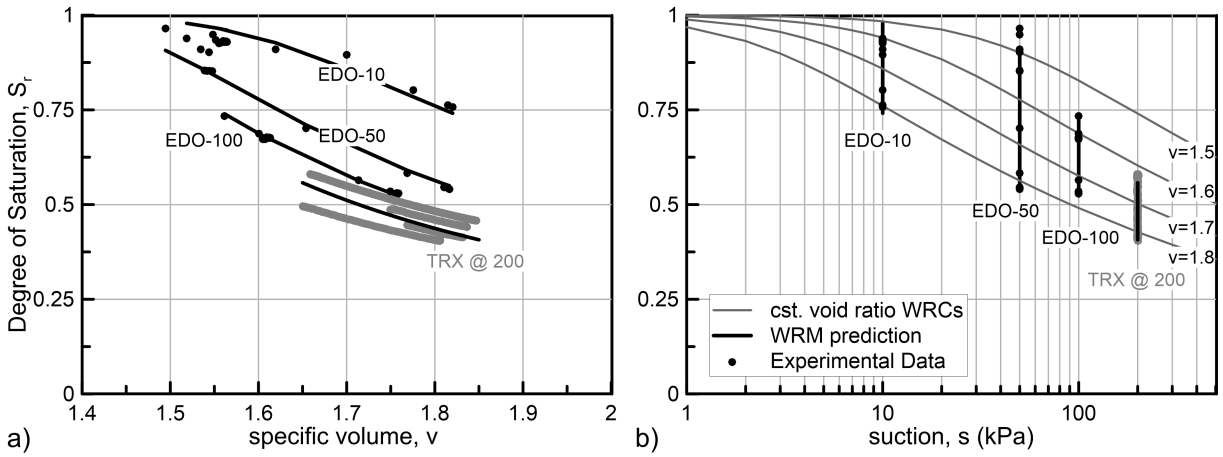


**Figure 9.13:** Comparison of the Gallipoli et al. (2003) WRM predictions with experimental data; a) the $S_r$ vs $v$ plot and; b) the $S_r$ vs $s$ plot (WRCs).

### 9.3.3 Estimation of Mechanical Parameters

This paragraph discusses the procedure followed to estimate proper values for the model's mechanical parameters. Additionally, parameter $\alpha$ used in the Alonso et al. (2010) power law (effective degree of saturation) is calculated. Although parameter $\alpha$ is not considered part of the model's parameters (it is rather part of the water retention behaviour) its calibration is included in the present paragraph due to the fact that its value is estimated simultaneously with the slope of the critical state line in the $p-q$ space.

In more detail, calibration of both parameters is based on Bishop's stress ability to properly represent the shear strength of unsaturated soils, when the effective degree of saturation is used as the scaling parameter. In that end, the experimentally determined stress paths of the TRX tests (TX01, TX02, TX06 and TX07) are plotted in the $p-q$ space, as illustrated in figure 9.14. To calculate Bishop's stress, degree of saturation is scaled for macrostructure and we seek the suitable $\alpha$ value, which produces a unique critical state line of the form $q = M \cdot p$. An $\alpha = 1.5$ value provides the best results and the corresponding slope of the critical state line is $M = 1.15$.

The next calibration step deals with the material's saturated compressibility. The available experimental results include an oedometer test under saturated conditions, allowing for a straight forward calibration of the parameters related to saturated compression. Figure 9.15 plots the experimentally determined data points in the $v - \ln p$ plane. The mean effective stress is calculated assuming a constant $K_0 = 0.5$ value, as suggested in Casini (2008). From the available data we can acquire representative

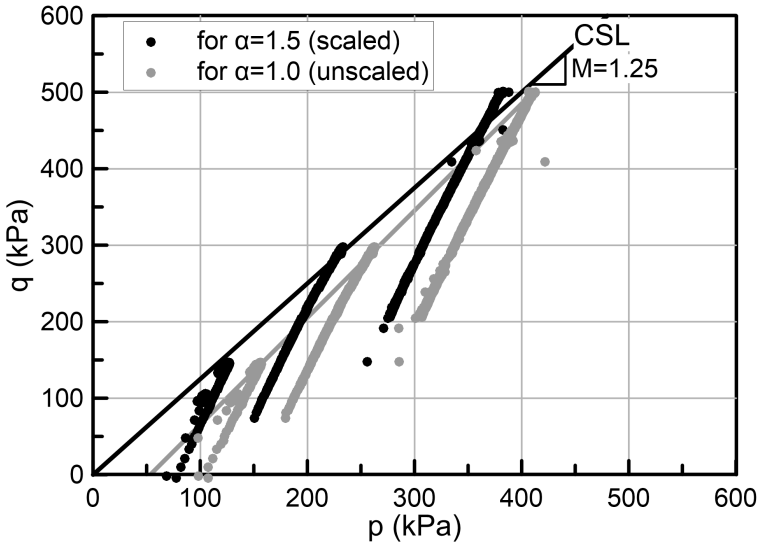


**Figure 9.14:** Triaxial loading tests plotted in the $p-q$ space to define the slope of the critical state line M and the Alonso et al. (2010) parameter $\alpha$.

values for: a) the slope of the virgin compression line under saturated conditions $\lambda(0)$; b) the slope of the swelling lines $\kappa$; c) the position of the $K_0$ compression line ($N_{K_0}$), and; d) the position of the isotropic compression line ($N_{iso}$).

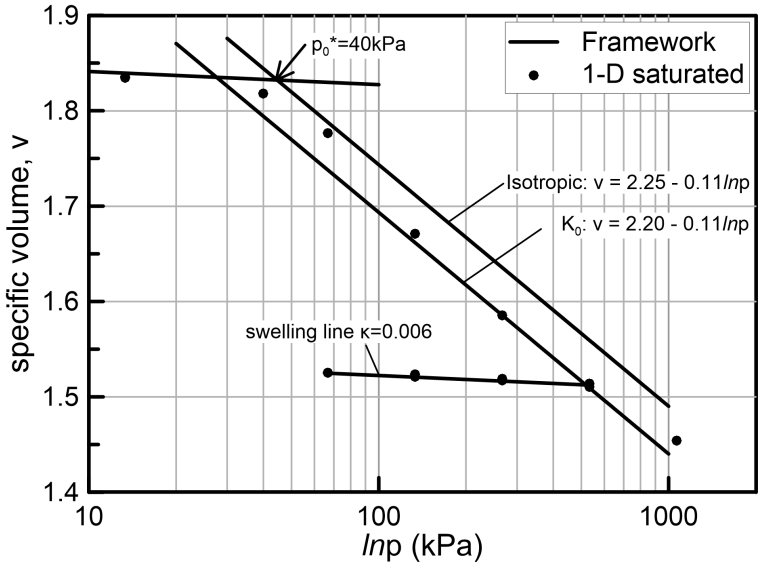


**Figure 9.15:** Elaboration of the EDO-SAT experimental data to determine the slope ($\lambda$) and position ($N$) of the isotropic and $K_0$ virgin compression lines, the slope of the swelling lines ($\kappa$) and the preconsolidation pressure under saturated conditions ($p_0^*$).

With the help of figure 9.15, we observe that the data points corresponding to a mean effective stress greater than 300kPa are indicative of the compression line

corresponding to $K_0$ conditions, leading to $N_{K_0} = 2.20$ and $\lambda(0) = 0.11$. We further assume that a parallel compression line, plotted marginally to the right of the first post yield data point, represents the isotropic compression line with $N_{iso} = 2.25$. The selected interpretation is based on the assumption that the preparation method, although involving compression under $1D$ conditions, is not sufficient to adjust the preferred directions of the material to $K_0$ loading. Thus, during subsequent oedometric compression, like the one examined here, stress induced anisotropy still evolves, justifying the anticipated behaviour.

Based on the unloading-reloading path of figure 9.15, a representative value for the slope $\kappa$ of the swelling lines is estimated, with $\kappa = 0.006$ providing the best fit.

Moreover, the intersection of the isotropic virgin compression line with a swelling line of slope $\kappa = 0.006$, describing the initial elastic reloading part of the EDO-sat test, defines the saturated preconsolidation pressure of the material $p_0^*$. A $p_0^* = 40kPa$ is selected.

At this point, we may assume that the yield surface aspect ratio $k$ is equal to that of the plastic potential function, with the latter corresponding to the previously defined slope of the critical state line $M = 1.25$. Thus, in the generalized stress space we end up with $k = c = 1.0206$.

Equation 9.4 is further utilized to calculate the position of the critical state line $\Gamma$ in the $v - \ln p$ plane, ending up with:

$$\Gamma = N_{iso} - (\lambda - \kappa) \ln \left(1 + \frac{c^2}{k^2}\right) \Rightarrow \tag{9.6}$$

$$\Gamma = 2.25 - (0.11 - 0.006) \ln \left(1 + \frac{1.0206^2}{1.0206^2}\right) \Rightarrow \tag{9.7}$$

$$\Gamma = 2.178 \tag{9.8}$$

Substituting the already defined $N_{iso}$, $\Gamma$, $c$, $k$ and $N_{K_0}$ values in equation 9.2 we may solve for the unknown parameter $r_s$:

$$2.20 = 2.178 + (2.25 - 2.178) \left(1 - \frac{(0.75)^2}{1.25^2}\right)^{r_s} \Rightarrow r_s \approx 2.0 \tag{9.9}$$

A $K_0 = 0.5$ was used in equation 9.9, and also further utilized here to calibrate the flow rule. Using equation 6.68 with $\nu = 1/3$ we derive $\chi = 0.4945$.

The last calibration step deals with the estimation of a proper set of parameters

for the unsaturated compressibility of the examined soil. The reference pressure $p^c$, as well as parameters $r$, $\beta$ and $\gamma$, related to the evolution of compressibly with partial saturation, are calibrated against suitable data regarding compression under different suction levels. For the examined case, the compression curves defined during the oedometer tests EDO-10 to EDO-200 are utilized. The calibration procedure includes the following steps:

1. available compression curves are plotted in terms of Bishop's mean stress $p$;
2. an initial post yield compressibility, corresponding to each suction level is gross estimated, as the slope of the first portion of the post yield compression line. An average value of degree of saturation relevant to this initial part of the compression line is also calculated from the available data;
3. the apparent preconsolidation pressure is determined as the intersection of the aforementioned initial post yield compressibility with a proper swelling line representative of the initial elastic loading branch.

Figure 9.16 offers a schematic representation of the aforementioned calibration procedure for two of the utilized experiments the EDO-50 and EDO-100 oedometric compression tests.

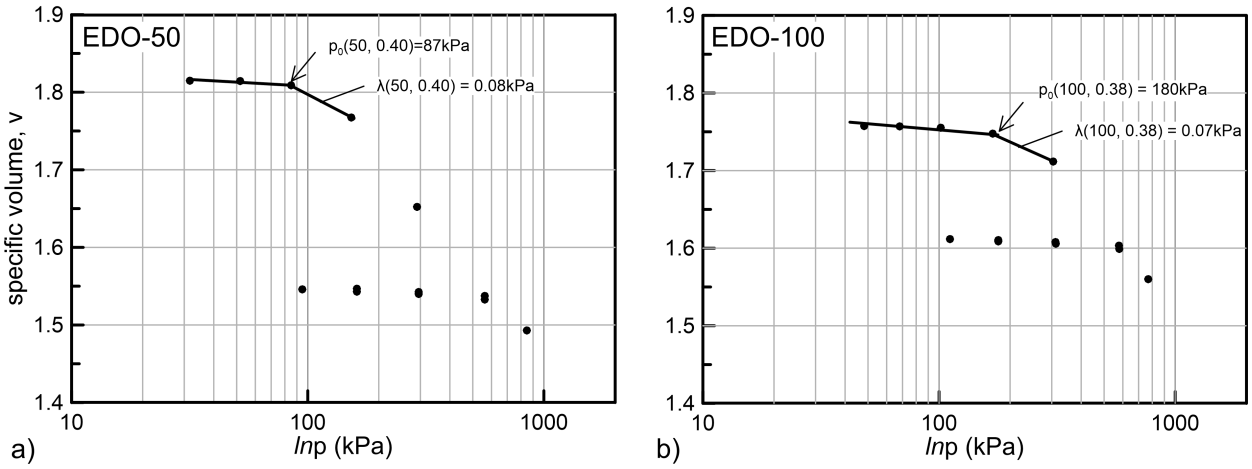


**Figure 9.16:** Elaboration of the EDO-50 and EDO-100 experimental results to determine the evolution of compressibility with partial saturation and thus calibrate the related model parameters.

The determined post yield compressibility and apparent preconsolidation pressure data are plotted as a function of suction, taking always into consideration the corresponding degree of saturation. Figure 9.17 presents the derived data (black points)

and plots them together with the predictions of the unsaturated compressibility and of the apparent preconsolidation pressure, based on the proposed model's compressibility framework. Through this plot, we seek the set of parameters that can better describe the results.

It turns out that although such a procedure can provide a good estimation of the unsaturated compressibility parameters, further adjustment of their value, via a trial and error simulation, is inevitable. The compressibility framework's predictions plotted in 9.17 reflect the final selection of parameters after such a fine tuning through trial and error simulations. For that reason, we may observe that especially for the apparent preconsolidation pressure the predicted and experimentally determined behaviour do not match well. Nevertheless, in terms of simulations the selected set of parameters produces the most satisfactory results.

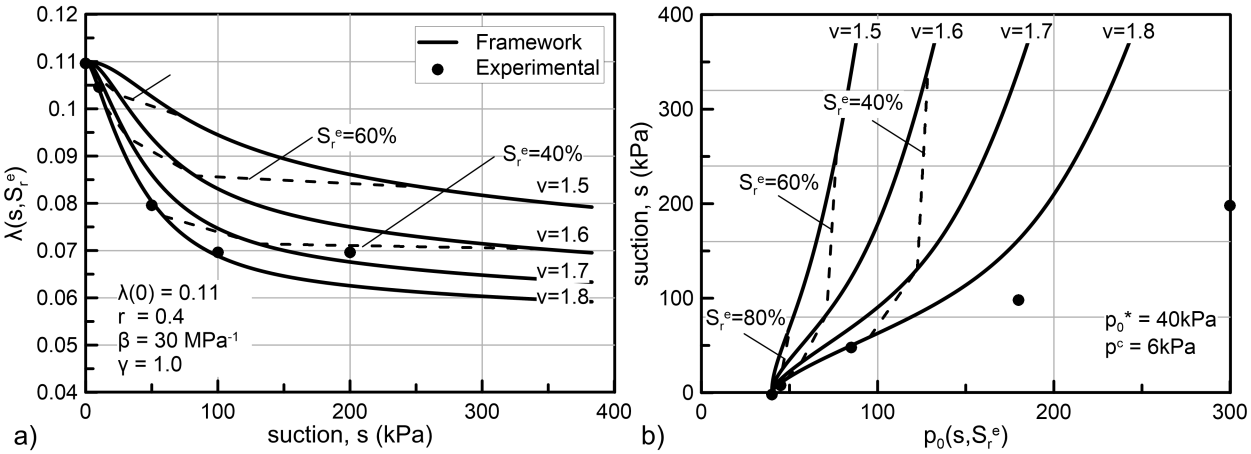


**Figure 9.17:** Calibration of the compressibility framework to accommodate the evolution of: a) compressibility with suction; and b) apparent preconsolidation pressure with suction, defined from the experimental data (EDO tests).

Table 9.8 summarizes the selected parameters. They are consistently used throughout the analysis presented in the following three paragraphs. Parameters $\psi$, $\zeta_q^p$, as well as the initial memory of stress induced anisotropy $b_q$ included in table 9.8 have been selected based on trial and error simulations.

**Table 9.8:** The calibrated model parameters corresponding to the Jossigny Silt behaviour.

| Basic Parameters | | Anisotropic Parameters | | Unsaturated Parameters | |
|---|---|---|---|---|---|
| Parameter | Value | Parameter | Value | Parameter | Value |
| $\kappa$ | 0.006 | $r_s$ | 2.0 | $r$ | 0.4 |
| $\lambda(0)$ | 0.11 | $\psi$ | 20.0 | $\beta$ | 30.0 $MPa^{-1}$ |
| $\nu$ | 0.333 | $\zeta_q^p$ | 20.0 | $\gamma$ | 1.0 |
| $c$ | 1.0206 | $\chi$ | 0.4945 | $p^c$ | 6 $kPa$ |
| $k$ | 1.0206 | Alonso et. al. (2010) power law | | | |
| $N_{iso}$ | 2.25 | $\alpha$ | 1.5 | | |
| $\Gamma$ | 2.178 | | | | |
| Initial Hardening Variables | | | | | |
| $P0^*$ | $40kPa$ | $b_q$ | 0.15 | | |

### 9.3.4 Simulation of Oedometric tests at five different suction levels

Figure 9.18 compares the simulation results with experimental data, regarding the oedometric test performed under saturated conditions (EDO-sat). The results are in good agreement with the experimental behaviour.

Graphs (c) and (d) plot the evolution of parameter $b_q$, reflecting the inclination of the yield surface in the triaxial stress space. The initial inclination ($b_q = 0.15$) represents the anisotropy induced in the tested soil during the samples preparation ($1D$ static compaction). During the oedometric test examined anisotropy further evolves and adjusts to the direction of the imposed stress path after approximately 20% of plastic volumetric straining.

Figure 9.19 extends the comparison to the oedometric tests under unsaturated conditions. Both the simulation and the experimental data are presented and compared under both in terms of Bishop's stress and net stress. Net stress representation offers a direct comparison between the measured and the predicted behaviour, independently of the assumption made in Bishop's stress representation (i.e, effective degree of saturation). For similar reasons, the comparison is given in terms of verti-

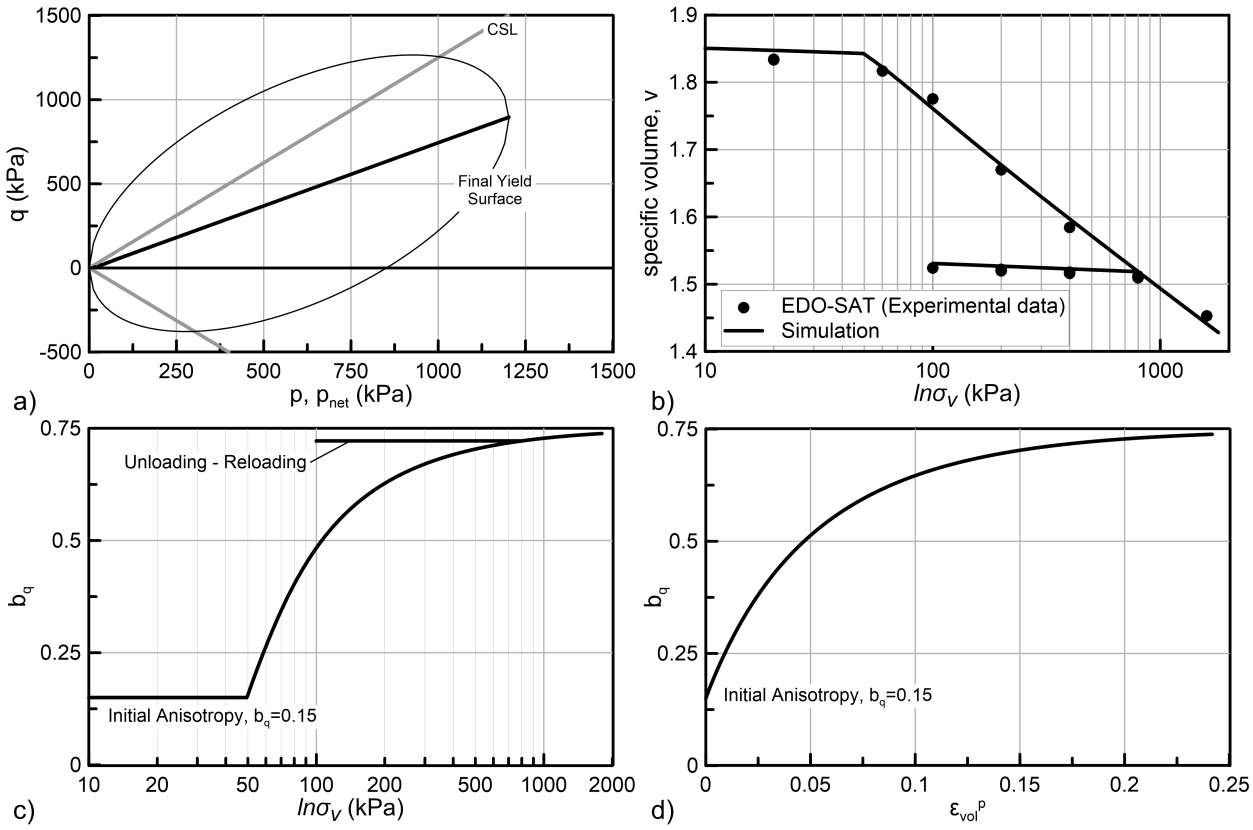


**Figure 9.18:** Simulation of the JS oedometer test under saturated conditions; a) the $p-q$ space; b) $v - \ln\sigma_v$ plot; c) the $b_q - \ln\sigma_v$ plot, and; d) $b_q - \varepsilon^p_{vol}$ plot.

cal stress, instead of octahedral stress, to avoid assumptions regarding the coefficient of lateral earth pressure at rest and its evolution during compression. Figure 9.20 provides supplementary information regarding the simulations of figure 9.19, to allow for an overall evaluation of the results.

Focusing on the comparison of figure 9.19, with the exception of the EDO-100 test, the model provides a very satisfactory representation of the oedometric Jossigny Silt behaviour under the examined suction levels. The proposed double dependance of the model's unsaturated compressibility on suction and degree of saturation plays a significant role in the success of the presented simulations, as it allows to sufficiently capture the evolving compressibility that the experimental results exhibit.

The anisotropic characteristics of the model also contribute to some extend to the successful prediction of the post yield compressibility. Nevertheless, a fair commentary of the results should recognise that the evolution of the compression curves due to anisotropy is not very profound. This is quite clear in the simulation of the EDO-sat test (see figure 9.18) where the evolution of the compression curve due to the evolv-

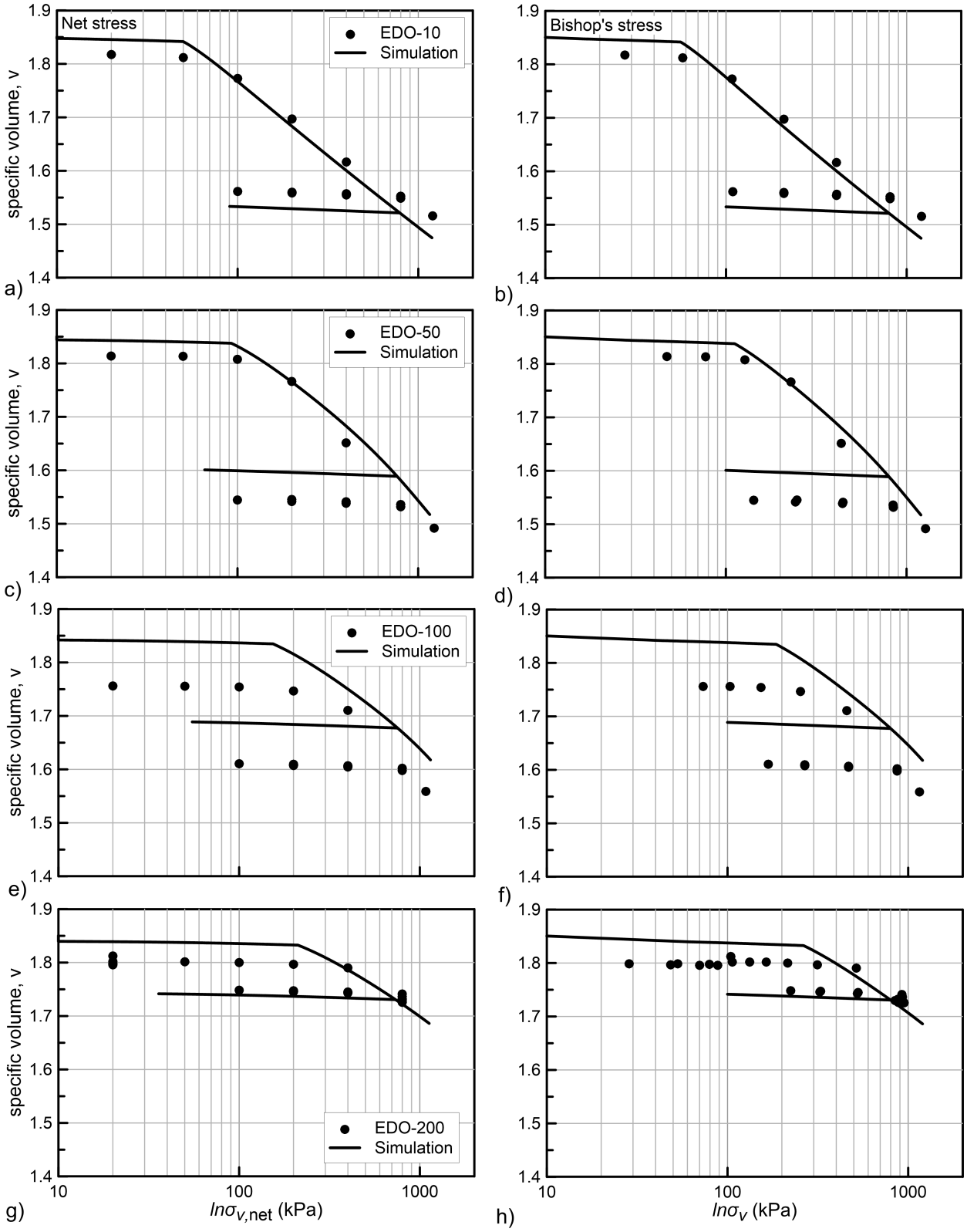


**Figure 9.19:** Simulation of the JS oedometer tests under different constant suction levels $s = 10kPa$ (a,b), $s = 50kPa$ (c,d), $s = 100kPa$ (e,f) and $s = 200kPa$ (g,h). In graphs a, c, e and g the compression curves in terms of net stress and in graphs b, d, f and h in terms of Bishop's stress.

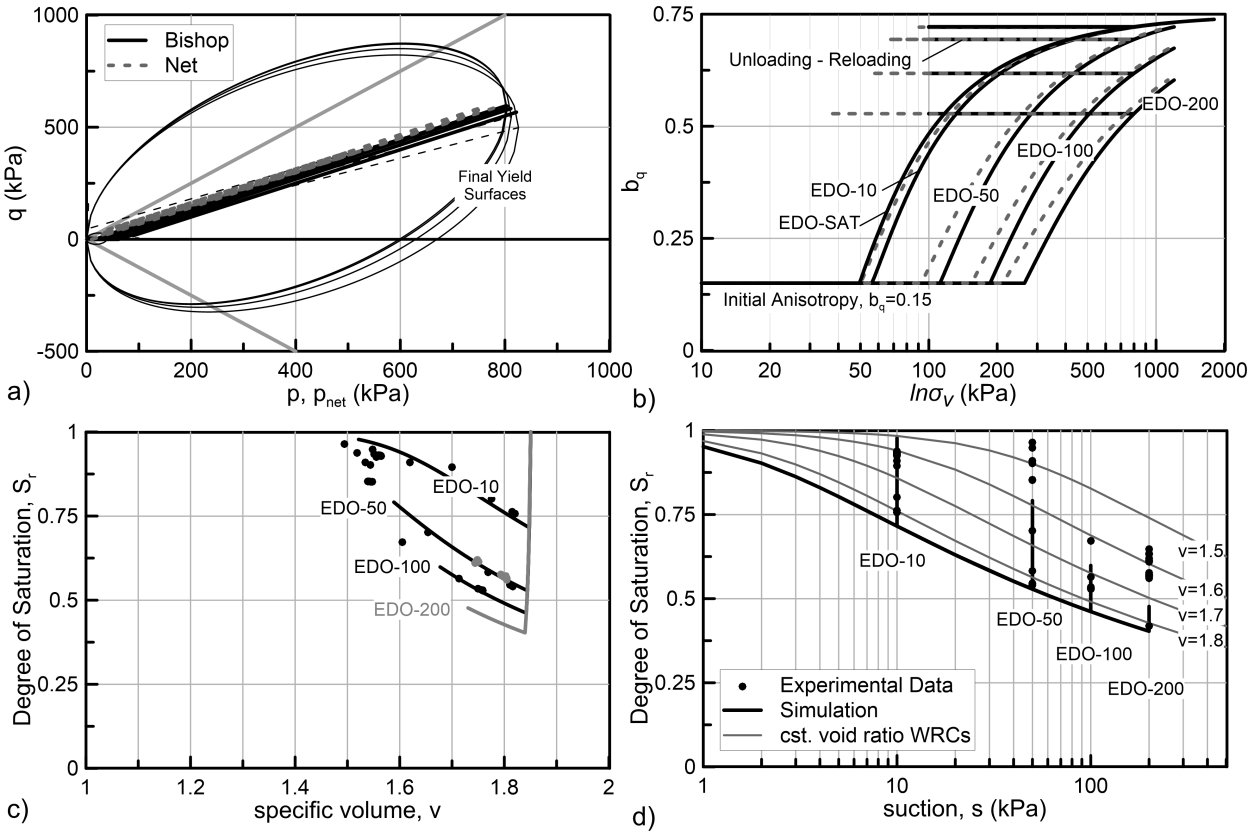


**Figure 9.20:** Simulation of the JS oedometer tests under different suction levels (see also figure 9.19). Additional information regarding: a) the stress paths on the $p, \overline{p} - q$ space; b) the evolution of anisotropy $b_q - \ln \sigma_v, \overline{\sigma_v}$; and the water retention behaviour in c) the $S_r - v$ and d) the $S_r - s$.

ing compressibility is practically negligible. Thus, it is expected that especially under unsaturated conditions, where the rate of anisotropy evolution is comparatively lower (see figure 9.20b), the effect of stress induced anisotropy in the reproduced compression curves is even more reduced, doubting the necessity to account for stress induced anisotropy, at least for the examined experimental data.

Regarding the EDO-100 test, the model captures well the evolution of compressibility and the apparent preconsolidation pressure of the sample, nevertheless, it fails in the prediction of the initial void ratio after drying. On that respect, one may raise the discussion on whether the model is capable of reproducing a realistic volumetric behaviour during drying. We believe that this is not the case, since it is more likely for the initial void ratio of the EDO-100 sample to be inconsistent with the rest of the results.

This belief is based on the fact that the rest of the samples, including also samples dried at higher suction levels (i.e., EDO-200 and the TRX@$s = 200kPa$), indicate a systematically higher post drying void ratio, in line with the predictions of the framework. Additionally, experimentally defined shrinkage curves usually indicate that with increasing suction, void ratio is decreasing, until reaching a residual value where the void ratio practically stabilizes for further drying. From such a perspective, it is really hard to see why the examined soil would deviate from such a well established behavioural trend to exhibit a minimum of void ratio for $s = 100kPa$ and an increasing void ratio for further drying.

The good simulation results are also highly attributed to the Gallipoli et al. (2003) WRM, which proves to be very capable of describing both the evolution of degree of saturation with suction and its evolution with void ratio as well. The comparison between experimentally measured values of degree of saturation and predicted ones, given in figures 9.20c and d, is quite representative of its modelling capabilities.

### 9.3.5 Simulation of Radial compression tests at $s = 200kPa$

Figures 9.21 and 9.22 present and compare the simulation results with the available experimental data from radial compression tests performed under a constant suction level $s = 200kPa$ and four different net stress ratios, namely: $\overline{n} = 0.0$, isotropic for the TRX03; $\overline{n} = 0.375$ for the TRX04; $\overline{n} = 0.75$ for the TRX08, and; $\overline{n} = 0.875$ for the TX09.

The examined experimental results were only used in the calibration of the water

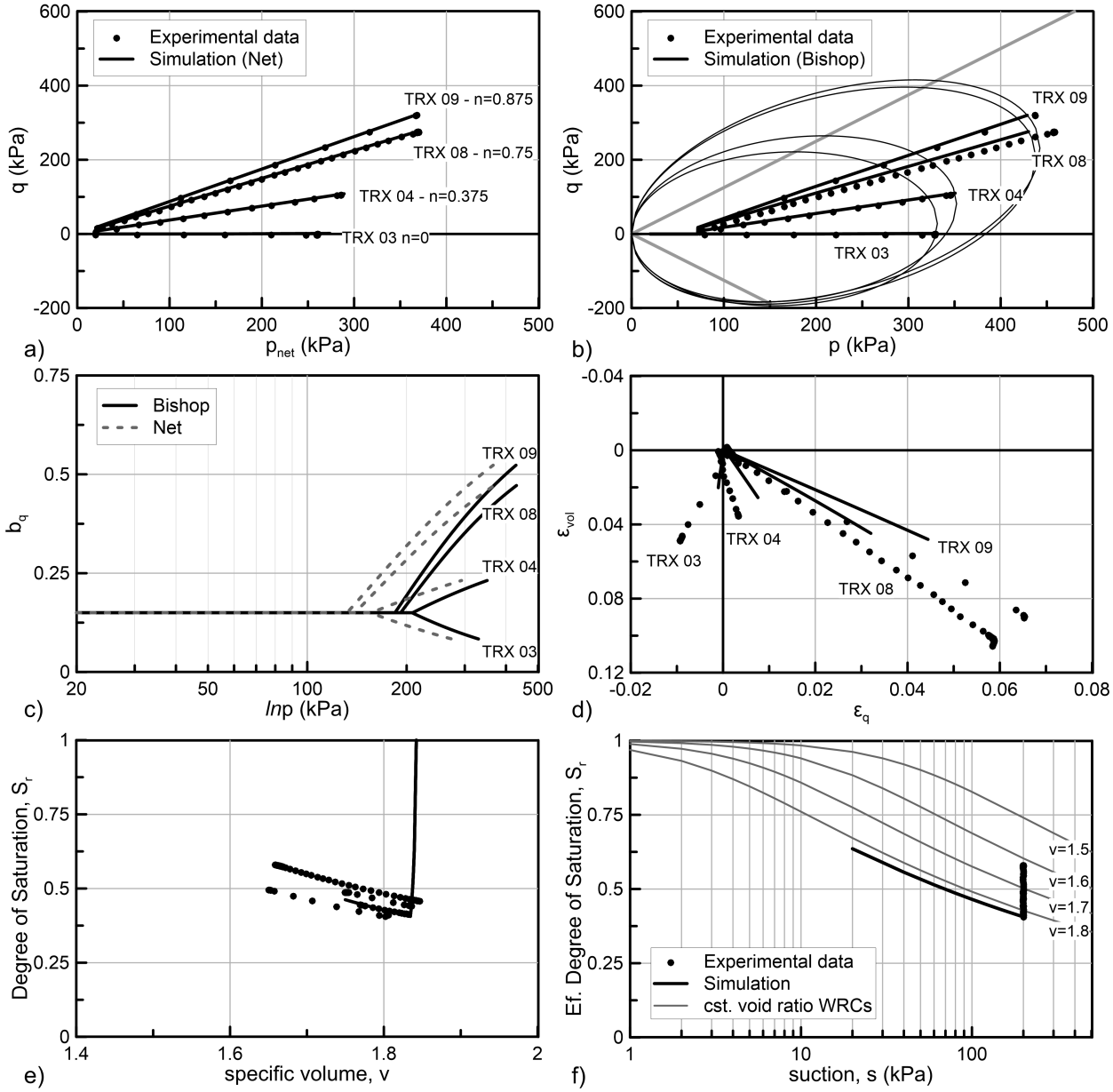


**Figure 9.21:** Simulation of the JS radial compression tests under different stress ratios ($\overline{n}$); a) the $\overline{p} - q$ space; b) the $p - q$ space; c) the evolution of anisotropy $b_q - \ln p, \overline{p}$; d) the $\varepsilon_q - \varepsilon_{vol}$ graph and the water retention behaviour in e) the $S_r - v$ and f) the $S_r - s$ planes. All tests performed under a constant suction $s = 200kPa$.

retention model and were not taken into consideration during the calibration of the mechanical parameters. This is reflected in the very accurate description of the evolution of degree of saturation with specific volume and suction in the relevant plots (see figure 9.21e and f).

Figure 9.21b highlights the importance of the accurate simulation regarding the

evolution of degree of saturation in Bishop's stress analyses. The proposed model, being a Bishop's stress model, can provide as accurate predictions as the imposed stress path in terms of Bishop's stress is. Loading conditions (in stress controlled simulations) are always imposed in terms of net stress, while Bishop's stress is calculated based on the WRM's predictions. If there is a significant difference between the WRM predicted degree of saturation and the experimentally determined one, then practically different tests are examined. The comparison of figure 9.21b reveals that the experimental stress paths (based on the experimentally determined degree of saturation) and the simulated stress paths (based on the WRM predicted degree of saturation), practically coincide, reflecting the successful WRM predictions.

The examined radial compression tests help in defining the initial yield surface inclination, or in other words, the initial stress induced anisotropy resulting from the preparation method. In more detail, test TRX03 is mainly used in this direction. Theoretically, an initially isotropic material, with no evidence of either stress induced or inherent anisotropy, should only undergo volumetric deformation when subjected to an isotropic compression test. The $\varepsilon_q - \varepsilon_{vol}$ plot of TX03 test (see fig. 9.21d), indicate that a certain amount of deviatoric strain[2] is also measured during the imposed isotropic compression.

Triggered by this observation, we assume that the preparation method induces preferred directions to the specimens, and through trial and error simulations, we seek for a suitable initial inclination which can reproduce the experimentally determined dilatancy. As already mentioned, a $b_q = 0.15$ value was finally selected.

Focusing on figure 9.22, the experimentally determined compression curves are not captured well by the model. The poor agrement between laboratory and simulation results is profound both in terms of net and of Bishop's stress interpretation. An exception is test TX04, while for the rest of the tests, although the model captures well the initial void ratio (with the exception of TX09 test), the initial elastic compressibility and the apparent preconsolidation pressure, it completely fails to reproduce the significantly increased post yield compressibility that the experimental results dictate.

An option would be to recalibrate the model by taking into account the radial compression tests in the calibration of the compressibility framework. Nevertheless, if attempted, it turns out that the proposed model cannot accommodate within a

[2] A negative $\varepsilon_q$ indicates that the accumulated radial strain is greater compared to the axial strain and lacks any other physical meaning.

single set of parameters both the oedometric and the triaxial behaviour of Jossigny silt. An alternative option would be to neglect the data from the oedometer tests and focus the calibration at a single suction level calibrating the model against the results of the TRX tests. It is evident that any model can easily describe the desired behaviour if only a single suction level is of interest. Nevertheless, we shall mention that even in this case, it turns out that the compressibility behaviour of the TRX radial compression laboratory results, calls for the adoption of strange values, which to some extend lack physical meaning.

Thus, we finally select to maintain the parameters of table 9.8 and compromise with the poor representation of the post yield compressibility during the examined radial compression tests.

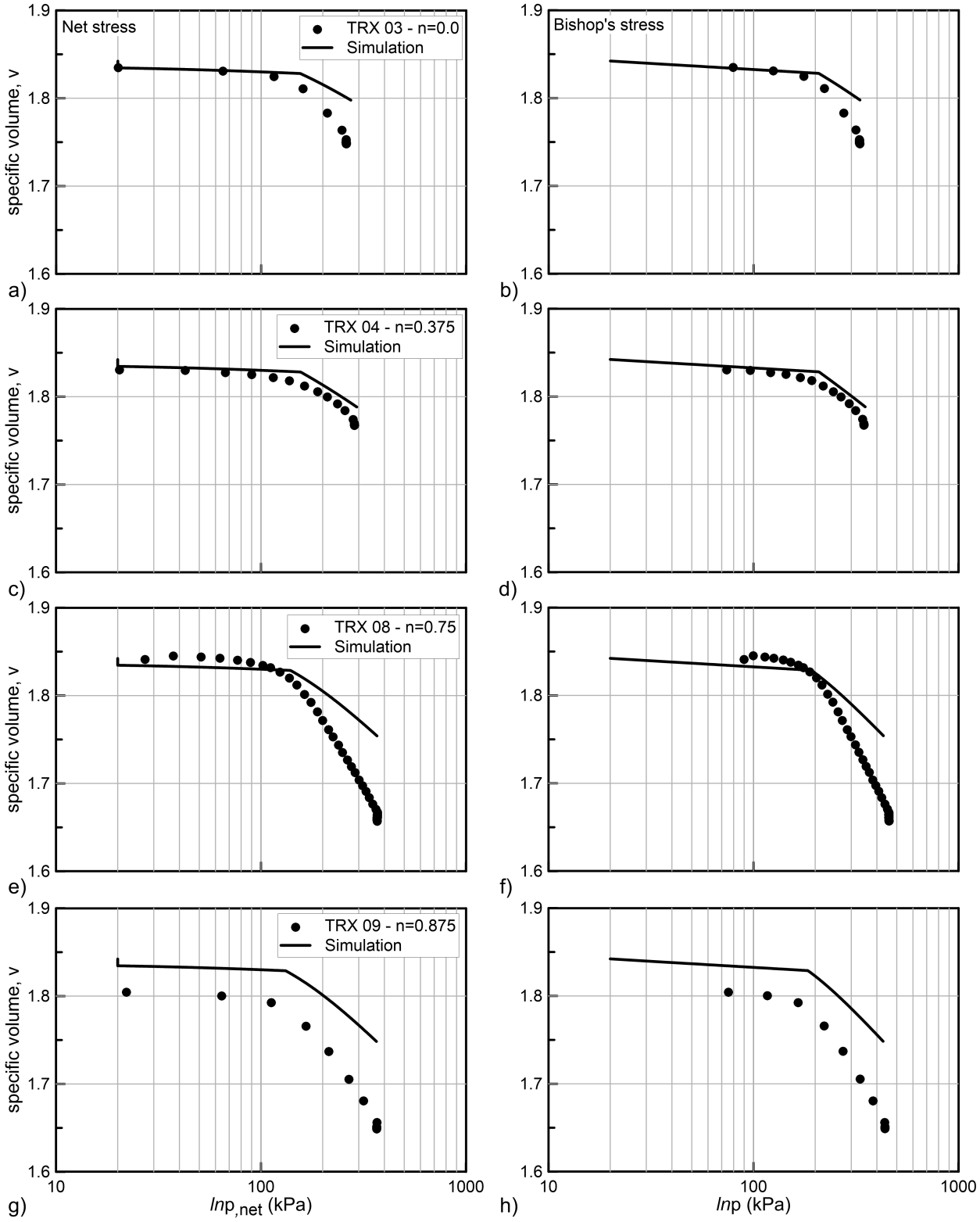


**Figure 9.22:** Simulation of the JS radial compression tests under a stress ratio $\overline{n} = 0$ (a,b), $\overline{n} = 0.375$ (c,d), $\overline{n} = 0.75$ (e,f) and $\overline{n} = 0875$ (g,h). In graphs a, c, e and g the compression curves in terms of net stress and in graphs b, d, f, h in terms of Bishop stress. All tests performed under a constant suction $s = 200kPa$.

### 9.3.6 Simulation of Triaxial compression tests at $s = 200kPa$

Figure 9.23 compares the simulation results regarding the triaxial loading tests with their experimental counterparts. The model can sufficiently reproduce the peak strength observed in the experiments, which in fact coincides with the residual one as all tests exhibit a continuously hardening stress - strain response. A closer look at the results reveals that especially for the TX02 and TX06 tests the simulation is almost excellent, while for the TX01 the deviatoric stress is slightly over-predicted and for the TX07 is slightly under-predicted.

The results are fully compatible with the calibration procedure followed to determine the critical state parameters. In more detail, if we look back at figure 9.14, where degree of saturation was scaled for macrostructural effects based on the triaxial loading behaviour, we may notice that with the selected parameters, the derived CSL line describes very accurately the stress path in terms of Bishop stress for the TX02 and TX06 tests, while plots slightly above the residual state of test TX01 and slightly below the residual state of test TX07, similarly to the simulations of figure 9.23.

Regarding the volumetric behaviour, the simulation results are less satisfactory. On one hand the model predicts quite well the contracting behaviour that TRX06 and TRX08 samples exhibit, while on the other hand it underestimates the dilatant behaviour of samples TX01 and TX02. The first two cases correspond to normally consolidated soil states, while the latter two refer to overconsolidated soil samples. Thus, it is quite possible that although the flow rule successfully captures the behaviour of normally consolidated samples ("wet side") it fails to do so in the "dry side", indicating a potential room for improvements in the proposed model. The inaccurate volumetric predictions during tests TRX01 and TRX02 are also reflected in the predicted evolution of the specific volume and as a consequence in the predicted degree of saturation as well.

With respect to the effect of anisotropy, no solid conclusions can be drawn. With the exception of the radial compression tests, where the isotropically compressed sample exhibits significant deviatoric strains and thus calls for an anisotropic constitutive model, anisotropy is not highly profound in the rest of the experimental data. Thus, from a more practical point of view, whether it is worth taking into account anisotropic effects or not to simulate the examined Jossigny Silt behaviour is open to discussion.

Summarizing, we may state that the proposed constitutive model provides at least

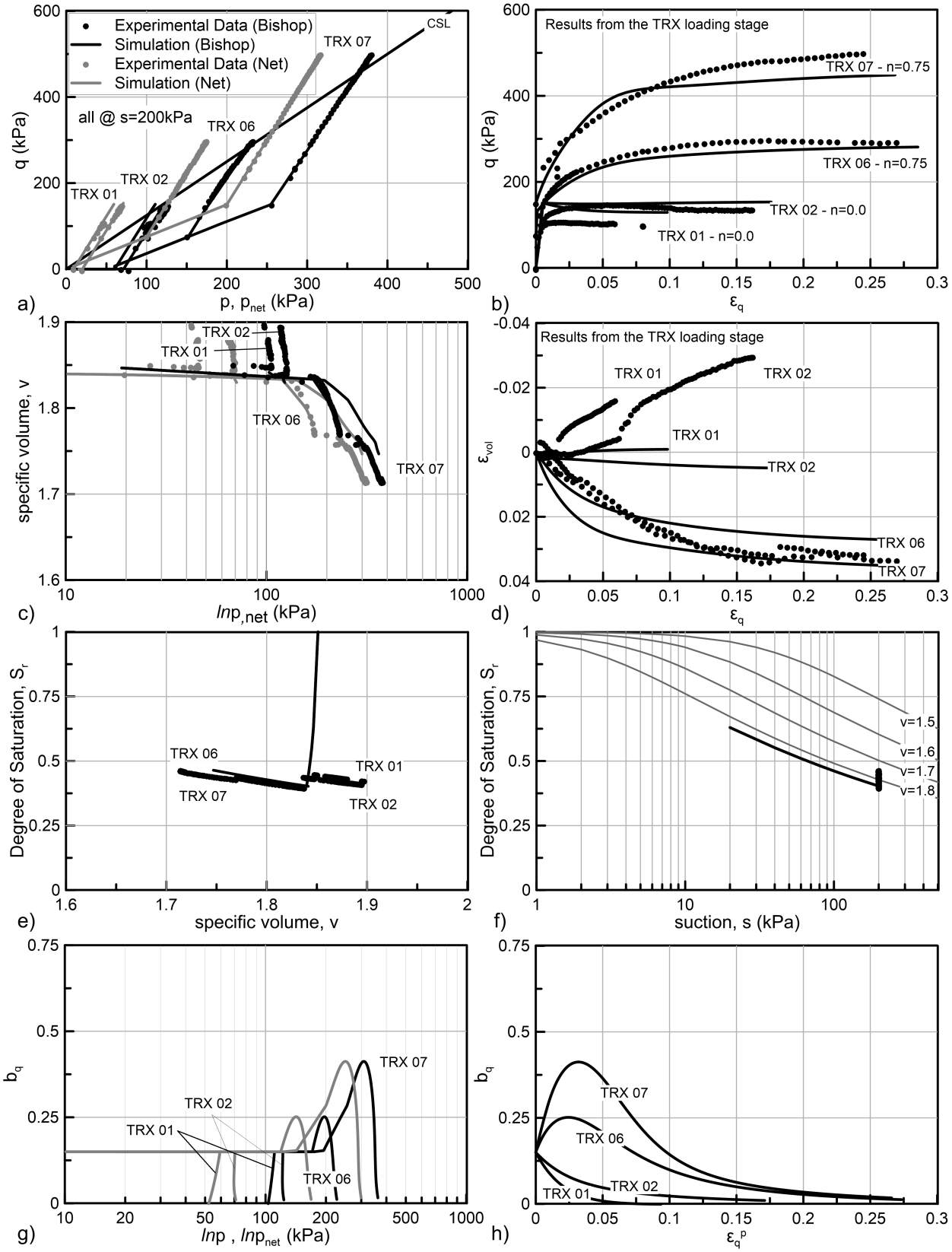


**Figure 9.23:** Simulation of the JS triaxial loading tests ($s = 200kPa$); a) the $p, p_{net} - q$ planes; b) the $q - \varepsilon_q$ plot; c) the $v - \ln p, \overline{p}$ plots; d)the $\varepsilon_q - \varepsilon_{vol}$ plot; e) the $S_r - v$ and f) the $S_r - s$ planes; g) $b_q - \ln p, \overline{p}$ plot and; h) $b_q - \varepsilon_q^p$.

fair descriptions of the experimental data of Casini (2008). According to the authors knowledge, at least in terms of the oedometric behaviour, the presented simulation is probably the most consistent and successful attempt to model the aforementioned experimental data, existing in the international literature. For comparisons the interested reader can refer to D'Onza et al. (2011) and to Casini (2008).

Moreover, the author would like to emphasize on the fact that the presented simulations have been based on a specific set of parameters, derived through a step by step calibration of the proposed model against the laboratory data while only a few of them are an output of trial and error simulations. Simultaneously the selected values, respect the physical meaning of each parameter, are quite coherent in terms of the expected geotechnical behaviour of a clayey silt, while the same set of parameters apply also to the Jossigny Silt behaviour under saturated conditions.

## 9.4 Evaluation of the Unsaturated Characteristics of the proposed model based on Barrera (2002) experimental results

### 9.4.1 General - The tested soil

Barrera (2002) presented en extensive study, addressing the hydromechanical behaviour of the Barcelona Clayey Silt (BCS). This section utilizes a set of data from the aforementioned investigation to mainly evaluate the proposed model's potential to simulate experimental results associated with volumetric collapse. In that respect, unlike to the previous two sections, the present section does not discuss a complete calibration procedure on the available experimental results.

We focus on modelling the results of three different triaxial compression tests, one of them including a wetting- drying cycle as an overconsolidation inducing mechanism. The tested soil is a Clayey Silt, taken from the campus of the Technical University of Catalonia (UPC) in Barcelona, Catalonia, Spain, while the experimental investigation was conducted at the laboratory of soil mechanics of the university. Table 9.9 summarizes the main properties of the tested soil, which according to the USCS classification system is classified as a Clay of Low plasticity (CL).

**Table 9.9:** Index properties of the Barcelona Clayey Silt (BCS) (Barrera 2002).

| Grain Size Distribution | | Atterberg Limits | | Other | |
|---|---|---|---|---|---|
| Gravel | 0% | LL | 32% | $G_s$ | 2.71 |
| Sand | 39.4% | PL | 16% | | |
| Silt | 44.5% | PI | 16% | | |
| Clay | 16.1%[*1] | | | | |

[*1] Illite is the dominant clay mineral.

### 9.4.2 Simulation of experimental results

Results from three triaxial loading tests are utilized, all performed under a constant suction level equal to $s = 800kPa$. One of the tests refer to a normally consolidated soil sample, while the other two to overconsolidated soil samples. Two different loading procedures where followed to result with an initially over-consolidated stress state. The first one refers to a classical isotropic loading and unloading stress path, while the second includes a wetting - drying cycle path during which the soil collapses.

Table 9.10 summarizes the utilized tests. The selected tests are referred to as Test 1, Test 2 and Test 3, while for the interested reader they correspond to IS-NC-06, IS-OC-06 and IWS-OC-01 respectively, in the Barrera (2002) doctoral thesis.

**Table 9.10:** The Barcelona Clayey Silt (BCS) laboratory tests examined.

| Test | Loading path prior to shearing |
|---|---|
| TEST 1 | IC[*1] to $\overline{p} = 600kPa$ |
| TEST 2 | IC to $\overline{p} = 1600kPa$ - IC (unloading) to $\overline{p} = 600kPa$ |
| TEST 3 | IC to $\overline{p} = 600kPa$ - Wetting[*2] to $s = 10kPa$ - Drying[*2] to $s = 800kPa$ |

[*1] IC denotes Isotropic Compression.
[*2] the wetting-drying cycle was performed under a constant net stress $\overline{p} = 1600kPa$.

Samples preparation included only isotropic compression, while additionally the examined stress paths are also isotropic. In that respect, we make the assumption that the tested specimens neither posses nor are going to develop any significant memory of stress induced anisotropy and thus, we deactivate the anisotropic characteristics of

the model, focusing exclusively on their unsaturated behaviour. Table 9.11 presents the model parameters used to simulate the aforementioned tests. Selection of the parameters regarding the water retention model and the basic model parameters (saturated parameters) follows the proposed values in Barrera (2002), where BCS behaviour was modelled using the Barcelona Basic Model. Regarding the unsaturated parameters, they have been calibrated to fit the experimental results.

**Table 9.11:** The calibrated model parameters corresponding to the Barcelona Clayey Silt behaviour.

| Basic Parameters | | Water Retention Model | | Unsaturated Parameters | |
|---|---|---|---|---|---|
| Parameter | Value | Parameter | Value | Parameter | Value |
| $\kappa$ | 0.015 | $\phi$ | 0.038 | $r$ | 0.892 |
| $\lambda$ | 0.095 | $\psi$ | 2.00 | $\beta$ | 100.0 $MPa^{-1}$ |
| $\nu$ | 0.333 | $n$ | 1.30 | $\gamma$ | 0.1 |
| $c$ | 0.9390[*1] | $m$ | 0.23 | $p^c$ | $1.5 \cdot 10^{-6}$ $kPa$ |
| $k$ | 0.9390 | Alonso et. al. (2010) power law | | | |
| $N_{iso}$ | 2.055 | $\alpha$ | 1.25 | | |
| $\Gamma$ | 1.999[*2] | | | | |

[*1] is equivalent to $M = 1.15$ in the triaxial stress space and corresponds to a material with $\phi \approx 28^o$ in compression.
[*2] corresponds to $\Gamma = N_{iso} - (\lambda - \kappa)\ln 2$ due to $k = c$ selection.

Figure 9.24 compares the model's predictions with the experimental results regarding TEST 1. The initial conditions describe a saturated, over-consolidated soil sample, at $\overline{p} = 24kPa$ with a preconsolidation pressure equal to $p_0^* = 71kPa$. The initial specific volume value ($v = 1.667$) is an output of the compressibility framework.

Experimental results (black solid symbols), are only available for the triaxial loading stage and not during the consolidation stage. Nevertheless , in terms of the model's output, figure 9.24 additionally includes the model's predictions for the drying stage (from $s = 0kPa$ to $s = 800kPa$) and the subsequent consolidation stage (net stress increase up to $\overline{p} = 600kPa$).

The model provides an excellent simulation of the stress - strain relation, depicted in figure 9.24b. It can capture the experimentally determined continuously strain

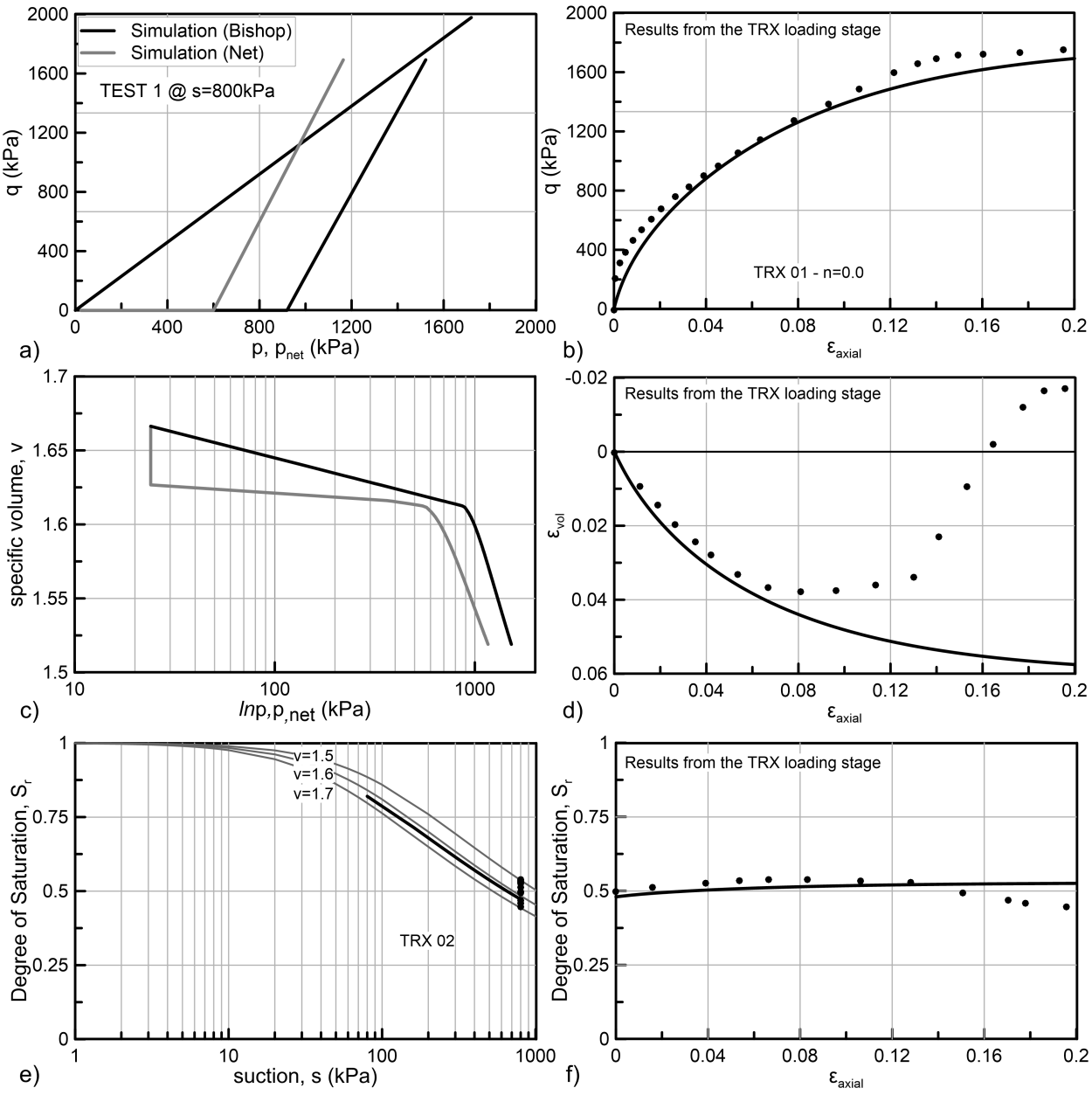


**Figure 9.24:** Test 1: Triaxial compression of a normally consolidated BCS specimen at $\overline{p} = 600kPa$ and $s = 800kPa$; a) the $p, \overline{p} - q$ planes; b) the $q - \varepsilon_{axial}$ plot; c) the $v - \ln p, \overline{p}$ plots; d)the $\varepsilon_{axial} - \varepsilon_{vol}$ plot; e) the water retention behaviour in the $S_r - s$ and; f) the $S_r - \varepsilon axial$ plot.

hardening response, leading to a very accurate prediction of the peak deviator stress. In terms of the volumetric response during shearing, the model predicts well the contracting behaviour at the initial loading stage up to an imposed axial strain equal to 8%. However, it cannot accommodate the significantly dilatant behaviour that the sample exhibits for larger axial strain. We shall mention that, such a behaviour plots

outside of the critical state framework underlying the proposed model, according to which normally consolidated, or even slightly over-consolidated samples are expected to constantly contract during triaxial loading.

In figures 9.24 e and f, we may notice that the WRM predictions are in a very good agreement with the experimentally determined degree of saturation values, both regarding the initial degree of saturation at the end of the drying stage as well as its evolution under constant suction during loading. The results only deviate for axial strains larger than 8%, when the sample begins to dilate and the degree of saturation drops. As previously discussed, the model fails to represent such a volumetric behaviour and it is inevitable that the problematic volumetric response is translated to a problematic prediction regarding the evolution of the degree of saturation.

Figure 9.25 compares the model predictions with the experimental results for Test 2, which involves a loading - unloading cycle, under constant suction prior to triaxial loading. The same loading - unloading cycle is simulated with the proposed model, starting from the initial conditions previously discussed for Test 1. Test 2 provides a good reference to additionally evaluate the selected parameters on their ability to describe the unsaturated compressibility of the BSC. A good agrement is achieved both in terms of the $v - \ln p$ and the $v - \ln \overline{p}$ compression curves (see figure 9.25c) and in terms of the water retention behaviour (see figure 9.25c).

During triaxial loading the model provides a fair simulation of the experimentally determined behaviour, yet less accurate compared to the normally consolidated soil (Test 1). The results describe well the peak strength and the continuously strain hardening response, but the model fails to precisely predict the size of the elastic region, reflected in the increased deviatoric stress corresponding to the initiation of significant plastic straining. Moreover, experimental results suggest a stiffer stress strain response in the elastic domain.

A slight recalibration of the model parameters can improve the elastic behaviour, without significant deleterious effects on the rest of the predictions. For instance, selecting a smaller aspect ratio value for the yield surface (lower $k$ value) can reduce the elastic domain, while selecting a smaller Poisson's ratio can stiffen the elastic deviatoric response[3].

With respect to the volumetric behaviour during loading, the model's inability to capture the dilatant response, observed after 8% of axial straining, is once again

[3]It is reminded that the Shear Modulus $G$ follows the evolution of the Bulk Modulus $K$, through the term $2G/K$, with the latter being a function of Poisson's ratio.

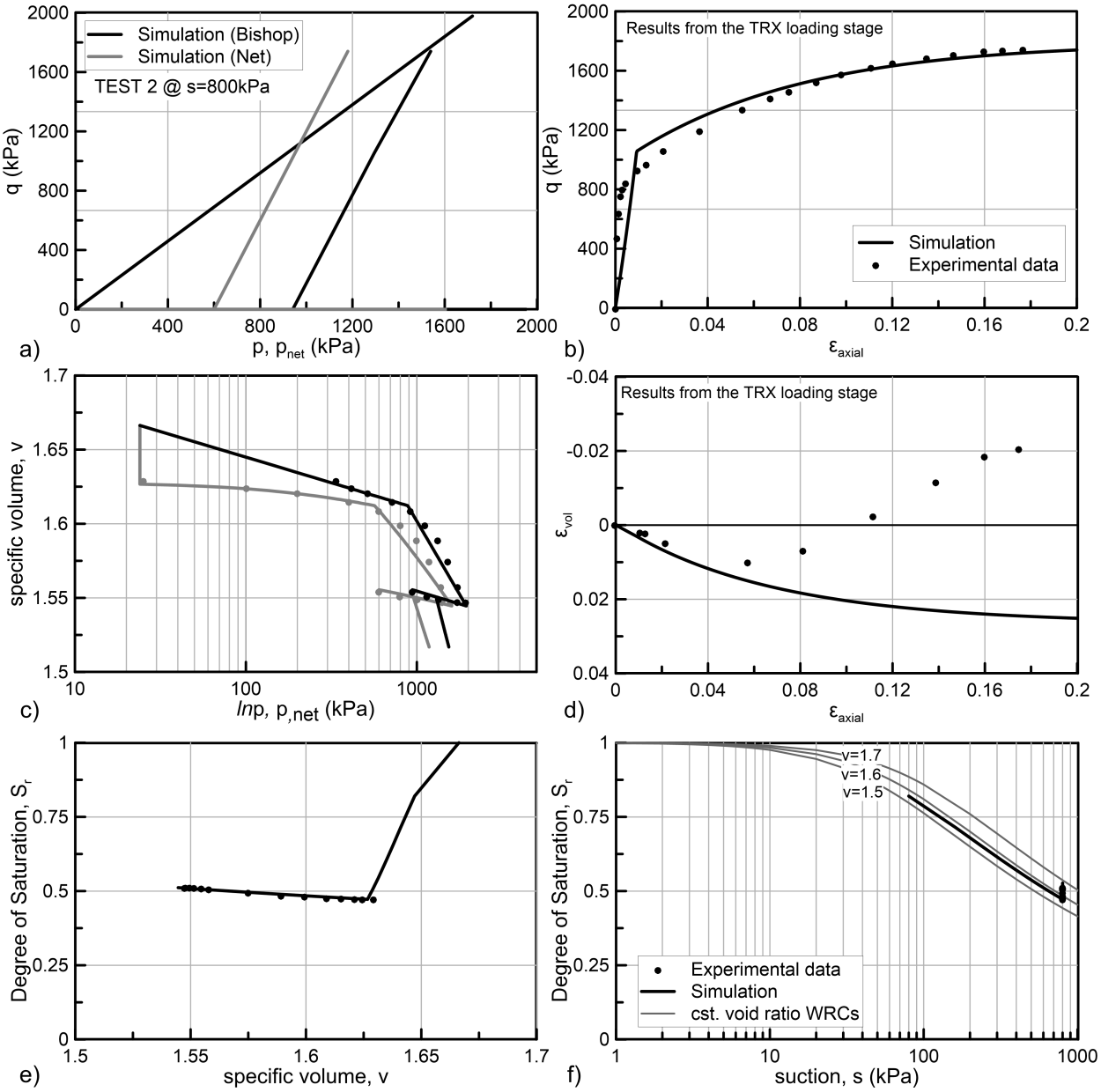


**Figure 9.25:** Test 2: Triaxial compression of an over-consolidated BCS specimen at $\overline{p} = 600kPa$ and $s = 800kPa$; a) the $p, \overline{p} - q$ planes; b) the $q - \varepsilon_{axial}$ plot; c) the $v - \ln p, \overline{p}$ plots; d)the $\varepsilon_{axial} - \varepsilon_{vol}$ plot; the water retention behaviour in e) the $S_r - v$ and f) the $S_r - s$ planes;

obvious. The experimental behaviour still plots outside the critical state framework, as although over-consolidated, the sample is loaded at the "wet" side. To the contrary, the initial contractant behaviour at small strains is very well predicted.

The last experiment utilized from Barrera (2002) work, Test 3, provides an excellent reference to test the model's volumetric predictions during a wetting - drying

cycle with predominant collapse. In more detail, starting from identical initial conditions with TESTS 1 and 2, in TEST 3 a BCS specimen is dried to $s = 800kPa$, isotropically compressed under constant suction to $\overline{p} = 600kPa$ and then subjected to a wetting - drying cycle under constant net stress. Suction is lowered to as low as 10kPa, before it is raised again back to 800kPa.

Figure 9.26 presents the simulation results. The experimentally determined evolution of specific volume with suction and the corresponding volumetric strains accumulated during the wetting - drying cycle are compared with the model's predictions in graphs c, d and e.

The model slightly underestimates the post compression void ratio and thus the wetting - drying cycle initiates from a higher void ratio compared to the experimental one. It should be mentioned that in Test 2, mainly used during calibration, the compression curve up to $\overline{p} = 600kPa$ was accurately predicted and thus the slight deviation observed in the present case is probably due to an initially smaller void ratio that the specimen possessed during preparation.

During wetting, the volumetric deformation was not continuously monitored. Barrera (2002) reports the specific volume at just one intermediate equilibrium stage at $s = 100kPa$ and at the end of the wetting phase for $s = 10kPa$. We may observe that at $s = 100kPa$ void ratio has not altered significantly while at the end of the wetting phase it has been significantly reduced, indicative of volumetric collapse. Regarding the simulation results, elastic swelling strains develop until the Loading - Collapse surface is crossed at $s = 30kPa$ and then behaviour reverses.

At this point we shall mention that several different combinations of parameters regarding the proposed model's unsaturated compressibility framework were, in fact trying different shapes of the LC curve. The selected set of parameters describes accurately the void ratio at the end of wetting and also at the end of the re-drying phase, while on the other hand the initial void ratio is slightly higher compared to the experimental results. In other words, we selected to over-predict the volumetric strain during wetting to end up with an accurate prediction of the void ratio at the end of the cycle. Such a selection ensures that the simulation of the triaxial compression test performed after the drying - wetting cycle, will initiate from a material state close to the experimental one, for a fair comparison of the behaviour during the subsequent TRX loading stage.

Finally, figure 9.27 presents the simulation results related to the TRX loading test

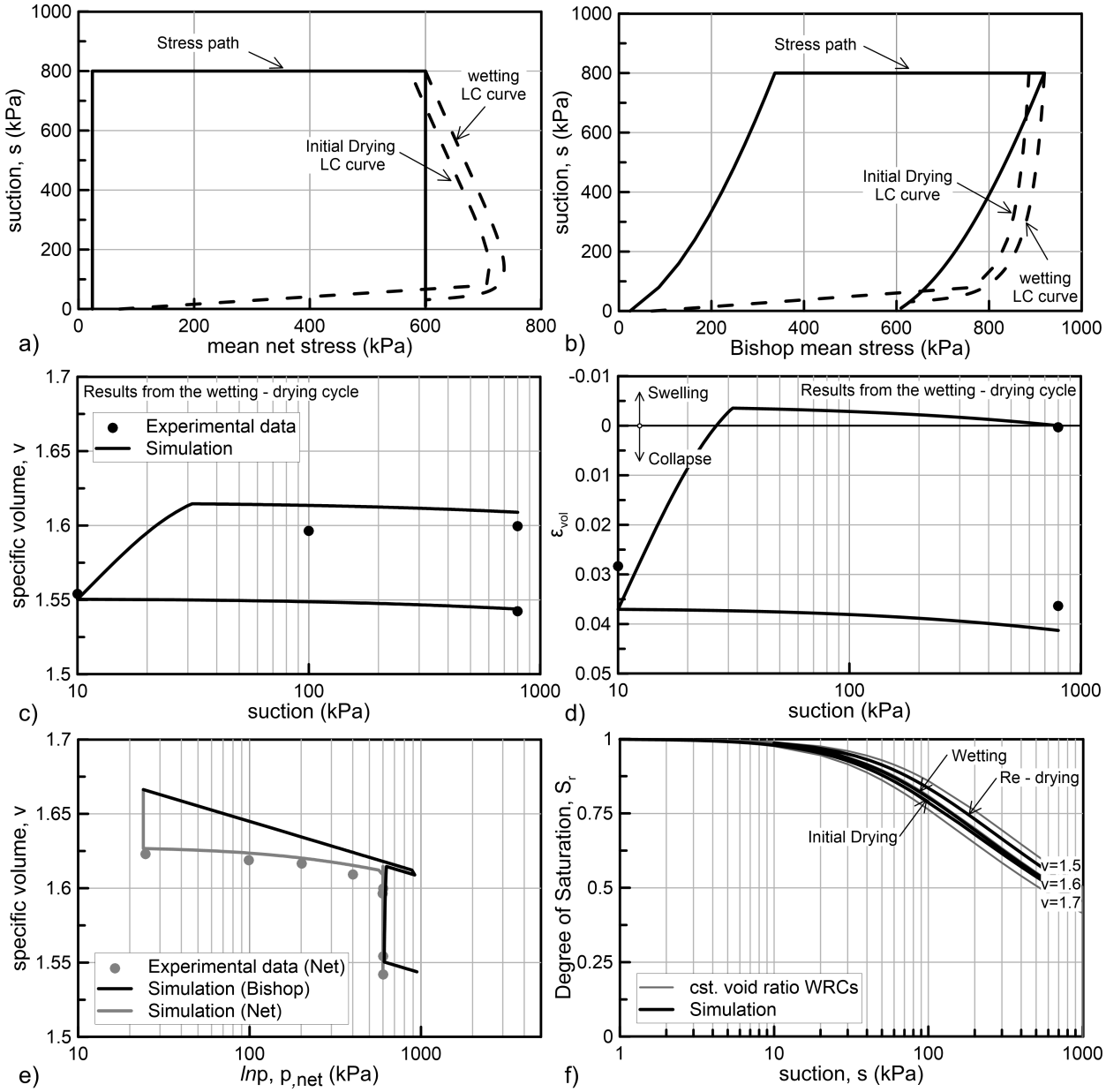


**Figure 9.26:** Test 3: Wetting - drying cycle at a normally consolidated BCS specimen under constant $\overline{p} = 600kPa$; a) the $\overline{p} - s$ space; b) the $p - s$ plane; c) the $v - \ln s$ plot; d) the $\varepsilon_{vol} - \ln s$ plot; e) the $v - \ln p, \overline{p}$ plots; and f) the $S_r - s$ plot.

under a constant suction level equal to $s = 800kPa$, following the wetting - drying cycle previously discussed. Comparison of the results with the experimental data reveals that the model over-predicts the size of the elastic region. This is clearly reflected on the elastic part of the stress - strain curve in figure 9.27d. The model describes a transition from elastic to elastoplastic behaviour at around $1300kPa$ of

deviatoric stress, while the experimental data indicate a significant lower transition at around 400kPa.

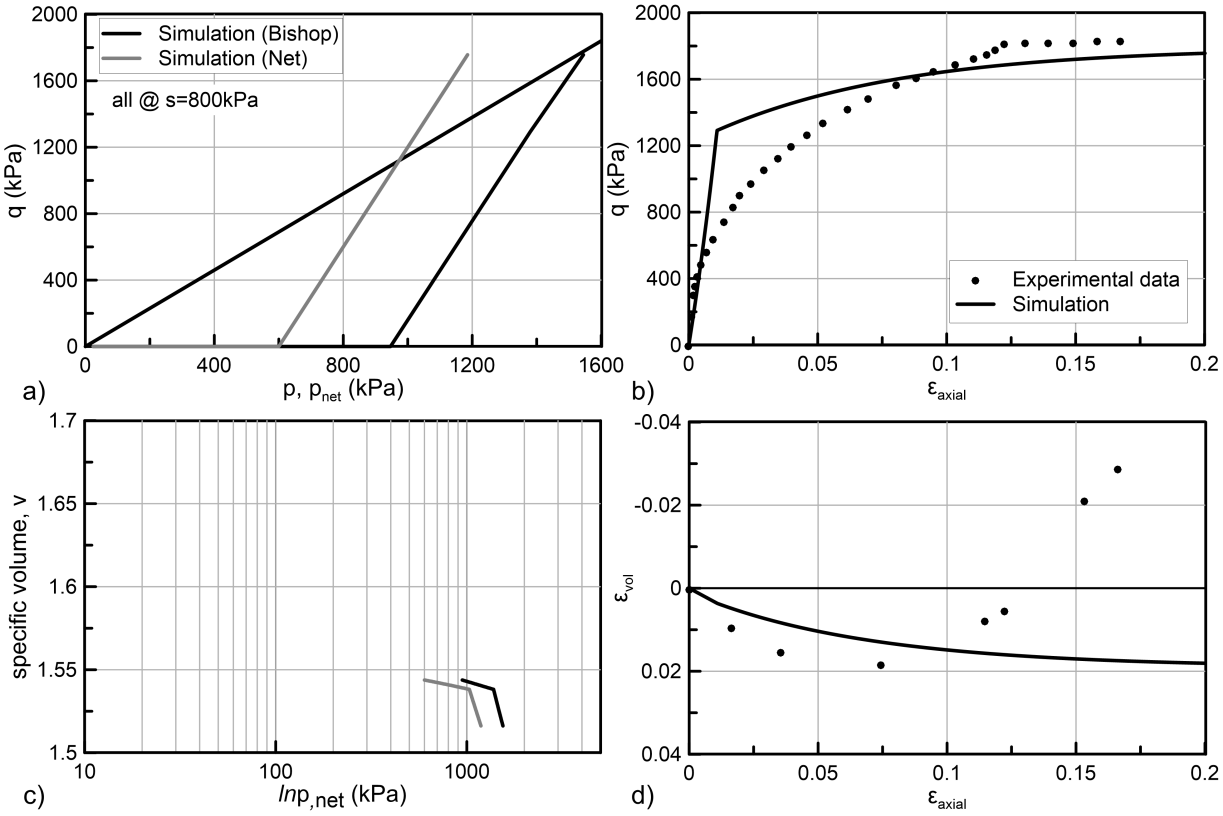


**Figure 9.27:** TEST 3: Triaxial compression of an over-consolidated BCS specimen at $\overline{p} = 600kPa$ and $s = 800kPa$; a) the $p, \overline{p} - q$ planes; b) the $q - \varepsilon_{axial}$ plot; c) the $v - \ln p, \overline{p}$ plots; d)the $\varepsilon_{axial} - \varepsilon_{vol}$ plot.

After initiation of plastic loading, the model's prediction and the experimental data converge, leading to a fair representation of the peak strength for large axial strains ($\varepsilon_a > 8\%$). The anticipated behaviour is indicative of an overestimation of the apparent preconsolidation pressure, possessed during the specimens redrying. During wetting, plastic loading increases the preconsolidation pressure of the material under saturated conditions. This is a fundamental principle of the Loading - Collapse surface, dictating that collapse and loading (stress increase) have a similar effect, both hardening the material. When redried, the hardened soil develops a new apparent preconsolidation pressure which is higher compared to its pre-wetting counterpart under the same suction level, explaining why fundamentally a wetting - drying cycle is considered an overconsolidation inducing mechanism.

It seems that with the selected parameters, the LC equation adopted in the pro-

posed model, overestimates the apparent preconsolidation pressure that BCS develops during a wetting - drying cycle, with the main parameter suspected being the unrealistically small (almost lucking physical meaning) reference pressure ($p^c$) value (see table 9.9). Nevertheless selection of such a small $p^c$ value was the only way to accommodate the significant apparent preconsolidation pressure that BCS exhibits during the initial drying and to simultaneously capture both the post yield compressibility and the examined volumetric collapse. Similar difficulties in successfully capturing the post-collapse behaviour of the examined Barcelona Clayey Silt behaviour have been reported by Gonzalez (2011).

## 9.5 Concluding Remarks

This chapter presented an extensive calibration exercise to evaluate the proposed model's simulation capabilities against well documented experimental results available in international literature. Three laboratory studies were selected namely, the Gens (1982) on the effects of stress induced anisotropy in a silty soil, the Casini (2008) on the effects of partial saturation in the Jossigny Silt behaviour and the Barrera (2002) study on the hydromechanical behaviour of the Barcelona Clayey Silt. The selected experimental investigations allowed for an extensive evaluation of the model's predictions under a variety of different loading conditions covering the entire range of the model's capabilities. Moreover, the calibration procedure required to estimate representative model parameters was discussed in detail.

The most interesting points of the conducted calibration and simulation exercises are summarized as follows:

- The model provides accurate predictions of the distinct compression lines corresponding to different levels of stress induced anisotropy, both under saturated and unsaturated conditions. Calibration of the compressibility framework under $K_0$ conditions proves sufficient in representing the soil behaviour under different stress ratios, without prior knowledge of the corresponding behaviour. This is of significant importance in practical applications, as the behaviour under $K_0$ conditions is usually available (i.e., oedometer testing).

- The adopted kinematic hardening rule, based on the idea of re-orienting the yield surface towards the isotropic axis with the accumulation of plastic deviatoric strain, proves capable of representing in a consistent way the residual

state of all the examined tests that lead to failure, irrespectively of the loading path and the initial anisotropy. Additionally, it successfully accommodates the strain softening behaviour exhibited during undrained loading, while at the same time it still predicts a continuously strain hardening behaviour during drained loading, both with a common set of parameters.

- During TRX loading of anisotropically consolidated soil samples, it turned out that the model has the tendency to overpredict the peak strength, at least based on the presented comparisons with Gens (1982) laboratory data. This behaviour is attributed to the strict assumption regarding the orientation of the yield surface towards the direction of the consolidation stress path included in the the hardening rule of Kavvadas (1982), that was adopted in the proposed constitutive model. Future versions of the model should include an increased versatility with respect to the orientation of the surface during anisotropic compression, while in the present version the simulation results are significantly improved if the model is recalibrated with an eye towards shear strength predictions.

- The model's unsaturated compressibility framework and especially its incorporated double dependance of the compressibility on both suction and effective degree of saturation, proves very capable of providing accurate predictions of the compressibility behaviour under different suction levels. The comparison of the model's predictions with the Casini (2008) oedometer tests, under five different suction level are very indicative.

- Bishop's stress, selected as the first constitutive variable of the proposed model, can sufficiently accommodate the evolution of shear strength with partial saturation as indicated by the results regarding both the unsaturated behaviour of the Jossigny Silt and of the BCS.

- The selected flow rule, despite its simplicity, provides a fair representation of the experimentally determined plastic dilatancy during both anisotropic consolidation stress paths as well as during drained triaxial loading. During unsaturated testing though, the predictions are less accurate, with the experimental results indicating an increased dilation with an increasing suction compared to the model's predictions. This highlights the necessity of a direct dependance of the flow rule on the state of partial saturation.

- The model can capture volumetric collapse and the overconsolidation induced during wetting-drying cycles. The successful predictions of the unsaturated behaviour are also highly attributed to the Gallipoli et al. (2003) WRM, systematically utilized in the present thesis, as it proved very capable of capturing the water retention behaviour of the examined soils.

Concluding this chapter we shall remind that all simulations used consistent material parameters defined through a step by step calibration procedure. The selected parameters was in line with their corresponding physical meaning, providing at least fair representations of the examined experimental results. As expected, simulation results can improve if the initially calibrated parameters are fine tuned according to specific mechanical characteristics (i.e., shear strength predictions, consolidation, wetting - drying). This is highly suggested for practical applications (i.e., FEM analysis of engineering boundary value problems) where usually the behaviour under a limited range of material states and loading paths is of concern.

# Chapter 10

# Application in Finite Element Analyses of Geotechnical Problems

## 10.1 Introduction

The present chapter deals with the numerical simulation (Finite Element Method) of two typical geotechnical problems, using the Simulia Abaqus finite element code. The proposed model's UMAT subroutine (see chapter 7) provides the constitutive behaviour.

The presented simulations serve two different objectives. The primary objective is related to the evaluation of the developed algorithms in 2D and 3D nonlinear, coupled hydromechanical FEM analyses, including a significant number of elements and nodes as well as complicated loading conditions. It is reminded that in chapters 7 and 8, the developed UMAT was used in simple finite element simulations of typical laboratory tests, emphasizing mainly on the precision of the obtained results. In this chapter, the presented analyses mainly evaluate the developed UMAT in terms of robustness and efficiency.

The second objective is to demontrate typical examples of common geotechnical problems where the proposed model can raise interesting results regarding the effects of anisotropy and partial saturation. Two different geotechnical problems are analyzed. The first one deals with face stability in mechanized tunnelling and the presented results are part of an extensive research study dealing with the impact of tunnelling in surface structures, conducted the last few years in the National Technical University of Athens (NTUA) within the frame of the research programme

"NeTTUN: New Technologies for Tunnelling and UNderground work", supported by the European Commission under the 7th Framework Programme (FP7). The proposed model is used in assessing the effects of anisotropy in tunnel excavation (i.e., face displacements and stability, surface settlements etc.).

The second application deals with the mechanical response of a swallow strip foundation, examining the influence of partial saturation and stress induced anisotropy in bearing capacity and deformation. This application is mainly related to the unsaturated characteristics of the model, including complicated hydromechanical phenomena which can only be addressed by proper constitutive models including a Loading - Collapse (LC) Surface.

The presented work does not comprise a complete investigation of the selected geotechnical problems. It is just indicative, mainly demonstrating that the developed UMAT can handle complicated FEM analyses. A detailed investigation of complex geotechnical problems calls for extensive parametric studies, including different ground and loading conditions as well as different geometries. Such an extensive research goes far beyond the scope of the present doctoral dissertation.

## 10.2 Application in numerical modelling of Mechanized Tunnelling

This section applies the proposed constitutive model to numerical modelling of mechanized tunnelling. It discusses the effects of primary anisotropy in face stability, quantified through face extrusion (horizontal face displacement). A brief description of the analyzed problem, giving emphasis on the numerical modelling and interpretation of the results is initially offered before presenting and discussing the obtained results.

### 10.2.1 Investigation of face stability in Mechanized Tunnelling

Face stability is one of the most important issues in urban tunnelling. Poor face stability conditions may lead to excessive ground deformation ahead of the tunnel face that can propagate all the way up to the surface and potentially affect existing structures and utilities. For that reason, in urban tunnelling applications, usually Earth Pressure Balanced (EPB) – Tunnel Boring Machines (TBM) are utilized. EPBs control face

stability by applying on the excavated face a stabilizing pressure to counterbalance the ground pressure (effective and water pressure). EPBs use the excavated material as the support medium by maintaining the excavation chamber filled with excavated ground. The applied face pressure is regulated by: a) controlling the forward thrust of the TBM; b) monitoring and controlling the air pressure in the upper part of the excavation chamber (air bubble) when it is not full, and; c) adjusting the rotation speed of the screw conveyor to control the discharge rate of the excavated material.

During excavation, TBM operators usually adjust the face pressure to the excavated ground conditions based on both information from the design and on feedback information related to various real time monitored parameters from the EPB operation. In some cases, mainly due to deteriorating unforseen or unforeseeable ground conditions, major over-excavations may occur before the face pressure is properly adjusted to the geotechnical conditions. The development and incorporation in EPBs of automated systems which are capable of early detecting over-excavations can prove very beneficial in eliminating the risk of tunnelling.

An attempt to develop such a system is currently under progress in the Geotechnical Department of NTUA within the frame of the research programme: "NeTTUN: New Technologies for Tunnelling and UNderground work", supported by the European Commission under the 7th Framework Programme (FP7). Part of the calibration of the developed system is based on results from finite element analyses which study the behaviour of the advancing excavation face, under various ground conditions, tunnel depths, geometries etc.

EPB machines are usually applied in clayey ground conditions. The mechanical behaviour of clayey soils depicts within the critical state soil mechanics framework. In that respect, critical state models are considered more appropriate to provide the crucial ground constitutive behaviour. For the "NeTTUN" research program, the Modified Cam Clay model is utilized as the reference model to study the effect of different ground conditions (strength and compressibility) in face stability, pre-convergence (radial displacement of the theoretical tunnel periphery ahead of the tunnel face), surface settlements etc. Additionally, advanced critical state models, developed in the Geotechnical Department of the NTUA offer the opportunity to study the effect of structure and small-strain stiffness (i.e., Belokas & Kavvadas (2010), Kalos (2014)) as well as the effect of anisotropy (the proposed model) in tunnel excavation.

This section presents preliminary results regarding the effect of stress induced

anisotropy in face extrusion. The presented results refer to a specific tunnel geometry, three different magnitudes of applied face pressure and various ground conditions.

### 10.2.2 The Abaqus Model - Input Parameters

The present investigation concentrates on a single tunnel geometry regarding the excavation of a $D = 8m$ diameter circular tunnel with $H_c = 16m$ depth of overburden (measured from the tunnel crown), corresponding to a tunnel axis depth (H) vs diameter (D) ratio of $H/D = 2.5$. The selected geometry and tunnel depth is typical of a metropolitan underground rail network. Figure 10.1 presents the utilized Simulia ABAQUS FEM model.

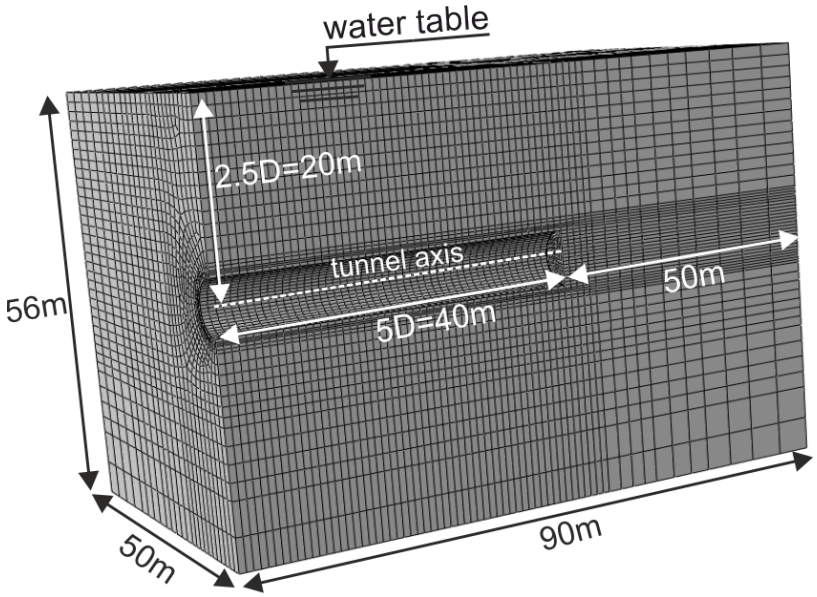


**Figure 10.1:** The FEM model in Simulia Abaqus.

Three – dimensional (3D) solid, pore pressure, 8-noded linear elements are used. The model includes a total of 71612 elements and 77117 nodes. A dense discretization was selected for the vicinity of the excavation (average characteristic element length of 1m), while the grid gets coarser as we move towards the boundaries of the model (max characteristic element length of 4m). To reduce the computational cost, the model takes advantage of the symmetry of the problem with respect to a vertical plane aligned with the tunnel axis, and thus only half of the model is simulated. Regarding the mechanical boundaries, rollers are assigned at the four sides of the model and hinges at the bottom.

EPB tunnelling excavation usually take place in saturated ground conditions under a significant hydraulic head (excavation takes place below the groundwater table). A realistic simulation of the excavation process calls for coupled hydromechanical analyses, to account for the pore water pressure redistribution taking place in the advancing face core (ground ahead of the tunnel face). In the presented analyses, the groundwater table coincides with the ground surface thus, a fully saturated soil profile is assigned. The analyses include 41 loading steps. In the first step, the geostatic stress field is established (body forces and gravity equilibrium), followed by the excavation of $40m$ of tunnel in an equal number of steps. Coupled hydromechanical analyses require a real time scale to reproduce hydraulic effects. A constant advance rate of one and a half hour for every meter of excavation ($1.5h/m$) is assumed as typical of EPB excavations. During excavation the tunnel face is supported by a predefined face pressure, followed by one slice of unsupported excavated ground to indirectly simulate cutterhead overcut and a series of stiff shell elements behind this slice to simulate the shield and tunnel lining.

As the analyses are coupled, separate total stress and pore pressure boundary conditions are assigned on the excavation face, permitting independent control of the total pressure and the effective stress in the muck filling the excavation chamber. Regarding face application, Sitarenios et al. (2015) present a discussion about the proper simulation of an EPB face pressure. They conclude that, based on the nature of the supporting medium inside the excavation chamber (usually being a mixture of the excavated soil with foam, water and other additives), the tunnel face is in fact retained by a pliable soil paste which is rather a heavy and viscous (compared to water) liquid than an ordinary soil mass. They assume that such a soil paste, being in a liquefied state, exerts an equal amount of total stress and pore water pressure to the soil boundary at the tunnel face or in other words that zero effective stress develop at the tunnel face.

The present investigation follows the same approach, assuming that an equal amount of mechanical and pore water pressure distribution is applied on the excavation face. Both pressure components have a trapezoidal distribution, linearly increasing with depth, following an assumed unit weight for the soil muck equal to $\gamma_m = 15kN/m^3$. The applied face pressure is expressed by parameter A (A=At=Aw) which is equal to the ratio of the face pressure at the tunnel crown (top of the excavation chamber) to the initial hydrostatic water pressure at the same level. Figure 10.2

gives a schematic representation of the assumed support pressure distribution.

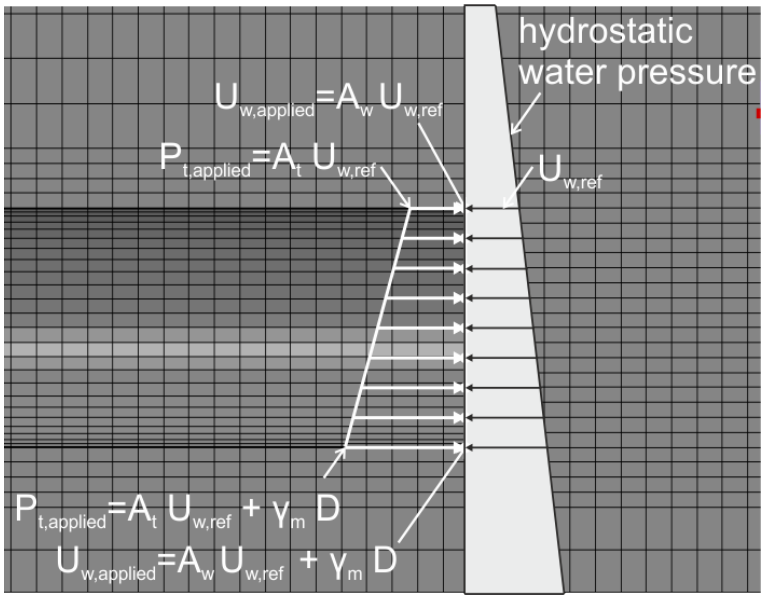


**Figure 10.2:** The applied face pressure distribution.

As face stability depends strongly on the mechanical properties of the excavated ground, different combinations of ground strength and deformation parameters are used in the analyses. Table 10.1 summarizes the selected geotechnical parameters. The performed analyses are divided in two main groups:

- **Isotropic - MCC**: The initial yield surface is assumed isotropic ($\boldsymbol{b} = \mathbf{0}$), while zero values are assigned to the hardening rule parameters $\psi$, $\zeta_q^p$. In other words, the yield surface remains isotropic throughout the analyses; moreover, considering that $k \equiv c$ (see table 10.1) the selected constitutive behaviour is identical to the MCC model.

- **Anisotropic**: For this group of analyses, we assume that the simulated ground has been deposited under 1-D conditions and that the coefficient of lateral earth pressure at rest under virgin compression is $K_{0,NC} = 0.5$. It is further assumed that the depositional mechanism involves sufficient plastic straining for soil fabric to adjust to the anisotropic geostatic stress field and thus, the initial inclination of the yield surface coincides with the stress path of consolidation. The initial components of the anisotropy tensor $\boldsymbol{b}$ are calculated according to the procedure described in appendix E.1.2, following the selected $K_{0,NC} = 0.5$.

**Table 10.1:** Geotechnical parameters used in the analyses.

| Parameter | Range of Values | Parameter | Range of Values |
|---|---|---|---|
| $OCR$ | $1-4$ | $r_s$ | $0.75^{*3}$ |
| $c$ | $0.7348^{*1}$ | $\psi$ | $30.0^{*3}$ |
| $k$ | 0.7348 | $\zeta_q^p$ | $30.0^{*3}$ |
| $\lambda$ | $0.10-0.20$ | $\chi$ | $0.7495^{*3,4}$ |
| $\kappa/\lambda$ | $0.10-0.20$ | Specific Density, $G_s$ | 2.65 |
| Poisson, $\nu$ | $1/3$ | $K_0$ | $0.5\cdot\sqrt{OCR}^{*5}$ |
| $N_{iso}$ | 2.5 | Permeability, $k$ (m/s) | $0.5\cdot10^{-7}$ |
| $\Gamma$ | $2.375-2.448^{*2}$ | | |

$^{*1}$ corresponds to $M=0.9$.
$^{*2}$ computed as $N_{iso}-(\lambda-\kappa)\ln 2$ depending on $\lambda,\kappa$ values.
$^{*3}$ only for anisotropic analyses.
$^{*4}$ calibrated for $K_{0,NC}=0.5$.
$^{*5}$ based on Mayerhof (1976) for $K_{0,NC}=0.5$.

As mentioned before, the first loading step establishes the initial geostatic stress and in order to involve negligible strains the user assigned initial geostatic stress field must be precisely calculated. According to the selected parameters, the initial conditions correspond to either a normally consolidated soil profile or to an over-consolidated soil profile with constant over-consolidation ratio (OCR) with depth. In both cases, void ratio is increasing with depth and an iterative procedure is required to calculate consistent initial conditions. The procedure followed is described in Appendix E.2.

### 10.2.3 Results - The effect of anisotropy

Prountzopoulos (2008) demonstrated how face stability conditions can be described and quantified using numerical analyses results. He presented graphs of face extrusion vs a stability factor ($\Lambda_F$) (see figure 10.3), with the latter describing different ground strength conditions. His work emphasized on conventional tunnelling methods (i.e., drill and blast) under dry conditions and thus primarily addresses the behaviour of an unsupported tunnel face. The proposed stability factor includes the well known

effective shear strength parameters, cohesion ($c$) and friction angle ($\phi$), while is properly formulated to correlate $\Lambda_F = 1.0$ with the transition between stable and unstable face conditions. The criterion used to distinguish between the two types of behaviour is the abrupt increase in face extrusion for a small reduction in the $\Lambda_F$ value.

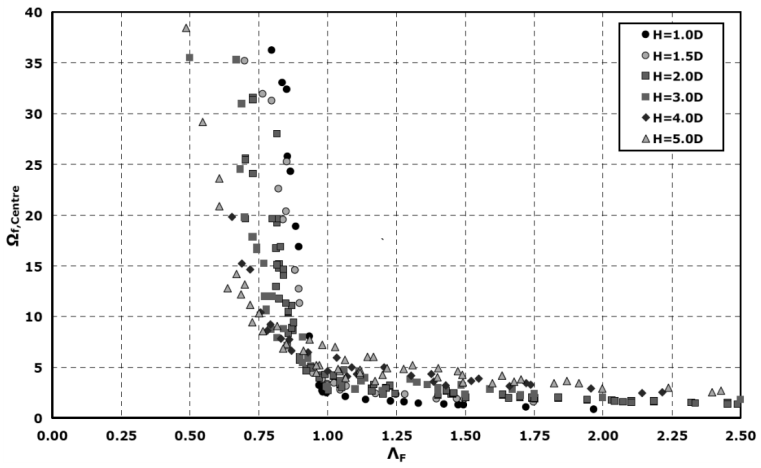


$$\Lambda_F = \frac{5.25 \cdot c \cdot (N_\varphi)^a}{\gamma \cdot H^{1-b} \cdot D^b}$$

$$a = 0.16 \cdot \frac{H}{D} + 0.59$$

$$b = \left(\frac{H}{D}\right)^{-0.37}$$

$$\Omega_f = \frac{U_h \cdot E_{soil}}{D \cdot P_0}$$

**Figure 10.3:** Typical results of normalized face extrusion vs the stability ratio $\Lambda_F$, for an unsupported tunnel face under dry conditions. (Prountzopoulos 2008)

Following Prountzopoulos (2008), Sitarenios et al. (2015) demonstrated that for EPB tunnelling, usually taking place in clayey soils under saturated ground conditions, a modified form of the stability factor is required to account for the undrained excavation conditions resulting from the reduced permeability of clayey soils combined with the high rate of advancement that TBMs can maintain. They concluded that the simplest form of such a stability factor is the ratio of the the undrained shear strength of the ground ($C_u$) over the vertical initial geostatic effective stress at the tunnel axis:

$$\Lambda_{F,CU} = \frac{2C_u}{\gamma \cdot H} \tag{10.1}$$

Undrained shear strength is not a direct input parameter in critical state models and thus, the need to calculate representative $C_u$ values based on the critical state parameters arises. Additionally, a soil profile with a constant OCR with depth, corresponds to an increasing over depth undrained shear strength. Considering that the presented investigation focuses on the behaviour of the tunnel face, mainly influenced from the strength of the ground in the vicinity of the tunnel axis, the undrained shear strength value corresponding to the tunnel (axis) depth is selected as a representative quantity.

Sitarenios et al. (2015) calculated the undrained shear strength by assuming that a soil element at the tunnel axis (with its initial geostatic void ratio) is loaded to failure under undrained triaxial conditions (under constant volume). The undrained shear strength is calculated from the deviatoric stress at critical state conditions as:

$$C_u = \frac{M}{2}\left(\frac{\sigma_v + 2\cdot\sigma_h}{3}\right)\left(\frac{1}{2}B\right)^{1-\frac{\kappa}{\lambda}} \tag{10.2}$$

where $\sigma_v$ and $\sigma_h$ the vertical and horizontal geostatic effective stress at the tunnel depth, $M$ the slope of the critical state line in the triaxial stress space $(p-q)$, while factor $B$ is computed through the following expression:

$$B = \left\{\left(\frac{0.75}{M}\right)^2 + 1\right\}\frac{1}{1+\sqrt{OCR}}OCR \tag{10.3}$$

The calculated $C_u$ value (eq. 10.2[1]) reflects the predictions of the critical state framework of the MCC model. Nevertheless, they are also representative for the set of anisotropic analyses performed with the proposed model due to the latter's assumption of an isotropic yield surface at critical state.

With respect to face extrusion, Prountzopoulos (2008) normalized the average face extrusion calculated from the analyses $(U)$, with the tunnel diameter $D$, the depth of the tunnel through the average geostatic stress at the tunnel axis $p_0 = (\sigma_v + \sigma_h)/2$[2] and for the ground's Young Modulus $(E)$, through the following expression:

$$\Omega_F = \frac{U}{D}\cdot\frac{E}{p_0} \tag{10.4}$$

Equation 10.4 is used in the present investigation as well and Young's modulus $E$ is calculated from the critical state parameters by assuming the initial elastic compressibility of a soil element at the tunnel axis level as a representative quantity. In more detail, Young's modulus $E$ is computed as:

$$E = 3K(1-2\nu) \tag{10.5}$$

where $\nu$ the Poisson's ratio and $K$ the elastic bulk modulus computed as (see eq. 2.59):

[1] Expression 10.3 holds true only for the assumed geostatic stress ratio $K_0 = 0.5\sqrt{OCR}$ and should not be generalized.

[2] $p_0$ should not be confused with the preconsolidation pressure.

$$K = \frac{v}{\kappa} \cdot p \tag{10.6}$$

where p the geostatic mean effective stress at the tunnel axis. The initial specific volume can be computed as:

$$v = N_n - \lambda \ln (B \cdot p) - \kappa \ln \frac{1}{B} \tag{10.7}$$

where $N_n$ depends on the initial anisotropy through equation 6.37, and factor $B$ calculates as precious (eq. 10.3).

Figure 10.4 plots the normalized face extrusion ($\Omega_F$) vs the modified stability ratio ($\Lambda_{F,CU}$) for sixty (60) coupled hydromechanical numerical analyses. The analyses refer to ten (10) different ground conditions combined with three different face pressures, namely $A = 50\%$, 100% and 150% leading to thirty (30) analyses for each one of the two main analyses sets (isotropic-MCC and Anisotropic).

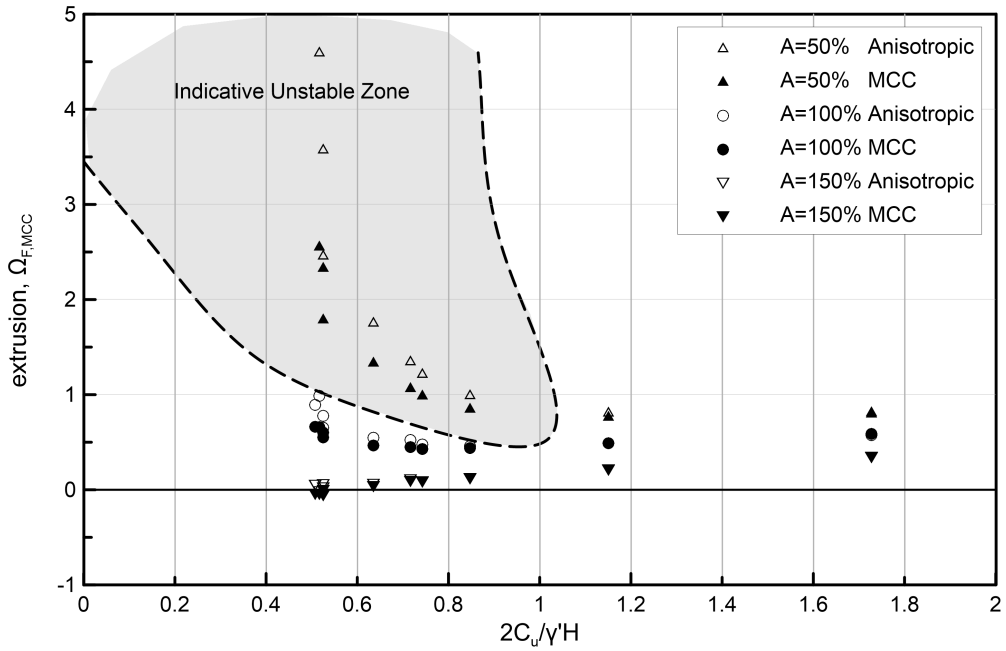


**Figure 10.4:** The results of the performed numerical analyses in terms of the normalized face extrusion ($\Omega_{F,MCC}$) vs the proposed stability factor $\Lambda_{F,CU}$.

The results of figure 10.4 indicate that:

- The selected stability ratio ($\Lambda_{F,CU}$) can satisfactory represent different geotechnical conditions, while as expected, the more unfavorable the geotechnical conditions are, the higher the calculated face extrusion.

- Under given geotechnical conditions an increased magnitude of the applied face pressure reduces the anticipated face extrusion.

- An indicative zone of potentially unstable tunnel face conditions is identified by the observed abrupt increase in face extrusion, enclosing results which correspond to face pressures less than $A = 100\%$ and to $\Lambda_{F,CU} < 0.9$, irrespectively of whether stress induced anisotropy is taken into account or not.

- A negligible increase in face extrusion is observed with improving ground strength for $\Lambda_{F,CU} > 0.8$. This is misleading and not connected to deteriorating face stability conditions. Instead, it reflects the assumed variation of the geostatic stress ratio ($K_0$) with the overconsolidation ratio ($OCR$). In more detail, an increased $OCR$ value corresponds to better geotechnical conditions, and thus to increasing stability ratio values, but at the same time the initial horizontal effective stress increases due to the increased $K_0$ ($K_0 = 0.5\sqrt{OCR}$). The applied face pressure is not following the aforementioned increase of the horizontal effective stress (face pressure is correlated with the initial hydrostatic pressure and not with the horizontal effective stress). Hence, if the support pressure is quantified in terms of the initial horizontal effective stress it reduces explaining why these analyses lead to an increased face extrusion.

- For the higher face pressure tested ($A = 150\%$) face extrusion constantly decreases with deteriorating ground strength, will for really adverse conditions it gets even negative. This behaviour indicates that the applied face pressure is too large and the tunnel face is rather being pushed over its geostatic conditions than retained. This is a quite common problem in EPB tunneling, where a face pressure significantly higher than the geostatic horizontal stress field may lead to undesired results, in some extremes leading to a generalized failure of the face core manifested as a blow out.

Focusing on the effect of stress induced anisotropy in face extrusion, we may note:

- Under stable conditions ($\Lambda_{F,CU} \geq 1.0$, $A = 150\%$), face extrusion is practically unaffected from stress induced anisotropy, while in some cases even a slight reduction in face deformation with increasing anisotropy is identified.

- Under unstable tunnel face conditions ($\Lambda_{F,CU} \leq 1.0$ and $A = 50\%$), stress induced anisotropy results to an increase in the calculated face extrusion.

- Stress induced anisotropy does not alter the general trend with respect to face stability (i.e., size and position of the indicative unstable zone).

For an insight on the mechanisms leading to the developed face extrusion, we need to examine in more detail the mechanical behaviour of the ground ahead of the tunnel face. In that respect, figures 10.5 and 10.6 present the evolution of stresses, strains, pore water pressure and yield surface inclination (anisotropy) for a soil element at the center of the tunnel face. Figure 10.5 presents results corresponding to different applied face pressures ($A = 50\%,\ 100\%,\ 150\%$) for relatively unfavourable ground conditions ($\Lambda_{F,CU} \approx 0.6$), while figure 10.6 plots similar results corresponding to the lower face pressure simulated ($A = 50\%$) for two different ground strengths, one corresponding to unfavourable ground conditions ($\Lambda_{F,CU} \approx 0.6$) and the other one to more favourable ($\Lambda_{F,CU} \approx 1.2$). Both figures contain results from both the "anisotropic" (left) and the "isotropic-MCC analyses" (right).

We may observe that tunnel excavation deconfines the face core, depicted in the progressive reduction of the mean total stress and to the corresponding increase in the deviatoric stress (see graphs a, b in both figure 10.5 and 10.6), while the mean effective stress may decrease or increase depending on the pore water pressure distribution ahead of the excavation face, with the latter being mainly controlled from the applied hydraulic conditions.

Depending on how excessive and extensive this stress redistribution is, plastic loading can be triggered if the stress state reaches the material's strength envelope. It seems that whether extensive plastification takes place or not governs the finally observed face extrusion. In more detail, an increased face pressure and/or strength, limits the onset of plastic deformation in the face core (see graphs g, h in both figures 10.5 and 10.6) and also results in a decreased face extrusion as observed in figure 10.4. In such cases, where the face core behaves primarily elastic, anisotropy is in favour of a slightly reduced face extrusion due to the fact that the peak strength of the material is slightly increased (at least for the loading direction corresponding to the examined case).

On the other hand, as the applied face pressure is reduced or/and ground conditions deteriorate, an extensive plastic zone appears, which explains why the analyses with the anisotropic constitutive law result to an increased face extrusion compared to their isotropic counterparts. Plastic loading activates the de-orientational hardening rule of the proposed model, and thus the ground strength degrades following

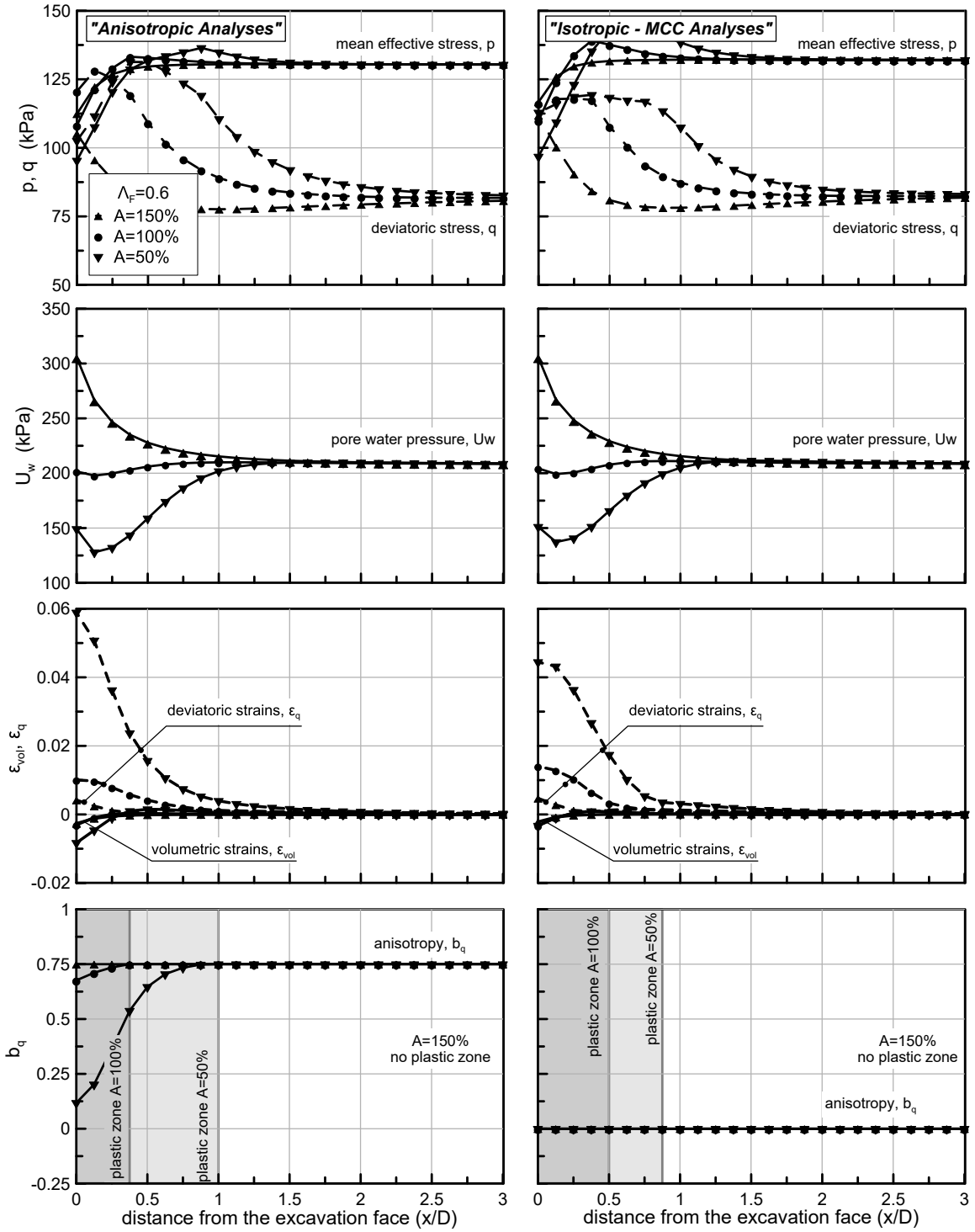


**Figure 10.5:** Stress and strain evolution of a soil element at the center of the tunnel face, for three different face support pressures; results from both isotropic and anisotropic analyses. a) the $p-q$ space; b) the $q-\varepsilon_q$ diagram; c) the $v-\ln p$ plane; d) the $\Delta U_w-\varepsilon_q$ diagram; e) the $b_q-\ln p$ diagram and; f) the $b_q-\varepsilon_q^p$ diagram.

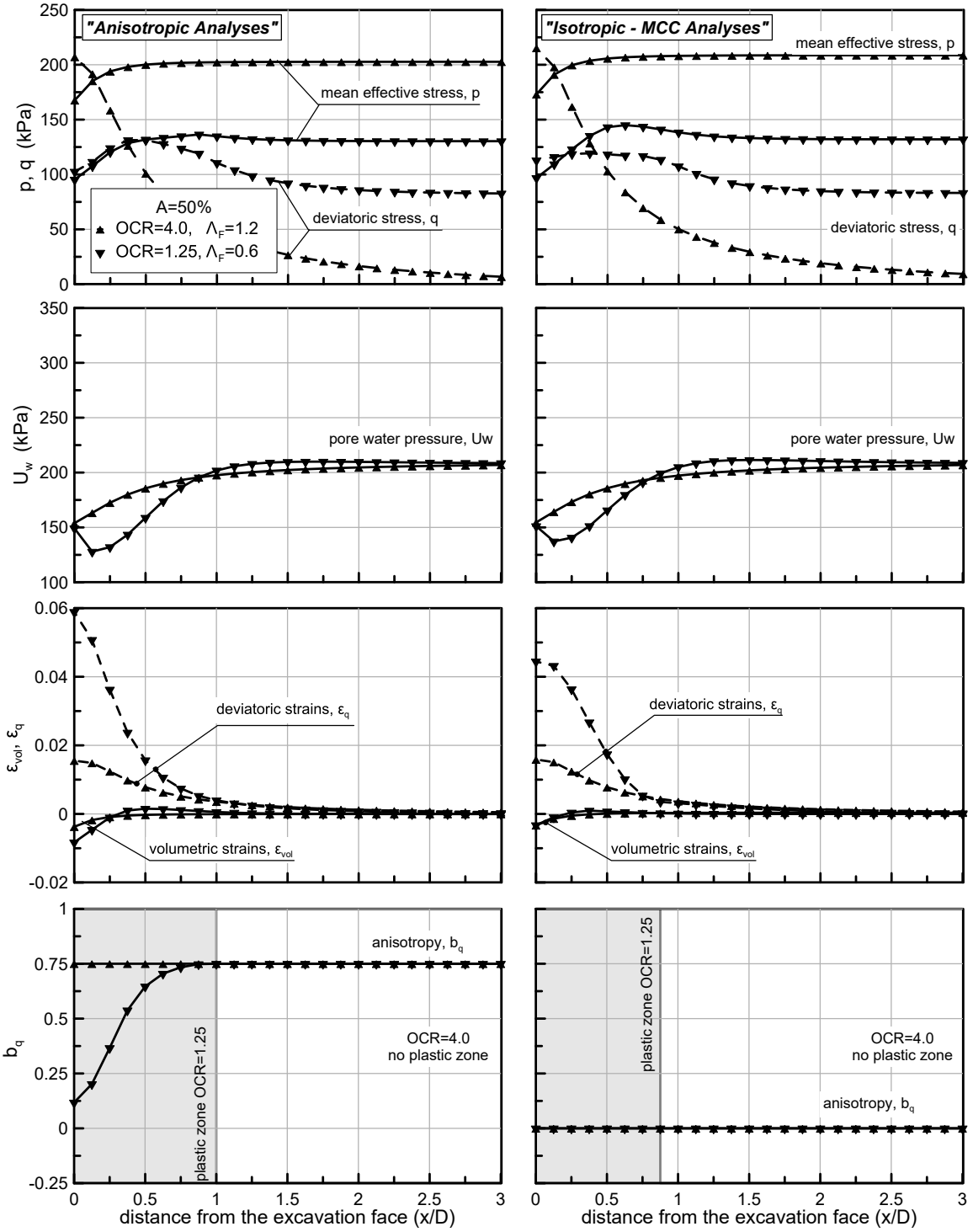


**Figure 10.6:** Stress and strain evolution of a soil element at the center of the tunnel face, for two different ground conditions; results from both isotropic and anisotropic analyses. a) the $p-q$ space; b) the $q-\varepsilon_q$ diagram; c) the $v-\ln p$ plane; d) the $\Delta U_w-\varepsilon_q$ diagram; e) the $b_q-\ln p$ diagram and; f) the $b_q-\varepsilon_q^p$ diagram.

the progressive loss of the memory of preferred directions with the onset of plastic deviatoric strains. Simultaneously, this strength degradation, further inflates plastic yielding, resulting to a self-triggering mechanism which increases face extrusion.

## 10.3 Application to strip foundation under unsaturated conditions

### 10.3.1 General - Problem Description

This section applies the proposed constitutive model to FEM analyses of the mechanical responce of a swallow strip footing founded on an unsaturated soil profile. Vertical load ($P$) - settlement ($\delta$) curves are calculated for different water table depths, while additionally the vertical displacement accompanying a lowering of the water table (drying the soil profile) and a rising of the water table (saturating the soil profile) are studied. Both "isotropic" and "anisotropic" analyses are conducted, the first group allowing for a clear manifestation of the effects of partial saturation in the analysed problem and the second one extending the discussion to the effect of stress induced anisotropy.

### 10.3.2 The Abaqus Model - Input Parameters

Figure 10.7 presents the Abaqus numerical model. It is a 2D numerical model with the dimensions given in the figure. A dense mesh discretization is selected and the model consists of 12808 two-dimensional, 8-noded (second order) solid elements with 9 integration points each. They are rectangular with a side length equal to $0.25m$.

The soil profile is realized through 12800 elements and typical boundary conditions are assigned, including rollers on the left and the ride side of the model and hinges at the bottom. Regarding the hydromechanical conditions, the water table is defined by suitably adjusting (assigning) the pore water pressure at the bottom of the model, while its distribution follows hydrostatic equilibrium.

A rigid strip foundation with a width equal to $B = 2.0m$ and with no embedded depth is simulated. It is realized by 8 solid elements placed directly on the top of the soil profile at the center of the model. To ensure a rigid body behaviour, their nodes are interconnected with rigid elements preventing elements deformation. A direct contact between the footing and the soil profile is simulated with no contact interface

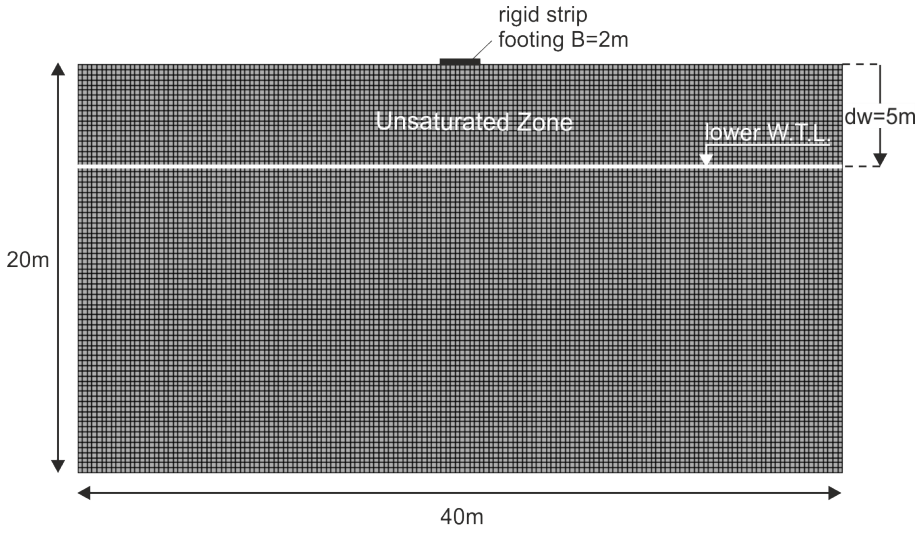


**Figure 10.7:** The FEM model in Simulia Abaqus.

elements. Such a selection simplifies the analysis with no deleterious effects on the results, as the examined footing is tested under vertical loading with no eccentricity. The footing is assumed weightless and the exact mechanical properties are irrelevant to the analyses results due to the rigid body assumption.

Table 10.2 summarizes the utilized model parameters for the soil profile. The performed analyses emphasize on the effects of partial saturation and thus, a relatively coarse grained soil of reduced water retention capacity is simulated to allow for a significant desaturation of the soil profile even under relatively low suction values. The model parameters corresponding to the Jossigny Silt soil are used, as these were defined through the calibration of the proposed model against the experimental results of Casini (2008) (see section 9.3).

None of the parameters is parametrically investigated. Regarding the two different sets of values for the hardening rule parameters $\psi$ and $\zeta_q^p$ appearing in table 10.2, they simply refer to the "isotropic" and the "anisotropic" analyses. For the isotropic analyses, the proposed model is reduced to the MCC model (no memory of preferred directions) focusing on the pure effects of partial saturation. For the second set of analyses the anisotropic characteristics of the model are activated while the initial orientation of the yield surface is assumed equal to $b_q = 0.25$. It is obvious that the selected orientation is smaller compared to the one corresponding to the assumed $K_0 = 0.5$ value. The selected reduced initial orientation favours a more realistic simulation, mainly due to the following two reasons:

**Table 10.2:** The constitutive parameters selected for the analyses.

| Basic Parameters | | Anisotropic Parameters | | Unsaturated Parameters | |
|---|---|---|---|---|---|
| Parameter | Value | Parameter | Value | Parameter | Value |
| $\kappa$ | 0.006 | $r_s$ | 2.0 | $r$ | 0.4 |
| $\lambda(0)$ | 0.11 | $\psi$ | 0, 20.0 | $\beta$ | 30.0 $MPa^{-1}$ |
| $\nu$ | 1/3 | $\zeta_q^p$ | 0, 20.0 | $\gamma$ | 1.0 |
| $c$ | 1.0206[*1] | $\chi$ | 0.4945[*2] | $p^c$ | 6 $kPa$ |
| $k$ | 1.0206 | | | | |
| $N_{iso}$ | 2.25 | | | | |
| $\Gamma$ | 2.178[*2] | | | | |

[*1] is equivalent to $M = 1.25$ in the triaxial stress space and corresponds to a material with $\phi \approx 30^o$ in compression.
[*2] corresponds to $\Gamma = N_{iso} - (\lambda - \kappa)\ln 2$ due to $k = c$ selection.
[*3] calibrated for $K_0 = 0.5$.

- In an almost normally consolidated soil profile, as the one simulated ($OCR = 1.2$), the upper soil layers have not undergone sufficient straining during their depositional history to justify a fully developed anisotropic fabric in line with the imposed stress path.

- The second reason is associated with the proposed model's tendency to overestimate the peak strength of initially anisotropic soils, while as discussed in chapter 9 the assumption of a reduced initial yield surface inclination significantly improves the simulation results.

The geostatic stress field (body forces and gravity equilibrium) is established under saturated conditions. This is achieved by prescribing a water pressure at the bottom of the model equal to 200kPa corresponding to 20m of water under hydrostatic conditions ($g = 10m/s^2$ and $\rho_w = 1.0Mgr/m^3$ are assumed). The procedure described in appendix E is used to calculate the initial geostatic field and the initial internal variables, while table 10.3 summarizes the additional parameters required to set up the mechanical problem in Simulia Abaqus.

The analysis of unsaturated porous media requires coupled hydromechanical analyses. For the hydraulic problem, the values reported in table 10.4 are used to de-

**Table 10.3:** Additional parameters required to set up the mechanical problem in Abaqus.

| Parameter | Value | Parameter | Value |
|---|---|---|---|
| $G_s$ | 2.65 | $b_q$ (isotropic set) | 0.0 |
| $OCR$ | 1.20 | $b_q$ (anisotropic set) | 0.25 |
| $K_0$ | 0.5 | | |

fine the WRC, the effective degree of saturation and the saturated and unsaturated permeability. Figure 10.8a presents the assumed water retention curve, based on the Gallipoli et al. (2003). It is reminded that Abaqus cannot account for a void ratio dependant water retention model and thus a constant WRC is assigned. The WRC corresponding to a relatively open soil fabric ($v = 1.8$) was selected as an input. It is further reminded that Abaqus incorporates directly the degree of saturation calculated through the WRC in the Bishop's stress equation and thus the effective degree of saturation must be directly provided through the water retention curve. The evolution of the $s \cdot S_r^e$ term corresponding to the modelled WRC is given in figure 10.8b.

**Table 10.4:** The WRC, effective degree of saturation and permeability parameters used in the analyses.

| WRM | | Effective $S_r$ | | Permeability | |
|---|---|---|---|---|---|
| Parameter | Value | Parameter | Value | Parameter | Value |
| $\phi$ | 1.318 | $\alpha$ | 1.5 | $k_{sat}$ $(m/s)$ | $10^{-4}$ |
| $\psi$ | 6.04 | | | $k_{Sr}$ | $k_{sat} \cdot (S_r)^3$ |
| $n$ | 1.34 | | | | |
| $m$ | 0.15 | | | | |
| $v$ | $1.8^{*1}$ | | | | |

$^{*1}$ a constant void ratio WRC is defined in Simulia Abaqus.

Additionally, figure 10.9 plots the evolution of compressibility and of the apparent preconsolidation pressure with suction, according to the assumed parameters. It is highlighted that the plots are just indicative of the assumed behaviour and do

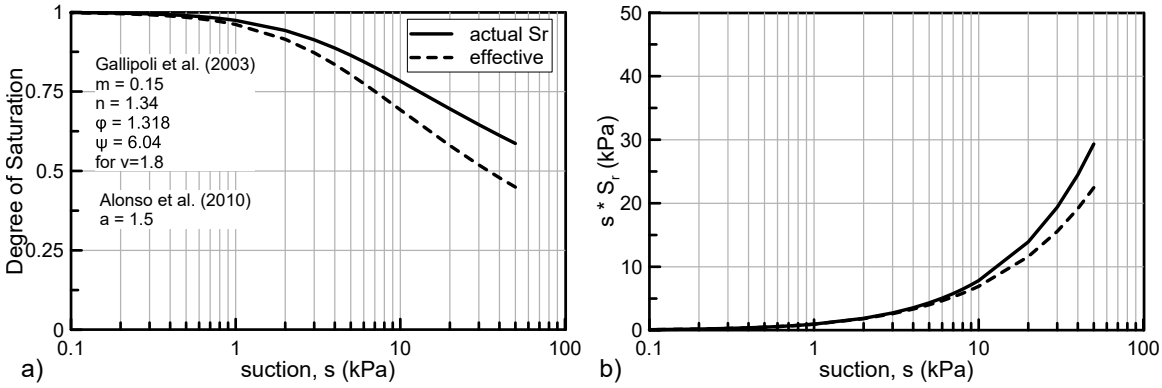


**Figure 10.8:** a) The assumed WRC and; b) the evolution of the $s \cdot S_r$ term.

not correspond to analyses' results. Regarding water flow, the selected saturated permeability corresponds to a typical sandy silt, while to account for a decreasing permeability with partial saturation, a simple power law is utilized (it is the default Abaqus option).

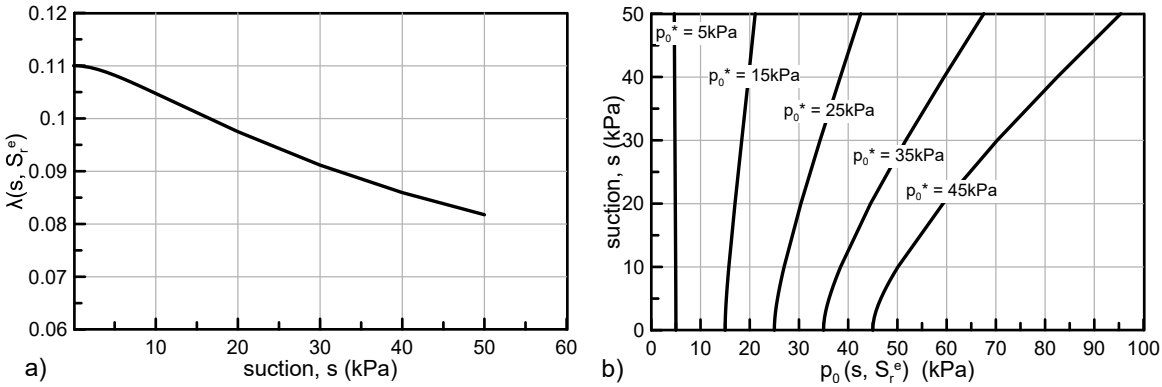


**Figure 10.9:** a) The evolution of compressibility with suction and; b) characteristic plots of the corresponding LC curve for five different $p_0^*$ values.

The present study includes a total of fourteen (14) coupled hydromechanical analyses. Twelve (12) are associated with the attempt to calculate load ($P$) - settlement ($\delta$) curves for the assumed surface strip footing. They are divided in the two main groups previously mentioned (the "isotropic" and the "anisotropic"), each one consisting of six (6) analyses related to an equal number of different water table depths ($d_w$); namely $d_w = 0$ (saturated), $d_w = 1.0$m, 2.0m, 3.0m, 4.0m and 5.0m. Finally,

two additional analyses (isotropic and anisotropic) are associated with the simulation of water table rise from its maximum depth ($d_w = 5.0m$) up to the surface ($d_w = 0.0$), to investigate the effect of such a wetting process on the displacement of a loaded footing.

### 10.3.3 Results

This section presents and discusses the results of the performed numerical analyses. It is divided in three paragraphs each one dealing with the results associated with: a) the initial drying of the soil profile; b) the loading stage to calculate $P$ - $\delta$ curves, and; c) the water table rise.

#### 10.3.3.1 Lowering the Water Table

Starting from the initially established fully saturated soil profile (geostatic conditions), the water table is gradually lowered to simulate the development of the unsaturated zone. The maximum water table depth analysed is $d_w = 5$m. Water table drop is realized through ten (10) individual loading steps, five (5) regarding the gradual lowering of the water table in equal steps of $\Delta d_w = 1.0m$ each and another five (5) regarding establishment of hysraulic equilibrium. In more detail, each of the former steps lasts 200hours and is followed by a consolidation step where water flow continuous under constant hydraulic boundary conditions until hydrostatic equilibrium is achieved. A rather strict criterion for $\Delta U_w = 10^{-4}$ is used to define equilibrium conditions (controls the end of each consolidation step).

Figure 10.10 presents the degree of saturation and suction profiles corresponding to equilibrium conditions for the maximum water table depth analyzed ($d_w = 5.0m$). Additionally, in figure 10.11, the distribution of pore water pressure and of the corresponding degree of saturation with depth are plotted at the end of each consolidation step. The initial saturated profile is also included for reference.

Drying an initially saturated soil profile is accompanied by settlement of the free surface. Figure 10.12 presents the evolution of surface settlement with drying for the performed analyses. Notice that substantial settlement develop ($s_max = 20 - 25cm$), with the anisotropic analysis resulting to slightly increased settlement with respect to its isotropic counterpart.

The calculated settlement is the output of a consolidation processes which condenses the soil profile as a result of the increasing average skeleton stress with drying.

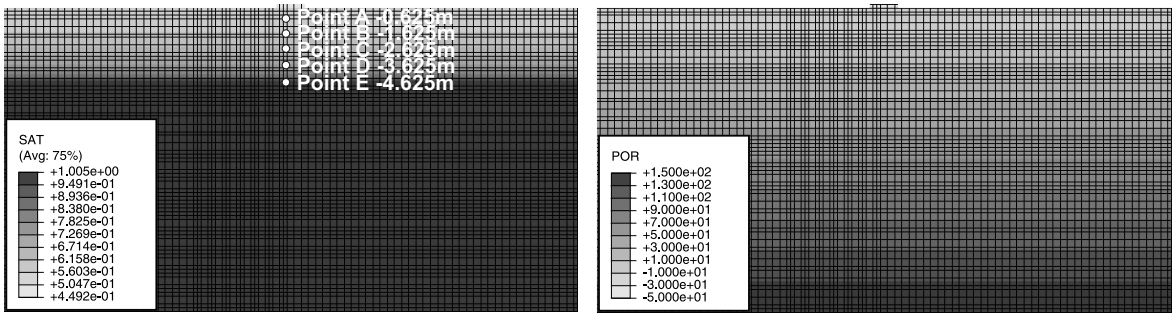


**Figure 10.10:** Distribution of the effective degree of saturation (left) and of the pore water pressure (right); water table at a depth equal to $d_w = 5.0m$.

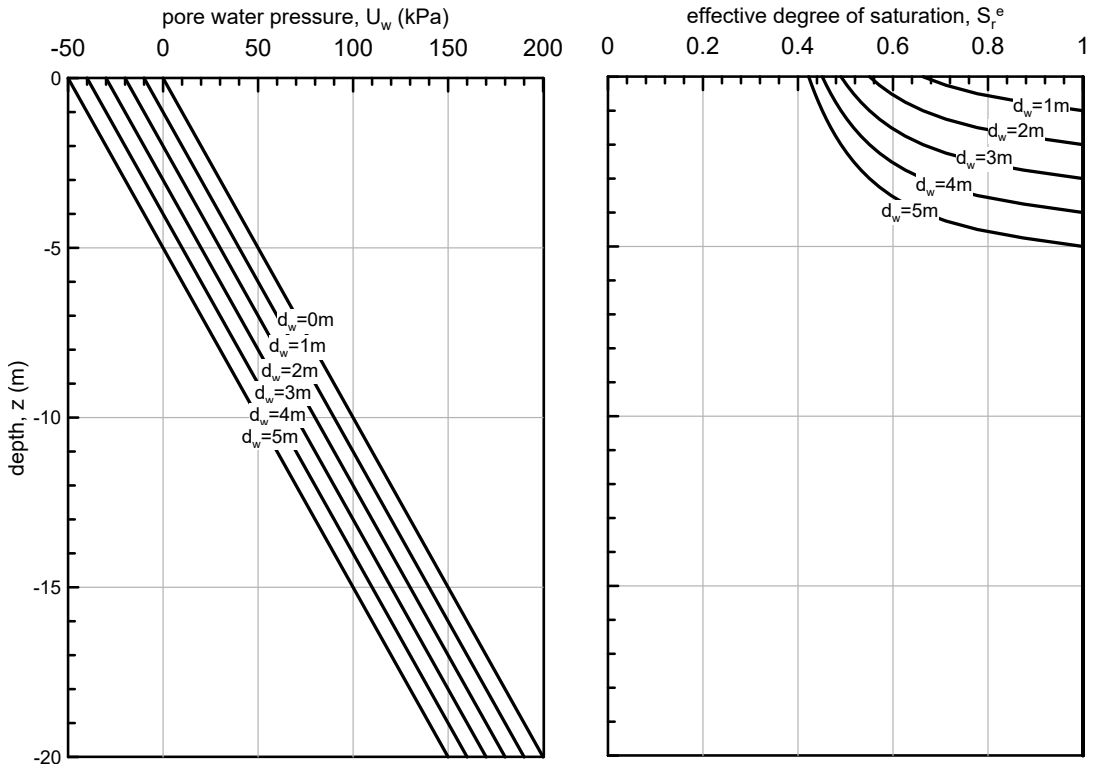


**Figure 10.11:** Distribution of the pore water pressure and of the effective degree of saturation with depth for 6 different water table depths (equilibrium conditions).

Figure 10.13 presents the evolution of various critical quantities during this drying process. Five characteristic points (Point A to E in figure 10.10) have been selected to monitor the evolution of various parameters. They are positioned along the axis of symmetry of the analyzed problem, corresponding to five different depths inside the

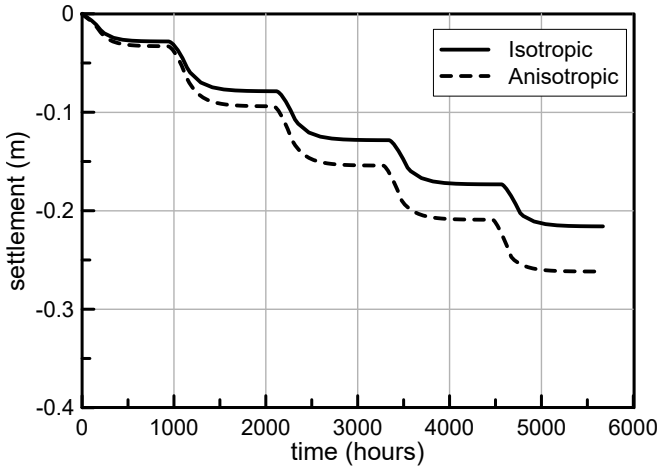


**Figure 10.12:** Surface settlements induced by the progressive lowering of the water table.

unsaturated zone.

In graphs 10.13 a and b we may monitor the gradual increase in suction and the reproduced drop of the effective degree of saturation with time. Notice that a substantial time was required after the initial 200 hours (duration of each water table drop step) for the hydraulic conditions to reach equilibrium. This is attributed to the strict equilibrium criterion selected ($\Delta U_w = 10^{-4}$) and offers little to the accuracy of the results. In practical terms, suction and degree of saturation has almost reached an equilibrium after 500 hours, indicating that a less strict criterion ($\Delta U_w$) can be selected.

The graphs (c) and (d) in figure 10.13 present the evolution of Bishop's mean stress, mean net stress and deviatoric stress with time. An increase in Bishop's stress and in the deviatoric stress is clearly identified while net stress slightly reduces. The increasing Bishop stress is a clear outcome of the pore water pressure reduction and is the main driving mechanism of the anticipated settlement. It is interesting to notice that at the same time the net stress (total stress) drops, reflecting the reducing specific weight of the material due to water drainage. Regarding the increase in the deviatoric stress, we shall consider that the simulated problem is in fact an $1D$ consolidation process, where the deviatoric stress adjusts according to the predictions of the constitutive law to maintain zero horizontal strains.

In figures 10.13e and f we may observe the deformation of the soil profile during drying. The increase in the average skeleton stress results in a continuous volumetric

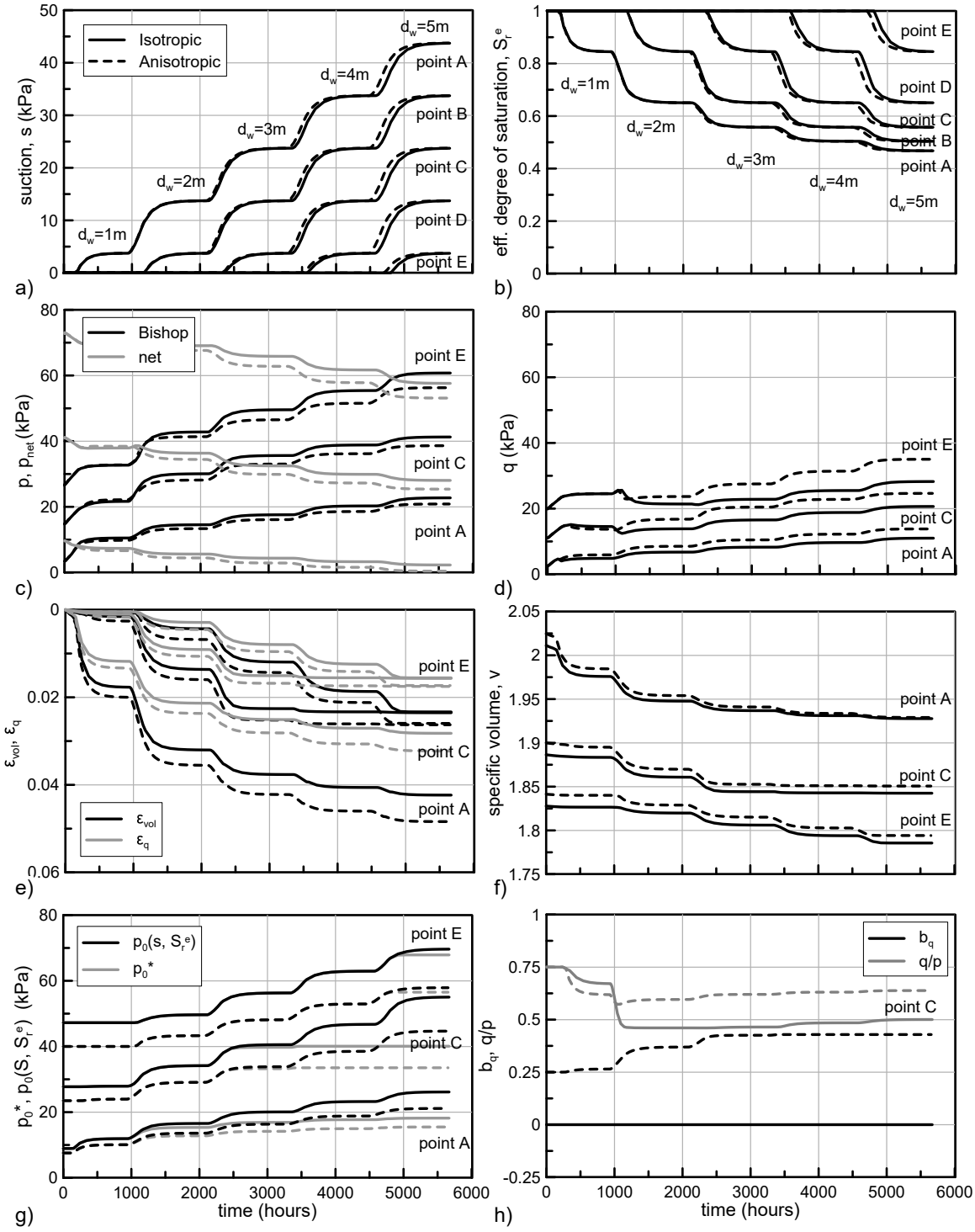


**Figure 10.13:** Evolution of: a) suction $s$; b) effective degree of saturation $S_r^e$; c) Bishop's mean stress $p$ and mean net stress $\overline{p}$; d) deviatoric stress $q$; e) volumetric strain $\varepsilon_{vol}$ and deviatoric strains $\varepsilon_q$; f) specific volume $v$; g) apparent preconsolidation pressure $p_0(s, S_r^e)$ and hardening variable $p_0^*$, h) yield surface orientation $b_q$ and stress ratio $n$ with time.

deformation, reflected also in the decrease in the void ratio, while the deviatoric strains follow the volumetric deformation according to a constant total dilatancy equal to $d = 2/3$ reflecting the analysis boundary and loading conditions.

Figure 10.13g presents the evolution of the tip of the unsaturated strength envelope ($p_0(s, S_r)$) and of the saturated strength envelope ($p_0^*$). These plots reveal how the yield stress increases with partial saturation and consolidation. Notice that as far as the soil remains saturated, the saturated and the unsaturated strength envelopes coincide with an increase in the mean effective stress hardening the material. When the water table reaches the examined point, further drying increases the apparent preconsolidation pressure $p_0(s, S_r)$, under a constant $p_0^*$, with the latter indicating an elastic stress path. In graph 10.14 the evolution of the apparent preconsolidation with suction is plotted, together with the corresponding evolution in terms of net stress and of the corresponding mean stress.

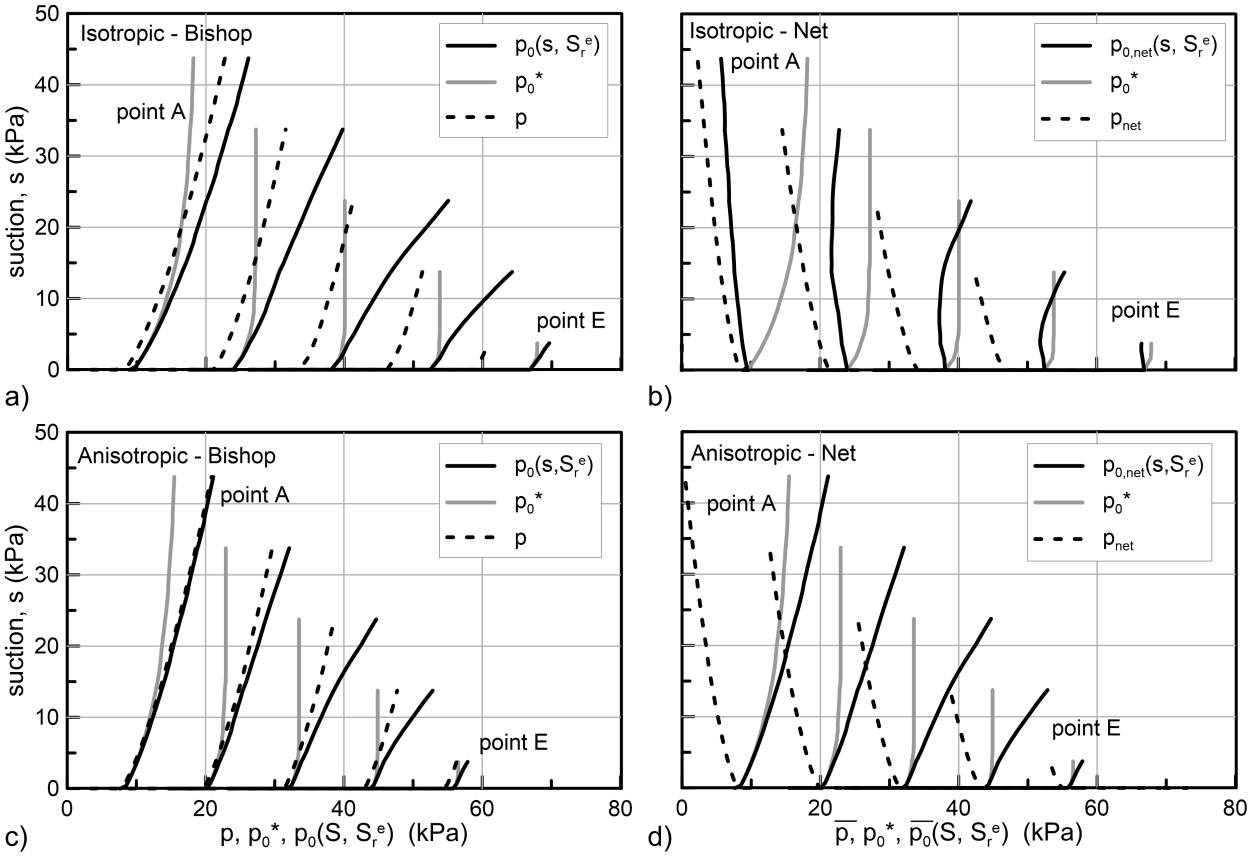


**Figure 10.14:** Evolution of the apparent preconsolidation pressure ($p_0(s, S_r^e)$), of the saturated preconsolidation pressure $p_0^*$ and of the octahedral stress $p$ with suction for the isotropic (top) and the anisotropic (bottom) analyses, in terms of Bishop' stress (left) and net stress (right).

With respect to the effect of stress induced anisotropy in the anticipated response, we may observe that anisotropy results in an increased volumetric deformation which explains the increased anticipated settlement. This is reasonable, as an anisotropic soil fabric usually results in a denser packing of the soil grains - particles reducing the void ratio of the soil.

In terms of constitutive modelling, it is the outcome of the flow rule which tries to accommodate the assumed $K_0$ value. In more detail, in figure 10.12h we may observe the evolution of the deviatoric stress and of the stress ratio $q/p$. Notice that for the anisotropic analysis, during plastic loading the ratio $q/p$ increases towards the value corresponding to the assumed $K_0 = 0.5$ ($n$=0.75). It is reminded that a reduced initial anisotropy with respect to the one corresponding to the selected $K_0$ has been assigned, explaining why the anisotropic analyses do not reproduce the assumed $K_0$. On the contrary, the analysis with an isotropic yield surface (MCC flow rule) produces a significant drop in the $q/p$ ratio towards the value $b_q$=0.50, which corresponds to $K_0 = 0.625$. Thus, the MCC analysis results to a "more isotropic" stress field (also reflected in the evolution of the deviatoric stress with drying in figure 10.12d) which is less efficient in reducing the void ratio.

#### 10.3.3.2 Loading under unsaturated conditions

This paragraph discusses the results of twelve (12) FEM analyses performed in order to calculate load ($P$) - settlement ($\delta$) curves for different partial saturation and anisotropic conditions. A significant vertical displacement equal to $1.0m$ is applied to the central node of the upper part of the rigid footing, relatively fast (within 1h), to ensure "undrained" loading conditions. The developing reaction force at the same node provides the desired load (P). The analyses performed correspond to six different positions of the water table, namely at a depth equal to $d_w = 0$ (saturated) and $d_w$ = 1.0m, 2.0m, 3.0m, 4.0m and 5.0m, each one of them initiating from the final state of the associated equilibrium stage of the previous paragraph's analyses.

Figure 10.15 presents the derived $P - \delta$ curves, where an increase in the load that the examined strip foundation can bear with an increasing thickness of the unsaturated zone is clearly identified. The anticipated results mainly reflect the failure mechanism and how the latter alters with water table depth.

In figure 10.16, the deformed mesh of the $d_w = 0.0m$ analyses (fully saturated soil profile) indicates an undrained failure mode, with a swallow plastic zone and a

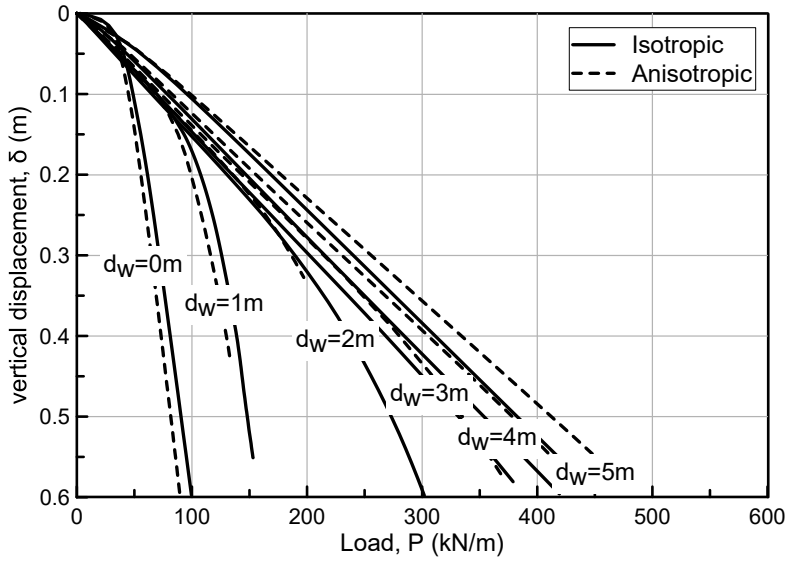


**Figure 10.15:** The calculated Load ($P$) - Settlement ($\delta$) curves (strip surface footing with $B = 2$m) for different depths of the water table.

typical uplift of the soil in the sides of the footing as a consequence of the constant volume deformation. The results suggest an almost similar response for the $d_w = 1.0m$ case with the increased bearing capacity in the latter case attributed to the fact that initially, the upper part of the soil although deforming under constant water conditions it undergoes volumetric deformation (air phase volume reduces), which stiffens and strengthens its behaviour. Nevertheless, at some point the soil underneath the footing saturates (as a result of the continuing loading) and further loading leads to constant volume deformation and an "undrained" failure mode.

On the other extreme, the significant increase in the soil stiffness and shear strength with an increase in the depth of the unsaturated zone, alters the anticipated response. The $P-\delta$ curves corresponding to a relatively deep water table ($d_w > 3.0m$) indicate an almost linear response with no clear trend towards a maximum load (bearing capacity). The deformed mesh reveals a punching mode of "failure" where the footing penetrates the soil below. Note that the contours of plastic deviatoric deformation corresponding to the maximum depth of the water table ($d_w = 5m$, see figure 10.16) imply a significant stress redistribution at a depth of approximately two times the footing's width ($2B$), resembling typical stress contours of elastic solutions below a loaded strip footing. Additionally it is interesting to notice that the accu-

mulated plastic strains are significantly decreased, by almost an order of magnitude, compared with the saturated ($d_w = 0m$) case.

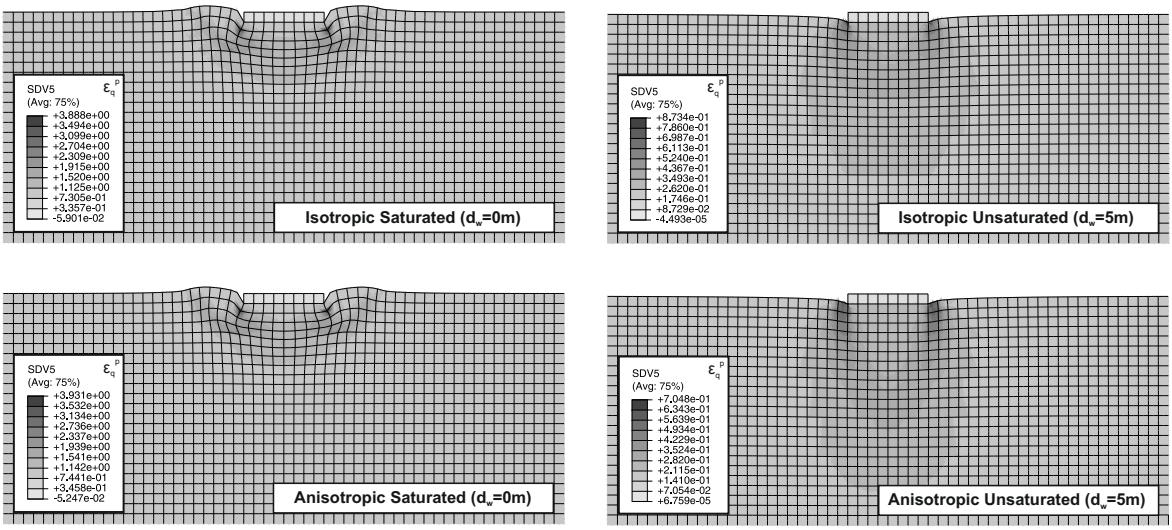


**Figure 10.16:** Distribution of the plastic deviatoric strains $\varepsilon_q^p$ (SDV5) at the end of loading, under saturated condition for the isotropic (top) and the anisotropic (bottom) analyses, and for the water table at the ground surface (left) and at a depth $d_w = 5.0m$ (right).

Comparison of the $P-\delta$ curves between the isotropic and the anisotropic analyses reveals a limited effect of stress induced anisotropy, especially if compared with the effect of an increase in the depth of the unsaturated zone. In other words, we may say that it is the partial saturation which govern the response of the examined footing with anisotropy having only secondary effects. Nevertheless, it is interesting to notice and discuss the fact that for the shallow water table cases, anisotropic analyses lead to a reduced "bearing capacity", with the trend reversing as the examined water table gets deeper. The anticipated behaviour reflects the different failure modes previously discussed. The undrained failure associated with a high water table favours the onset of significant plastic deviatoric strains, which result to intense anisotropy degradation. In other words, the response in terms of the $P-\delta$ curves is a reflection of the strain softening behaviour due to anisotropy degradation. On the other hand, the footing's deformation under unsaturated conditions, favours an increased soil strength and stiffness, limiting the plastic deviatoric strain accumulation and thus, the resulting anisotropy degradation. The described behaviour is also reflected in the plots of figure 10.17, presenting the distribution of quantity $b_q$, a measure of stress induced anisotropy.

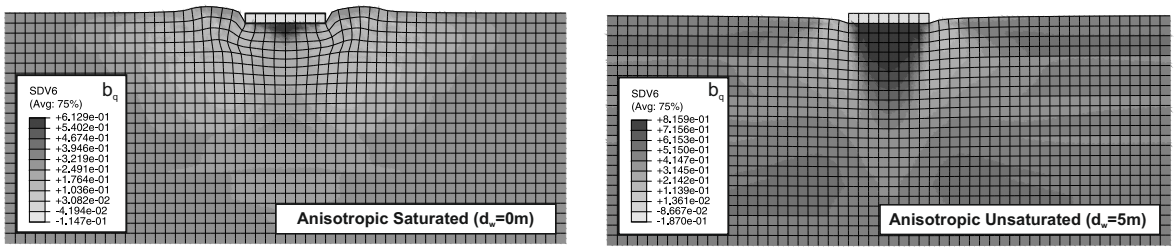


**Figure 10.17:** Distribution of the measure of the yield surface orientation $b_q$ ($b_q = \sqrt{3/2}\cdot$ SDV5) at the end of loading, for the water table at the ground surface (left) and at a depth equal to $d_w = 5.0m$ (right).

Finally, we shall mention that the increased bearing capacity calculated for the unsaturated analyses does not imply that in practical terms a surface structure can be designed for such an increased bearing capacity as the anticipated settlements are practically unrealistic for a $B = 2m$ footing. Moreover, the analyses lack some realism in the sense that a very soft ground is simulated (normally consolidated soil profile), leading to increased deformation. Porous elastic critical state models overestimate the compressibility of the upper parts of a given soil profile due to their framework dependance on the level of the applied stress. For that reason, it is quite common in numerical simulations to assume a significant overconsolidation for the upper part of the soil profile to better match the in situ behaviour. Nevertheless, in our comparative study an increased compressibility was deliberately selected as it: a) favours a clear demonstration of the anticipated behaviour, and b) increases the complexity of the numerical analyses due to the severe deformation and distortion of the finite elements.

#### 10.3.3.3 Raising the Water Table

With the water table at its maximum (examined) depth ($d_w = 5.0m$), a vertical load equal to $P = 120$kN/m is applied to the examined strip footing and then, water table is gradually raised under constant load until the soil profile completely saturates. Load application is realized by applying a concentrated vertical load at the central node of the upper part of the rigid footing and the step's duration is $1h$. If we compare the selected load with the $P-\delta$ curves previously discussed, we will observe that it is higher than the bearing capacity under saturated conditions, but significantly lower compared to the maximum load defined from the analyses with the water table at $5m$ depth.

To simulate the water table rise, we define a reversed loading sequence with respect

to the drying process. The pore water pressure at the bottom of the model is increased by 10kPa in five equal steps lasting 200h each, while at the end of each water table rise step, a consolidation step ensures hydraulic equilibrium. Figure 10.18a plots the calculated vertical movement of the examined strip foundation during both the load application stage and the subsequent wetting stage.

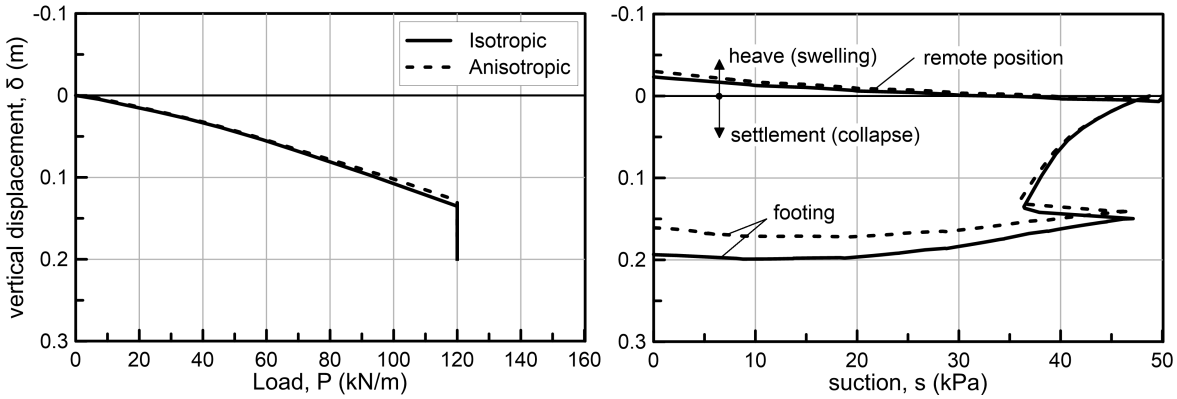


**Figure 10.18:** Evolution of vertical displacement versus the: a) applied Load (P) and; b) suction.

Load application leads to a settlement of 12cm, while the subsequent suction decrease under a constant load further increases settlement by another 8cm, the latter a consequence of wetting induced volumetric collapse. In figure 10.18b we may further observe how settlement evolves with suction, with the latter monitored at the top of the soil profile. The vertical displacement at two different positions is monitored, both at the ground surface. The first one is located directly under the examined footing, while the other one in a remote position away from the footing. Note that during load application, under the footing, suction drops as a result of the relatively quick load application. During the wetting stage, initially suction at the soil surface increases, trying to reach an equilibrium with the surrounding soil (away from the footing), while at the same time settlement increases as a consequence of the progressive rise of the water table which causes plastic volumetric deformation in the unsaturated zone. This trend soon reverses as the wetting front moves towards the surface, with suction progressively decreasing and at the same time settlement continuously increasing.

Away from the footing, neither suction nor the vertical displacement is influenced by the load application. During the wetting stage though, heave is observed as a result of swelling of the soil profile away from the footing. This continuous heave

away from the footing seems to also affect the vertical displacement of the footing to some extend as well. This is depicted in figure 10.18b, where footing's settlement reaches a maximum when the water table is at a depth of around 1m, while further wetting leads to a slight heave (settlement reduction) of the footing. This is the result of the decreased stress field under which wetting takes place at the upper $1m$ of the soil leading to a significant swelling of the surrounding ground. Thus, although the soil elements underneath the footing slightly collapse it is the swelling of the adjacent soil that governs the overall footing's response.

Figure 10.19 presents the variation of: a) the apparent preconsolidation pressure; b) saturated preconsolidation pressure (hardening variable) and; c) of the octahedral stress with suction, for points A to E, (see figure 10.10). The plots highlight the importance of the Loading - Collapse surface in capturing the mechanical behaviour of unsaturated soils. We may observe that the increasing stress field during loading moves the stress point towards the yield surface and also hardens the material. As a result, the initial state after loading is plastic and thus, during wetting, the decreasing suction tends to drag the material state outside of the yield surface (the LC curve), triggering plastic loading which leads to the anticipated plastic volumetric deformation.

Regarding the effect of stress induced anisotropy, we may observe that away from the footing the calculated heave is not significantly influenced. On the other hand, regarding the footing settlement, the simulation reveals that stress induced anisotropy favours a reduced collapse and thus decreased settlement.

In terms of constitutive modelling, this is attributed to the plastic volumetric strains accumulating during wetting which favour an evolving stress induced anisotropy towards the direction of loading. The rotation of the yield surface makes the current stress state and the tip of the yield surface (lying on the LC curve) to approach. Two opposite mechanisms evolve and interact. From on hand, wetting produces plastic loading which increases the preconsolidation pressure, while on the other hand, simultaneously the yield surface rotates to accommodate the evolving anisotropy. This evolving anisotropy reduces the wetting induced plastic straining due to the fact that the "current" stress state and the tip of the yield surface approach. This is depicted in figure 10.19, where the gray lines indicating the evolution of the saturated preconsolidation pressure reveal a significantly increased hardening for the isotropic analyses.

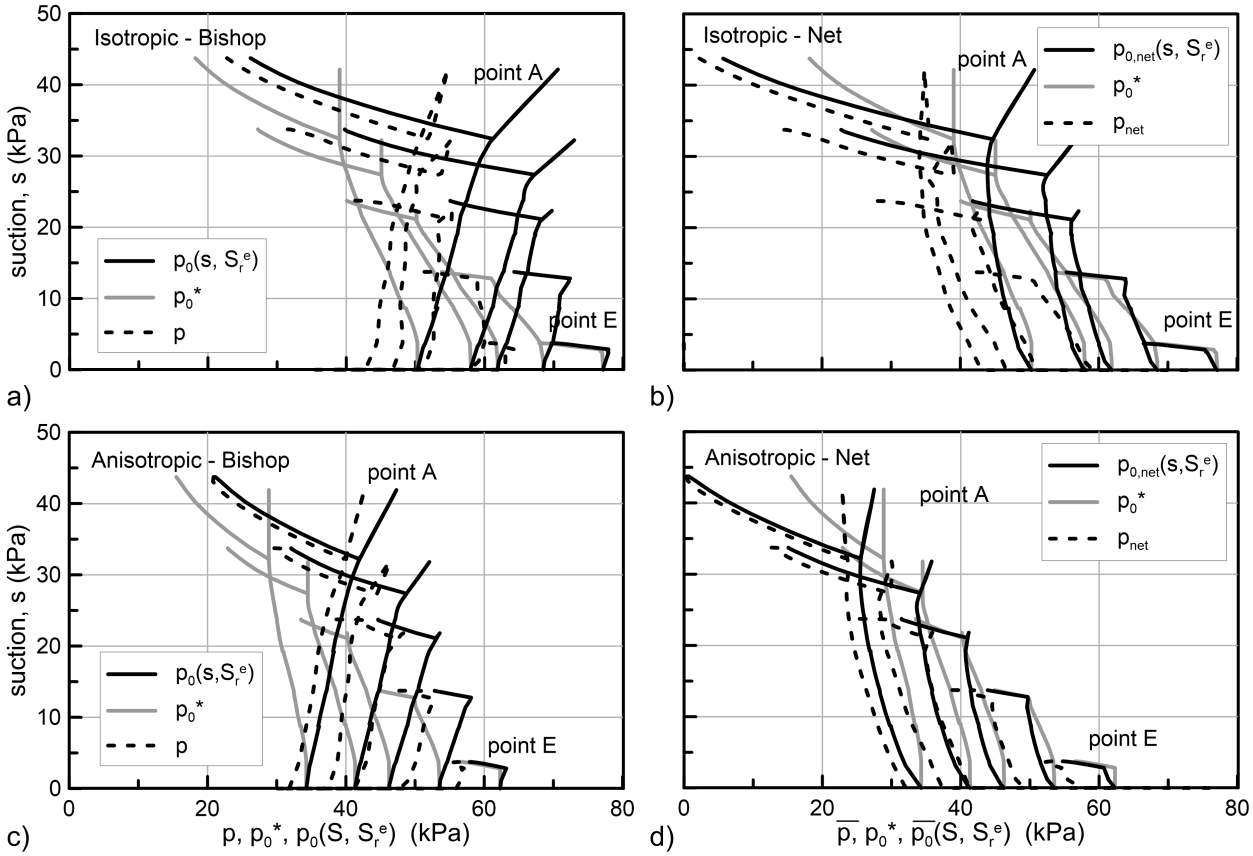


**Figure 10.19:** Evolution of the apparent preconsolidation pressure ($p_0(s, S_r^e)$), of the saturated preconsolidation pressure $p_0^*$ and of the octahedral stress $p$ with suction for the isotropic (top) and the anisotropic (bottom) analyses, in terms of Bishop' stress (left) and net stress (right).

## 10.4 Concluding Remarks

The present chapter applied the proposed constitutive model in finite element analyses of large scale geotechnical problems. The effect of stress induced anisotropy on face stability conditions of a mechanically excavated (TBM-EPB) circular tunnel (diameter $8m$ and height of overburden $16m$), as well as the mechanical response of a strip footing ($B = 2m$) founded on an unsaturated soil profile were analyzed with the Simulia Abaqus FEM computer code.

The tunnel analyses were realized using a $3D$ numerical model, while the footing analyses using a $2D$ model. Both problems involved coupled hydromechanical analyses, while the proposed model's UMAT subroutine, presented in chapter 7, provided the constitute behaviour.

A total of 74 analyses were conducted and all turned out reasonable results. The

developed UMAT performed efficiently with the analyses requiring reasonable time, given the complexity of the simulated problems (large models including a significant number of steps, extensive plastic loading, etc.). Suction increase and suction decrease steps prove the most time consuming. This is attributed to the Simulia Abaqus' inability to account for the hydraulic Jacobian(s) $\boldsymbol{W}_s$ and $\boldsymbol{W}_{S_r^e}$, inevitably influencing the accuracy of the predicted, imposed strain increment and thus delaying convergence.

It is highlighted once again that the strong unsymmetrical matrices resulting from the model's non-associated flow rule necessitate the activation of the Abaqus' unsymmetrical solver and also the addition of the UNSYMM option in the material definition. In general even when the previously mentioned unsymmetrical options are activated, the numerical solution of anisotropic analyses proves quite demanding. The analyses related to the $P$-$\delta$ calculation for the strip footing under unsaturated conditions ($d_w > 1m$) and with the anisotropic characteristic's of the model activated (rotated yield surface and non-associated flow rule) could not be completed. The solution did not convergence even with the minimum time increment assigned, indicating a highly nonlinear response. Nevertheless, we should mention that a quite increased vertical displacement ($1m$) was assigned as the targeted displacement for the footing, leading to a highly nonlinear response. In practical terms, the aforementioned (not completed) cases, still yielded sufficient information, as analysis progressed until a vertical displacement larger than $0.5m$ before terminating.

The values obtained by the term $H + \boldsymbol{Q} : \boldsymbol{C}^e : \boldsymbol{P}$ during plastic loading where systematically monitored. In chapter 2 we demonstrated that if the selected flow rule ensures that inequality $\boldsymbol{Q} : \boldsymbol{C}^e : \boldsymbol{P} > 0$ holds true and the hardening rule ensures that $H + \boldsymbol{Q} : \boldsymbol{C}^e : \boldsymbol{P} > 0$, then the constitutive model ensures a stable numerical solution. The $H + \boldsymbol{Q} : \boldsymbol{C}^e : \boldsymbol{P}$ values, at least during the performed analyses, where systematically positive during plastic loading, a strong indication that the proposed constitutive model ensures such numerical stability. In any case, as also mentioned in chapter 7, the aforementioned term is systematically monitored inside the developed UMAT and a warning message appears in case of negative values.

Tunnelling analyses focused on the effect of stress induced anisotropy on face stability, the latter assessed in a qualitative way through face extrusion. The analyses indicate that anisotropy favours a slightly decreased face extrusion when the face core behaves primarily elastic (good geotechnical conditions or increased face pressure)

and an increased face extrusion when the face core behaves primarily plastic (bad geotechnical condition and reduced face pressure). Overall, stress induced anisotropy has only secondary effects, with face stability conditions governed by the strength of the soil and the applied face pressure.

With respect to the analyzed strip foundation, results indicate that an unsaturated soil profile favours an increased "bearing capacity", mainly attributed to the transition of the footing's failure mechanism from an undrained failure mode, associated with a swallow unsaturated zone, towards a punching type of failure as the depth of the water table increases. Additionally, the analyses demonstrated the potential of a water table rise to produce excessive settlement to a footing under a working load as a consequence of volumetric collapse of the foundation ground.

# Chapter 11

# Conclusions

The present thesis presented and evaluated an advanced critical state constitutive model for anisotropic and unsaturated, non-expansive soils. The proposed constitutive behavioural framework was established on existing constitutive ideas, combined and enhanced to end up with novel constitutive relations which: a) improve the modelling capabilities and thus the accuracy of the simulation; b) minimize the constitutive parameters and; c) simplify the mathematical formulation with an eye towards efficiency and robustness of the proposed numerical framework.

## 11.1 Summary of Main Points

The proposed constitutive model builds on the principles of Theory of Soil Plasticity suitably modified to accommodate unsaturated behavioural characteristics. It accounts for the effect of stress induced anisotropy and partial saturation in soil behaviour. In doing so, the anisotropic constitutive model proposed by Kavvadas (1982) was used as a reference. Its flow rule was simplified and the hardening rule enhanced, prior to introducing the unsaturated principles of the Barcelona Basic Model (Alonso et al. 1990) (i.e., a Loading - Collapse constitutive surface), suitably modified for Bishop's stress applications, based on an extension of the Belokas & Kavvadas (2011) intrinsic compressibility framework for unsaturated material states developed within the present thesis.

The proposed constitutive model tries to accommodate most of the mechanical aspects of both anisotropic and unsaturated soils, within a simple and robust mathematical framework. It includes a total of fifteen (15) parameters. It can reduce to

either an anisotropic model for saturated soils or to an isotropic model for unsaturated soils. Under both circumstances eleven (11) parameters are required. All parameters hold a strong physical background, while most of them can be directly calibrated from experimental results, with only two demanding trial and error simulations. In the lack of available experimental data, the total number of parameters in all cases can be further reduced by two, through reasonable assumptions. Finally the model reduces to the Modified Cam Clay constitutive model upon saturation for isotropic material states.

The main characteristics of the developed model are:

- It incorporates the anisotropic, distorted elliptical yield surface proposed by Kavvadas (1982) to account for the yield locus of anisotropically consolidated soils.

- Plastic strains are described by means of a non-associated flow rule, defined through a plastic potential surface with a similar shape but different orientation, with respect to the yield surface. The proposed flow rule can be calibrated to account for the desired plastic dilation in radial stress paths (with emphasis on $1D$ compression) and further enhances the control over the position of the critical state line in the void ratio – mean effective stress plane.

- It incorporates a new hardening rule consisting of three different parts:

  a) an isotropic part based on the Intrinsic Compressibility Framework proposed by Belokas & Kavvadas (2010), which in combination with the kinematic part of the rule describes the dependence of the virgin compression lines on the level of stress induced anisotropy;

  b) the kinematic hardening rule of Kavvadas (1982) to describe the evolution of the orientation of the yield surface with plastic straining, and;

  c) a kinematic hardening rule module, which describes a progressive loss of the soil's memory of anisotropy (de-orientation of the material fabric) with the onset of plastic strain.

- The extension of the constitutive model in the unsaturated regime through Bishop's average skeleton stress, using the macrostructural (effective) degree of saturation as a scaling parameter;

- It includes a Loading – Collapse (LC) surface, derived from a new compressibility framework. The latter describes a double dependence of the unsaturated compressibility on suction and effective degree of saturation.

The proposed constitutive model was implemented in an incremental driver, which solves the constitutive equations using an explicit integration scheme (non-adaptive). The developed incremental driver was utilized to simulate common laboratory stress paths at a single material point, but also to implement the model in the Finite Element Method computer code Simulia Abaqus as a user defined material, to facilitate the solution of boundary-value problems. To allow for unsaturated simulations, the developed code for single material point testing incorporates a simple hydromechanical coupling based on the Gallipoli et al. (2003) water retention model.

To evaluate the constitutive model the following three steps where undertaken:

1) A parametric study was performed with an eye towards: a) validating the model predictions against the underlying mechanical framework; b) a qualitative comparison of the model's predictions against common experimental observations; c) investigating the effect of various model parameters, and; d) comparing the simulation results derived with the single material point algorithm with the results of finite element analyses, both concerning simple common laboratory stress paths in order to validate the proposed numerical tools.

2) Calibration and evaluation against available experimental data. Laboratory measurements from three individual experimental studies were used (Gens (1982), Casini (2008) and Barrera (2002)), carefully selected to allow for the evaluation of the entire range of the model's simulation capabilities.

3) Study of two common engineering problems, by means of Finite Element Analyses. The first application is related to the anisotropic features of the model and deals with face stability of an EPB excavated tunnel, while the second study focuses on the effect of partial saturation on the response of a vertically loaded shallow strip foundation.

In general, the proposed constitutive model and the developed numerical tools where found to provide sound results, in accordance with the exhibited experimental behaviour of anisotropically consolidated and partially saturated soils. In more detail, note that:

- The proposed constitutive model can efficiently describe the evolution of the intrinsic compression curves with evolving stress induced anisotropy. Distinct compression curves are precisely reproduced in line with the proposed compressibility framework, while the hardening rule's parameter $\psi$ can sufficiently accommodate different rates of anisotropy evolution, with suggested values in the order of $\psi = 20$ to 40. Calibrating the compressibility framework under $K_0$ conditions proves sufficient in representing the soil behaviour under different stress ratios, without prior knowledge of the corresponding behaviour. This is of significant importance in practical application as the behaviour under $K_0$ conditions is usually available (i.e., oedometer testing).

- The proposed kinematic hardening rule module, succeeds in describing a strain softening response together with a unique critical state independent of the initial anisotropy and the stress path followed, as the outcome of an anisotropy degradation mechanism associated with the onset of plastic deviatoric strain. The incorporated material constant $\zeta_q^p$ efficiently controls the intensity of the described anisotropy degradation, ranging from $\zeta_q^p = 20$ to 50. By properly selecting parameters $\psi$ and $\zeta_q^p$, the model can simultaneously simulate a strain softening response during undrained triaxial loading and a continuous strain hardening response during drained triaxial loading.

- The incorporated flow rule can successfully represent the accumulation of plastic strains during both radial compression and drained triaxial compression tests, provided that parameter $\chi$, controlling the relative orientation of the plastic potential envelope with respect to the yield surface, has been properly calibrated. It accounts for increasing dilatancy with increasing anisotropy.

- The proposed model reproduces a nonlinear increase of the post-yield compressibility with suction along with an increasing elastic domain, reflecting the beneficial effect of partial saturation in strengthening and stiffening soil response, in agreement with the proposed framework and common experimental observations.

- During constant suction compression tests, the model adequately represents a constantly increasing compressibility following the increasing degree of saturation; it results in convex compression lines in the net stress domain and thus reproduces a maximum in the volume reduction (maximum of collapse) during

wetting. The collapse potential depends on both the applied suction and the level of applied net stress in line with common experimental observations.

- The model succeeds in reproducing a nonlinear increase in shear strength with suction, as an outcome of Bishop's stress formulation. Its evolution follows the nonlinearity of the $s \cdot S_r^e$ term, while the beneficial effect of suction in shear strength becomes less profound as the confining stress increases. Moreover, it reproduces unique critical state conditions in terms of Bishop's stress and suction dependant in terms of net stress, with partial saturation favouring an increased void ratio (at critical state).

- Regarding the combined effects of partial saturation and anisotropy, it should be emphasized that: a) partial saturation results to a decrease in the rate of anisotropy evolution, b) any radial stress path imposed in terms of net stress corresponds to a smaller stress ratio in terms of Bishop's stress, and c) the model predicts a decreasing coefficient of lateral earth pressure at rest with an increase in suction.

- The developed numerical tools proved robust and capable of efficiently handling complicated numerical analyses, within a reasonable computational time. It is emphasized that the incorporated non-associated flow rule, leads to strong unsymmetrical Jacobian(s).

- Regarding the application of the model in analyses of large boundary-value problems, the model proved capable of representing the main effects of stress induced anisotropy and partial saturation in the behaviour of a supported tunnel face and a shallow strip foundation. Tunnelling analyses, which focused on the effects of stress induced anisotropy on face stability, indicate that anisotropy favours a slightly decreased face extrusion when the face core behaves primarily elastic (good geotechnical conditions or increased face pressure) and an increased face extrusion when the face core behaves primarily plastic (bad geotechnical condition and reduced face pressure). Overall though, stress induced anisotropy has only secondary effects, with face stability conditions governed by the soil strength and the applied face pressure. With respect to the analyzed strip foundation, results indicate that an unsaturated soil profile favours an increased "bearing capacity", mainly attributed to the transition of the footing's failure

mechanism from an undrained failure mode, associated with a swallow unsaturated zone, towards a punching type of failure as the depth of the water table increases, while additionally it was demonstrated that a potential rise of the water table may lead to excessive settlements as a result of volumetric collapse.

## 11.2 Recommendations for Future Research

Future research can focus on three different directions, namely: a) improving the model's predictions; b) enhancing the numerical implementation in the Simulia Abaqus and; c) applying the proposed constitutive model in the analyses of complex engineering problems.

An improvement of the model's simulation capabilities can be facilitated by addressing its main simulation shortcomings, focusing on:

a) modifying the Kavvadas (1982) hardening rule towards an increased versatility, for the orientation of the yield surface during radial stress paths. Attention needs to focus in reducing the model's tendency to over-predict the peak strength of anisotropically consolidated soil samples, as this was identified during the calibration exercise performed on the experimental results of Gens (1982). The analyses indicate that the orientation of the yield surface during anisotropic consolidation should be bounded to a smaller inclination with respect to the stress ratio of the imposed consolidation stress path, for a more accurate prediction of the stress - strain response during subsequent triaxial loading. Such a limitation in the rotation can be achieved by including a proper stress attractor in the definition of the hardening rule. In the present model's edition, an accurate representation of the peak strength is realized through proper calibration;

b) reducing the elastic domain to improve the simulations regarding highly overconsolidated soils (on the "dry side"), as they lack in precision compared to their normally consolidated (on the "wet side") counterparts. Hence, the behavioural framework needs to account for the Bounding Surface Soil Plasticity principles, where the elastic states are enclosed within the Plastic Yield Envelope (PYE) which in turn lies within the Structure Strength Envelope (SSE) facilitating all possible elastoplastic states. Bounding surface plasticity requires a proper mapping rule to account for the evolution of the Plastic Modulus ($H$) for material states on the PYE and inside the SSE. In that respect, the advanced mapping

rule of Kalos (2014) can be extended for non-isotropic models following the Belokas & Kavvadas (2010) model;

c) modifying the flow rule in order to better accommodate the increase in dilatancy with increasing suction, typically observed in laboratory results. A possible improvement towards this direction may stem from the inclusion of a direct dependance of the plastic potential function on the state of partial saturation.

Improvement of the developed numerical tools can potentially involve the following actions:

a) Incorporating in the Simulia Abaqus code of a void ratio dependant water retention model. The existing Simulia Abaqus editions do not provide such a module, a severe drawback, which hinders the proposed model's unsaturated features and especially the constantly evolving post yield compressibility and the model's representation of a maximum of collapse. Unfortunately, the code does not allow for a user defined water retention model and thus, the specific intervention requires action from the Abaqus developers.

b) Suitably modifying the UMAT environment to easily account for the analysis of unsaturated material states which should reduce the time required for convergence. Modifications need to include: a) a direct exchange of suction and degree of saturation between the main code and the UMAT (User defined MATerial) subroutine; b) incorporation of suction and degree of saturation related Jacobian(s) in the solution process and also; c) increased versatility in the selection of Bishop's stress scaling parameter (i.e., by adopting the Alonso et al. (2010) power law). It should be mentioned that similar to (a), such modifications require access to the internal Simulia Abaqus code and thus cannot be only realized by the code's developers.

c) Incorporate adaptive capabilities in the proposed integration scheme. Such an enhancement will allow for the infinitesimal strain, suction and effective degree of saturation increments involved in the solution of the constitutive equations, to be automatically adjusted to the nonlinearity of the examined problem, thus reducing the computational time. The adaptive integration schemes proposed by Sheng et al. (2003) or Karamitros (2010) hold as a possible reference in trying such an intervention. In the present version the developed numerical tools are

based on the user's selection of a relatively small infinitesimal increment for the aforementioned quantities.

Regarding any future applications of the proposed constitutive model, it can be employed in a variety of different boundary-value problems, to investigate the effect of stress induced anisotropy and partial saturation. An indicative list of suggested projects includes:

- Shallow and deep foundations: The model can be used to investigate the effect of the vadose zone on the engineering behaviour of shallow foundations, as well as on the response of piles and pile groups during vertical and lateral loading.
- Man-made and natural slopes: Slope stability is significantly affected by partial saturation mainly due to the increasing soil strength with suction. The model can be utilized in either direct assessments of slope stability and parametric studies of the water table and the water flow on slope stability or in back analyses of slope failures where neglecting the effects of partial saturation may lead to severe overestimation of the residual shear strength of the examined soil profile.
- Tunnelling: The model allows for the investigation of the effect of stress induced anisotropy and partial saturation in tunneling induced ground movements.

# Appendices

# Appendix A

# Detailed calculations related to the constitutive model formulation

## A.1 Calculating parameter $\Gamma$ (Critical State Line)

This appendix includes the analytical mathematical calculation of parameter $\Gamma$ defining the position of the critical state line in the $v-\ln p$ plane. The presented calculation is based on the following assumptions:

- A saturated stress state is examined.
- Critical state conditions correspond to an isotropic yield surface.
- Model parameters $c$, $k$ are independent of the examined deviatoric sub-plane.

According to the assumed hardening rule, yield surface at critical state is isotropic $\sqrt{\boldsymbol{b}:\boldsymbol{b}}=0$ and the plastic potential surface orientation follows equation 6.30 thus, $\sqrt{\boldsymbol{d}:\boldsymbol{d}}=0$ as well. Point A in figure A.1 represents such a material state. The corresponding stress state lies on the top of the isotropic ellipse representing the PPS as indicated by point A. For such a stress state we may write that:

$$q=\sqrt{\frac{3}{2}}(\boldsymbol{s}:\boldsymbol{s}) \tag{A.1}$$

end

$$p=\sigma=\theta \tag{A.2}$$

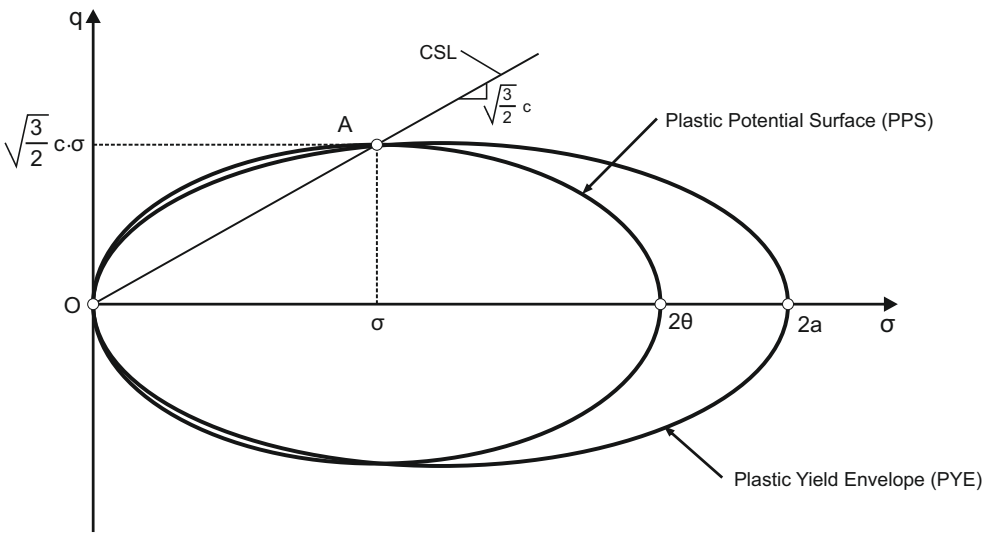


**Figure A.1:** Critical state

Substituting in equation 6.27 we derive:

$$\frac{1}{c^2}\cdot\frac{2}{3}\cdot q^2 - p(2p-p) = 0 \tag{A.3}$$

and further elaborating we calculate the corresponding stress ratio $(q/p)$ at point A, which is also equal to the slope of the critical state line in the $p-q$ plane:

$$\frac{q}{p} = \sqrt{\frac{3}{2}}c \tag{A.4}$$

Critical state is a plastic material state and thus, lies always on the yield surface. From the yield surface equation (see eq. 6.12) we can calculate the ratio $2a/p$ as follows:

$$\begin{aligned}
&\frac{1}{k^2}\cdot\frac{2}{3}\cdot q^2 - p(2\alpha - p) = 0 \Rightarrow \\
&\frac{1}{k^2}\cdot\frac{2}{3}\cdot q^2 - 2\alpha\cdot p + p^2 = 0 \Rightarrow \\
&2\alpha\cdot p = \frac{1}{k^2}\cdot\frac{2}{3}\cdot q^2 + p^2
\end{aligned} \tag{A.5}$$

Dividing both parts with $p^2 \neq 0$ we obtain:

$$\frac{2\alpha}{p} = \frac{\frac{2}{3}\left(\frac{q}{p}\right)^2}{k^2} + 1 \tag{A.6}$$

and additionally considering that at point A the stress ratio $q/p$ is given by equation A.4 we finally obtain:

$$\frac{2\alpha}{p} = \frac{\frac{2}{3}\left(\sqrt{\frac{3}{2}}c\right)^2}{k^2} + 1 \Rightarrow$$
$$\frac{2\alpha}{p} = 1 + \frac{c^2}{k^2} \tag{A.7}$$

Equation A.7 is used to calculate the specific volume corresponding to state A according to the assumed compressibility framework. According to the hardening rule (see subchapter 6.6) if an isotropic yield surface under saturated conditions is examined, the hardening variable $a$ corresponds to:

$$a = a^* = \frac{1}{2} exp\left(\frac{N_{iso} - v - \kappa \ln \sigma}{\lambda - \kappa}\right) \tag{A.8}$$

Solving for the specific volume we obtain:

$$v = N_{iso} + \kappa \ln 2a - \kappa \ln p - \lambda \ln 2a \Rightarrow$$
$$v = N_{iso} + \kappa \ln \frac{2a}{p} p - \kappa \ln p - \lambda \ln \frac{2a}{p} p \Rightarrow$$
$$v = N_{iso} + \kappa \ln \frac{2a}{p} - \lambda \ln \frac{2a}{p} - \lambda \ln p \Rightarrow$$
$$v = N_{iso} - (\lambda - \kappa) \ln \frac{2a}{p} - \lambda \ln p \tag{A.9}$$

At the same time the specific volume at point A corresponds to a point on the CSL of the material in the $v - \ln p$ plane and thus:

$$v = \Gamma - \lambda \ln p \tag{A.10}$$

Comparing equations A.9 and A.12 parameter $\Gamma$ corresponds to:

$$\Gamma = N_{iso} - (\lambda - \kappa) \ln \frac{2a}{p} \tag{A.11}$$

while finally by substituting the term $2a/p$ with expression A.7 we finally derive:

$$\Gamma = N_{iso} - (\lambda - \kappa) \ln \left(1 + \frac{c^2}{k^2}\right) \tag{A.12}$$

## A.2 Calculating parameter $\chi$ (flow rule)

This appendix presents the analytical calculation of parameter $\chi$ (see equation 6.30) defining the inclination of the plastic potential surface with respect to the inclination of the yield surface. The presented calculation is based on the assumption that experimental results from at least one anisotropic consolidation test (i.e., either radial consolidation or 1D consolidation) under saturated conditions are available. The required input, apart from the model parameters, includes: a) the stress ratio under which the test was performed, and; b) the measured total dilatancy.

In more detail, lets assume that a triaxial radial consolidation test under a constant and known stress ratio $n_q = q/p = \dot{q}/\dot{p}$ is performed. After reaching stabilized anisotropic conditions, the examined soil element will deform under a constant total dilatancy equal to $D_q = \dot{\varepsilon}_q/\dot{\varepsilon}_v$. Provided that both quantities are known, the flow rule of the constitutive model can be calibrated to reproduce this behaviour. Note that, the flow rule provides the increment of plastic deformation and thus describes the plastic dilatancy, while, the experimentally determined dilatancy additionally includes an elastic part. In that respect, we need to initially calculate the plastic dilatancy out of the measured (desired) total one to be able to calibrate the flow rule.

### A.2.1 Calculation of Plastic Dilatancy

The basic kinematic assumption enables the decomposition of any total strain increment to an elastic and a plastic component and thus, we may write that total dilation corresponds to:

$$D_q = \frac{\dot{\varepsilon}_q}{\dot{\varepsilon}_v} = \frac{\dot{\varepsilon}_q^e + \dot{\varepsilon}_q^p}{\dot{\varepsilon}_v^e + \dot{\varepsilon}_v^p} \tag{A.13}$$

Using the flow rule to substitute for the increment of the plastic strains we get:

$$D_q = \frac{\dot{\varepsilon}_q^e + \dot{\Lambda}\sqrt{\frac{2}{3}\boldsymbol{P}' : \boldsymbol{P}'}}{\dot{\varepsilon}_v^e + \dot{\Lambda}P} \tag{A.14}$$

The assumed elastic law is used to calculate the elastic strain increment as:

$$\dot{\varepsilon}_q^e = 3G\dot{q} \tag{A.15}$$

and

$$\dot{\varepsilon}_v^e = K\dot{p} \tag{A.16}$$

while dividing the two equations and solving for $\dot{\varepsilon}_q^e$ we obtain:

$$\dot{\varepsilon}_q^e = \frac{K}{3G} \cdot \frac{\dot{q}}{\dot{p}} \cdot \dot{\varepsilon}_v^e \tag{A.17}$$

Equation 6.8 can be used to substitute the term $K/3G$ with Poisson's ratio to obtain:

$$\dot{\varepsilon}_q^e = \frac{2(1+\nu)}{9\,(1-2\nu)} \cdot \frac{\dot{q}}{\dot{p}} \cdot \dot{\varepsilon}_v^e \tag{A.18}$$

The elastic volumetric strains are calculated according to the porous-elastic behaviour as:

$$\dot{\varepsilon}_v^e = \frac{\kappa}{v \cdot p}\dot{p} \tag{A.19}$$

Considering that the computed stress increment represents a normally consolidated stress state under stabilized anisotropic conditions, the stress state lies constantly at the tip of the yield surface. For that case, an increment of the isotropic stress is equal to the isotropic enlargement of the yield surface and thus we may write:

$$\dot{p} = 2\dot{\alpha} \tag{A.20}$$

and

$$p = 2\alpha \tag{A.21}$$

enabling the calculation of the elastic volumetric increment as:

$$\dot{\varepsilon}_v^e = \frac{\kappa}{v}\frac{\dot{\alpha}}{\alpha} \tag{A.22}$$

Moreover, when a radial stress path is imposed and the orientation of the yield surface has adjusted to the imposed stress path $b_q = n_q = \dot{q}/\dot{p}$ the kinematic part of the employed hardening rule deactivated ($\dot{\boldsymbol{b}} = \mathbf{0} \Rightarrow \dot{A} = 0$). Under established anisotropic conditions, the isotropic part of the hardening rule (eq. 6.40) reduces to:

$$\dot{a} = A\dot{a^*} \tag{A.23}$$

Additionally considering that $\alpha = A \cdot \alpha^*$, the elastic volumetric increment can be computed as:

$$\dot{\varepsilon}_v^e = \frac{\kappa}{v}\frac{\dot{\alpha}^*}{\alpha^*} \tag{A.24}$$

while finally employing equation 6.43 we obtain:

$$\dot{\varepsilon}_v^e = \frac{\kappa}{\lambda - \kappa}\dot{\Lambda} P \tag{A.25}$$

for the elastic volumetric strain increment, allowing to further elaborate equation A.18 as:

$$\dot{\varepsilon}_q^e = \frac{2(1+\nu)}{9\,(1-2\nu)} \cdot \frac{\dot{q}}{\dot{p}} \cdot \frac{\kappa}{\lambda - \kappa}\dot{\Lambda} P \tag{A.26}$$

to derive the elastic deviatoric strain increment as well.

Equations A.25 and A.26 facilitate the calculation of the total dilatancy (eq. A.14), as:

$$D_q = \frac{\frac{2(1+\nu)}{9(1-2\nu)} \cdot \frac{\dot{q}}{\dot{p}} \cdot \frac{\kappa}{\lambda-\kappa}\dot{\Lambda} P + \dot{\Lambda}\sqrt{\frac{2}{3}\boldsymbol{P}' : \boldsymbol{P}'}}{\frac{\kappa}{\lambda-\kappa}\dot{\Lambda} P + \dot{\Lambda} P} \tag{A.27}$$

According to the flow rule definition, the reproduced plastic dilatancy corresponds to:

$$d_q^p = \frac{\dot{\varepsilon}_q^p}{\dot{\varepsilon}^p} = \frac{\sqrt{\frac{2}{3}\dot{\boldsymbol{e}}^p : \dot{\boldsymbol{e}}^p}}{\dot{\varepsilon}^p} = \frac{\sqrt{\frac{2}{3}\boldsymbol{P}' : \boldsymbol{P}'}}{P} \tag{A.28}$$

Equation A.28, is used in the denominator of eq. A.30 to substitute term $\sqrt{\frac{2}{3}\boldsymbol{P}' : \boldsymbol{P}'}$ obtaining:

$$D_q = \frac{\frac{2(1+\nu)}{9(1-2\nu)} \cdot \frac{\dot{q}}{\dot{p}} \cdot \frac{\kappa}{\lambda-\kappa}\dot{\Lambda} P + d_q^p \cdot \dot{\Lambda} P}{\frac{\kappa}{\lambda-\kappa}\dot{\Lambda} P + \dot{\Lambda} P} \tag{A.29}$$

where the term $\dot{\Lambda} P$ is eliminated to result with:

$$D_q = \frac{\frac{2(1+\nu)}{9(1-2\nu)} \cdot \frac{\dot{q}}{\dot{p}} \cdot \frac{\kappa}{\lambda-\kappa} + d_q^p}{\frac{\kappa}{\lambda-\kappa} + 1} \tag{A.30}$$

Solving for plastic dilation $d_q^p$ we obtain:

$$d_q^p = D_q\left(\frac{\kappa}{\lambda - \kappa} + 1\right) - \frac{2}{9} \cdot \frac{1+\nu}{1-2\nu} \cdot \frac{\kappa}{\lambda - \kappa} \cdot \frac{\dot{q}}{\dot{p}} \tag{A.31}$$

where additionally considering that $n_q = b_q = q/p = \dot{q}/\dot{p}$ plastic dilation is finally

computed as:

$$d_q^p = D_q \left( \frac{\kappa}{\lambda - \kappa} + 1 \right) - \frac{2}{9} \cdot \frac{1+\nu}{1-2\nu} \cdot \frac{\kappa}{\lambda - \kappa} \cdot b_q \tag{A.32}$$

### A.2.2 Orientation of the Plastic Potential Surface (PPS)

Provided that the desired plastic dilatancy has been computed (eq. A.32), the flow rule is now adjusted to reproduce the same plastic dilatancy. Starting with the definition of the plastic dilatancy (eq. A.28), we may substitute the isotropic ($P$) and the deviatoric ($\boldsymbol{P}^{'}$) component of the plastic potential tensor with equations 6.29a and 6.29b respectively. The obtained expressions correlate the orientation of the plastic potential surface with plastic dilatancy as:

$$d_q^p = \frac{\sqrt{\frac{2}{3}\frac{4}{c^4}(\boldsymbol{s} - \sigma \boldsymbol{d}) : (\boldsymbol{s} - \sigma \boldsymbol{d})}}{2(\sigma - \theta) - \frac{2}{c^2}\boldsymbol{d} : (\boldsymbol{s} - \sigma \boldsymbol{d})} \tag{A.33}$$

Further considering that the examined case corresponds to a radial stress path under stabilized yield surface orientation, the stress state $(\sigma, \boldsymbol{s})$ is located at the tip of an inclined yield surface where the deviatoric stress tensor corresponds to:

$$\boldsymbol{s} = \sigma \boldsymbol{b} \tag{A.34}$$

Simultaneously, the orientation of the plastic potential surface follows the yield surface orientation through:

$$\boldsymbol{d} = \chi \boldsymbol{b} \tag{A.35}$$

where $\chi$ the unknown parameter, trying to calculate. Incorporating equations A.34 and A.35 in eq. A.33, after some algebra we can calculate the plastic dilatancy according to:

$$d_q^p = \frac{\frac{2}{c^2} \cdot \sigma(1-\chi) \cdot \sqrt{\frac{2}{3}\boldsymbol{b} : \boldsymbol{b}}}{2(\sigma - \theta) - \frac{2}{c^2} \cdot \sigma \cdot \chi \cdot (1-\chi)\boldsymbol{b} : \boldsymbol{b}} \tag{A.36}$$

while dividing both the numerator and the denominator with $\sigma > 0$ we obtain:

$$d_q^p = \frac{\frac{2}{c^2} \cdot (1-\chi) \cdot \sqrt{\frac{2}{3}\boldsymbol{b} : \boldsymbol{b}}}{2(1 - \frac{\theta}{\sigma}) - \frac{2}{c^2} \cdot \chi \cdot (1-\chi)\boldsymbol{b} : \boldsymbol{b}} \tag{A.37}$$

The term $\theta/\sigma$ can be calculated through the equation of the plastic potential surface (eq. 6.27) as:

$$g(\sigma, \boldsymbol{s}, \theta, \boldsymbol{d}) = \frac{1}{c^2}(\boldsymbol{s} - \sigma\boldsymbol{d}) : (\boldsymbol{s} - \sigma\boldsymbol{d}) - \sigma(2\theta - \sigma) = 0 \Rightarrow$$
$$\sigma(2\theta - \sigma) = \frac{1}{c^2}(\boldsymbol{s} - \sigma\boldsymbol{d}) : (\boldsymbol{s} - \sigma\boldsymbol{d})$$

where once again incorporating equations A.34 and A.35 we obtain:

$$\sigma(2\theta - \sigma) = \frac{1}{c^2} \cdot \sigma^2 \cdot (1 - \chi)^2 \boldsymbol{b} : \boldsymbol{b}$$

while finally dividing both parts with $\sigma^2 > 0$ we obtain:

$$(2\frac{\theta}{\sigma} - 1) = \frac{1}{c^2} \cdot (1 - \chi)^2 \boldsymbol{b} : \boldsymbol{b} \Rightarrow$$
$$\frac{\theta}{\sigma} = \frac{1}{2} + \frac{1}{2} \cdot \frac{1}{c^2} \cdot (1 - \chi)^2 \boldsymbol{b} : \boldsymbol{b} \tag{A.38}$$

Equation A.38 is used to substitute the term $\theta/\sigma$ in eq. A.37:

$$d_q^p = \frac{\frac{2}{c^2} \cdot (1 - \chi) \cdot \sqrt{\frac{2}{3}\boldsymbol{b} : \boldsymbol{b}}}{1 - \frac{1}{c^2} \cdot (1 - \chi)^2 \boldsymbol{b} : \boldsymbol{b} - \frac{2}{c^2} \cdot \chi \cdot (1 - \chi)\boldsymbol{b} : \boldsymbol{b}} \tag{A.39}$$

while multiplying both the nominator and the denominator with $c^2$ we have:

$$d_q^p = \frac{2 \cdot (1 - \chi) \cdot \sqrt{\frac{2}{3}\boldsymbol{b} : \boldsymbol{b}}}{c^2 - (1 - \chi)^2 \boldsymbol{b} : \boldsymbol{b} - 2 \cdot \chi \cdot (1 - \chi)\boldsymbol{b} : \boldsymbol{b}} \tag{A.40}$$

At the same time the deviatoric measure of the anisotropy tensor is:

$$b_q = \sqrt{\frac{3}{2}\boldsymbol{b} : \boldsymbol{b}} \Rightarrow \boldsymbol{b} : \boldsymbol{b} = \frac{2}{3}(b_q)^2$$

allowing as to substitute the inner product $\boldsymbol{b} : \boldsymbol{b}$ in equation A.40 with the imposed (stabilized anisotropic fabric is assumed) stress ratio $b_q$, to end up with:

$$d_q^p = \frac{\frac{4}{3} \cdot (1 - \chi) \cdot b_q}{c^2 - \frac{2}{3}(1 - \chi)^2 \cdot (b_q)^2 - \frac{4}{3} \cdot \chi \cdot (1 - \chi)(b_q)^2} \tag{A.41}$$

Equation A.41 can be further reordered to derive the following quadratic equation of

the unknown quantity $\chi$:

$$\left(\frac{2}{3}(b_q)^2 d_q^p\right)\chi^2 + \left(\frac{4}{3}b_q\right)\chi + \left(c^2 d_q^p - \frac{2}{3}(b_q)^2 d_q^p - \frac{4}{3}b_q\right) = 0 \tag{A.42}$$

# Appendix B

# The transformed space of stresses and strains

## B.1 The transformed stress space (TSS)

$$\sigma = \frac{\sigma_x + \sigma_y + \sigma_z}{3} \tag{B.1}$$

$$\boldsymbol{s} = \{S_1, S_2, S_3, S_4, S_5\} \tag{B.2}$$

$$S_1 = \frac{2\sigma_y - \sigma_x - \sigma_z}{\sqrt{6}} \tag{B.3}$$

$$S_2 = \frac{\sigma_z - \sigma_x}{\sqrt{2}} \tag{B.4}$$

$$S_3 = \sigma_{xy} \cdot \sqrt{2} \tag{B.5}$$

$$S_4 = \sigma_{xz} \cdot \sqrt{2} \tag{B.6}$$

$$S_5 = \sigma_{yz} \cdot \sqrt{2} \tag{B.7}$$

## B.2 The corresponding energy conjugate strains

$$\varepsilon = \varepsilon_x + \varepsilon_y + \varepsilon_z \tag{B.8}$$

$$\boldsymbol{\varepsilon} = \{E_1, E_2, E_3, E_4, E_5\} \tag{B.9}$$

$$E_1 = \frac{2\varepsilon_y - \varepsilon_x - \varepsilon_z}{\sqrt{6}} \tag{B.10}$$

$$E_2 = \frac{\varepsilon_z - \varepsilon_x}{\sqrt{2}} \tag{B.11}$$

$$E_3 = \frac{\gamma_{xy}}{\sqrt{2}} \text{ or } \varepsilon_{xy} \cdot \sqrt{2} \tag{B.12}$$

$$E_4 = \frac{\gamma_{xz}}{\sqrt{2}} \text{ or } \varepsilon_{xz} \cdot \sqrt{2} \tag{B.13}$$

$$E_5 = \frac{\gamma_{yz}}{\sqrt{2}} \text{ or } \varepsilon_{yz} \cdot \sqrt{2} \tag{B.14}$$

## B.3 The anisotropy tensor

$$\boldsymbol{b} = \{b_1, b_2, b_3, b_4, b_5\} \tag{B.15}$$

$$S_1 = \frac{2b_y - b_x - b_z}{\sqrt{6}} \tag{B.16}$$

$$S_2 = \frac{b_z - b_x}{\sqrt{2}} \tag{B.17}$$

$$S_3 = b_{xy} \cdot \sqrt{2} \tag{B.18}$$

$$S_4 = b_{xz} \cdot \sqrt{2} \tag{B.19}$$

$$S_5 = b_{yz} \cdot \sqrt{2} \tag{B.20}$$

# Appendix C

# Implementation of "unsaturated" capabilities in the Single Material Point testing code

This appendix presents the main mathematical calculations associated with the enchantment of the Single Material Point (SMP) testing code (see chapter 7) to enable simulations under unsaturated material states.

## C.1 Drained unsaturated simulations

As discussed in chapter 7, the developed SMP testing code can impose either constant suction tests or varying suction tests (i.e., wetting, drying). In saturated soil mechanics, it is common to correlate a drained test with a constant pore water pressure test. Nevertheless, fundamentally the term drained accommodates any test where water can be either expelled or absorbed from a soil specimen undergoing loading. In that respect, when it comes to unsaturated soil states, constant suction tests as well as drying and wetting test are drained tests.

Analysis under unsaturated conditions necessitates knowledge of the water retention characteristics of the examined soil. It is reminded that suction is the only external variable which can be arbitrarily controlled and imposed to any given problem, while degree of saturation is an outcome of the water retention characteristics of the soil. In that end, in the developed SMP analysis numerical tool, suction is handled as a user input while to calculate degree of saturation, the Gallipoli et al.

(2003) Water Retention Model (WRM) is incorporated.

The Gallipoli et al. (2003) WRM was presented in subchapter 4.2.2.4. It is reminded that it is a modified Van Genuchten model with void ratio dependance, described by the following expression:

$$S_r = \frac{1}{\left[1 + \left(\left(\phi(v-1)^{\psi}\right) s\right)^n\right]^m} \tag{C.1}$$

where $\phi$, $\psi$, $n$ and $m$ material constants and $v$ the current specific volume.

Equation C.1 provides the degree of saturation $S_r$, under any given suction level ($s$) and specific volume value ($v$). Furthermore, differentiating equation C.1 we obtain the increment of degree of saturation ($\dot{S}_r^e$) corresponding to any given suction increments ($\dot{s}$) and volumetric stain ($\dot{\varepsilon}$) increment. In detail, $\dot{S}_r^e$ is calculated as:

$$\dot{S}_r = \frac{\partial S_r}{\partial s}\dot{s} + \frac{\partial S_r}{\partial v}(-v)\dot{\varepsilon} \tag{C.2}$$

where:

$$\frac{\partial S_r}{\partial s} = \frac{-nmS_r}{1 + \left[\phi(v-1)^{\psi} s\right]^n}\left[\phi(v-1)^{\psi}\right]^n s^{n-1} \tag{C.3}$$

and

$$\frac{\partial S_r}{\partial v} = \frac{-nm\psi(\phi s)^n S_r}{1 + \left[\phi(v-1)^{\psi} s\right]^n}(v-1)^{\psi n-1} \tag{C.4}$$

Effective degree of saturation is calculated through equation 6.4, while the corresponding increment of the effective degree of saturation is calculated as:

$$\dot{S}_r^e = \frac{\partial S_r^e}{\partial S_r}\dot{S}_r = a(S_r)^{a-1}\dot{S}_r \tag{C.5}$$

where $a$ the scaling parameter used in the power law of Alonso et al. (2010). Equations C.2 and C.5 are used in the developed numerical tool whenever a drained unsaturated test is performed. We should mention that even during constant suction tests, effective degree of saturation changes due to its dependance on specific volume.

## C.2 Undrained unsaturated simulations

Regarding undrained testing, it is well know that under saturated conditions an undrained test corresponds to a constant volume test[1], facilitating simplified sim-

[1] Water is assumed incompressible.

ulations where $\dot{\varepsilon} = 0$ is imposed, with the developed algorithm following such an approach. To extend undrained testing for unsaturated soil conditions we need to consider that fundamentally, an undrained test is not a constant volume test but instead it is a constant water content test. No water can flow either outwards or inwards the soil pores and as a result both suction and degree of saturation evolve following the volumetric deformation of the material. In that respect, to enable calculations we shall consider that the only constant quantity during an undrained test is the gravimetric water content ($\dot{w} = 0$).

This latter allows us to take advantage of the fundamental relationship of soil mechanics connecting degree of saturation with the gravimetric water content and the specific volume:

$$S_r = \frac{w \cdot G_s}{v - 1} \tag{C.6}$$

where $G_s$ the specific gravity of the solid soil phase. Differentiating with respect to the specific volume we may calculate the evolution of degree of saturation ($\dot{S}_r$) in any soil system subjected to a volumetric strain increment $\dot{\varepsilon}$ as:

$$\dot{S}_r = -S_r \cdot \frac{1}{v - 1} \cdot \dot{v} = S_r \cdot \frac{v}{v - 1} \cdot \dot{\varepsilon} \tag{C.7}$$

With the increment of degree of saturation calculated, the WRM is utilized to calculate the corresponding suction increment ($\dot{s}$). Towards that direction, equation C.1 is solved for suction to obtain:

$$s = \frac{1}{\phi(v - 1)^{\psi}} \cdot ({S_r}^{-\frac{1}{m}} - 1)^{1/n} \tag{C.8}$$

We observe that suction evolves following the evolution of degree of saturation and the evolving water retention curve due to volumetric straining as well. Equation C.8 is rewritten as:

$$s = f(v) \cdot g(S_r) \tag{C.9}$$

and utilizing the chain rule we finally obtain:

$$\dot{s} = -g(S_r) \cdot \frac{\partial f(v)}{\partial v} \cdot v \cdot \dot{\varepsilon} + f(v) \cdot \frac{\partial g(S_r)}{\partial S_r} \cdot \dot{S}_r \tag{C.10}$$

where:

$$f(v) = \frac{1}{\phi(v-1)^{\psi}} \tag{C.11a}$$

$$g(S_r) = \left(S_r^{-\frac{1}{m}} - 1\right)^{1/n} \tag{C.11b}$$

$$\frac{\partial f(v)}{\partial v} = -\frac{\phi\psi}{\sqrt{\phi(v-1)^{\psi}}} \cdot (v-1)^{(\psi-1)} \tag{C.11c}$$

$$\frac{\partial g(S_r)}{\partial S_r} = -\frac{1}{n \cdot m} \cdot g(S_r)^{(1-n)} \cdot S_r^{\left(-\frac{1}{m}-1\right)} \tag{C.11d}$$

Summarizing when an undrained test is performed beginning from a known unsaturated soil state, equations C.7 and C.10 are used to define the corresponding degree of saturation and suction increments to be imposed simultaneously with the strain increment in the main incremental driver.

# Appendix D

# The PROPS, STATEV and PREDEF arrays (Simulia Abaqus UMAT subroutine)

The present appendix contains information about the user specified arrays PROPS (material constants), STATEV (solution dependant variables) and DPRED (predefined field variables), related to the Abaqus UMAT subroutine of the proposed model. It is taken for granted that the potential user is familiar with the UMAT subroutine in Simulia Abaqus.

## D.1 The PROPS array (material constants)

PROPS is the user-specified array of material constants associated with the user defined material. Its dimension is defined by the NPROPS value. In the proposed model, the number of the required material constants (NPROPS) depends on the dimension of the stress tensor NTENS, through:

$$NPROPS = 17 + 2 * NTENS \tag{D.1}$$

Thus:

- for **axis - symmetric** or **2D** models $NTENS = 4 \Rightarrow NPROPS = 25$, while;
- for **3D** models $NTENS = 6 \Rightarrow NPROPS = 29$

The following table presents the correspondence between the $PROPS(i)$ array components and the proposed model's material constants. The full array of the 29 parameters necessary for a 3D problem are presented. For axis-symmetric and 2D models the four lines in gray are omitted (any following lines are shifted upwards) resulting with 25 parameters. Parameters *beta* and $p^c$ follow the stress dimensioning selected for the simulation (i.e., Pascal), while the rest of them are dimensionless.

| **PROPS(i)** | **constant** | **Short description** |
|---|---|---|
| 1 | 2 | related to the incremental driver; always 2 for ABAQUS STD |
| 2 | 5 | related to the incremental driver; always 5 for ABAQUS STD |
| 3 | $2G/K$ | elasticity |
| 4 | $\lambda$ | slope of the virgin compression lines under saturated conditions |
| 5 | $\kappa$ | slope of the swelling lines |
| 6 | $\beta$ | unsaturated compressibility |
| 7 | $r$ | unsaturated compressibility |
| 8 | $\gamma$ | unsaturated compressibility |
| 9 | $p^c$ | unsaturated compressibility |
| 10 | $N_{iso}$ | position of the isotropic NCL |
| 11 | $\Gamma$ | position of the CSL |
| 12 | $r_s$ | compressibility framework; defines relative position of Anisotropic NCLs |
| 13 | $\chi$ | flow rule |
| 14 | $\psi$ | hardening rule |
| 15 | 0 | standby parameter; assign a zero value |
| 16 | $\zeta_q^p$ | hardening rule |
| 17 | $k1$ | YS aspect ratio; 1st deviatoric plane of the Transformed Stress Space (TSS) |
| 18 | $k2$ | YS aspect ratio; 2nd deviatoric plane of the TSS |
| 19 | $k3$ | YS aspect ratio; 3rd deviatoric plane of the TSS |
| 20 | $k4$ | YS aspect ratio; 4th deviatoric plane of the TSS |
| 21 | $k5$ | YS aspect ratio; 5th deviatoric plane of the TSS |
| 22 | $c1$ | PPS aspect ratio; 1st deviatoric plane of the TSS |

| PROPS(i) | constant | Short description |
|---|---|---|
| 23 | $c2$ | PPS aspect ratio; 2nd deviatoric plane of the TSS |
| 24 | $c3$ | PPS aspect ratio; 3rd deviatoric plane of the TSS |
| 25 | $c4$ | PPS aspect ratio; 4th deviatoric plane of the TSS |
| 26 | $c5$ | PPS aspect ratio; 5th deviatoric plane of the TSS |
| 27 | $DLIMIT$ | maximum infinitesimal strain increment; suggested value: $10^{-6}$ |
| 28 | $DLIMSUC$ | maximum infinitesimal suction increment; suggested value: $10^{-3}$ |
| 29 | $DLIMSR$ | maximum infinitesimal degree of saturation increment; suggested value: $10^{-3}$ |

**Attention**: The optional parameter **UNSYMM** must be included in the *USER MATERIAL command to store the full unsymmetric Jacobian deriving from the non-associated flow rule of the proposed constitutive model.

## D.2 The STATEV array (solution dependant variables)

STATEV is the user-specified array of the solution dependant variables associated with the user defined material. Its dimension is defined by the NSTATV value. In the proposed model, the number of the required solution - dependant variable (NSTATV) depends on the dimension of the stress tensor NTENS, through:

$$NSTATV = 4 + NTENS \tag{D.2}$$

Thus:

- for **axis - symmetrical** or **2D** models $NTENS = 4 \Rightarrow NSTATV = 8$, while;
- for **3D** models $NTENS = 6 \Rightarrow NSTATV = 10$

The following table presents the correspondence between the $STATEV(i)$ array components and the solution dependent variables of the developed UMAT. The 10 solution dependant variables necessary in a 3D problem are presented. For axis-symmetric and 2D models the two lines in gray are omitted resulting with 8 variables.

The isotropic hardening variable $\alpha$ follows the stress dimensioning selected for the simulation (i.e., Pascal), while the rest of them are dimensionless.

| **STATEV(i)** | **variable** | **Short description** |
|---|---|---|
| 1 | $\alpha$ | isotropic hardening variable |
| 2 | $NSURF$ | flag identifier; $NSURF = 0.0$ elastic state/ $NSURF =$ 1.0 plastic state |
| 3 | $v$ | specific volume |
| 4 | $\varepsilon_v^p$ | accumulated plastic volumetric strains |
| 5 | $\varepsilon_q^p$ | accumulated plastic deviatoric strains |
| 6 | $b1$ | anisotropy tensor; 1st deviatoric plane of the TSS |
| 7 | $b2$ | anisotropy tensor; 2nd deviatoric plane of theTSS |
| 8 | $b3$ | anisotropy tensor; 3rd deviatoric plane of the TSS |
| 9 | $b4$ | anisotropy tensor; 4th deviatoric plane of the TSS |
| 10 | $b5$ | anisotropy tensor; 5th deviatoric plane of the TSS |

## D.3 The PREDEF array (predefined field variables)

PREDEF is the user-specified array of the predefined field variables associated with the user material. The proposed model utilizes two field variables, given in the following table.

| **PREDEF(i)** | **variable** | **Short description** |
|---|---|---|
| 1 | $U_w$ | pore water pressure |
| 2 | $S_r$ | degree of saturation |

# Appendix E

# Calculation of initial conditions for ABAQUS applications

The scope of this appendix is to familiarize the potential user with the proper calculation and assignment of initial conditions with respect to the analyses of boundary value problems with the Simulia Abaqus FEM code in conjunction with the proposed constitutive model. Emphasis is given on the proper calculation of: a) the initial values for the anisotropy tensor's components and; b) consistent initial stress field and solution dependant variables under geostatic conditions.

## E.1 Initial Anisotropy Tensor

The anisotropy tensor $\boldsymbol{b}$ is always computed and also stored (as solution dependant variables) in the Transformed Stress Space (TSS). This may pose difficulties to the potential user of the proposed constitutive model, due to limited familiarization. The present section provides a short guide on how initial values for the anisotropy tensor can be estimated based on the stress path responsible for the anisotropic fabric (preferred directions). It additionally helps in clarifying the correspondence between the TSS stress components and conventional stress quantities.

The presented calculation corresponds to common initial geostatic conditions for which we assume that the initial preferred directions follow the anisotropy of the consolidation stress path. In other words, the calculated values represent the anisotropy induced during a K-test. This is just an assumption for the presented example; in general, any value can be assigned to the components of tensor $\boldsymbol{b}$ to represent the

desired initial memory of preferred directions.

Regarding ABAQUS implementation, calculation depends on whether an axis-symmetric, a two-dimensional (2D) or a three-dimensional (3D) problem is simulated. Differences rise from the fact that Abaqus assumes a different vertical axis depending on the simulated problem and in more detail, in axis-symmetric and 2D problems, the vertical axis is the y-axis, while in 3D problems vertical axis is the z-axis. In geotechnical FEM analyses, the axis corresponding to the vertical direction is of significant importance as it dictates the direction of the gravitational forces.

### E.1.1 Two - dimensional (2D) and Axis - Symmetric models

In 2D and axis-symmetric problems, the vertical direction coincides with the y-axis. Figure E.1 shows how a common geostatic stress field defined by a geostatic stress ratio $K = \frac{\sigma_h}{\sigma_v}$ is translated in terms of the cartesian coordinates in the Abaqus FEM model.

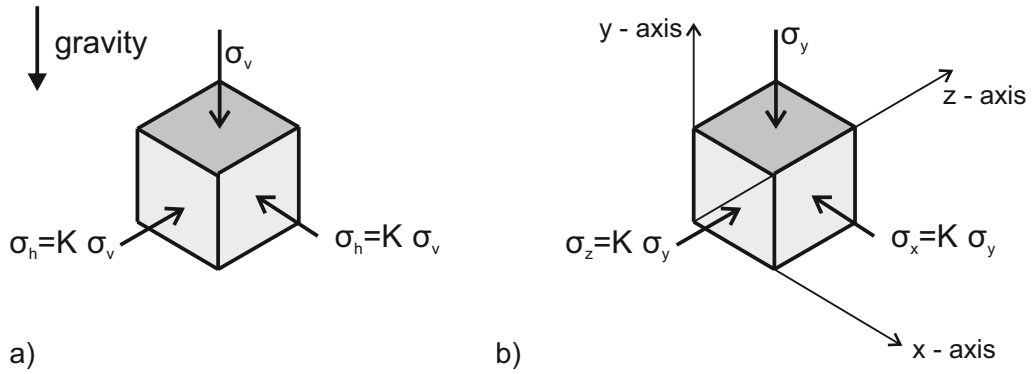


**Figure E.1:** a) Geostatic stress field and b) its corresponding state for 2D and axis - symmetric models in Simulia ABAQUS.

We observe that:

$$\sigma_y = \sigma_v \tag{E.1}$$

and

$$\sigma_x = \sigma_z = \sigma_h = K \cdot \sigma_y \tag{E.2}$$

Moreover, assuming a relative flat topography, vertical and horizontal geostatic stresses are also principal stress. In other words, no shear stresses develop on the vertical and horizontal planes and thus:

$$\sigma_{xy} = 0 \tag{E.3}$$

In the transformed stress space, such a geostatic stress field corresponds to:

$$\boldsymbol{\sigma} = \left\{ \begin{array}{c} \sigma \\ S_1 \\ S_2 \\ S_3 \end{array} \right\} = \left\{ \begin{array}{c} \frac{\sigma_x+\sigma_y+\sigma_z}{3} \\ \frac{2\sigma_y-\sigma_x-\sigma_z}{\sqrt{6}} \\ \frac{\sigma_z-\sigma_x}{\sqrt{2}} \\ \sigma_{xy} \cdot \sqrt{2} \end{array} \right\} = \left\{ \begin{array}{c} \frac{1+2K}{3}\sigma_v \\ \frac{2(1-K)}{\sqrt{6}}\sigma_v \\ 0 \\ 0 \end{array} \right\} \tag{E.4}$$

Finally, assuming that initial anisotropy follows the consolidation stress path we can calculate the initial anisotropy tensor $\boldsymbol{b}$ according to:

$$\boldsymbol{b} = \left\{ \begin{array}{c} b_1 \\ b_2 \\ b_3 \end{array} \right\} = \left\{ \begin{array}{c} S_1/\sigma \\ S_2/\sigma \\ S_3/\sigma \end{array} \right\} = \left\{ \begin{array}{c} \frac{\sqrt{6}(1-K)}{1+2K} \\ 0 \\ 0 \end{array} \right\} \tag{E.5}$$

*Note: Axis - symmetric and 2D numerical models activate only the first four components of the stress tensor.*

### E.1.2 Three - dimensional (3D) models

In 3D problems, the vertical direction coincides with the z-axis. Figure E.2 shows how a common geostatic stress field defined by a geostatic stress ratio $K = \frac{\sigma_h}{\sigma_v}$ is translated in terms of the cartesian coordinates in ABAQUS for a 3D FEM model.

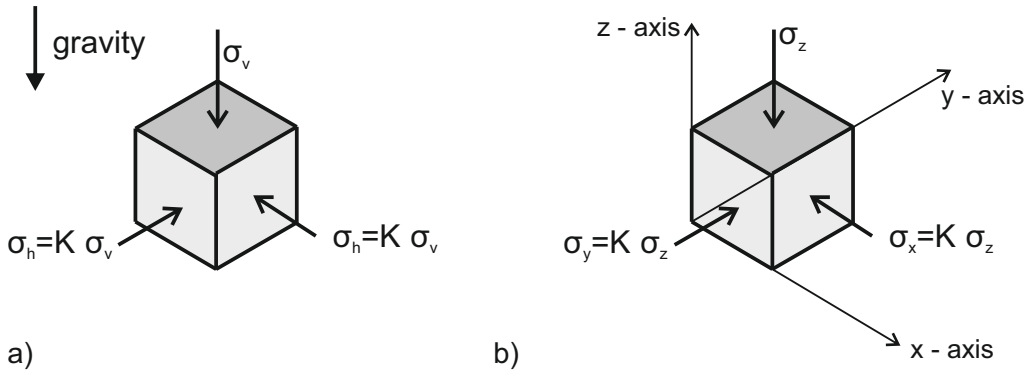


**Figure E.2:** a) Geostatic stress field and b) its corresponding state for 3D models in Simulia ABAQUS.

Note that:

$$\sigma_z = \sigma_v \tag{E.6}$$

and

$$\sigma_x = \sigma_y = \sigma_h = K \cdot \sigma_z \tag{E.7}$$

Moreover, assuming a relative flat topography, vertical and horizontal geostatic stresses are also principal stress. In other words, no shear stresses develop on the vertical and horizontal planes and thus:

$$\sigma_{xy} = 0 \tag{E.8}$$

$$\sigma_{xz} = 0 \tag{E.9}$$

$$\sigma_{yz} = 0 \tag{E.10}$$

In the transformed stress space, such a geostatic stress field corresponds to:

$$\boldsymbol{\sigma} = \begin{Bmatrix} \sigma \\ S_1 \\ S_2 \\ S_3 \\ S_4 \\ S_5 \end{Bmatrix} = \begin{Bmatrix} \frac{\sigma_x+\sigma_y+\sigma_z}{3} \\ \frac{2\sigma_y-\sigma_x-\sigma_z}{\sqrt{6}} \\ \frac{\sigma_z-\sigma_x}{\sqrt{2}} \\ \sigma_{xy} \cdot \sqrt{2} \\ \sigma_{xz} \cdot \sqrt{2} \\ \sigma_{yz} \cdot \sqrt{2} \end{Bmatrix} = \begin{Bmatrix} \frac{(2K+1)}{3}\sigma_v \\ \frac{(K-1)}{\sqrt{6}}\sigma_v \\ \frac{(1-K)}{\sqrt{2}}\sigma_v \\ \\ 0 \\ 0 \\ 0 \end{Bmatrix} \tag{E.11}$$

Finally, assuming that initial anisotropy follows the consolidation stress path we can calculate the initial anisotropy tensor $\boldsymbol{b}$ according to:

$$\boldsymbol{b} = \begin{Bmatrix} b_1 \\ b_2 \\ b_3 \end{Bmatrix} = \begin{Bmatrix} S_1/\sigma \\ S_2/\sigma \\ S_3/\sigma \end{Bmatrix} = \begin{Bmatrix} \sqrt{\frac{3}{2}} \cdot \frac{(K-1)}{(2K+1)} \\ \frac{3\sqrt{2}}{2} \cdot \frac{(1-K)}{(2K+1)} \\ 0 \end{Bmatrix} \tag{E.12}$$

*Note: Three - dimensional models activate all components of the stress tensors.*

## E.2 Initial Geostatic Conditions

A realistic simulation of geotechnical problems must take into account the decreasing void ratio with depth usually observed in natural soil deposits. In porous materials, a varying void ratio results in an increasing (with depth) density and thus to a nonlinear distribution of the initial geostatic stress field. To assign consistent initial conditions,

corresponding to varying with depth soil properties, we select to divide the model in multiple vertical layers. Each layer should contain at least on row of elements.

Figure E.3 presents a typical layer with a tickness ($h$), containing a single row of elements. For each soil layer we need to define:

- **the material constants**; as a material constant, apart from the constitutive models' parameters, the specific gravity of the solid phase $G_s$ is assumed. Material constants are assigned at the integration points.
- **the initial hardening and other solution dependant variables**; their values are calculated and assigned at the integration points as well.
- **the initial stress field**; the initial stress field is calculated and the corresponding stress variables at the top and the bottom of each layer are assigned.

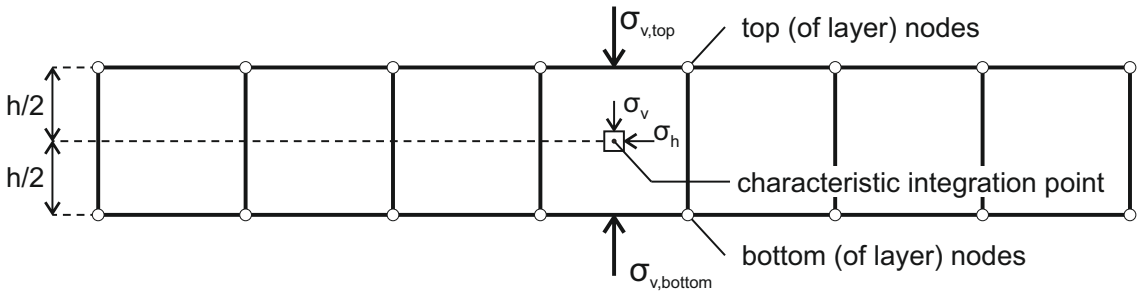


**Figure E.3:** A typical layer of solid elements in Abaqus and the assignment of the initial conditions.

In the following lines, an iterative procedure is presented to calculate varying with depth initial conditions. In the present example, initial conditions are calculated under saturated conditions, additionally assuming that the water table coincides with the top of the model (fully saturated soil profile). Calculating initial conditions for an unsaturated soil profile is also possible, nevertheless, the required calculations are quite complicated and demanding. For this reason, it is suggested that in order to calculate the initial conditions of an unsaturated soil profile to simulate a suitable drying process from an initially saturated profile.

The required iterative procedure includes the following steps:

1. **STEP 1 - Effective stress calculation**: A trial void ratio value $e$ is assumed for each layer and the saturated density of the material ($\rho$) is calculated

according to:

$$\rho = \frac{\rho_w \left(G_s + e\right)}{1 + e} \tag{E.13}$$

where $\rho_w$ the water density usually (assumed equal to $\rho_w = 1.0 Mgr/m^3$) and $G_s$ the specific gravity of the solid phase. Then with the effective stress at the top of the layer known (it is the one calculated for the bottom of the layer above) we can calculate the vertical and horizontal effective stress at the middle of the layer (assumed representative of the stress state at the integration points):

$$\sigma_v = \sigma_{v,top} + (\rho - \rho_w) \cdot g \cdot \frac{h}{2} \tag{E.14}$$

$$\sigma_h = K_0 \cdot \sigma_v \tag{E.15}$$

and also at the bottom of the layer:

$$\sigma_{v,bottom} = \sigma_{v,top} + (\rho - \rho_w) \cdot g \cdot h \tag{E.16}$$

$$\sigma_{h,bottom} = K_0 \cdot \sigma_{v,bottom} \tag{E.17}$$

where $K_0$ the desired coefficient of lateral earth pressure at rest, $g$ the gravitational acceleration ($g = 9.81 m/s^2$) and $h$ the thickness of the layer.

In the transformed stress space (assuming a 2D problem) the stress state at the middle of the layer corresponds to:

$$\sigma = \frac{1 + 2K_0}{3}\sigma_v \tag{E.18}$$

$$S_1 = \frac{2\left(1 - K_0\right)}{\sqrt{6}}\sigma_v \tag{E.19}$$

2. **STEP 2 - Initial hardening and other solution dependant variables**: With the stress state at the middle of the layer calculated, the initial hardening variables can be estimated, based on reasonable assumptions for the soil profile. In the present analysis the following assumptions are made:

   - A constant overconsolidation ratio with depth; It is reminded that $OCR = \sigma_{v,p}/\sigma_v$) where $\sigma_{v,p}/$ denotes the preconsolidation pressure.
   - The initial anisotropy corresponds to the stress path followed during the consolidation history up to the preconsolidation pressure $\sigma_{v,p}$ and thus is calculated according to the selected $K_{0,NC}$ value.

Following these assumptions we may calculate the vertical and horizontal effective stresses representing the preconsolidation stress state:

$$\sigma_{v,p} = OCR \cdot \sigma_v \tag{E.20}$$

$$\sigma_{h,p} = K_{0,NC} \cdot \sigma_{v,p} \tag{E.21}$$

while in the transformed stress space:

$$\sigma_p = \frac{1 + 2K_{0,NC}}{3}\sigma_{v,p} \tag{E.22}$$

$$S_{1,p} = \frac{2\left(1 - K_{0,NC}\right)}{\sqrt{6}}\sigma_{v,p} \tag{E.23}$$

The initial inclination of the yield surface is computed according to expression E.5 with $K \equiv K_0$, resulting to:

$$b_1 = \frac{\sqrt{6}\left(1 - K_{0,NC}\right)}{1 + 2K_{0,NC}} \tag{E.24}$$

During consolidation the stress state lies on the yield surface, while during unloading to the desired $OCR$ level the stress path retracts from the yield surface following an elastic stress path. Thus, the initial size of the yield surface "remembers" the preconsolidation stress state, and in that respect, we may substitute the stress state and the initial inclination corresponding to the preconsolidation pressure (equations E.22 and E.24 respectivelly) into the yield function 6.12:

$$f\left(\sigma, \boldsymbol{s}, \alpha\left(s, S_r^e\right), \boldsymbol{b}\right) = \frac{1}{k^2}(S_{1,p} - \sigma_p b_1)^2 - \sigma(2\alpha\left(s, S_r^e\right) - \sigma) \tag{E.25}$$

Solving the aforementioned equation for $2\alpha\left(s, S_r^e\right)$, which due to $S_r = 1.0$, is also equal to $2\alpha$ we obtain the desired initial size of the saturated strength envelope.

3. **STEP 3 - Recalculating the void ratio**: With the stress state and also the initial hardening variables known we can recalculate the void ratio to conform with the compressibility framework of the proposed model. It is calculated as:

$$e = v - 1 \tag{E.26}$$

where

$$v = N_n - (\lambda - \kappa) \ln 2\alpha - \kappa \ln \sigma_v \tag{E.27}$$

while $N_n$ is defined through equation 6.37:

$$N_n = \Gamma + (N_{iso} - \Gamma) \left( 1 - \frac{1}{c^2} \boldsymbol{b} : \boldsymbol{b} \right)^{r_s} \tag{E.28}$$

The void ratio value calculated from STEP3 is inserted as a new trial value at STEP1 to repeat the calculation until the trial and the calculated void ratio coincide. It is obvious that the described iterative procedure is performed for every layer simultaneously, as the stress at the bottom of any given layer is an input for the top of the layer below. Thus a suitable computer software is required (i.e., MS EXCEL, Matlab, etc.). When convergence is achieved, the calculated stress field and solution dependant variables obtained are the desired initial condition for the ABAQUS geostatic step.

# References


Aitchison, G. (1960). Relationships of moisture stress and effective stress functions in unsaturated soils. In *Conference of the British National Society of The International Society for Soil Mechanics and Foundation Engineering, 1960, London, United Kingdom*.

Aitchison, G. & Donald, I. (1956). Effective stresses in unsaturated soils. In *Proc. 2on Aus.–New Zeal. SM Conf., Christchurch*, pp. 192–199.

Allman, M. & Atkinson, J. (1992). Mechanical properties of reconstituted bothkennar soil. *Géotechnique 42*(2), 289–301.

Alonso, E. (2012). Unsaturated soils: Basic concepts and applications. Webinar of the ISSMGE, July, 2012, http://www.issmge.org/en/resources/recorded-webinars/556-unsaturated-soils-basic-concepts-and-applications-part-1-and-part-2.

Alonso, E., Gens, A., & Hight, D. (1987). Special problem soils. general report. In *Proceedings of the 9th European conference on soil mechanics and foundation engineering, Dublin*, Volume 3, pp. 1087–1146.

Alonso, E., Gens, A., & Josa, A. (1990). A constitutive model for partially saturated soils. *Géotechnique. 40*(3), 405–430.

Alonso, E. & Lloret, A. (1996). Settlement of a 12 storey building due to desiccation induced by trees: a case study. In *UNSAT'95/Paris/France/6-8 Semptember 1995. Vol. 3*.

Alonso, E., Olivella, S., & Pinyol, N. (2005). A review of beliche dam. *Géotechnique 55*(4), 267–285.

Alonso, E., Pinyol, N., & Gens, A. (2012). Compacted soil behaviour: initial state, structure and constitutive modelling. *Geotechnique 63*(6), 463–478.

Alonso, E., Vaunat, J., & Gens, A. (1999). Modelling the mechanical behaviour of expansive clays. *Engineering geology 54*(1), 173–183.

Alonso, E. E., Pereira, J.-M., Vaunat, J., & Olivella, S. (2010). A microstructurally based effective stress for unsaturated soils. *Géotechnique. 60*(12), 913–925.

Amerasinghe, S. (1973). *The stress-strain behaviour of clay at low stress levels and high overconsolidation ratio*. Ph. D. thesis, Cambridge University.

Andersen, K. H., Rosenbrand, W. F., Brown, S. F., & Pool, J. H. (1980). Cyclic and static laboratory tests on drammen clay. *Journal of the Geotechnical Engineering Division 106*(5), 499–529.

Arairo, W., Prunier, F., Djeran-Maigre, I., & Millard, A. (2014). On the use of effective stress in three-dimensional hydro-mechanical coupled model. *Computers and Geotechnics 58*, 56–68.

Arya, L. M. & Paris, J. F. (1981). A physicoempirical model to predict the soil moisture characteristic from particle-size distribution and bulk density data. *Soil Science Society of America Journal 45*(6), 1023–1030.

Atkinson, J. & Bransby, P. (1977). The mechanics of soils, an introduction to critical state soil mechanics. Technical report.

Atkinson, J., Richardson, D., & Robinson, P. (1987). Compression and extension of k 0 normally consolidated kaolin clay. *Journal of geotechnical engineering 113*(12), 1468–1482.

Balasubramannian, A. (1969). *Sane factors influencing the stress-strain behaviour of clay*. Ph. D. thesis, University of Cambridge.

Barbour, S. L. (1998). Nineteenth canadian geotechnical colloquium: The soil-water characteristic curve: a historical perspective. *Canadian Geotechnical Journal 35*(5), 873–894.

Bardanis, M. (2016). *Experimental and Analytical Investigation of the Mechanical Beahaviour of Unsaturates Soils (in Greek)*. Ph. D. thesis, School of Civil Engineering, National Technical University of Athens (NTUA).

Bardanis, M. & Grifiza, S. (2011). Measuring the soil-water characteristic curve of structured and recomposed soils. In *Proceedings of the 15th European Conference on Soil Mechanics and Geotechnical Engineering. Geotechnics of hard soils-weak rocks*, Volume 1, pp. 609–614. IOS Press.

Bardanis, M. & Kavvadas, M. (2005). Laboratory investigation of the virgin drying of the corinth marl. In *Unsaturated Soils: Experimental Studies*, pp. 421–432. Springer.

Bardanis, M. & Kavvadas, M. (2006). Prediction of the limiting void ratio of clayey soils after drying. Number 147, pp. 1085–1096.

Bardanis, M. & Kavvadas, M. (2008a). Modifying the barcelona basic model to account for residual void ratio and subsequent decrease of shear strength relative to suction. In *Advances in Geo-Engineering - Proceedings of the 1st European Conference on Unsaturated Soils, Durham, UK*, pp. 589–595.

Bardanis, M. & Kavvadas, M. (2008b). Soil-water characteristic curves and void ratio changes relative to suction for soils from greece. In *Unsaturated Soils. Advances in Geo-Engineering: Proceedings of the 1st European Conference, E-UNSAT 2008, Durham, United Kingdom, 2-4 July 2008*, pp. 263. CRC Press.

Barden, L., Madedor, A., & Sides, G. (1969). Volume change characteristics of unsaturated clay. *Journal of Soil Mechanics & Foundations Div*.

Barrera, B. (2002). *Estudio experimental del comportamiento hidro-mecánico de suelos colapsables*. Ph. D. thesis, Universitat Politècnica de Catalunya.

Belokas, G. (2008). *Simulating the Mechanical Behaviour of Structured and Anisotropic Soils*. Ph. D. thesis, School of Civil Engineering, National Technical University of Athens (NTUA).

Belokas, G., Amorosi, A., & Kavvadas, M. (2007). The behaviour of a normally loaded clayey soil and its simulation. In *Soil Stress-Strain Behavior: Measurement, Modeling and Analysis*, pp. 707–718. Springer.

Belokas, G. & Kavvadas, M. (2010). An anisotropic model for structured soils: Part i: Theory. *Computers and Geotechnics 37*(6), 737 – 747.

Belokas, G. & Kavvadas, M. (2011). An intrinsic compressibility framework for clayey soils. *Geotechnical and Geological Engineering 29*(5), 855–871.

Belokas, G., Kavvadas, M., & Amorosi, A. (2005). Modelling the behaviour of reconstituted soils under radial stress paths. In *Prediction, analysis and design in geomechanical application (Proc. 11th Int. Conf. on Computer Methods and Advances in Geomechanics)*, pp. 249–256.

Bishop, A. W. (1959). *The principles of effective stress*. Teknick Ukeblad, 39 : 859-863, Norges Geotekniske Institutt.

Bishop, A. W., Alpan, I., Blight, G., & Donald, I. (1960). Factors controlling the strength of partly saturated cohesive soils. In *Proc. Res. Conf. on Shear Strength of Cohesive Soils, Boulder*, pp. 503–532.

Bishop, A. W. & Blight, G. (1963). Some aspects of effective stress in saturated and partly saturated soils. *Geotechnique 13*(3), 177–197.

Bishop, A. W. & Eldin, G. (1950). Undrained triaxial tests on saturated sands and their significance in the general theory of shear strength. *Geotechnique 2*(1), 13–32.

Bjerrum, L. (1973). Problems of soil mechanics and construction on soft clays and structurally unstable soils (collapsible, expansive and others). In *Proc. of 8th ICSMFE*, Volume 3, pp. 111–159.

Bland, D. (1957). The associated flow rule of plasticity. *Journal of the Mechanics and Physics of Solids 6*(1), 71–78.

Bolton, M. D. (1991). *A guide to soil mechanics*. Universities Press.

Bolzon, G., Schrefler, B., & Zienkiewicz, O. (1996). Elastoplastic soil constitutive laws generalized to partially saturated states. *Géotechnique 46*(2), 279–289.

Bondok, A. (1989). *Constitutive relations for anisotropic soils*. Ph. D. thesis, University of Wales, College of Cardiff,.

Bouyoucos, G. & Mick, A. (1940). Comparison of absorbent materials employed in the electrical resistance method of making a continuous measurement of soil moisture under field conditions. In *Proc Soil Sci Soc Am*, Volume 5, pp. 77–79.

Broms, B. & Casbarian, A. (1965). Effects of rotation of the principal stress axes and of the intermediate principal stress on the shear strength. *Proceedings of the 6th ICSMFE, Montreal 1*, 179–183.

Broms, B. & Ratman, M. (1963). Shear strength of an anisotropically consolidated clay. *Journal of the Soil Mechanics and Foundations Division 89*(6), 1–26.

Brooker, E. W. & Ireland, H. O. (1965). Earth pressures at rest related to stress history. *Canadian Geotechnical Journal 2*(1), 1–15.

Brutsaert, W. (1966). Probability laws for pore-size distributions. *Soil Science 101*(2), 85–92.

Buisson, M. & Wheeler, S. (2000). Inclusion of hydraulic hysteresis in a new elasto-plastic framework for unsaturated soils. *Experimental evidence and theoretical approaches in unsaturated soils*, 109–119.

Burdine, N. et al. (1953). Relative permeability calculations from pore size distribution data. *Journal of Petroleum Technology 5*(03), 71–78.

Burland, J. (1965). Some aspects of the mechanical behaviour of partly saturated soils. In *Moisture Equilibria and Moisture Changes in Soils Beneath Covered Areas, A Symposium in Print, Butterworth, Sidney, Australia*, pp. 270–278.

Burland, J. (1990). On the compressibility and shear strength of natural clays. *Géotechnique. 40*(3), 329–378.

Calabresi, G. (1968). Deformazioni plastiche di una terra argillosa. *Rivista italiana di Geotecnica* (4).

Callisto, L. & Calabresi, G. (1998). Mechanical behaviour of a natural soft clay. *Geotechnique 48*(4), 495–513.

Casagrande, A. & Carillo, N. (1944). Shear failure of anisotropic materials. *Journal of Boston Society of Civil Engineers 31*(4), 74–81.

Casini, F. (2008). *Effecti Del Grado Di Saturazione Sul Comportamento Meccanico Del Limo (in Italian)*. Ph. D. thesis, La Sapienza University, Rome, Italy.

Casini, F. (2012). Deformation induced by wetting: a simple model. *Canadian Geotechnical Journal. 49*(8), 954–960.

Casini, F., Serri, V., & Springman, S. M. (2012). Hydromechanical behaviour of a silty sand from a steep slope triggered by artificial rainfall: from unsaturated to saturated conditions. *Canadian Geotechnical Journal 50*(1), 28–40.

Casini, F., Vaunat, J., Romero, E., & Desideri, A. (2012). Consequences on water retention properties of double-porosity features in a compacted silt. *Acta Geotechnica 7*(2), 139–150.

Chandler, R. J. (1986). The filter-paper method of suction measurement. *Géotechnique 36*, 265–268(3).

Chen, Z.-H., Fredlund, D., & Gan, J. K. (1999). Overall volume change, water volume change, and yield associated with an unsaturated compacted loess. *Canadian geotechnical journal 36*(2), 321–329.

Collins, B. D. & Znidarcic, D. (2004). Stability analyses of rainfall induced landslides. *Journal of Geotechnical and Geoenvironmental Engineering 130*(4), 362–372.

Coop, M. (1990). The mechanics of uncemented carbonate sands. *Geotechnique 40*(4), 607–626.

Cotecchia, F. & Chandler, R. (1997). The influence of structure on the pre-failure behaviour of a natural clay. *Géotechnique 47*(3), 523–544.

Croney, D., Coleman, J., & Black, W. (1958). The movement and distribution of water in soil in relation to highway design and performance. Technical report, Highway Research Board Special Report No. 40, Washington, D.C.

Cui, Y. & Delage, P. (1996). Yielding and plastic behaviour of an unsaturated compacted silt. *Géotechnique 46*(2), 291–311.

Cui, Y., Ye, W., Chen, B., & Chen, Y. (Eds.) (2009). *Proccedings of the International Symposium on Unsaturated Soil Mechanichs and Deep Geological Nuclear Waste Disposal (UNSAT-WASTE 2009)*, UNSAT-WASTE.

Cunningham, M., Ridley, A., Dineen, K., & Burland, J. (2003). The mechanical behaviour of a reconstituted unsaturated silty clay. *Géotechnique 53*(2), 183–194.

Dafalias, Y. (1986). An anisotropic critical state soil plasticity model. *Mechanics Research Communications 13*(6), 341–347.

Dafalias, Y. & Herrmann, L. (1982). Bounding surface formulation of soil plasticity, chapter 10 in soil mechanics: transient and cyclic loads, eds gn pande & oc zienkiewicz.

Dafalias, Y. & Popov, E. (1975). A model of nonlinearly hardening materials for complex loading. *Acta Mechanica 21*(3), 173–192.

Dafalias, Y. F., Manzari, M. T., & Akaishi, M. (2002). A simple anisotropic clay plasticity model. *Mechanics research communications 29*(4), 241–245.

Dafalias, Y. F., Manzari, M. T., & Papadimitriou, A. G. (2006). Saniclay: simple anisotropic clay plasticity model. *International Journal for Numerical and Analytical Methods in Geomechanics 30*(12), 1231–1257.

Darve, F., Flavigny, E., & Meghachou, M. (1995). Constitutive modelling and instabilities of soil behaviour. *Computers and Geotechnics 17*(2), 203–224.

Davis, R. O. & Selvadurai, A. P. (2002). *Plasticity and geomechanics*. Cambridge University Press.

Delage, P., Audiguier, M., Cui, Y.-J., & Howat, M. D. (1996). Microstructure of a compacted silt. *Canadian Geotechnical Journal 33*(1), 150–158.

Delage, P. & Graham, J. (1996). Mechanical behaviour of unsaturated soils: understanding the behaviour of unsaturated soils requires reliable conceptual models. In *UNSAT'95/Paris/France/6-8 Semptember 1995. Vol. 3*.

Desai, C. S. & Siriwardane, H. J. (1984). *Constitutive laws for engineering materials with emphasis on geologic materials*. Prentice-Hall.

Diaz-Rodriguez, J., Leroueil, S., & Aleman, J. (1992). Yielding of mexico city clay and other natural clays. *Journal of geotechnical engineering 118*(7), 981–995.

Donaghe, R. & Townsend, F. (1978). Effects of anisotropic consolidation in consolidated-undrained triaxial compression tests of cohesive soils. *ASTM Geotechnical Testing Journal 1*(4), 173–189.

Donald, I. B. (1956). hear strength measurements in unsaturated non-cohesive soils with negative pore pressures. In *Proc. 2nd Australia-New Zealand Conference on Soil Mechanics & Foundation Engineering, Christchurch, New Zealand*, pp. 200–205.

D'Onza, F., Gallipoli, D., & Wheeler, S. (2010). Effect of anisotropy on the prediction of unsaturated soil response under triaxial and oedometric conditions.

D'Onza, F., Gallipoli, D., Wheeler, S., Casini, F., Vaunat, J., Khalili, N., Laloui, L., Mancuso, C., Mašín, D., Nuth, M., et al. (2011). Benchmark of constitutive models for unsaturated soils. *Géotechnique 61*(4), 283–302.

Drucker, D. & Prager, W. (1952). Soil mechanics and plastic analysis for limit design. *Quarterly of Applied Mathematics 10*(2), 157–165.

Drucker, D. C. (1951). A more fundamental approach to plastic stress-strain relations. In *Journal Of Applied Mechanics-Transactions of the ASME*, Volume 18, pp. 323–323. ASME-AMER SOC MECHANICAL ENG.

Drucker, D. C., Gibson, R. E., & Henkel, D. J. (1957). Soil mechanics and work-hardening theories of plasticity. *Transactions of the American Society of Civil Engineers 122*(1), 338–346.

Dudley, J. H. (1970). Review of collapsing soils. *Journal of Soil Mechanics & Foundations Div 97*(SM1).

Escario, V. & Juca, J. (1989). Strength and deformation of partly saturated soils. In *Proc. 12th Int. Conf. Soil Mech. Found. Eng., Rio de Janeiro*, Volume 1, pp. 43–46.

Escario, V. & Saez, J. (1973). Measurement of the properties of swelling and collapsing soils under controlled suction. In *Proc. 3rd Int. Conf. Expansive Soils, Haifa*, Volume 2, pp. 195–200.

Escario, V. & Saez, J. (1986). The shear strength of partly saturated soils. *Géotechnique 36*(3).

Esteban, F. (1990). *Caracterización experimental de la expansividad de una roca evaporítica. Identificación de los mecanismos de hinchamiento*. Ph. D. thesis, Universidad de Camtrabria, Santander, Spain.

Fredlund, D., Morgenstern, N., & Widger, R. (1978). The shear strength of unsaturated soils. *Canadian Geotechnical Journal 15*(3), 313–321.

Fredlund, D., Rahardjo, H., & Gan, J. (1987). Non-linearity of strength envelope for unsaturated soils. In *Proc. 6th Int. Conf. Expansive Soils, New Delhi*, Volume 1, pp. 49–54.

Fredlund, D. G. (2006). Unsaturated soil mechanics in engineering practice. *Journal of geotechnical and geoenvironmental engineering 132*(3), 286–321.

Fredlund, D. G. & Morgenstern, N. R. (1977). Stress state variables for unsaturated soils. *Journal of Geotechnical and Geoenvironmental Engineering 103*(ASCE 12919).

Fredlund, D. G. & Rahardjo, H. (1993). *Soil mechanics for unsaturated soils*. John Wiley & Sons.

Fredlund, D. G. & Xing, A. (1994). Equations for the soil-water characteristic curve. *Canadian geotechnical journal 31*(4), 521–532.

Fredlund, D. G., Xing, A., Fredlund, M. D., & Barbour, S. (1996). The relationship of the unsaturated soil shear to the soil-water characteristic curve. *Canadian Geotechnical Journal 33*(3), 440–448.

Fredlund, M. D., Fredlund, D., & Wilson, G. (1997a). Estimation of unsaturated soil properties using a knowledge-based system. In *Proceedings of the Fourth Congress on Computing in Civil Engineering, ASCE, Philadelphia, PA, June', Citeseer*, pp. 16–18.

Fredlund, M. D., Fredlund, D. G., & Wilson, G. (1997b). Prediction of the soil-water characteristic curve from grain-size distribution and volume-mass properties. In *Proc., 3rd Brazilian Symp. on Unsaturated Soils*, Volume 1, pp. 13–23. Rio de Janeiro.

Fredlund, M. D., Wilson, G. W., & Fredlund, D. G. (2002). Use of the grain-size distribution for estimation of the soil-water characteristic curve. *Canadian Geotechnical Journal 39*(5), 1103–1117.

Gallipoli, D., Gens, A., Sharma, R., & Vaunat, J. (2003). An elasto-plastic model for unsaturated soil incorporating the effects of suction and degree of saturation on mechanical behaviour. *Géotechnique. 53*(1), 123–136.

Gallipoli, D., Wheeler, S., & Karstunen, M. (2003). Modelling the variation of degree of saturation in a deformable unsaturated soil. *Géotechnique. 53*(1), 105–112.

Gan, J. K. & Fredlund, D. (1996). Shear strength characteristics of two saprolitic soils. *Canadian Geotechnical Journal 33*(4), 595–609.

Ganjian, N., Pisheh, Y. P., & Hosseini, S. M. M. M. (2007). Prediction of soil–water characteristic curve based on soil index properties. In *Experimental Unsaturated Soil Mechanics*, pp. 355–367. Springer.

Gao, Y.-B. (2013). Compression and extension yield of an anisotropically consolidated soil. *Soils and Foundations 53*(3), 431–442.

Gens, A. (1982). *Stress-strain and strength characteristics of a low plasticity clay*. Ph. D. thesis, Imperial College London.

Gens, A. (1996). Constitutive modelling: Application to compacted soils. In *UNSAT'95/Paris/France/6-8 Semptember 1995. Vol. 3*.

Gens, A. (2010). Soil - environment interactions in geotechnical engineering. *Géotechnique. 60*(1), 3–74.

Gens, A. & Alonso, E. (1992). A framework for the behaviour of unsaturated expansive clays. *Canadian Geotechnical Journal 29*(6), 1013–1032.

Gens, A., Alonso, E., & Lloret, A. (1995). Effect of structure on the volumetric behaviour of a compacted soil. In *UNSAT'95/Paris/France/6-8 Semptember 1995. Vol. 1*.

Gens, A., Sánchez, M., Guimaraes, L. D. N., Alonso, E., Lloret, A., Olivella, S., Villar, M., & Huertas, F. (2009). A full-scale in situ heating test for high-level nuclear waste disposal: observations, analysis and interpretation. *Géotechnique 59*(4), 377–399.

Gens, A., Sánchez, M., & Sheng, D. (2006). On constitutive modelling of unsaturated soils. *Acta Geotechnica 1*(3), 137–147.

Georgiadis, K. (2003). *Development, implementation and application of partially saturated soil models in finite element analysis*. Ph. D. thesis, Imperial College.

Georgiannou, V. N. (1988). *The behaviour of clayey sands under monotonic and cyclic loading*. Ph. D. thesis, Imperial College London (University of London).

Gonzalez, N. (2011). *Development of a family of constitutive models for geotechnical applications*. Ph. D. thesis, Universitat Politècnica de Catalunya.

Gonzalez, N. & Gens, A. (2011). Evaluation of a constitutive model for unsaturated soils: stress variables and numerical implementation. In E. Alonso & A.Gens (Eds.), *Unsaturated Soils - Proc. of the 5th Inter. Conf. on Unsat. Soils, Barcelona, Spain, 6-8 September, 2010*. CRC Press/Balkema.

Graham, J. & Houlsby, G. (1983). Anisotropic elasticity of a natural clay. *Geotechnique 33*(2), 165–180.

Henkel, D. (1956). The effect of overconsolidation on the behaviour of clays during shear. *Geotechnique 6*(4), 139–150.

Henkel, D. (1959). The relationships between the strength, pore-water pressure, and volume-change characteristics of saturated clays. *Geotechnique 9*(3), 119–135.

Henkel, D. (1960). The relationships between the effective stresses and water content in saturated clays. *Geotechnique 10*(2), 41–54.

Henkel, D. & Sowa, V. (1963). The influence of stress history on stress paths in undrained triaxial tests on clay. *Laboratory shear testing of soils*, 280–291.

Hight, D., Bond, A., & Legge, J. (1992). Characterization of the bothkennaar clay: an overview. *Géotechnique 42*(2), 303–347.

Hilf, J. W. (1956). An investigation of pore water pressure in compacted cohesive soils. *Technical Memorandum 654, U.S. Dept. of Interior, Bureau of Reclamation, Denver, Colo*.

Hill, R. (1958). A general theory of uniqueness and stability in elastic-plastic solids. *Journal of the Mechanics and Physics of Solids 6*(3), 236–249.

Honda, M. (2000). *Research on the prediction methods for the mechanical behaviors of unsaturated soils*. Ph. D. thesis, PhD thesis, Kobe University, Kobe, Japan.

Houlsby, G. (1997). The work input to an unsaturated granular material. *Géotechnique 47*(1), 193–196.

Huang, S. (1994). *Evaluation and laboratory measurement of the coefficient of permeability in deformable, unsaturated soils*. Ph. D. thesis, Department of Civil Engineering, University of Saskatchewan, Saskatoon.

Jaky, J. (1944). The coefficient of earth pressure at rest. *Journal of the Society of Hungarian Architects and Engineers 78*(22), 355–358.

Jardine, R., Gens, A., Hight, D., & Coop, M. (2004). Developments in understanding soil behaviour. In *Advances in geotechnical engineering: The Skempton conference*, pp. 103–206. Thomas Telford.

Jefferies, M. (1993). Nor-sand: a simle critical state model for sand. *Geotechnique 43*(1), 91–103.

Jennings, J. (1957). Discussion on ms youssef's paper. In *Proc. 4th Int. Conf. on Soil Mech., ISSMFE*, Volume 3, pp. 168.

Jennings, J. (1961). A revised effective stress law for use in the prediction of the behaviour of unsaturated soils. *Pore pressure and suction in soils*, 26–30.

Jennings, J. & Burland, J. (1962). Limitations to the use of effective stresses in partly saturated soils. *Géotechnique 12*(2), 125–144.

Jommi, C. (2000). Remarks on the constitutive modelling of unsaturated soils. *Experimental evidence and theoretical approaches in unsaturated soils*, 139–153.

Josa, A., Balmaceda, A., Gens, A., & Alonso, E. (1992). An elastoplastic model for partially saturated soils exhibiting a maximum of collapse. In *3rd international conference on computational plasticity, Barcelona*, Volume 1, pp. 815–826.

Kalos, A. (2014). *Investigation of the Nonlinear Time-Dependent Soil Behaviour*. Ph. D. thesis, School of Civil Engineering, National Technical University of Athens (NTUA).

Karamitros, D. (2010). *Development of a Numerical Algorithm for the Dynamic Elastoplastic Analysis of Geotechnical Structures in Two (2) and Three (3) Dimensions*. Ph. D. thesis, School of Civil Engineering, National Technical University of Athens (NTUA).

Karube, D. & Kawai, K. (2001). The role of pore water in the mechanical behavior of unsaturated soils. *Geotechnical & Geological Engineering 19*(3-4), 211–241.

Kassiff, G. & Shalom, A. B. (1971). Experimental relationship between swell pressure and suction. *Géotechnique 21*(3), 245–255.

Kavvadas, M. (1982). *Non - Linear Consolidation around driven piles in Clays*. Ph. D. thesis, Massachussets Institute of Technology (MIT), Cambridge, MA.

Kavvadas, M. (1995). A plasticity approach to the mechanical behaviour of bonded soils. In *Proceedings of the 4th International Conference on Computational Plasticity, Barcelona*.

Kavvadas, M. (2000). General report: Modelling the soil behaviour - selection of soil parameters. In A. Evangelista & L. Picarelly (Eds.), *The Geotec. of hard soils - soft rocks. Proc. of the 2nd Int. Conf. Geotech. Hard Soils-Soft Rocks, Naples, Italy, 12 -14 Oct. 1998*, Volume 3, pp. 1441–1481.

Kavvadas, M. & Amorosi, A. (2000). A constitutive model for structured soils. *Geotechnique 50*(3), 263–273.

Kavvadas, M. & Anagnostopoulos, A. (1998). A framework for the mechanical behaviour of structural soils. In *Proc. 2nd Int. Symp. on the Geotechnics of Hard Soils – Soft Rocks, Napoli*, Volume 2, pp. 591–601. Balkema. Rotterdam.

Kavvadas, M., Anagnostopoulos, A., & Kalteziotis, N. (1993). A framework for the mechanical behaviour of the cemented corinth marl. *Geotechnical Engineering of Hard Soils-Soft Rocks 1*, 577–583.

Kavvadas, M. & Belokas, G. (2001). An anisotropic elastoplastic constitutive model for natural soils. In *Computer Methods and Advances in Geomechanics: Proceedings of the 10th International Conference on Computer Methods and Advances in Geomechanics, Tucson, Arizona, USA, 7-12 January 2001*, pp. 335. CRC Press.

Kayadelen, C., Sivrikaya, O., Taşkıran, T., & Güneyli, H. (2007). Critical-state parameters of an unsaturated residual clayey soil from turkey. *Engineering Geology 94*(1), 1–9.

Khalili, N. & Khabbaz, M. (1998). A unique relationship of chi for the determination of the shear strength of unsaturated soils. *Geotechnique 48*(5).

Khera, R. (1967). *Strength responce of an anisotropically consolidated clay.* Ph. D. thesis, Northwestern University.

Kikumoto, M., Kyokawa, H., Nakai, T., & Shahin, H. M. (2011). A simple elastoplastic model for unsaturated soils and interpretations of collapse and compaction behaviours. Volume 2, pp. 849–855.

Ko, H. & Sture, S. (1980). Data reduction and application for analytical modelling. In *State-of-the-Art-Paper presented at ASTM Symposium*, Volume I11.

Kohgo, Y., Nakano, M., & Miyazaki, T. (1993). Theoretical aspects of constitutive modelling for unsaturated soils. *Soils & Foundations 33*(4), 49–63.

Koutsoftas, D. (1981). Undrained shear behavior of a marine clay. *Laboratory shear strength of soil, ASTM STP 740*, 254–276.

Ladd, C. C. & Lambe, T. W. (1963). *The strength of" undisturbed" clay determined from undrained tests*. Department of Civil Engineering, Massachusetts Institute of Technology.

Ladd, C. C. & Varallyay, J. (1965). The influence of stress system on the behavior of saturated clays during undrained shear. Technical report, DTIC Document.

Lade, P. V. & Duncan, J. M. (1975). Cubical triaxial tests on cohesionless soil. *Journal of Geotechnical and Geoenvironmental Engineering 101*(ASCE# 11269 Proceeding).

Lagioia, R. & Nova, R. (1995). An experimental and theoretical study of the behaviour of a calcarenite in triaxial compression. *Géotechnique 45*(4), 633–648.

Lagioia, R., Puzrin, A., & Potts, D. (1996). A new versatile expression for yield and plastic potential surfaces. *Computers and Geotechnics 19*(3), 171–191.

Lambe, T. W. (1960). A mechanistic picture of shear strength in clay. In *Research Conference on shear strength of cohesive soils*, pp. 555–580. ASCE.

Lawton, E. C., Fragaszy, R. J., & Hardcastle, J. H. (1989). Collapse of compacted clayey sand. *Journal of Geotechnical Engineering 115*(9), 1252–1267.

Le Lievre, S. (1967). *The yielding and flow of cohesive soils in triaxial compression.* Ph. D. thesis, Waterloo University.

Lee, K. L. & Morrison, R. A. (1970). Strength of anisotropically consolidated compacted clay. *Journal of the Soil Mechanics and Foundations Division 96*(6), 2025–2043.

Lehane, B. & Faulkner, A. (1998). Stiffness and strength characteristics of a hard lodgement till. In *Proc. Int. Symp. on the Geotechnical Engineering of Hard Soils – Soft Rocks, Napoli*, Volume 2, pp. 637–646. Balkema. Rotterdam.

Leon, J. & Alberro, J. (1972). Extension and compression tests on mexico city clay. *Proceedings of the 9th ICSMFE, Tokyo 1*, 193–196.

Leong, E., He, L., Rahardjo, H., & Fredlund, D. (2003). A comparative study of constitutive models for unsaturated soils. In *Proc., 2nd Asian Conf. on Unsaturated Soils, Osaka*, pp. 41–46.

Leong, E. C. & Rahardjo, H. (1997). Review of soil-water characteristic curve equations. *Journal of geotechnical and geoenvironmental engineering 123*(12), 1106–1117.

Leroueil, S. & Vaughan, P. (1990). The general and congruent effects of structure in natural soils and weak rocks. *Géotechnique. 40*(3), 467–488.

Lewin, P. & Burland, J. B. (1970). Stress-probe experiments on saturated normally consolidated clay. *Géotechnique. 20*(1), 38–56.

Li, X. (2003). Effective stress in unsaturated soil: a microstructural analysis. *Géotechnique 53*(2), 273–277.

Lloret, A. (2012). Mecanica de suelos no saturados. Based on personal notes and material from the master course Mechanica de Suelos No Saturados In Universitat Politecnica de Catalunya (UPC), Barcelona, Spain.

Lloret, A., Alonso, E., Gens, A., & Batlle, F. (1988). Analysis of a foundation on swelling rock. rock mechanics and power plants. In *ISRM Symposium. M. Romana, ed. Balkema*, Volume 2.

Länsivaara, T. (1996). *Modelling the Mechanical Behaviour of Soil*. Ph. D. thesis, Licenciate Thesis @ Tampere University of Technology, Geotechnical Laboratory, Publication 34, Tampere, Finland.

Loret, B. & Khalili, N. (2000). A three-phase model for unsaturated soils. *International Journal for Numerical and Analytical Methods in Geomechanics 24*(11), 893–927.

Lu, N. & Likos, W. J. (2004). *Unsaturated soil mechanics*. J. Wiley.

Maâtouk, A., Leroueil, S., & La Rochelle, P. (1995). Yielding and critical state of a collapsible unsaturated silty soil. *Géotechnique 45*(3), 465–477.

Mandel, J. (1966). Conditions de stabilité et postulat de drucker. In *Rheology and Soil Mechanics/Rhéologie et Mécanique des Sols*, pp. 58–68. Springer.

Manzari, M. T. & Dafalias, Y. F. (1997). A critical state two-surface plasticity model for sands. *Geotechnique 47*(2), 255–272.

Mašín, D. & Khalili, N. (2008). A hypoplastic model for mechanical response of unsaturated soils. *International Journal for Numerical and Analytical Methods in Geomechanics 32*(15), 1903–1926.

Maswoswe, J. (1985). *Stress paths for compacted soil during collapse due to wetting*. Ph. D. thesis, Imperial College London (University of London).

Matsuoka, H. & Nakai, T. (1974). Stress-deformation and strength characteristics of soil under three different principal stresses. In *Proc. JSCE*, Volume 232, pp. 59–70.

Matyas, E. L. & Radhakrishna, H. (1968). Volume change characteristics of partially saturated soils. *Géotechnique 18*(4), 432–448.

Mayerhof, G. (1976). Bearing capacity and settlement of pile foundations. *Journal of Geotechnical and Geoenvironmental Engineering 102*(ASCE# 11962).

Mayne, P. W. & Kulhawy, F. H. (1982). $k_0$-ocr relationships in soil. *Journal of the Geotechnical Engineering Division 108*(6), 851–872.

Mitachi, T. & Kitago, S. (1979, jun). The influence of stress history and stress system on the stress-strain-strength properties of saturated clay. *Soils and Foundations 19*(2), 45–61.

Mitchell, J. & Soga, K. (2005). *Fundamentals of Soil Behaviour*. John Wiley and Sons Inc.

Mohamad, T. A., Ali, F. H., Hashim, S., & Haut, B. B. (2006). Relationship between shear strength and soil water characteristic curve of an unsaturated granitic residual soil. *American Journal of Environmental Sciences 2*(4), 142.

Monroy, R., Zdravkovic, L., & Ridley, A. (2009). Evolution of microstructure in compacted london clay during wetting and loading. *Géotechnique 60*(2), 105–119.

Mroz, Z. (1963). Non associated flow laws in plasticity. *Journal de Mecanique 2*(1), 21–42.

Mualem, Y. (1976). A new model for predicting the hydraulic conductivity of unsaturated porous media. *Water resources research 12*(3), 513–522.

Nadarajah, V. (1973). *Stress-Strain properties of lightly overconsolidated clays.* Ph. D. thesis, University of Cambridge.

Namy, D. (1970). *An investigation of certain aspects of stress-strain relationships for clay soils.* Ph. D. thesis, Cornell University.

Naylor, D., Maranha, J., Neves, E. M. D., & Pinto, A. V. (1997). A back-analysis of beliche dam. *Geotechnique 47*(2), 221–233.

Naylor, D., Neves, E. M. D., Mattar, D., & Pinto, A. V. (1986). Prediction of construction performance of beliche dam. *Geotechnique 36*(3), 359–376.

Newson, T. & Davies, M. (1996). A rotational hardening constitutive model for anisotropically consolidated clay. *Soils and foundations 36*(3), 13–20.

Noorany, I. & Seed, H. (1965). In-situ strength characteristics of soft clays. *Journal of Soil Mechanics & Foundations Div 91*(Proc. Paper 4274).

Nuth, M. & Laloui, L. (2008a). Advances in modelling hysteretic water retention curve in deformable soils. *Computers and Geotechnics 35*(6), 835–844.

Nuth, M. & Laloui, L. (2008b). Effective stress concept in unsaturated soils: Clarification and validation of a unified framework. *International journal for numerical and analytical methods in Geomechanics 32*(7), 771–801.

Öberg, A.-L. & Sällfors, G. (1997). Determination of shear strength parameters of unsaturated silts and sands based on the water retention curve. *ASTM geotechnical testing journal 20*(1), 40–48.

Olivella, S., Carrera, J., Gens, A., & Alonso, E. (1994). Nonisothermal multiphase flow of brine and gas through saline media. *Transport in porous media 15*(3), 271–293.

Olivella, S., Gens, A., Carrera, J., & Alonso, E. (1996). Numerical formulation for a simulator (code_bright) for the coupled analysis of saline media. *Engineering computations 13*(7), 87–112.

Papadimitriou, A. & Agapoylaki, G. (2013). On improving a simple anisotropic clay model. In S. Pietruszczak & G.N.Pande (Eds.), *Comp. Geomech. - Proc. of the 3rd Inter. Symp. on Comp. Geomech. (ComGeo III), Krakow, Poland, 21-23 Aug., 2013*, pp. 214–226.

Papadimitriou, A. G., Bouckovalas, G. D., & Dafalias, Y. F. (2001). Plasticity model for sand under small and large cyclic strains. *Journal of Geotechnical and Geoenvironmental Engineering 127*(11), 973–983.

Parry, R. & Nadarajah, V. (1974). Observations on laboratory prepared, lightly overconsolidated specimens of kaolin. *Geotechnique 24*(3), 345–357.

Parry, R. H. G. (1960). Triaxial compression and extension tests on remoulded saturated clay. *Géotechnique 10*, 166–180(14).

Pastor, M., Zienkiewicz, O., & Chan, A. (1990). Generalized plasticity and the modelling of soil behaviour. *International Journal for Numerical and Analytical Methods in Geomechanics 14*(3), 151–190.

Pestana, J. M. & Whittle, A. J. (1999). Formulation of a unified constitutive model for clays and sands. *International Journal for Numerical and Analytical Methods in Geomechanics 23*(12), 1215–1243.

Pham, H. Q. (2002). An engineering model of hysteresis for soil-water characteristic curves. Master's thesis, Univ. of Saskatchewan, Saskatoon, Sask., Canada.

Pham, H. Q., Fredlund, D. G., & Barbour, S. L. (2005). A study of hysteresis models for soil-water characteristic curves. *Canadian Geotechnical Journal 42*(6), 1548–1568.

Prager, W. (1949). Recent developments in the mathematical theory of plasticity. *Journal of Applied Physics 20*(3), 235–241.

Prevost, J.-H. & Höeg, K. (1975). Soil mechanics and plasticity analysis of strain softening. *Geotechnique 25*(2), 279–297.

Prountzopoulos, G. (2008). *Investigation of the excavation face stability in shallow tunnels*. Ph. D. thesis, School of Civil Engineering, National Technical University of Athens (NTUA).

Rahardjo, H., Ong, T., Rezaur, R., & Leong, E. C. (2007). Factors controlling instability of homogeneous soil slopes under rainfall. *Journal of Geotechnical and Geoenvironmental Engineering 133*(12), 1532–1543.

Rampello, S., Viggiani, G., & Amorosi, A. (1997). Small-strain stiffness of reconstituted clay compressed along constant triaxial effective stress ratio paths. *Géotechnique. 47*(3).

Rampello, S., Viggiani, G., & Georgiannou, V. (1993). Strength and dilatancy of natural and reconstituted vallericca clay. In *Proc. Int. Symp. on the Geotechnical Engineering of Hard Soils – Soft Rocks, Athens*, Volume 1, pp. 761–768. Balkema. Rotterdam.

Rampino, C., Mancuso, C., & Vinale, F. (2000). Experimental behaviour and modelling of an unsaturated compacted soil. *Canadian Geotechnical Journal 37*(4), 748–763.

Rendulic, L. (1936). Relation between void ratio and effective principal stresses for a remoulded silty clay. In *Proc. of 1st International Conference on Soil Mechanics and Foundation Engineering*, Volume 3, pp. 48–51.

Richards, B. (1965). Measurement of free energy of soil moisture by the psychrometric technique, using thermistors. Technical report.

Richards, B. (1966). The significance of moisture flow and equilibria in unsaturated soils in relation to the design of engineering structures built on shallow foundations in australia. In *Symposium on Permeability and Capillarity, American Society for Testing and Materials, Atlantic City, N.J.*

Richards, L. (1941). A pressure-membrane extraction apparatus for soil solution. *Soil science 51*(5), 377–386.

Ridley, A. & Burland, J. (1993). A new instrument for the measurement of soil moisture suction. *Géotechnique* (43), 321–324.

Romero, E., Gens, A., & Lloret, A. (1999). Water permeability, water retention and microstructure of unsaturated compacted boom clay. *Engineering Geology 54*(1), 117–127.

Romero, E. & Vaunat, J. (2000). Retention curves of deformable clays. *Experimental evidence and theoretical approaches in unsaturated soils*, 91–106.

Roscoe, K. & Burland, J. (1968). On the generalized stress-strain behaviour of wet clay.

Roscoe, K. & Poorooshasb, H. (1963). A theoretical and experimental study of strains in triaxial compression tests on normally consolidated clays. *Geotechnique 13*(1), 12–38.

Roscoe, K. H., Schofield, A., & Wroth, C. (1958). On the yielding of soils. *Geotechnique 8*(1), 22–53.

Schmidt, B. (1966). Earth pressures at rest related to stress history. *Canadian Geotechnical Journal 3*(4), 239–242.

Schofield, A. & Wroth, P. (1968). Critical state soil mechanics.

Sheng, D. (2011). Review of fundamental principles in modelling unsaturated soil behaviour. *Computers and Geotechnics 38*(6), 757–776.

Sheng, D. & Fredlund, D. G. (2008). Elastoplastic modelling of unsaturated soils: an overview. In *Keynote lecture, 12th Int conf int assoc computer methods & advances in geomechanics (IACMAG)*, pp. 1–6.

Sheng, D., Fredlund, D. G., & Gens, A. (2008). A new modelling approach for unsaturated soils using independent stress variables. *Canadian Geotechnical Journal 45*(4), 511–534.

Sheng, D., Sloan, S., & Gens, A. (2004). A constitutive model for unsaturated soils: thermomechanical and computational aspects. *Computational Mechanics 33*(6), 453–465.

Sheng, D., Sloan, S. W., Gens, A., & Smith, D. W. (2003). Finite element formulation and algorithms for unsaturated soils. part i: Theory. *International Journal for Numerical and Analytical Methods in Geomechanics 27*(9), 745–765.

Sheng, D., Zhou, A., & Fredlund, D. G. (2011). Shear strength criteria for unsaturated soils. *Geotechnical and Geological Engineering 29*(2), 145–159.

Sheng, D. & Zhou, A.-N. (2011). Coupling hydraulic with mechanical models for unsaturated soils. *Canadian Geotechnical Journal 48*(5), 826–840.

Shi, C. N. Q. (2003). The stability of unsaturated soil slopes subjected to rainfall infiltration. *Numerical Analysis and Modelling in Geomechanics*, 104.

Shibata, T. & Karube, D. (1965). Influence of the variation of the intermediate principal stress on the mechanical properties of normally consolidated clays. In *Proc. 6th Int. Conf. on Soil Mech. and Found Engrg*, Volume 1, pp. 359–363.

Sitarenios, P., Bardanis, M., & Kavvadas, M. (2011). Modelling the soil-water characteristic curve of structured and recomposed hard soils - soft rocks. In *15th European Conference on Soil Mechanics and Geotechnical Engineering*, pp. 665–670. IOS Press.

Sitarenios, P., Bardanis, M., & Kavvadas, M. (2012). Evaluation of various soil-water characteristic curve models for soils from greece. In *Unsaturated Soils: Research and Applications, Proccedings of the 2nd E-UNSAT (2012), Naples, Italy*, pp. 69–76. Springer.

Sitarenios, P., Belokas, G., & Kavvadas, M. (2013). The incorporation of new isotropic and kinematic hardening rules in an anisotropic constitutive model. In S. Pietruszczak & G.N.Pande (Eds.), *Comp. Geomech. - Proc. of the 3rd Inter. Symp. on Comp. Geomech. (ComGeo III), Krakow, Poland, 21-23 Aug., 2013*, pp. 85–97.

Sitarenios, P., Litsas, D., Papadakos, A., & Kavvadas, M. (2015). Effect of hydraulic conditions in controlling the face in epb excavated tunnels.

Sivakumar, V. & Doran, I. (2000). Yielding characteristics of unsaturated compacted soils. *Mechanics of Cohesive-frictional Materials 5*(4), 291–303.

Sivakumar, V., Doran, I. G., Graham, J., & Johnson, A. (2001). The effect of anisotropic elasticity on the yielding characteristics of overconsolidated natural clay. *Canadian geotechnical journal 38*(1), 125–137.

Sivakumar, V. & Wheeler, S. (1993). Elasto-plastic volume change of unsaturated compacted clay. In *Unsaturated Soils*, pp. 127–138. ASCE.

Smith, P., Jardine, R., & Hight, D. (1992). The yielding of bothkennar clay. *Géotechnique 42*(2), 257–274.

Springman, S., Askarinejad, A., Casini, F., Friedel, S., Kienzler, P., Teysseire, P., & Thielen, A. (2012). Lesson learnt from field tests in some potentially unstable slopes in switzerland. *Acta Geotechnica Slovenica 1*, 5–29.

Stropeit, K., Wheeler, S., & Cui, Y. (2008). An anisotropic elasto-plastic model for unsaturated soils. pp. 625–631.

Sun, D., Sheng, D., & Sloan, S. W. (2007). Elastoplastic modelling of hydraulic and stress–strain behaviour of unsaturated soils. *Mechanics of Materials 39*(3), 212–221.

Suriol, J., Gens, A., & Alonso, E. (2002). Volumetric behaviour of a compacted soil upon wetting. In *Proc. 3rd International Conference on Unsaturated Soils. Recife (Brasil)*, Volume 2, pp. 619–623.

Taiebat, M. & Dafalias, Y. F. (2013). Rotational hardening and uniqueness of critical state line in clay plasticity. In *Constitutive Modeling of Geomaterials*, pp. 223–230. Springer.

Tang, G. X. & Graham, J. (2002). A possible elastic plastic framework for unsaturated soils with high-plasticity. *Canadian Geotechnical Journal 39*(4), 894–907.

Tarantino, A. (2007). A possible critical state framework for unsaturated compacted soils. *Géotechnique 57*(4), 385–389.

Tarantino, A., Romero, E., & Cui, Y. J. (2009). *Laboratory and field testing of unsaturated soils*. Springer.

Tarantino, A. & Tombolato, S. (2005). Coupling of hydraulic and mechanical behaviour in unsaturated compacted clay. *Géotechnique 55*(4), 307–317.

Tasiopoulou, P. & Gerolymos, N. (2016). Constitutive modeling of sand: Formulation of a new plasticity approach. *Soil Dynamics and Earthquake Engineering 82*, 205 – 221.

Tavenas, F. & Leroueil, S. (1977). Effects of stresses and time on yielding of clays. In *Proceedings of the 9th International Conference on Soil Mechanics and Foundation Engineering*, Volume 1, pp. 319–326.

Terzaghi, K. (1925). Erdbaumechanik auf bodenphysikalischer grundlage.

Thu, T. M., Rahardjo, H., & Leong, E.-C. (2007). Critical state behavior of a compacted silt specimen. *Soils and Foundations 47*(4), 749–755.

Toll, D. (1990). A framework for unsaturated soil behaviour. *Géotechnique 40*(1), 31–44.

Toll, D. (1995). A conceptual model for the drying and wetting of soil. In *UNSAT'95/Paris/France/6-8 Semptember 1995. Vol. 2*.

Tsiampousi, A., Zdravković, L., & Potts, D. (2013a). A new hvorslev surface for critical state type unsaturated and saturated constitutive models. *Computers and Geotechnics 48*, 156–166.

Tsiampousi, A., Zdravković, L., & Potts, D. (2013b). A three-dimensional hysteretic soil-water retention curve. *Geotechnique 63*(2), 155–164.

Vaid, Y. P. & Campanella, R. G. (1974). Triaxial and plane strain behavior of natural clay. *Journal of Geotechnical and Geoenvironmental Engineering 100*(Proc. Paper 10421).

Van Genuchten, M. T. (1980). A closed-form equation for predicting the hydraulic conductivity of unsaturated soils. *Soil science society of America journal 44*(5), 892–898.

Vanapalli, S., Fredlund, D., & Pufahl, D. (1999). The influence of soil structure and stress history on the soil–water characteristics of a compacted till. *Géotechnique 49*(2), 143–159.

Vanapalli, S., Fredlund, D., Pufahl, D., & Clifton, A. (1996). Model for the prediction of shear strength with respect to soil suction. *Canadian Geotechnical Journal 33*(3), 379–392.

Vaughan, P. (1999). Special lecture: Problematic soil or problematic soil mechanichs? In *Proccedings of the international symposium on problematic soils, Sendai, Vol.2, pp. 803-814*.

Vaughan, P., Maccarini, M., & Mokhtar, S. (1988). Indexing the engineering properties of residual soil. *Quarterly Journal of Engineering Geology and Hydrogeology 21*(1), 69–84.

Vaunat, J., Romero, E., & Jommi, C. (2000). An elastoplastic hydromechanical model for unsaturated soils. *Experimental evidence and theoretical approaches in unsaturated soils*, 121–138.

VICOL, T. (1990). *Comportement hydraulique et mécanique d'un sol fin non saturé. Application à la modélisation*. Ph. D. thesis, ENPC.

Wheeler, S. (1991). An alternative framework for unsaturated soil behaviour. *Geotechnique 41*(2).

Wheeler, S. (1996). Inclusion of specific water volume within an elasto-plastic model for unsaturated soil. *Canadian Geotechnical Journal 33*(1), 42–57.

Wheeler, S. & Karube, D. (1996). Constitutive modelling. In *UNSAT'95/Paris/France/6-8 Semptember 1995. Vol. 3*.

Wheeler, S., Näätänen, A., Karstunen, M., & Lojander, M. (2003). An anisotropic elastoplastic model for soft clays. *Canadian Geotechnical Journal 40*(2), 403–418.

Wheeler, S., Sharma, R., & Buisson, M. (2003). Coupling of hydraulic hysteresis and stress–strain behaviour in unsaturated soils. *Géotechnique 53*(1), 41–54.

Wheeler, S. J. & Sivakumar, V. (1995). An elasto-plastic critical state framework for unsaturated soil. *Géotechnique 45*(1), 35–53.

Whittle, A. J. (1987). *A constitutive model for overconsolidated clays with application to the cyclic loading of friction piles*. Ph. D. thesis, Massachusetts Institute of Technology.

Whittle, A. J. & Kavvadas, M. J. (1994). Formulation of mit-e3 constitutive model for overconsolidated clays. *Journal of Geotechnical Engineering 120*(1), 173–198.

Wilde, P. (1977). Two-invariants-dependent model of granular media. *Archwm Mech. Stosow 29* (4), 799–809.

Wood, D. (1980). True triaxial tests on boston blue clay. In *Proceedings of the 10th International Conference on Soil Mechanics and Foundation Engineering, Session 4*, pp. 825–830.

Wood, M. (1995). Kinematic hardening model for structured soil. In *Proceedings of the International symposium on numerical models in geomechanics, Davos*, pp. 83–88.

Wroth, C. (1978). In situ measurement of initial stresses and deformation characteristics: Proc conference on in-situ measurements of soil properties, raleigh, nc, 1–4 june 1975, v2, p181–230, disc p231–277. In *International Journal of Rock Mechanics and Mining Sciences & Geomechanics Abstracts*, Volume 15, pp. 67. Pergamon.

Wu, T. H., Loh, A. K., & Malvern, L. (1963). Study of failure envelope of soils. *Journal of the Soil Mechanics and Foundations Division, ASCE 89*, 145–181.

Zapata, C. E., Houston, W. N., Houston, S. L., & Walsh, K. D. (2000). Soil-water characteristic curve variability. *GEOTECH SPEC PUBL* (99), 84–124.

Zhang, F. & Ikariya, T. (2011). A new model for unsaturated soil using skeleton stress and degree of saturation as state variables. *Soils and Foundations 51*(1), 67–81.

Zhou, A. & Sheng, D. (2015). An advanced hydro-mechanical constitutive model for unsaturated soils with different initial densities. *Computers and Geotechnics 63*, 46–66.

Zhou, A.-N., Sheng, D., Sloan, S. W., & Gens, A. (2012a). Interpretation of unsaturated soil behaviour in the stress–saturation space, i: Volume change and water retention behaviour. *Computers and Geotechnics. 43*, 178–187.

Zhou, A.-N., Sheng, D., Sloan, S. W., & Gens, A. (2012b). Interpretation of unsaturated soil behaviour in the stress–saturation space: Ii: Constitutive relationships and validations. *Computers and Geotechnics 43*, 111–123.